NASA Contractor Report 3737

Statistical Analysis of Turbulence Data From the NASA Marshall Space Flight Center Atmospheric Boundary Layer Tower Array Facility

Walter Frost and Ming-Chang Lin

25

25th Anniversary
1958-1983

NASA

NASA Contractor Report 3737

Statistical Analysis of Turbulence Data From the NASA Marshall Space Flight Center Atmospheric Boundary Layer Tower Array Facility

Walter Frost and Ming-Chang Lin
University of Tennessee Space Institute
Tullahoma, Tennessee

NASA

National Aeronautics
and Space Administration

Scientific and Technical
Information Branch

1983

ACKNOWLEDGMENTS

TABLE OF CONTENTS

LIST OF TABLES

LIST OF FIGURES

NOMENCLATURE

A	Span area of the airfoil
a_1	Slope of the lift curve
a_{ij}	Decay parameter for i velocity component, j direction of position
b	Span width of aircraft
b_t	Horizontal tail span width
B_e	Bandwidth
$B_{xy}(\tau)$, $B_{w_i w_j}$	Correlation coefficient
C_L	Lift coefficient
$C_{xy}(f)$	Coincident spectral density function (one-sided)
E_r	Normalized standard error
f	Frequency in cycle per second
f_c	Cut-off frequency (1/2h)
G(f)	Normalized spectrum ($f\phi/\sigma^2$)
$G_u(f)$	Normalized spectrum for longitudinal wind fluctuation
$G_w(f)$	Normalized spectrum for vertical wind fluctuation
h	Time interval
h(t,y)	Indicial response function at time t and position y
$h_t(t)$	Indicial response function which depends on time only
$h_y(y)$	Indicial response function which depends on position only
H(f), $H_i(f)$	Frequency response function at ith position
H*(f)	Complex conjugate of H(f)
J_o	Bessel function
k	Gust reduction factor

K	Reduced spatial frequency $(2\pi f / \overline{W})$ or wave number
K_0	Highest reduced spatial frequency
K_1	Lowest reduced spatial frequency
ℓ	Gust gradient distance
ℓ^t	Tail moment arm of length measured from the center of gravity
ℓ^W	Wing moment arm of length measured from the center of gravity
L	Lift
L_g	Lift due to gust
L_i	Length scale calculated by method i
$M_{R_i}(t)$	Rolling moment for i ($i = w_x$, longitudinal; $i = w_y$, lateral; $i = w_z$, vertical)
$M_p(t)$	Pitching moment
N_0	Average number of times per unit distance that the response Δn crosses the value of zero with positive slope
$N(\Delta n_s)$	Average number of times per unit distance that the response Δn crosses the specified value Δn_s
$p(\Delta n)$	Probability of exceeding the design load factor, Δn
$p(x)$	Probability of density function of x
$Q_{xy}(f)$	Quadrature spectral density function (one-sided)
r	Distance $(\overline{W} \cdot t)$ or lag number
$R_L(\tau)$	Lift correlation function
$R_{W_i W_i}(\tau)$	Correlation function of wind velocity fluctuation for component i

$\hat{R}_{w_i w_i}(\tau)$	Effective correlation function of wind velocity fluctuation for component i
$R_{w_n w_n}$	Conventional longitudinal turbulence correlation
$R_{w_p w_p}$	Conventional lateral turbulence correlation
$R_{xy}(\tau)$	Correlation function
s	Separation distance
S	Design effective wing area
$S_x(f)$	Auto-spectral density function (two-sided)
$S_{xy}(f)$	Two-point spectral density function (two-sided)
t	Time
T, T_r	Total record time
T_x	Total amount of time that x(t) falls inside the range $(x, x+\Delta x)$
U	Gust velocity
V	Airspeed
$\tilde{w}$	Gross weight of aircraft
$w_i(t,y)$	Wind velocity fluctuation at time t and position y (i = x, longitudinal; i = y, lateral, i = z, vertical)
$\overline{W}$	Mean wind velocity
x_t	Distance between the wing and the horizontal tail
x(t), y(t)	Time history record
X(f)	Fourier transfer of x(t)
z	Height above ground
z_0	Surface roughness

Greek Letters

α	Angle of attack

ρ	Density of air
γ^2	Coherence
Γ	Dihedral angle
Δn	Load factor
Δn_d	Design load factor
Δn_s	Specified magnitude
η	Reduced frequency $(sf/\overline{W})$
λ	Eddy side (associated with frequency f if $\overline{W}/f$)
σ	Standard deviation
$\sigma^2_{\Delta n}$	Variance of quantity Δn
σ_T	Truncated root mean square value
τ	Lag time
$\phi_{\Delta n}(f)$	Aircraft response spectrum
ϕ_{ii}	Auto-spectrum of gust at segment i
ϕ_{ij}	Two-point spectrum between gusts at segment i and segment j
$\phi_L(f)$	Lift spectrum
$\phi_{W_x}(f)$	Spectrum for the longitudinal fluctuation wind speed component
$\phi_{W_i W_j}$	Spectrum
$\hat{\phi}_{W_i W_j}$	Effective spectrum
$\phi_x(f)$, $\phi_{ii}(f)$	Auto-spectral density function (one-sided) at x direction
$\phi_{xy}(f)$, $\phi_{ij}(f)$	Two-point spectral density function (one-sided)

Superscripts

$(\overline{})$	Average
$(\ )^t$	Tail
$(\ )^w$	Wing

CHAPTER I

INTRODUCTION

Spatial variation of turbulence over aircraft is known to strongly influence the structural and control design of the aircraft (Houbolt 1973; Etkin 1972; Bisplinghoff et al. 1957). Techniques for computing rolling and pitching moments and other aerodynamic forces, which are influenced by spatial turbulence, have been developed theoretically and, in general, utilize isotropic homogeneous turbulence (Diederich and Drischler 1957; Eichenbaum 1972; Eggleston and Diederich 1956; Houbolt 1973; Lichtenstein 1978; Kordes and Houbolt 1953; Eichenbaum 1971; Houbolt 1972; Pastel, Caruthers, and Frost 1981; Akkari and Frost 1982; Diederich 1957). It is well known, however, that the turbulence in the atmospheric boundary layer close to the earth's surface, which is encountered by an aircraft during approach and takeoff, and turbulence associated with thunderstorms and clear-air roll waves is generally not isotropic. Additionally, turbulence shed by large buildings near aircraft runways can also create relatively large-scale turbulence that has been known to affect not only small general aviation and corporate aircraft but also the larger commercial airliners (Woodfield 1983). No experimental data exist which can be utilized to verify the current theoretical models nor develop new and improved design criteria.

In general, spatial turbulence statistics have been computed from data measured with single towers to heights not exceeding much more than 100 m. An individual tower, however, provides spatial turbulence information only in the vertical, which is, in general, uninteresting to

1

aircraft design (Davenport 1961; Brooke 1975; Panofsky 1973). Some studies have been carried out with tower arrays based on two or three towers located at various horizontal separation distances. The data normally reported from these studies is the coherence function for longitudinal velocities (Panofsky and Mizuno 1975; Panofsky et al. 1974; Kristensen and Jensen 1979; Pielke and Panofsky 1970). These towers are normally less than 20 to 30 m in height. Due to the fact that turbulence information is required for aircraft in the terminal region, roughly from 500 m to the surface, these data are somewhat limited in their application. NASA, therefore, planned and is now carrying out the NASA B-57 gust gradient program. This program utilizes a B-57 Canberra bomber equipped with velocity measuring probes on both wing tips and at the nose. The separation distance between the two wing tip probes is approximately 20 m, allowing spatial turbulence of that horizontal length scale to be investigated.

Prior to the initiation of the gust gradient program, a large amount of atmospheric boundary layer data had been gathered with the NASA/Marshall Space Flight Center (NASA/MSFC) Atmospheric Boundary Layer Facility's eight tower array. These data were ideally suited to supplement the B-57 gust gradient program by providing ground truth data. Also the necessary statistical, analytical tool needed for analyzing the B-57 data, when it becomes available, can be developed and verified with these data. Unfortunately, the purpose of the original study, for which the tower array data were gathered, was to investigate the influence of a block geometry, simulated buildings, on the atmospheric mean wind fields and turbulence. Thus, the data were contaminated by the presence

of a solid rectangular body located amongst the towers. Figure 1.1
illustrates the tower array geometry and the location of the building.
The details of this arrangement are described in Chapter III. Despite
the presence of the block building, it is believed that the atmospheric
data obtained from the towers at the upper levels, i.e., 20 m above the
surface, and from the towers at the ends of the array, are not appre-
ciably influenced by the building disturbance. Thus, statistical
analysis of correlations between measurements at different towers and of
the auto-correlation at individual towers were expected to be representa-
tive of undisturbed surface flow. These statistical analyses are pre-
sented and compared with analytical models in Chapters IV through VIII
of this study.

Chapter II reviews the current design techniques for predicting
aircraft lift, drag, yaw, rolling, and pitching moments due to turbu-
lence spatially distributed over the aircraft. The purpose of Chapter II
is to identify some of the necessary and needed statistical correlations
for aircraft design. It is shown that the two-point spatial correlation
for velocity or turbulence distribution over the airfoil is of prime
interest.

In this study, a distinction is made between a two-point spatial
correlation and the commonly used term "cross-correlation." The termi-
nology cross-correlation in this study is reserved for a correlation
between velocity components in a different direction; for example,
between the lateral and longitudinal components or the vertical and
longitudinal components, etc. The terminology "two-point" spatial
correlation in this study refers to a correlation between velocity

3
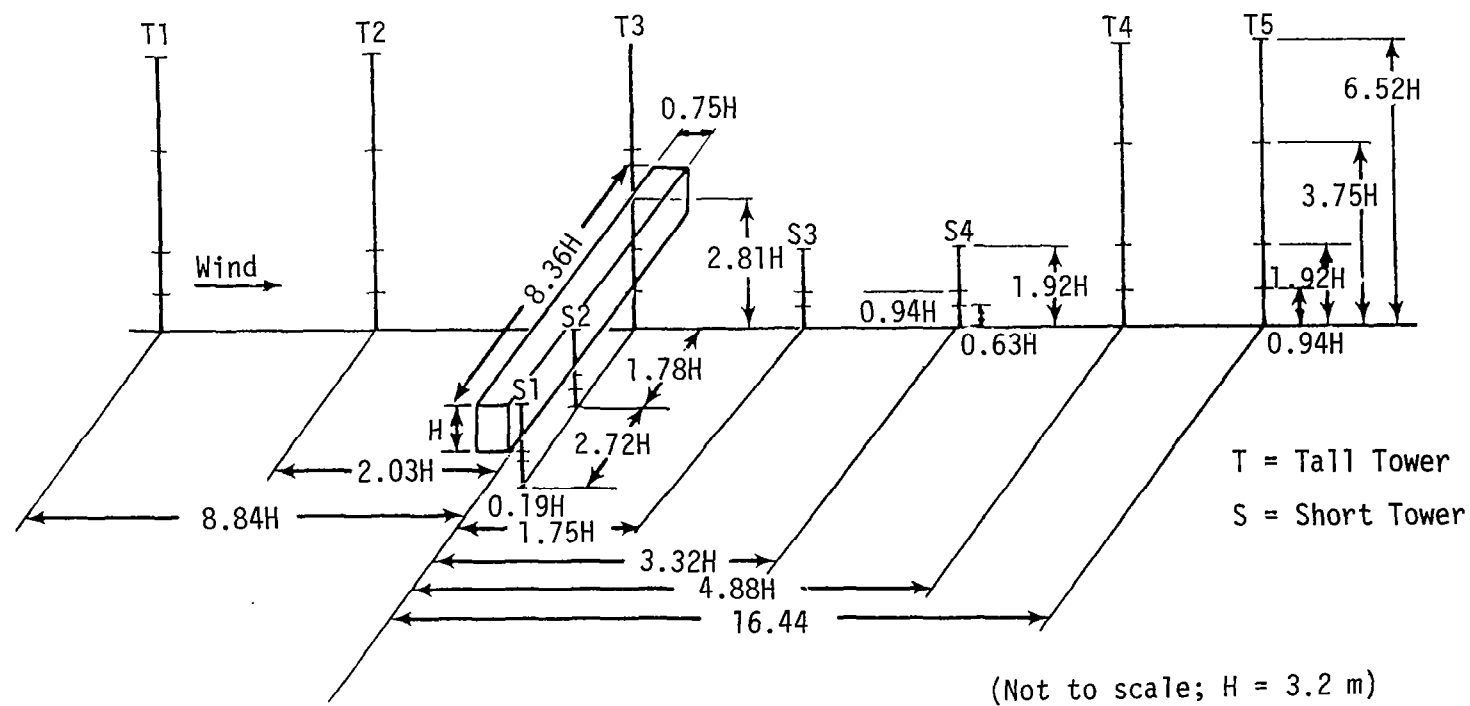
Figure 1.1. Schematic of the current configuration of the NASA/MSFC Boundary Layer Facility.

components measured at stations separated in space. This can be either a two-point cross-correlation where dissimilar velocity components are correlated over a spatially separated distance or it can be a two-point auto-correlation where the same velocity components are correlated over a spatial distance. Only results for two-point auto-correlations are presented. A single-point spatial correlation is a correlation between velocity fluctuations measured at the same point but possibly separated in time. Note that a two-point spatial correlation can also be separated in time (i.e., time dependent or lagged in time). Chapter VI describes in more detail the terminology for correlations and spectra used in this study.

Three analytical models of turbulence spectra, which are commonly used in the literature, are frequently referred to in this study; these are the von Karman, Dryden, and Kaimal spectra (mathematical expressions are given in Chapter VII). Although reference is made to these spectra throughout the earlier chapters, a more thorough discussion of them is given in Chapters VI and VII where comparison is made with the experimental data. The spectra models of von Karman and Dryden rely heavily upon the choice of length scale. Throughout this study the analytical predictions were found to be extremely sensitive to length scale in obtaining agreement with experimental results. Chapter V of this study addresses four different methods of computing length scales. All four different length scales are used sequentially in each analyt-

both models are generally assumed valid only for isotropic homogeneous turbulence. However, the Kaimal spectra does not predict the experimental results well either. Since the Kaimal model is in effect an empirical correlation of data gathered during the Kansas experiment from towers of similar height to those used in this study, this poor agreement is surprising. It should be noted, however, as discussed in Chapter III, that the terrain features surrounding the tower array used in the present study are not homogeneous over a large fetch.

Finally, Chapter VIII of this study addresses the two-point spatial spectra and the coherence function. Comparison of the two-point spectra with a theoretical model by Houbolt and Sen (1972) and the coherence with semi-empirical models are made in this chapter. In general, the experimental data do not agree extremely well with the theoretical results, indicating that additional work is required to develop correlations of the experimental data which can be used for aircraft design.

Finally, the appendices of this study contain the time histories of all anemometer readings, spectral analysis of all longitudinal components, additional correlations, and probability density functions which are too numerous to put in the text of the report.

CHAPTER II

AIRCRAFT DESIGN REQUIREMENTS RELATIVE

TO SPATIAL TURBULENCE

This chapter discusses various aspects of aircraft design associated with spatial variations in turbulence. Gusts affect the control of attitude, altitude, and power setting of the aircraft and the structural integrity, such as wing bending, fatigue, etc.

Initially, the design of aircraft for gust encounters was based on the concept of a single gust model or gust load factor. The gust load factor is computed as follows. When a sharp edge gust is encountered, the angle of attack, α, changes by $\Delta\alpha = KU/V$ where U is the gust velocity, K is the gust reduction factor normally computed numerically, and V is the indicated airspeed assumed constant through the gusts. If the lift coefficient C_L is given by $a_1\alpha$, then the change in C_L is $\Delta C_L = a_1\Delta\alpha = KUa_1/V$. The load factor is defined as $\Delta n = \Delta C_L/C_L = \rho KUVSa_1/2\tilde{W}$ where $\tilde{W}$ is the gross weight, S is the design effective wing area, and ρ is the density of air. Rather than a sharp-edged gust, the shape of the gust velocity was later taken as $(1 - \cos \pi Vt/\ell)$ where ℓ is the gust gradient distance. Experimental measurements of vertical accelerations coupled with this model were used to calculate an effective gust magnitude for computing design loads.

In recent years, the design of aircraft for gust penetration has used spectral concepts. Given the spectrum for the longitudinal fluctuating wind speed component, $\phi_{w_x}(f)$, of atmospheric turbulence (where f is the cyclic frequency) and multiplying by the square of the absolute

7

value of the aircraft frequency response function, $|H(f)|^2$, yields the aircraft response spectrum, $\phi_{\Delta n}(f)$, i.e.,

$$\phi_{\Delta n}(f) = |H(f)|^2 \phi_{w_x}(f) \qquad (2.1)$$

This model assumes homogeneous turbulence and the aircraft is entirely engulfed in the velocity fluctuations (i.e., the aircraft is a point mass). In general, near the ground, the atmospheric turbulence is not homogeneous and the typical spatial scale is such that the turbulence gusts vary over the airplane. Therefore, the spatial structure of the turbulence must be known.

To analyze the effects of gust variations across the airfoil, the wing of the aircraft is normally divided into segments. Each segment is considered to "see" locally homogeneous turbulence. The response spectrum of the aircraft then becomes

$$\phi_{\Delta n}(f) = \phi_{11}(f)|H_1(f)|^2 + \phi_{22}(f)|H_2(f)|^2 + \cdots$$
$$+ 2Re[\phi_{12}(f)H_1^*(f)H_2(f) + \phi_{13}H_1^*(f)H_3(f) + \cdots$$
$$+ \phi_{23}(f)H_2^*(f)H_3(f) + \cdots] \qquad (2.2)$$

where $\phi_{\Delta n}(f)$ is the spectrum of the n response of the aircraft; Δn can be a bending moment, a displacement, etc.

$\phi_{ii}(f)$ is the auto-spectrum of gusts at segment i.

$\phi_{ij}(f)$ is the two-point spatial spectrum between gusts at segment i and segment j.

$H_i(f)$ is the frequency response function for the parameter Δn due to a unit sinusoidal gust acting on segment i.

Re denotes the real part of the complex number.

$H_i^*(f)$ denotes the complex conjugate of $H_i(f)$.

The need for analytical expressions for spatial spectra over the airfoil is apparent from Equation 2.2. However, very little experimental information on $\phi_{ij}(f)$ is available. Therefore, the NASA B-57 gust gradient program was initiated to measure data from which expressions for $\phi_{ij}(f)$ can be determined.

Having established $\phi_{\Delta n}(f)$, a number of design parameters can be derived. For example, integrating under the $\phi_{\Delta n}(f)$ curve provides the variance $\sigma_{\Delta n}^2$ of the quantity Δn, i.e.,

$$\sigma_{\Delta n}^2 = \int_0^\infty \phi_{\Delta n}(f) df \qquad (2.3)$$

The gust load factor Δn for design is then given by

$$\Delta n_{design} = P(\Delta n_d) \sigma_{\Delta n} \qquad (2.4)$$

The factor $P(\Delta n_d)$ is a measure of the probability of exceeding the design load factor, Δn_d.

The fatigue strength of an aircraft component can also be investigated from a known value of the spectrum. The approximate number of peaks in Δn per unit distance travel by the aircraft that exceed a specified magnitude, Δn_s, are given by the equations

$$N(\Delta n_s) = N_o e^{-\frac{\Delta n_s^2}{2\sigma_{\Delta n}^2}} \qquad (2.5)$$

9

where

$$\sigma_{\Delta n}^2 = \int_0^\infty \phi_{\Delta n}(f)df \qquad (2.6)$$

and

$$N_0 = \left[\frac{\int_0^\infty f^2 \phi_{\Delta n}(f)df}{\int_0^\infty \phi_{\Delta n}(f)df} \right]^{1/2} \qquad (2.7)$$

The value of N_0 represents the average number of times per unit distance that the response Δn crosses the value zero with positive slope. The value of $N(\Delta n_s)$ represents a needed input to the design of an aircraft for fatigue loading.

To understand how a nonuniform distribution of wind, i.e., gust gradients across the airfoil, enter the analysis of lift and other aerodynamic parameters, the following example analyses are reviewed.

A. Lift Due to Vertical Wind Speed Fluctuations

The instantaneous value of the lift due to the normal fluctuating component of the wind vector can be written as:

$$L_g(t) = \int_{-\infty}^\infty \int_{-b/2}^{b/2} h(t_1,y)w_z[V(t - t_1),y]dy dt_1 \qquad (2.8)$$

The function $h(t,y)$ is the indicial response function which represents

the lift generated by the wing due to a unit sinusoidal gust applied at time, t, and at position, y, measured along the wing. The parameter b is span width, V is the uniform horizontal speed of the aircraft, t is time, and w_z is the vertical wind velocity fluctuation at position y and time $t - t_1$. Note the vertical wind speed w_z is assumed to be a function of position y on the airfoil and of distance $x = v(t - t_1)$ along the flight path. The latter relationship assumes the validity of Taylor's hypothesis.

For an upswept wing, the function $h(t_1, y)$ can be written as the product of a function which depends only on time and one which depends only on the distance along the span; that is,

$$h(t_1, y) = \frac{1}{b} h_t(t_1) h_y(y) \tag{2.9}$$

Therefore, Equation 2.8 can be rewritten as

$$L_g(t) = \int_{-\infty}^{\infty} h_t(t_1) \frac{1}{b} \int_{-b/2}^{b/2} h_y(y) w_z[V(t - t_1), y] dy dt_1 \tag{2.10}$$

The lift correlation function can now be written as

$$R_L(\tau) = \int_{-\infty}^{\infty} \int_{-\infty}^{\infty} h_t(t_1) h_t(t_2) \hat{R}_{w_z w_z}[V(\tau + t_1 - t_2)] dt_1 dt_2 \tag{2.11}$$

where, considering the nomenclature illustrated in Figure 2.1,

$$\hat{R}_{w_z w_z}(\xi) = \frac{1}{b^2} \int_0^b \int_{-b/2}^{(b/2) - \eta} h_y(y) h_y(\eta + y) R_{w_z w_z}(\xi, \eta) dy d\eta \tag{2.12}$$

where

11
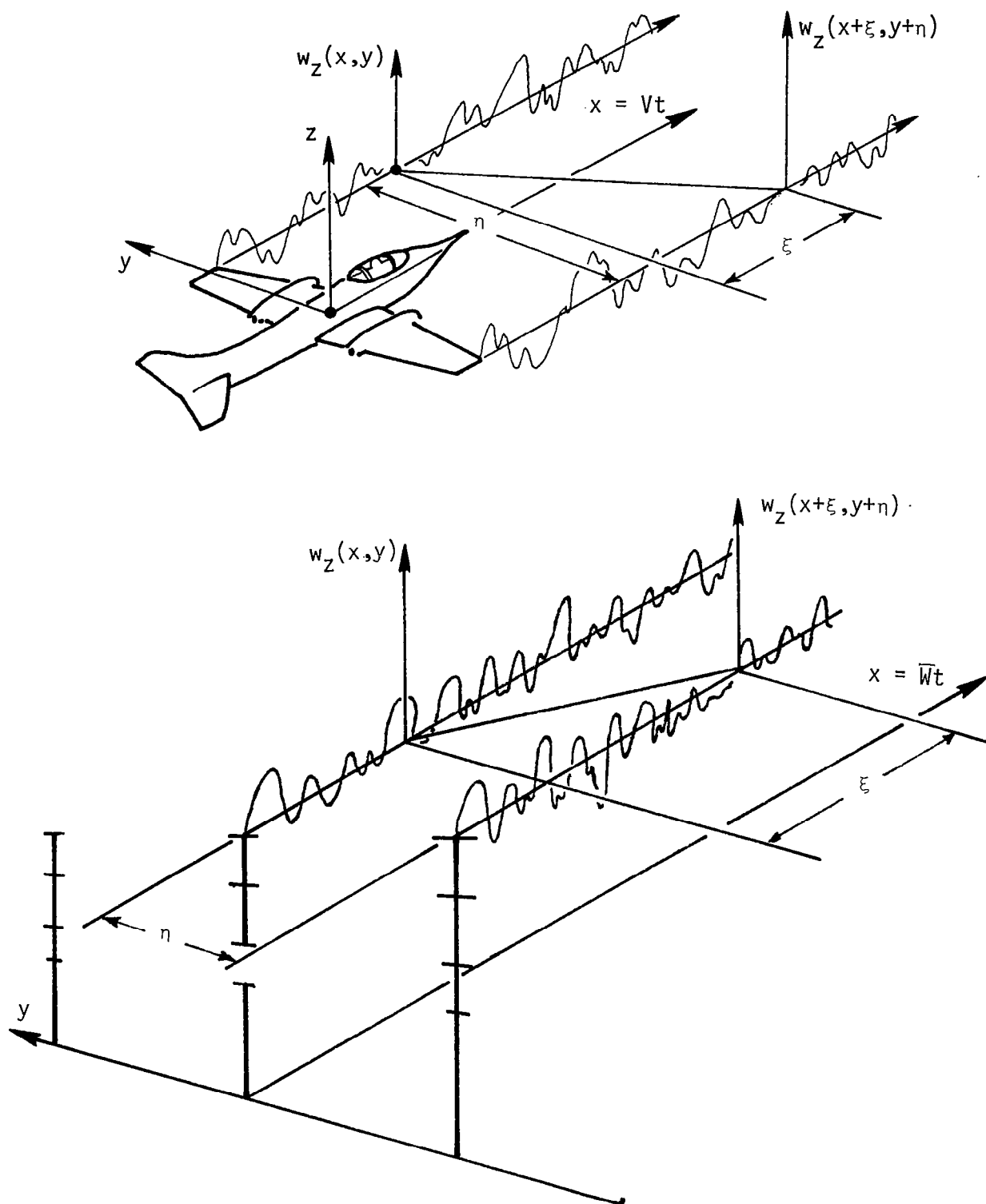
Figure 2.1.   Illustration of coordinate system for either the aircraft or the tower array.

$$R_{w_z w_z}(\xi, \eta) = \overline{w_z(x,y)w_z(x+\xi,y+\eta)} \qquad (2.13)$$

and

$$\xi = V(\tau + t_1 - t_2), \quad \eta = y_2 - y_1, \quad y = y_1 \qquad (2.14)$$

Thus, the spatial correlation of the vertical wind fluctuations enter the computation of the aircraft lift. These correlations can be computed from the tower array at NASA/Marshall Space Flight Center as illustrated in Figure 2.1. Thus, values of $R_{w_z w_z}(\xi, \eta)$ for computing lift of an airfoil very near to the earth's surface can be carried out with the tower array to provide ground-level information for establishing design criteria.

The power spectrum of the lift can be obtained by calculating the Fourier transform of the correlation function that is

$$\phi_L(f) = \int_{-\infty}^{\infty} R_L(\tau) e^{-i2\pi f\tau} d\tau \qquad (2.15)$$

If we define

$$R_y(\eta) = \frac{1}{b} \int_{-b/2}^{(b/2)-\eta} h_y(y) h_y(y + \eta) dy \qquad (2.16)$$

then

$$\hat{R}_{w_z w_z}(\xi) = \frac{1}{b} \int_0^b R_y(\eta) R_{w_z w_z}(\xi, \eta) d\eta \qquad (2.17)$$

After some algebra (see Appendix A), Equation 2.15 reduces to

$$\phi_L(f) = |H_t(f)|^2 \hat{\phi}_{w_z w_z}(f) \tag{2.18}$$

where $\hat{\phi}_{w_z w_z}(f)$ is the effective spectrum of the vertical gust defined as

$$\hat{\phi}_{w_z w_z}(f) = \frac{1}{V} \int_{-\infty}^{\infty} \hat{R}_{w_z w_z}(\xi) e^{-i2\pi f \xi/V} d\xi \tag{2.19}$$

It is apparent from Equation 2.17 that the effective spectrum $\hat{\phi}_{w_z w_z}(f)$ is dependent on the aerodynamic characteristics of the airplane through the $h_y(y)$ function. Thus, the lift spectrum cannot be simply computed from knowledge of the wind field spectra and $|H(f)|^2$ as is generally possible for isotropic turbulence and a point mass aircraft analysis.

For axisymmetric or isotropic turbulence, the procedure for computing $\phi_L(f)$ can be somewhat simplified as follows:

$$\phi_{w_z w_z}(f,\eta) = \frac{1}{V} \int_{-\infty}^{\infty} e^{-i2\pi f \xi/V} R_{w_z w_z}(\xi,\eta) d\xi \tag{2.20}$$

and

$$\phi_{w_z w_z}(f_1,f_2) = \frac{1}{V^2} \int_{-\infty}^{\infty} \int_{-\infty}^{\infty} e^{-i2\pi(f_1\xi+f_2\eta)/V} R_{w_z w_z}(\xi,\eta) d\xi d\eta \tag{2.21}$$

Values of $R_{w_z w_z}(\xi,\eta)$ can be computed from the B-57 data where η is the span width or distance between the wing tip and nose probes and $\xi = V(t_1 - t_2)$. Also, $R_{w_z w_z}(\xi,\eta)$ can be computed from the tower data where

14

η is the separation distance between the towers and $\xi = \overline{W}(t_1 - t_2)$. The parameter $\overline{W}$ is the mean wind speed relative to the ground.

For axisymmetric or isotropic turbulence

$$R_{W_z W_z}(\xi, \eta) = R_{W_z W_z}(\zeta) \tag{2.22}$$

where

$$\zeta = \sqrt{\xi^2 + \eta^2}$$

and $\phi_{W_z W_z}(f, \eta)$ can then be written

$$\phi_{W_z W_z}(f, \eta) = \frac{1}{V} \int_{-\infty}^{\infty} e^{-i2\pi f\xi/V} R_{W_z W_z}(\sqrt{\xi^2 + \eta^2}) d\xi \tag{2.23}$$

In turn, $\phi_{W_z W_z}(f_1, f_2)$ becomes a function of a single variable $\hat{f} = \sqrt{f_1^2 + f_2^2}$ given by the expression (see Appendix A)

$$\phi_{W_z W_z}(f) = \frac{2\pi}{V^2} \int_{0}^{\infty} \zeta J_0(2\pi f\zeta/V) R_{W_z W_z}(\zeta) d\zeta \tag{2.24}$$

where

$$\hat{\phi}_{W_z W_z}(\hat{f}) = \int_{0}^{\infty} |H_y(f_1)|^2 \phi_{W_z W_z}(\hat{f}) df_1 \tag{2.25}$$

and $H_y(f)$ is the Fourier transfer of $h_y(y)$ given by

$$H_y(f) = \frac{1}{b} \int_{-b/2}^{b/2} e^{-i2\pi fy/V} h_y(y) dy \tag{2.26}$$

15

The results of the preceding analysis for axisymmetric or isotropic turbulence simplify the computation of the lift spectrum due to vertical gusts since $R_{w_z w_z}(\xi, \eta)$ can be computed simply from $R_{w_z w_z}(\zeta)$ where $\zeta = \sqrt{\xi^2 + \eta^2}$ is a spatial lag. Standard expressions for the correlations are then applicable to design analysis. A similar statement can be made about $\phi_{w_z w_z}(\hat{f})$ where $\hat{f} = \sqrt{f_1^2 + f_2^2}$.

B. Lift Due to Longitudinal Wind Speed Fluctuations

The above results pertain to vertical gusts. However, loading on the aircraft arises not only from the vertical wind vector component but also from the longitudinal components. The following analysis serves to indicate the relative influence of the vertical and longitudinal gusts. Consider an aircraft flying at a uniform horizontal speed which encounters an inclined gust having a vertical component w_z and a horizontal component w_x as shown in Figure 2.2.
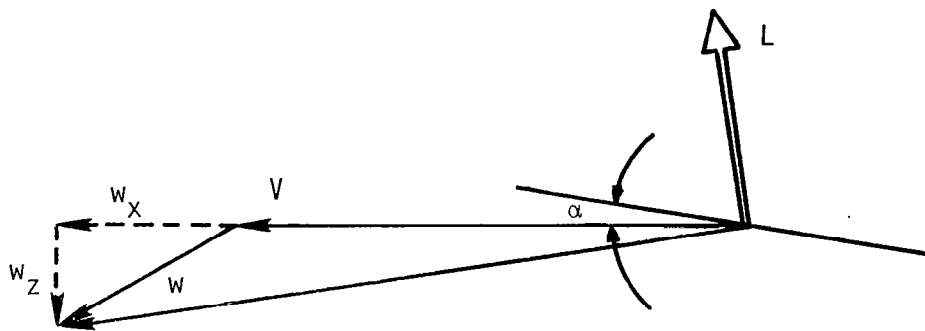
Figure 2.2. Affect of an inclined gust on aircraft lift.

The lift is given by

$$L = \frac{a_1}{2} \rho A (V + w_x)^2 \left[\alpha + \frac{w_z}{V + w_x} \right]$$

(2.27)

where

a_1 = slope of the lift curve

A = span area of the airfoil

ρ = air density

α = angle of attack

Before the gust, the lift was equal to the weight, or

$$\tilde{W} = \frac{a_1}{2} \rho A V^2 \alpha$$

(2.28)

therefore, dividing Equation 2.27 by $\tilde{W}$ gives

$$\frac{L}{\tilde{W}} = \left(1 + \frac{w_x}{V} \right)^2 \left(1 + \frac{w_z}{\alpha (V + w_x)} \right)$$

(2.29)

Figure 2.3 compares values of $L/\tilde{W}$ for conditions neglecting w_x and for conditions including w_x. This comparison is based on standard atmospheric boundary layer theory where it is assumed that $\sigma_{w_z}/\sigma_{w_x} \simeq 0.77$, a surface roughness $z_0 = 0.1$ m, and a mean wind speed at 10 m height of $\overline{W}_{z=10m} = 20$ m/s and 10 m/s, respectively. The results show that near the ground at typical approach speeds of commercial airliners, the influence of w_x can become significant. Near thunderstorms and other severe weather conditions, w_x can conceivably dominate this relationship. Subchapter C reviews the influence of the longitudinal gust on lift.

17
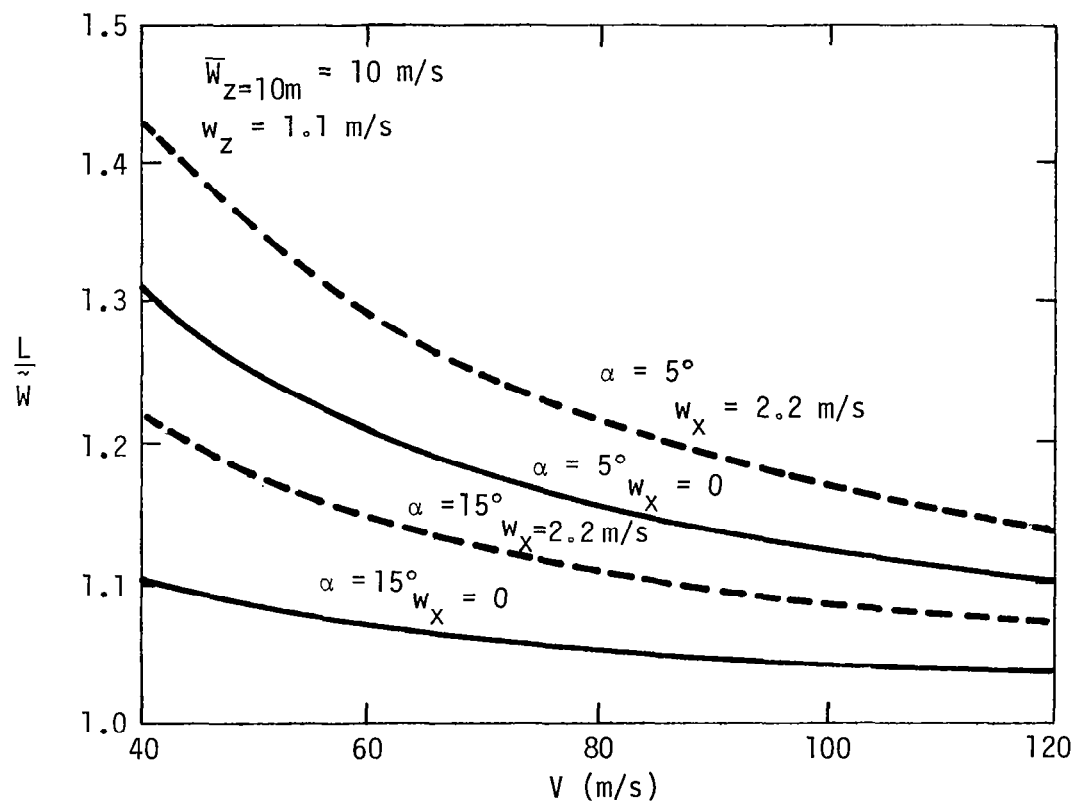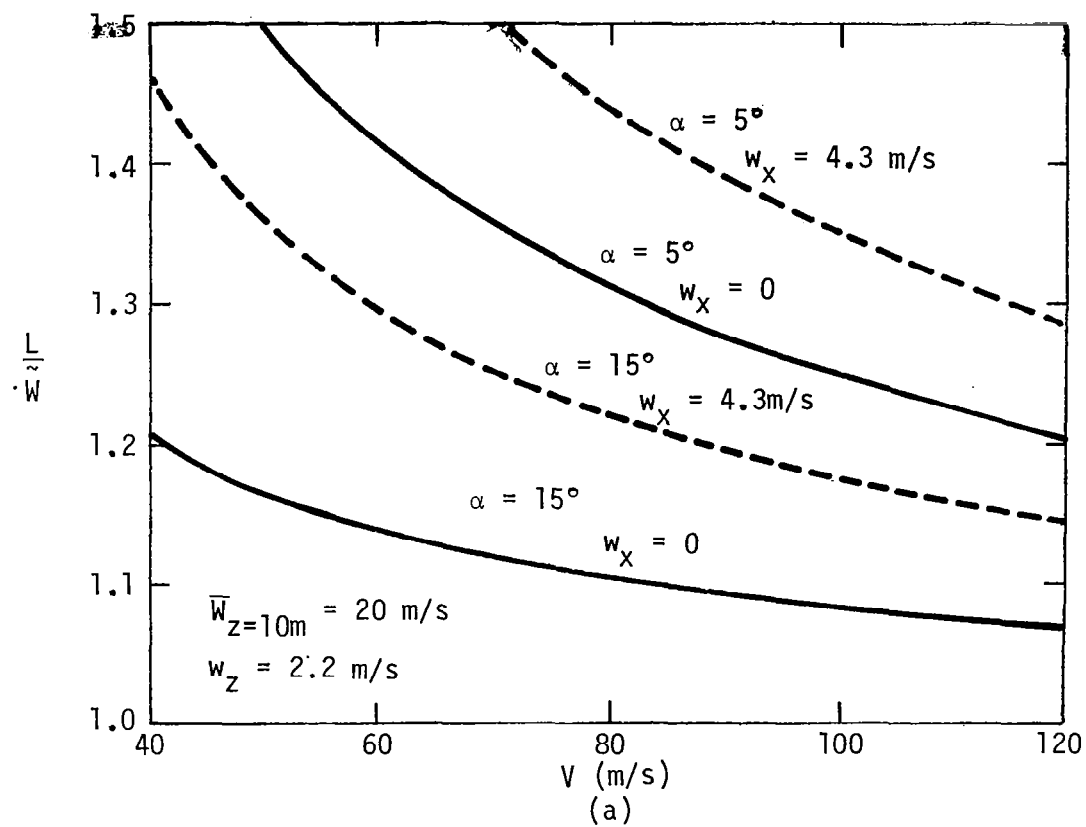
Figure 2.3. Affect of longitudinal gust on load factor.

18

The instantaneous value of the lift due to the longitudinal component of turbulence can be written as (see Diederich and Drischler 1957)

$$L_g(t) = 2\alpha \int_{-\infty}^{\infty} \int_{-b/2}^{b/2} h(t_1, y) w_x [V(t - t_1), y] dy dt_1 \tag{2.30}$$

(assumes angle of attack is constant along the span). The lift correlation function can thus be written as

$$R_L(\tau) = 4\alpha^2 \int_{-\infty}^{\infty} \int_{-\infty}^{\infty} h_t(t_1) h_t(t_2) \hat{R}_{w_x w_x} [V(\tau + t_1 - t_2)] dt_1 dt_2 \tag{2.31}$$

where similar to Equations 2.12 and 2.13

$$\hat{R}_{w_x w_x}(\xi) = \frac{1}{b^2} \int_0^b \int_{-b/2}^{(b/2)-\eta} h_y(\eta + y) h_y(y) R_{w_x w_x}(\xi, \eta) dy d\eta \tag{2.32}$$

and

$$R_{w_x w_x}(\xi, \eta) = \overline{w_x(x, y) w_x(x+\xi, y+\eta)} \tag{2.33}$$

For axisymmetric or isotropic turbulence

$$R_{w_x w_x}(\xi, \eta) = R_{w_x w_x}(\zeta) \tag{2.34}$$

In this case, however, $R_{w_x w_x}(\zeta)$ where $\zeta = \sqrt{\xi^2 + \eta^2}$ is different from the standard vertical correlation for isotropic turbulence given in the literature. Figure 2.4 illustrates this difference. The expression for $R_{w_x w_x}(\zeta)$ in terms of $R_{w_n w_n}(\zeta)$ and $R_{w_p w_p}(\zeta)$ is

$$R_{w_x w_x}(\zeta) = \frac{\eta^2}{\xi^2 + \eta^2} R_{w_n w_n}(\zeta) + \frac{\xi^2}{\xi^2 + \eta^2} R_{w_p w_p}(\zeta) \tag{2.35}$$

19
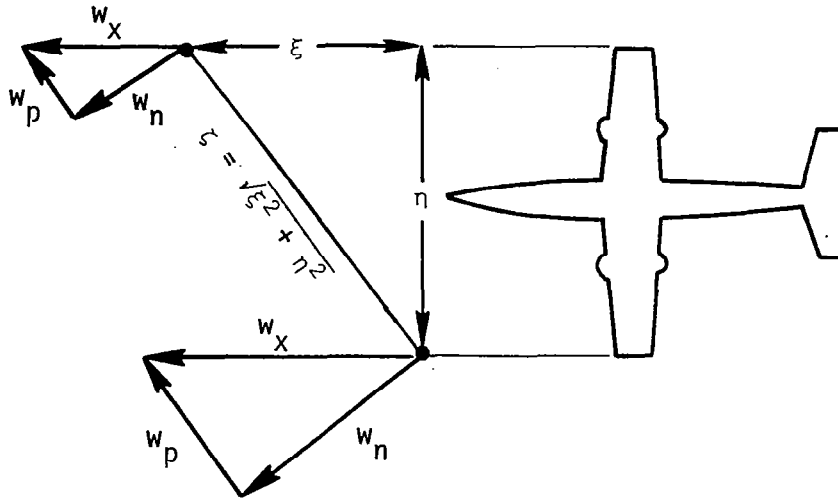
Figure 2.4. Illustration of coordinates and wind speed components.

where $R_{w_n w_n}(\varsigma)$ and $R_{w_p w_p}(\varsigma)$ are the conventional longitudinal and lateral turbulence correlations (Frost and Moulden 1977).

Following a similar approach as for the vertical wind speed, we can establish an effective spectrum

$$\hat{\phi}_{w_n w_n}(f) = \frac{1}{b} \int_0^b R_y(\eta)\phi_{w_x w_x}(f,\eta)d\eta \qquad (2.37)$$

Note, however, that the function $\phi_{w_x w_x}(f_1,f_2)$ cannot be expressed in terms of $\sqrt{f_1^2 + f_2^2}$ as used in Equation 2.25. The lift spectrum now becomes

$$\phi_L(\omega) = 4a^2|H_t(\omega)|^2 \hat{\phi}_{w_x w_x}(f) \qquad (2.38)$$

For isotropic turbulence, the normal and longitudinal components of turbulence are statistically independent and the total lift spectrum due to both components can be treated as the sum of the individual spectra.

C. Rolling Moment

A rolling moment occurs if the gust components w_x and w_z are non-uniform in the spanwise direction. The rolling moment due to the longitudinal component and the vertical component can be derived as follows:

$$M_{R_{w_x}}(t) = 2\alpha \int_{-\infty}^{\infty} \int_{-b/2}^{b/2} h(t_1,y)\, w_x[V(t-t_1),y]y\,dy\,dt_1 \qquad (2.38)$$

$$M_{R_{w_z}}(t) = \int_{-\infty}^{\infty} \int_{-b/2}^{b/2} h(t_1,y)\, w_z[V(t-t_1),y]y\,dy\,dt_1 \qquad (2.39)$$

The corresponding rolling moment correlations for w_x become

$$R_{M_{w_x}}(\tau) = 4\alpha^2 \int_{-\infty}^{\infty} \int_{-\infty}^{\infty} h_t(t_1)h_t(t_2)\, \hat{R}_{w_x w_x}[V(\tau + t_1 - t_2)]dt_1 dt_2 \qquad (2.40)$$

where

$$\hat{R}_{w_x w_x}(\xi) = \frac{1}{b^2} \int_{-b/2}^{b/2} \int_{-b/2}^{b/2} h_y(y_1)h_y(y_2)\, R_{w_x w_x}[V(\tau + t_1 - t_2),$$

$$(y_2 - y_1)]y_1 y_2 dy_1 dy_2 \qquad (2.41)$$

and, as before, the atmospheric parameter of interest becomes

$$R_{w_x w_x}(\xi,\eta) = \overline{w_x(x,y)\, w_x(x+\xi,y+\eta)} \qquad (2.42)$$

Similarly

$$R_{M_{w_z}}(\tau) = \int_{-\infty}^{\infty} \int_{-\infty}^{\infty} h_t(t_1)h_t(t_2)\, \hat{R}_{w_z w_z}[V(\tau + t_1 - t_2)]dt_1 dt_2 \qquad (2.43)$$

where

$$\hat{R}_{w_z w_z}(\xi) = \frac{1}{b^2} \int_{-b/2}^{b/2} \int_{-b/2}^{b/2} h_y(y_1) h_y(y_2) \ R_{w_z w_z}[V(\tau + t_1 - t_2),$$

$$(y_2 - y_1)] y_1 y_2 dy_1 dy_2 \qquad (2.44)$$

$$R_{w_z w_z}(\xi, \eta) = \overline{w_z(x,y) \ w_z(x+\xi, y+\eta)} \qquad (2.45)$$

The rolling moment due to lateral fluctuations, w_y, is associated with a dihedral effect. The local angle of attack due to a wind speed component from the side can be written as Houbolt (1972):

$$\alpha = \Gamma w_y / V$$

where Γ is the dihedral angle. Since the dihedral angles of the right and left wings are opposite in sign, the lift will be opposite, also. Thus, the rolling moment correlation due to w_y can be derived as:

$$R_{R_{w_y}}(\tau) = \frac{4}{V^2} \int_{-\infty}^{\infty} \int_{-\infty}^{\infty} h_t(t_1) h_t(t_2) \ \hat{R}_{w_y w_y}[V(\tau + t_1 - t_2)] dt_1 dt_2 \qquad (2.46)$$

where

$$\hat{R}_{w_y w_y}(\xi) = \frac{1}{b^2} \int_{-b/2}^{b/2} \int_{-b/2}^{b/2} h_y(y_1) h_y(y_2) \ R_{w_y w_y}[V(\tau + t_1 - t_]),$$

$$(y_2 - y_1)] y_1 y_2 dy_1 dy_2 \qquad (2.47)$$

and

$$R_{w_y w_y}(\xi, \eta) = \overline{w_y(x,y) \ w_y(x+\xi, y+\eta)} \qquad (2.48)$$

Generally, the affect of a lateral gust is smaller than the affect of a longitudinal gust. However, in severe weather conditions, gusts perpendicular to the flight direction may create rolling moment which must be considered in control design.

D. Pitching Moment

The tail of an aircraft strikes a given gust some time after the wing does, generating a pitching moment. Defining an effective moment arm of length ℓ^w (wing) and ℓ^t (tail) measured from the center of gravity, the pitching moment due to the vertical component of atmospheric turbulence can be written as

$$
M_p(t) = \int_{-\infty}^{\infty} \int_{-b/2}^{b/2} \ell^w h^w(t_1,y) \; w_z[V(t + t_1),y]dydt_1
$$

$$
+ \int_{-\infty}^{\infty} \int_{-b_t/2}^{b_t/2} \ell^t h^t(t_1,y) \; w_z[x_t + V(t + t_1),y]dydt_1 \qquad (2.49)
$$

where the assumption that turbulence varies along the flight path but not across the airfoil is made. The corresponding correlation of pitching moment is

23

$$R_{p_{W_z}}(\tau) = \int_{-\infty}^{\infty} \int_{-\infty}^{\infty} \{ h_t^W(t_1) h_t^W(t_2) \; \hat{R}_{W_z}^{WW}[V(\tau + t_2 - t_1)] + h_t^t(t_1) h_t^t(t_2)$$

$$\times \; \hat{R}_{W_z}^{tt}[x_t + V(\tau + t_2 - t_1)] + h_t^W(t_1) h_t^t(t_2)$$

$$\times \; \hat{R}_{WZ}^{wt}[x_t + V(\tau + t_1 - t_2)] + h_t^W(t_2) h_t^t(t_1)$$

$$\times \; \hat{R}_{WZ}^{tw}[x_t + V(\tau + t_1 - t_2)] \} dt_1 dt_2 \qquad (2.50)$$

where

$$\hat{R}_{W_z}^{WW}[V(\tau + t_2 - t_1)] = \frac{(\ell^W)^2}{b^2} \int_{-b/2}^{b/2} \int_{-b/2}^{b/2} h_y^W(y_1) h_y^W(y_2)$$

$$\times \; R_{W_z}^W[V(\tau + t_2 - t_1), y_2 - y_1] dy_1 dy_2 \qquad (2.51)$$

$$R_{W_z}^W(\xi, \eta) = \overline{w_z(x,y) \; w_z(x+\xi, y+\eta)} \qquad (2.52)$$

$$\hat{R}_{W_z}^{tt}[x_t + V(\tau + t_2 - t_1)] = \frac{(\ell^t)^2}{b_t^2} \int_{-b_t/2}^{b_t/2} \int_{-b_t/2}^{b_t/2} h_y^t(y_1) h_y^t(y_2)$$

$$\times \; R_{W_z}^t[x_t + V(\tau + t_2 - t_1),$$

$$(y_2 - y_1)] dy_1 dy_2 \qquad (2.53)$$

$$R_{W_z}^t(x_t + \xi, \eta) = \overline{w_z(x+x_t, y) \; w_z(x+x_t+\xi, y+\eta)} \qquad (2.54)$$

$$\hat{R}_{W_z}^{wt}[x_t + V(\tau + t_2 - t_1)] = \frac{\ell^{W}\ell^{t}}{bb_t} \int_{-b/2}^{b/2} \int_{-b_t/2}^{b_t/2} h_y^{W}(y_1) h_y^{t}(y_2)$$

$$\times R_{W_z}^{wt}[x_t + V(\tau + t_2 - t_1),$$

$$(y_2 - y_1)]dy_2 dy_1 \qquad (2.55)$$

$$R_{W_z}^{wt}(x_t + \xi, \eta) = \overline{w_z(x,y)\ w_z(x + x_t + \xi, y + \eta)} \qquad (2.56)$$

$$\hat{R}_{W_z}^{tw}[x_t + V(\tau + t_1 - t_2)] = \frac{\ell^{t}\ell^{W}}{b_t b} \int_{-b_t/2}^{b_t/2} \int_{-b/2}^{b/2} h_y^{W}(y_2) h_y^{t}(y_1)$$

$$\times R_{W_z}^{tw}[x_t + V(\tau + t_1 - t_2),$$

$$(y_2 - y_1)]dy_2 dy_1 \qquad (2.57)$$

$$R_{Wz}^{tw}(x_t + \xi'', \eta) = \overline{w_z(x,y)\ w_z(x + x_t + \xi'', y + \eta)} \qquad (2.58)$$

$$\xi'' = V(\tau + t_1 - t_2) \qquad (2.59)$$

$h^{W}(t,y)$ and $h^{t}(t,y)$ are the indicial lift responses to a gust hitting the wing and tail, respectively, at $t = 0$. The parameter b_t is the horizontal tail span, and x_t is the distance between the wing and the horizontal tail. Thus, correlations for winds blowing along the tower array are the parameters which influence pitching motions. These can be computed from the tower array data, but the B-57 aircraft is not equipped to measure correlations in the turbulence between the wing and tail assemblies.

The analyses presented throughout this chapter (although not inclusive of all possible combinations of wind loads and resulting aerodynamic forces) serve to illustrate the types of wind speed correlations arising from spectral analyses of aerodynamic loading in a turbulent environment. In general, the correlations of interest are those between like wind speed components in the horizontal plane of the aircraft's flight path. The reason for this is that the analyses assume each of the three gust components, i.e., longitudinal, lateral, and vertical, act independently of each other. In reality, this is not the case. However, the necessary indicial functions for carrying out more complex analyses are not generally available in the literature and would probably be too costly for practical design methods if they were available.

Thus, for the moment, limiting ourselves to the spectral approaches outlined in the foregoing, we see that the general design and motion analyses call for correlations as given by Equations 2.13, 2.33, 2.45, 2.48, 2.52, 2.54, and 2.58. It is possible to construct these correlations from the tower data and from the B-57 aircraft flight data (see Figure 2.1, page 12). Because of the instrument configuration for both the tower array and aircraft, the correlations given by Equations 2.54 and 2.58 must be computed using Taylor's hypothesis. It would have been preferable to have a "T" configuration of anemometers but economics and aircraft structural constraints prohibit such an arrangement. The spectra and correlations computed from the tower data are presented in Chapters V, VI, VII, and VIII of this study.

CHAPTER III

TOWER ARRANGEMENT AND DATA QUALIFICATION

A. Tower Array and Field Site

The experiments were conducted in the NASA Marshall Space Flight
Center, Atmospheric Sciences Division, Atmospheric Boundary Layer
Facility, located near Huntsville, Alabama. The specific tower arrange-
ment used in this study and a brief description of the field site are
given in this section. Additional details are given in Steely and Frost
(1981).

The field site is not exactly level, having slight undulations
along the line of towers. The elevation of the ground with respect to
the profile of the tower array is shown in Figure 3.1. The measurement
of elevation with respect to Tower 3 as the zero elevation datum plane
are shown in Table 3.1. From this table it can be determined that the
building is located on an approximate 6.3:1 upgrade.

The surrounding topography is shown in Figure 3.2. There are moun-
tains to the northeast, east, and southeast which are approximately 2439
m (8000 ft) away from the tower site. The height of the mountains are
about 300 m (1000 ft) above mean sea level, whereas the height of the
tower array site is about 190 m (630 ft) above mean sea level. There
are flat areas to the north, south, and west of the tower array which
are approximately the same elevation as the tower site.

Cross sections of the terrain along a line parallel to the array
and perpendicular to the array are shown in Figure 3.3. It is antici-
pated that the wind blowing from the northeast, east, or southeast will

Figure 3.1. Cross-sectional contour of the eight-tower array.

⊙ indicates the base of each tower

x indicates ground level

Note: δ ∿ height of ground relative to zero at
at the base of Tower 3; h ∿ height of
building (h = 3.2 m)

TABLE 3.1. Tower Location and Elevation

Location	Horizontal		Elevation	
	Building Heights	Meters	Building Heights	Meters
Ground	-24.12	-77.18	-0.045	-0.144
T1	-9.04	-28.93	-0.039	-0.125
T2	-2.22	-7.10	-0.008	-0.026
Building[a]	-0.19	-0.61	-0.002	-0.006
T3	0.0	0.0	0.0	0.0
S3	1.56	4.99	0.012	0.038
S4	3.13	10.02	0.031	0.099
T4	4.69	15.01	0.043	0.138
T5	16.25	52.00	0.103	0.330

[a]Building dimensions: Height (H) = 3.2 m
Width = 2.4 m
Length = 26.8 m
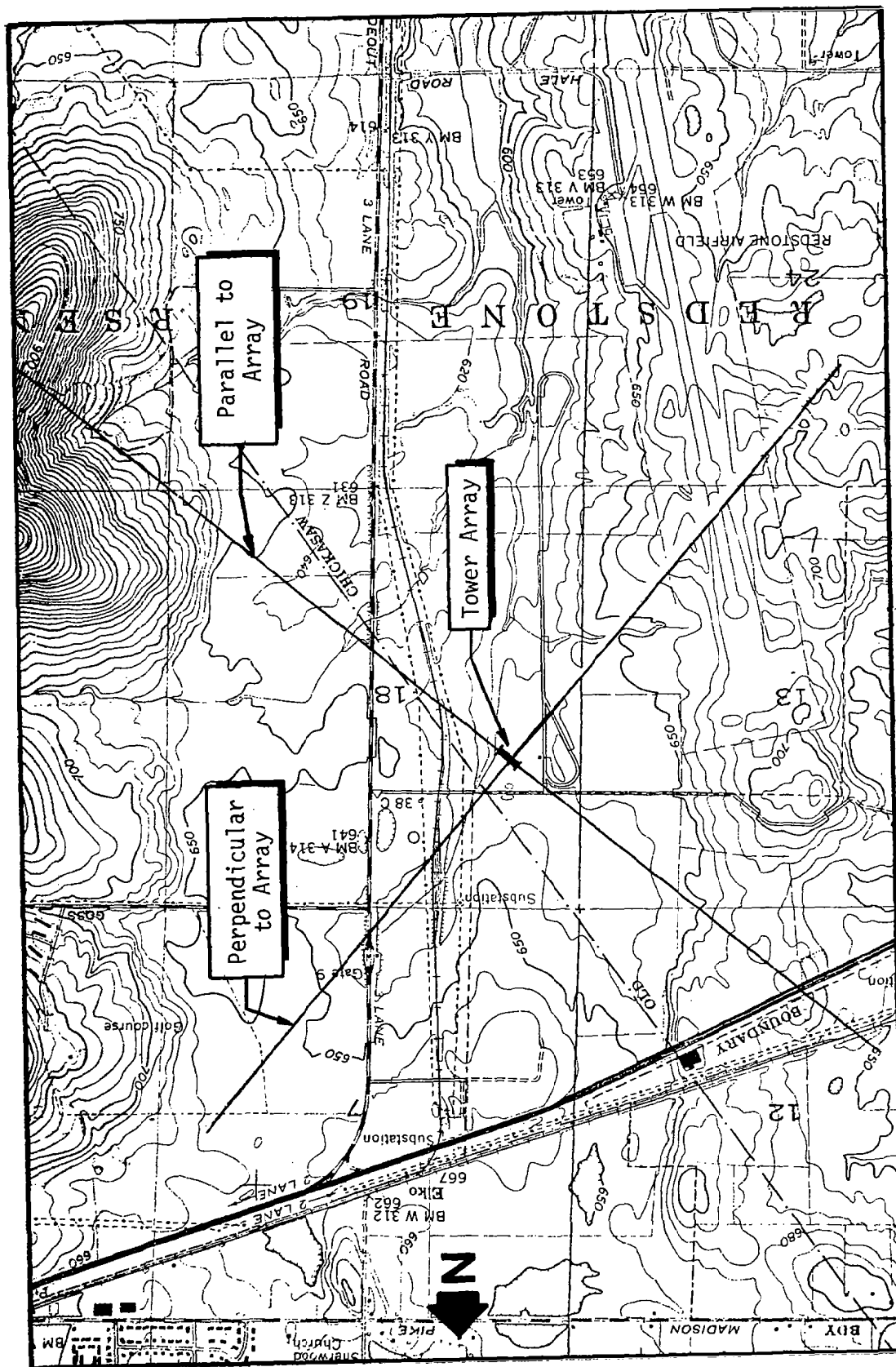
Figure 3.2. Topography map of the terrain surrounding the field site.

30

Height
Feet Meters
400 (122)

300 (91)

200 (61)

Northwest   100 (31)   Southeast

-8000 -6000 -4000 -2000   2000   4000   6000   8000 Feet
(-2439)(-1829)(-1220) (-610)   (610) (1220) (1829) (2439) Meters
                                -100 (-31)
                                                          Distance
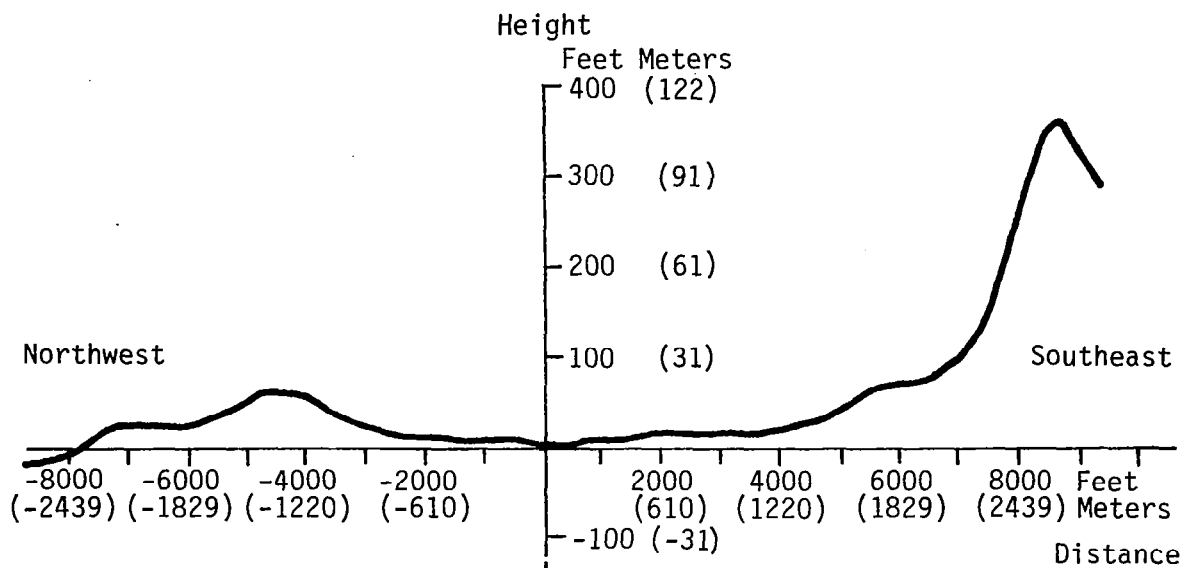
(a) Along the tower array (Run #8624)

Distance
Feet Meters
400 (122)

300 (91)

200 (61)

Northeast   100 (31)   Southwest

-8000 -6000 -4000 -2000   2000   4000   6000   8000 Feet
(-2439)(-1829)(-1220) (-610)   (610) (1220) (1829) (2439) Meters
                                -100 (-31)
                                                          Distance
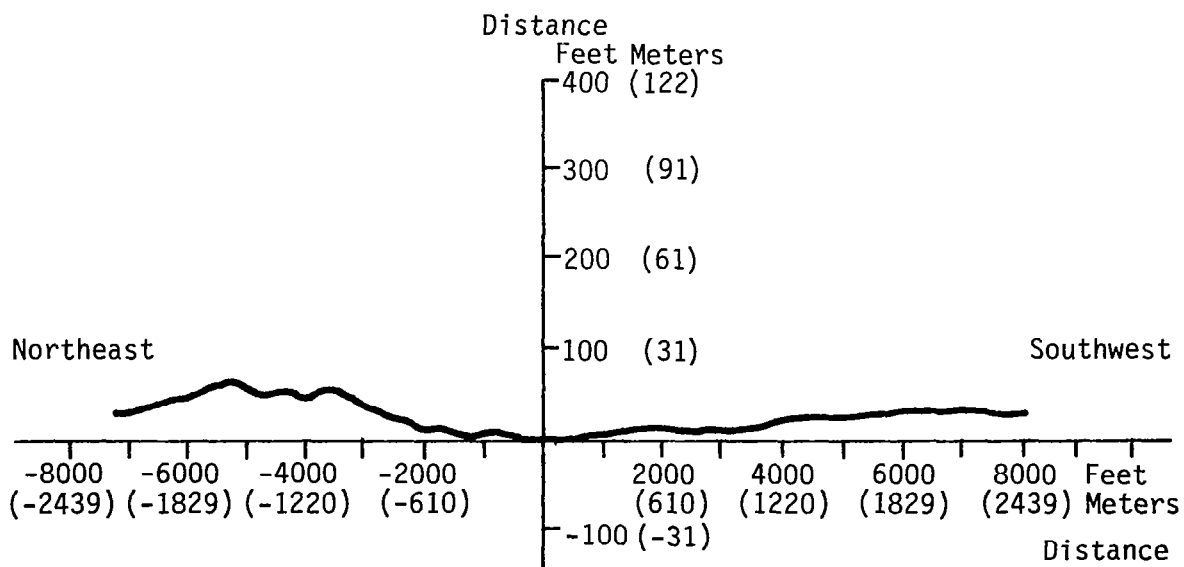
(b) Perpendicular to tower array (Run #8623)

Figure 3.3 Cross section of the terrain features.

31

be affected by the mountains and will be nonuniform. On the other hand, a wind blowing from north, south, or west will be relatively uniform.

The towers are lined 52 degrees counterclockwise from north. Therefore, a wind blowing along the tower array (from Tower 1 to Tower 5) will be reasonably undisturbed. Run #8624, discussed later, was along this direction. The wind blowing perpendicular to the tower array from the northeast approaches over relatively flat land and can also be considered undisturbed. Run #8623, also discussed later, was from the northeast.

The present experimental setup is shown in Figure 1.1, page 4. The tower arrangement consists of five in-line 20-m towers (indicated by T1 through T5) and four short towers (indicated by S1 through S4). The tall towers are instrumented at the 3-m, 6-m, 12-m, and 20-m levels (referred to as Levels 1, 2, 3, and 4, respectively) with the exception of T3 on which the instruments from the 20-m level were lowered to the 9-m level and recorded as Level 4. The short towers are instrumented at the 2-m, 3-m, and 6-m levels (referred to as Levels 1, 2, and 3, respectively). Towers S1 and S2 are stationed behind the block building laterally from T3, while S3 and S4 are stationed in-line with the tall towers between T3 and T4. Throughout this study instrument locations (or measuring stations) for the tall towers are designated by TnLm where n is the tower number and m is the level (e.g., T5L2 is Tower 5, Level 2). For the short towers, the designation in SnLm.

32

B. Data Qualification

The data reduction procedures are described in detail in Steely and Frost (1981). The data used in this report were qualified visually by plotting time histories for each level and tower as shown in Appendix B and through inspection of the mean values tabulated in Tables B.1 and B.2. Data from the measuring positions given in Table 3.2 have been eliminated from the data set. Justification for eliminating these data is also given in Appendix B.

TABLE 3.2. Measuring Positions from Which Data Have Been Eliminated

Run No.	Station
8623	T1L1 (vertical only)
8623	T1L2 (vertical only)
8623	T2L1 (vertical only)
8624	T1L2 (vertical only)
8623	T3L4
8623	T5L3
8623	S1L3
8624	T3L4
8624	T5L3
8623	S4L2
8624	S4L2

CHAPTER IV

VELOCITY PROBABILITY DISTRIBUTIONS

The probability density distributions are discussed in this chapter. The data were measured for Run #8623 and Run #8624. Data samples at 0.1 second for a 900-second record length were used. Plots of the probability density of the measured data as compared with a Gaussian probability density distribution are given in Appendix C. The probability density function for the velocity fluctuation is computed as follows. Consider the time history records x(t) illustrated in Figure 4.1. The probability that x(t) assumes a value within the range between x and (x + Δx) may be obtained by taking the ratio of T_x/T, where T_x is the total amount of time that x(t) falls inside the range (x,x+Δx) during the total record time T. This ratio will approach an exact probability description as T approaches infinity. In equation form:

$$\text{prob}[x < x(t) \leq x + \Delta x] = \lim_{T \to \infty} \frac{T_x}{T} \tag{4.1}$$

For small Δx, a probability density function p(x) can be defined as follows:

$$\text{prob}[x < x(t) \leq x + \Delta x] \simeq p(x)\Delta x \tag{4.2}$$

therefore

$$p(x) = \lim_{\Delta x \to 0} \frac{\text{prob}[x < x(t) \leq x + \Delta x]}{\Delta x} = \lim_{\Delta x \to 0} \frac{1}{\Delta x} \left[\lim_{T \to \infty} \frac{T_x}{T} \right] \tag{4.3}$$
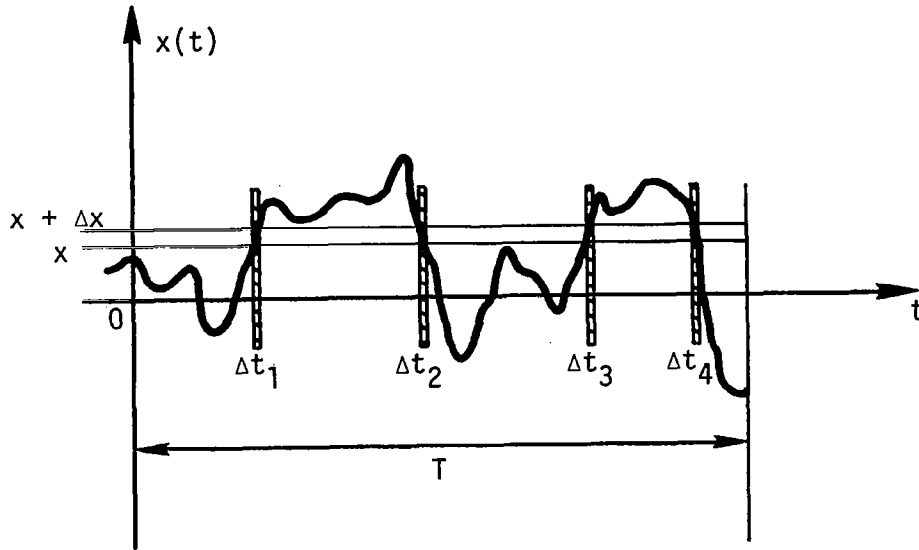
Figure 4.1. Calculation of probability function p(x) for a random
process.

The Gaussian function is given by

$$p(x) = \frac{1}{\sigma\sqrt{2\pi}} e^{-\frac{(x - \bar{x})^2}{2\sigma^2}}$$ (4.4)

The probability density of the turbulence data matches reasonably well
with the Gaussian distribution. There is, however, a definite trend
toward more smaller fluctuations and less larger fluctuation than the
Gaussian curve predicts, i.e., greater Kurtosis.

CHAPTER V

LENGTH SCALE

An important characteristic of the structure of turbulence is the length scale. This length scale is to a certain extent a measure of the longest connection, or correlation distance, between the velocity at two points of the flow field. It is reasonable to expect that the degree of correlation will decrease with increasing separation of the points and that beyond some finite displacement this correlation will approach zero. In general, the length scale varies with height, with surface roughness, and with the direction of the velocity component relative to the mean wind, i.e., the longitudinal direction versus the lateral and vertical directions.

There are a number of methods available for estimating the numerical value of L. The most common method is to integrate the auto-correlation coefficient from zero to infinity with respect to lag time or separation distance:

$$L_1 = \overline{W} \int_0^\infty B_{w_i w_i}(\tau)d\tau = \int_0^\infty B_{w_i w_i}(\ell)d\ell \qquad (5.1)$$

where Taylor's hypothesis has been used to relate the spatial correlation to the time correlation, i.e., $\ell = \overline{W}\tau$; this is called the integral length scale and is referred to as Method 1 for computing length scales throughout this study. In general, when the length scale is denoted by L without a subscript, the integral length scale is implied.

A second method of determining the length scale is to integrate the correlation coefficient from zero to a specific value of $\ell = S_k$ instead of to infinity.

$$L_2 = 0.746S_k = 2 \int_0^{S_k} B_{w_i w_i}(\ell)d\ell \qquad (5.2)$$

S_k is chosen such that twice the area under the correlation coefficient up to a value of S_k is equal to 0.746 S_k, a product which can be shown to represent a measure of L. This method is referred to as Method 2. Equation 5.2 is based on the von Karman spectra theory. The same theory applied to Dryden spectra is given by:

$$L_2 = S_D = 2 \int_0^{S_D} B_{w_i w_i}(\ell)d\ell \qquad (5.3)$$

L_2 is defined such that it is equal to twice the area under the auto-correlation coefficient integrated to a value of S_D.

In computing the length scale by the above integral techniques, two segments of the data tapes consisting of 8192 digitized values each (approximately 10 minutes) were used to compute the correlation. The two values of length scale computed from the respective correlation coefficients for each segment were then averaged to give the reported value of L. The values of L computed by Method 1 at each measuring station are shown in Figure 5.1. Those in parentheses are for Run #8624, whereas those not in parentheses are for Run #8623. The values of length scale computed by Method 2 are shown in Figures 5.2 and 5.3 for the von Karman (Equation 5.2) and Dryden (Equation 5.3) definitions,

37

Figure 5.1. Spatial variation of the integral length scale in meters as comp by Method 1. (Component 1: Numbers not in parentheses, Run #86 crosswind; numbers in parentheses, Run #8624, along wind).
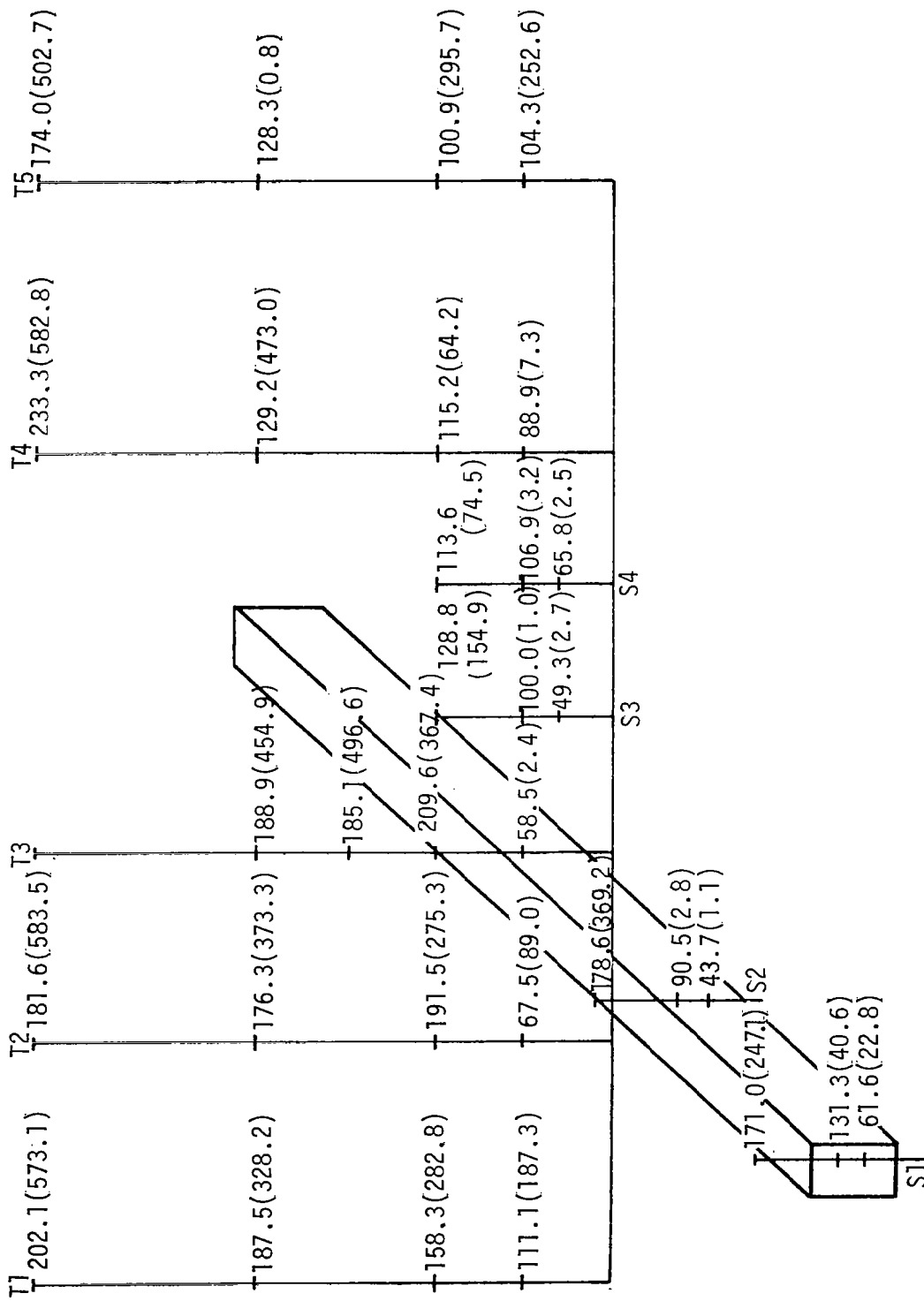
Figure 5.2. Spatial variation of the integral length scale in meters as computed by Method 2, Equation 5.2. (Component 1: Numbers not in parentheses, Run #8623, crosswind; numbers in parentheses, Run #8624, along wind).

39
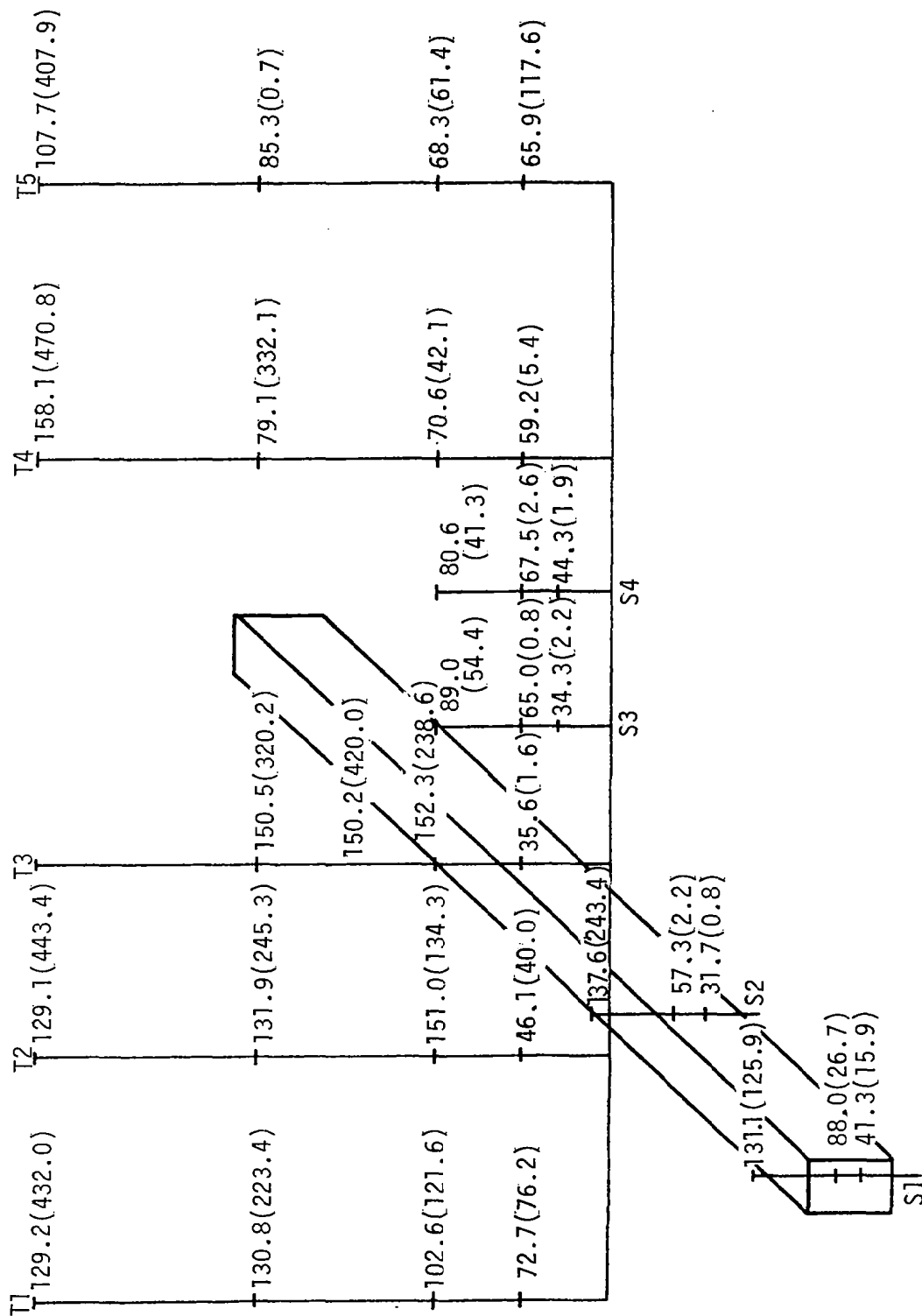
Figure 5.3. Spatial variation of the integral length scale in meters as computed by Method 2, Equation 5.3. (Component 1: Numbers not in parentheses, Run #8623, crosswind; numbers in parentheses, Run #8624, along wind).

40

respectively. (The von Karman and Dryden forms of $B_{w_i w_i}$ are given in Chapter VI.)

In computing the integral length scale, large variations in the computed value occurred depending on the length of recorded use. Figure 5.4 illustrates this variation. As an example, when the length scale was computed using 2048 datum points (approximately 3 minutes), values for different sections of the time history ranged from 34 m to 134 m. The length scale tends to have more stable values as the record length used to compute the auto-correlation increases. This is, of course, evident from an error analysis of the correlation coefficient which shows the rms error decreases with increasing record length. Since 16,384 data points were unwieldy from the economics of computer uses, two segments of 8192 datum points each (as mentioned before) were used to compute two correlation coefficients for each measuring station and the average value of L computed from these is used throughout this study.

A third method of computing the length scale employs the turbulence energy spectrum (see Chapter VII). This method defines L in terms of the truncated root mean square value, σ_T, computed from the measured spectrum and the total root mean square value, σ, as computed by the direct method.

$$\left\{ k_0 \qquad \right\}^{1/2}$$
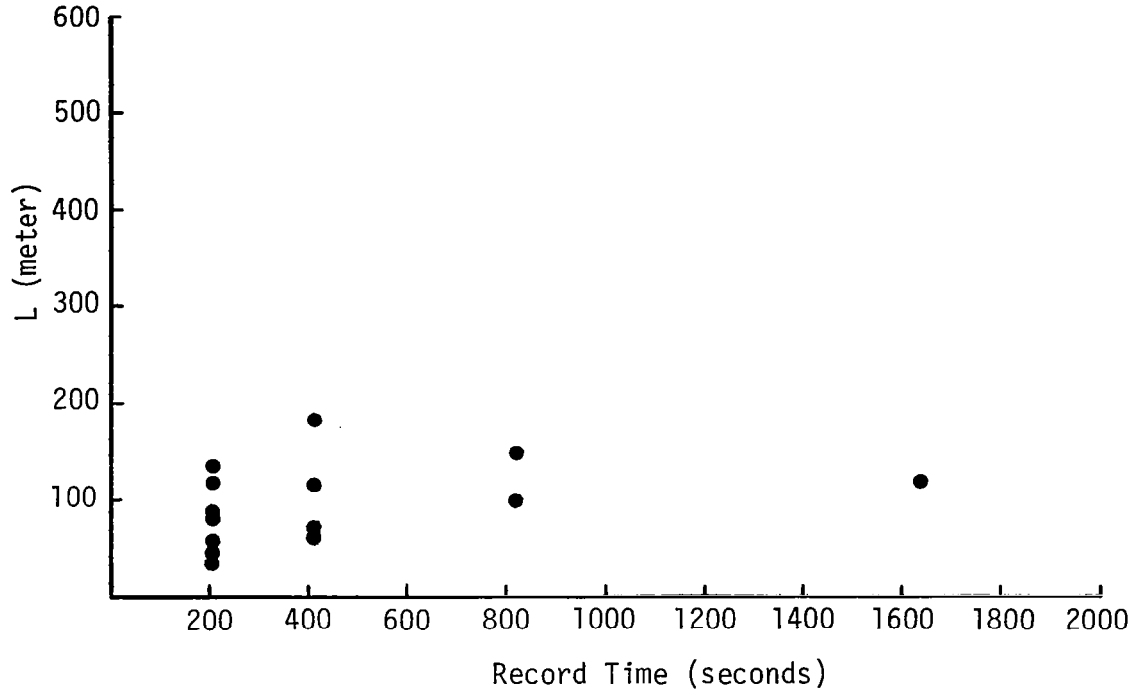
Figure 5.4. The variation of integral length scale with different record times.

$$\sigma = \left(\frac{1}{N} \sum_{i=1}^{N} U_i^2 \right)^{1/2} \tag{5.5}$$

where $\phi(k)$ is the turbulence energy spectrum and k is the reduced spatial frequency $2\pi f/\overline{W}$. Integration of Equation 5.4 from k_1 to k_0, the lowest and highest measured frequencies assuming a straight-line spectrum over this range, gives:

$$L_3 = 0.692 \left(\frac{\sigma}{\sigma_T} \right)^3 \left(\frac{1}{k_1^{2/3}} - \frac{1}{k_0^{2/3}} \right)^{3/2} \tag{5.6}$$

for a von Karman spectrum, and

$$L_3 = \frac{3}{\pi} \left(\frac{\sigma}{\sigma_T} \right)^2 \left(\frac{1}{k_1} - \frac{1}{k_0} \right) \tag{5.7}$$

for a Dryden spectrum.

42

In evaluating Equations 5.6 and 5.7, values of σ computed from $\sigma_{ij} = (\overline{u_i u_j})^{1/2}$, which are tabulated in Tables 6.1 through 6.4, pages 57 through 60, were employed. Values of σ_T were found by integrating the computed spectrum given in Appendix D from the lowest measured frequency of 0.0098 Hz to the highest measured frequency of 2 Hz. Figure 5.5 shows values of L_3 computed from Equation 5.6 for Runs #8623 and #8624, respectively. Figure 5.6 shows values of L_3 computed from Equation 5.7 for Runs #8623 and #8624, respectively. Finally, a fourth method (Method 4) of computing the length scale is based on the value of the frequency $f = f_p$, at which the computed spectrum multiplied by frequency $f\phi(f)$ takes on its maximum value. For the von Karman spectrum model

$$L_4 = 0.146 \; \overline{W}/f_p \qquad\qquad (5.8)$$

Values of f_p were determined from the spectra presented in Appendix D by multiplying the value of $\phi(f)$ by the corresponding frequency. The computer was programmed to select the value of f_p. In some cases, the computer does not make the same selection as a human observer would make.

Figures 5.1 through 5.3 and 5.5 through 5.7 show that the length scales computed by the four different methods described above, although differing in magnitude, have the same general trends. Length scales computed by the integral methods are typically larger by at least a factor of two than those computed by the spectral methods. All length scales are for longitudinal components of the gust. In Run #8623, the

Figure 5.5. Spatial variation of the integral length scale in meters as compu
by Method 3, Equation 5.6. (Component 1: Numbers not in parenth
Run #8623, crosswind; numbers in parentheses, Run #8624, along wi
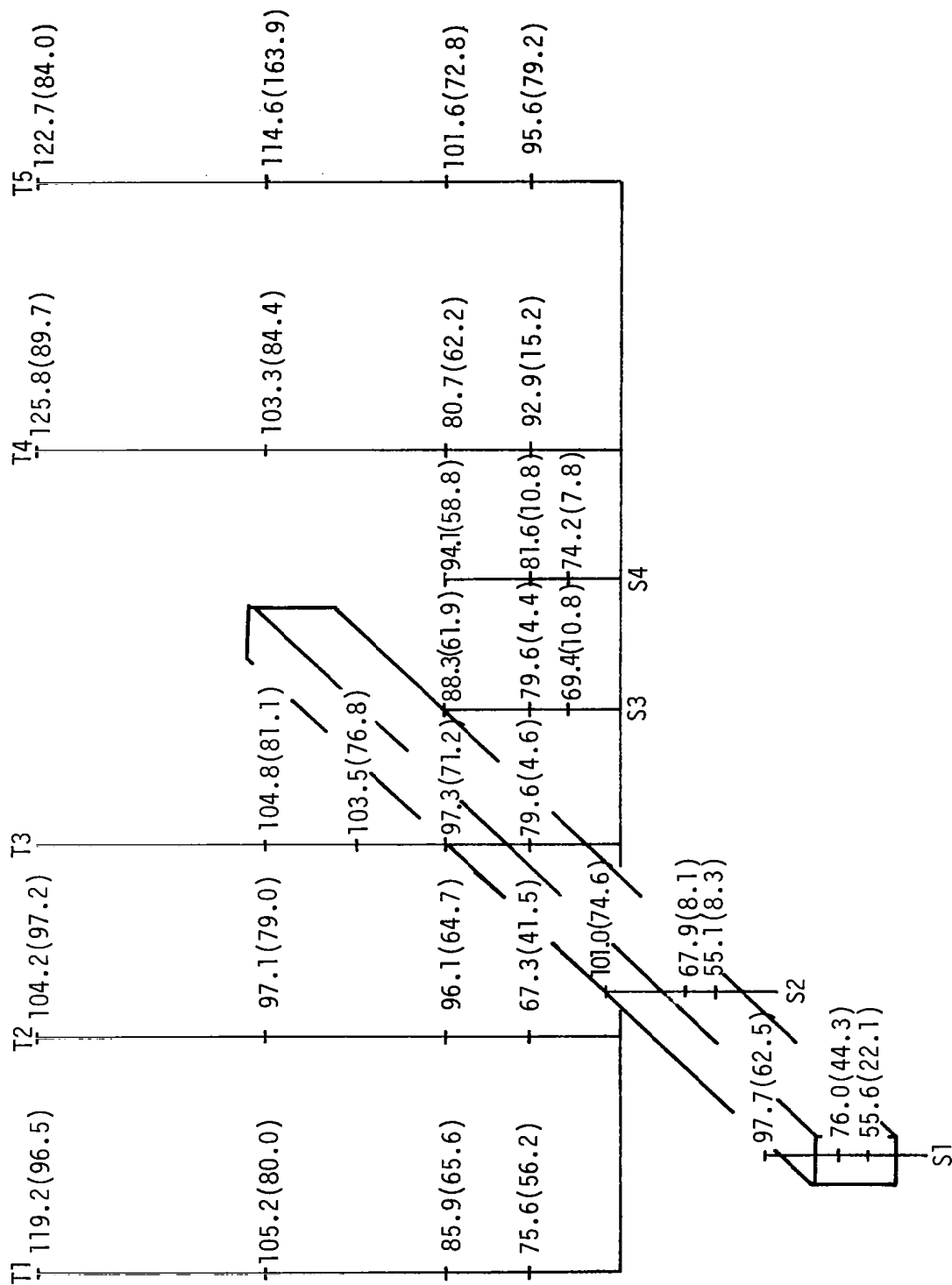
Figure 5.6. Spatial variation of the integral length scale in meters as computed by Method 3, Equation 5.7. (Component 1: Numbers not in parentheses, Run #8623, crosswind; numbers in parentheses, Run #8624, along wind).
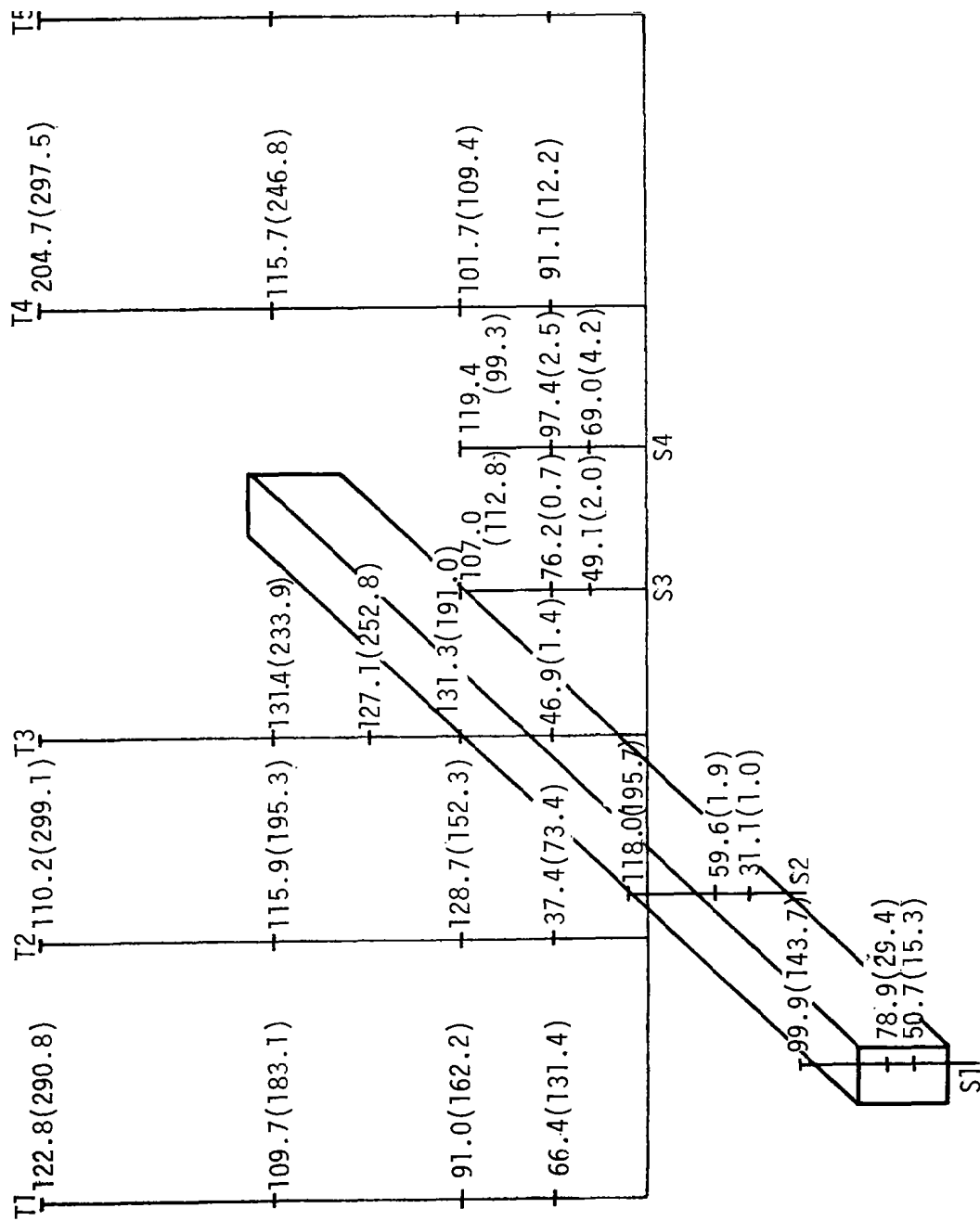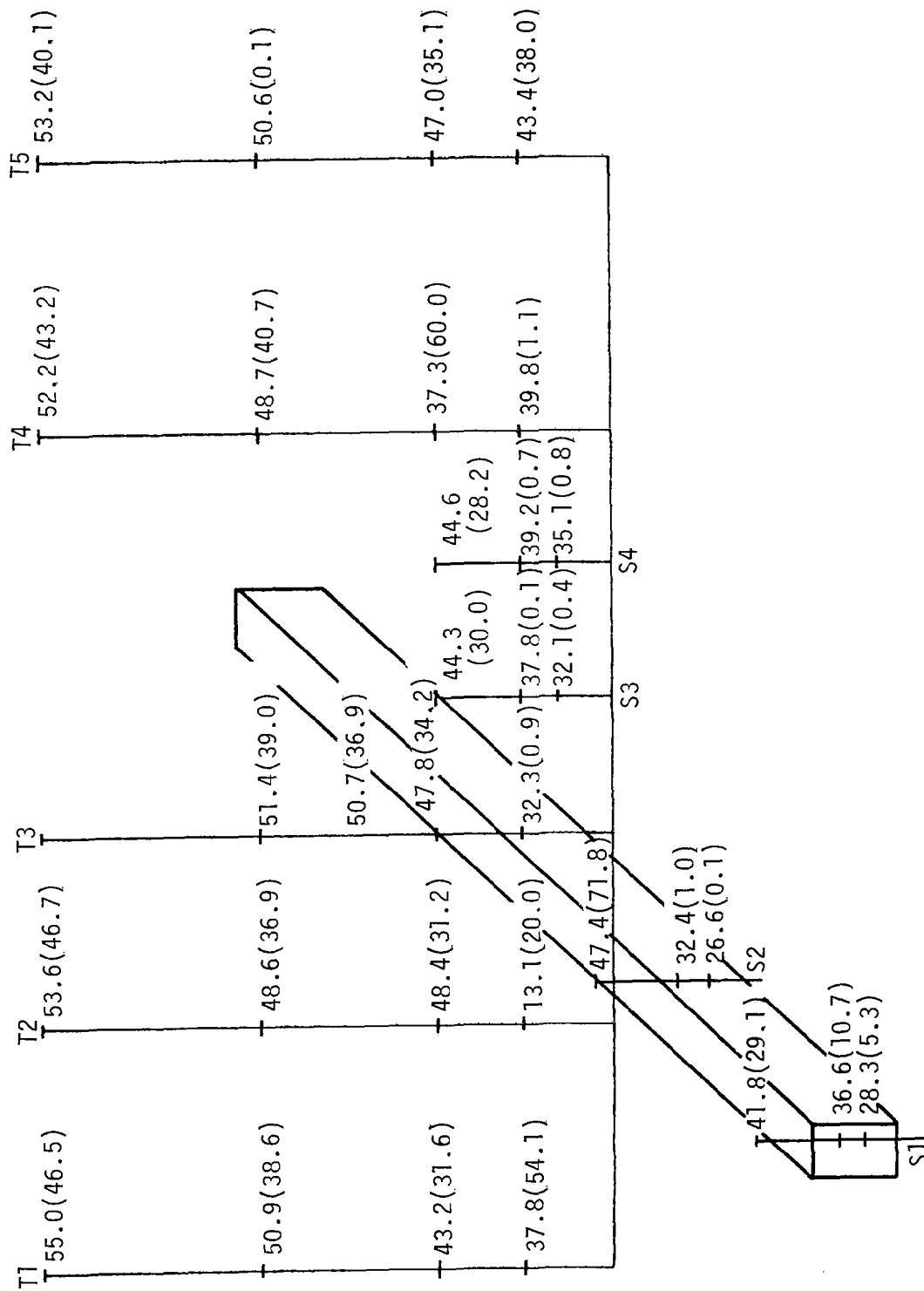
Figure 5.7. Spatial variation of the integral length scale in meters as computed by Method 4, Equation 5.8. (Component 1: Numbers not in parentheses, Run #8623, crosswind; numbers in parentheses, Run #8624, along wind).

46

wind blows perpendicular to the line of the tower array. The length scales in this case are not expected to be influenced by the block building except for those measurements immediately next to the block building. For Run #8624, on the other hand, where the wind blows along the line of towers, the length scale is significantly influenced by the flow wake generated behind the building.

The length scales in the stagnant region of the wake are very small; that is, measurements at T3L1, T4L1, S2L1, S2L2, S3L1, S3L2, S4L1, and L4L2. In turn, the integral length scales at T4L4 and T5L4 are very large, suggesting a stretching of the turbulence perhaps due to acceleration of the flow over the separation region (see Frost and Shieh 1981). In theory, length scales are an indication of the size of the eddies. Therefore, at the higher tower levels, larger length scales generally occur.

Most references show the length scales for the longitudinal component to increase with height. Shiotani (1975) proposes that L increases with height z to the 0.19 power, i.e.,

$$L = 207(z/80.8)^{0.19} \tag{5.9}$$

This expression is for high average wind speed ($\overline{W} \geq 10$ m/s). Kaimal (1973) suggests

$$L = 0.0374 \frac{z}{(n)} \tag{5.10}$$

$$L = 25 \ z^{0.35}/z_0 \ 0.063 \tag{5.11}$$

for strong winds or a neutral atmosphere where z_0 is the surface roughness. For the NASA/MSFC Boundary Layer Facility, the surface roughness for the direction along the array is approximately 0.01 m (see Frost and Shahabi 1977). Etkin (1972) suggests

$$L = 20\sqrt{z} \tag{5.12}$$

Duchene-Marullaz (1975) calculated the length scale from full-scale measured data in a suburban area. Similarly, Neal (1982) calculated the length scale from measured data in flat approach terrain upstream of an escarpment. Values reported in these references along with values computed from Equations 5.9 through 5.12 at the 20-m level are given in Table 5.1. In Run #8623 the average value of length scale at the 20-m level range from 50 m to 250 m, depending on the method of calculation. For Run #8624 the average length scale ranged from 40 m to 580 m.

Thus, the values reported in the literature tend to bracket the results computed in this field study.

TABLE 5.1. Measured and Computed Integral Length Scales at the 20-m Level Based on Reported Results

Reference	Length Scale (m)
Shiotani (1975)	158.8
Kaimal (1973)	51.9
ESDU (1974)	95.3
Etkin (1972)	89.4
Duchene-Marullaz (1975)	95.0
Neal (1982)	290.0

CHAPTER VI

CORRELATIONS

A. Definitions and Nomenclature

Space-time correlations of the atmospheric flow have been computed from the data of this study. These correlations are presented in this chapter. In general, given two sets of data x(t) and y(t) with means equal to zero ($\overline{x(t)} = \overline{y(t)} = 0$), a correlation function $R_{xy}(\tau)$ is defined as

$$R_{xy}(\tau) = \lim_{T \to \infty} \frac{1}{T} \int_0^T x(t)y(t + \tau)dt \qquad (6.1)$$

A correlation coefficient is then defined as

$$B_{xy}(\tau) = R_{xy}(\tau)/(\sigma_x \sigma_y) \qquad (6.2)$$

where σ_x and σ_y are the standard deviations of x(t) and y(t), respectively. As defined, $B(\tau)$ is normalized and theoretically bound within the range $-1 \leq B(\tau) \leq 1$. Computation of the correlation coefficients $B(\tau)$ was accomplished by digital techniques, explained in detail by Steely and Frost (1981). The fast Fourier transform (FFT) technique has been used throughout. As reported in Steely and Frost (1981), this technique is more efficient and gives almost identical agreement with the direct method (see Figure 6.1).

In this study, the symbol for the correlation coefficient, $B_{U_{ij}U_{k\ell}}(\tau)$, will be used where U_{ij} and $U_{k\ell}$ are longitudinal velocity components with U_{ij} being measured at tower "i" and level "j" while
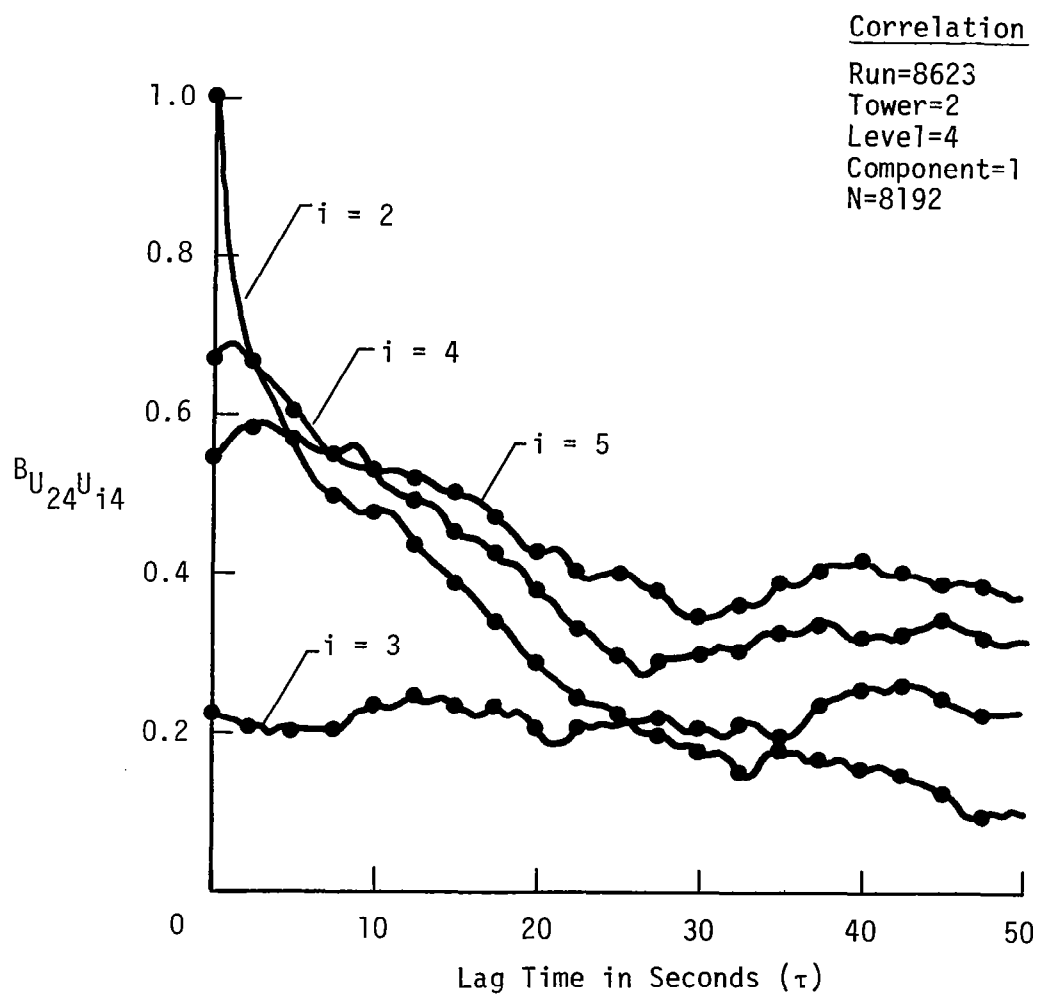
Figure 6.1. Comparison of the correlation coefficient computed by the direct method and by the FFT method (• represents the FFT computed values).

$U_{k\ell}$ is measured at tower "k" and level "ℓ." When $i \neq k$ and $j \neq \ell$; $B_{U_{ij}U_{k\ell}}(\tau)$ is called a two-point spatial correlation coefficient. If $i = k$ and $j = \ell$, then it is called a one-point correlation coefficient and is written as $B_{U_{ij}}(\tau)$ to indicate only the tower and level at which the measurements were made. The terminology "auto-" and "cross-" correlations, used frequently in the literature, are used to denote velocity components. For the longitudinal components, as an example $B_{U_{ij}}(\tau)$, is called an auto-correlation coefficient, whereas $B_{U_{ij}V_{ij}}(\tau)$, when u and v are velocity components in different directions, indicates a cross-correlation coefficient. Figure 6.2 further defines this nomenclature.

B. Experimental Results

In Figures 6.3 and 6.4, two-point spatial correlations have been plotted relative to their tower position and level. The correlations have been computed with respect to the position designated in the caption. For example, in Figure 6.3 the correlations have been computed relative to T1L1, which is evident from the fact that the correlation coefficient is unity at that position.

Values in parentheses in Figures 6.3 and 6.4 denote values for the wind parallel to the building axis (Run #8623) or perpendicular to the line of towers. Thus, the unparenthesized values are along-wind correlations; whereas those in parentheses are crosswind correlations.

Some interesting properties of the correlation coefficient are observed in Figures 6.3 and 6.4. Again, taking Figure 6.3 as an example, it can be seen that directly behind the block building there is very little correlation with the upstream position T1L1 for the along-wind

Definition:

$$R_{xy}(\tau) = \lim_{T \to \infty} \frac{1}{T} \int_0^T x(t)y(t + \tau)dt$$

$$B_{xy}(\tau) = R_{xy}(\tau)/\sigma_x\sigma_y; \quad (-1 \leq B_{xy}(\tau) \leq 1)$$

Nomenclature:

$B_{U_{ij}U_{k\ell}}(\tau)$ where U_{ij} is velocity measured at Tower i, Level j

$U_{k\ell}$ is velocity measured at Tower k, Level ℓ

$\tau \neq 0$ $i \neq k$ and $j \neq \ell \approx$ Two-point time-dependent spatial correlation

$\tau = 0$ $i \neq k$ and $j \neq \ell \approx$ Two-point spatial correlation

$\tau \neq 0$ $i = k$ and $j = \ell \approx$ One-point time-dependent spatial correlation

$\tau = 0$ $i = k$ and $j = \ell \approx$ One-point spatial correlation

Figure 6.2. Spatial time-dependent correlation terminology.

52
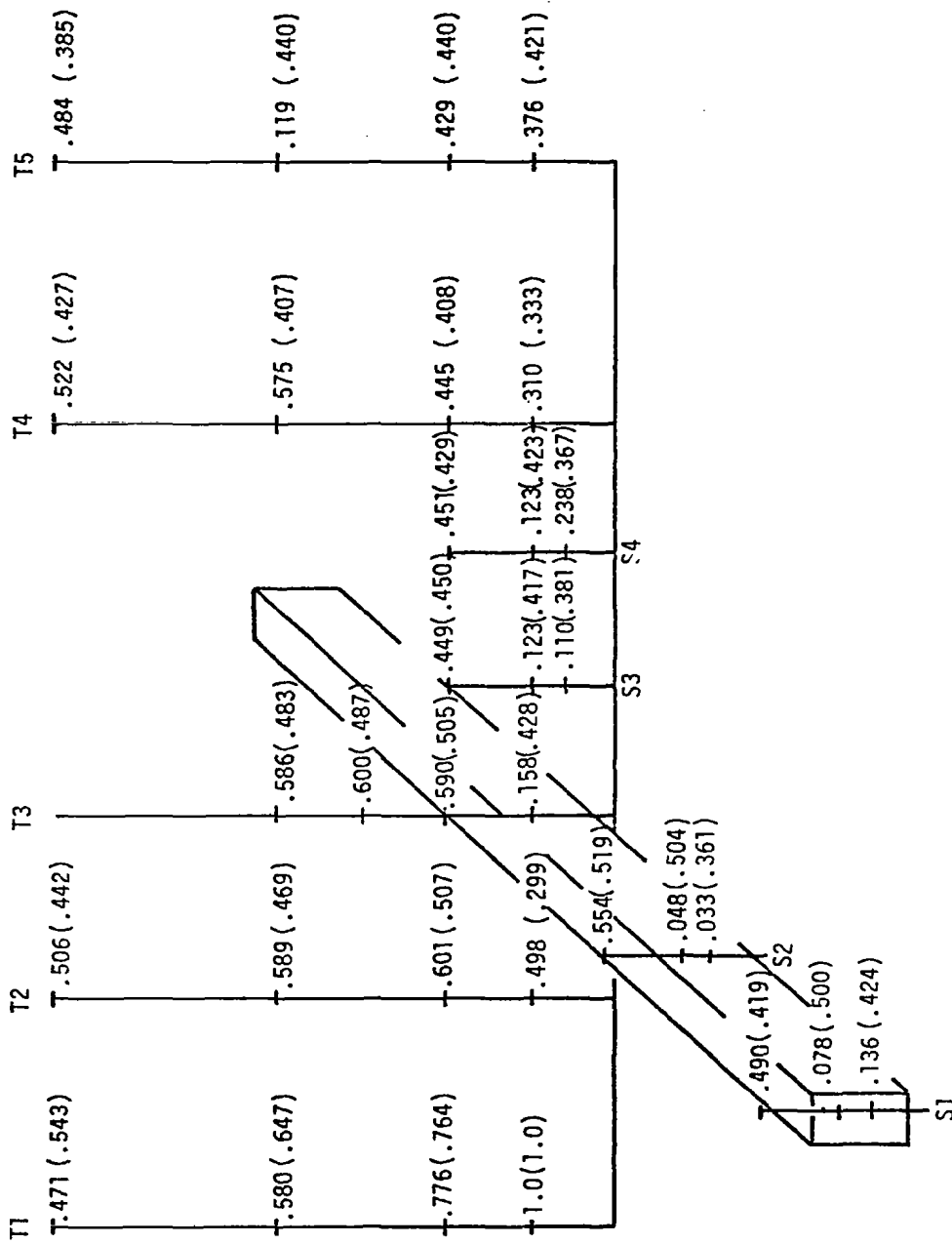
Figure 6.3. Two-point spatial correlations of the longitudinal velocity component relative to T1L1. (Numbers in parentheses, Run #8623, crosswind; numbers not in parentheses, Run #8624, along wind).
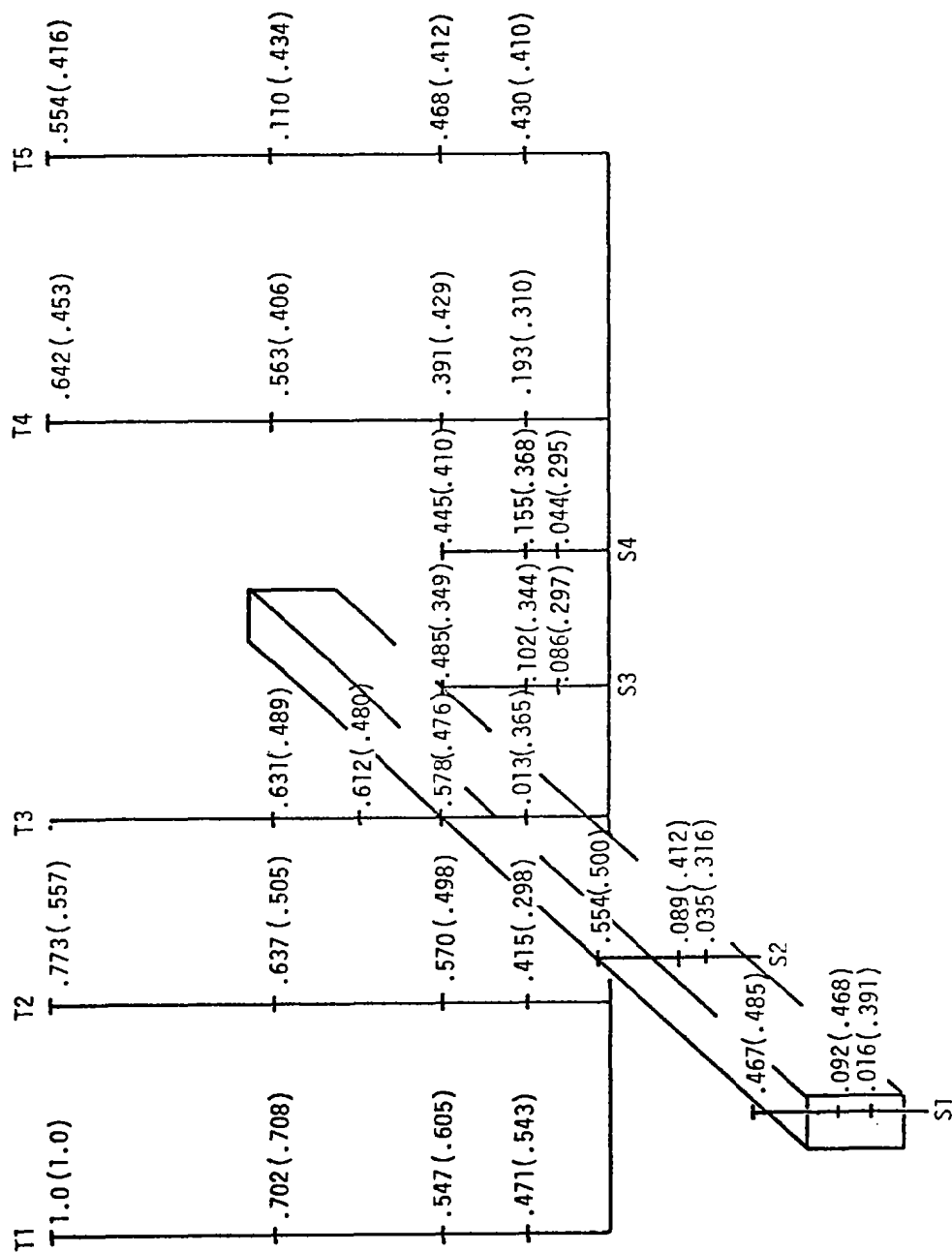
Figure 6.4. Two-point spatial correlations of the longitudinal velocity component relative to T1L4. (Numbers in parentheses, Run #8623, crosswind; numbers not in parentheses, Run #8624, along wind).

54

case, which is not true, however, for the crosswind case. A wake obviously occurs in the former case causing a breakdown in the flow structure between the undisturbed flow upstream and the wake region behind the building. In fact, the wake which typically extends 10 to 14 building heights downstream is outlined by the low correlation values. On the other hand, when the flow approaches the narrow end or small aspect ratio of the building, very little degradation of the correlation occurs. Although one might anticipate longitudinal vortices being shed and rolling up along side the building; no evidence of this is observed in the data. As expected, the correlations in the free-stream (upper levels) increase with a decrease in the distance separating the two points of correlation. It might be noted that due to the definition of the two-point spatial correlation, $R_{U_{ij}U_{k\ell}}(0) = R_{U_{k\ell}U_{ij}}(0)$. Also, if $\sigma_{U_{ij}} = 0$, then $R_{U_{ij}U_{ij}}$ is undefined. A negative correlation between two points suggests a structured reverse flow region where a longitudinal fluctuation in the positive direction at one point results in a negative fluctuation at another point. Some negative values of the along-wind correlations are observed immediately behind the builidng on the off-axis towers. These negative values indicate reverse flow in the wake. One might anticipate stronger negative values along the centerline; however, these are not observed.

The extent to which a signal is felt at two different points depends on the time it takes the signal to travel from one point to the other, plus any changes which may have occurred during this time. A two-point space-time correlation, $R_{U_{ij}U_{k\ell}}(\tau)$, describes the general dependence of the velocities at one tower and level position to those at

55

another position. Information relative to the time required for a signal to pass from one point to another in the wind field can be determined from the space-time correlation. As the signal at one point is displaced in time relative to another point, the space-time correlation function will peak at the value of τ equal to the time required for the signal to propagate at the speed of the wind to the second point.

Values of the correlation are nondimensionalized with $\sigma_{U_{ij}} \sigma_{U_{k\ell}}$ where $\sigma_{U_{ij}}$ and $\sigma_{U_{k\ell}}$ are the turbulent intensities at the tower and level indicated. Tables 6.1 and 6.3 present the turbulent intensities $\sigma_{U_{ij}}$ for Runs #8624 and #8623, respectively. Note $\sigma_{U_{ij}}$ is the absolute value (i.e., dimensional value) of the auto-correlation for zero spatial separation and zero time lag. Similar values of the cross-correlations are given in Tables 6.2 and 6.4. Mean wind speeds for all measuring stations are given in Tables 6.5 and 6.6 for Runs #8624 and #8623, respectively.

Figures 6.5 and 6.6 are plots of two-point space-time correlations. Figure 6.5 illustrates vertical correlations, whereas Figure 6.6 illustrates horizontal correlations. Figures 6.5a and 6.5b are plots of the correlation of L4 with all other levels on T1 and of L4 with all other levels on T5, respectively. These correlations for the wind perpendicular and parallel to the building or line of towers will not be appreciably different for Towers 1 and 5 where the flow is relatively undisturbed in both cases. Inspection of the data show that the correlations are very similar. The peaks in the correlation which shift to greater times with decreasing height are associated with the decreasing mean wind speed near the ground (e.g., logarithmic velocity profile).

TABLE 6.1. Value of $\sigma^2 U_{ij}$ for Run #8624 (number of digitized points used is 8192)

		T1	T2	T3	T4	T5	S1	S2	S3	S4
L1	$U_{1j}U_{1j}$	1.31	1.05	0.84	1.75	1.39	1.78	1.05	1.00	1.82
	$V_{1j}V_{1j}$	0.71	1.17	0.46	2.06	0.87	0.86	1.05	1.36	1.37
	$W_{1j}W_{1j}$	29.69	0.24	0.02	0.83	0.27	0.11	0.18	0.11	0.75
L2	$U_{2j}U_{2j}$	1.49	1.33	1.45	2.74	1.61	1.67	0.64	1.69	1.83
	$V_{2j}V_{2j}$	0.87	0.81	0.82	1.15	0.93	1.09	0.53	1.64	1.43
	$W_{2j}W_{2j}$	29.69	0.52	1.14	0.58	0.11	0.51	0.32	0.72	29.69
L3	$U_{3j}U_{3j}$	1.75	1.64	1.68	2.03	17.93	1.60	1.70	1.67	2.51
	$V_{3j}V_{3j}$	1.01	0.86	0.81	0.77	0.00	1.16	1.03	1.05	1.24
	$W_{3j}W_{3j}$	0.39	0.57	0.32	0.33	0.46	0.39	1.04	0.34	0.05
L4	$U_{4j}U_{4j}$	1.97	2.05	1.52	2.00	2.39	--	--	--	--
	$V_{4j}V_{4j}$	0.96	0.87	1.68	0.75	0.83	--	--	--	--
	$W_{4j}W_{4j}$	0.50	0.48	0.01	0.43	0.58	--	--	--	--

57

TABLE 6.2. Values of Cross-Correlation $\sigma^2_{U_{ij}V_{ij}}$ for Run #8624 (number of digitized points used is 8192)

		T1	T2	T3	T4	T5	S1	S2	S3	S4
L1	$U_{1j}V_{1j}$	0.29	0.25	-0.18	-0.24	0.19	-0.46	-0.35	-0.09	-0.03
	$V_{1j}W_{1j}$	-2.07	0.00	0.00	-0.35	-0.12	-0.03	0.03	0.00	0.12
	$U_{1j}W_{1j}$	-0.64	0.06	0.00	0.36	0.00	0.02	0.02	0.00	0.34
L2	$U_{2j}V_{2j}$	0.26	0.26	0.11	0.20	0.27	-0.37	0.04	-0.26	-0.09
	$V_{2j}W_{2j}$	2.19	-0.17	0.25	-0.44	-0.13	0.03	0.00	-0.34	0.00
	$U_{2j}W_{2j}$	0.75	0.00	0.05	-0.03	-0.05	-0.07	0.02	0.29	-0.05
L3	$U_{3j}V_{3j}$	0.32	0.30	0.29	0.37	0.00	0.11	0.23	0.02	0.00
	$V_{3j}W_{3j}$	-0.23	-0.34	-0.22	-0.31	-0.34	-0.02	-0.31	-0.06	0.01
	$U_{3j}W_{3j}$	0.07	-0.02	0.03	0.00	0.00	0.01	-0.12	0.04	0.00
L4	$U_{4j}V_{4j}$	0.22	0.26	0.46	0.20	-0.05	--	--	--	--
	$V_{4j}W_{4j}$	-0.31	-0.31	0.00	-0.34	-0.52	--	--	--	--
	$U_{4j}W_{4j}$	0.04	0.03	0.00	0.00	0.11	--	--	--	--

TABLE 6.3. Value of $\sigma^2_{U_{ij}}$ for Run #8623 (number of digitized points used is 8192)

		T1	T2	T3	T4	T5	S1	S2	S3	S4
L1	$\overline{U_{1j}U_{1j}}$	2.17	2.58	1.80	1.77	1.75	1.34	1.60	1.39	1.61
	$\overline{V_{1j}V_{1j}}$	1.51	3.28	2.47	1.44	1.49	1.81	0.79	1.25	1.40
	$\overline{W_{1j}W_{1j}}$	3.95	2.03	0.85	0.20	0.21	0.02	0.21	0.42	0.15
L2	$\overline{U_{2j}U_{2j}}$	2.62	2.99	2.47	2.59	1.85	1.71	1.40	1.66	1.76
	$\overline{V_{2j}V_{2j}}$	1.69	2.27	1.68	1.05	1.79	1.86	1.36	1.45	1.47
	$\overline{W_{2j}W_{2j}}$	29.70	0.28	1.09	0.35	0.09	0.27	0.71	0.40	0.17
L3	$\overline{U_{3j}U_{3j}}$	2.65	2.54	2.95	2.07	2.04	12.23	2.49	2.03	2.04
	$\overline{V_{3j}V_{3j}}$	1.88	1.56	1.81	1.61	0.00	9.97	1.80	1.63	1.72
	$\overline{W_{3j}W_{3j}}$	0.50	0.45	0.53	0.53	0.32	0.33	0.63	0.61	0.01
L4	$\overline{U_{4j}U_{4j}}$	2.68	2.46	2.73	1.88	2.34	--	--	--	--
	$\overline{V_{4j}V_{4j}}$	1.85	1.63	0.03	1.63	1.56	--	--	--	--
	$\overline{W_{4j}W_{4j}}$	0.93	0.68	0.00	0.84	0.85	--	--	--	--

TABLE 6.4. Values of Cross-Correlation $\sigma^2_{U_{ij}V_{ij}}$ for Run #8623 (number of digitized points used is 8192)

		T1	T2	T3	T4	T5	S1	S2	S3	S4
L1	$\overline{U_{1j}V_{1j}}$	-0.47	0.45	0.45	-0.13	0.08	-0.29	0.27	-0.12	-0.07
	$\overline{V_{1j}W_{1j}}$	-0.16	0.11	-0.24	0.02	0.01	-0.01	0.03	-0.08	-0.02
	$\overline{U_{1j}W_{1j}}$	0.14	0.10	-0.30	-0.20	-0.11	-0.04	-0.10	-0.18	-0.11
L2	$\overline{U_{2j}V_{2j}}$	-0.55	-0.68	-0.36	-0.17	0.02	-0.34	0.24	-0.20	-0.14
	$\overline{V_{2j}W_{2j}}$	-0.21	0.09	-0.30	-0.06	0.00	-0.05	-0.33	-0.16	-0.02
	$\overline{U_{2j}W_{2j}}$	-1.59	0.04	-0.35	-0.30	0.05	-0.17	-0.09	-0.15	-0.11
L3	$\overline{U_{3j}V_{3j}}$	-0.66	-0.55	-0.79	-0.02	0.00	-9.26	-0.38	-0.32	-0.29
	$\overline{V_{3j}W_{3j}}$	-0.06	0.02	-0.10	-0.01	0.00	0.04	-0.24	-0.19	0.02
	$\overline{U_{3j}W_{3j}}$	-0.33	-0.21	-0.24	-0.35	-0.28	-0.25	-0.38	-0.25	0.05
L4	$\overline{U_{4j}V_{4j}}$	-0.66	-0.44	-0.01	-0.38	0.11	--	--	--	--
	$\overline{V_{4j}W_{4j}}$	0.07	0.03	0.00	-0.03	-0.12	--	--	--	--
	$\overline{U_{4j}W_{4j}}$	-0.23	-0.30	-0.02	-0.49	-0.43	--	--	--	--

60

TABLE 6.5. Mean Wind Speed (m/s) at All Stations, Run #8623

	T1	T2	T3	T4	T5	S1	S2	S3	S4
L1	5.04	4.38	4.32	5.32	5.80	3.78	3.56	4.29	4.69
L2	5.77	6.48	6.39	4.99	6.29	4.88	4.30	5.06	5.25
L3	6.81	6.50	6.86	6.50	6.76	5.50	6.33	5.93	5.96
L4	7.36	7.16	6.79	6.97	7.12	--	--	--	--

TABLE 6.6. Mean Wind Speed (m/s) at All Stations, Run #8624

	T1	T2	T3	T4	T5	S1	S2	S3	S4
L1	3.62	2.67	0.29	0.98	5.08	1.41	0.47	0.69	0.50
L2	4.22	4.17	4.57	4.00	4.69	2.85	0.51	0.28	0.68
L3	5.16	4.92	5.22	5.44	3.52	3.89	4.79	3.97	3.76
L4	6.21	6.23	4.94	5.78	5.35	--	--	--	--

(a) Vertical correlation relative to T1L4.
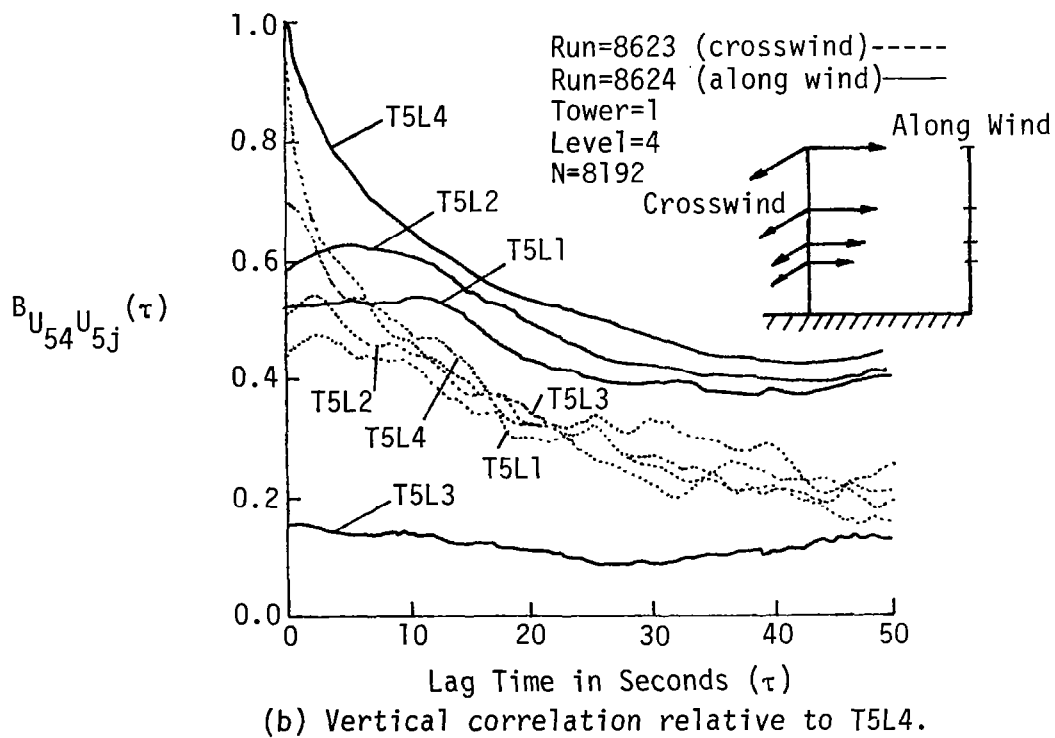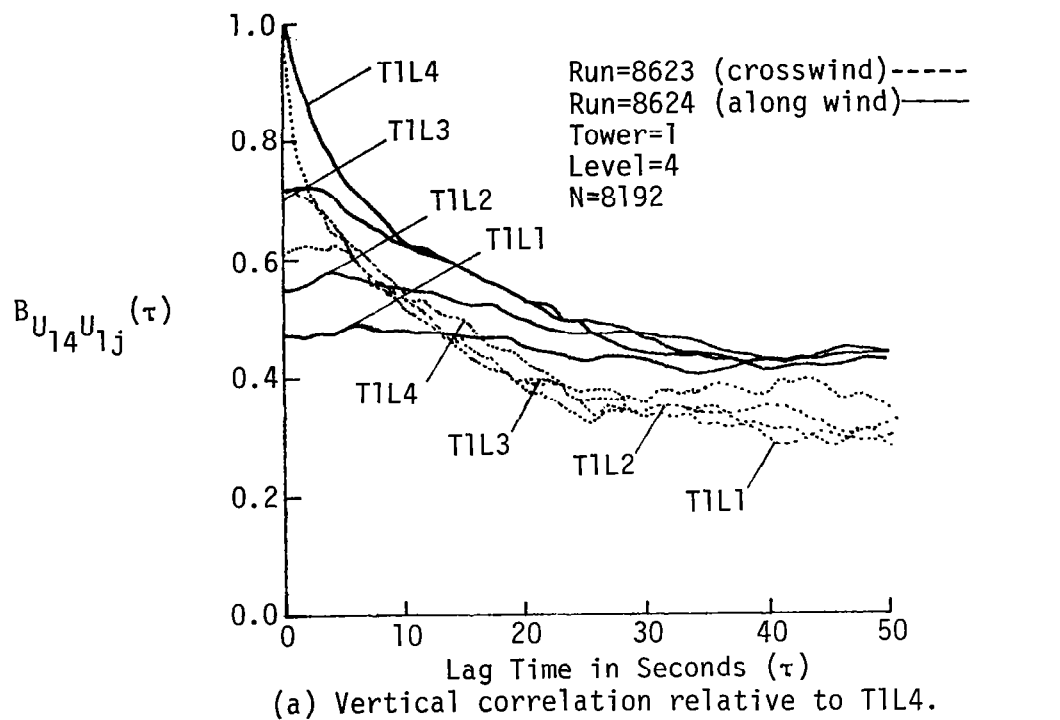
(b) Vertical correlation relative to T5L4.

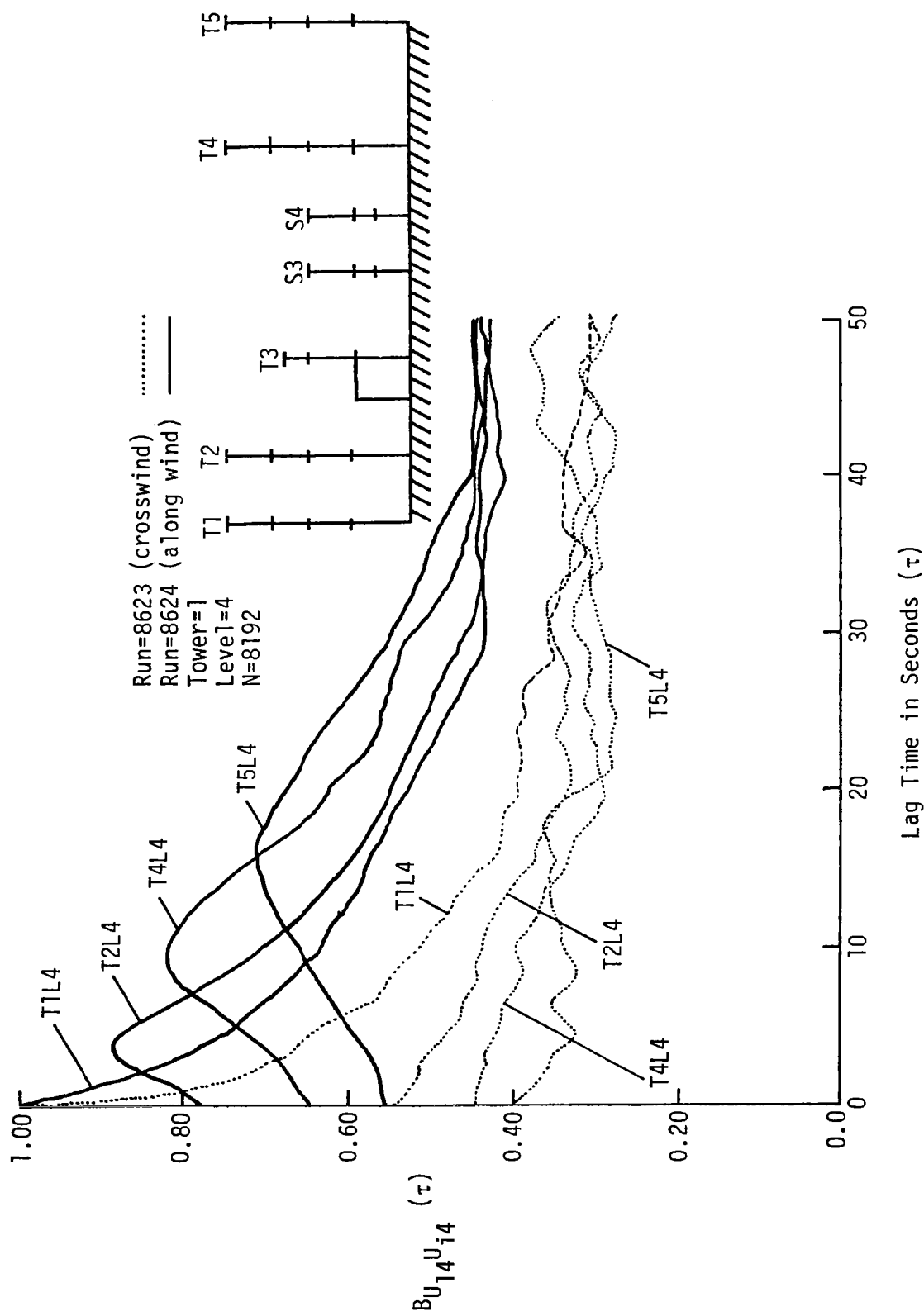Figure 6.5. Two-point vertical space-time correlations.

Figure 6.6. Two-point horizontal space-time correlation relative to T1L4.

(Note that the instrumentation on T5L3 was not operating correctly.)
The increase in lag time at which the peak in the correlation occurs can
be explained by the fact that the boundary layer has not fully recovered
at T5. The lower mean velocities in the unrecovered region results in
the signal propagating at a lower speed and thus requiring a longer time
to traverse a given distance.

In Figure 6.6 (horizontal two-point space-time correlations),
considerable difference in the correlations for Run #8624 (along the
tower array) and Run #8623 (across the tower array) is observed. This
is as expected since Run #8624 now represents the along-wind correla-
tion, whereas Run #8623 is the crosswind correlation. Peaks occur in
the along-wind correlation and are associated with the turbulence being
carried with the mean flow (i.e., Taylor's hypothesis). It should be
noted that the instrumentation on T3L4 was moved to the 9-m level, and
for this reason, it has been excluded in Figure 6.6. No peaks are
observed in the crosswind correlations and their overall magnitude is
considerably less than the along-wind correlation.

The differences in the along-wind and crosswind correlations
suggest a stretching and transport of the eddies in the along-wind
direction.

Figure 6.7 shows the two-point horizontal space-time correlation at
Level 2 which is just slightly above the wake region created by the
building. One sees the same general characteristic of the correlation
for the along-wind direction. For the crosswind direction, however, one
observes peaks at approximately a 2-second lag time between S3L3 and
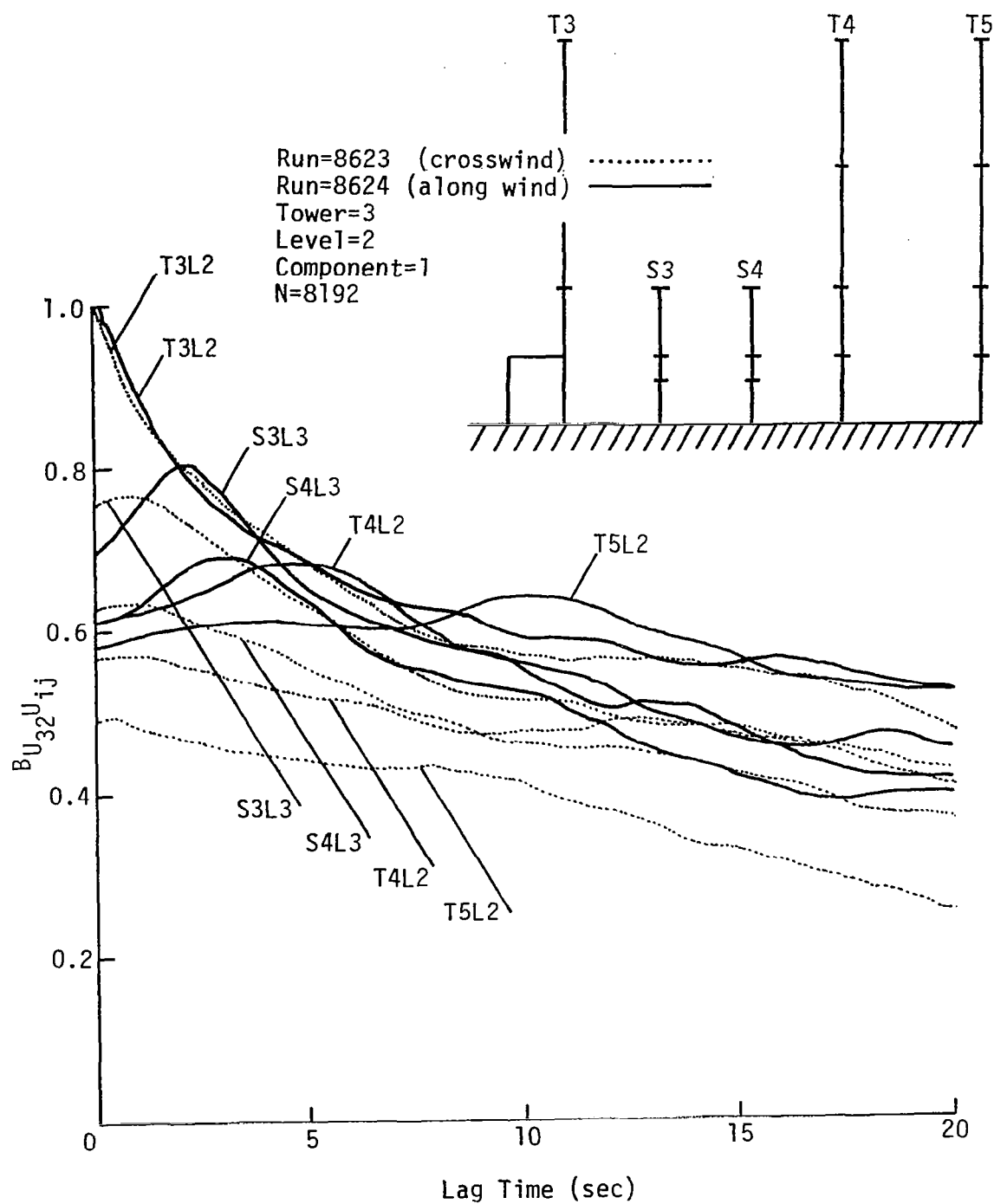S4L3. These peaks may possibly be related to some organized shedding of

Figure 6.7. Two-point horizontal space-time correlation slightly above the wake region relative to T3L2.

the flow from the building. That is, the peaks may be associated with a vortex pattern or result due to a component of wind acting along the direction of the tower due to the displacement of the flow of the building.

Figure 6.8 further illustrates the effect of the presence of the building on the flow field. It shows the two-point horizontal space-time correlation at Level 1 (i.e., in the wake region). The correlation of T3L1 with itself drops off very quickly and approaches zero within ten seconds. The correlation with T3L1 and all the other measuring positions along Level 1 is almost zero. An interesting effect, however, is seen in the correlation with T5L1. This correlation starts out negative and becomes positive in approximately ten seconds. This suggests an organized fluctuation of the reattachment point of the wake. Since, in general, the wake region would extend roughly ten building heights downstream, it is anticipated that the flow will reattach somewhere between Towers 4 and 5. It is well known that the reattachment point of a turbulent flow will oscillate, and further examination of this correlation might shed some light on this particular aspect of turbulent wakes. It is not the purpose of this study, however, to pursue this investigation further.

The crosswind correlations do not show any characteristic peaks as they do for Level 2. However, they tend to remain more constant at approximately a value of 0.4 showing very little drop off out to values of 20 seconds. The correlation of T3L1 with itself drops off somewhat faster at Level 1 than at Level 2, reaching a value on the order of 0.4 in 10 seconds for the former case and a value of approximately 0.6 at 10 seconds for the latter case.
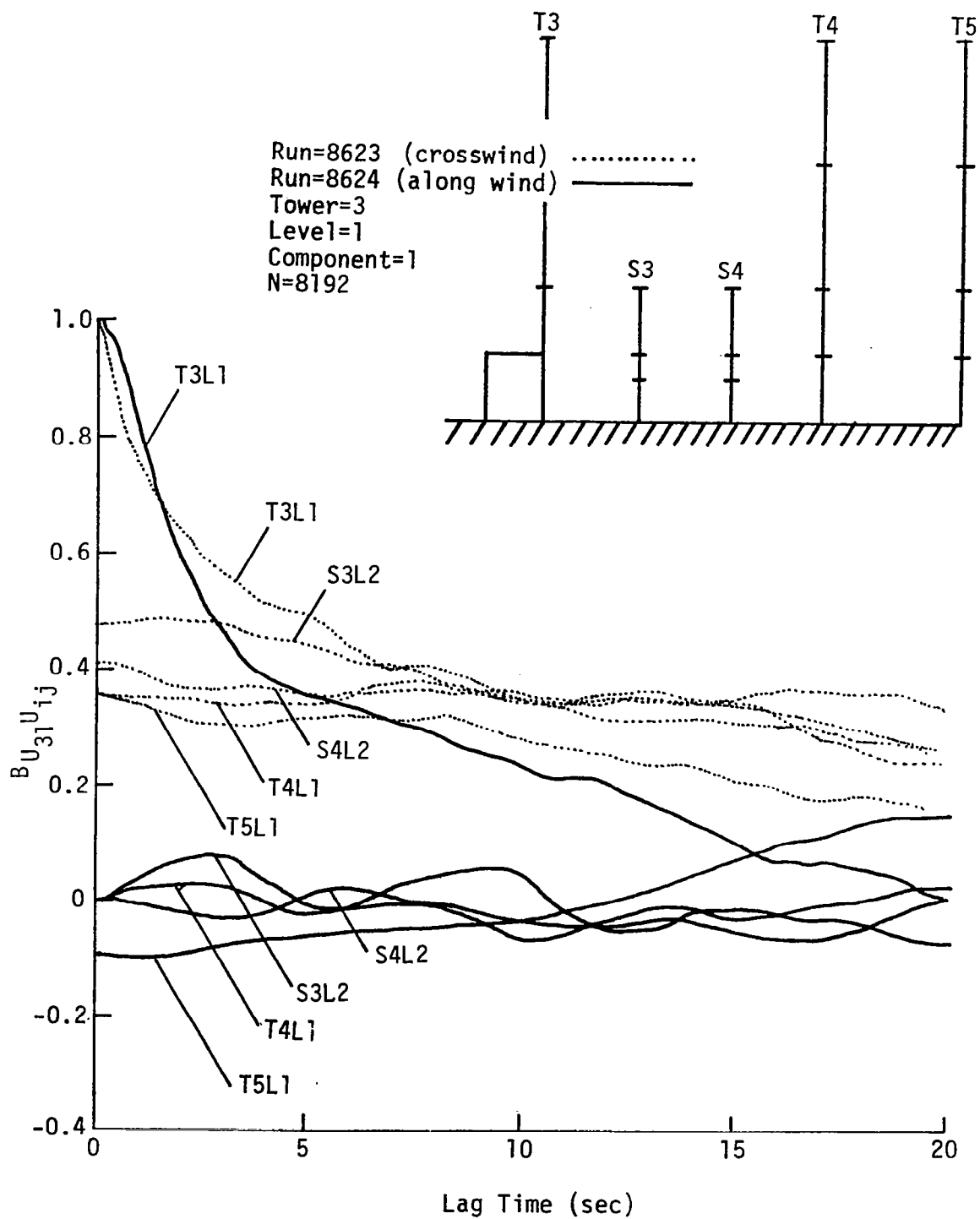
66

Figure 6.8. Two-point horizontal space-time correlation in the wake region relative to T3L1.

Figures 6.9 and 6.10 show the correlation between the towers positioned immediately behind the building at Level 2 and Level 1, respectively, for the tall towers. For this case, the correlation for Run #8623 now becomes essentailly the along-wind correlation whereas that for Run #8624 becomes a crosswind correlation. One can see that the general characteristics of the correlations are thus reversed. The crosswind correlation, or dashed line (now the along-wind correlation), shows peaks in the correlation due to the fact that the mean wind transports some of the turbulence along the wind direction. The along-wind correlation, solid line (now the crosswind correlation), shows a peak at Level 2 in a similar manner to that shown in Figure 6.10. For Run #8624 (along-wind), the correlation at Level 1 is essentially zero for S2L2 and S1L2. The reason for this is undoubtedly due to the fact that the anemometers are almost level with the building; and, consequently, this region of flow is essentially stagnant and no correlation occurs. Correlations for other velocity components are given in Appendix C.

C. Comparison with Theory

A number of empirical and semi-empirical equations for predicting the behavior of the longitudinal and transverse correlations have been developed. Notable among these are the von Karman and the Dryden methods. Figure 6.11 defines the theoretical correlations. Note that the transverse correlation function defined (see sketch in Figure 6.11) is not the same correlation as the crosswind correlation computed in the preceding subchapters. The correlations are also expressed in terms of a length scale rather than a separation distance and a lag time. The
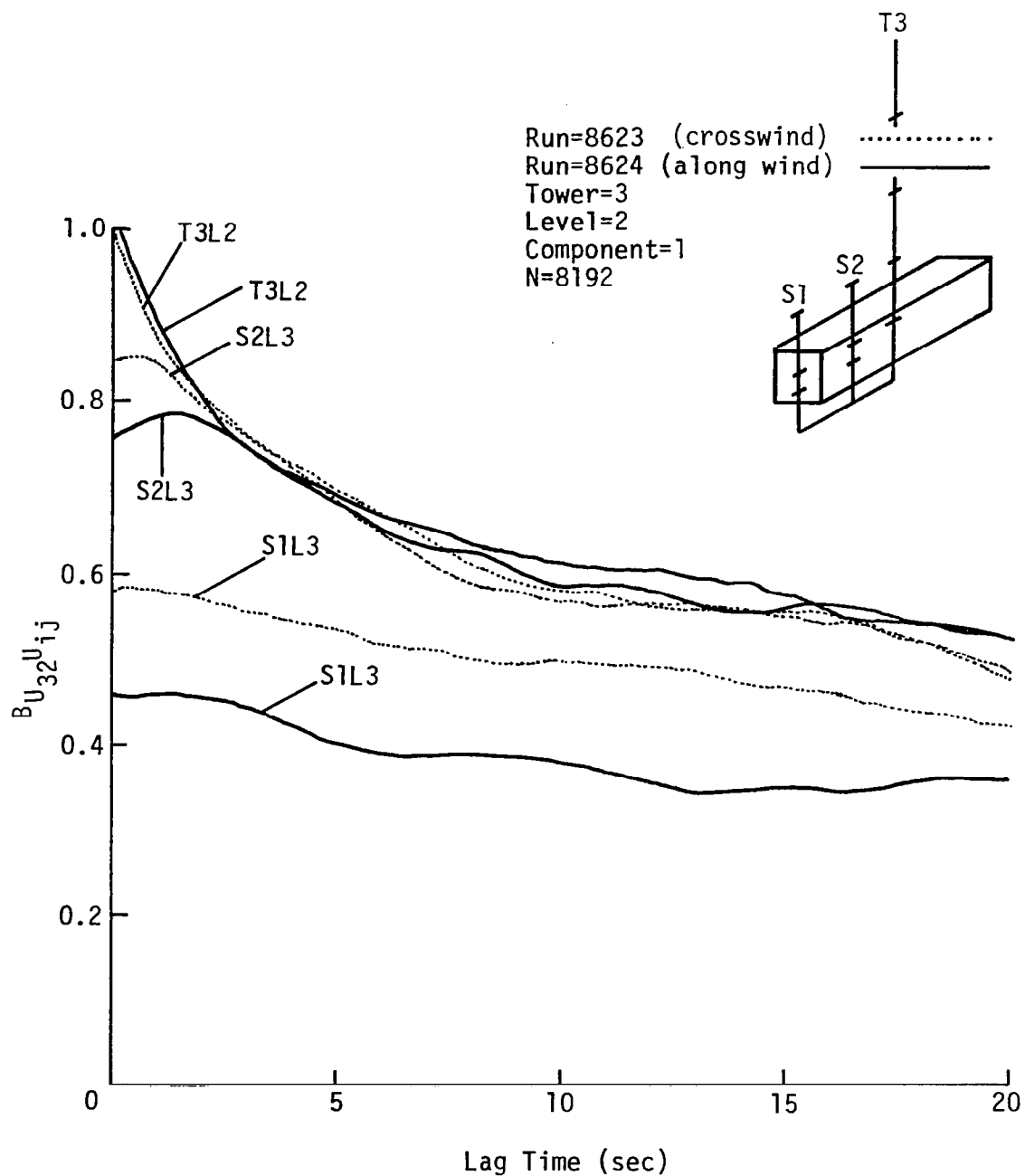
Figure 6.9.   Two-point horizontal space-time correlation immediately behind the building and slightly above wake relative to T3L2.
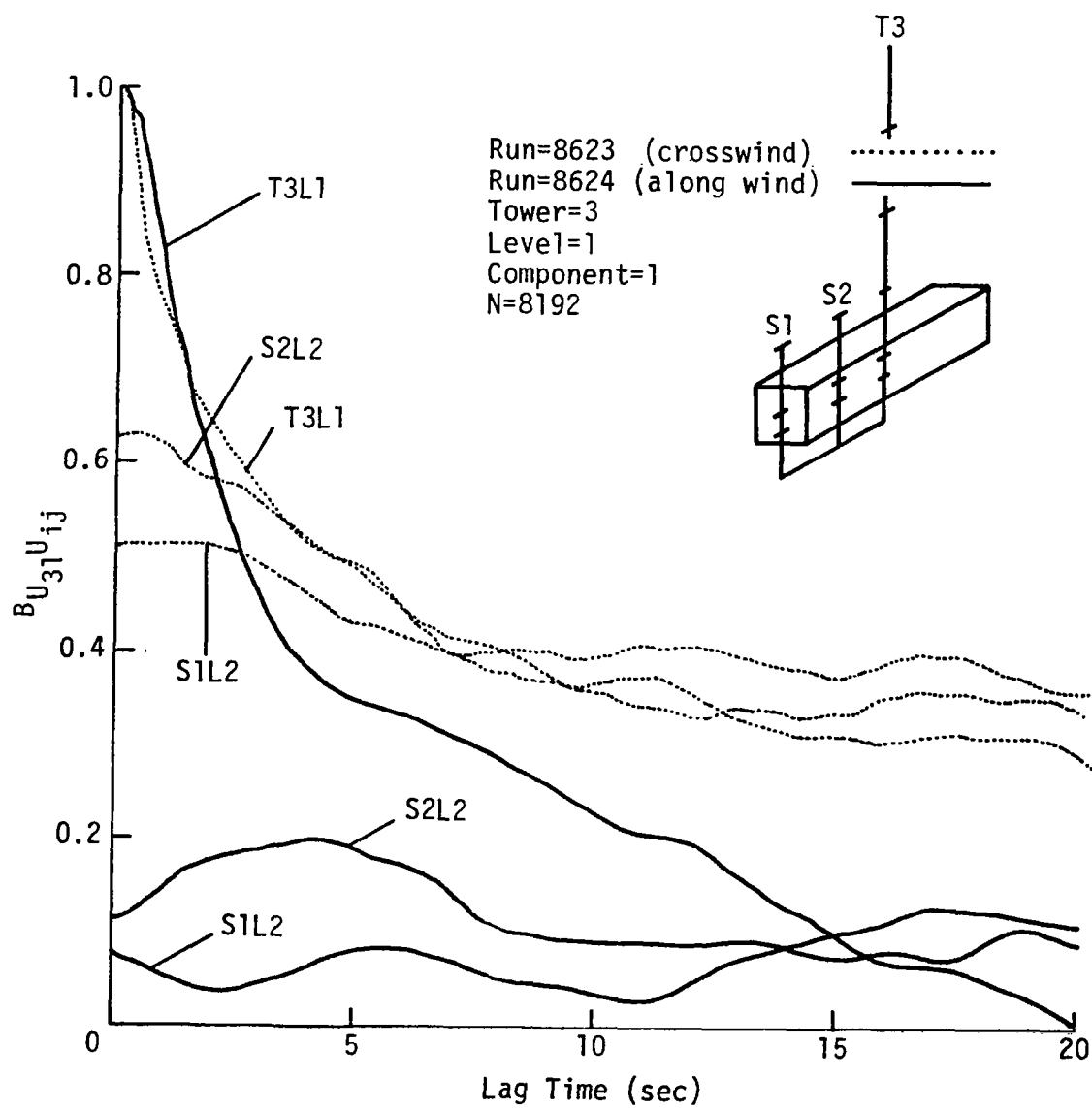
Figure 6.10. Two-point horizontal space-time correlation immediately behind the building and in the wake region relative to T3L1.
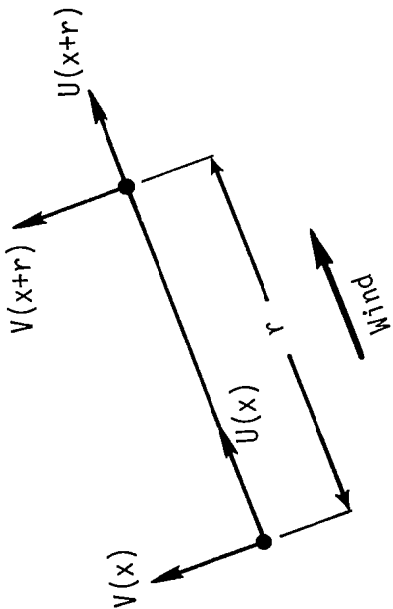
$$B_{U_{ij}} = \frac{\langle U(x)U(x+r)\rangle}{\sigma_u^2}$$

$$B_{V_{ij}} = \frac{\langle V(x)V(x+r)\rangle}{\sigma_v^2}$$

<u>von Karman</u>

Longitudinal Correlation Function:

$$B_{U_{ij}}(r) = \frac{2^{2/3}}{\Gamma(1/3)} \left(\frac{r}{aL}\right)^{1/3} K_{1/3}\left(\frac{r}{aL}\right)$$

Transverse Correlation Functions:

$$B_{V_{ij}}(r) = \frac{2^{2/3}}{\Gamma(1/3)} \left(\frac{r}{aL}\right)^{1/3} \left\{K_{1/3}\left(\frac{r}{aL}\right) - \left(\frac{r}{2aL}\right) K_{2/3}\left(\frac{r}{aL}\right)\right\}$$

a = 1.339

K = modified Bessel function of the second kind

L = longitudinal isotropic turbulence integral scale

<u>Dryden</u>

$$B_{U_{ij}}(r) = e^{-r/L}$$

$$B_{V_{ij}}(r) = e^{-r/L}\left[1 - \frac{1}{2}\right]$$

Figure 6.11. von Karman and Dryden expressions for the correlation coefficients:

von Karman and the Dryden spectrum, therefore, are based on the assumption that Taylor's hypothesis is valid and that, in general, time-dependent correlations can be converted to a spatial correlation by the relationship $r = \overline{W}t$. The validity of Taylor's hypothesis is well justified by the data. Figure 6.12 compares the spatial correlation converted to time with Taylor's hypothesis to the computed time correlation. The agreement is excellent.

The Dryden and von Karman correlations were computed using length scales L_1 and L_4 discussed in Chapter V. As shown in Chapter VII, L_4 results in the best agreement of the spectra with the von Karman and Dryden models. Comparison of the theory with the experimental data are shown in Figures 6.13 through 6.24.

The agreement with the theory, in general, is varied. Figures 6.13 and 6.14 show reasonable agreement with the experimental results; however, Figure 6.16 shows poor agreement. This could possibly be explained if Run #8623 was along the array (that is, perpendicular to the building) where it might be anticipated that Tower 4 should be disturbed by the presence of the building.

Considering the results in Figures 6.16 through 6.18, the theoretical correlations do not show the initial sharp drop-off that is indicated by the experimental data; however, at values of lag time greater than 5 to 10 seconds, the analytical models take on the same characteristic slope as the experimental data.

The analytical correlations in Figures 6.13 through 6.18 are computed with a length scale based on Method 1, i.e., L_1. If one computes the length scale by Method 4 (see Chapter V), the theoretical curves now
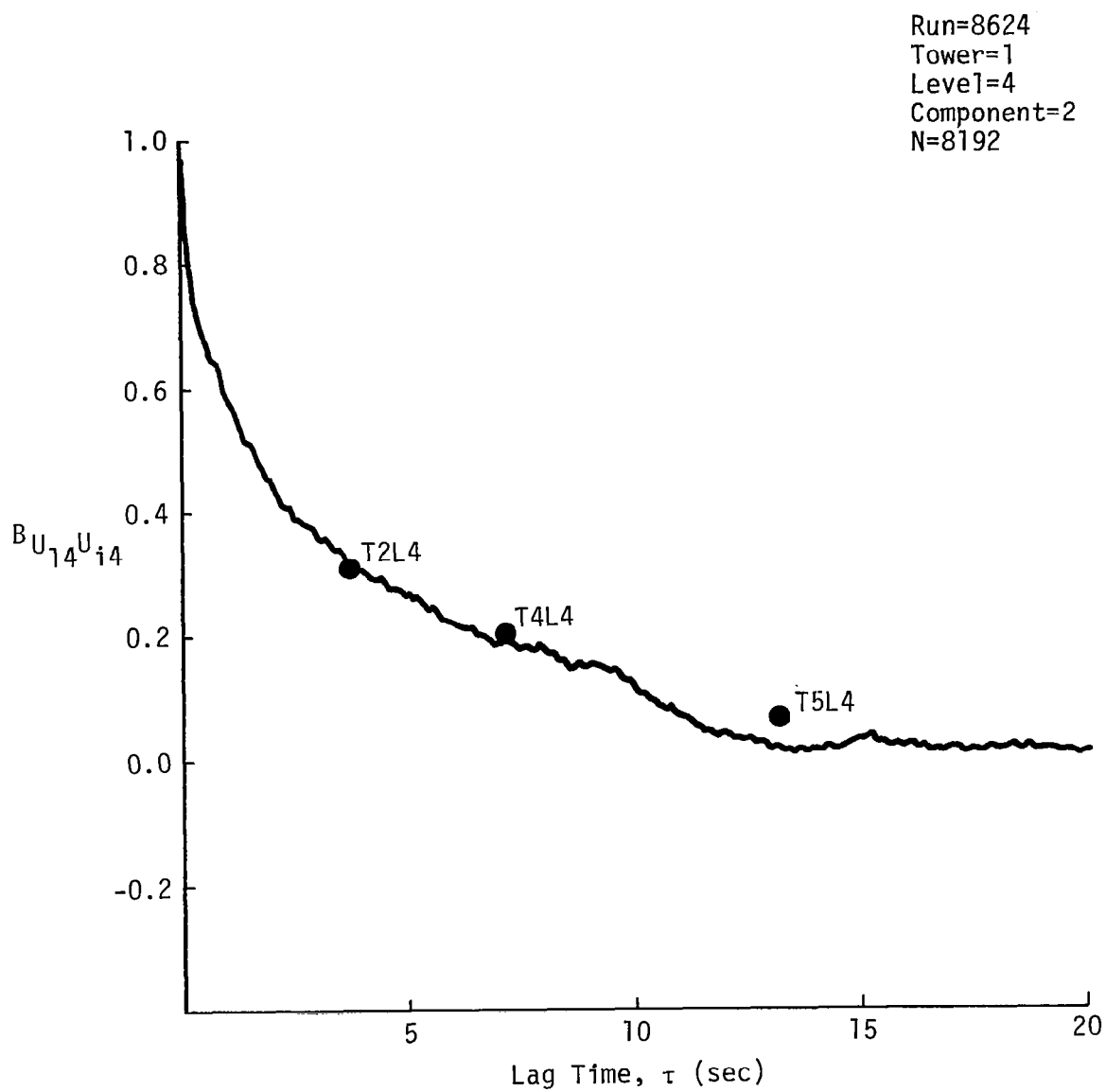
Figure 6.12. Illustration of validity of Taylor's hypothesis (● spatial correlation converted to a time correlation with the relationship $\ell = \overline{W}\tau$).
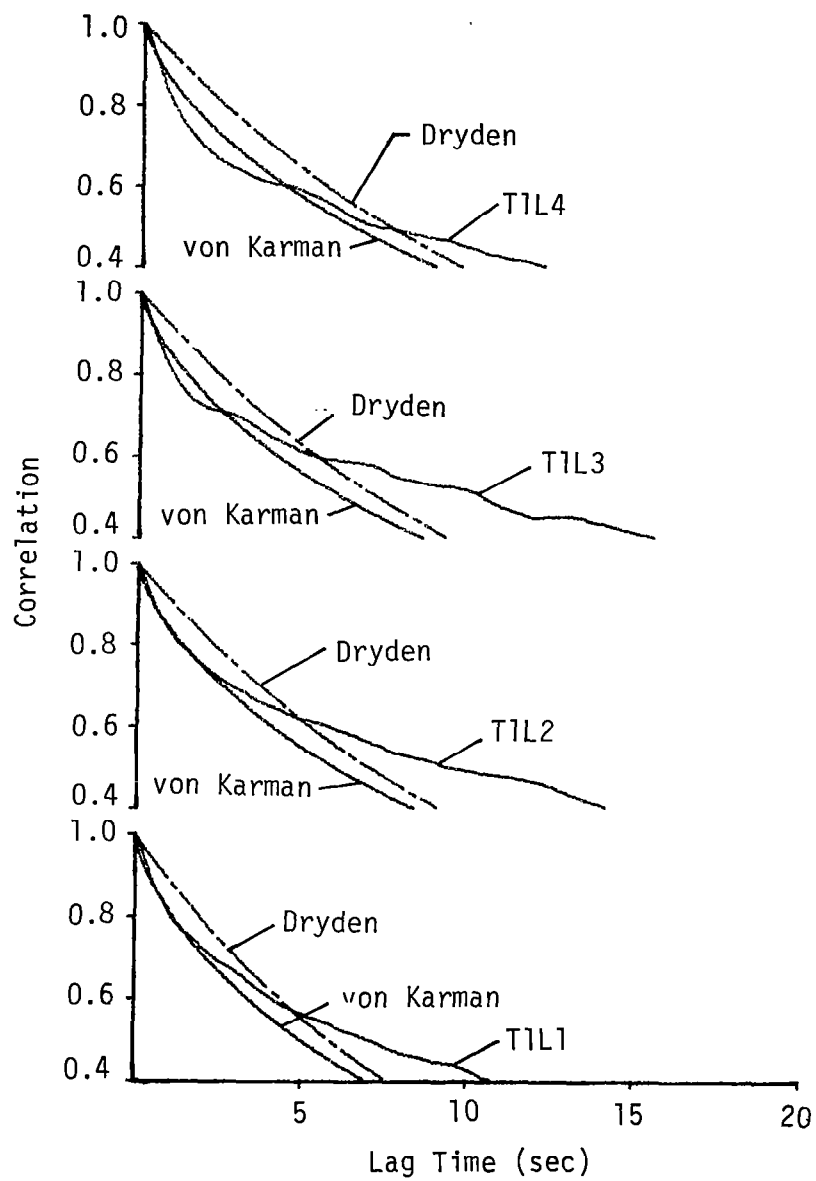
Figure 6.13. Comparison with von Karman and Dryden expressions for the longitudinal correlation (length scale L_1, T1, Run #8623).

74
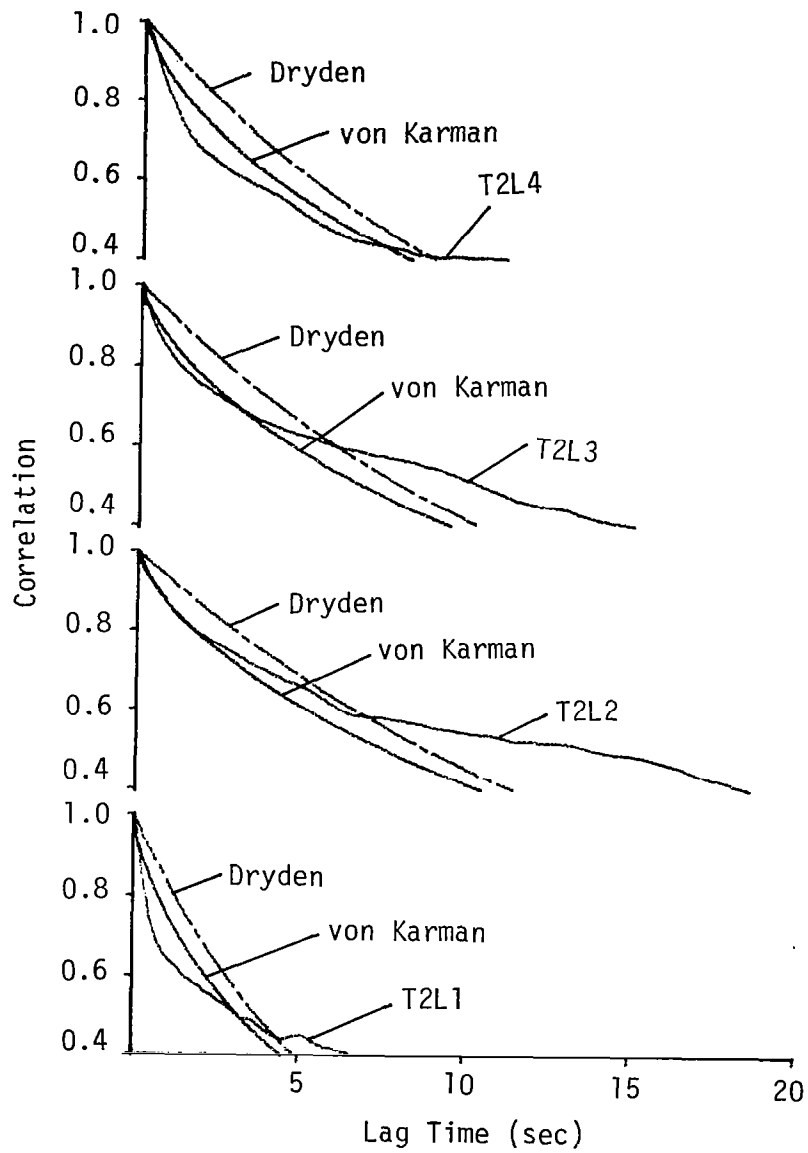
Figure 6.14. Comparison with von Karman and Dryden expressions for the longitudinal correlation (length scale L_1, T2, Run #8623).
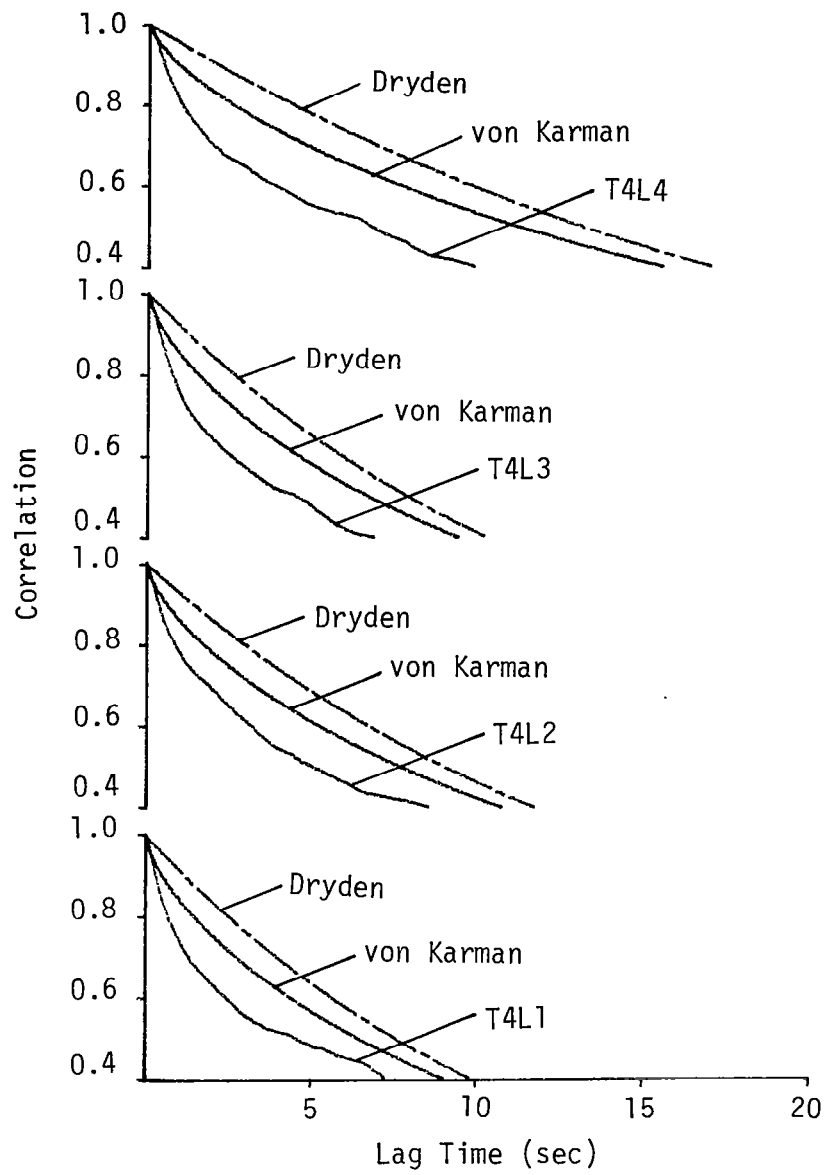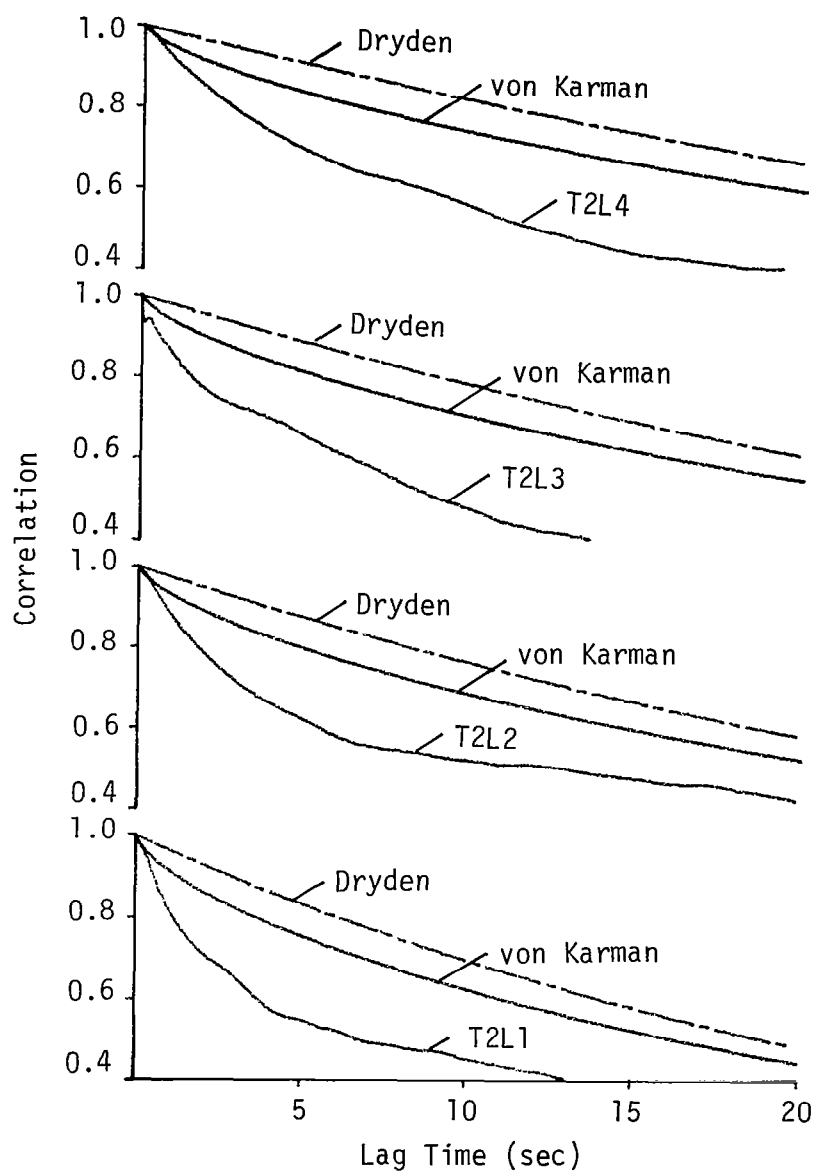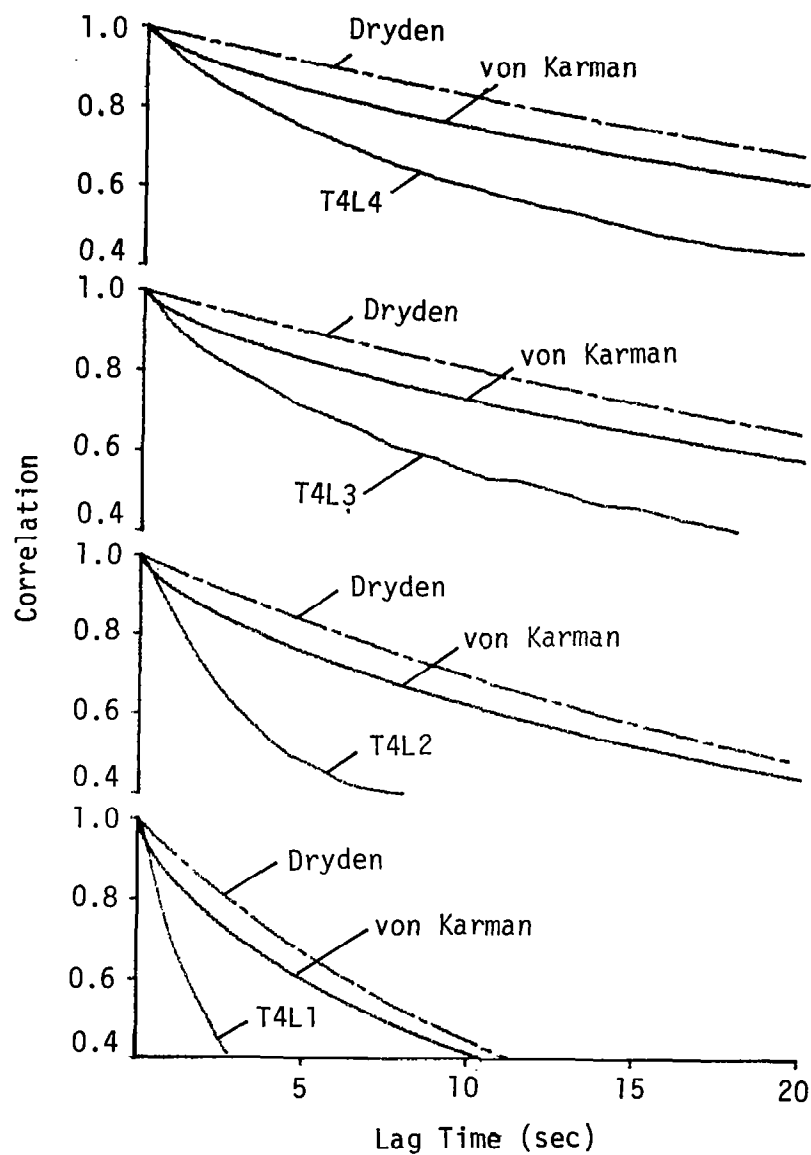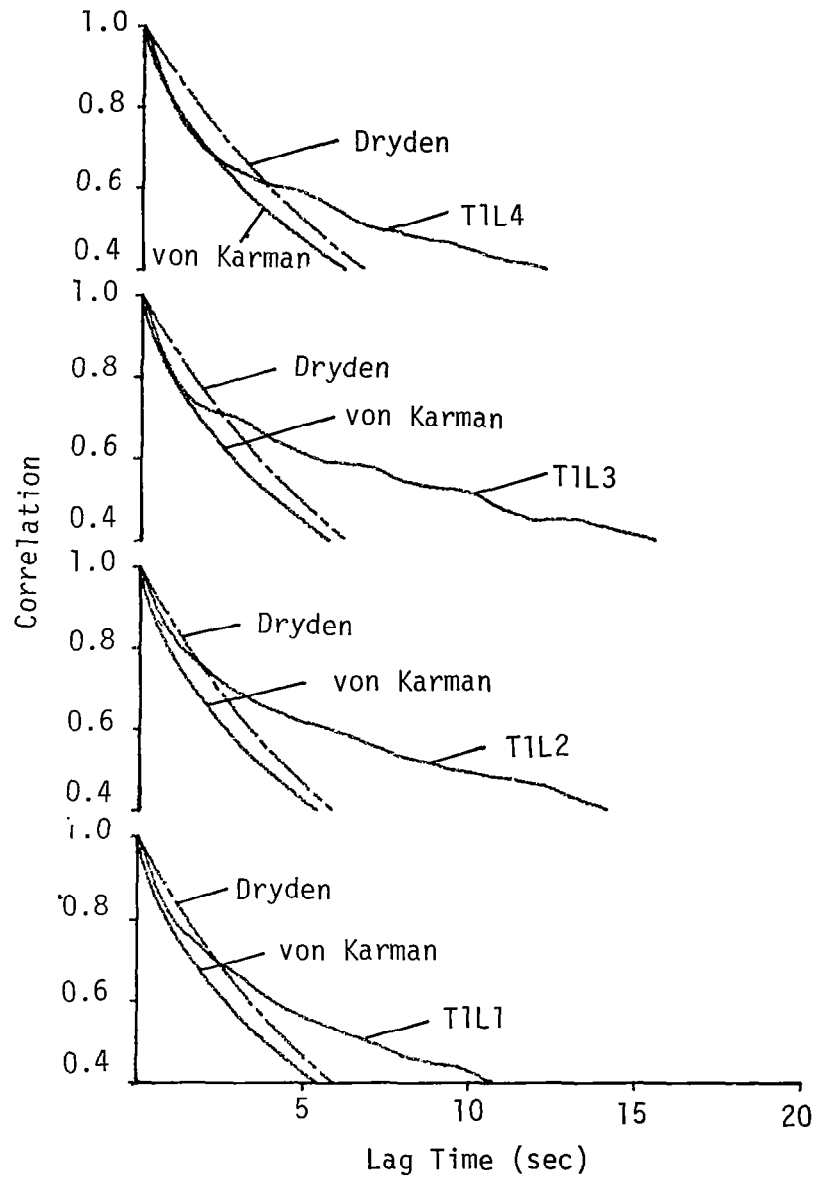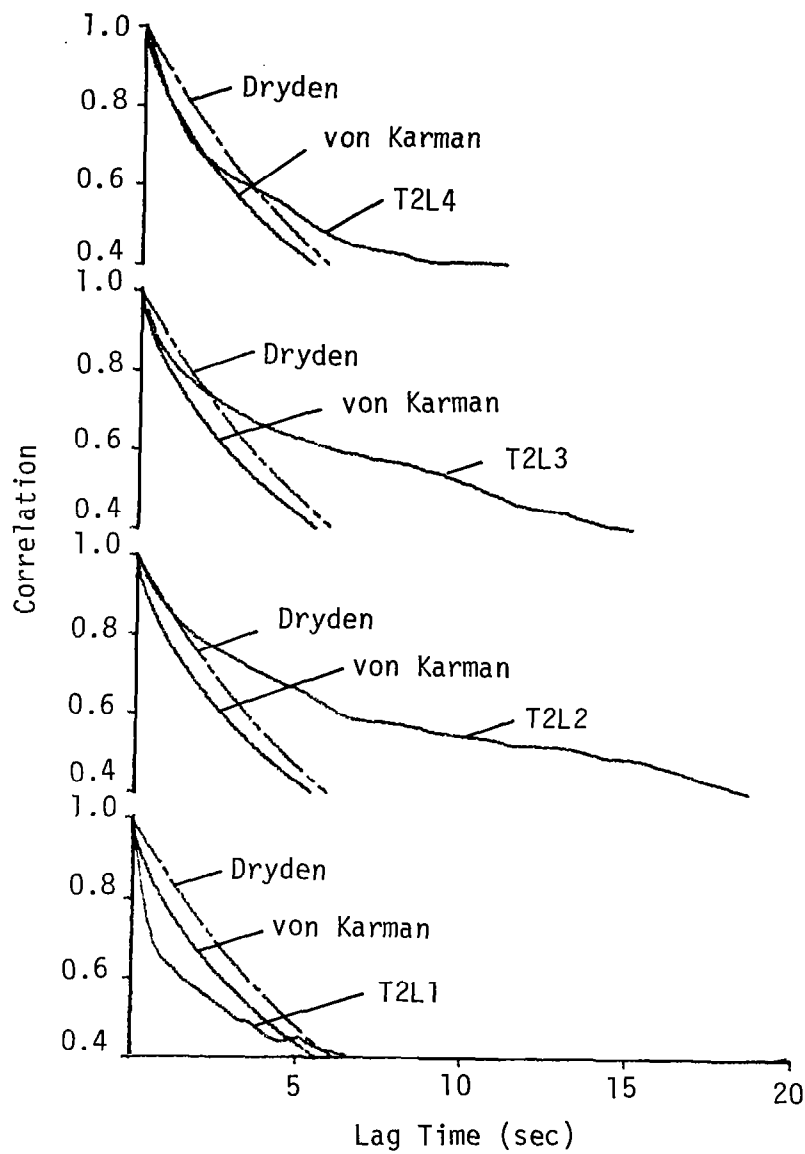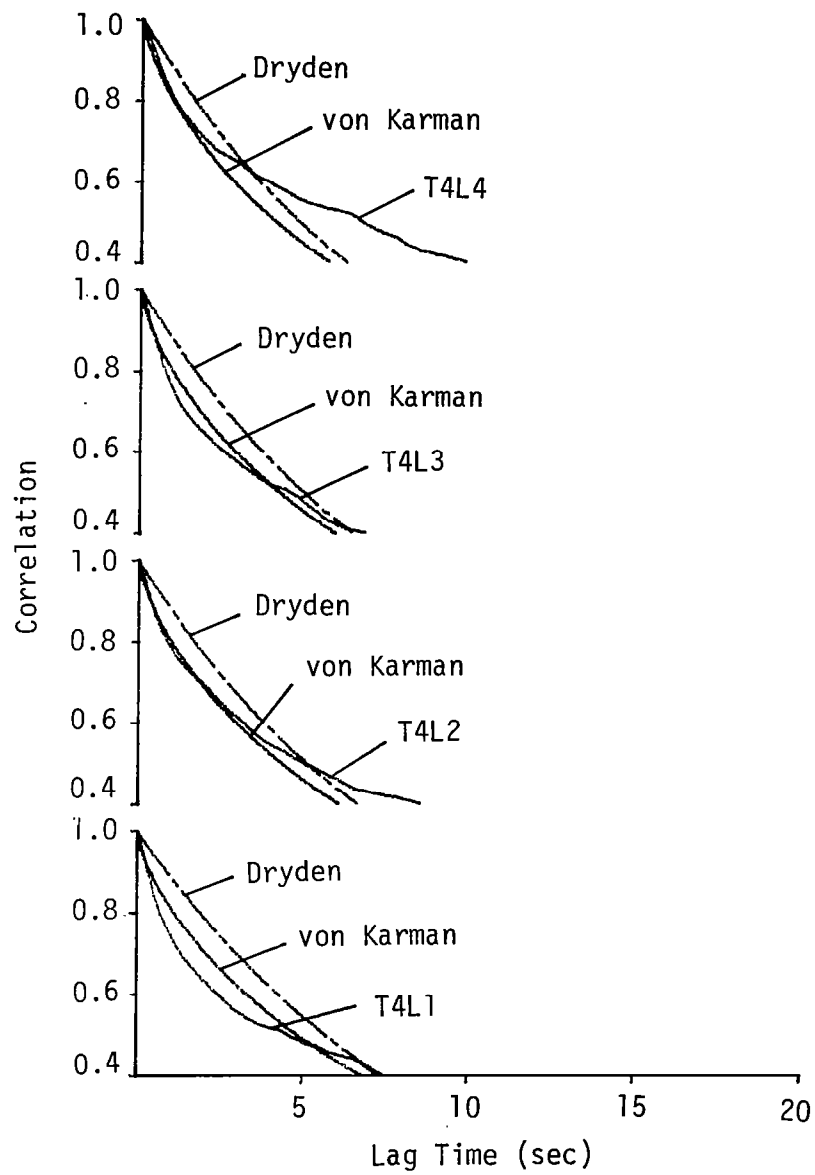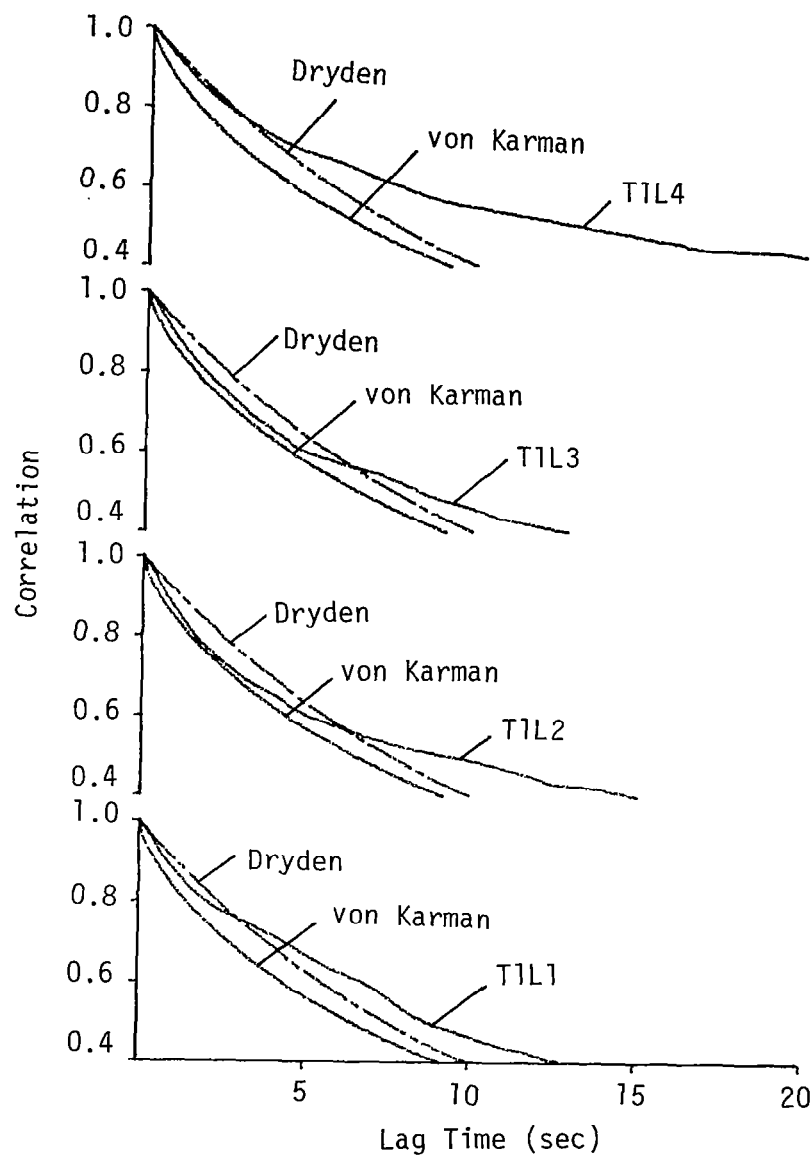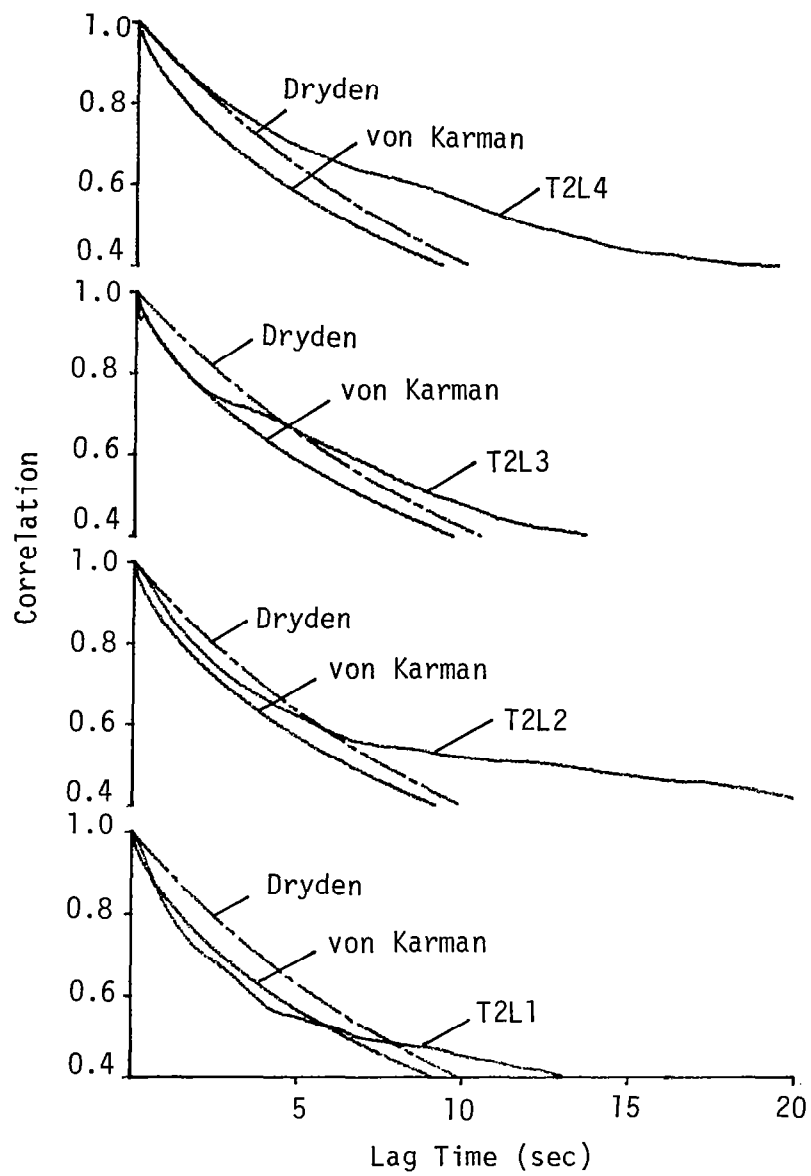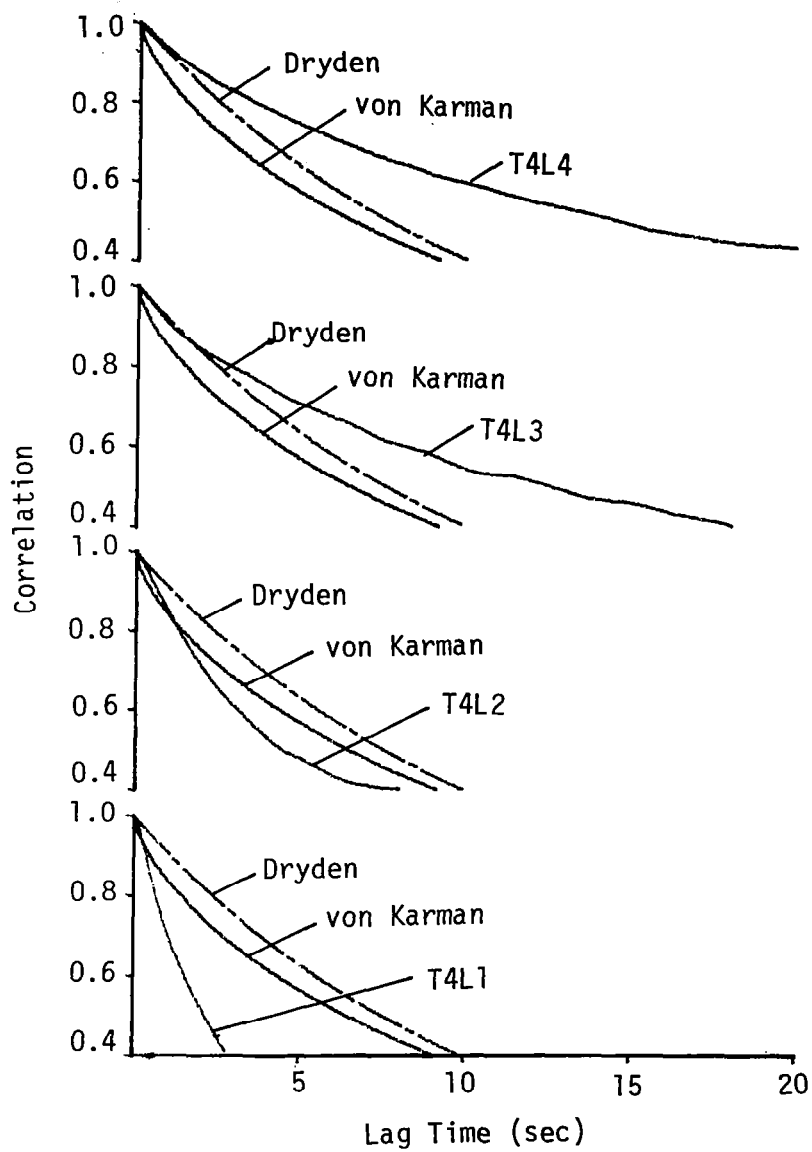
Figure 6.15. Comparison with von Karman and Dryden expressions for the longitudinal correlation (length scale L_1, T4, Run #8623).
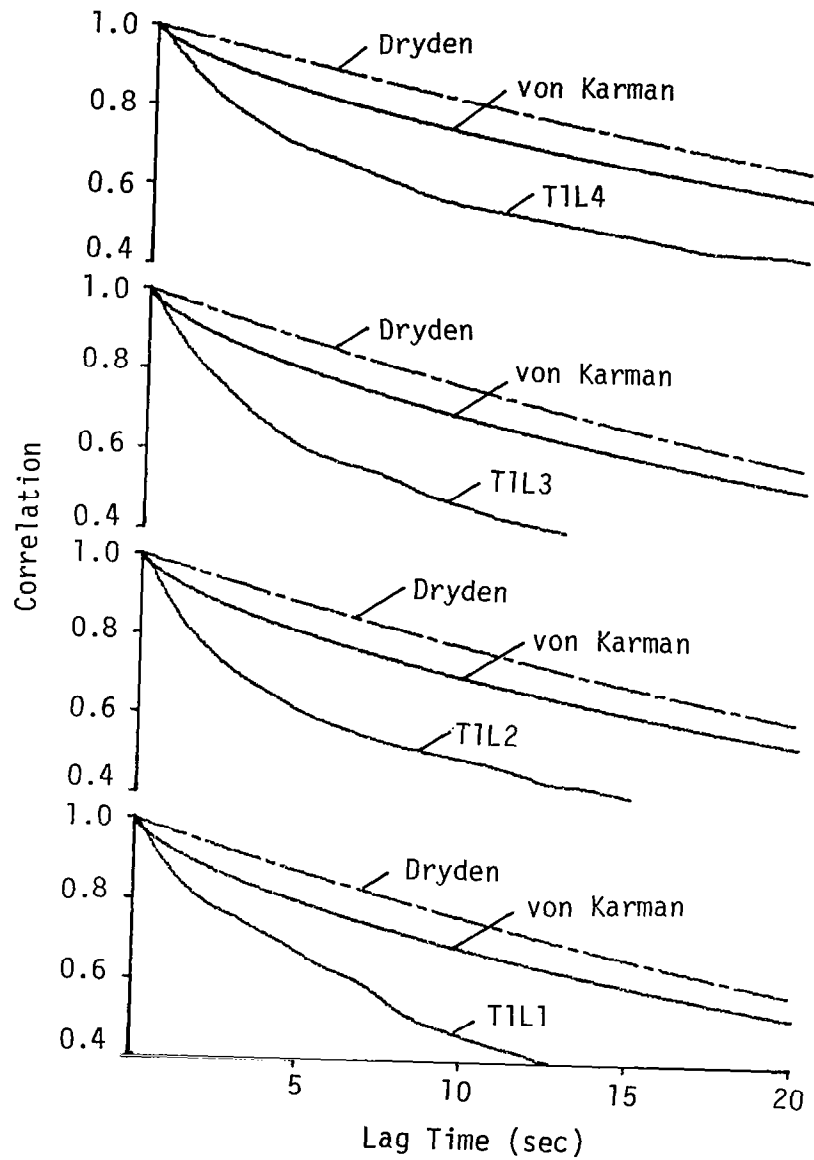
Figure 6.16. Comparison with von Karman and Dryden expressions for the longitudinal correlation (length scale L_1, T1, Run #8624).

Figure 6.17. Comparison with von Karman and Dryden expressions for the longitudinal correlation (length scale L_1, T2, Run #8624).

Figure 6.18. Comparison with von Karman and Dryden expressions for the longitudinal correlation (length scale L_1, T4, Run #8624).

Figure 6.19. Comparison with von Karman and Dryden expressions for the longitudinal correlation (length scale L_4, T1, Run #8623).

Figure 6.20.   Comparison with von Karman and Dryden expressions for the longitudinal correlation (length scale L_4, T2, Run #8623).

Figure 6.21. Comparison with von Karman and Dryden expressions for the longitudinal correlation (length scale L_4, T4, Run #8623).

Figure 6.22. Comparison with von Karman and Dryden expressions for the longitudinal correlation (length scale L_4, T1, Run #8624).

Figure 6.23. Comparison with von Karman and Dryden expressions for the longitudinal correlation (length scale L_4, T2, Run #8624).

Figure 6.24. Comparison with von Karman and Dryden expressions for the longitudinal correlation (length scale L_4, T4, Run #8624).

show very good agreement with the data for the first 2 to 3 seconds and then depart at a slope which more closely approximates the slope shown in Figures 6.13 through 6.18 based on a length scale computed by Method 1. Figure 6.24 shows that the correlation, particularly near the ground, does not behave like the theoretical correlation in either case. This is to be expected, however, in view of the fact that the anemometers on Tower 4 at Levels 1 and 2 are in the wake region behind the simulated block building.

It is apparent that by selecting a length scale which behaves more like the length scale calculated by Method 4 for values of lag time on the order of 2 to 3 seconds and then converting to a length scale more similar to that computed by Method 1, good correlation of the data would be given. At present, however, there is no theoretical justification for this approach. It seems, however, by empirically selecting the length scale, relatively good agreement with the experimental data could be obtained using either the von Karman or the Dryden spectra. The choice of the von Karman versus the Dryden models for spectra is described and elaborated upon in Chapter VII.

The comparison of experiment with theory clearly indicates that new empirical correlations which incorporate the effects of surface rough-ness and other ground effects are needed to provide better agreement between theory and the experimental results of this study.

CHAPTER VII

SPECTRUM ANALYSES

This chapter addresses the auto-spectra for the wind speed data. Only the longitudinal and vertical components at Level 4 are considered. The theory of the spectra is first addressed. Then three correlation models--von Karman, Dryden, and Kaimal--are reviewed. These models are compared with the experimental results.

A. Theory

The two-sided power spectral density of a random process {x} is defined as the Fourier transform of its auto-correlation function (Bendat and Persol 1971).

$$S_X(f) = \int_{-\infty}^{\infty} R_X(\tau)e^{-i2\pi f\tau}d\tau \qquad (7.1)$$

where f is frequency in cycles per second. From the symmetry properties of stationary correlation functions, it follows that

$$S_X(f) = S_X(-f) \qquad (7.2)$$

These equations state that the two-sided power spectral density function is real, non-negative, and an even function of f; therefore, the one-sided power spectral density function, $\phi_X(f)$ where f varies only over $(0,\infty)$, is defined by

$$\phi_X(f) = 2S_X(f) \qquad (7.3)$$

or

$$\phi_X(f) = 4 \int_0^\infty R_X(\tau) \cos 2\pi f \tau d\tau \tag{7.4}$$

It is noted that negative f has no physical significance; and hence, the power spectrum contains no phase information.

For stationary random data, two common methods for computing the power spectral density function are (1) the standard method based on computing the power spectral density function from a straightforward Fourier transform of the auto-correlation function, and (2) the direct Fourier transform method based on computing the power spectral density function via a finite-range fast Fourier transform (FFT) of the original data.

Briefly, the standard method is computed as follows. For sampled data from a transformed record x(f), which is stationary with $\bar{x} = 0$, a raw estimate $\phi_X'(f)$ of a true power spectral density function $\phi_X(f)$ is defined for an arbitrary f in the range $0 \leq f \leq f_c$ by

$$\phi_X'(f) = 2h \left[R_0' + 2 \sum_{r=1}^{m-1} R_r' \cos\left(\frac{\pi r f}{f_c}\right) + R_m' \cos\left(\frac{\pi m f}{f_c}\right) \right] \tag{7.5}$$

where h is the time interval between samples, R_r' is the estimate of the auto-correlation function at lag r, m is the maximum lag number, $f_c = 1/2h$ is the cut-off frequency, and $\phi_X'(f)$ is the raw estimate of true value $\phi_X(f)$ at frequency f. Equation 7.5 is a discrete approximation to the theoretical relation of Equation 7.1. For this method, the discrete frequencies are given by

$$f = \frac{kf_c}{m} \qquad k = 0, 1, 2, \cdots m \tag{7.6}$$

The FFT is computed as follows. The direct Fourier transform method is used to compute estimates of power spectral density functions directly from the original data value. This method has been used throughout most of this report. A raw estimate of the power spectral density function, $\phi_x'(f)$, at any frequency f is given by the formula

$$\phi_x'(f) = \frac{2}{T}\left|X(f,T)\right|^2 \tag{7.7}$$

Here, T is Nh and

$$X(f,T) = h \sum_{n=0}^{N-1} x_n \exp(-i2\pi fnh) \tag{7.8}$$

At the usual FFT discrete frequency values

$$f_R = \frac{k}{T} = \frac{k}{Nh} \qquad k = 0, 1, 2, \cdots N-1 \tag{7.9}$$

the Fourier components are defined by

$$X_k = \frac{X(f_k,T)}{h} = \sum_{n=0}^{N-1} x_n \exp\left(-i\,\frac{2\pi kn}{N}\right) \tag{7.10}$$

Hence, the power spectrum estimate becomes

$$\phi_k' = \phi_x'(f) = \frac{2}{Nh}\left|X(f_k,T)\right|^2 = \frac{2h}{N}\left|X_k\right|^2 \tag{7.11}$$

The following steps were used to compute power spectra estimates via the FFT procedures. Assume that the sample size for the data sequence x_n is initially of arbitrary size N.

1. Truncate the data sequence or add zeros so that $N = 2^P$.

2. Taper the resulting sequence using the cosine taper data
   window or some other appropriate tapering.

3. Compute the

$$X_k = \frac{X(f_k, T)}{h} = \sum_{n=0}^{N-1} x_n \exp\left(-i \frac{2\pi kn}{N}\right) \qquad k = 0, 1, \cdots N-1$$

   using the FFT method.

4. Compute the ϕ_k' of Equation 7.11 for $k = 0, 1, \cdots N-1$.

5. Adjust these estimates for the scale factor due to taper-
   ing. (Example: By replacing ϕ_k' by $(1/0.875)\phi_k'$ if the
   cosine tapering is used.)

Steps 2 and 5 were not used in the present report since N is rela-
tively large and, as shown later, no significant effect was observed
between tapered and untapered spectra.

The discrete frequency of the two computational methods described
above are not the same for the same k, except when N = 2 m. In the FFT
method, adding zeros (Step 1 above) affects the discrete frequency value.
The usual spacing is given by

$$\Delta f = \frac{1}{Nh} \tag{7.12}$$

If zeros are added to a data sequence, the spacing of the estimates
become

$$\Delta f' = \frac{1}{(N + N_z)h} \tag{7.13}$$

where N_z represents the number of added zeros. Thus, comparing $\phi(f)$
values computed by the two different methods at frequency values corres-
ponding to k are only in agreement if N = 2 m. In computing Figure 7.1

90
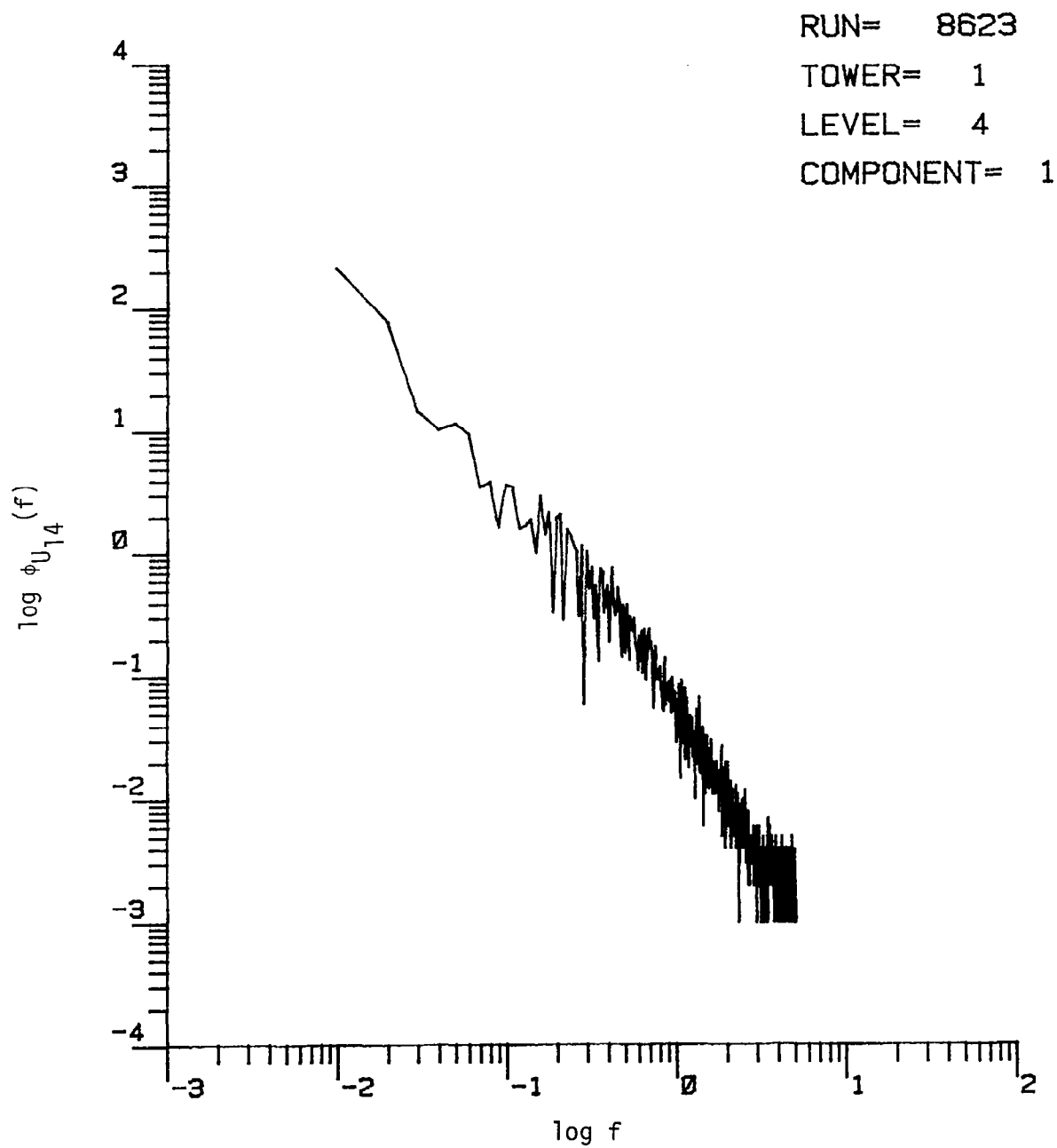
Figure 7.1. Power spectral density function calculated by the standard method (Equation 7.5).

by the power spectral density function by the standard method, the time history was divided into 10 segments of 1024 datum points each. These 1024 datum points were introduced into Equation 7.5 to calculate each of the 10 spectra and the 10 segments were ensemble averaged to give the smoothed spectrum value. Figure 7.2 shows the power spectral density function calculated by the FFT method. The same segment averaging procedure was employed. Comparison of Figure 7.1 and Figure 7.2 indicates that the spectrum in Figure 7.1 is slightly larger than that in Figure 7.2 at low frequency. For higher frequencies, the spectrum in Figure 7.1 is less than that of Figure 7.2. This difference, however, is certainly negligible. Thus because of the significant saving of computer time associated with the FFT method, it was used throughout this study.

In using the FFT method, the tapering window was found to not have a significant effect on the result. Figure 7.3 shows the spectrum calculated with a cosine taper data window. Comparison of this figure with Figure 7.2 shows no noticeable difference in the spectrum.

As mentioned earlier, smoothing was accomplished by segment averaging for all spectra. The smoothing procedure is carried out as follows. The original time record, T_r, is divided into q separate time slices, where each time slice is of length T_r'; therefore, $T_r = q \cdot T_r'$. The smooth spectrum is given by

$$\phi_k' = \frac{1}{q}\left(\phi_{k,1}' + \phi_{k,2}' + \cdots + \phi_{k,q}'\right) \tag{7.14}$$

where $\phi_{k,q}'$ is the raw spectrum at frequency f_k of the qth time slice.
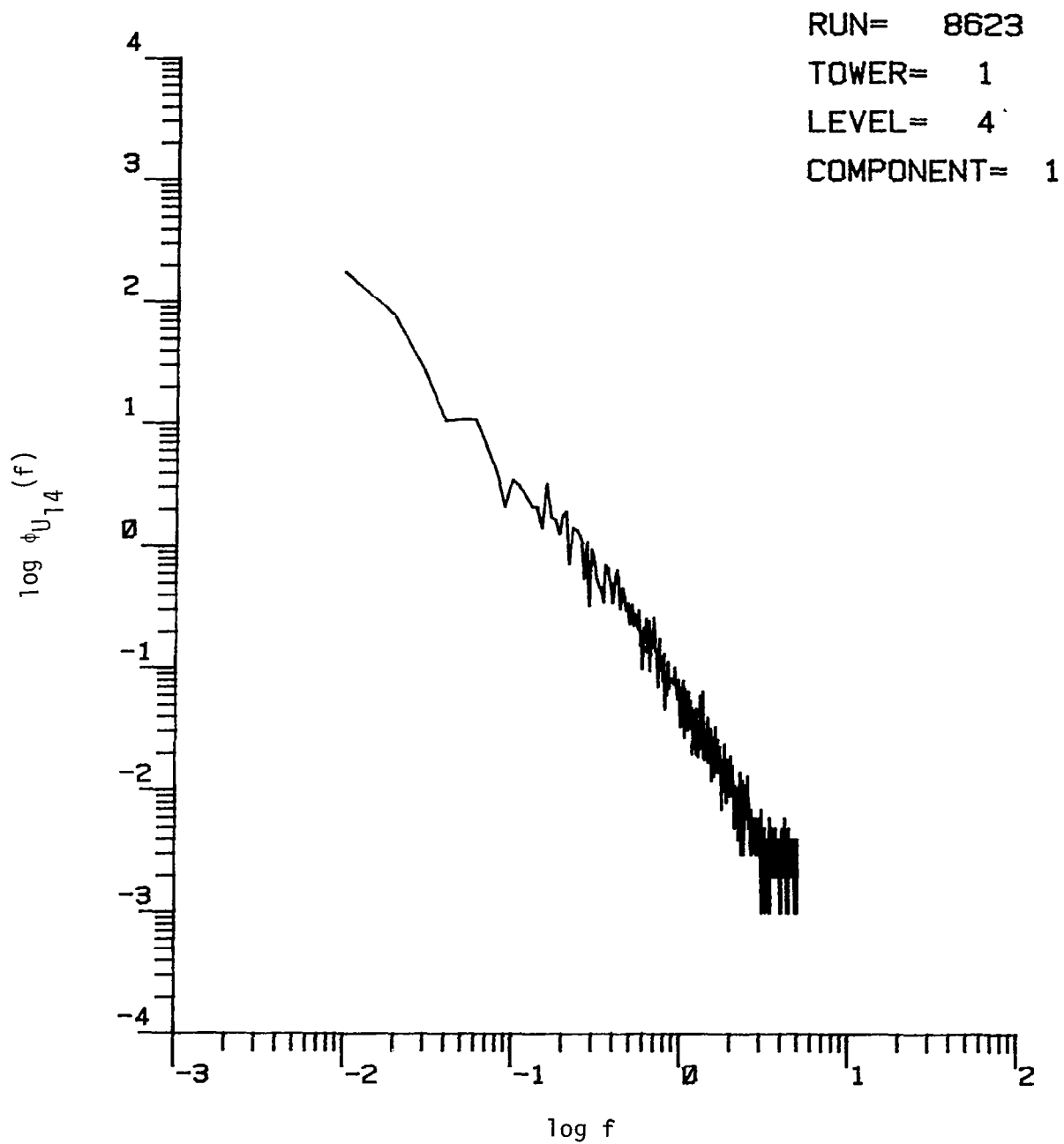
Figure 7.2. Power spectral density function calculated by the FFT method without using a tapering window.
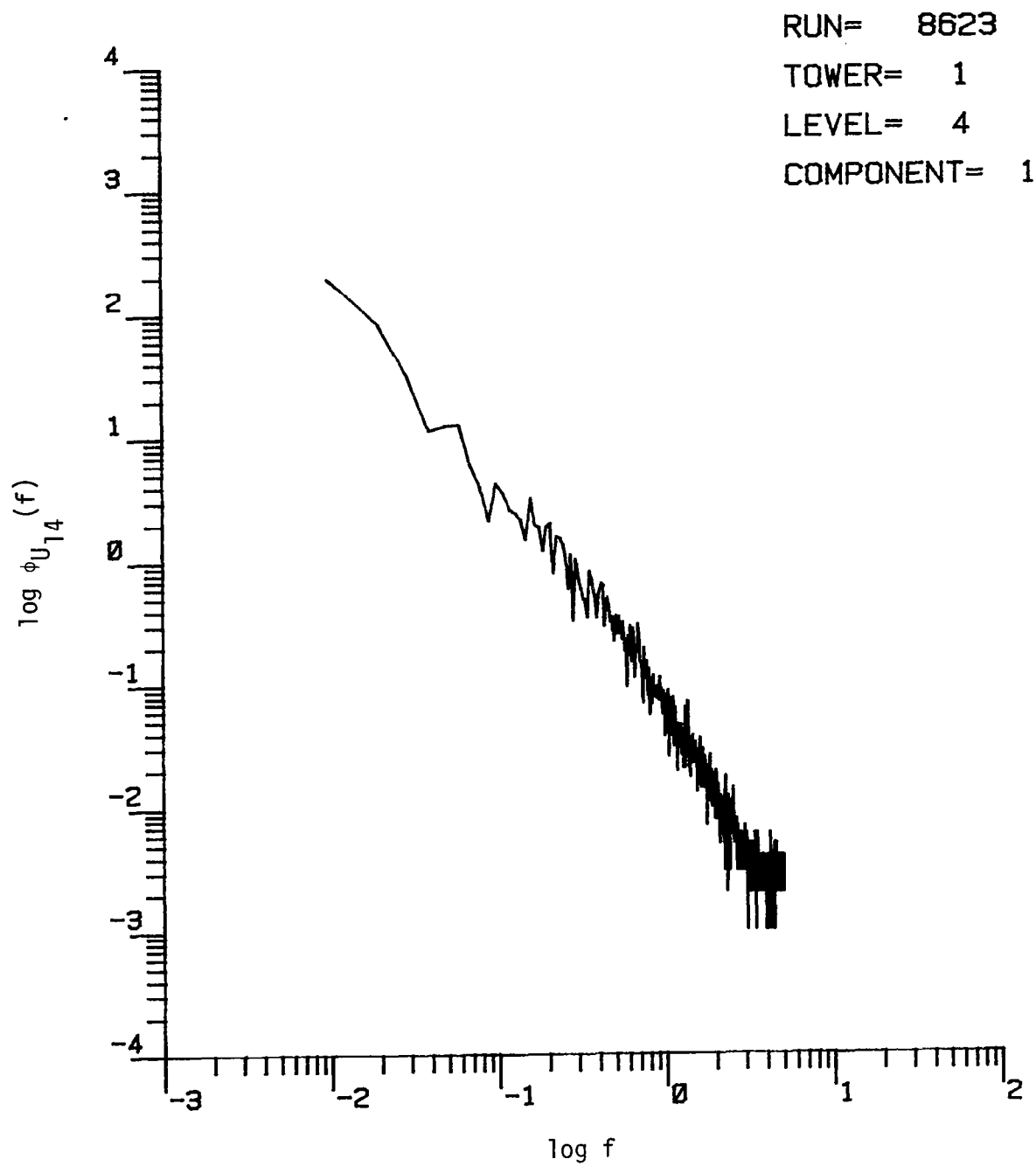
Figure 7.3. Power spectral density function calculated by the FFT
method with a cosine tapering window.

The bandwidth B_e for this approach becomes $1/T_r'$. Thus the degree of freedom is $n = 2B_eT_r = 2q$. The normalized standard error, E_r, is then given by

$$E_r = \sqrt{\frac{1}{B_eT_r}} = \sqrt{\frac{1}{q}} \tag{7.15}$$

Therefore, the larger the value of q, the smaller the normalized standard error. In the present study, the FFT paraments are given by

$h = 0.1$ second; $f_c = 1/2h = 5$ cycles/second; $q = 10$

$T_r = 1024$ seconds; $T_r' = T_r/q = 102.4$ seconds; $N = T_r/h = 10240$

Thus,

$B_e = 1/T_r' = 0.00977$ cycle/second

and

$$E_r = \sqrt{\frac{1}{q}} = 0.316$$

This gives an rms error of approximately 32 percent for all spectra presented.

B. Spectra Correlation Models

Several semi-mathematical models have been suggested to describe the power spectral density of the three turbulence gust components. Notable among these are the von Karman, Dryden, and Kaimal. von Karman (1961) suggested the following forms of the one-dimensional spectrum function, ϕ, for each velocity fluctuation component:

$$\phi_{w_x}(K) = \sigma_{w_x}^2 \frac{2L_{w_x}}{\pi} \frac{1}{[1 + (1.339L_{w_x}K)^2]^{5/6}}$$

$$\phi_{w_y}(K) = \sigma_{w_y}^2 \frac{L_{w_y}}{\pi} \frac{1 + 8/3(1.339L_{w_y}K)^2}{[1 + (1.339L_{w_y}K)^2]^{11/6}}$$

(7.16)

$$\phi_{w_z}(K) = \sigma_{w_z}^2 \frac{L_{w_z}}{\pi} \frac{1 + 8/3(1.339L_{w_z}K)^2}{[1 + (1.339L_{w_z}K)^2]^{11/6}}$$

where the subscripts w_x, w_y, and w_z represent longitudinal, lateral, and vertical fluctuations, respectively. σ is the standard deviation or rms value; L is the integral length scale; K is the wave number, $2\pi f/\overline{W}$; and $\overline{W}$ is the mean wind velocity at the height, z. von Karman's spectra functions are specifically for isotropic, homogeneous turbulence. For spectra measured at the higher levels, i.e., Level 4, reasonable agreement may be expected with the data. However, near the ground and in the vicinity of the building it is not likely that the spectra correlations will agree with experiment. Thus, the results in Subchapter C are presented only for Level 4.

Dryden (1961), on the other hand, suggested that the shape of the velocity correlation curve can be approximated by an exponential function. In this case, the one-dimensional Dryden spectra become:

$$\phi_{w_x}(K) = \sigma_{w_x}^2 \frac{2L_{w_x}}{\pi} \frac{1}{1 + L_{w_x}^2 K^2}$$

(7.17a)

$$\phi_{w_y}(K) = \sigma_{w_y}^2 \frac{L_{w_y}}{\pi} \frac{1 + 3L_{w_y}^2 K^2}{(1 + L_{w_y}^2 K^2)^2} \tag{7.17b}$$

$$\phi_{w_z}(K) = \sigma_{w_z}^2 \frac{L_{w_z}}{\pi} \frac{1 + 3L_{w_z}^2 K^2}{(1 + L_{w_z}^2 K^2)^2} \tag{7.17c}$$

These spectra, although receiving considerable use because of their simpler form, are normally reported as not representing atmospheric data well. However, as shown in Subchapter C, depending on the choice of length scale, reasonable agreement is shown for data from Run #8624.

In a recent series of papers describing the spectral properties of atmospheric turbulence over a flat homogeneous field site, Kaimal (1973) shows for stable conditions that with appropriate nondimensionalization, the spectra can be correlated with a universal curve having the empirical formula

$$\frac{f}{\sigma^2} \phi(f) = \frac{0.164(\eta/\eta_o)}{1 + 0.164(\eta/\eta_o)^{5/3}} \tag{7.18}$$

where f is frequency in cycles/second, $\eta = fz/\overline{W}$ is the reduced frequency, z is height above level terrain, and η_o is a scaling parameter related to the prevailing atmospheric stability. Frost et al. (1978) suggest the extension of this relationship to neutral conditions by specifying reduced frequency scaling factors of:

$$\eta_{oW_x} = 0.0144 \tag{7.19a}$$

$$\eta_{oW_y} = 0.0265 \tag{7.19b}$$

$$\eta_{oW_z} = 0.0962 \tag{7.19c}$$

Frost (1980) later found these values to vary slightly with height.

The Kaimal model, in effect, uses height z above level terrain as a length scale. The von Karman and Dryden models employ derived length scales. Normally the integral length scale, Method 1 of Chapter V, is used. However, as also shown in Chapter V, several other analytical forms of the length scale have been suggested. The von Karman and Dryden spectra models show strong dependence on length scale, and considerable disagreement exists as to the best model of L to use. Subchapter C makes comparison of the data with the spectra using different length scales and presents some conclusion regarding the best value.

C. Results and Comparison with Correlation Models

This subchapter presents only spectra computed for the upper tower levels, Level 4, for both Runs #8623 and #8624. This level is expected to be least affected by the presence of the block building in the flow field. Spectra at Level 4 for both the longitudinal and vertical wind speed fluctuations are presented. Turbulence spectra plotted as log $\phi(f)$ versus log (f) for the longitudinal component at all towers and levels are given in Appendix D.

The computed spectra in this subchapter are plotted in normalized form, i.e.,

$$G_{u_{ij}}(f) = f\phi_{u_{ij}}(f)/\sigma^2_{u_{ij}} \tag{7.20}$$

versus $\eta = fz/\overline{W}$. In comparing the correlation models with the data, LK is written as $L2\pi f/\overline{W} = (2\pi L/z)(fz/\overline{W}) = \eta/\eta_o$ where $\eta_o = z/2\pi L$.

Before comparing the correlation models with the data, some general characteristics of the data are pointed out. Figures 7.4 and 7.5 show typical spectra for Tower 1 at Level 4 for Runs #8623 and #8624, respectively. Both spectra tail-off at high reduced frequency ($2 > \eta > 4$) to an approximate slope of -2.9 (i.e., $\phi(f) \simeq f^{-3.9}$), suggesting the end of the inertial subrange and the beginning of the viscous dissipation range. Interestingly, however, at low reduced frequencies ($\eta < 1$), the data for Run #8623 have a slope of -2/3 (i.e., $\phi(f) \simeq f^{-5/3}$) and for Run #8624 a slope of -1 (i.e., $\phi(f) \simeq f^{-2}$). Thus, in the inertial subrange, the data for Run #8623 best fit a von Karman or Kaimal spectrum; whereas, the data for Run #8624 best fit a Dryden spectrum. The explanation for this is not clear. The building is not expected to affect these results because measurements at Tower 1 Level 4 should be essentially undisturbed by the block building. Moreover, inspection of Figures 3.2 and 3.3, pages 31 and 32, show that the wind for each run approaches over similar terrain. Thus, terrain effects should not be a factor. Finally, although the atmospheric stability is unknown, it is generally not reported to affect the slope of the spectra in the inertial subrange. Moreover, at the high mean wind speeds (approximately 7.2 m/s at Level 4 for Run #8623 and 5.9 m/s for Run #8624), the atmospheric boundary layer is expected to be close to neutral for both runs.

Figures 7.6 through 7.9 and Figures 7.10 through 7.13 compare the three analytical spectra models (von Karman, Dryden, and Kaimal) with
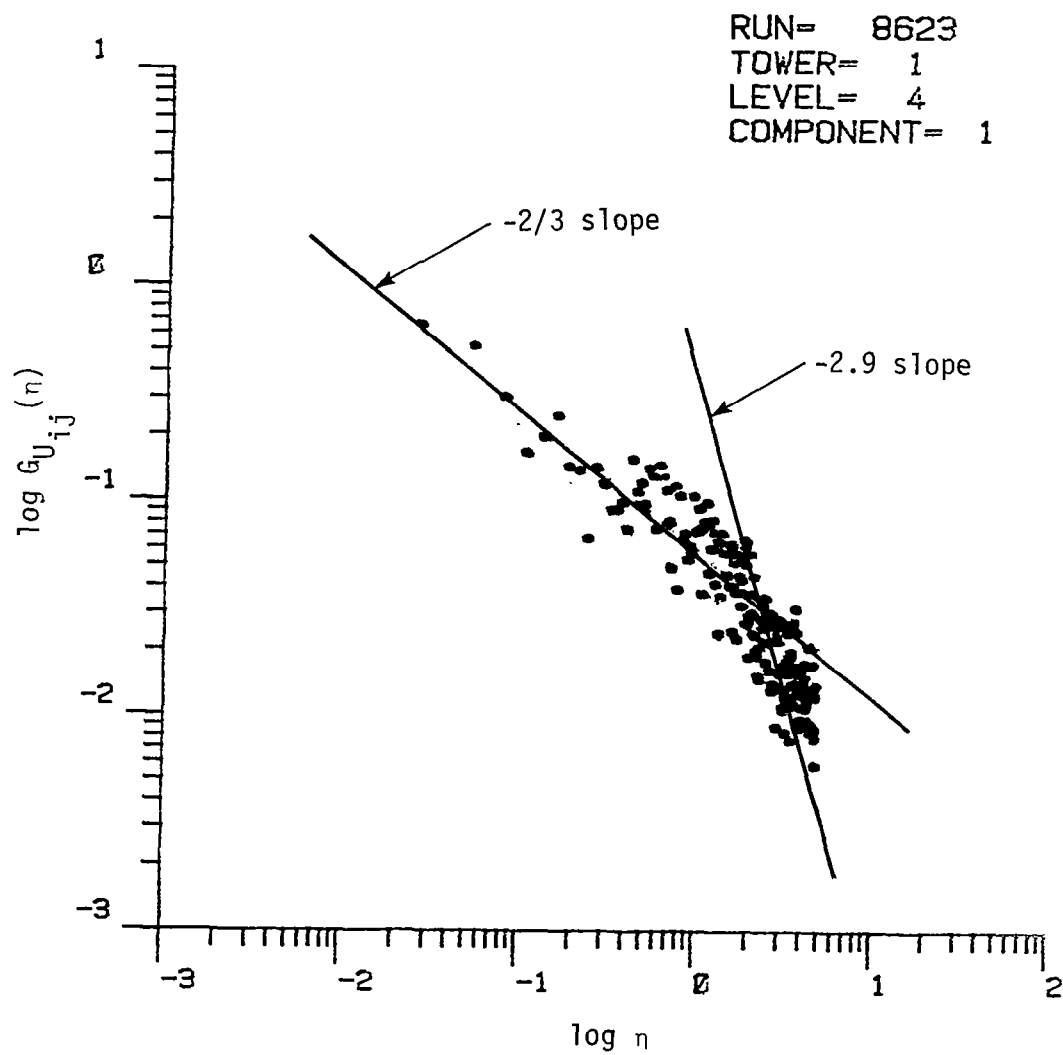
Figure 7.4. Characteristic slope of spectra is -2/3 at L4 for Run #8623.

Figure 7.5. Characteristic slope of spectra is -1 at L4 for Run #8624.
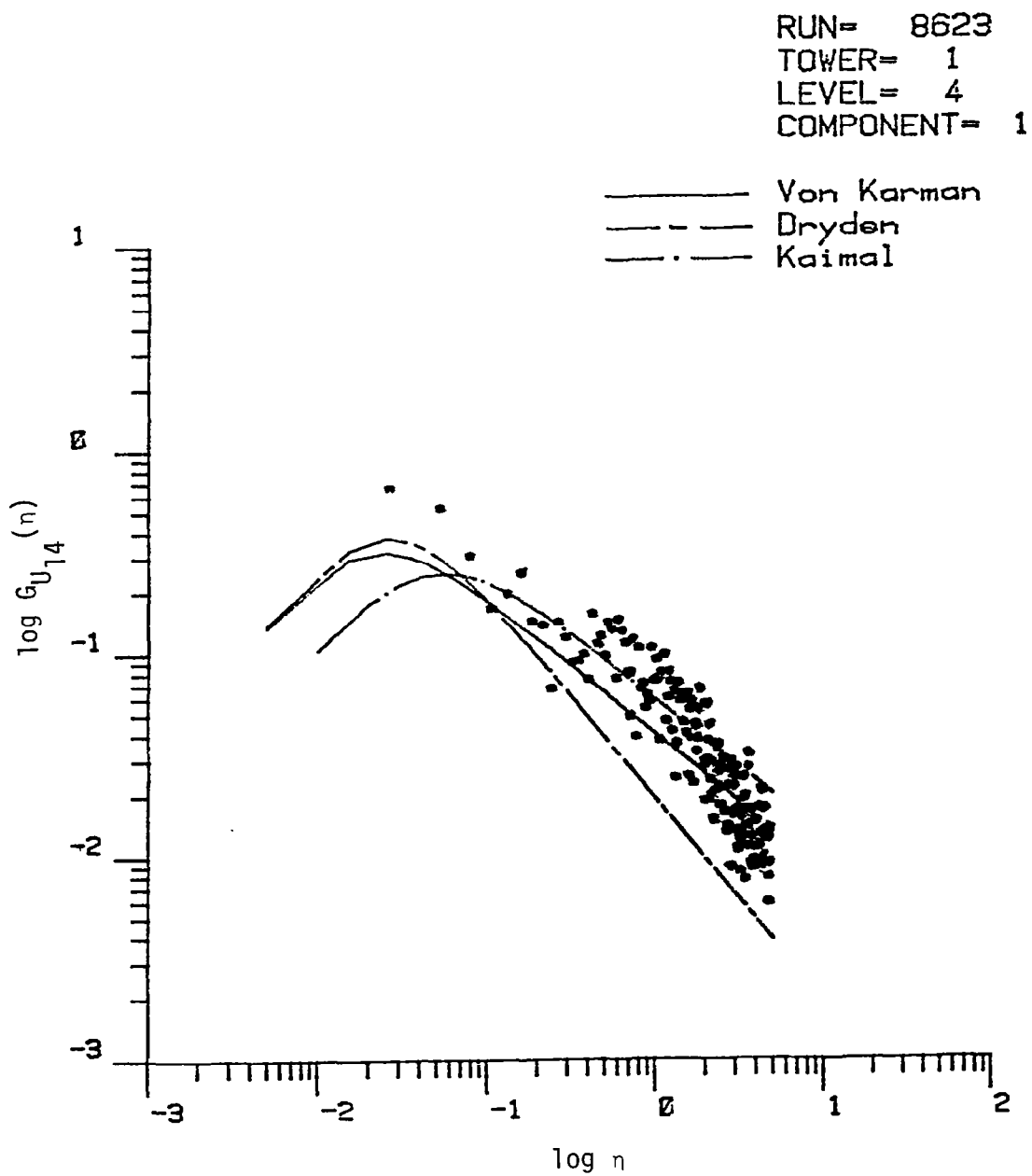
Figure 7.6. Comparison of longitudinal turbulence spectrum with three correlation models. (The length scale is calculated by Method 1, Chapter V, Run #8623).
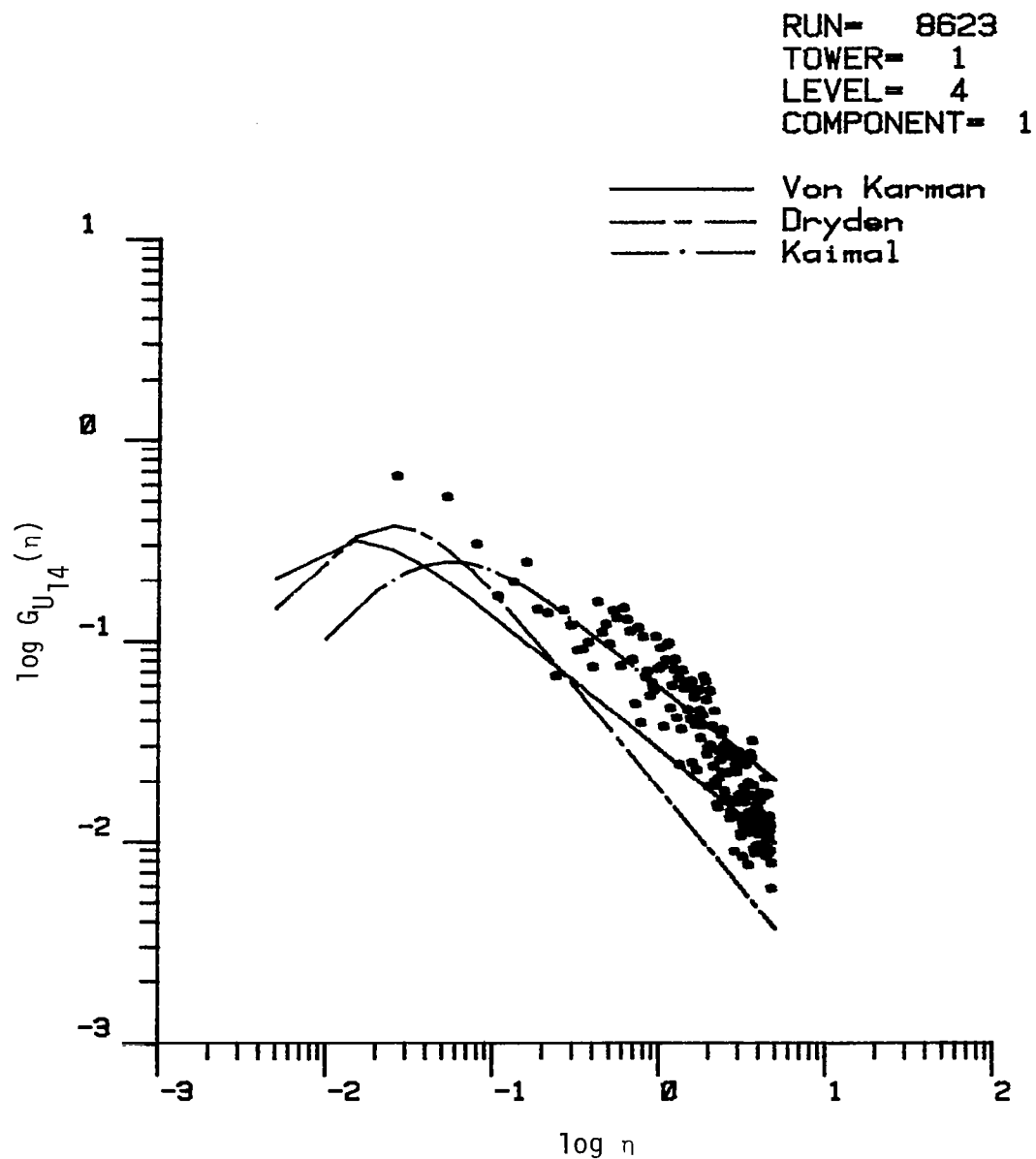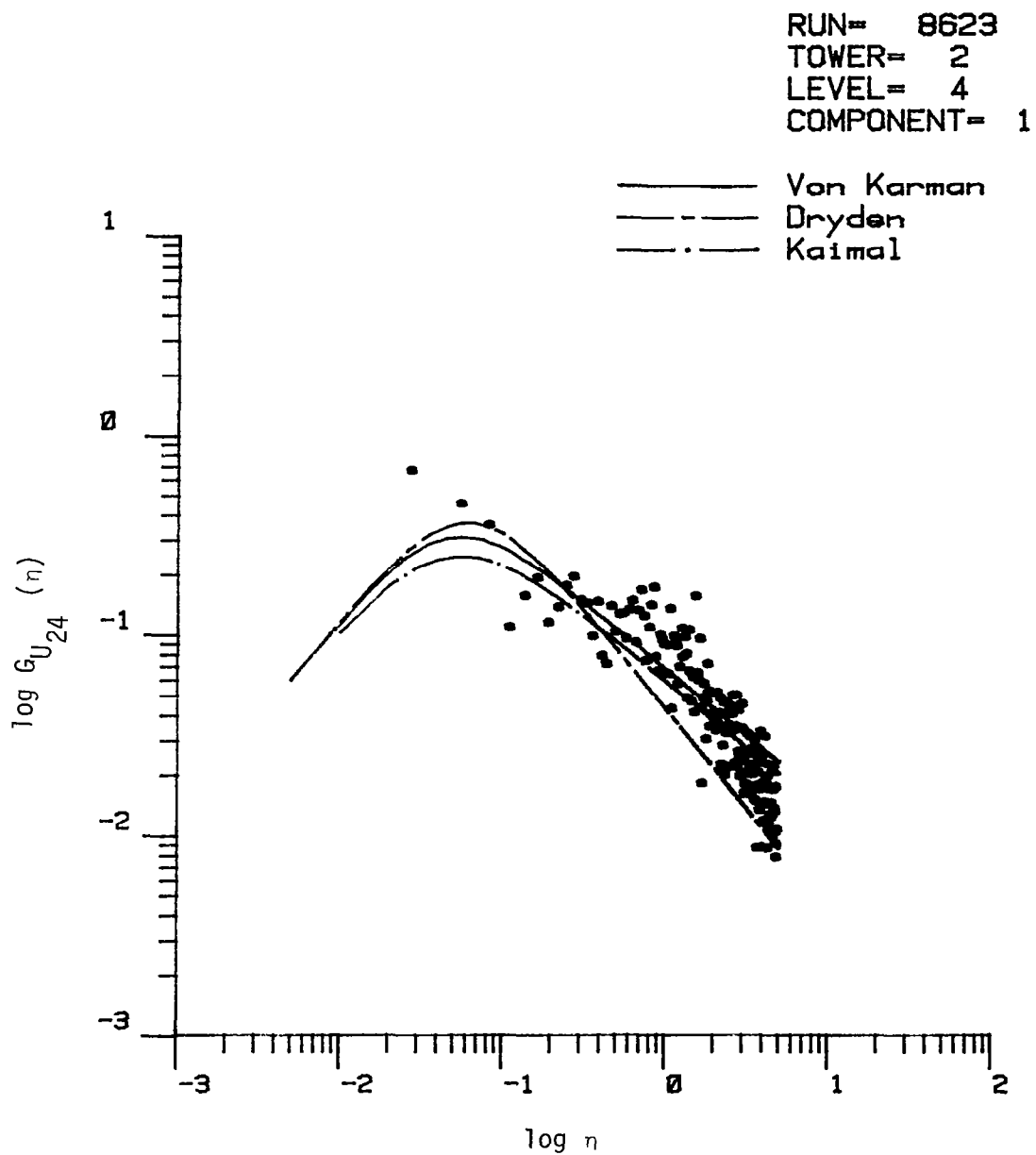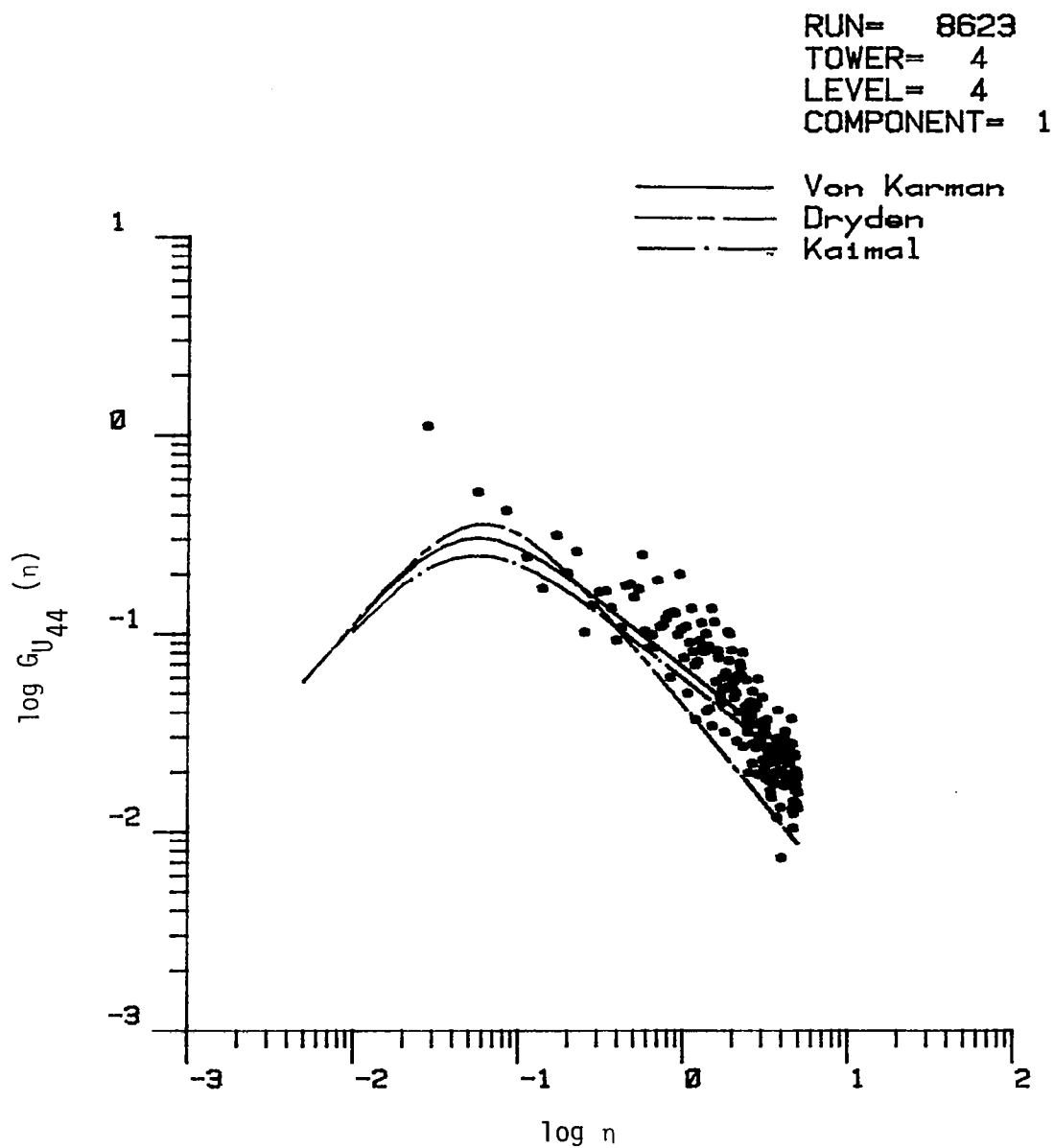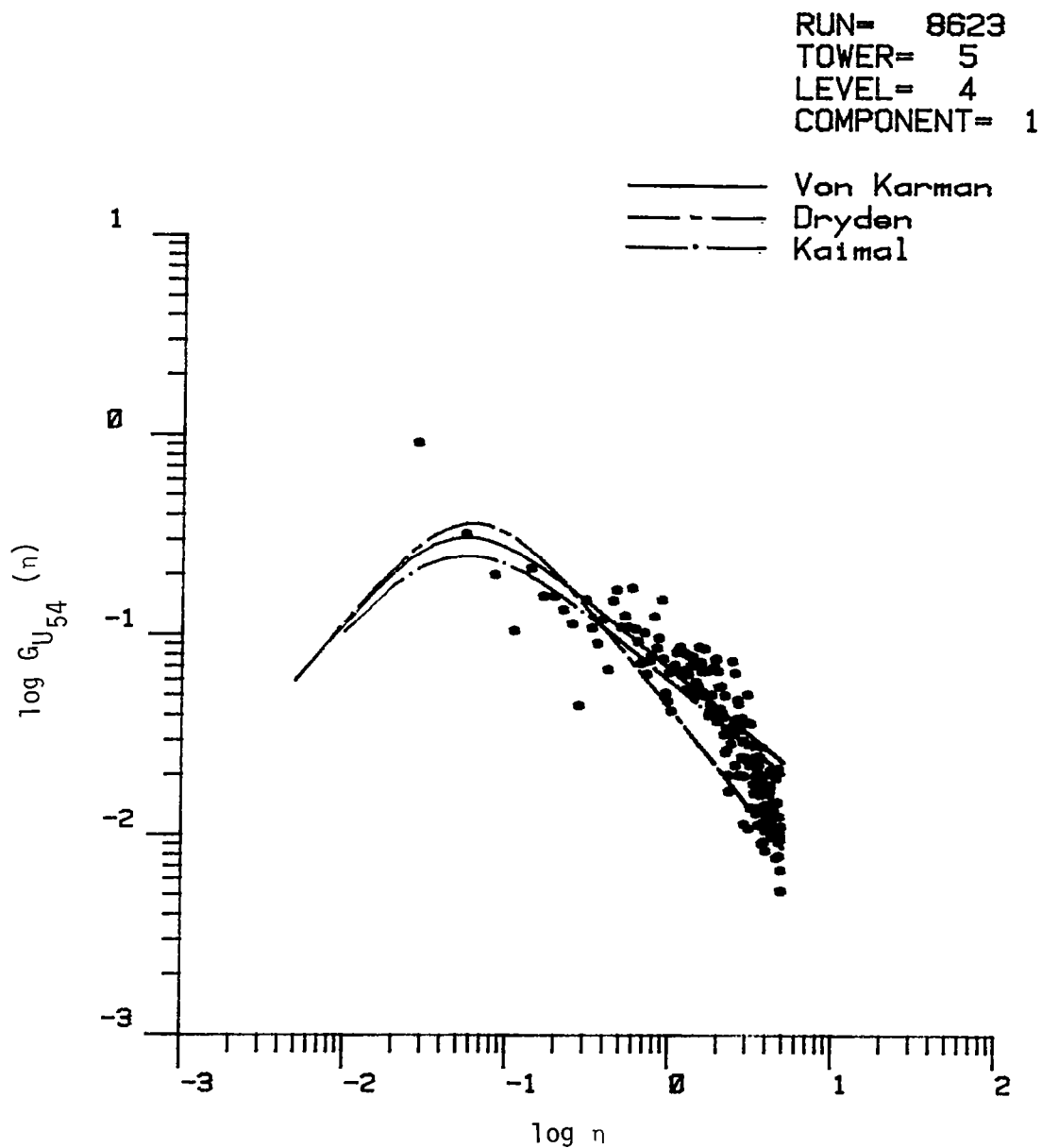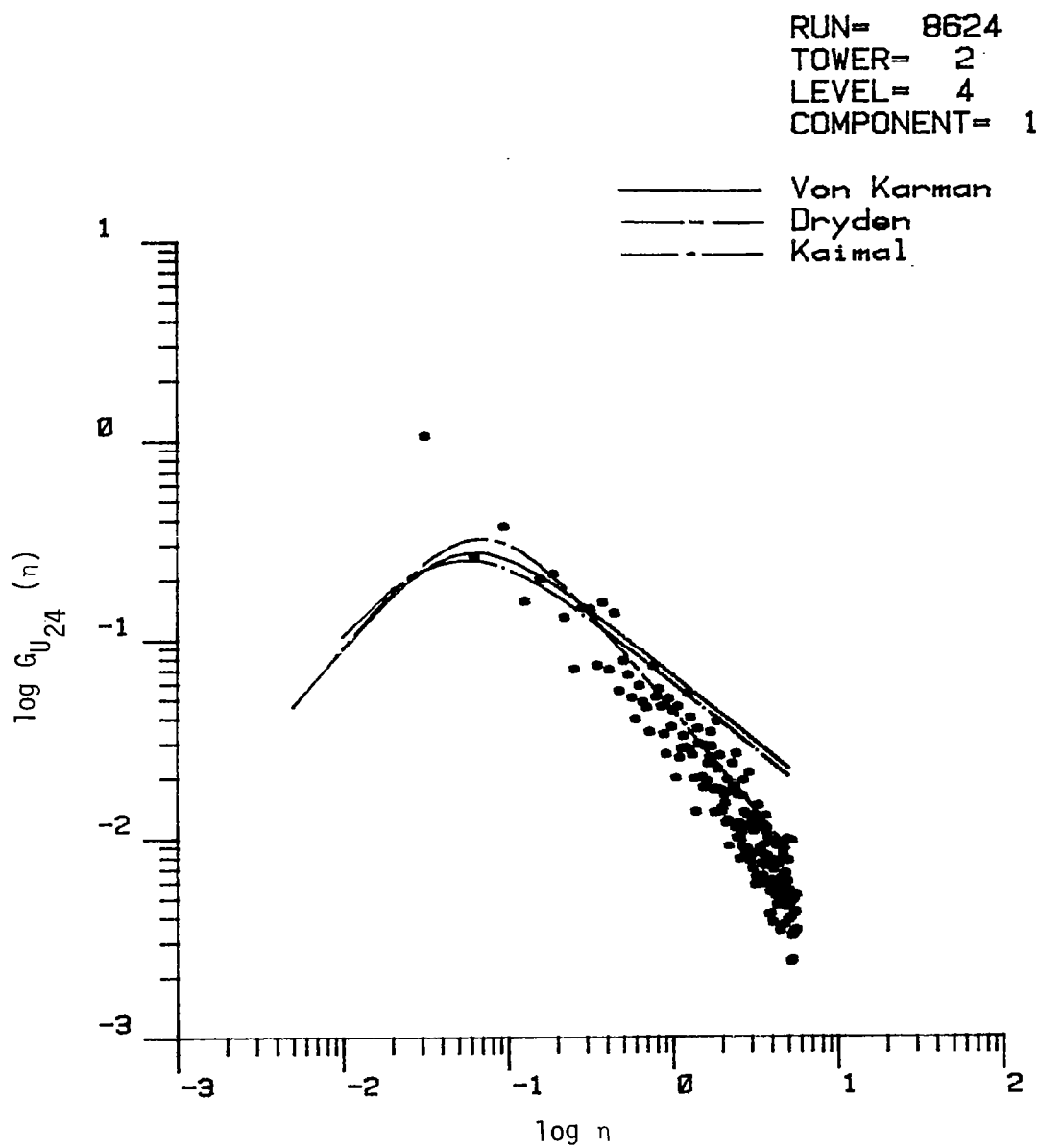
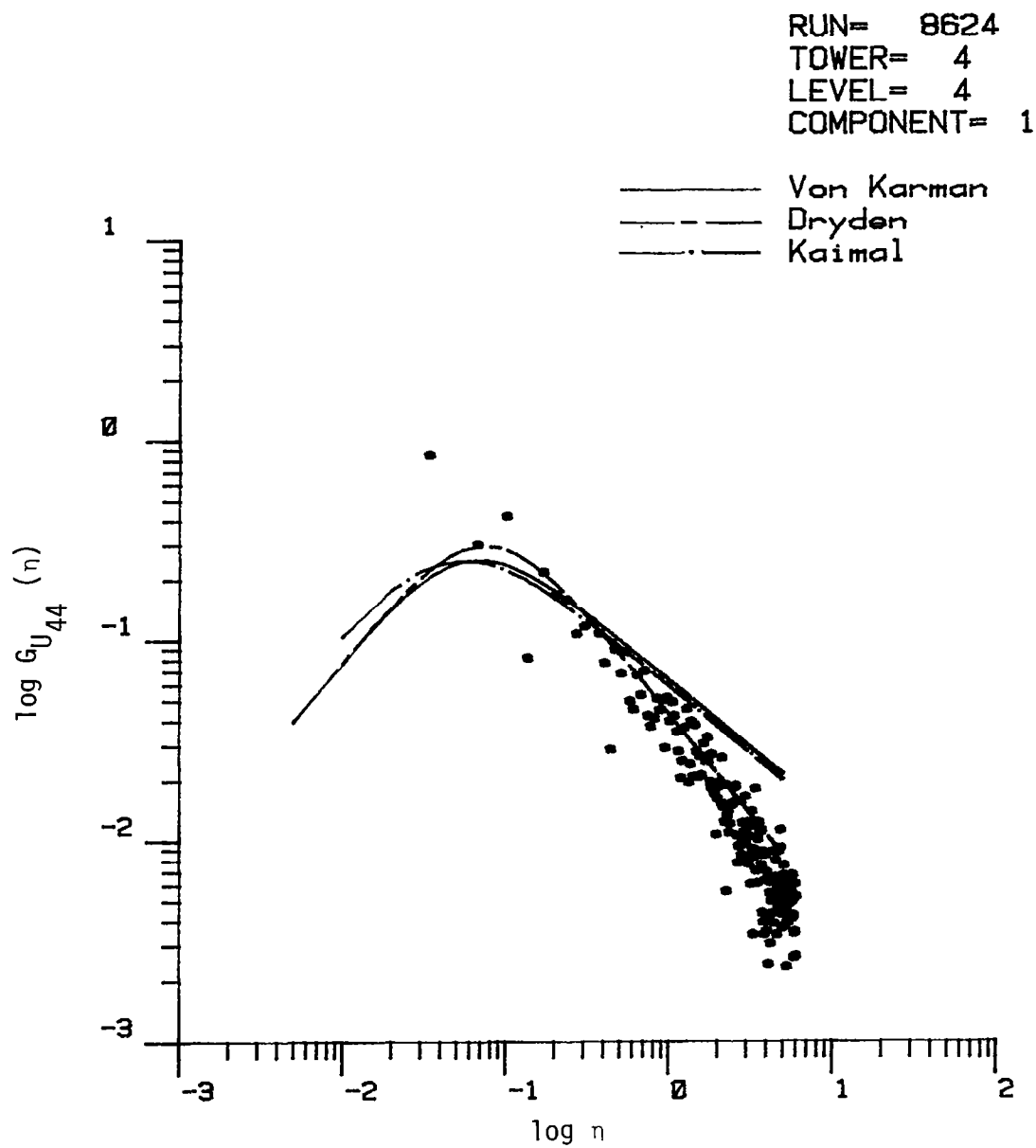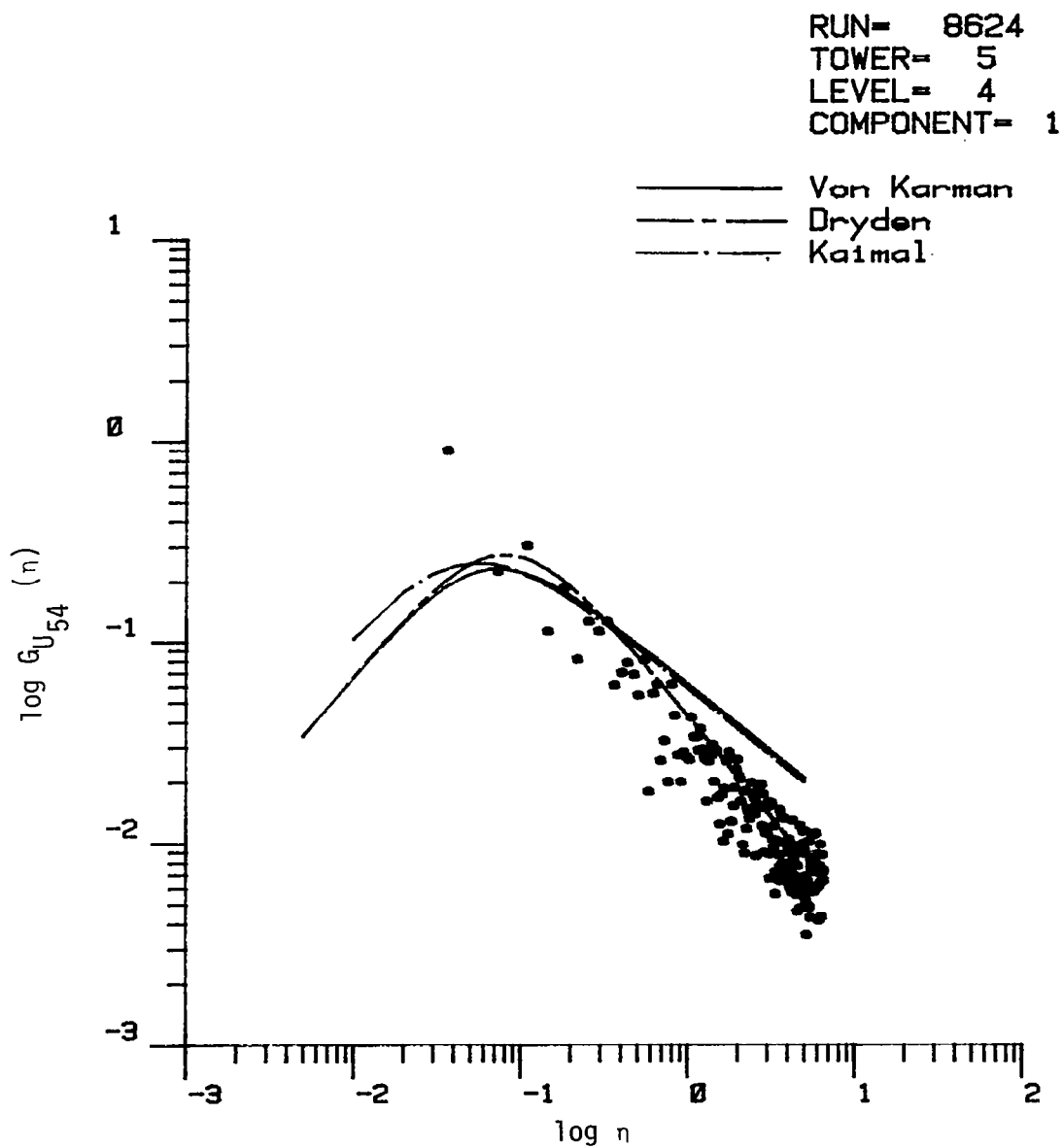Figure 7.7. Comparison of longitudinal turbulence spectrum with three correlation models. (The length scale is calculated by Method 2, Chapter V, Run #8623).

RUN= 8623
TOWER= 1
LEVEL= 4
COMPONENT= 1

——————— Von Karman
——— — —— Dryden
——— · —— Kaimal
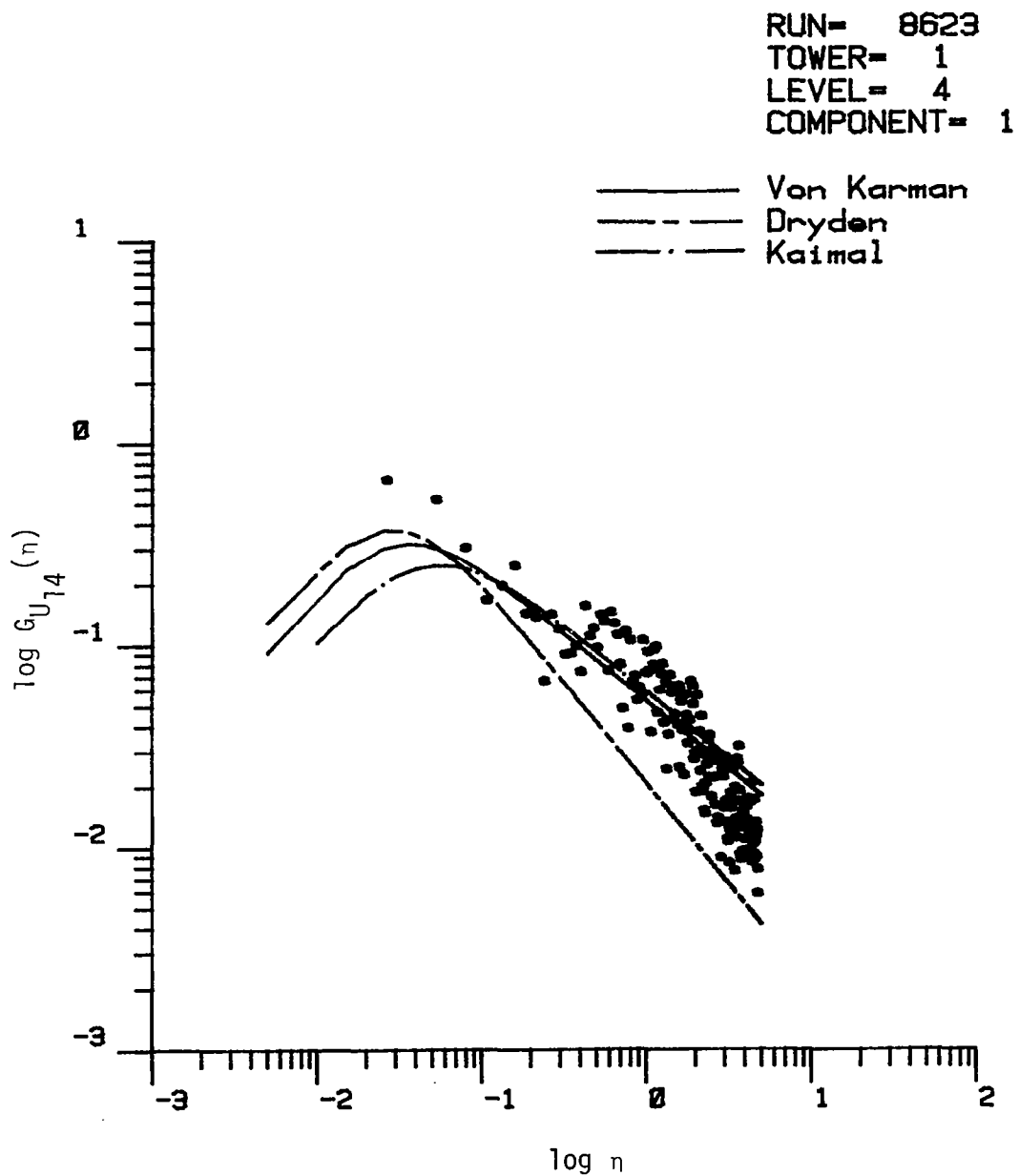
Figure 7.8. Comparison of longitudinal turbulence spectrum with three correlation models. (The length scale is calculated by Method 3, Chapter V, Run #8623).

RUN= 8623
TOWER= 1
LEVEL= 4
COMPONENT= 1

——————— Von Karman
———–—— Dryden
——–·—— Kaimal
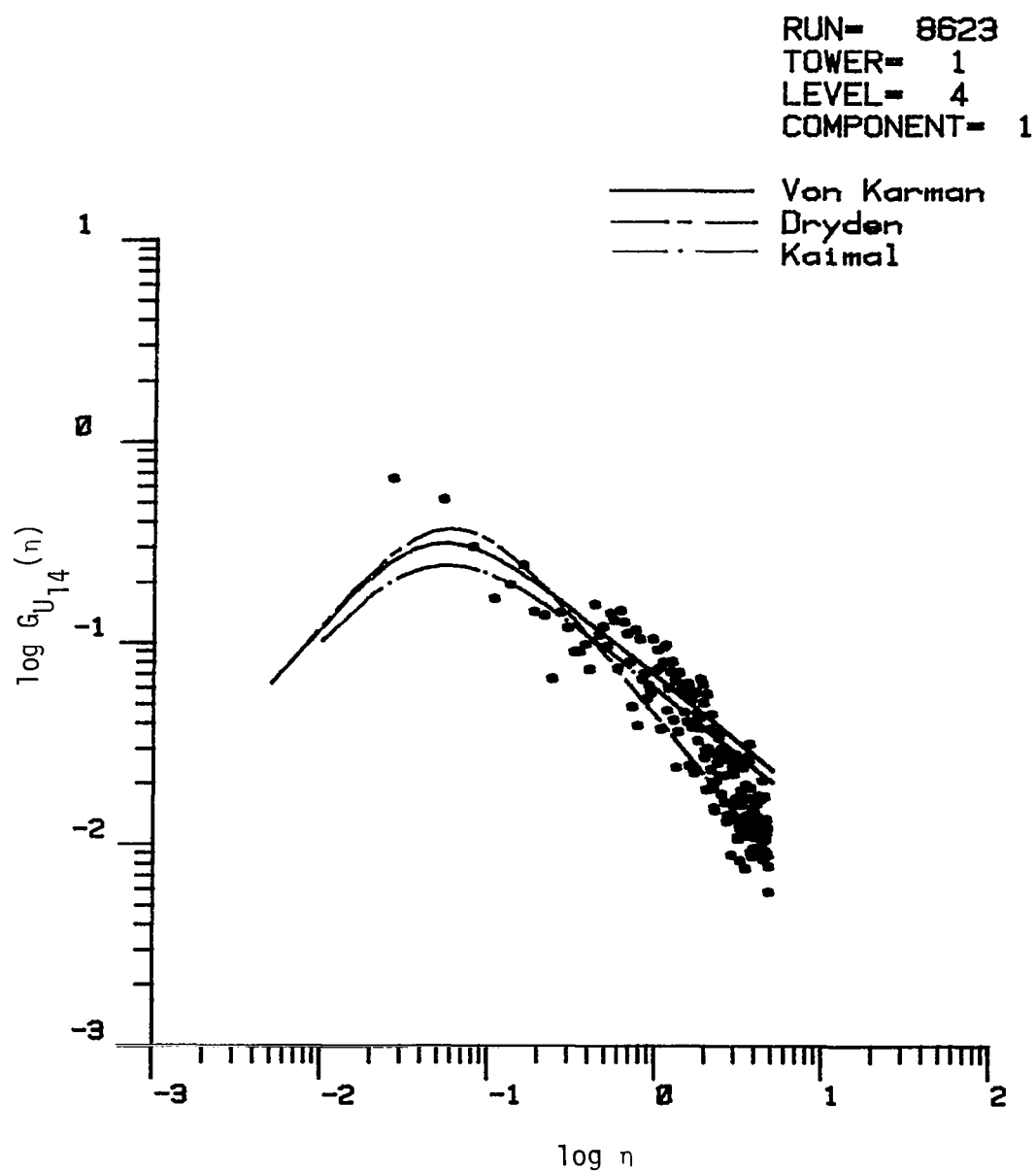
Figure 7.9. Comparison of longitudinal turbulence spectrum with three correlation models. (The length scale is calculated by Method 4, Chapter V, Run #8623).

RUN= 8624
TOWER= 1
LEVEL= 4
COMPONENT= 1

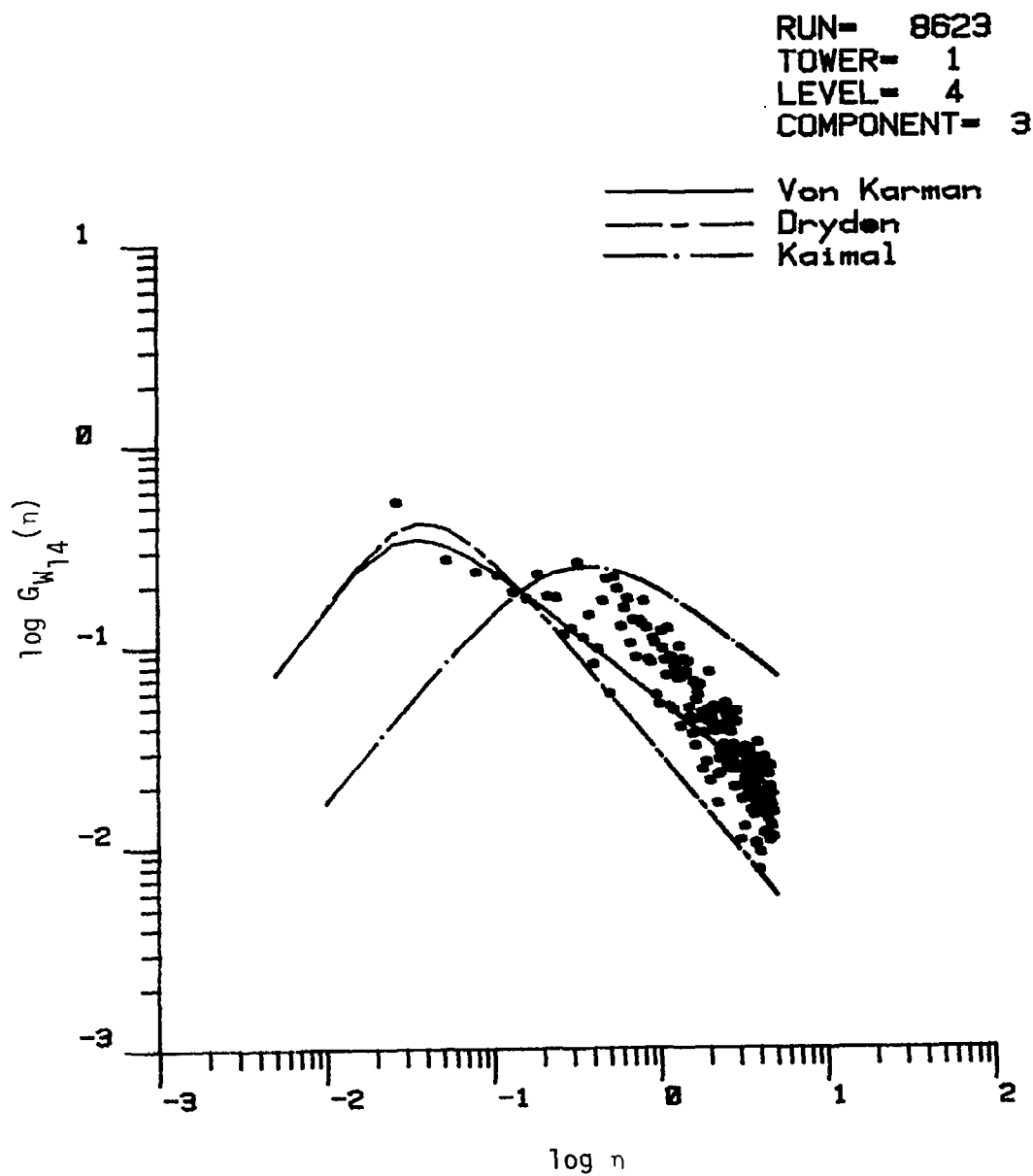——————— Von Karman
——— — —— Dryden
——— · —— Kaimal
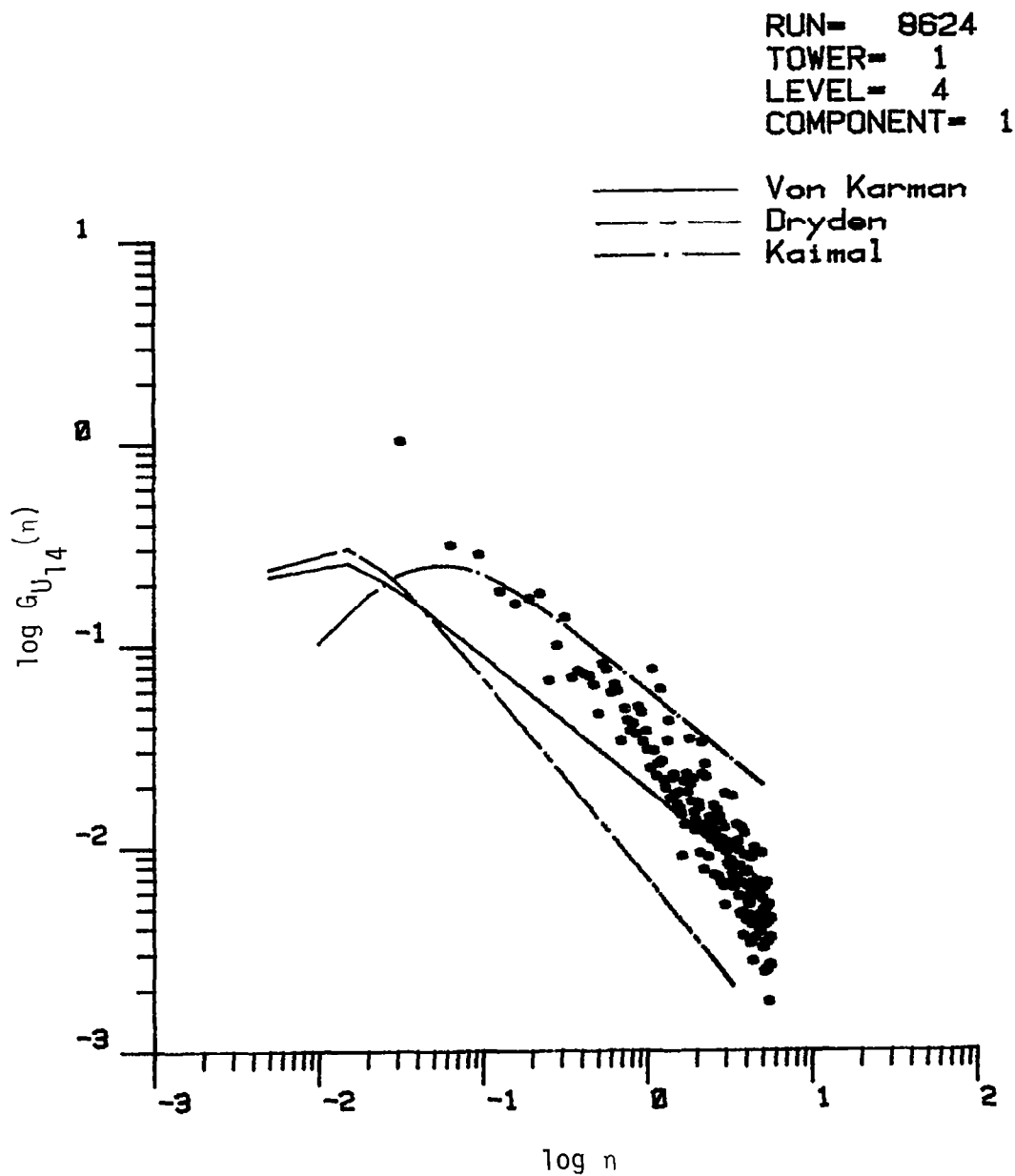
Figure 7.10. Comparison of longitudinal turbulence spectrum with three correlation models. (The length scale is calculated by Method 1, Chapter V, Run #8624).

RUN= 8624
TOWER= 1
LEVEL= 4
COMPONENT= 1
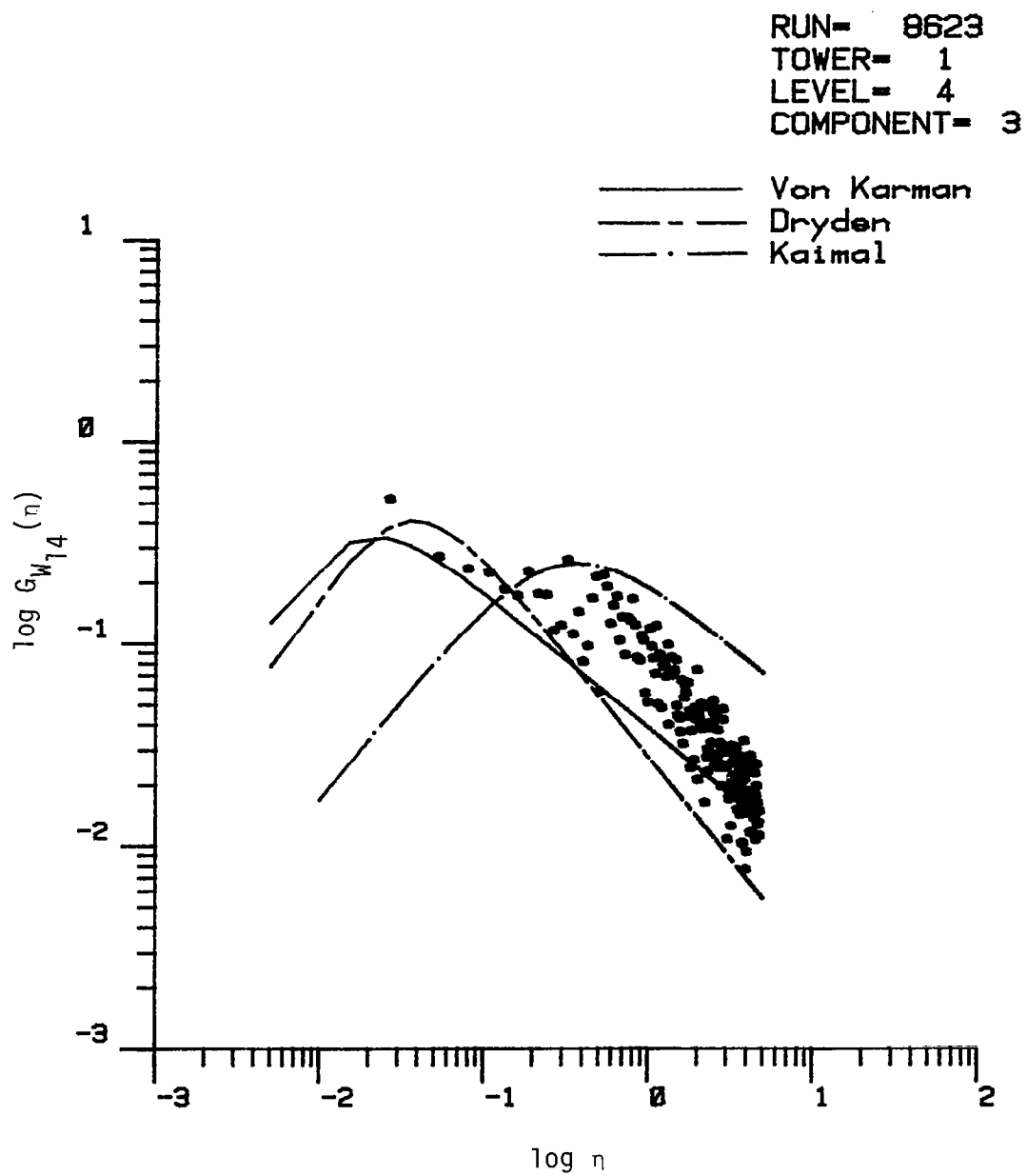
——————— Von Karman
— — — — Dryden
——·—— Kaimal
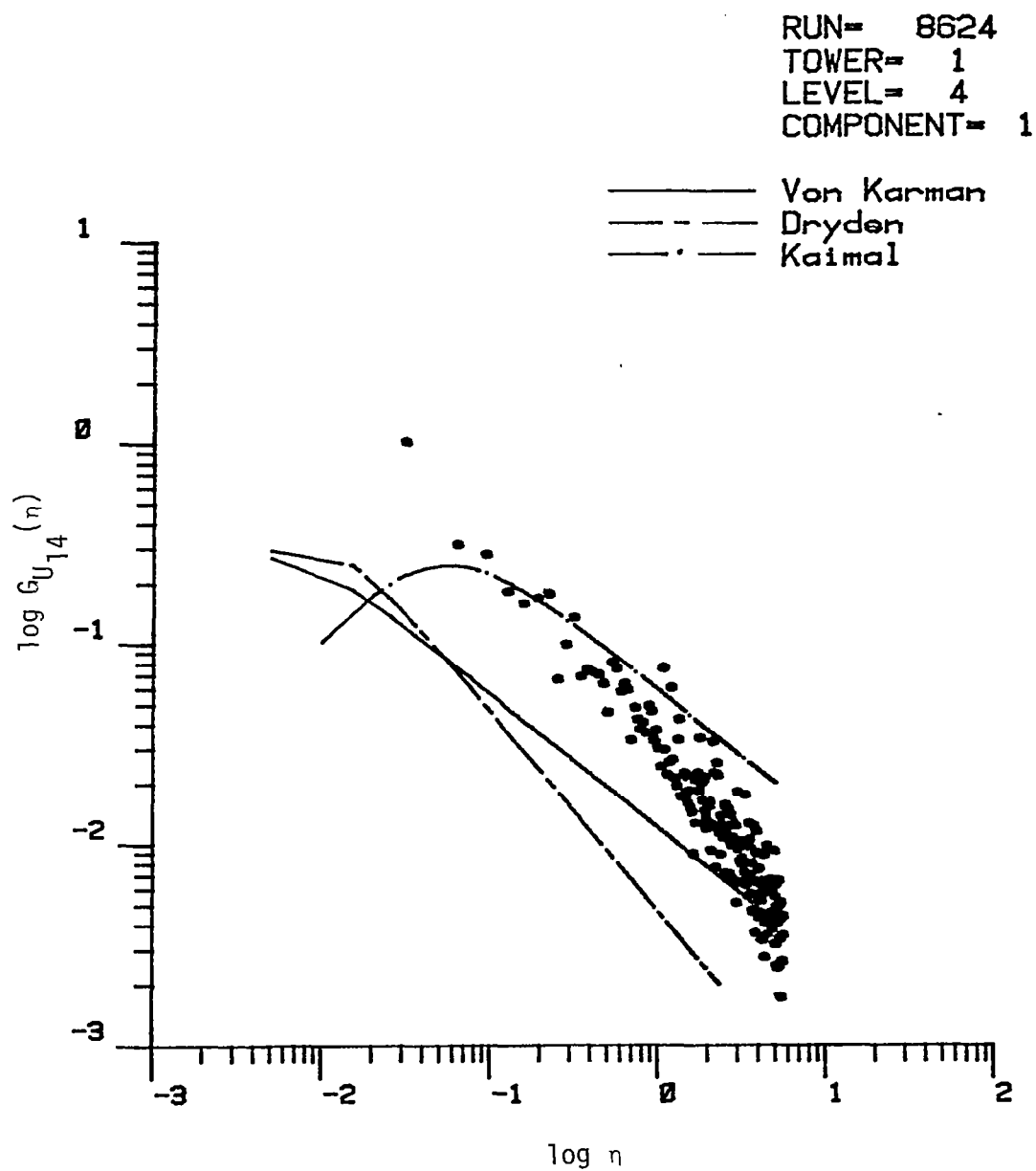
Figure 7.11. Comparison of longitudinal turbulence spectrum with three correlation models. (The length scale is calculated by Method 2, Chapter V, Run #8624).
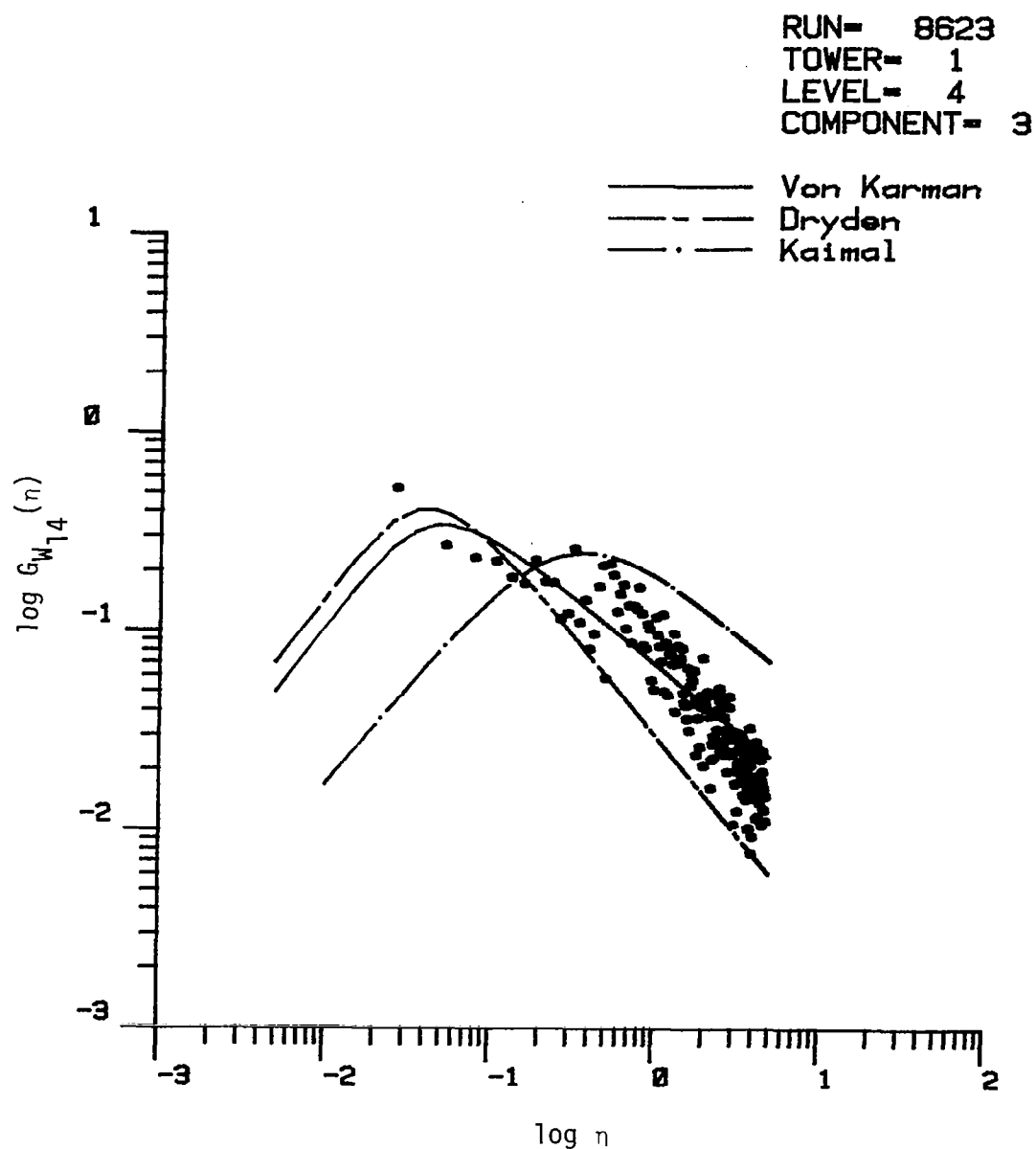
107
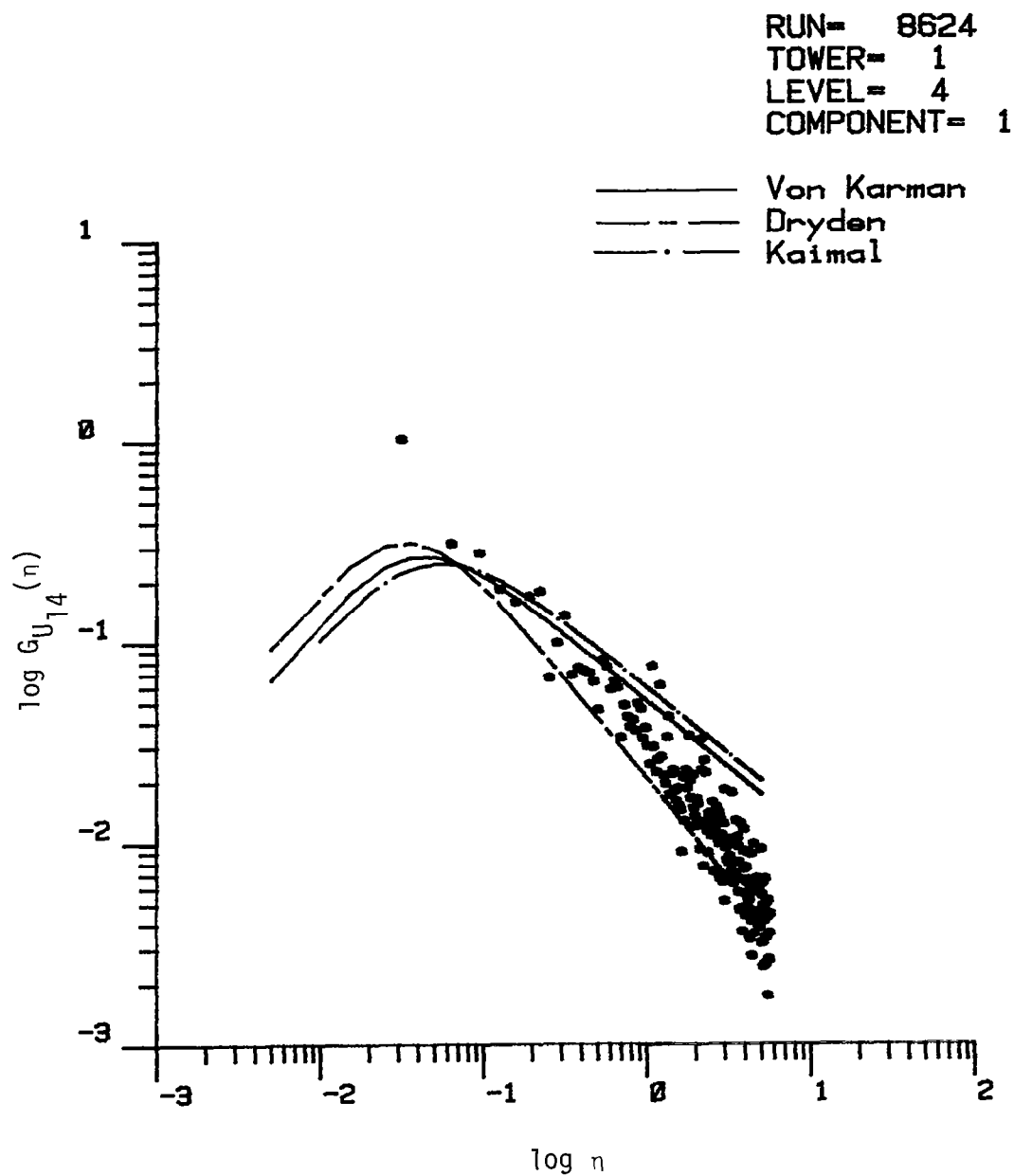
Figure 7.12. Comparison of longitudinal turbulence spectrum with
three correlation models. (The length scale is
calculated by Method 3, Chapter V, Run #8624).

RUN= 8624
TOWER= 1
LEVEL= 4
COMPONENT= 1
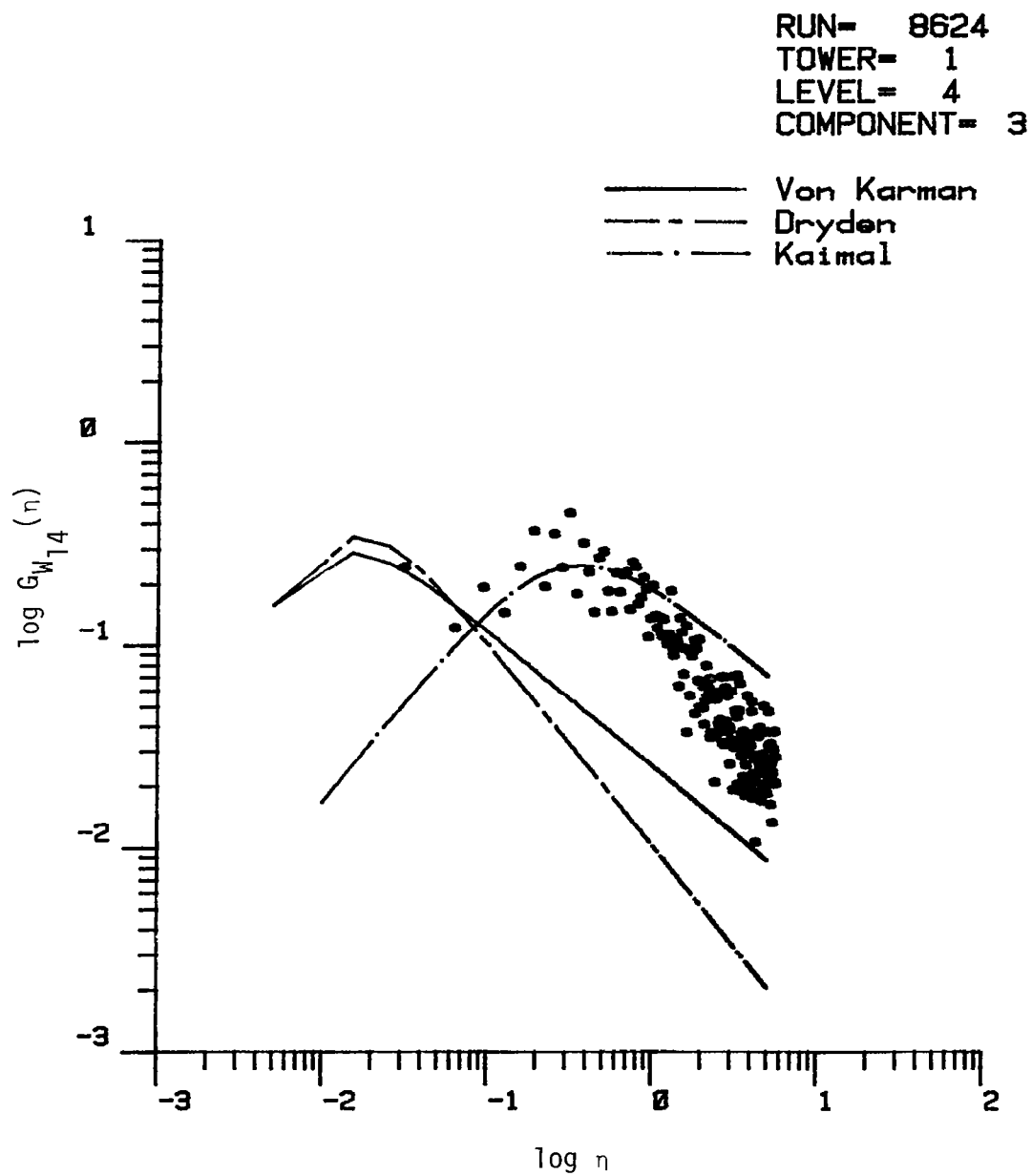
———————— Von Karman
— — — Dryden
—·— Kaimal
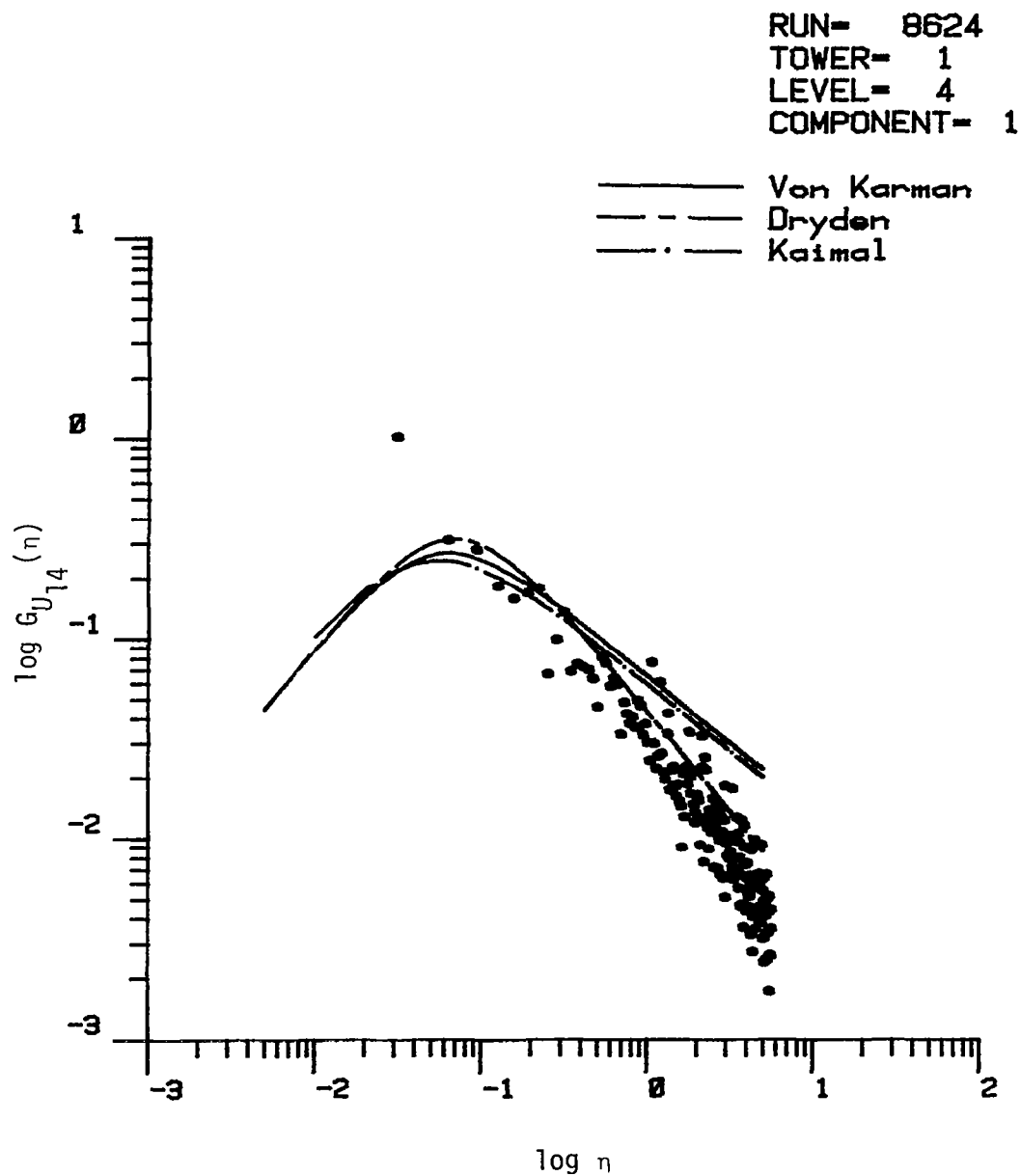
Figure 7.13. Comparison of longitudinal turbulence spectrum with three correlation models. (The length scale is calculated by Method 4, Chapter V, Run #8624).

109

the experimentally computed spectra for Tower 1 Level 4, Runs #8623 and #8624, respectively. Each figure illustrates the analytical spectrum based on length scales calculated by the four different methods described in Chapter V. Notice that the Kaimal spectrum is the same in each figure since it is based on height above level terrain as a length scale, which remains constant. In general, the von Karman spectrum fits the data for Run #8623 quite well in the inertial subrange when based on a length scale calculated either by Method 3 or Method 4. For these length scales, the von Karman spectrum essentially coincides with the Kaimal spectrum in the inertial subrange. The von Karman spectrum, however, generally shows a higher peak value than the Kaimal. On the other hand, the data in all cases do not show a peak; in fact, there is no apparent knee in the experimental data. This implies that more energy is contained in the low-frequency range of the experimental results than predicted by the analytical models. The peak in the analytical spectra occurs in the range $0.055 > \eta > 0.032$. As noted earlier, the data for Run #8623 does not fit the Dryden spectrum well regardless of the method for calculating length scale.

Directing attention to the four curves, Figures 7.10 through 7.13, for Run #8624, however, one sees that the Dryden curve shows better agreement with the data in the inertial subrange than either of the von Karman or Kaimal spectra. The length scale computed by Method 4 results in the best fit of the Dryden spectrum with the data. The Dryden spectrum, based on a length scale computed by Method 3, fits the data reasonably well but gives low values for the magnitude for $G(\eta)$. Once again the data show considerably higher energy levels at low frequency

than predicted by the analytical spectra. It is quite apparent from inspection of Figures 7.10 through 7.13 that the von Karman and Kaimal spectra do not fit the data for Run #8624. They have an incorrect slope in the region which would typically be the inertial subrange.

Length scales computed by Method 4 best correlate the experimental spectra for both the von Karman and Dryden spectra models in the respective cases where they agree with the data. Therefore, L_4 was used as the length scale for comparing the analytical models with spectra at other towers. Figures 7.14 through 7.19 compare the three analytical correlation models with data at Level 4 but different tower positions. In general, the von Karman and Kaimal spectra agree well with data from Run #8623, and similarly the Dryden model agrees with the data from Run #8624. In practically all cases for Run #8623, however, the analytical spectra tend to show lower values than indicated by the data. That is, the correlations fall below the major data in the inertial subrange. This is not true for the data of Tower 1 and less apparent for the data of Tower 5 than for Towers 2 and 4, respectively. The Dryden spectra surprisingly show good agreement in the inertial subrange for all cases. Although the upper levels of the towers were not expected to be influenced by the building, the results suggest that the presence of the building has added energy to the turbulence. This results in higher values of $G(n)$ than predicted by analytical spectra models, which are based on atmospheric boundary flow over uniform, homogeneous terrain. For flow parallel to the major axis of the building (Run #8623), the presence of the building seems to add energy at low frequencies but does not influence the spectral content at high frequencies. For flow

111

Figure 7.14. Comparison of longitudinal turbulence spectra with three analytical models. (The length scale is calculated by Method 4, T2).

RUN= 8623
TOWER= 4
LEVEL= 4
COMPONENT= 1

——————— Von Karman
——— — — Dryden
——— · ——⁻ Kaimal

Figure 7.15. Comparison of longitudinal turbulence spectra with three analytical models. (The length scale is calculated by Method 4, T4).

113

Figure 7.16. Comparison of longitudinal turbulence spectra with three analytical models. (The length scale is calculated by Method 4, T5).

RUN=   8624
TOWER=   2
LEVEL=   4
COMPONENT= 1

—————— Von Karman
——— —— Dryden
—— · —— Kaimal

Figure 7.17. Comparison of longitudinal turbulence spectra with three
analytical models. (The length scale is calculated by
Method 4, T2).

RUN= 8624
TOWER= 4
LEVEL= 4
COMPONENT= 1

——————— Von Karman
——-——— Dryden
——-—— Kaimal

Figure 7.18. Comparison of longitudinal turbulence spectra with three analytical models. (The length scale is calculated by Method 4, T4).

116

Figure 7.19. Comparison of longitudinal turbulence spectra with three
analytical models. (The length scale is calculated by
Method 4, T5).

117

perpendicular to the building (Run #8624), the presence of the building increases energy at low frequencies and changes the structure of the distributions with frequency at higher values. That is, it makes the turbulence more Dryden-like and thus characteristic of wind tunnel turbulence.

Figures 7.20 through 7.25 show the same comparison of theory with experimental data for the vertical velocity component as described earlier for the longitudinal component. The analytical curves for three different length scales are compared with the data from Tower 1, Level 4, in Figures 7.20 through 7.22 (Run #8623) and in Figures 7.23 through 7.25 (Run #8624). Again the Kaimal spectra does not change with length scale and is the same on all figures. Very little, if any, agreement with the theory is demonstrated by the data. The experimental results tend to have some anomalous variations at low frequencies. As discussed in Appendix D, this may be associated with a harmonic oscillation in the vertical data or with a lag in the propeller anemometers when reversing direction suggested by inspection of the time histories for vertical velocities (see Appendix B) which appear to be chopped. Harmonic oscillation will create a spike in the data, and one appears at a value of η roughly between 0.022 and 0.032. This spike, if real, represents a harmonic period of 130 to 190 seconds. Further study of these data is needed to resolve the reliability of the data and to develop empirical correlations which will provide a better prediction of the data than given by the existing correlation.

Finally, Figures 7.26 through 7.31 show vertical velocity spectra for Towers 2, 4, and 5 for Runs #8623 and #8624, respectively. In these

Figure 7.20. Comparison of vertical turbulence spectrum with three correlation models. (The length scale is calculated by Method 1, Chapter V, Run #8623).

Figure 7.21. Comparison of vertical turbulence spectrum with three
correlation models. (The length scale is calculated by
Method 2, Chapter V, Run #8623).

Figure 7.22. Comparison of vertical turbulence spectrum with three correlation models. (The length scale is calculated by Method 3, Chapter V, Run #8623).

121

Figure 7.23. Comparison of vertical turbulence spectrum with three correlation models. (The length scale is calculated by Method 1, Chapter V, Run #8624).

122
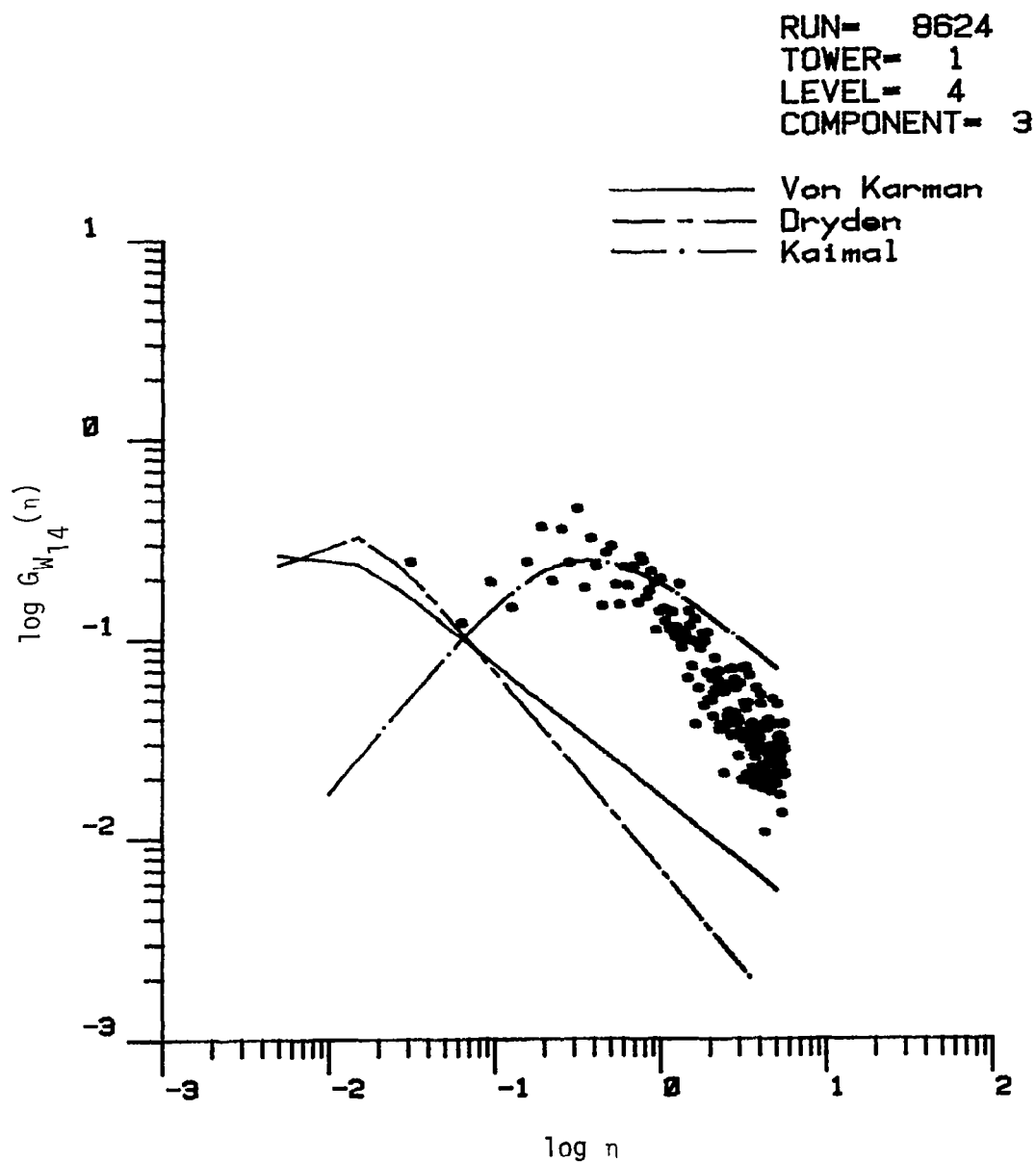
Figure 7.24. Comparison of vertical turbulence spectrum with three
correlation models. (The length scale is calculated by
Method 2, Chapter V, Run #8624).
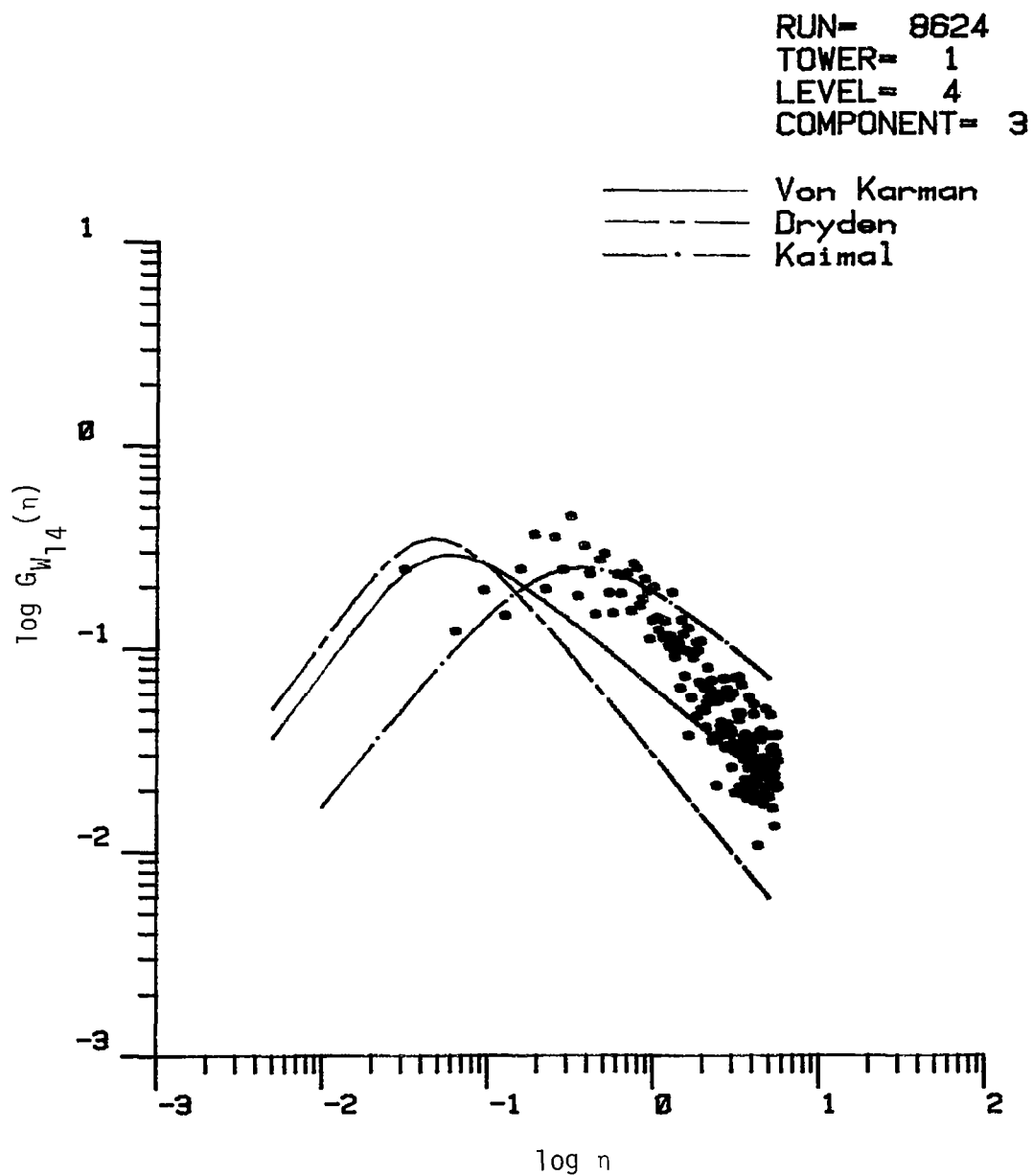
Figure 7.25. Comparison of vertical turbulence spectrum with three correlation models. (The length scale is calculated by Method 3, Chapter V, Run #8624).

124
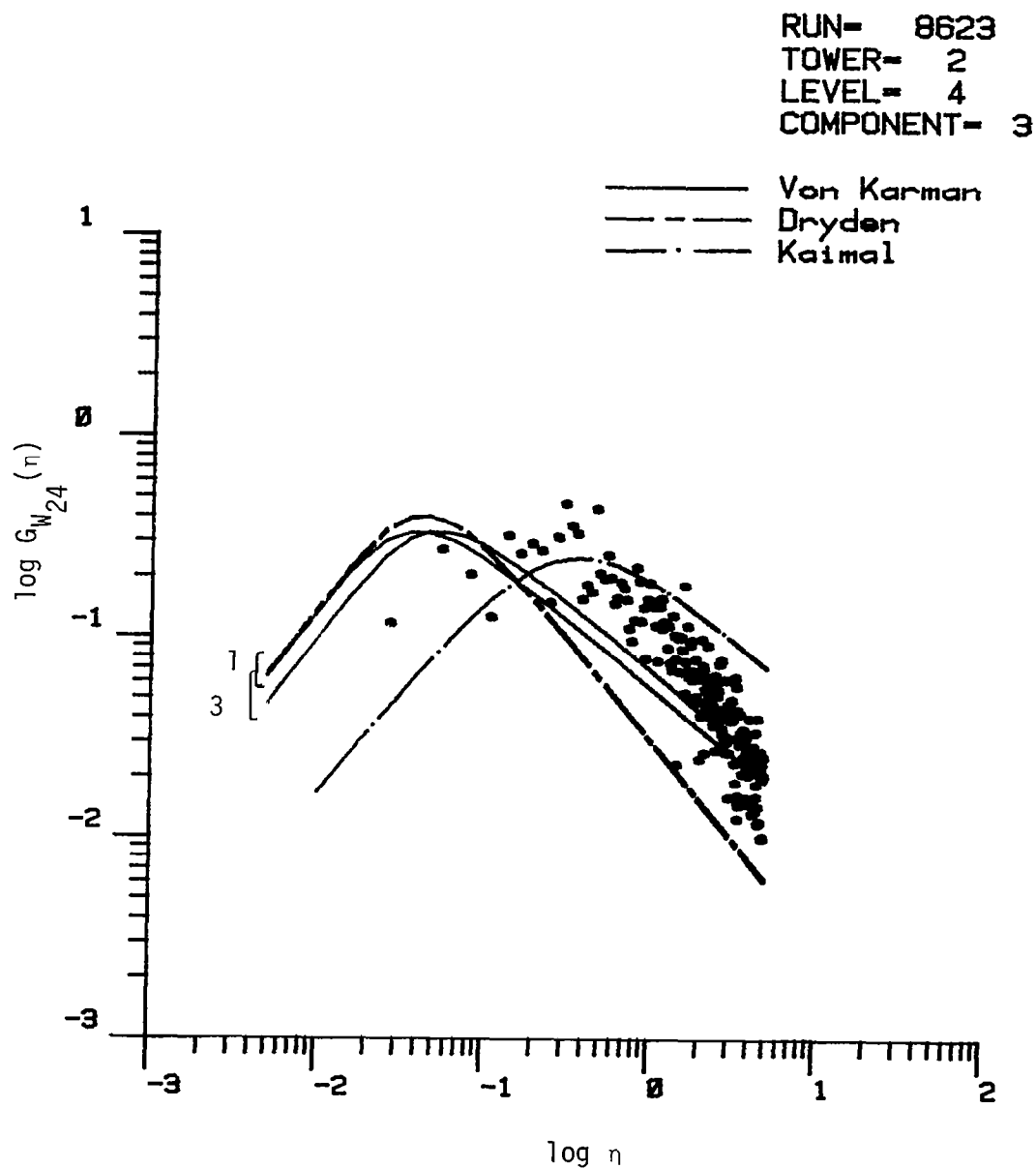
Figure 7.26. Comparison of vertical turbulence spectrum with three correlation models. (The length scale is calculated by Methods 1 and 3, Chapter V, T2, Run #8623).

125
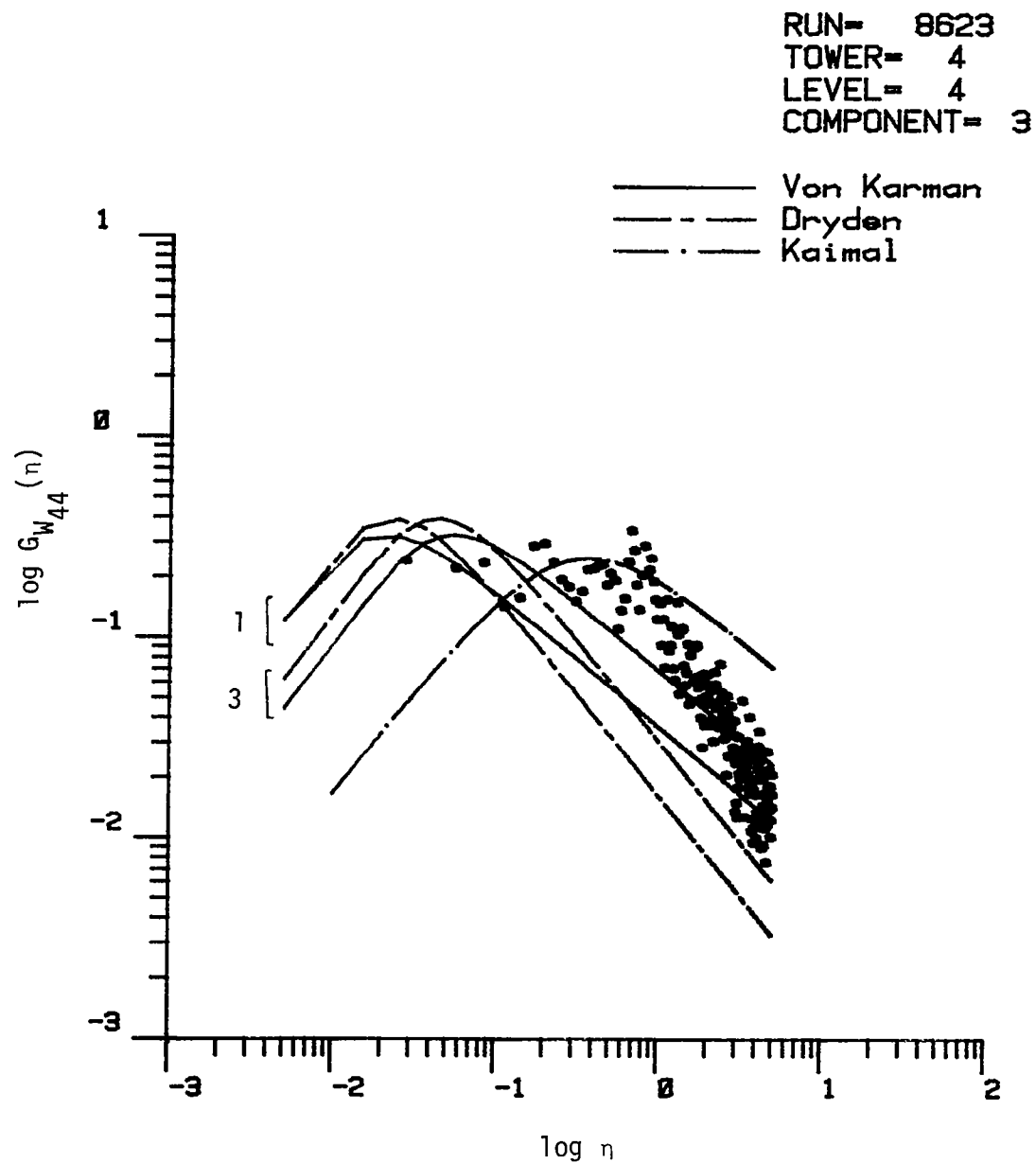
Figure 7.27. Comparison of vertical turbulence spectrum with three correlation models. (The length scale is calculated by Methods 1 and 3, Chapter V, T4, Run #8623).
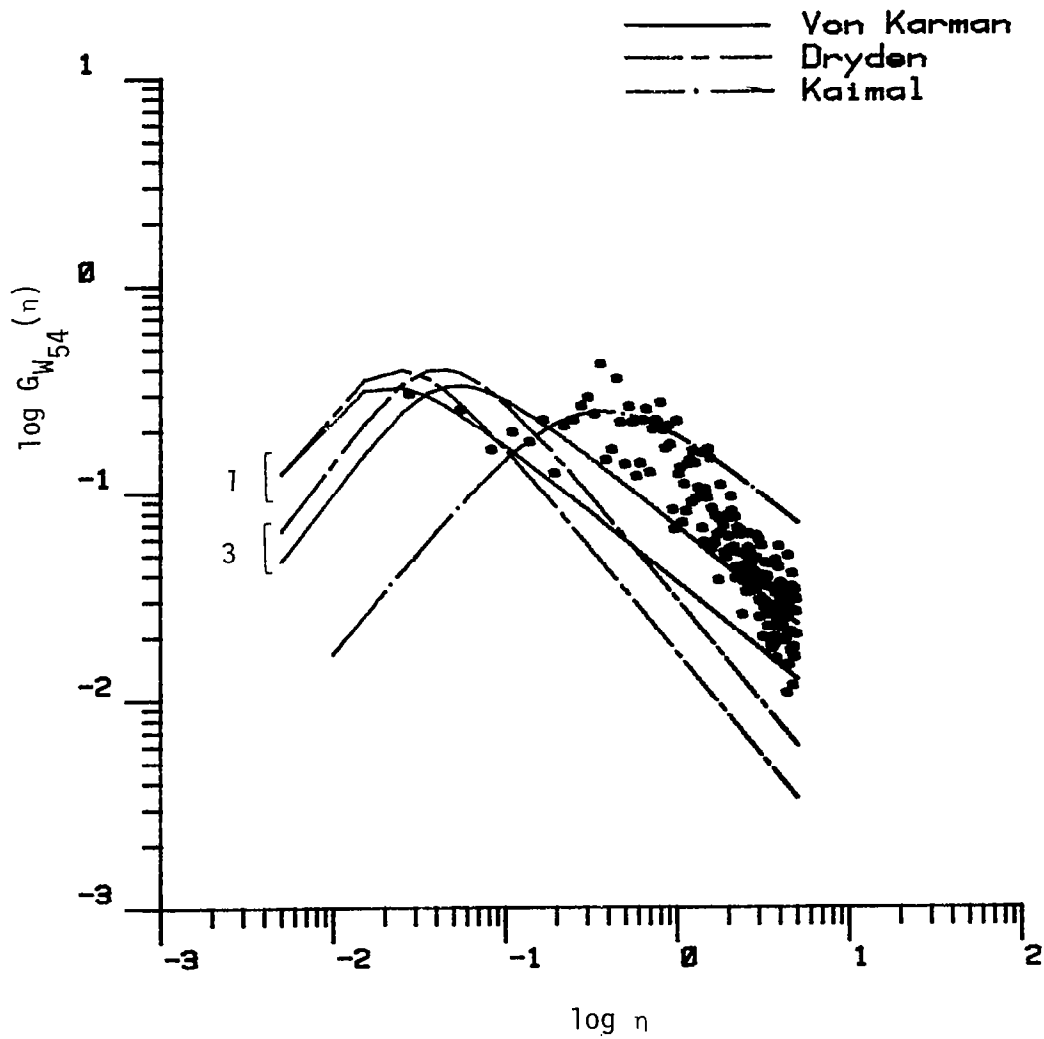
Figure 7.28. Comparison of vertical turbulence spectrum with three correlation models. (The length scale is calculated by Methods 1 and 3, Chapter V, T5, Run #8623).

127

RUN= 8624
TOWER= 2
LEVEL= 4
COMPONENT= 3

——————— Von Karman
——— ——— Dryden
——— · ——— Kaimal
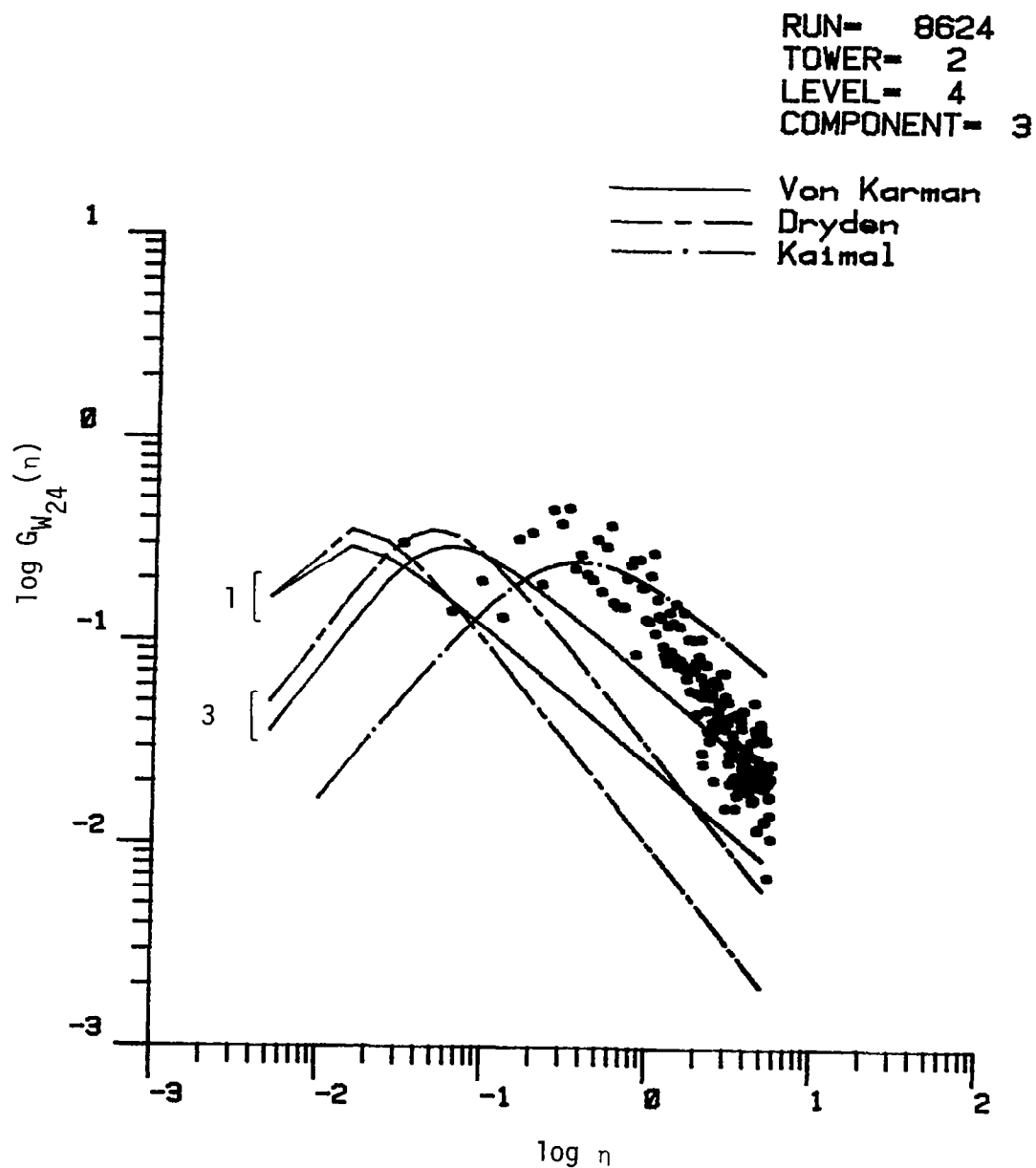
Figure 7.29. Comparison of vertical turbulence spectrum with three correlation models. (The length scale is calculated by Methods 1 and 3, Chapter V, T2, Run #8624).

128
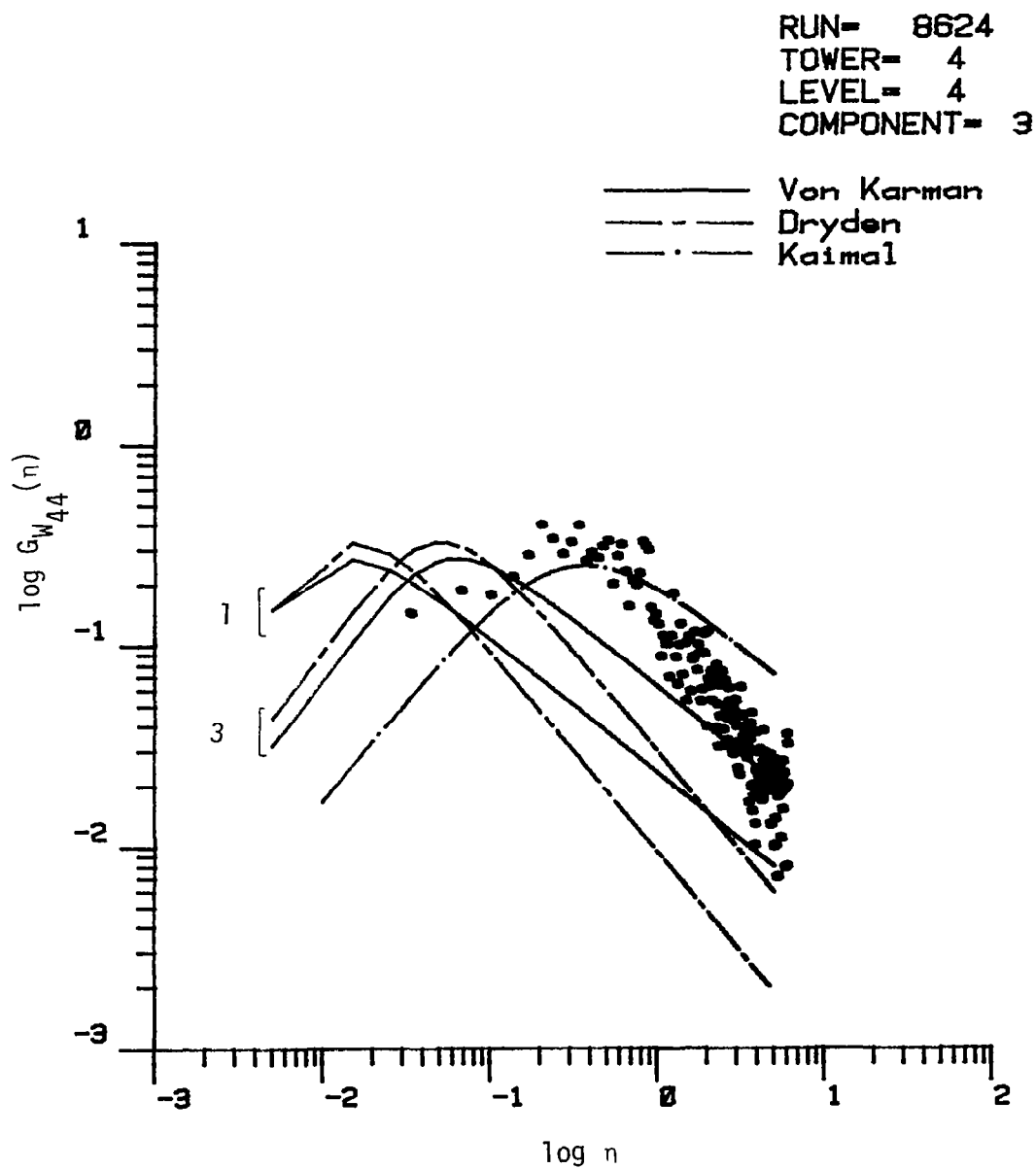
Figure 7.30. Comparison of vertical turbulence spectrum with three correlation models. (The length scale is calculated by Methods 1 and 3, Chapter V, T4, Run #8624).

129
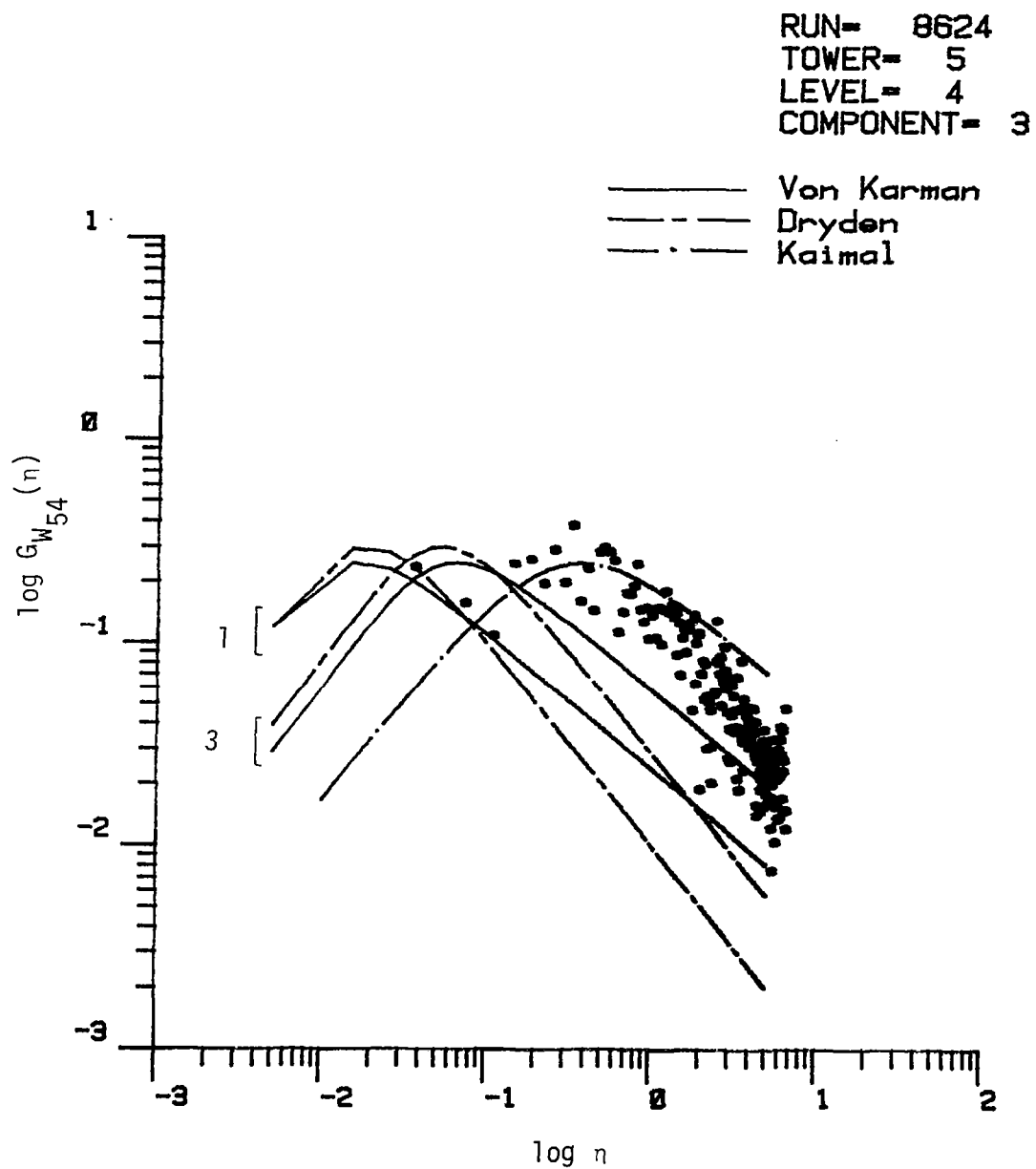
Figure 7.31. Comparison of vertical turbulence spectrum with three correlation models. (The length scale is calculated by Methods 1 and 3, Chapter V, T5, Run #8624).

130

plots, the von Karman and Dryden spectra are computed both for length scales L_1 and L_3, respectively. In general, these spectra show poor agreement with the experimental results. Of all the analytical models, however, the Kaimal spectra more closely resembles the data. It is not unexpected that the vertical spectra depart from the predicted results of an isotropic, homogeneous turbulence model near the ground due to the fact that the vertical downward velocity must decay to zero at the surface. The Kaimal spectra were, however, measured with towers of approximately the same height as those used in this study, and it was anticipated that better agreement with the Kaimal spectra would be observed. Further study of the results is needed, however, to resolve this anomaly between the experimental results and the analytical models.

CHAPTER VIII

TWO-POINT SPECTRUM ANALYSES

The two-point spatial spectrum is discussed in this chapter. The
theory is initially reviewed, then the analytical model for the two-
point spectrum proposed by Houbolt and Sen (1972) is described. Note
that Houbolt and Sen refer to the two-point spatial spectra as the
cross-spectra. In this report cross-spectra refers to a spectral corre-
lation between different velocity components rather than between like
components separated in spatial position. In the present terminology,
the results reported in this chapter are two-point auto-spectra.
Analytical models and measured data are compared in Subchapter C.
Finally, the lateral coherence of the longitudinal velocity component is
presented in Subchapter D and compared with theoretical models.

As shown in Chapter II, the two-point spectra play an important
role in determining the rolling and pitching moments due to spatial varia-
tion in turbulence over an airfoil. The major thrust of the NASA B-57
gust gradient program is to gather spatial turbulence data at altitude.
The thrust of this study is to utilize the tower array to measure
spatial turbulence variation at ground level. In general, the two-point
spectra calculated for Run #8623 are representative of turbulence distri-
bution across an airfoil, in view of the fact that the wind is perpen-
dicular to the array. The data from Run #8624 are representative of wind
along the body of the aircraft; for example, similar to the longitudinal
component of the wind when the airplane is flying into the wind. The
results show, in general, that the analytical two-point spectrum model

132

proposed by Houbolt and Sen (1972) is sensitive to the length scale model; also, it does not predict the high turbulence kinetic energy at the low frequencies observed in the experimental data.

A. Theory

Similar to the one-point auto-spectra discussed in Chapter VII, the two-sided spatial spectrum density function is calculated by the Fourier transform of the two-point time-dependent spatial correlation function, as follows

$$S_{xy}(s,f) = \int_{-\infty}^{\infty} R_{xy}(s,\tau)e^{-i2\pi f\tau}d\tau \tag{8.1}$$

where s is the spatial separation distance between the stations at which $x(t)$ and $y(t)$ are measured. The two-point spatial correlation function, however, is not an even function; therefore, the spectrum density function is generally a complex number.

For the one-sided two-point space-time spectrum

$$\phi_{xy}(s,f) = 2 \int_{-\infty}^{\infty} R_{xy}(s,\tau)e^{-i2\pi f\tau}d\tau = C_{xy}(s,f) - iQ_{xy}(s,f) \tag{8.2}$$

where the real part, $C_{xy}(s,f)$, is called the coincident spectral density function and the imaginary part, $Q_{xy}(s,f)$, is called the quadrature spectral density function.

There are two methods to calculate two-point spectrum, the standard method is computed as follows. For two time histories, $x(t)$ and $y(t)$, which are stationary in time with $\bar{x} = \bar{y} = 0$, raw estimates for $C'_{xy}(f)$ and $Q'_{xy}(f)$ (where s has been dropped for convenience), are

$$C'_{xy}(f) = 2h\left\{A'_0 + 2\sum_{r=1}^{m-1} A'_r \cos\left(\frac{\pi rf}{f_c}\right) + A'_m \cos\left(\frac{\pi mf}{f_c}\right)\right\} \qquad (8.3)$$

$$Q'_{xy}(f) = 2h\left\{2\sum_{r=1}^{m-1} B''_r \sin\left(\frac{\pi rf}{f_c}\right) + B''_m \sin\left(\frac{\pi mf}{f_c}\right)\right\} \qquad (8.4)$$

where

$$A'_r = A'_{xy}(rh) = \frac{1}{2}\left[R'_{xy}(rh) + R'_{yx}(rh)\right]$$

$$B''_r = B''_{xy}(rh) = \frac{1}{2}\left[R'_{xy}(rh) - R'_{yx}(rh)\right]$$

R'_{xy} and R'_{yx} are the estimates of the two-point correlation function at lag r, h is the time interval between samples, m is the maximum lag number, f_c is the cut-off frequency. For this method, the discrete frequencies are given by

$$f = \frac{kf_c}{m} \qquad k = 0, 1, \cdots m \qquad (8.5)$$

The second method of computation is direct Fourier transform of the original data values $x(t)$ and $y(t)$. A raw estimate of the two-point spectrum density function, $\phi'_{xy}(f)$, at any frequency f is given by the formula

$$\phi'_{xy}(f) = \frac{2h}{N}\left|X^*_k Y_k\right| \qquad (8.6)$$

where X^*_k is the complex conjugate of X_k.

The following steps were used to compute the two-point spectral density function via the FFT procedures in this report. Assume that the sample size for each of the two data sequences x_n and y_n is initially the arbitrary size N.

134

1. Truncate the two data sequences or add zero so that each sequence has $N = 2^P$ data values.

2. Taper the two resulting sequences using the cosine taper window, or some other appropriate tapering.

3. Store the tapered x_n in the real part and the tapered y_n in the imaginary part of the complex variable $z_n = x_n + iy_n$, $n = 0, 1, \cdots N-1$.

4. Compute the N-point FFT giving the z_k for $k = 0, 1, \cdots N-1$, using the FFT procedure.

5. Compute x_k and y_k for $k = 0, 1, \cdots N-1$,

$$X(k) = \frac{1}{2} [Z(k) + Z^*(N - k)] \tag{8.7}$$

$$Y(k) = \frac{1}{2i} [Z(k) - Z^*(N - k)] \tag{8.8}$$

where Z^* is the complex conjugate of Z.

6. Compute the raw cross-spectral density estimate $\phi'_{xy}(f_k)$ for $k = 0, 1, \cdots N-1$, and $f_k = k/(Nh)$ by Equation 8.6.

7. Adjust these estimates for the scale factor due to tapering, i.e., by replacing ϕ'_{xy} by $(1/0.875)\phi'_{xy}$ if the cosine tapering is used.

8. Finally, obtain smooth estimates by either frequency smoothing or segment averaging.

Note in this study, Steps 2 and 7 were not used since N is relatively large and the results showed little difference with or without tapering.

Similar to the power spectrum, the normalized standard error, E_r, is given by

135

$$E_r = \sqrt{1/q}$$

In the present study, the FFT parameters are given by h = 0.1 second; f_c = 1/(2h) = 5 cycles/second; q = 10 T_r = 1024 seconds; T_r' = 102.4 seconds; N = 10,240. Thus, the band error B_e is

$$B_e = 1/T_r' = 0.00977 \text{ cycle/second}$$

and

$$E_r = \sqrt{1/q} = 0.316$$

This gives an rms error of approximately 32 percent for all of the two-point spectra presented.

B. Two-Point Spectrum Analytical Model

Houbolt and Sen (1972) analytically developed a model of the two-point spectrum function from the von Karman spectrum for both vertical and longitudinal turbulence. The longitudinal two-point analytical expression is given by:

$$\phi_{w_x w_x}(\zeta, \hat{n}) = 0.3889784 \ \sigma_{w_x}^2 \ \frac{\zeta^{5/3}}{B^{5/6}} \ K_{5/6}(B) \tag{8.9}$$

where

$$\hat{n} = \frac{2\pi f L}{\overline{W}}$$

$$\zeta = s/L$$

$$B = \frac{\zeta}{1.339} \sqrt{1 + (1.339\hat{n})^2}$$

For vertical component turbulence the expression is

136

$$\phi_{w_x w_y}(\zeta, \hat{n}) = 0.01853 \; \sigma^2_{w_z} \left\{ 4.78 \; \frac{\zeta^{5/3}}{B^{5/6}} \; K_{5/6}(B) - \frac{\zeta^{11/3}}{B^{11/6}} \; K_{11/6}(B) \right\} \qquad (8.10)$$

where $K_{5/6}$ and $K_{11/6}$ are modified Bessel function of the second kind of order 5/6 and 11/6, respectively.

C. Comparison of Analytical Model with Experimental Results

Figures 8.1 through 8.3 for Run #8623 and Figures 8.4 through 8.6 for Run #8624 compare the experimental data with the analytical model of Houbolt and Sen (1972). The theoretical model is computed using both the length scale by Method 1 and the length scale by Method 3. Figures 8.1 and 8.4 contain experimental results for three separation distances. The separation distances are the distance between Tower 1 and Tower 2, Tower 1 and Tower 4, and Tower 1 and Tower 5 at Level 4, respectively. Figures 8.2 and 8.5 show similar results; however, in this case, there are only two separation distances between Tower 2 and Tower 4 and Tower 2 and Tower 5. Finally, Figures 8.3 and 8.6 show the results for Tower 4 with one separation distance Tower 4 to Tower 5. All data are for Level 4.

In each figure, the log of the cross-spectra, $\phi_{U_{ij}U_{k\ell}}$, is normalized with the product of the standard deviation at each tower position, $\sigma_{U_{ij}}$, $\sigma_{U_{k\ell}}$, versus the log of the frequency times separation distance divided by the mean wind speed, $fs/\overline{W}$. In general, the analytical curves do not fit the data particularly well. In most cases, the data essentially follow a straight line which does not show the characteristic knee in the curve as predicted by the theory. Also, the slope of the experimental data does not agree with the slope of the theoretical curve. In

137

log $\left[\{ {}^{\phi U_{14} U_{i4}} \} / \{ {}^{\sigma U_{14}}{}^{\sigma}U_{i4} \} \right]$

	Method 1		Method 3		
	s/L	L_1	s/L	L_3	T_i-T_j
⊖——⊖	0.19	116.5	0.28	77.6	T1T2
▲――――▲	0.27	163.8	0.55	80.1	T1T4
▣—·—▣	0.49	163.7	0.92	87.5	T1T5

log fs/$\overline{W}$
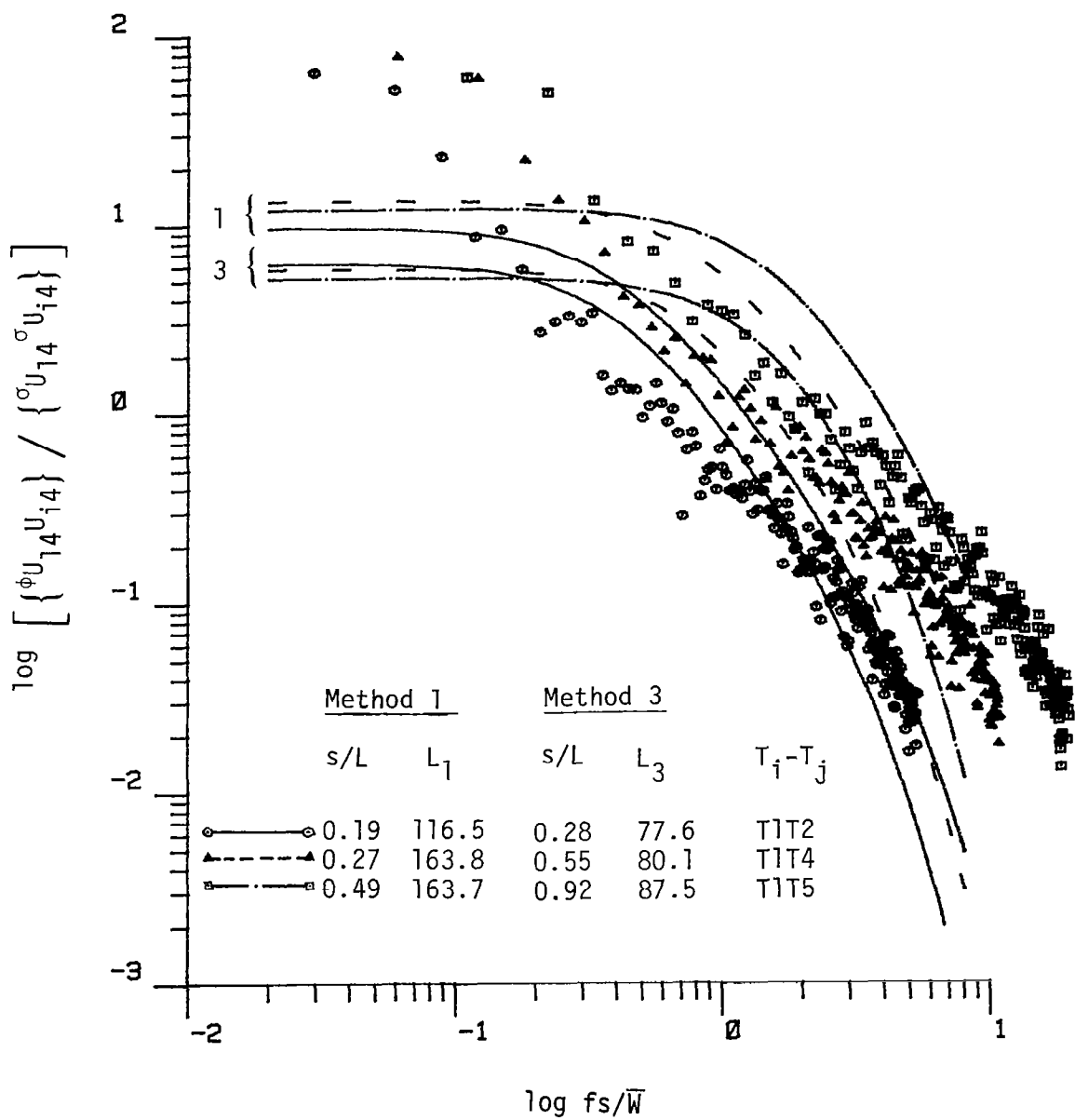
Figure 8.1. Comparison of computed two-point spatial spectra with the theoretical model of Houbolt and Sen (1972) (Run #8623, L4, Component 1).

138
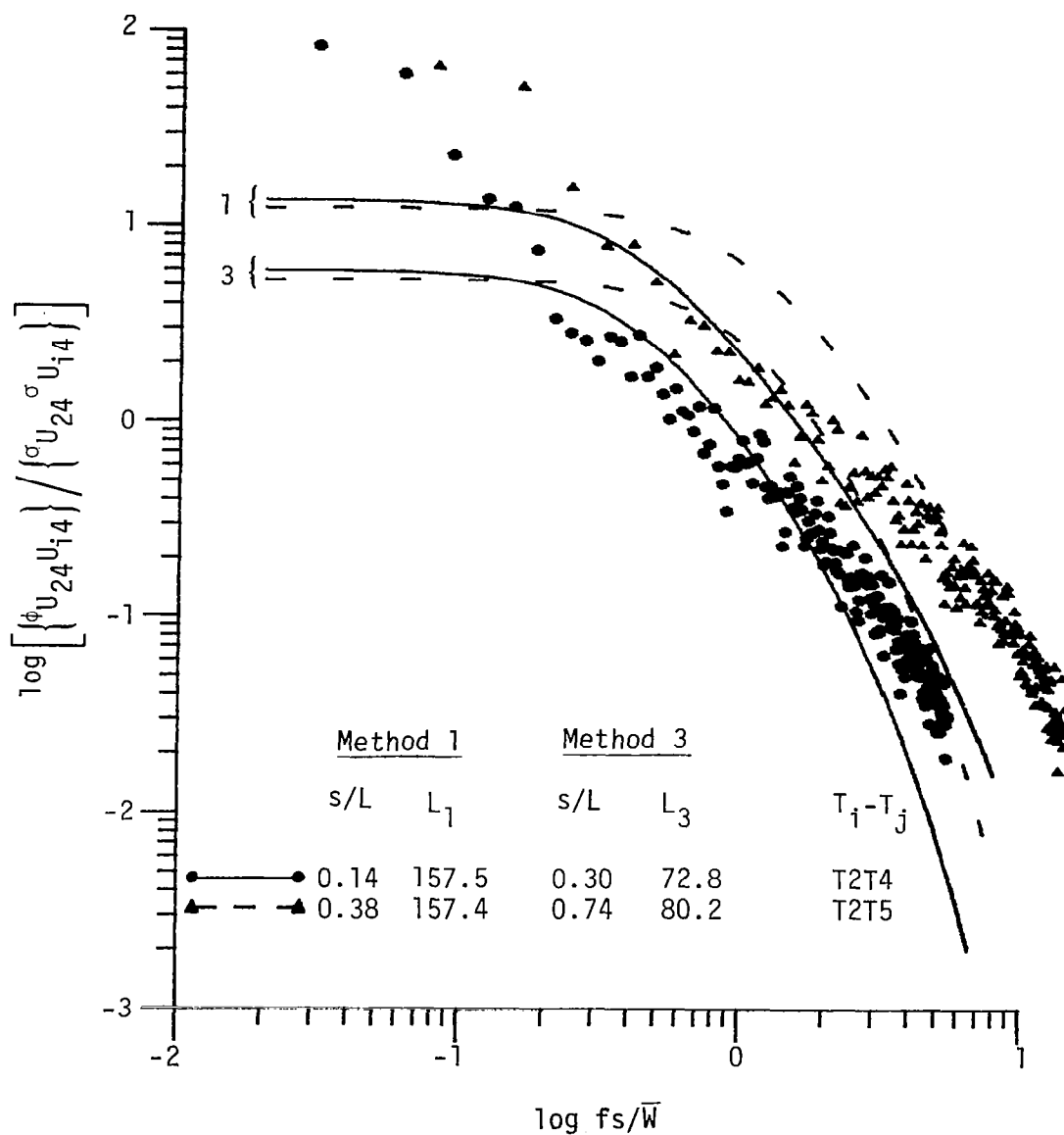
Figure 8.2. Comparison of computed two-point spatial spectra with the theoretical model of Houbolt and Sen (1972) (Run #8623, L4, Component 1).

139
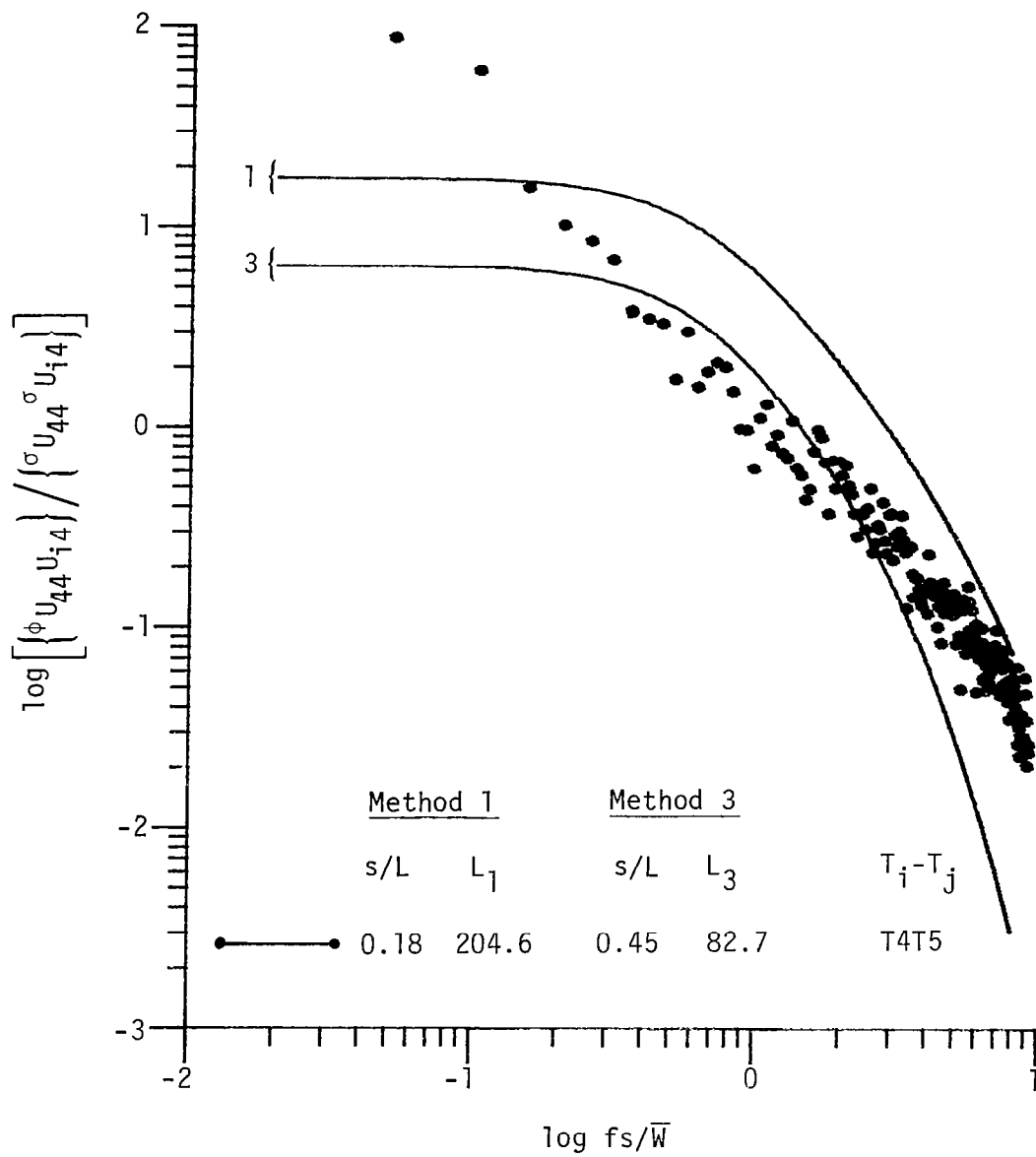
Figure 8.3. Comparison of computed two-point spatial spectra with the theoretical model of Houbolt and Sen (1972) (Run #8623, L4, Component 1).
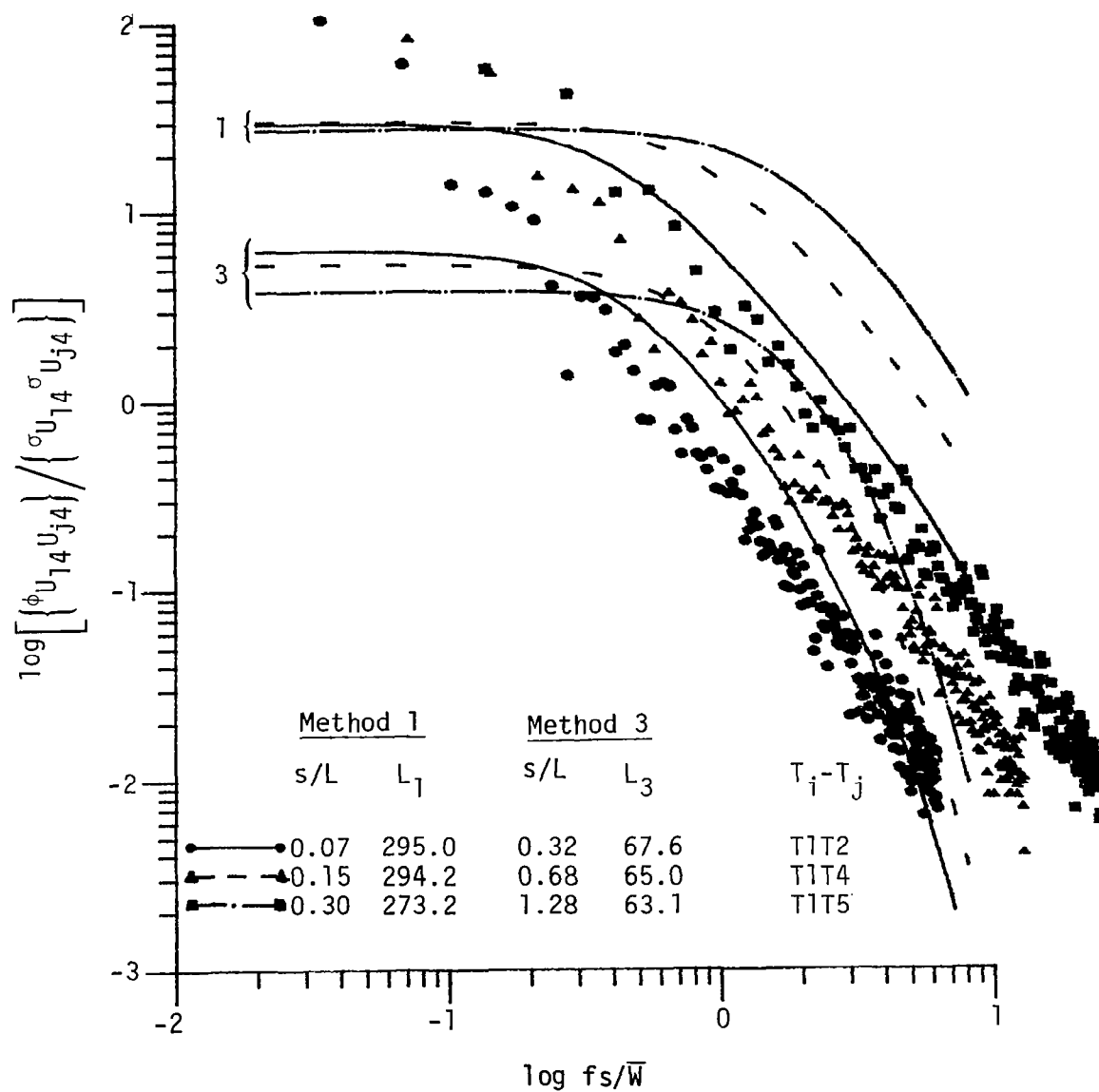
Figure 8.4. Comparison of computed two-point spatial spectra with the
theoretical model of Houbolt and Sen (1972) (Run #8624,
L4, Component 1).

141
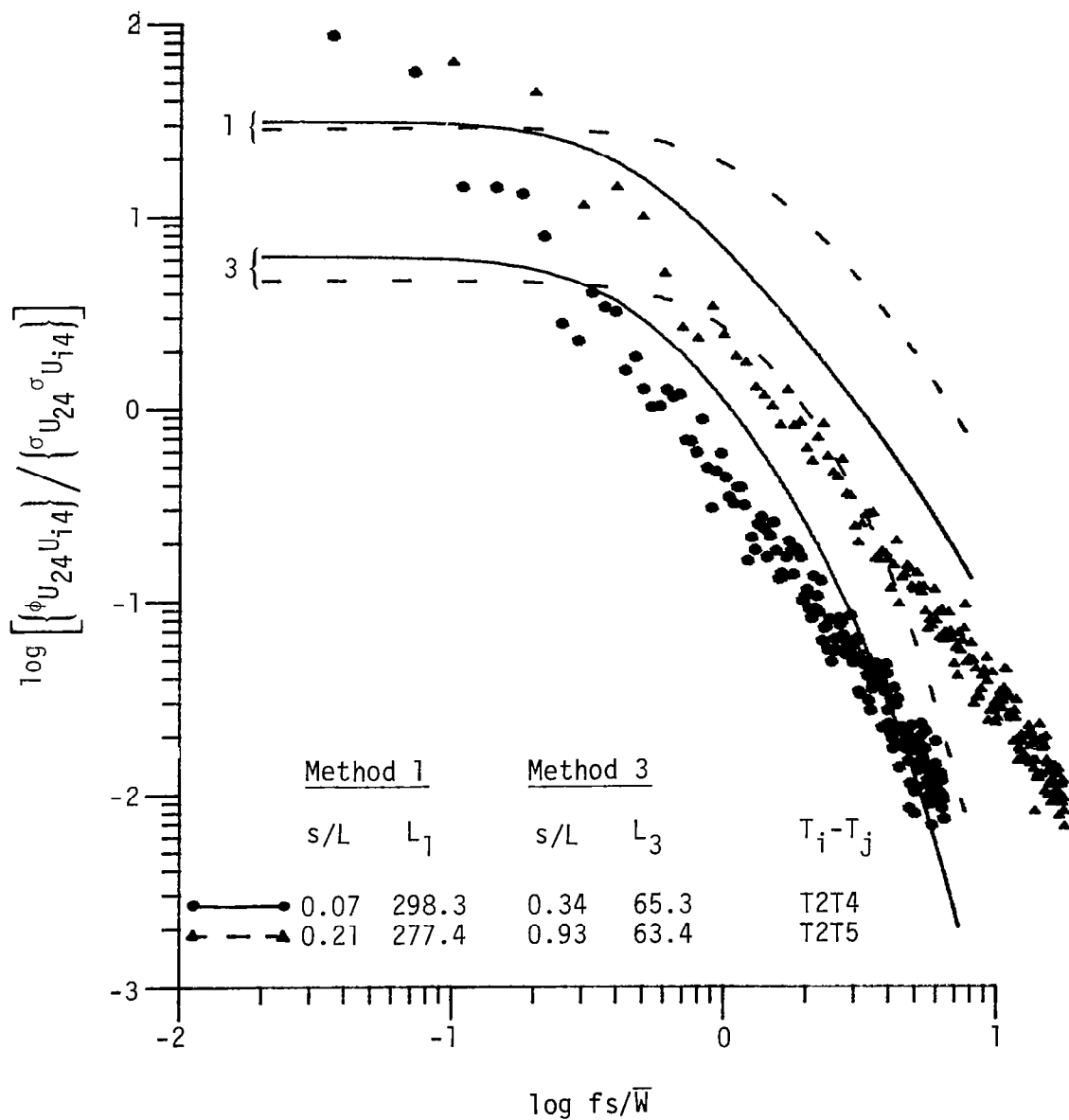
Figure 8.5. Comparison of computed two-point spatial spectra with the theoretical model of Houbolt and Sen (1972) (Run #8624, L4, Component 1).
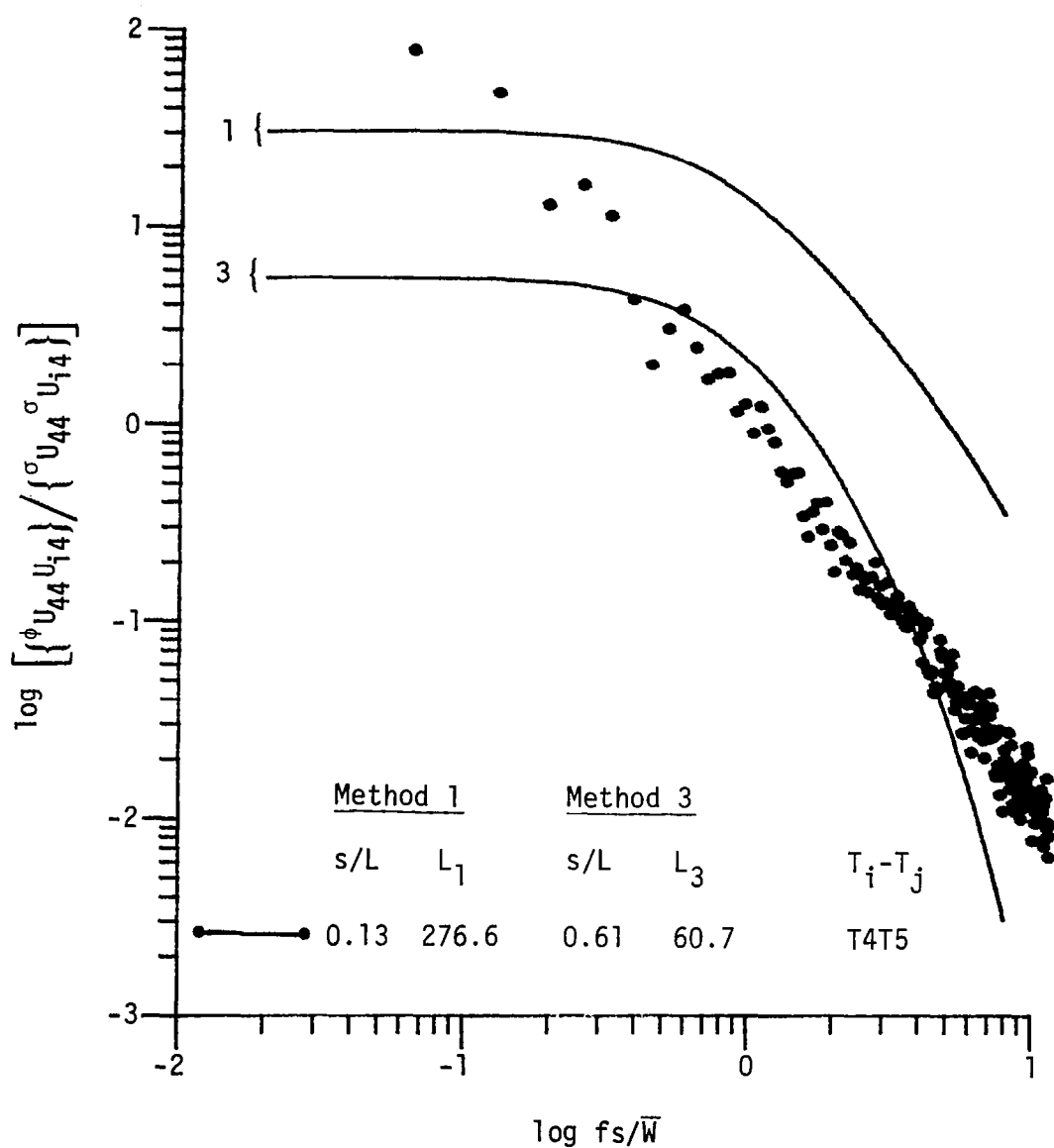
Figure 8.6.. Comparison of computed two-point spatial spectra with the theoretical model of Houbolt and Sen (1972) (Run #8624, L4, Component 1).

all cases, the experimental data show much higher energy in the low frequency level than predicted by the analytical model.

It is apparent from these results that the assumption of isotropic turbulence is not valid near the ground. Empirical models correlating the experimental results are needed. Also, the data are stratified according to separation distance. For values of s/L increasing in magnitude, the data show more significant energy at a given value of fs/$\bar{W}$. In addition to the isotropic assumption inherent in the analytical model, there is another assumption in the development of the two-point spatial spectra for the longitudinal velocity component that may cause disagreement with the data.

Houbolt and Sen (1972), in developing their spectrum expression, began with the von Karman correlation function (see Chapter VI). In their analysis, the separation distance was ζ, shown in Figure 2.4, page 20, and the correlation was taken between $w_x(x,y)$ and $w_x(x+\xi,y+n)$. The theoretical von Karman correlation, however, is based on $w_p(x,y)$ and $w_p(w+\xi,y+n)$ for the longitudinal correlation and $w_n(x,y)$ and $w_n(x+\xi,y+n)$ for the lateral correlation. The author believes that Houbolt and Sen (1972) should have begun their analysis with Equation 2.35, page 19. Thus, the disagreement between theory and experiment for the case of the longitudinal velocity component may be, in part, due to this assumption.

Figures 8.7 through 8.13 show the same comparison of theory with results for the vertical velocity component. In this case, slightly better agreement with the data and theory is obtained; however, the agreement is still not good. The better agreement is demonstrated by the fact that the data tend to take on a slope similar to the analytical

144
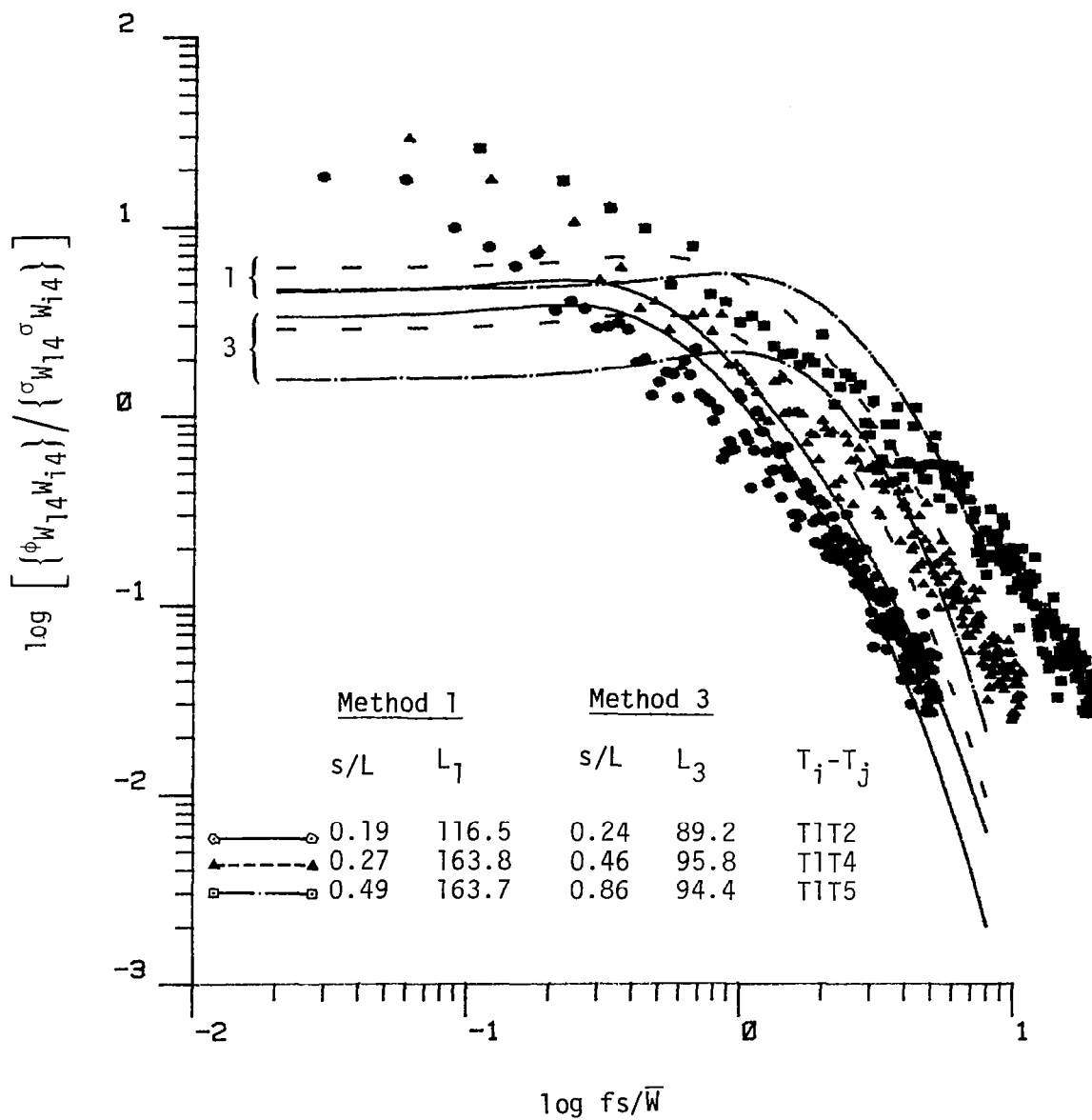
Figure 8.7. Comparison of computed two-point spatial spectra with the theoretical model of Houbolt and Sen (1972) (Run #8623, L4, Component 3).

145
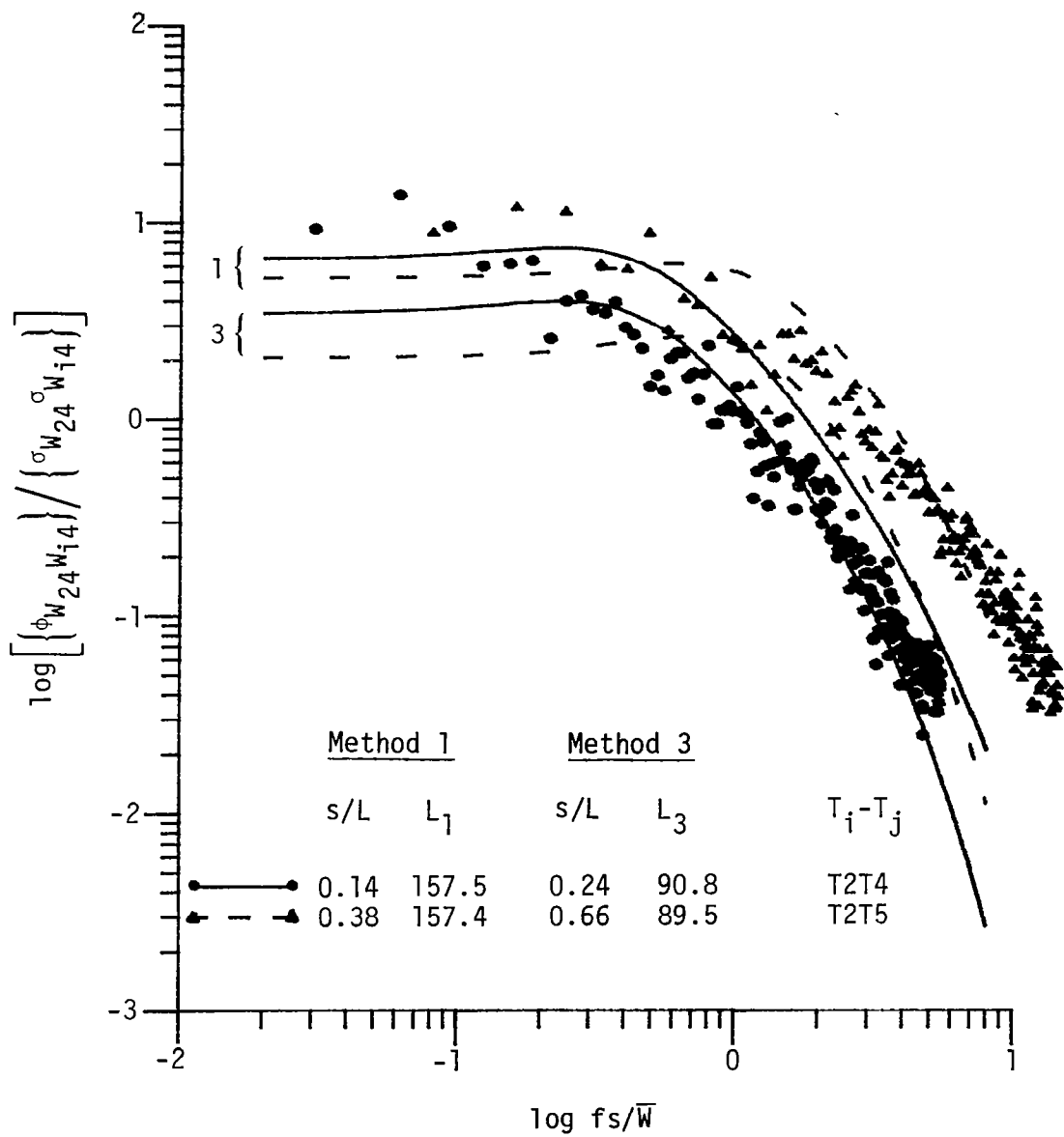
Figure 8.8. Comparison of computed two-point spatial spectra with the theoretical model of Houbolt and Sen (1972) (Run #8623, L4, Component 3).
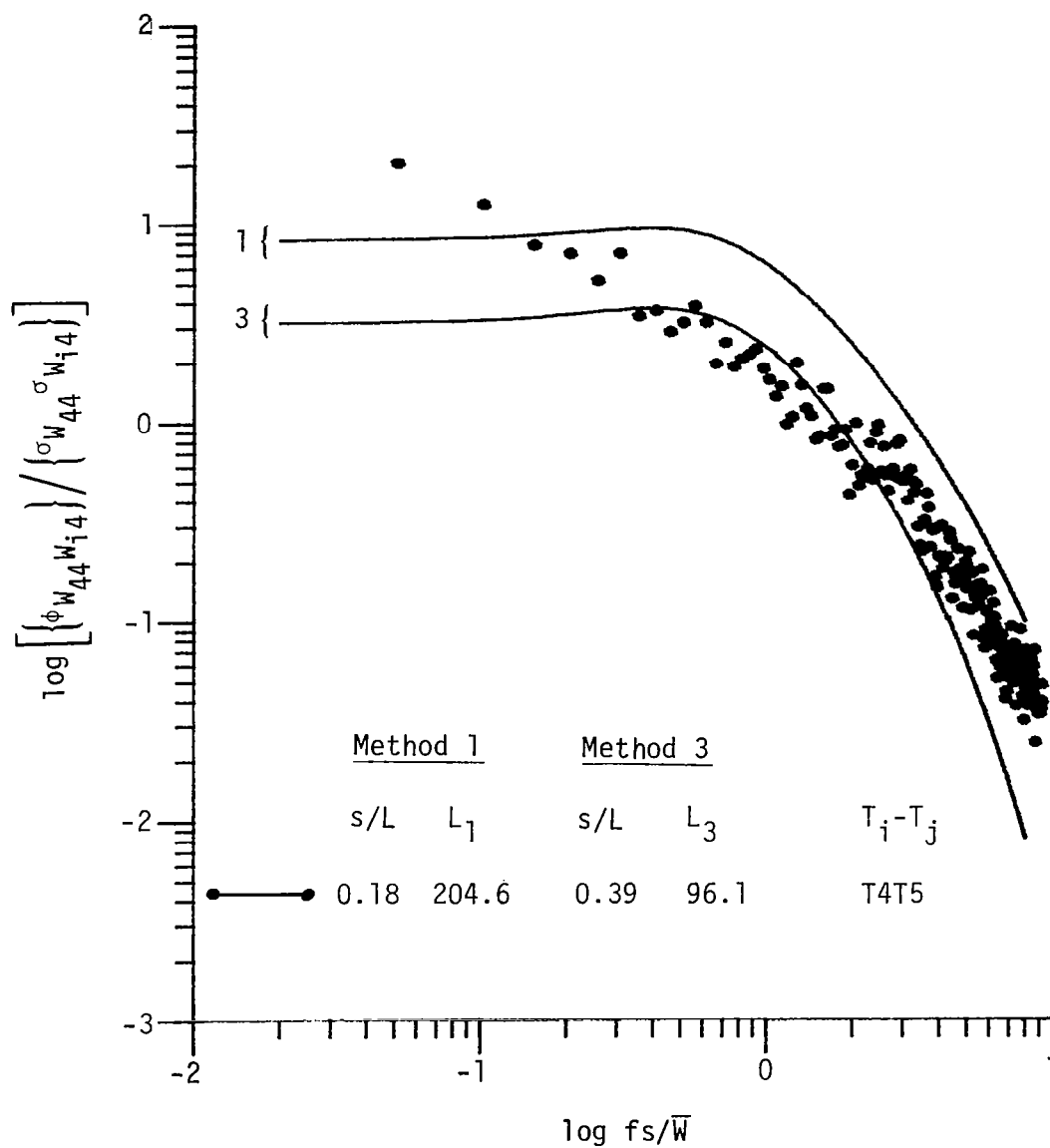
Figure 8.9. Comparison of computed two-point spatial spectra with the theoretical model of Houbolt and Sen (1972) (Run #8623, L4, Component 3).
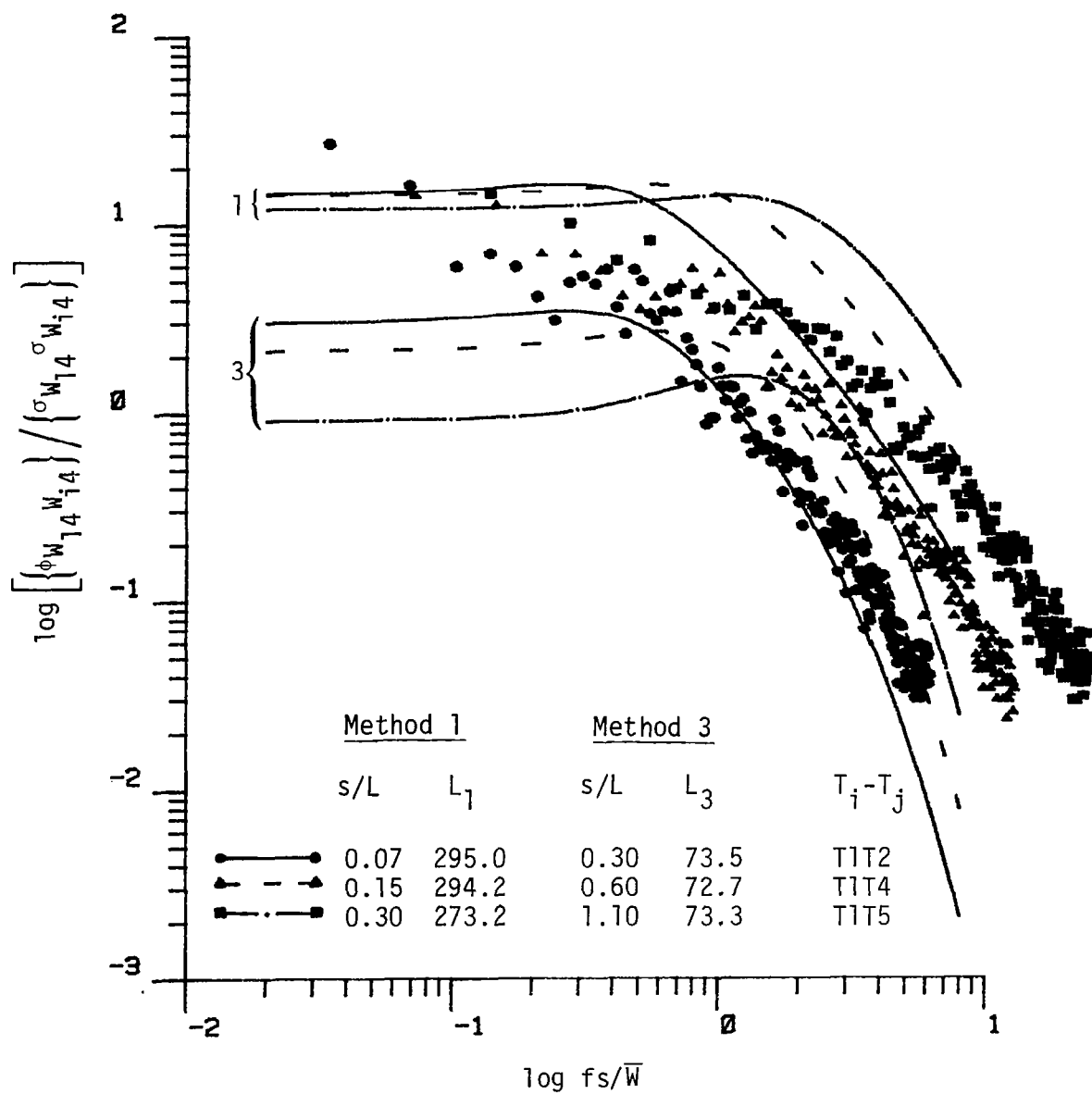
Figure 8.10. Comparison of computed two-point spatial spectra with the
theoretical model of Houbolt and Sen (1972) (Run #8624,
L4, Component 3).
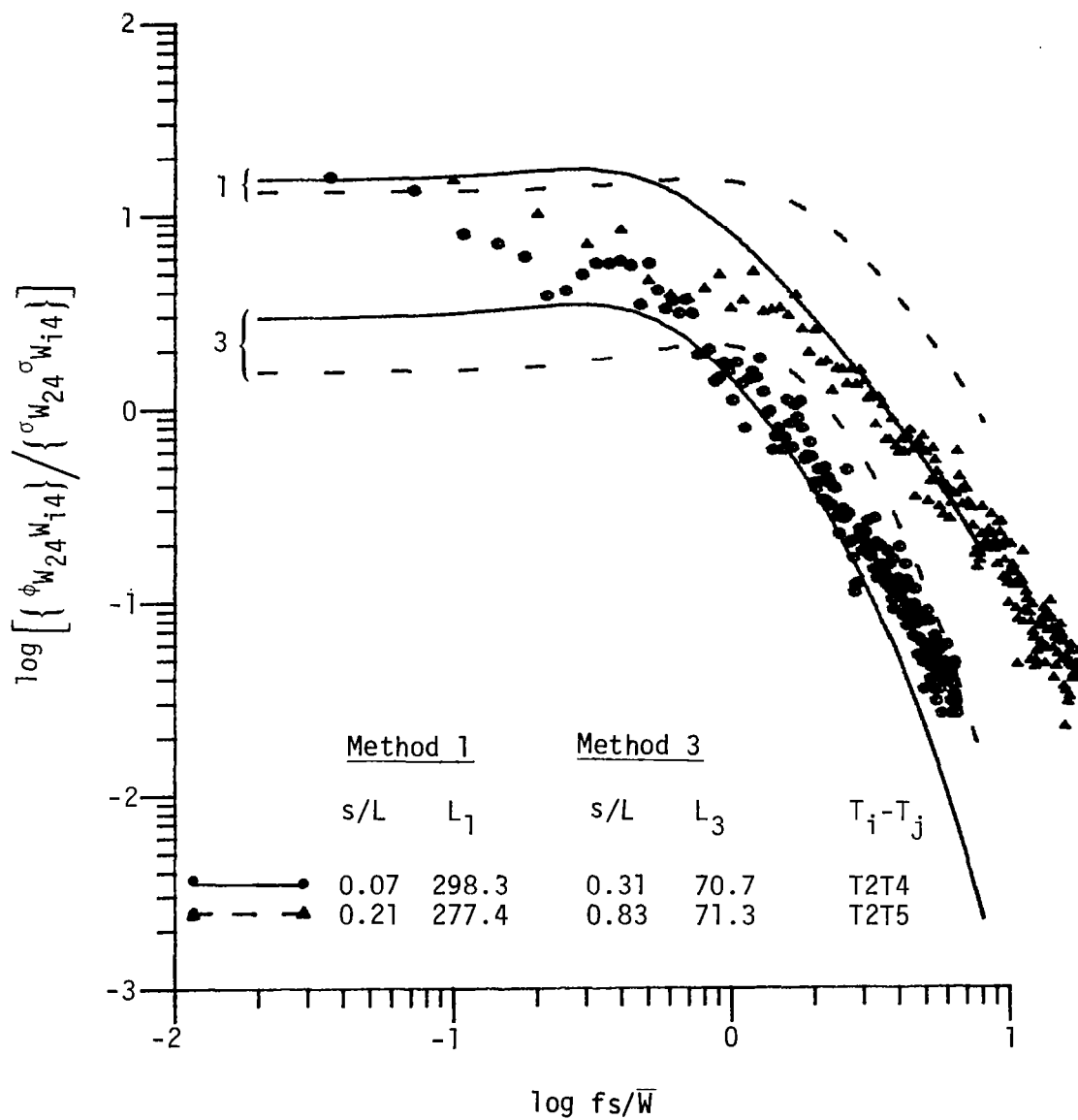
Figure 8.11. Comparison of computed two-point spatial spectra with the theoretical model of Houbolt and Sen (1972) (Run #8624, L4, Component 3).

149
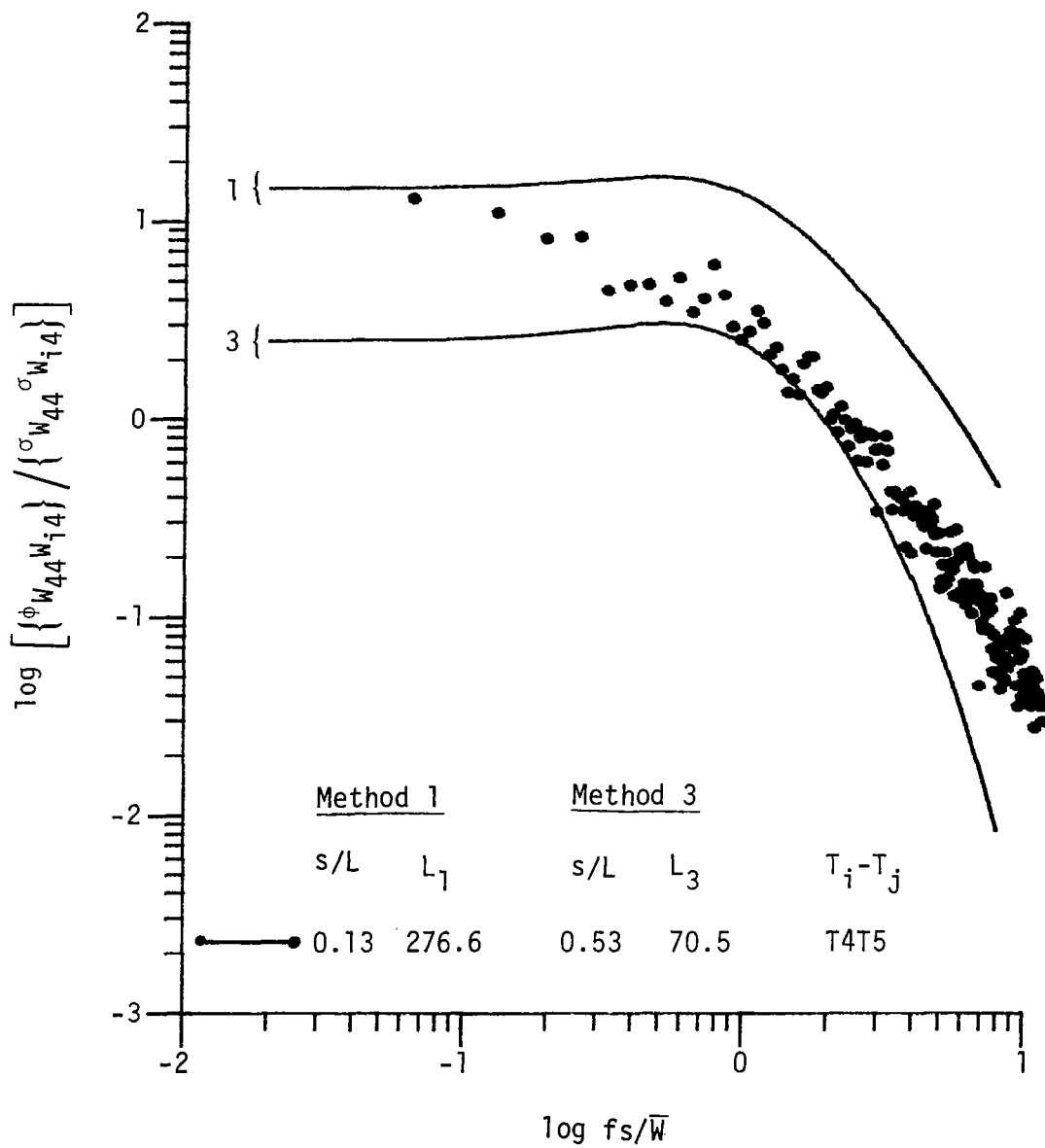
Figure 8.12. Comparison of computed two-point spatial spectra with the theoretical model of Houbolt and Sen (1972) (Run #8624, L4, Component 3).

150

models at higher frequencies and begin to show a "knee" at lower frequencies.

It is readily apparent, however, from comparing the experimental results with the analytical model that the assumption of isotropic, homogeneous turbulence near the surface of the earth is not valid. Design analysis based on isotropic analytical models of two-point spatial correlations may, thus, provide spurious results. In general, the analytical curves tend to predict more energy in the higher frequencies than the experimental data show. On the other hand, at the lower frequencies, the data generally contain considerably more energy than is predicted by the analytical model. Again, the results of the comparison are highly sensitive to the length scale. For the integral length scale (Method 1), which is the typical method of computing length scales used in the literature, higher values of the two-point spatial spectra are predicted at higher frequencies than are demonstrated experimentally and lower values at lower frequencies. The analytical model based on length scale computed by Method 3 tends to pass through the data at higher frequencies and, in some cases, fits the data reasonably well.

It should be observed, however, that in all cases, the analytical curves representing different separation distances cross one another near the knee of the curve. Similar crossing of the experimental data is not shown at all by the experimental results. It is apparent that additional analysis of the data is required to establish meaningful design criteria that represents the experimental results and can be applied to calculations of rolling and pitching moments as described in Chapter II.

151

D. Coherence Function

The coherence function is a two-point spatial spectrum normalized by the product of the one-point spectra at the separation points. Thus, the coherence function is an expression of the correlation or coherence between fluctuations of the individual frequencies.

Davenport (1961) suggests the coherence between wind velocity components in the atmospheric surface layer is generally expressed by

$$\gamma^2(\eta) = \exp(-a\eta) \tag{8.11}$$

where a is a nondimensional parameter called the decay parameter, η is defined as before by $sf/\overline{W}$, and $\overline{W}$ is the average mean wind speed between the two measuring positions. Because the decay parameter, a, depends on many factors, Pielke and Panofsky (1976) generalized Equation 8.11 by

$$\gamma_{ij}^2(\eta) = \exp(-a_{ij}\eta) \tag{8.12}$$

where the first subscript represents the direction of the velocity component (1 = longitudinal, 2 = lateral, and 3 = vertical) and the second subscript represents the direction of separation of the measuring stations. For the longitudinal wind component and longitudinal separation, Ropelewski et al. (1973) suggests that the coherence should decrease with travel time according to

$$\gamma_{11}^2(\eta) = \exp(-t/\tau) \tag{8.13}$$

where τ is the eddy decay time which is of order λ/σ_{w_x}, λ is an eddy of size associated with frequency f and can be written as $\lambda = \overline{W}/f$, and $t = s/\overline{W}$ is the time it takes the eddy to be advected downstream. With these

estimates and the definition of the nondimensional frequency, the expression for the coherence becomes

$$\gamma_{11}^2(n) = \exp\left(-\frac{fs}{\overline{W}}\frac{\sigma_{W_x}}{\overline{W}}\right) = \exp\left(-\frac{\sigma_{W_x}}{\overline{W}}n\right) \qquad (8.14)$$

Thus, the decay parameter for the longitudinal wind component for longitudinal separation may be written as

$$a_{11} = c\frac{\sigma_{W_x}}{\overline{W}}$$

where c is an undetermined constant to be evaluated by experiment; therefore, the longitudinal coherence decay parameter, a_{11}, is strongly dependent on roughness.

For the lateral separation and the longitudinal wind component, there is no lag time involved, and the coherence may be written in complete analogy with Davenport's expression as

$$\gamma_{12}^2(n) = \exp\left(-c\frac{L_{W_x}}{L_{W_y}}n\right) \qquad (8.15)$$

where L_{W_x} and L_{W_y} are integral length scales (Method 1, Chapter V) computed from $R_{W_x W_x}$ and $R_{W_y W_y}$, respectively, and c is an unknown nondimensional constant. The ratio of the length scale is a function of stability; therefore, the decay parameter a_{12} is a strong function of stability.

The coherence function for the longitudinal velocity component separated laterally was computed for the data from the previously

153

discussed spectra. From curve fitting techniques, the decay parameter a_{12} was obtained. Figures 8.13 through 8.16 show the lateral coherence computed between different heights of towers for Levels 1, 2, 3, and 4, respectively. At the lower levels, the coherence is more scattered; but in general, the decay parameter increases with decreasing height.

Kristensen and Jensen (1979) report that a_{12} is approximately 14 at the 20-m level, whereas Panofsky et al. (1974) find a_{12} is approximately 12 for neutral boundary layer conditions. The value of a_{12} for the present data is approximately 10.3 at the 20-m level. They also suggest that the decay parameter a_{12} is a function of height and separation distance in isotropic turbulence. Thus,

$$a_{12} \simeq \frac{18\left(\frac{s}{10}\right)^{0.26}}{\left(\frac{z}{10}\right)^{0.13}}$$

(8.16)

where s is the separation distance and z is height. Figure 8.17 compares the decay parameter a_{12} from the measured data with Equation 8.16 at different heights. At the 3-m level, the comparison is reasonable. The decay parameter is expected to be a function of separation distance, but at the 6-m and 12-m levels the decay parameter is scattered and shows no clear dependence on separation distance. At the 20-m level, the decay parameter appears to remain constant with separation distance.

Table 8.1 lists the decay parameter a_{13} for the longitudinal velocity component separated in the vertical direction, which is approximately 13.6. Brook (1975) reports a_{13} values of about 17 for a neutral boundary layer; whereas, Panofsky et al. (1974) report that a_{13} varies
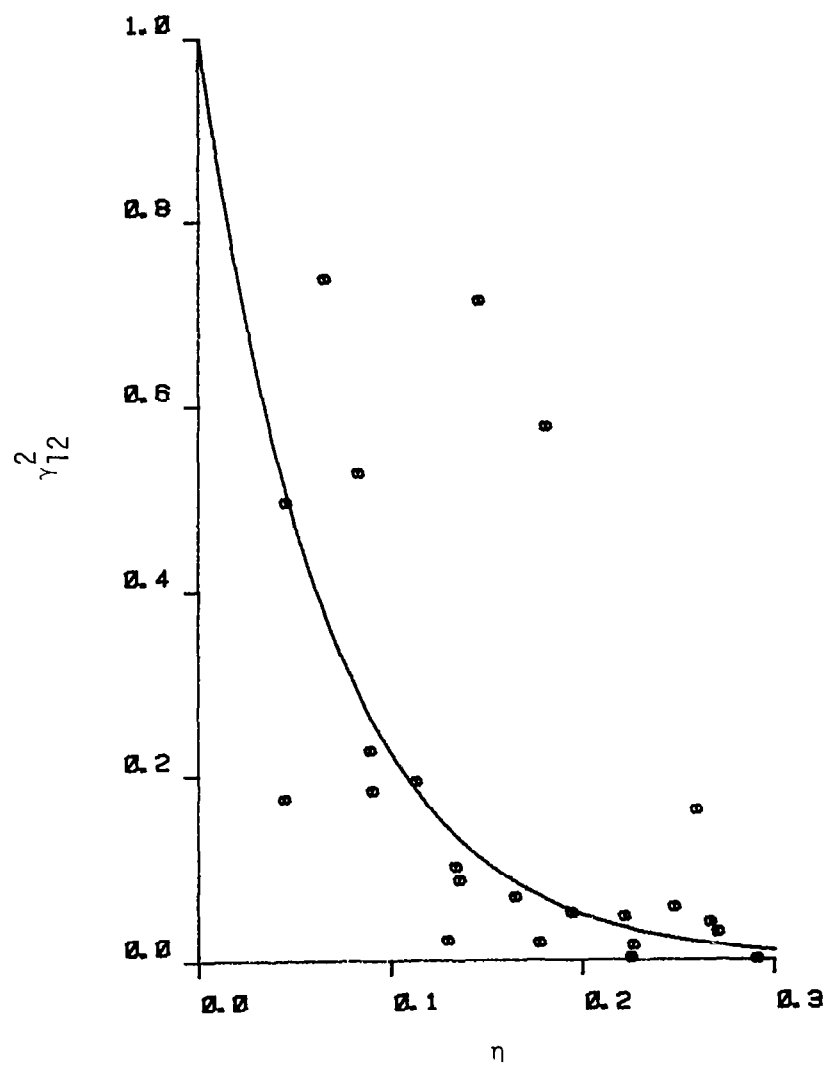
Figure 8.13. The lateral coherence γ_{12}^2 for the longitudinal velocity component at the 3-m level.
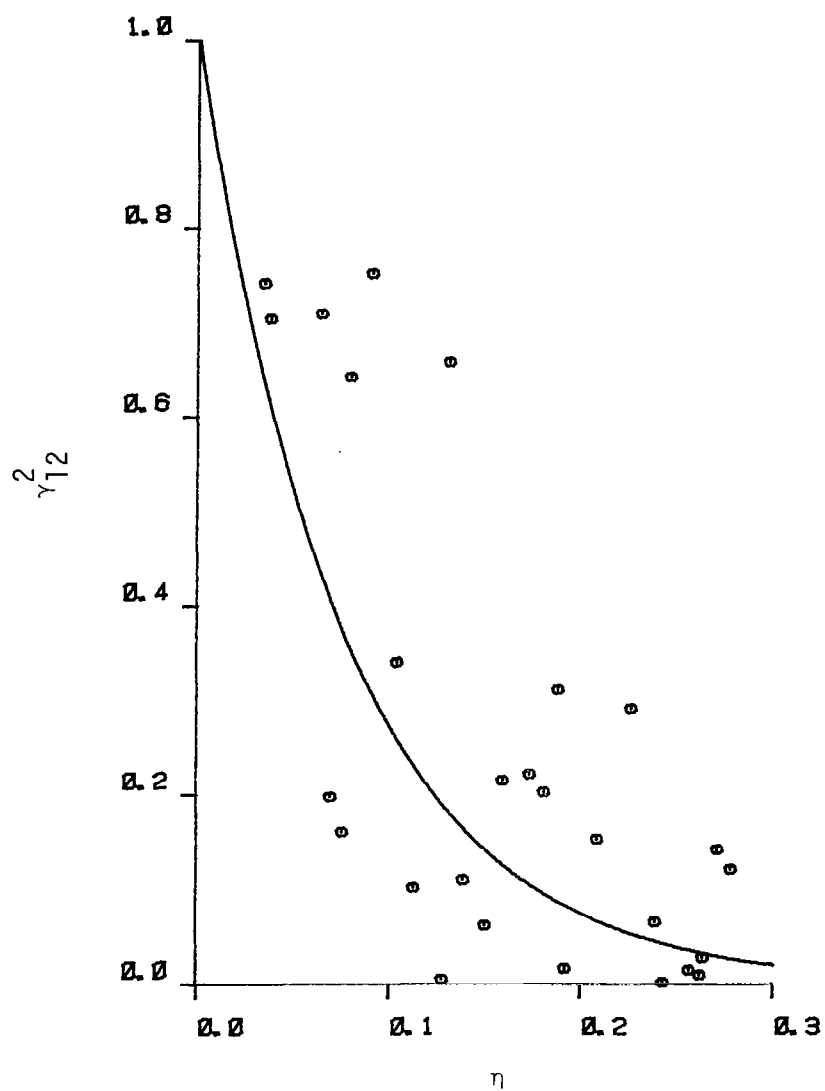
Figure 8.14. The lateral coherence γ_{12}^2 for the longitudinal velocity component at the 6-m level.
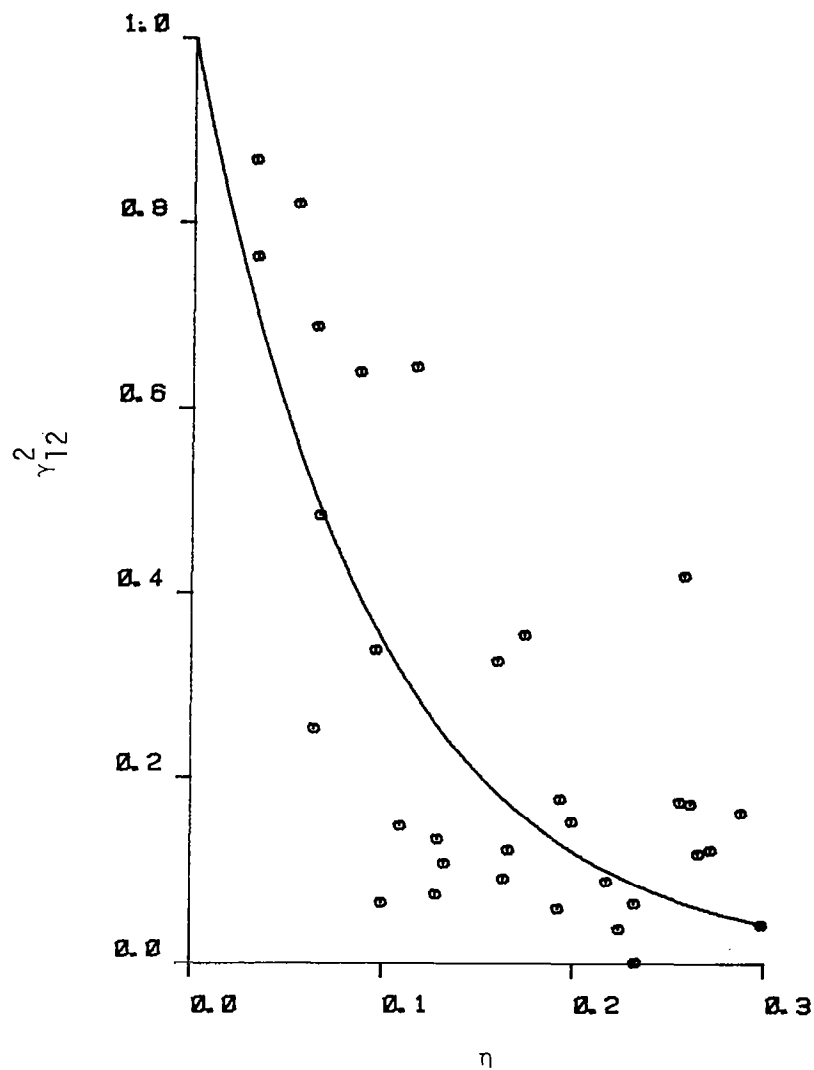
Figure 8.15. The lateral coherence γ_{12}^2 for the longitudinal velocity component at the 12-m level.
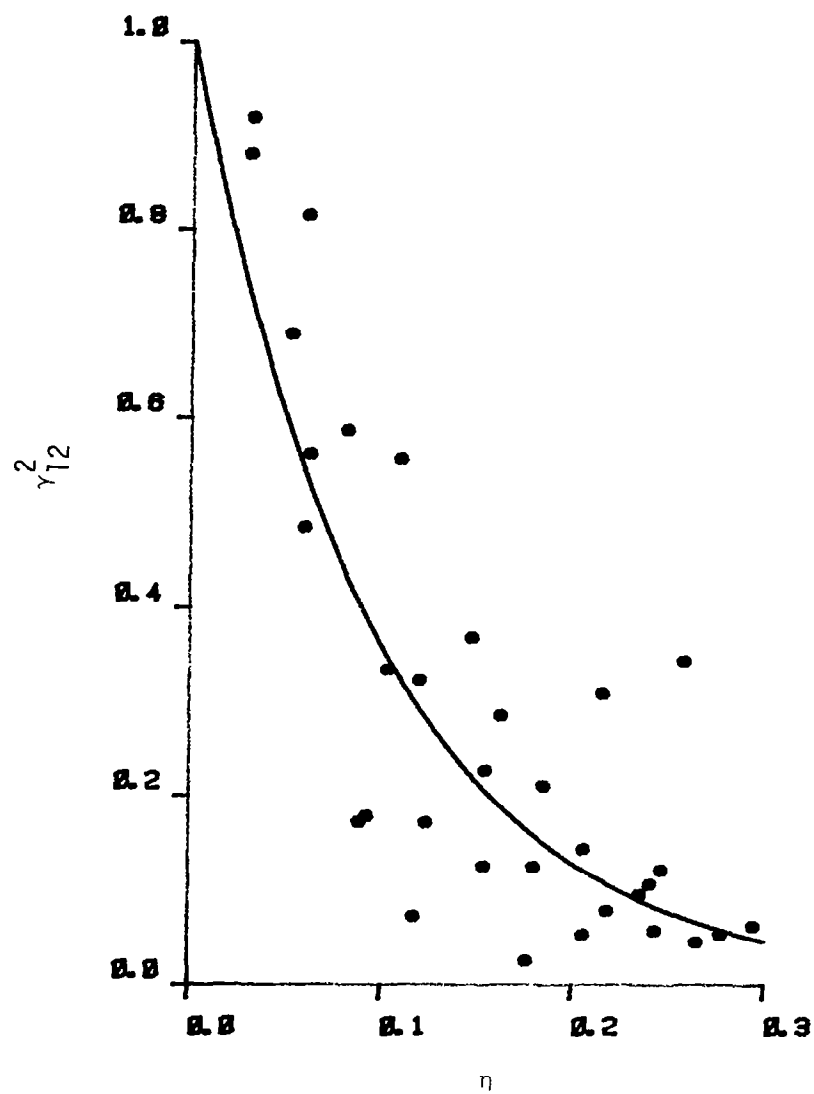
Figure 8.16. The lateral coherence γ_{12}^{2} for the longitudinal velocity component at the 20-m level.
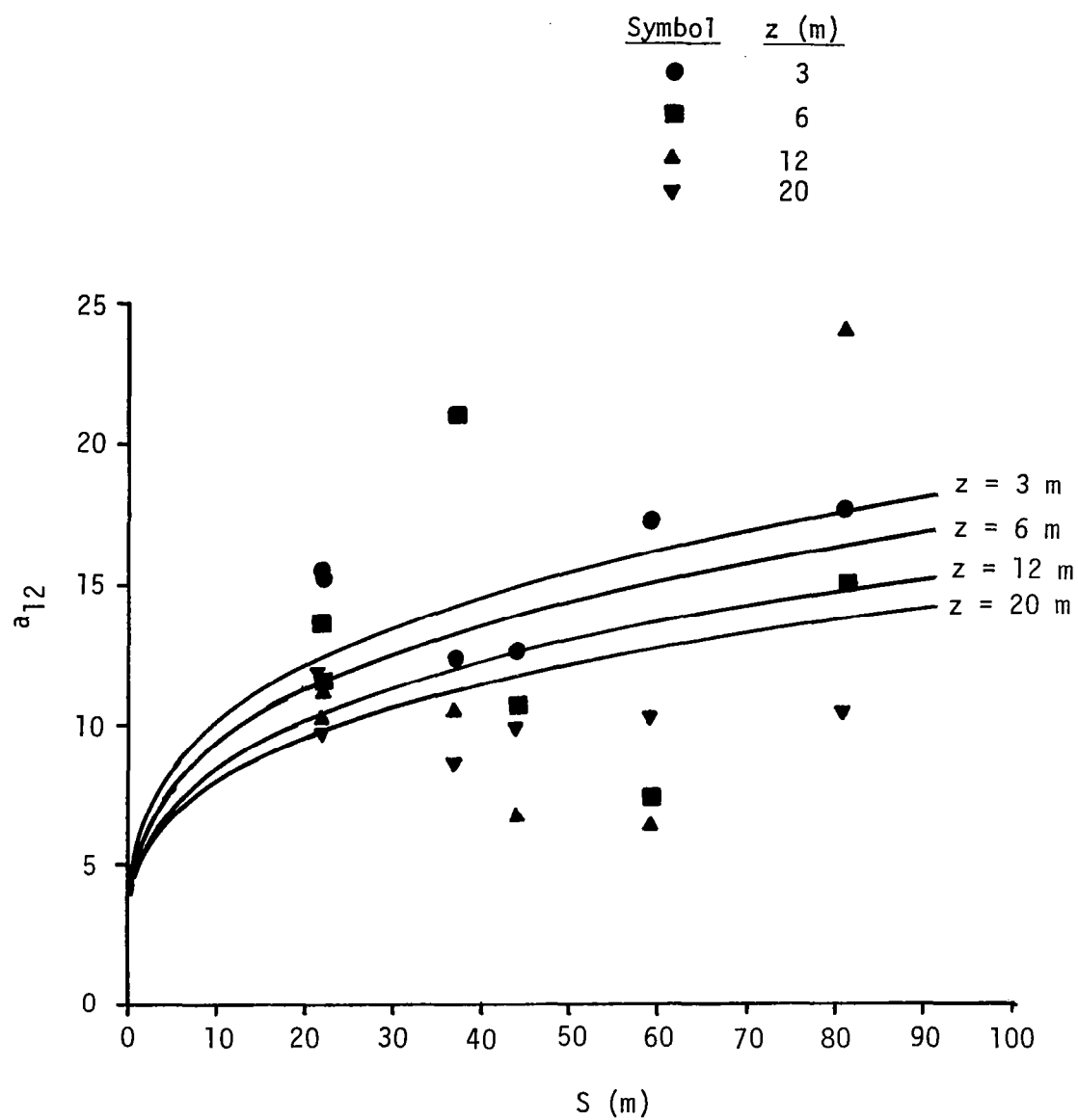
Figure 8.17. Comparison of the decay parameter a_{12} with Equation 8.16.

TABLE 8.1. Decay Parameter a_{13}

z_{max}	Δz	T1	T2	T4	T5
20	8	12.8	12.6	15.8	14.2
20	14	14.3	13.5	13.6	14.5
20	17	12.7	12.1	12.0	17.6
12	7	12.1	13.2	13.3	12.4
12	9	12.1	14.5	15.7	14.0
6	3	12.6	14.6	13.5	13.3

from values of 30 during stable conditions to values less than 10 during unstable conditions. They report that a_{13} has a value of about 20 in neutral stratification.

In general, the decay parameter a_{13} is reported to increase with increasing separation height, Δz, and decrease with increasing height, z_{max}. In the present data, there is no obvious indication that a_{13} depends on the separation distance Δz.

CHAPTER IX

CONCLUSIONS

Statistical analyses of the wind speed data measured with the eight-tower array for Run #8623 mean wind perpendicular to the array and Run #8624 mean wind parallel to the array have been carried out. Not all analyses possible with this gigantic data set have been carried out, but most of the analyses important to aeronautical applications have been made.

Probability density distributions of the longitudinal and vertical components of the velocity at each tower and level were calculated. The probability density function of the turbulence data demonstrates, as is typical of atmospheric turbulence, a distribution of greater kurtosis than a Gaussian distribution. In turn, the vertical distribution behaves very strangely, which is possibly due to what appears to be a typical chopping of the velocity fluctuations in the time history records.

The length scale of the turbulence was calculated by four different methods. Method 4, based on computing the length scale in terms of the frequency at which the computed turbulence spectrum has a maximum value, resulted in a length scale, which gave best comparison of theory with experimental results. Computed values of the length scale for Run #8623 at the 20-m level ranged from 50 m to 250 m depending on the method of calculation. Whereas, for Run #8624, the average length scale ranged from 40 m to 580 m.

Two-point spatial correlation coefficients for each run have been computed for the longitudinal velocity components at each measuring

161

station. Two-point time-dependent velocity correlations have been computed for both the longitudinal and vertical velocities. These have been computed for various combinations of measuring stations, both vertically and horizontally spaced, but have not been computed for all possible combinations. Comparison with the theoretical models of von Karman and Dryden were carried out. The correlations show poor agreement with the theoretical models. This is not surprising in view of the fact that the models are based on isotropic homogeneous turbulence; whereas, the turbulence near the surface is highly nonisotropic. Also, the correlations are strongly dependent upon the length scale used. The length scale based on Method 4 gave good agreement at small lag times, less than 3 seconds; whereas, the correlations computed on length scale based on Method 1 gave better agreement at lag times in excess of 2 to 3 seconds.

One-point spectra for the longitudinal and vertical components for Level 4 on all towers for both runs have been compared with three separate analytical models. The agreement with the theoretical models is poor. This is not surprising for the von Karman model based on isotropic and homogeneous turbulence nor for the Dryden model based on mainly laboratory flows. It was anticipated, however, that better agreement with Kaimal's model would be shown by the data in view of the fact that it is an empirical formulation based on data measured with towers of approximately the same level as those used in the present study. As with the correlations, the theoretical spectral models are extremely sensitive to the choice of length scale. In general, when the spectra are computed with length scale based on Method 4, best agreement

162

with the data is achieved. The spectra for Run #8623 shows a short
inertial subrange which has a slope of -5/3 as is generally reported for
atmospheric turbulence. Surprisingly, the spectra for Run #8624 show a
corresponding inertial subrange which varies as the -2 power showing
best agreement with the Dryden spectrum model. This is unusual for
atmospheric turbulence and is believed to be a terrain or an internal
boundary layer effect.

Two-point spatial spectra were also computed. The two-point
spectra play an important role in the rolling and pitching moments due
to spatial variation in turbulence over an airfoil. In general, the
two-point spectra calculated for Run #8623 are representative of the
turbulence distribution across the airfoil; whereas, the results of Run
#8624 are representative of wind along the body of the aircraft.

The results show, in general, that the analytical two-point spectrum
model proposed by Houbolt and Sen (1972) is highly sensitive to the
length scale and also does not predict the high-turbulence kinetic
energy at the low frequencies observed in the experimental data. The
vertical velocity two-point spatial spectra, however, show better
agreement with the theory than the longitudinal component. It is appar-
ent from the results that additional analysis of the data is required to
establish meaningful design criteria which represent the experimental
results and which can be applied to calcultions of aircraft rolling,
yawing, and pitching moments.

Coherence functions, which are the two-point spatial spectra normal-
ized by the product of the one-point spectra at the separation points,
were also computed. The results were found to compare (with the reported

exponential variation of the coherence function; the argument of the function being the separation distance scaled with reduced frequency). In general, however, the scatter in the data is quite large. In all cases, the lateral coherence of the longitudinal velocity components were computed. The decay parameter in the exponential correlation of the coherence function was found to increase with increasing altitude, but did not show the dependence on separation distance reported in the literature.

Considerable data remains to be analyzed from this overall measurement program. Additionally, analyses of the results presented in here are required to adapt the experimental results into useful design criteria for aeronautical applications.

LIST OF REFERENCES

LIST OF REFERENCES

Akkari, Safwan H., and Walter Frost (1982). "Analysis of Vibration
    Induced Error in Turbulence Velocity Measurements from an Aircraft
    Wing Tip Boom, NASA CR 3571.

Bendat, J. S., and A. G. Piersol (1971). Random Data: Analysis and
    Measurement Procedures. New York: John Wiley & Sons, Inc.

Bisplinghoff, R. L., and H. Ashley (1957). Aeroelasticity. Menlo Park,
    California: Addison-Wesley Publishing Company.

Brook, R. R. (1975). "A Note on Vertical Coherence of Wind Measured in
    an Urban Boundary Layer," Boundary-Layer Meteorology, 9:11-20.

Davenport, A. G. (1961). "The Spectrum of Horizontal Gustiness Near the
    Ground in High Winds," Quarterly Journal of the Royal Meteorolog-
    ical Society, 87:194-211.

Diederich, Franklin W. (1957). "The Response of an Airplane to Random,"
    NACA TN 3910.

Diederich, Franklin W., and Joseph A. Drischler (1957). "Effect of
    Spanwise Variation in Gust Intensity on the Lift Due to Atmospheric
    Turbulence," NACA TN 3920.

Dryden, H. L. (1961). "A Review of the Statistical Theory of Turbu-
    lence," Turbulence Classic Papers on Statistical Theory. New York:
    Interscience Publishers, Inc.

Duchene-Marullaz, P. (1975). "Full-Scale Measurements of Atmospheric
    Turbulence in Suburban Area," Wind Effects on Buildings and Struc-
    ture. London: Cambridge University Press, pp. 23-31.

ESDU (1974). "Characteristic of Atmospheric Turbulence Near the Ground,"
    Part II, Item No. 74031.

Eggleston, J. M., and F. W. Diederich (1956). "Theoretical Calculation
    of the Power Spectra of the Rolling and Yawing Moments on a Wing in
    Random Turbulence," NACA TN 3864.

Eichenbaum, F. D. (1972). "Response of Aircraft to Three-Dimensional
    Random Turbulence," AFFDL-TR-72-28.

Etkin, B. (1972). Dynamics of Atmospheric Flight. New York: John
    Wiley & Sons, Inc.

Frost, Walter (1980). "Standard Deviations and Confidence Intervals for
    Atmospheric Design Criteria Used in WECS Development," Proceedings
    of the Third International Symposium on Wind Energy Systems.
    Bedford, England: BHRA Fluid Engineering.

Frost, Walter, Bryan H. Long, and Robert E. Turner (1978). "Engineering Handbook on the Atmospheric Environmental Guidelines for Use in Wind Turbine Generator Development," NASA TP 1359.

Frost, Walter, and Trevor H. Moulden (1977). Handbook on Turbulence. New York: Plenum Press.

Frost, Walter, and Alireza M. Shahabi (1977). "A Field Study of Wind Over a Simulated Block Building," NASA CR 2804.

Houbolt, J. C. (1973). "Atmospheric Turbulence," AIAA Journal, 4:421-437.

Houbolt, John C., and Asim Sen (1972). "Cross-Spectral Functions Based on von Karman's Spectral Equation," NASA CR 2011.

Kaimal, J. C. (1973). "Turbulence Spectra, Length Scales and Structure in the Stable Surface Layer," Boundary-Layer Meteorology, 4:287-309.

Kordes, E. E., and J. C. Houbolt (1953). "Evaluation of Gust Response Characteristics of Some Existing Aircraft with Wing Bending," NACA TN 2897.

Kristensen, L., and N. O. Jensen (1979). "Lateral Coherence in Isotropic Turbulence and in the Natural Wind," Boundary-Layer Meteorology, 17:353-373.

Lichtenstein, J. H. (1978). "Comparison of Wing-Span Averaging Effects Rolling Moment, and Bending Moment for Two Span Load Distributions and for Two Turbulence Representatives," NASA TM-78699.

Neal, D. (1982). "Full-Scale Measurements of the Wing Regime Over a Saddle, and Correlation with Wind-Tunnel Tests," Boundary-Layer Meteorology, 22:351-371.

Panofsky, Hans A., and Tateke Mizuno (1975). "Horizontal Coherence and Pasquill's Beta," Boundary-Layer Meteorology, 9:247-256.

Panofsky, Hans A., D. W. Thomson, D. A. Sullivan, and D. E. Moravek (1974). "Two-Point Velocity Statistics Over Lake Ontario," Boundary-Layer Meteorology, 7:301-321.

Pastel, Robert L., John E. Caruthers, and Walter Frost (1981). "Airplane Wing Vibrations Due to Atmospheric Turbulence," NASA CR 3431.

Pielke, R. A., and H. A. Panofsky (1976). "Turbulence Characteristics Along Several Towers," Boundary-Layer Meteorology, 1:115-130.

Ropelewski, C. F., H. Tennekes, and H. A. Panofsky (1973). "Horizontal Coherence of Wind Fluctuations," Boundary-Layer Meteorology, 5:353-363.

Shieh, Chih Fang, and Walter Frost (1981). "Numerical Solutions of Atmospheric Flow Over Semi-Empirical Simulated Hills," NASA CR 3430.

Shiotani, Masao (1975). "Turbulence Measurements at the Sea Coast During High Wind," The Research Institute of Industrial Technology Report No. 1, Nihon University, Japan.

Steely, Sidney L., Jr., and Walter Frost (1981). "Statistical Analysis of Atmospheric Turbulence About a Simulated Block Building," NASA CR 3366.

von Karman, T. (1961). "Progress in the Statistical Theory of Turbulence," Turbulence Classic Papers on Statistical Theory. New York: Interscience Publishers, Inc.

Woodfield, Alan A. (1983). "Wind Shear and Vortex Wake Research in UK. 1982," Proceedings: Sixth Annual Workshop on Meteorological and Environmental Inputs to Aviation Systems, NASA CP-2274, DOT/FAA/RD-83-/67, pp. 69-86.

APPENDICES

APPENDIX A

DERIVATION OF EQUATIONS 2.18 AND 2.24

A.1 Derivation of Equation 2.18

The spectrum of lift, ϕ_L, is given by the Fourier transfer of $R_L(\tau)$

$$\phi_L(f) = \int_{-\infty}^{\infty} R_L(\tau)e^{-i2\pi f\tau}d\tau \qquad (A.1)$$

where from Equation 2.11

$$R_L(\tau) = \int_{-\infty}^{\infty}\int_{-\infty}^{\infty} h_t(t_1)h_t(t_2)\left\{\frac{1}{b^2}\int_{-b/2}^{b/2}\int_{-b/2}^{b/2} h_y(y_1)h_y(y_2)\right.$$

$$\left. \times R_{w_z w_z}[V(\tau + t_1 - t_2),(y_2 - y_1)]dy_1 dy_2\right\}dt_1 dt_2 \qquad (A.2)$$

therefore,

$$\phi_L(f) = \int_{-\infty}^{\infty} e^{-i2\pi f\tau}\left\{\int_{-\infty}^{\infty}\int_{-\infty}^{\infty} h_t(t_1)h_t(t_2)\left[\frac{1}{b^2}\int_{-b/2}^{b/2}\int_{-b/2}^{b/2} h_y(y_1)h_y(y_2)\right.\right.$$

$$\left.\left. \times R_{w_z w_z}[V(\tau + t_1 - t_2),(y_2 - y_1)]dy_1 dy_2\right]dt_1 dt_2\right\}d\tau \qquad (A.3)$$

Inserting the factor $e^{i2\pi f(t_1-t_2)}e^{-i2\pi f(t_1-t_2)} = 1$ gives

$$\phi_L(f) = \int_{-\infty}^{\infty} h_t(t_1)e^{i2\pi ft_1}dt_1 \int_{-\infty}^{\infty} h_t(t_2)e^{-i2\pi ft_2}dt_2 \left\{ \int_{-\infty}^{\infty} e^{-i2\pi f(\tau+t_1-t_2)} \right.$$

$$\left[\frac{1}{b^2} \int_{-b/2}^{b/2} \int_{-b/2}^{b/2} h_y(y_1)h_y(y_2)R_{w_zw_z}[V(\tau + t_1 - t_2),(y_2 - y_1)] \right.$$

$$\left. \left. \times\ dy_1 dy_2 \right] d\tau \right\} \qquad\qquad (A.4)$$

Now change the variable $\hat{\tau} = \tau + t_1 - t_2$ and $d\hat{\tau} = d\tau$.

$$\phi_L(f) = H_t^*(f)H_t(f) \int_{-\infty}^{\infty} \left\{ \frac{1}{b^2} \int_{-b/2}^{b/2} \int_{-b/2}^{b/2} h_y(y_1)h_y(y_2)R_{w_zw_z}[V\hat{\tau},(y_2 - y_1)] \right.$$

$$\left. \times\ dy_1 dy_2 \right\} e^{-i2\pi f\hat{\tau}}d\hat{\tau}$$

$$= |H_t(f)|^2 \int_{-\infty}^{\infty} \tilde{R}_{w_zw_z}(V\hat{\tau})e^{-i2\pi f\hat{\tau}}d\hat{\tau} \qquad\qquad (A.5)$$

where $\tilde{R}_{w_zw_z}(V\hat{\tau})$ is the effective correlation function along the wing. Therefore,

$$\phi_L(f) = |H_t(f)|^2 \tilde{\phi}_{w_zw_z}(f) \qquad\qquad (A.6)$$

where

$$\phi_{w_zw_z}(f) = \int_{-\infty}^{\infty} \tilde{R}_{w_zw_z}(V\hat{\tau})e^{-i2\pi f\hat{\tau}}d\hat{\tau} \qquad\qquad (A.7a)$$

171

$$\tilde{\phi}_{w_z w_z}(f) = \frac{1}{V} \int_{-\infty}^{\infty} \tilde{R}_{w_z w_z}(\xi) e^{-i2\pi f \xi / V} d\xi \qquad (A.7b)$$

where $\hat{\tau}$ is $(\tau + t_1 - t_2)$ and $\xi = V\hat{\tau}$.

A.2 Derivation of Equation 2.24

For axisymmetric turbulence, the correlation and spectrum can be expressed as

$$R_{w_z w_z}(\xi, \eta) = R_{w_z w_z}(\zeta) \qquad (A.8)$$

and

$$\phi_{w_z w_z}(f_1, f_2) = \phi_{w_z w_z}(f) \qquad (A.9)$$

where $\zeta^2 = \xi^2 + \eta^2$ and $f^2 = f_1^2 + f_2^2$, respectively. From Equation 2.21

$$\phi_{w_z w_z}(f_1, f_2) = \frac{1}{V^2} \int_{-\infty}^{\infty} \int_{-\infty}^{\infty} e^{-i2\pi(f_1 \xi + f_2 \eta)/V} R_{w_z w_z}(\xi, \eta) d\xi d\eta \qquad (A.10)$$

$$\phi_{w_z w_z}(f) = \frac{1}{V^2} \int_{0}^{\infty} \int_{0}^{2\pi} e^{-i2\pi f \zeta \cos(\theta - \phi)/V} R_{w_z w_z}(\zeta) \zeta d\zeta d\theta \qquad (A.11)$$

where $\xi + i\eta = \zeta e^{i\theta}$

$$f_1 + if_2 = fe^{i\phi} \qquad (A.12)$$

Then

$$\phi_{w_z w_z}(f) = \frac{1}{V^2} \int_{0}^{\infty} R_{w_z w_z}(\zeta) \left\{ \int_{0}^{2\pi} e^{-i2\pi f \zeta \cos\theta/V} d\theta \right\} \zeta d\zeta \qquad (A.13)$$

172

APPENDIX B

TURBULENCE TIME HISTORIES AND JUSTIFICATION
FOR ELIMINATION OF SOME DATA

Data measured at the tower position and level indicated in Table
3.2, page 34, have been eliminated from the data set. These data are
believed to be bad due to instrument malfunction. Tables B.1 and B.2
show mean values for the measured data. Inspection of these tables shows
that for measuring stations T1L1, T1L2, and T2L1 for Run #8623 and T1L2
for Run #8624 a much higher than realistic vertical component for flow
near the surface was measured. Therefore, the vertical velocity data in
this case are erroneous and have been omitted. This, however, does not
influence the longitudinal and lateral velocity data and they are left
in the data set. It is also observed that T3L2 has a higher vertical
wind component for Run #8624. However, this is justifiable in view of
the fact that this anemometer is immediately behind the building where a
vertical flow exists due to the wake created by flow over the building.

Further inspection of the tabulated data indicates that either the
mean zonal wind component and/or the mean direction at stations T3L4,
T5L1, T5L3, S1L3 (T6L3) for Run #8623 and T3L4 and T5L3 for Run #8624
are inconsistent with the remainder of the data. Therefore, measure-
ments at S4L2 (T8L3) do not correlate well with other results. Inspec-
tion of the time history of the fluctuating components given in Figures
B.1 through B.54 for these measurements indicate that the measurements
were seriously in error and that the anemometer was not working. There-
fore, they have also been eliminated from the data set. Figures B.1

173

through B.54 are time history plots of the fluctuation components of the wind speed. The vertical scale is velocity in meters per second and the horizontal scale is time in seconds. In each figure the time history is plotted at the scaled level of the measurement station. The component number given in the caption designates the wind direction: Component 1 is along the direction of the mean wind, i.e., longitudinal, w_x; Component 2 is perpendicular to the mean wind, i.e., lateral, w_y; and Component 3 is vertical to the earth's surface, w_z.

TABLE B.1. Mean Values for Test Run #8623

Tower	Level	Mean Zonal	Mean Meridional	Mean Scalar	Mean Direction	Vertical Velocity
1	1	-4.9406	-1.0354	5.0479	78.1785	2.7358
1	2	-5.7322	-0.7237	5.7777	82.8202	3.9514
1	3	6.7323	-1.0466	6.8132	81.1789	0.1854
1	4	-7.3635	0.1308	7.3647	91.0345	-0.4789
2	1	-4.2044	-1.2547	4.3877	73.3972	-1.2962
2	2	-6.3918	-1.0856	6.4833	80.3759	-0.3243
2	3	-6.5052	-0.0359	6.5053	89.7007	-0.1350
2	4	-7.1013	0.9769	7.1682	97.8514	-0.1018
3	1	-3.1094	3.0003	4.3209	134.0021	0.8810
3	2	-6.1063	-1.9131	6.3990	72.6183	0.8744
3	3	-6.8302	-0.7344	6.8696	83.8788	0.0959
3	4	-0.0643	-6.7920	6.7923	0.5467	0.0396
4	1	-5.3100	-0.4432	5.3285	85.2445	0.0684
4	2	-4.9962	-0.1094	4.9974	88.7624	0.2059
4	3	-6.5158	0.1633	6.5079	91.4551	0.1287
4	4	-6.9119	-0.6906	6.9768	84.2859	0.2323
5	1	-5.5352	1.7541	5.8065	107.6034	0.1737
5	2	-6.2623	0.6350	6.2944	95.8076	-0.0630
5	3	0.0079	-6.7687	6.7687	360.0000	0.3037
5	4	-7.1130	0.4085	7.1247	93.3044	0.1849
6 a	1	-3.7003	-0.7748	3.7811	78.1895	0.0883
6	2	-4.7602	-0.6754	4.8879	81.9398	0.3508
6	3	-0.9212	-5.5098	5.5063	9.4935	0.0914
6	4	-3.4786	0.7634	3.5614	102.3962	-0.0202
7 b	1	-4.3364	0.1141	4.3078	91.5070	0.6519
7	2	-6.3344	0.1581	6.3364	91.4471	0.5364
7	3	-4.2900	0.0762	4.2907	91.0341	0.5756
7 c	4	-5.0558	-0.2411	5.0616	87.2858	0.4841
8	1	-5.9071	-0.5221	5.9301	84.9647	0.6191
8	2	-4.6894	-0.2029	4.6938	87.5391	0.1167
8 d	3	-5.2420	0.3515	5.2538	93.8532	0.0622
8	4	-5.9079	0.8431	5.9678	98.1404	-0.0754

[a]Short Tower 1.

[b]Short Tower 2.

[c]Short Tower 3.

[d]Short Tower 4.

TABLE B.2.   Mean Values for Test Run #8624

Tower	Level	Mean Zonal	Mean Meridional	Mean Scalar	Mean Direction	Vertical Velocity
1	1	2.0487	2.9895	3.6241	214.4623	0.0272
1	2	2.3735	3.4968	4.2263	214.2065	4.8259
1	3	2.5700	4.4788	5.1638	209.8875	0.1272
1	4	3.9871	4.7714	6.2179	219.9246	0.2569
2	1	1.9003	2.1630	2.6792	221.3415	0.2170
2	2	2.8738	3.0276	4.1743	223.5492	0.5090
2	3	3.2904	3.6659	4.9260	221.9519	0.4624
2	4	3.6427	4.9111	6.2357	218.0823	0.2592
3	1	0.0169	0.2914	0.2919	3.3279	0.0311
3	2	2.0817	4.0728	4.5740	207.1117	1.0011
3	3	2.5370	4.5621	5.2201	209.1173	0.1225
3	4	2.7828	4.0849	4.9427	34.2704	0.0009
4	1	0.9223	0.3413	0.9834	249.7402	0.0255
4	2	2.3095	3.2753	4.0077	215.2295	0.1064
4	3	3.2612	4.3579	5.4430	216.8496	0.1676
4	4	2.4891	5.2211	5.7841	205.5273	0.0070
5	1	3.2851	2.4210	5.0809	233.6546	0.1119
5	2	3.2226	3.4132	4.6941	223.3969	0.1622
5	3	0.0015	3.5265	3.5265	180.0093	0.2154
5	4	2.9834	4.4481	5.3559	213.8905	0.2271
6 a	1	0.9096	1.0851	1.4159	220.0140	0.1513
6	2	1.7511	2.2599	2.8590	217.8114	0.3075
6	3	2.3261	3.1185	3.8905	216.7596	0.2740
6	4	0.0408	0.4768	0.4786	355.1710	0.4562
7 b	1	0.4594	0.2393	0.5180	297.5690	0.2601
7	2	3.1289	3.6387	4.7990	220.7332	0.9213
7	3	0.1628	0.6726	0.6920	346.4559	0.0126
7 c	4	0.2682	0.0937	0.2841	250.7872	0.0452
8	1	2.1279	3.3532	3.9714	212.4383	0.1263
8	2	0.4505	0.2266	0.5043	296.7586	0.0909
8 d	3	0.4531	0.5182	0.6884	221.2112	0.0166
8	4	2.5293	2.7937	3.7686	222.1989	0.0049

[a]Short Tower 1.

[b]Short Tower 2.

[c]Short Tower 3.

[d]Short Tower 4.
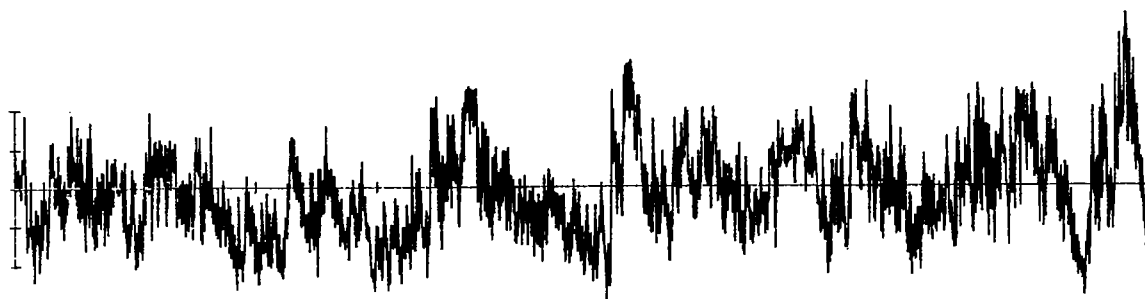
Time Scale

0   200 Seconds

Velocity Scale
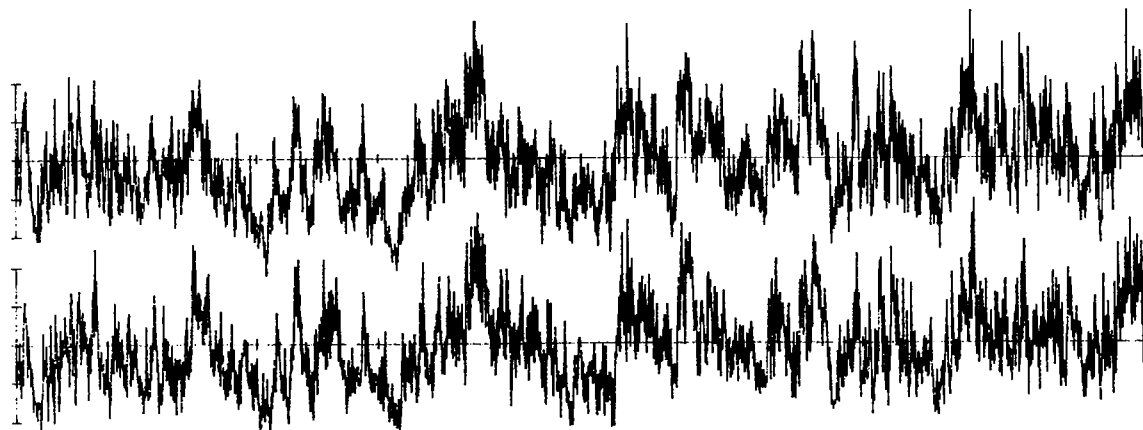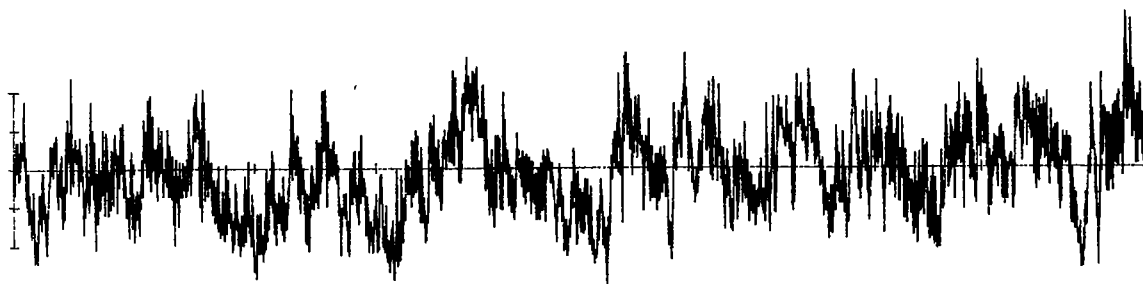
0 1 2 3 M/S

Figure B.1. Time history of turbulent fluctuations. (Run #8623, T1, Component 1).

177
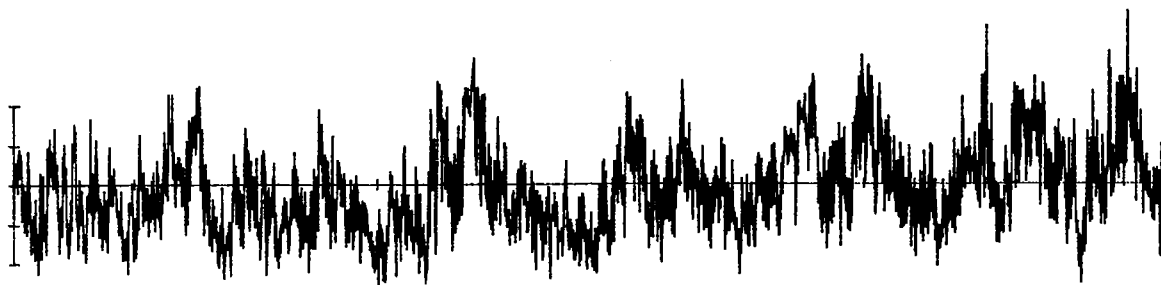
Time Scale ├──────────┤
          0   200 Seconds

Velocity Scale ├──┼──┼──┤
               0 1 2 3   M/S
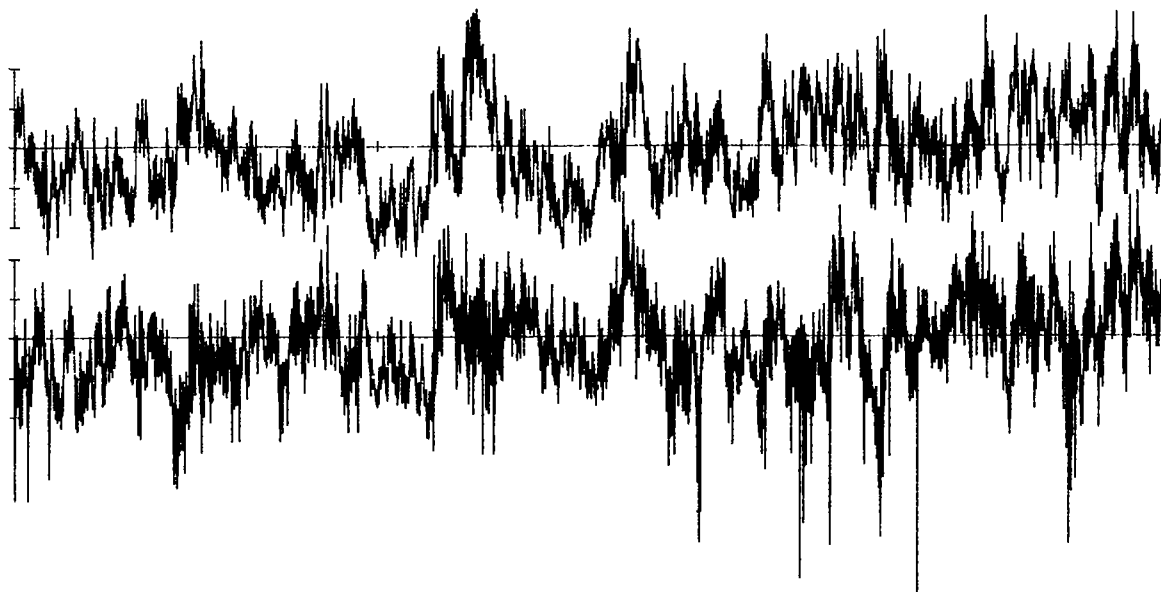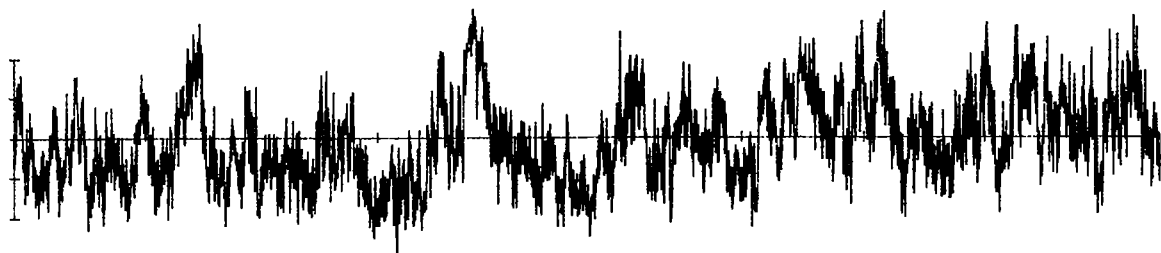
Figure B.2. Time history of turbulent fluctuations. (Run #8623, T2, Component 1).

178
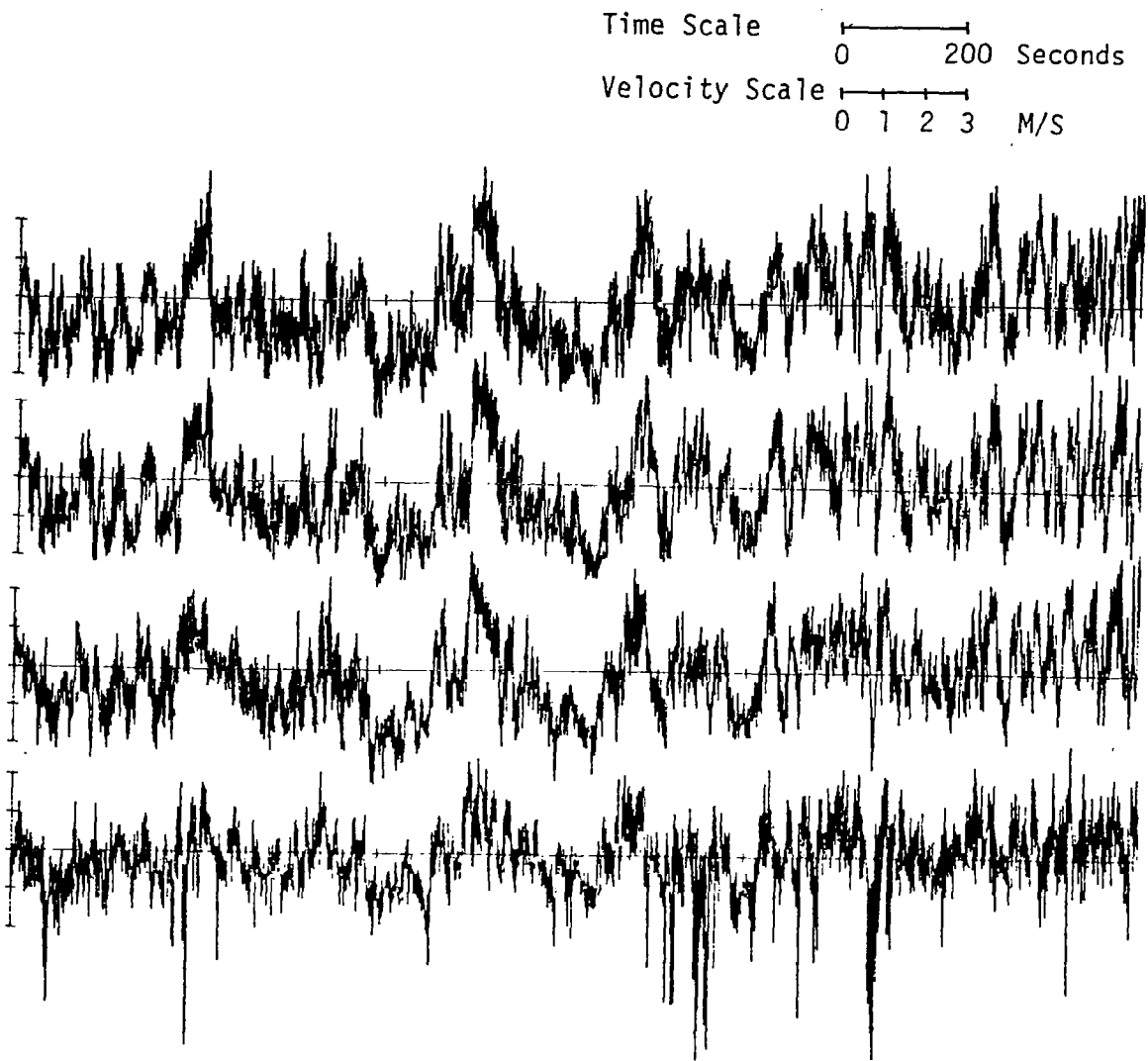
Figure B.3. Time history of turbulent fluctuations. (Run #8623, T3, Component 1).
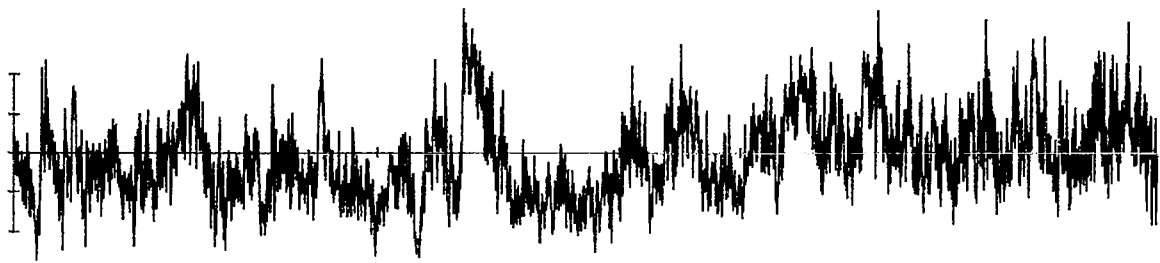
Time Scale

0   200 Seconds

Velocity Scale
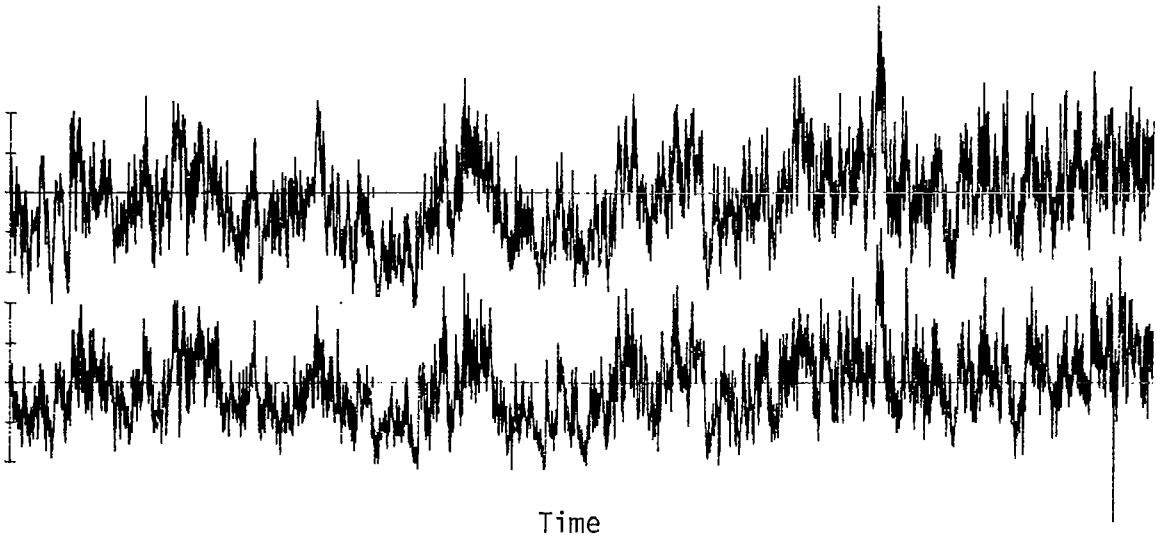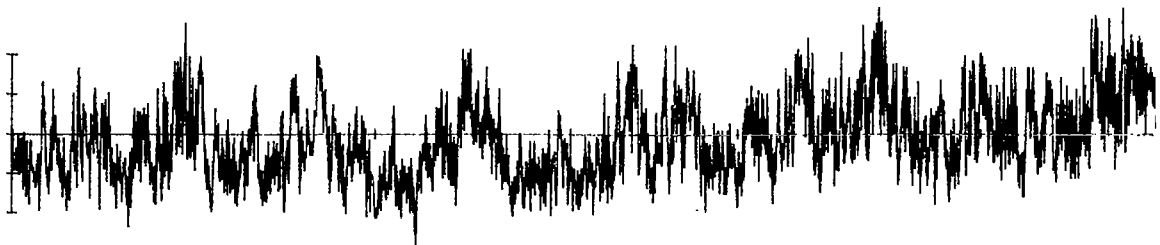
0 1 2 3 M/S

Time

Figure B.4. Time history of turbulent fluctuations. (Run #8623, T4, Component 1).
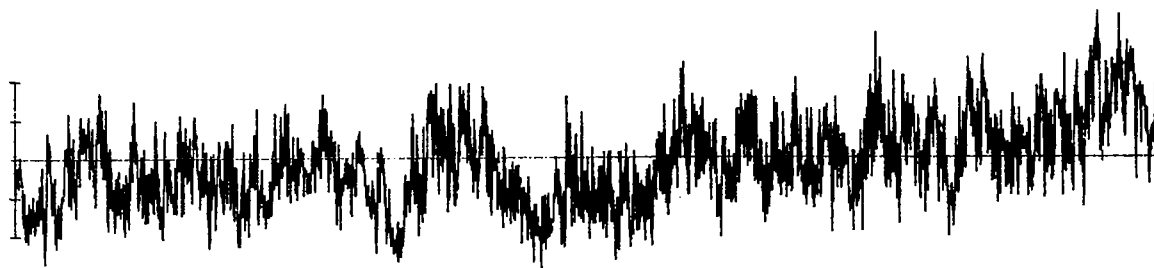
Time Scale

0   200 Seconds

Velocity Scale

0   1   2   3   M/S
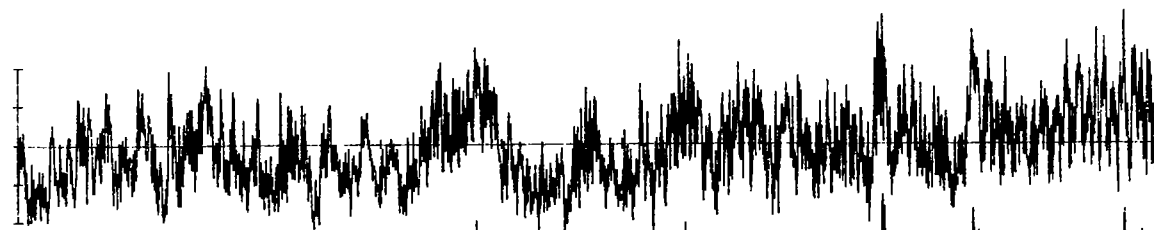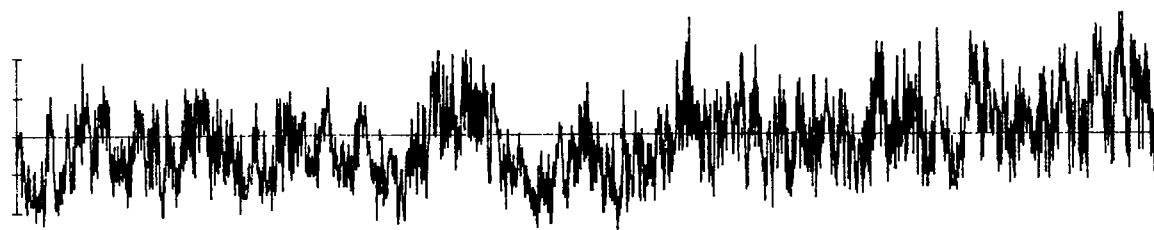
Time

Figure B.5.   Time history of turbulent fluctuations. (Run #8623, T5, Component 1).

Time Scale

0   200 Seconds

Velocity Scale

0 1 2 3 M/S
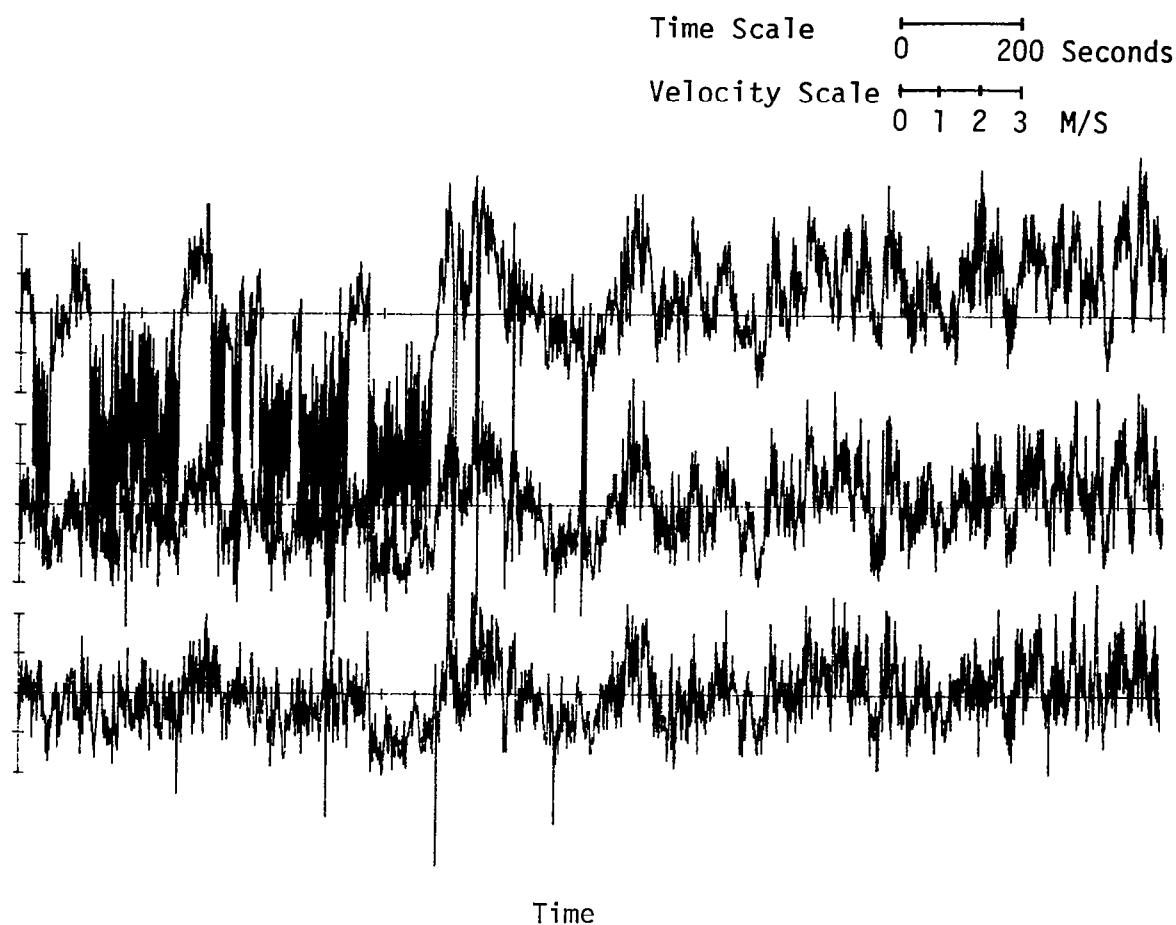
Time

Figure B.6. Time history of turbulent fluctuations. (Run #8623, S1, Component 1).
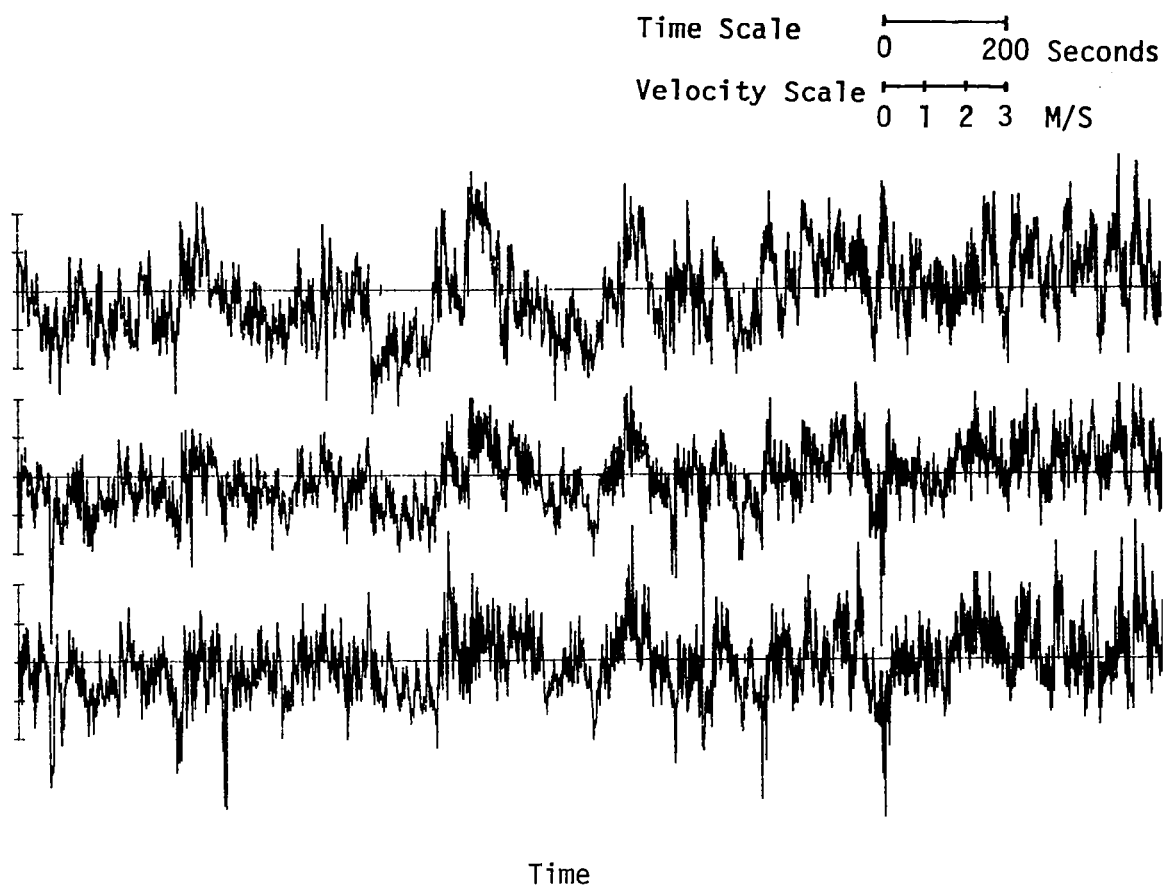
Figure B.7. Time history of turbulent fluctuations. (Run #8623, S2, Component 1).

183
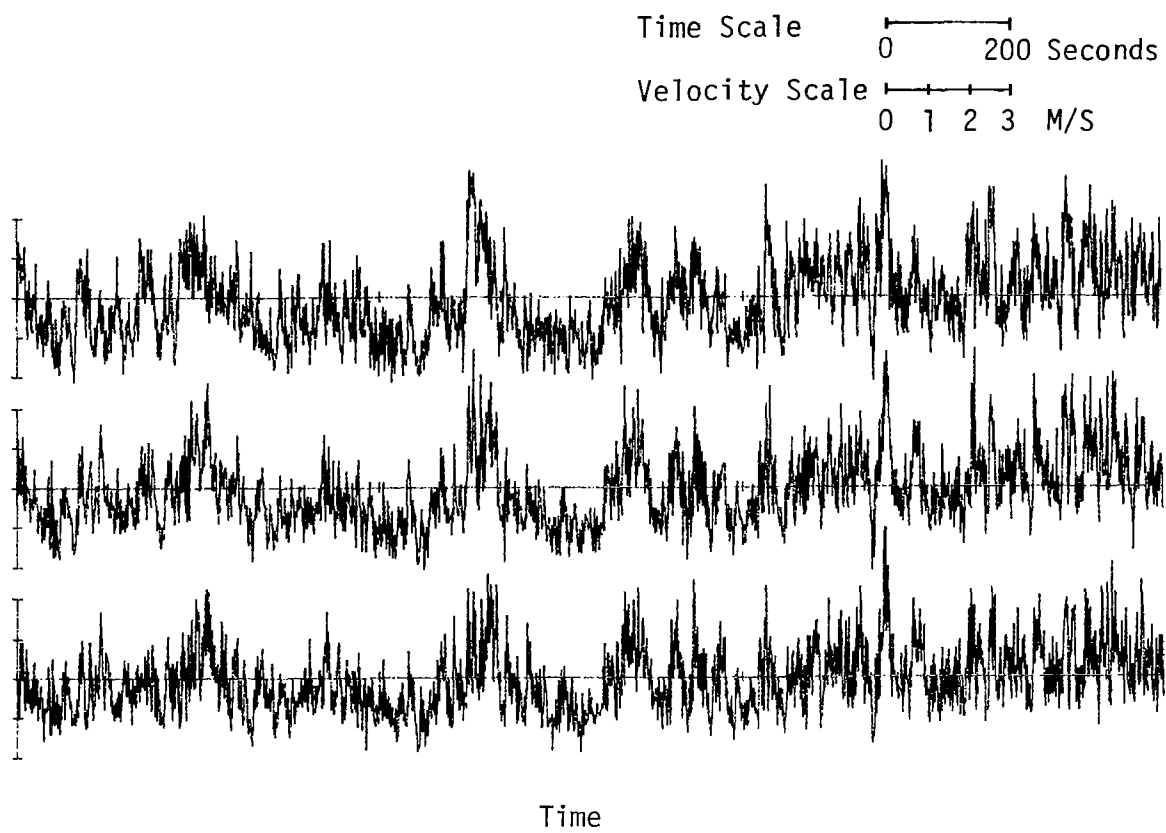
Figure B.8. Time history of turbulent fluctuations. (Run #8623, S3, Component 1).

Time Scale

Velocity Scale

0   200 Seconds
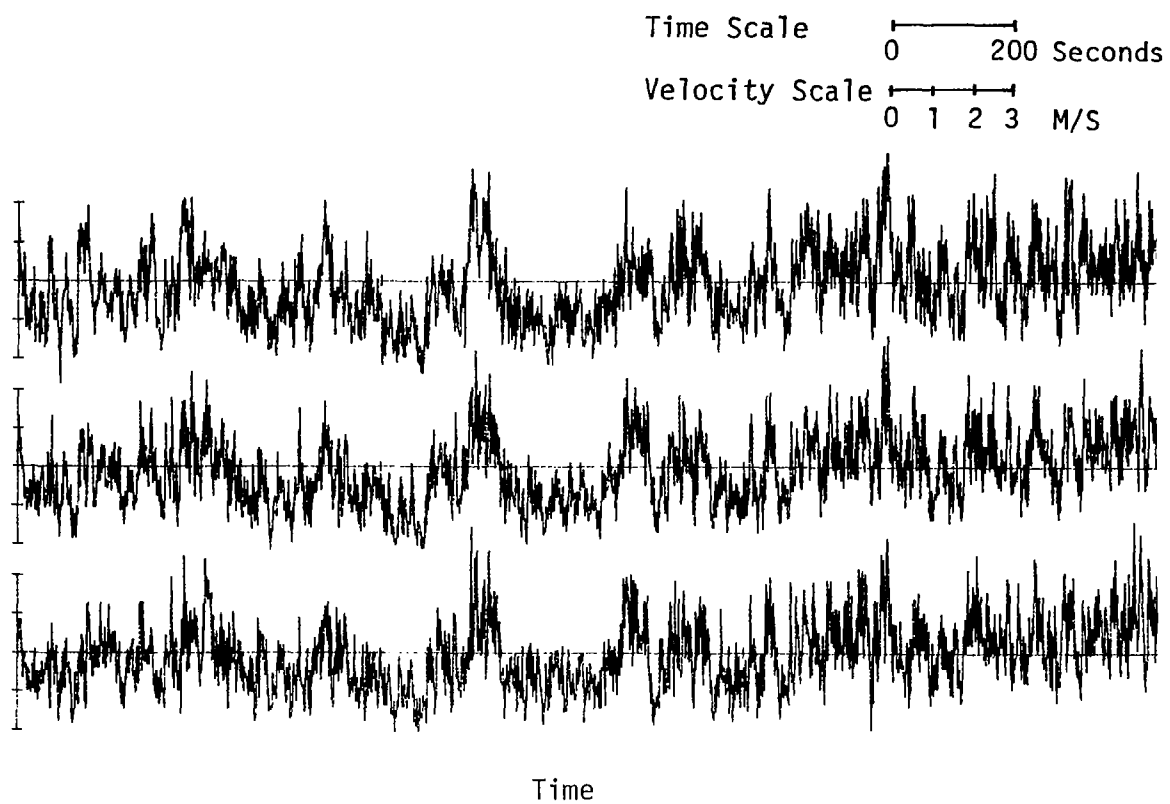
0 1 2 3   M/S

Time

Figure B.9.   Time history of turbulent fluctuations.   (Run #8623, S4,
              Component 1).

185
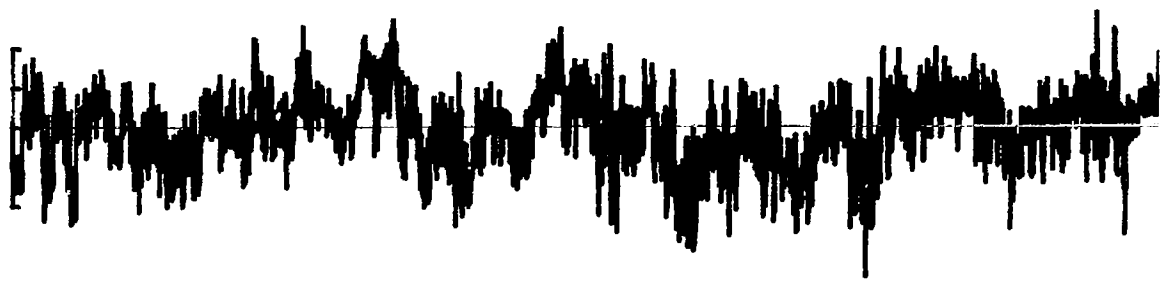
Time Scale |———————|
            0   200 Seconds

Velocity Scale |—+—+—|
               0 1 2 3 M/S
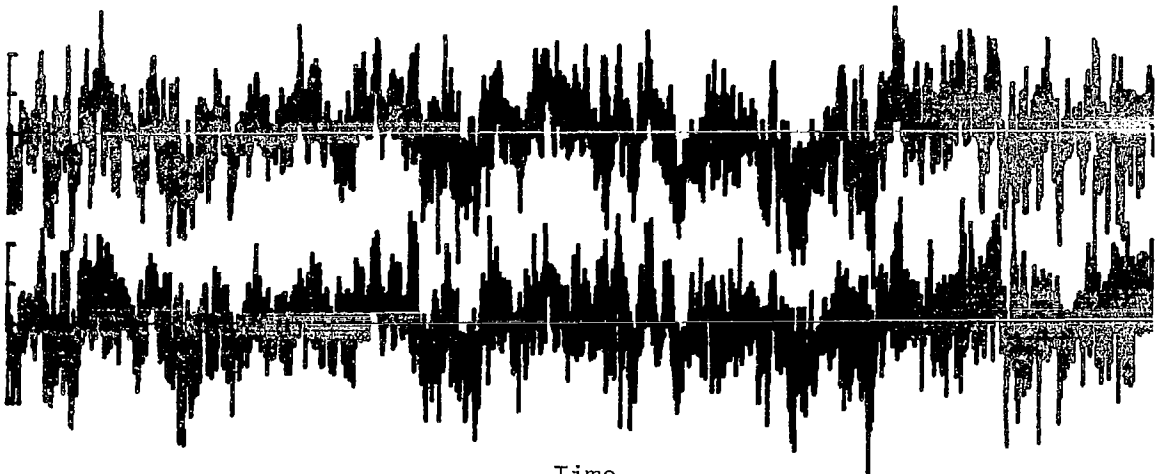
Time

Figure B.10. Time history of turbulent fluctuations. (Run #8623, T1, Component 2).

186

Time Scale |————————|
0   200 Seconds

Velocity Scale |——+——+——|
0 1 2 3 M/S
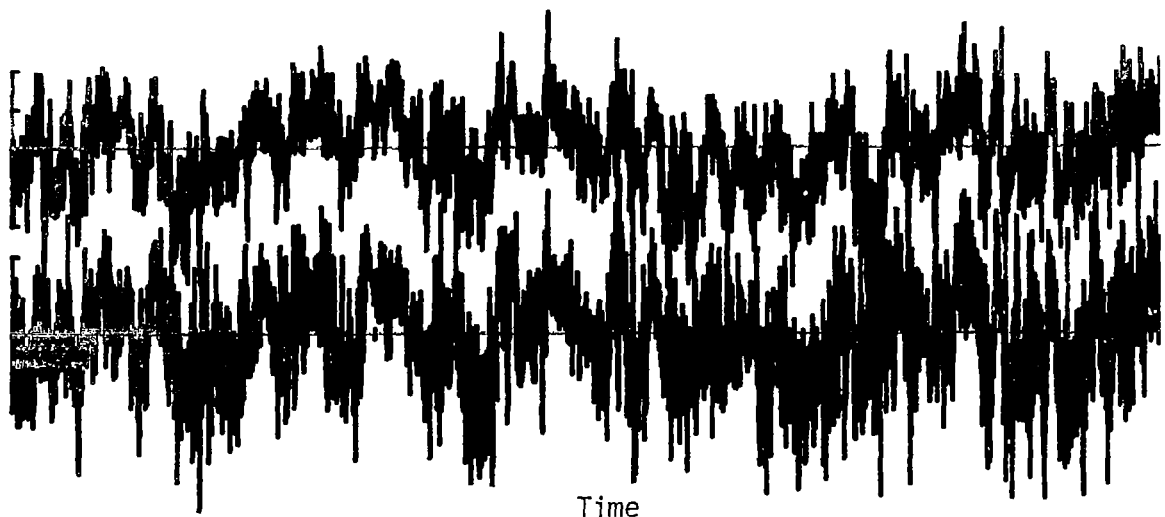
Time

Figure B.11. Time history of turbulent fluctuations. (Run #8623, T2, Component 2).

187

Time Scale ⊢————————⊣
         0   200 Seconds

Velocity Scale ⊢—+——+——⊣
             0 1 2 3 M/S
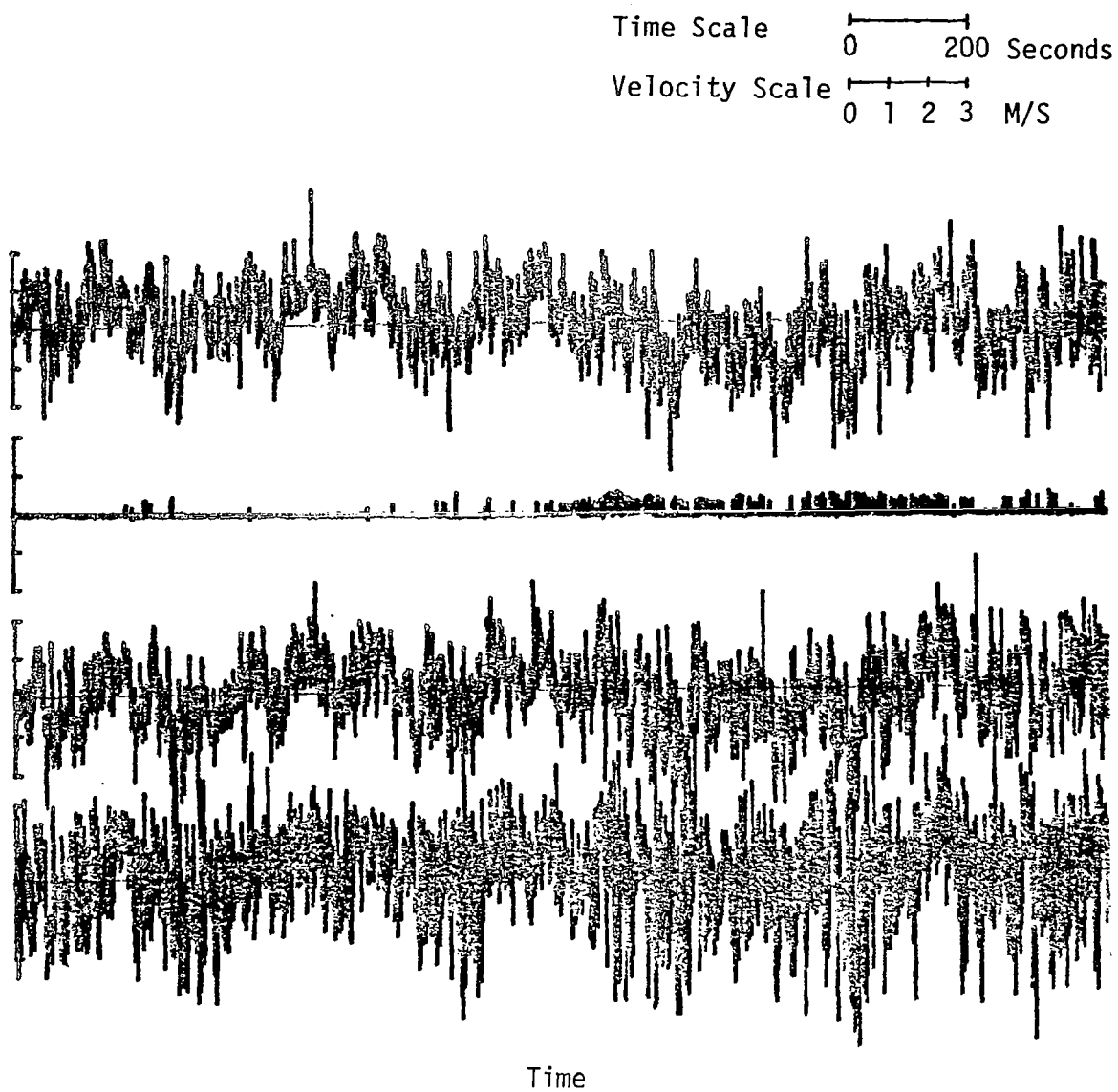
Time

Figure B.12. Time history of turbulent fluctuations. (Run #8623, T3, Component 2).

188

Time Scale

0   200 Seconds

Velocity Scale
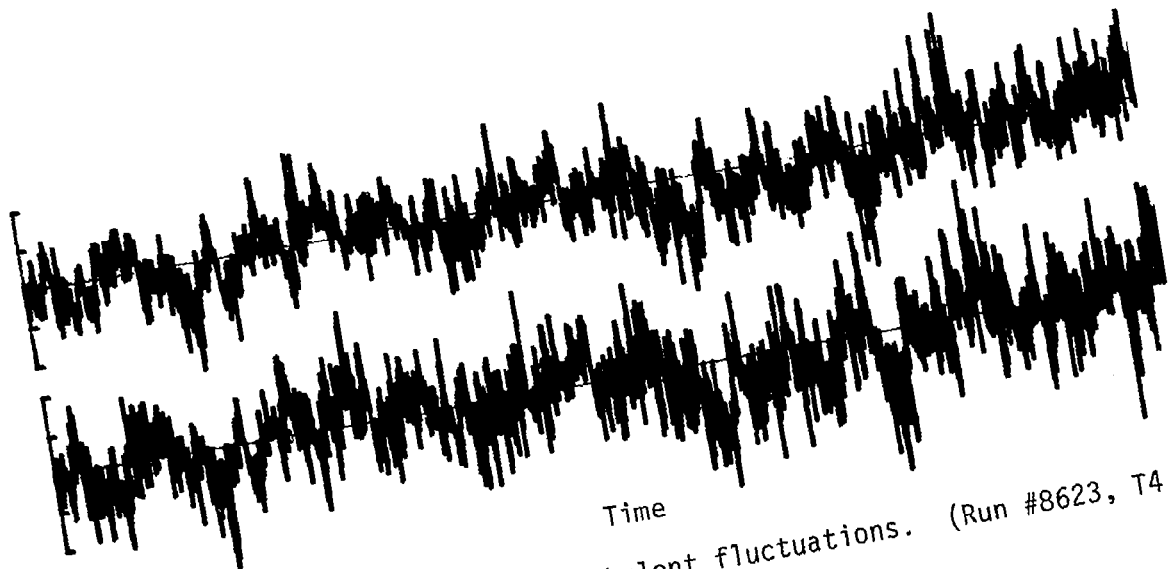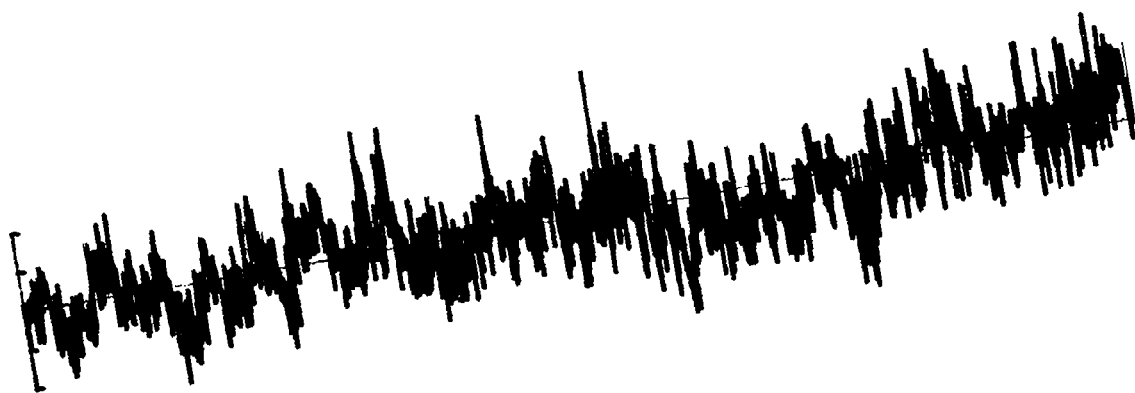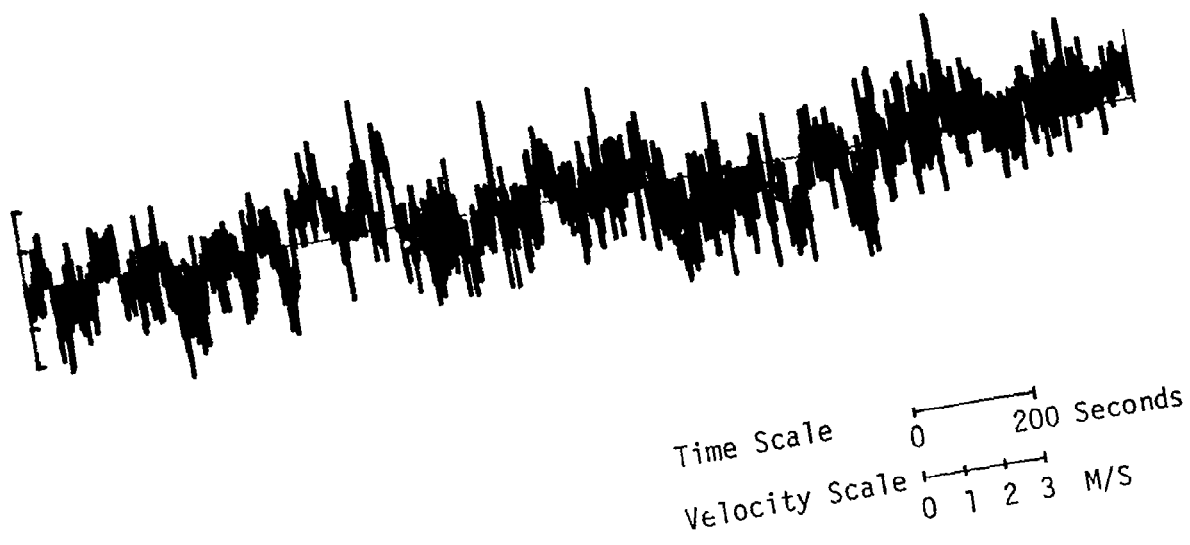
0 1 2 3 M/S

Time

Figure B.13. Time history of turbulent fluctuations. (Run #8623, T4, Component 2).
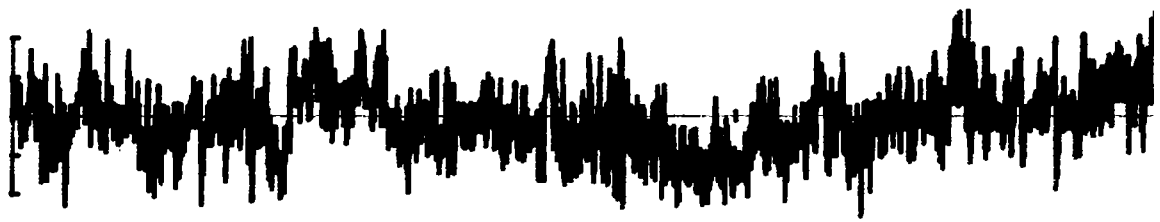
Time Scale ┣━━━━━━━━┫
0   200 Seconds

Velocity Scale ┣━━╋━━╋━━┫
0 1 2 3 M/S
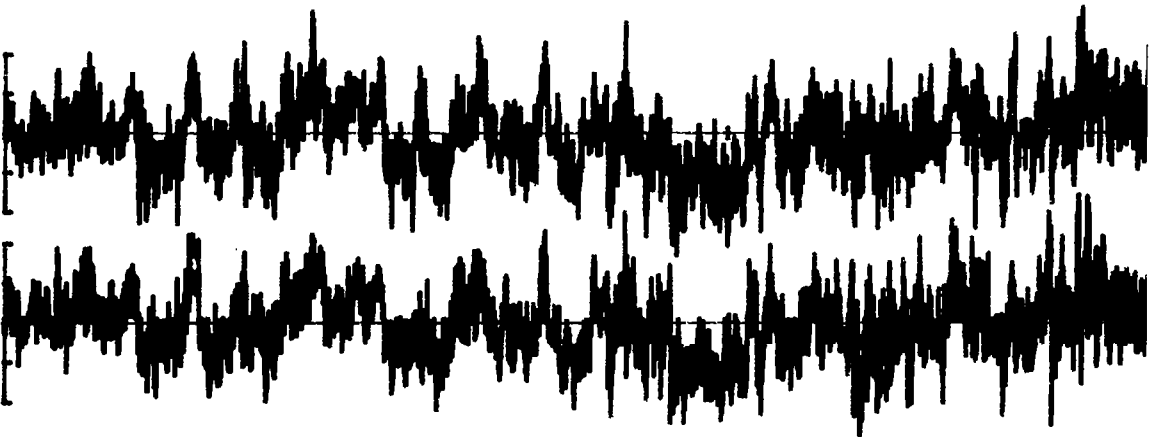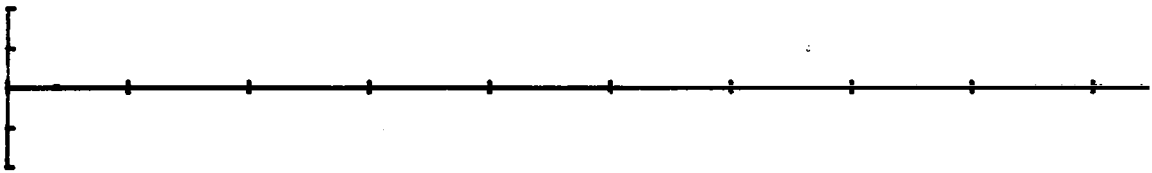
Time

Figure B.14. Time history of turbulent fluctuations. (Run #8623, T5,
Component 2).

190
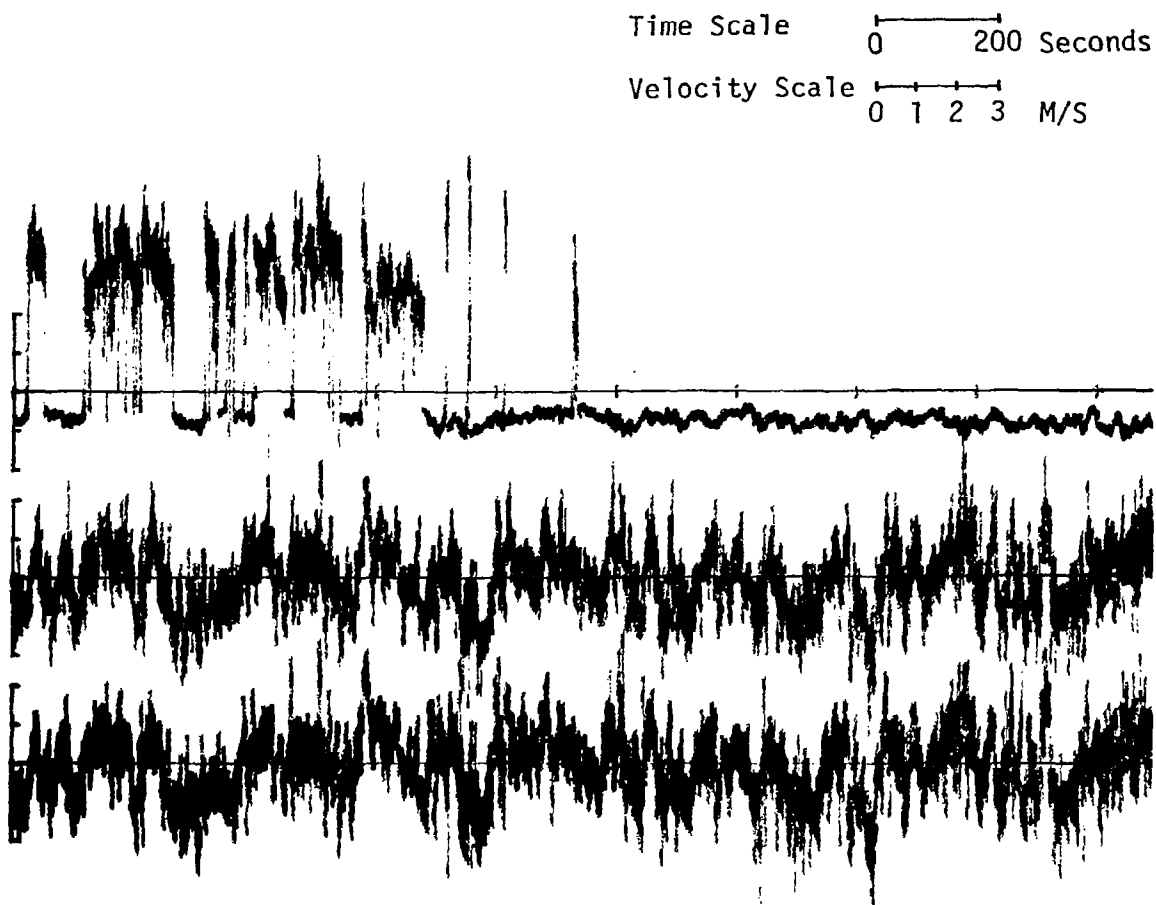
Figure B.15.   Time history of turbulent fluctuations.   (Run #8623, S1, Component 2).

Time Scale ⊢————⊣
0   200 Seconds

Velocity Scale ⊢—+—+—⊣
0 1 2 3 M/S
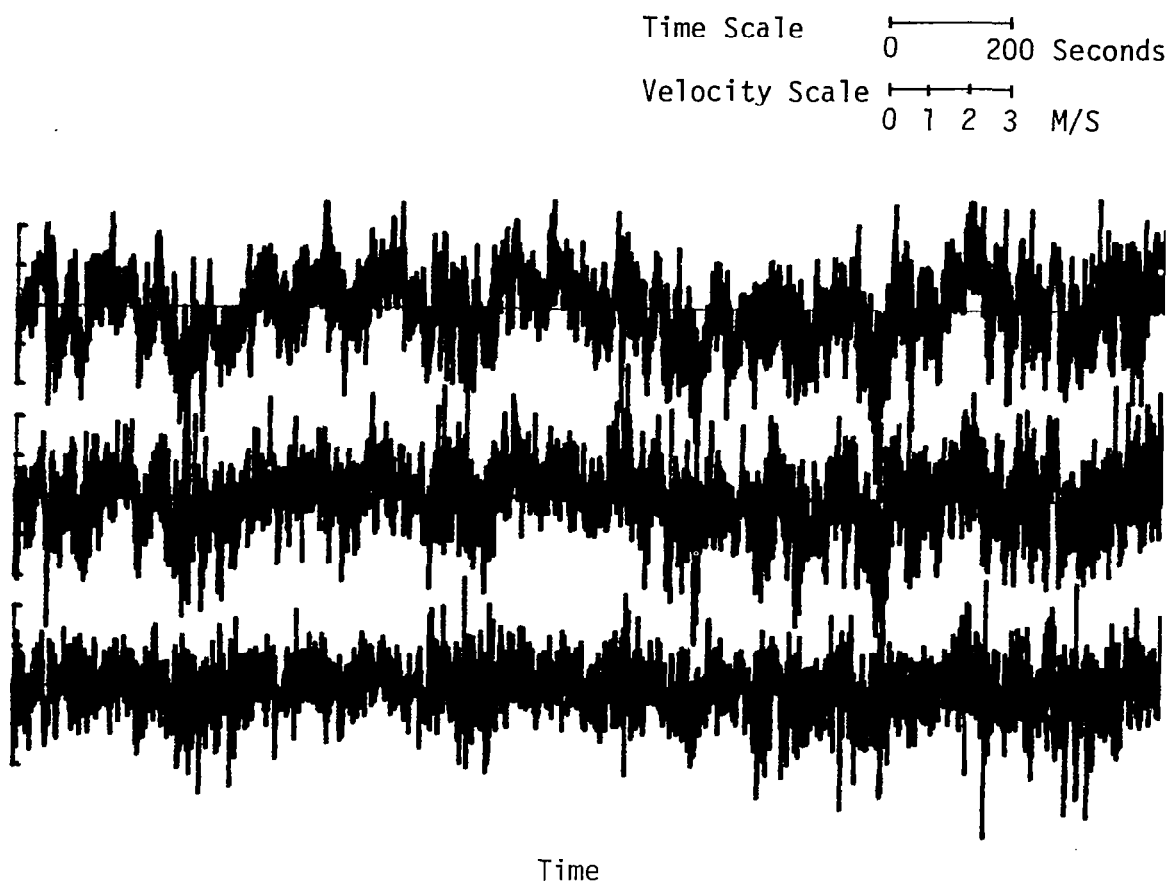
Time

Figure B.16.   Time history of turbulent fluctuations.   (Run #8623, S2, Component 2).

Time Scale ├─────────┤
           0   200 Seconds
Velocity Scale ├──┼──┼──┤
               0 1 2 3 M/S
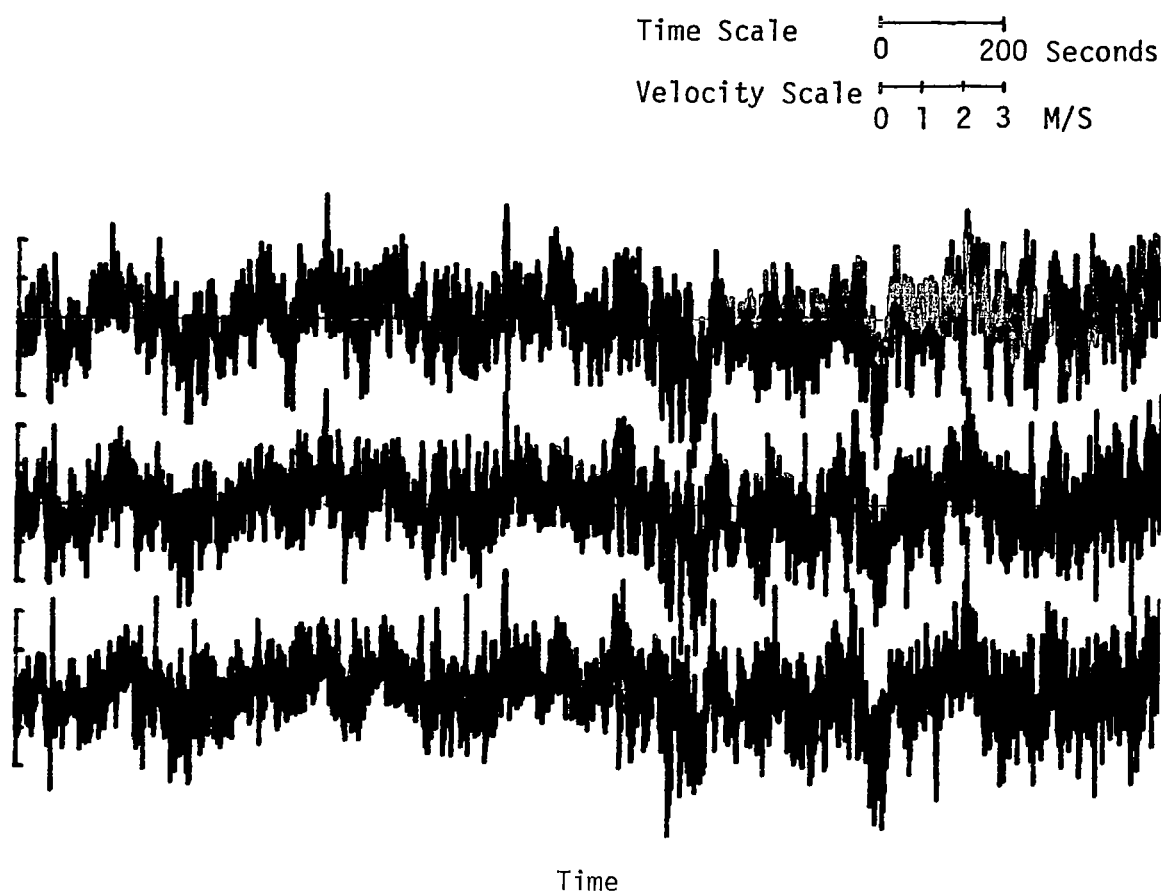
Time

Figure B.17.   Time history of turbulent fluctuations.   (Run #8623, S3,
               Component 2).

Time Scale ├────────────┤
            0   200 Seconds
Velocity Scale ├──┼──┼──┤
                0 1 2 3 M/S
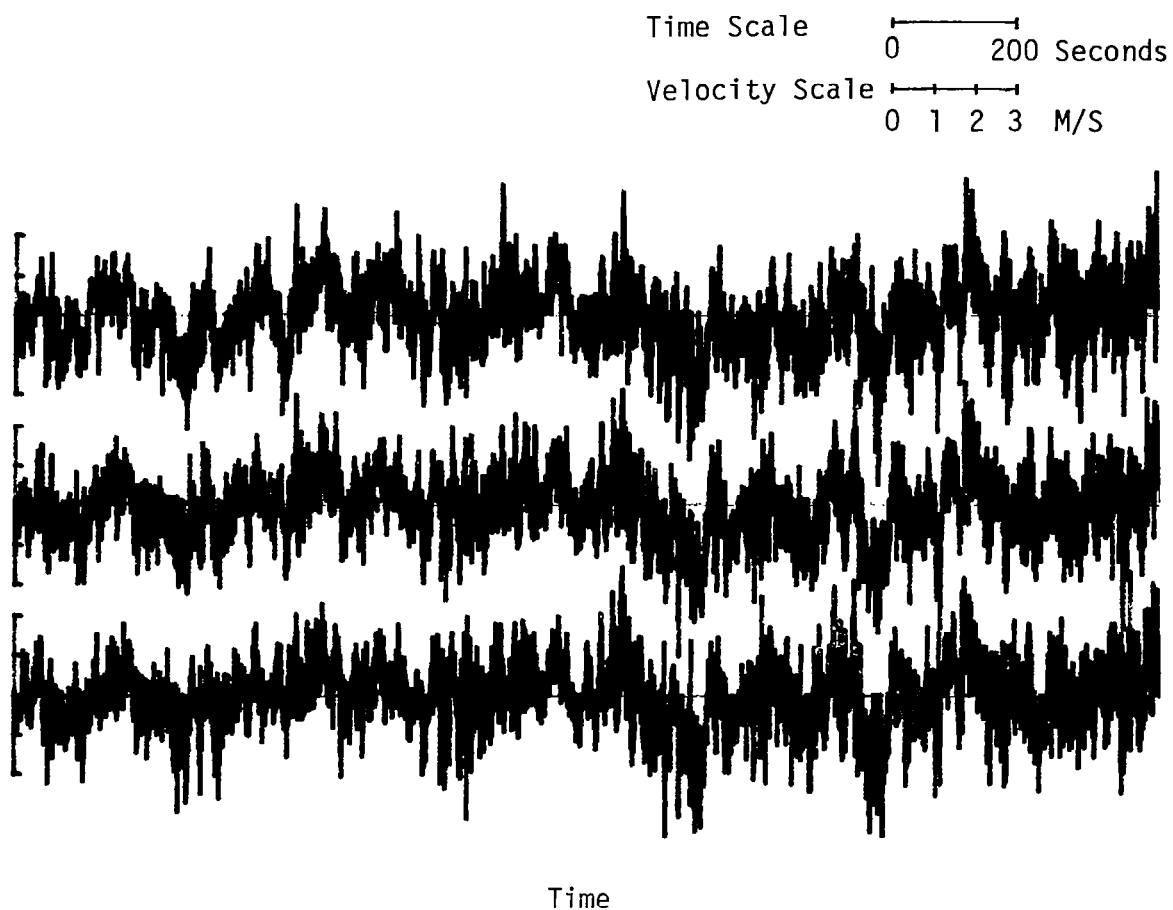
Time

Figure B.18.   Time history of turbulent fluctuations.   (Run #8623, S4,
               Component 2).

194

Time Scale ├──────┤
0   200 Seconds

Velocity Scale ├──┬──┬──┤
0 1 2 3 M/S
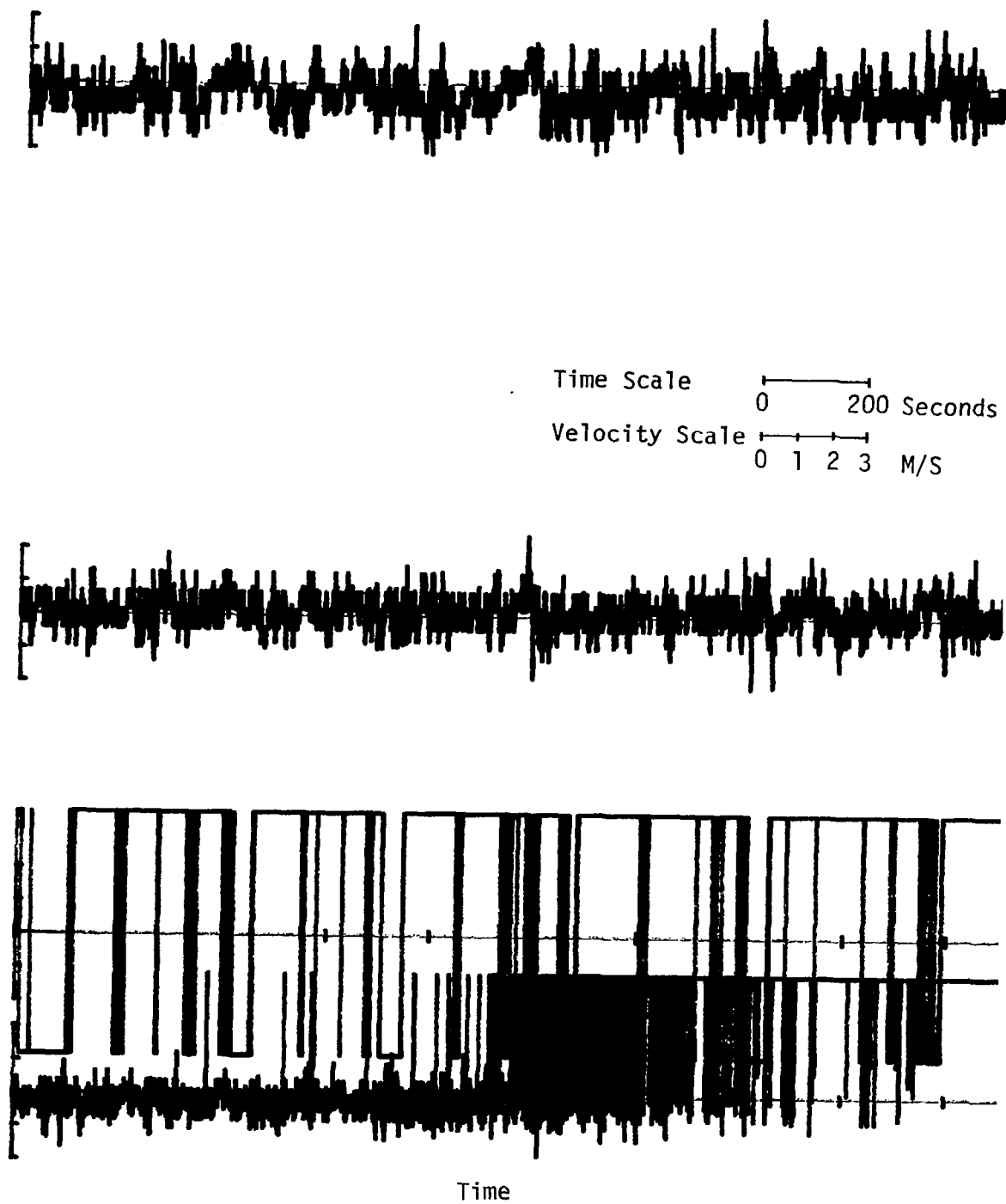
Time

Figure B.19. Time history of turbulent fluctuations. (Run #8623, T1, Component 3).

Time Scale   ├──────────┤
              0   200 Seconds
Velocity Scale ├──┬──┬──┤
               0 1 2 3 M/S

Time

Figure B.20. Time history of turbulent fluctuations. (Run #8623, T2,
             Component 3).

196
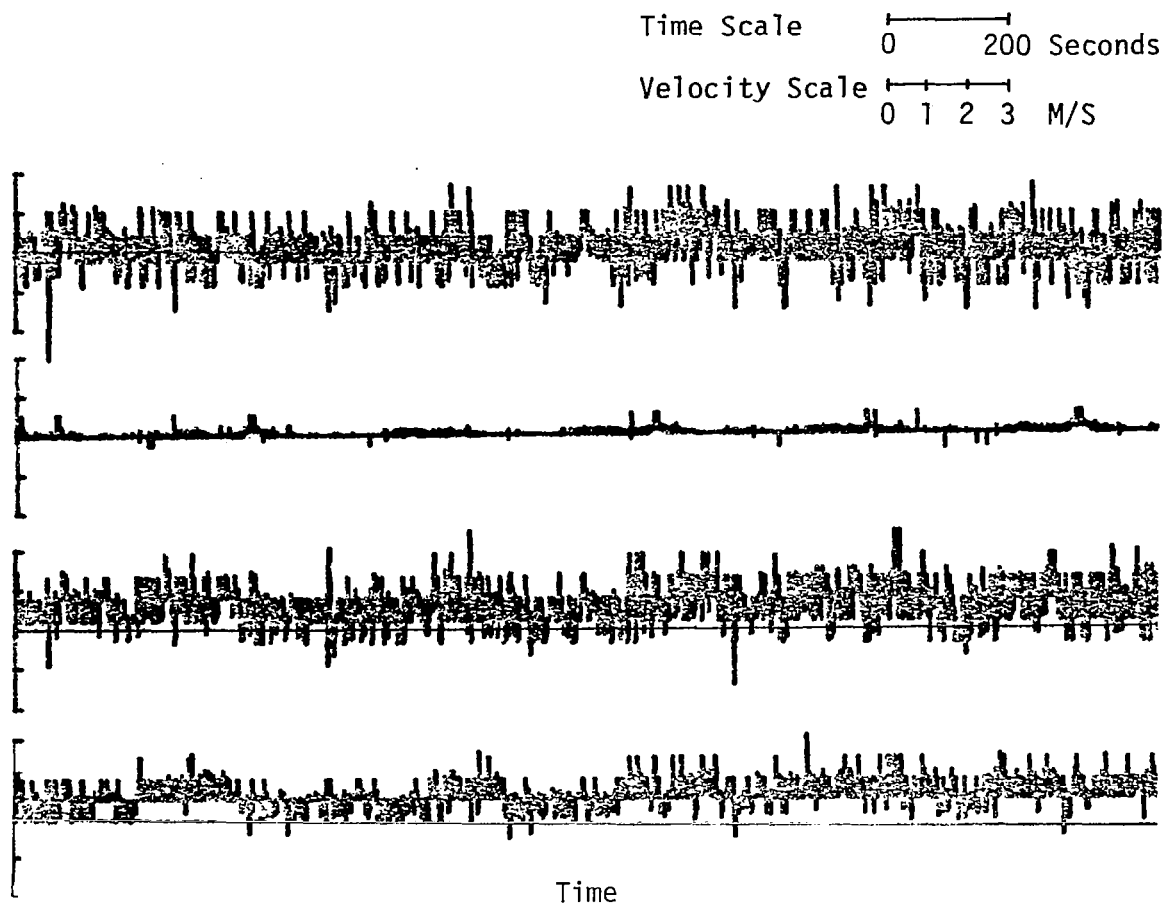
Figure B.21. Time history of turbulent fluctuations. (Run #8623, T3, Component 3).

197

Time Scale ├────────┤
0   200 Seconds

Velocity Scale ├──┼──┼──┤
0 1 2 3 M/S
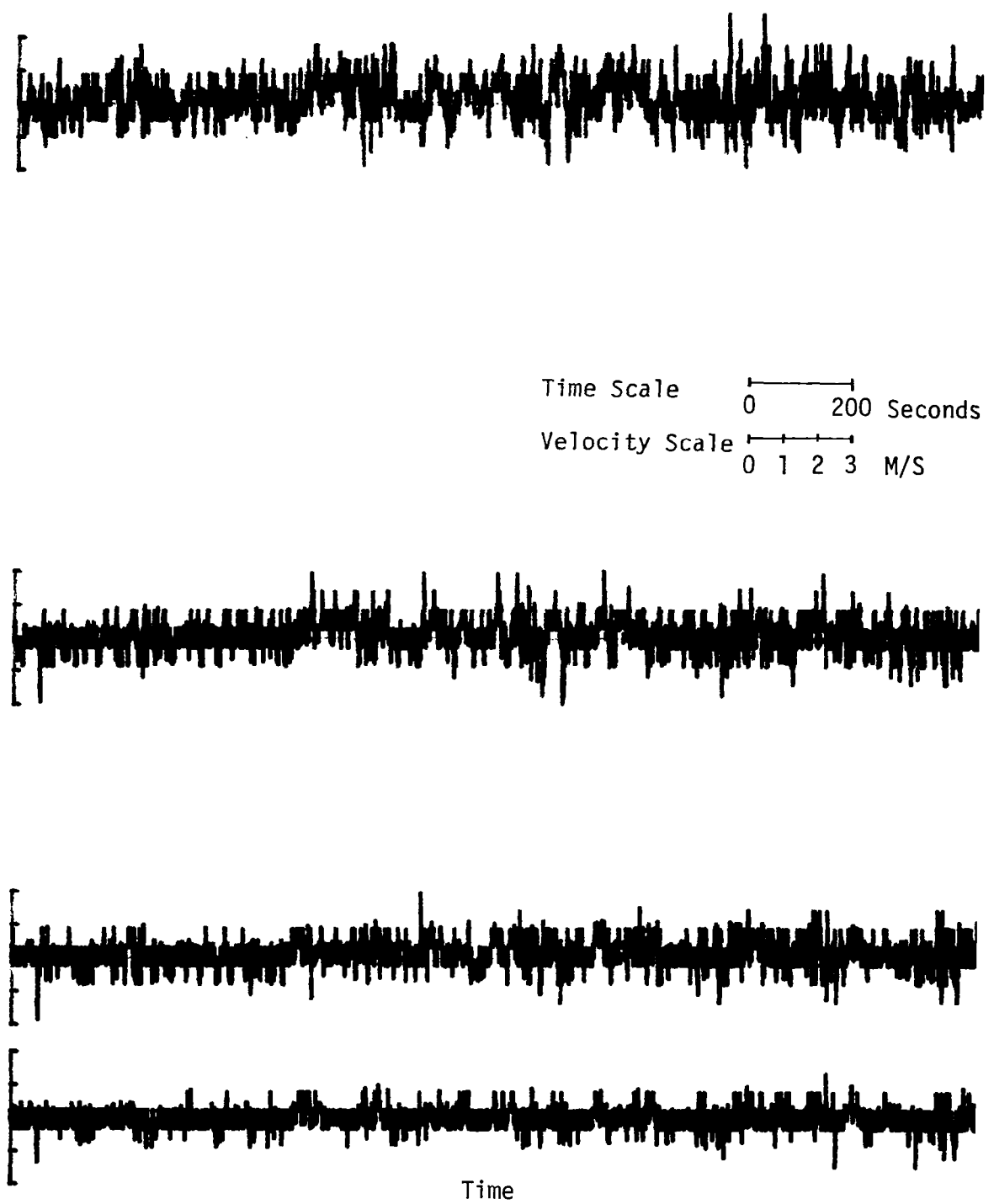
Time

Figure B.22. Time history of turbulent fluctuations. (Run-#8623, T4, Component 3).

198

Time Scale ⊢————————⊣
              0   200 Seconds
Velocity Scale ⊢——+——+——⊣
                  0 1 2 3 M/S

Time

Figure B.23. Time history of turbulent fluctuations. (Run #8623, T5, Component 3).

Time Scale

0   200 Seconds

Velocity Scale
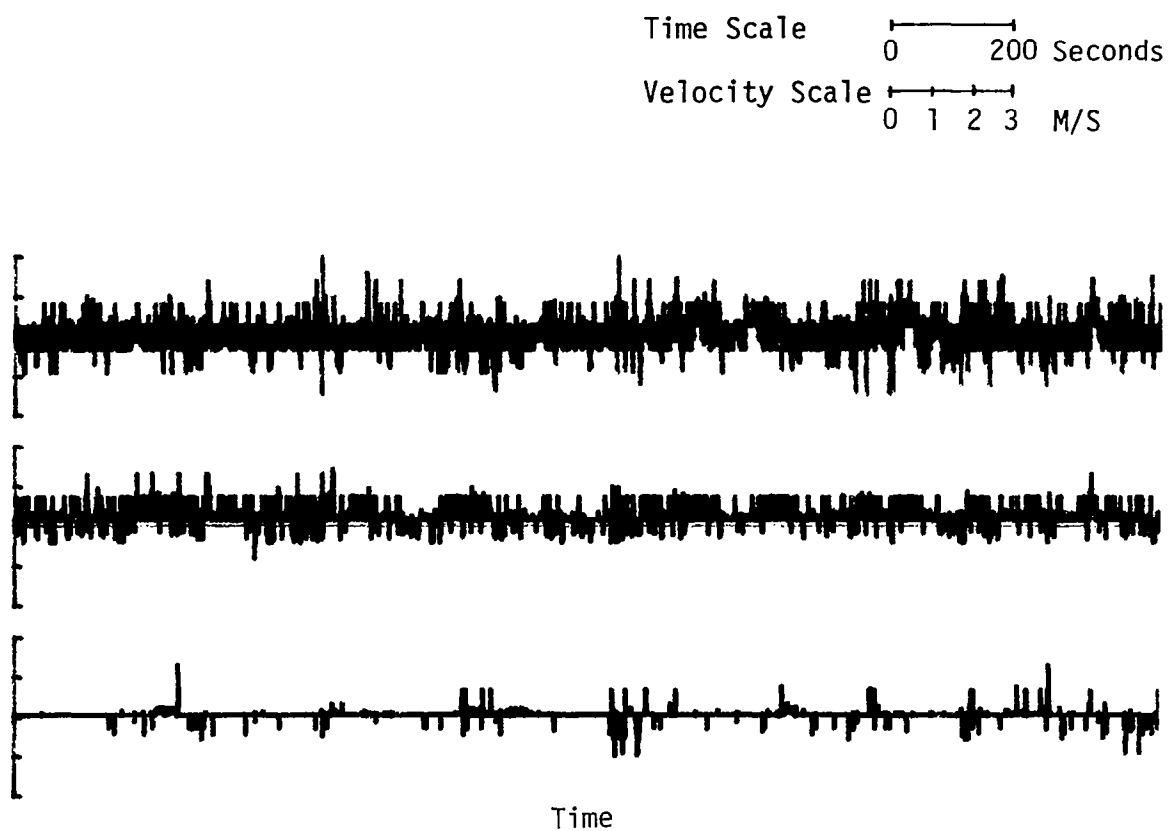
0 1 2 3 M/S

Time

Figure B.24. Time history of turbulent fluctuations. (Run #8623, S1, Component 3).

200

Time Scale 0 ——— 200 Seconds

Velocity Scale 0 1 2 3 M/S
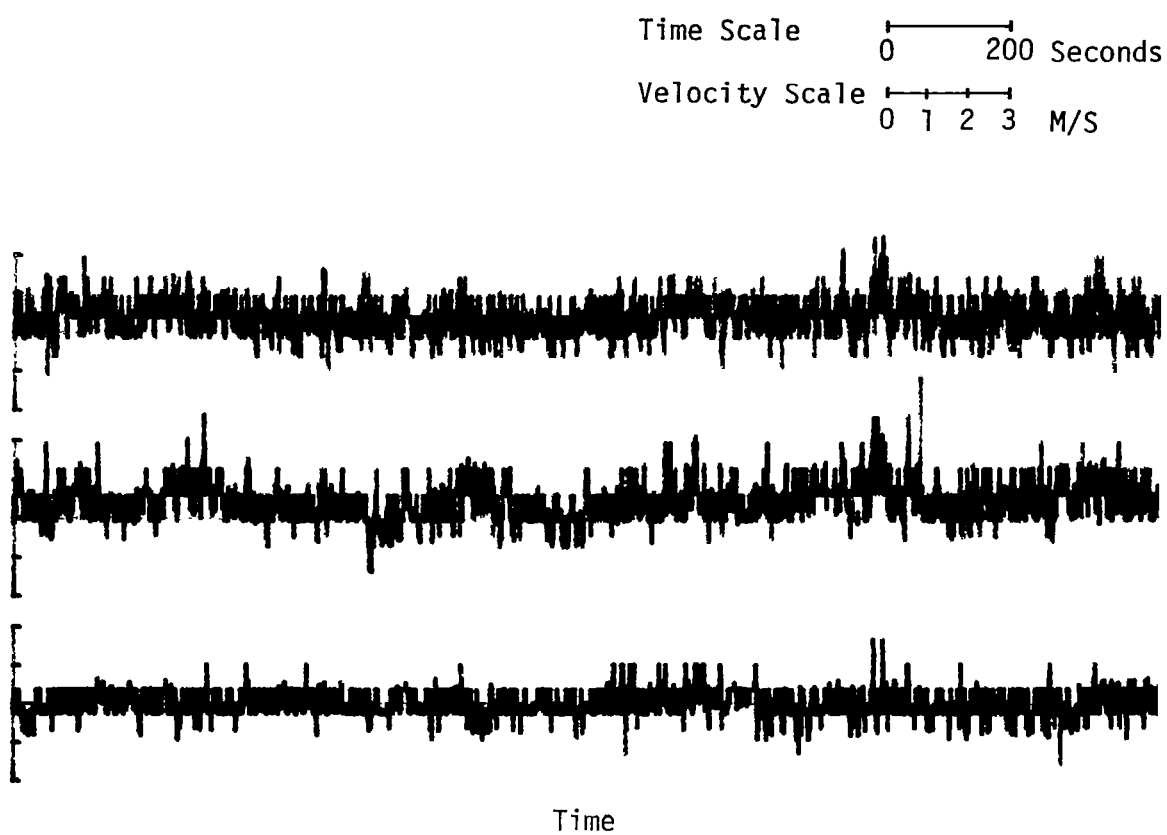
Time

Figure B.25. Time history of turbulent fluctuations. (Run #8623, S2, Component 3).

Time
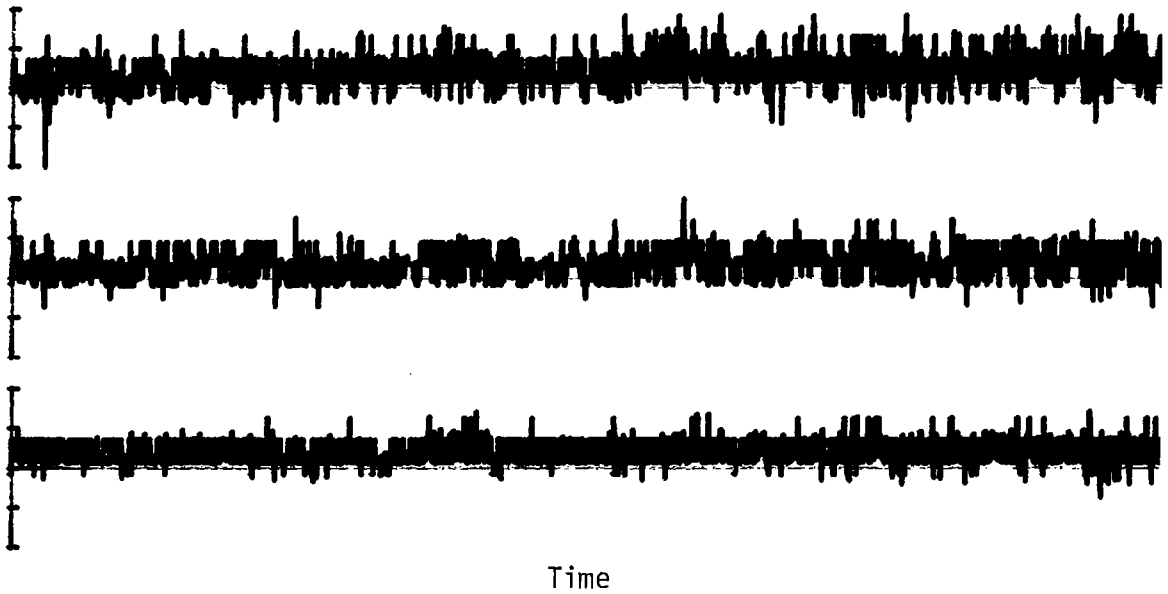
Figure B.26. Time history of turbulent fluctuations. (Run #8623, S3, Component 3).

Time Scale

0   200 Seconds

Velocity Scale

0 1 2 3 M/S
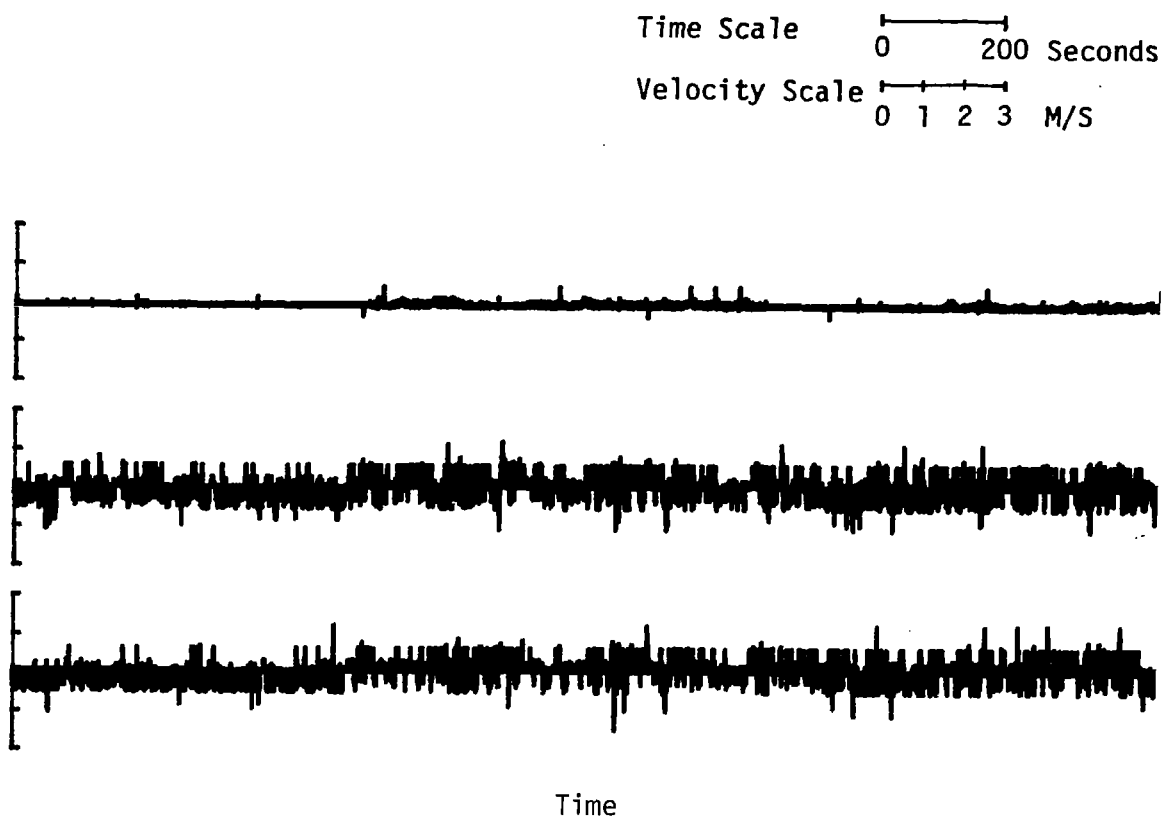
Time

Figure B.27. Time history of turbulent fluctuations. (Run #8623, S4, Component 3).

Time Scale ⊢————⊣
0   200 Seconds
Velocity Scale ⊢—+—+—⊣
0 1 2 3 M/S
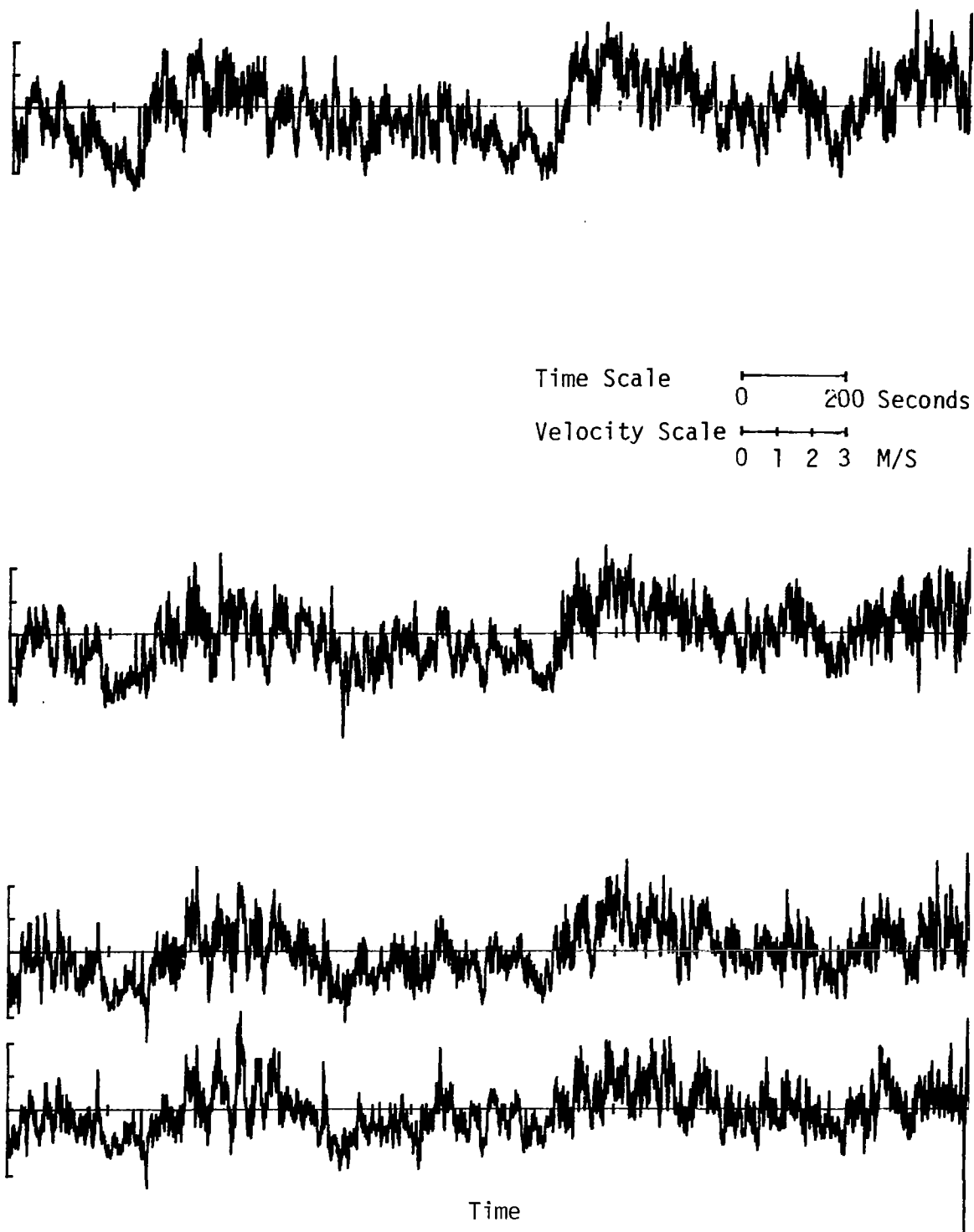
Figure B.28. Time history of turbulent fluctuations. (Run #8624, T1,
Component 1).

Time Scale ⊢————————⊣
0   200 Seconds

Velocity Scale ⊢—⊢—⊢—⊣
0 1 2 3   M/S
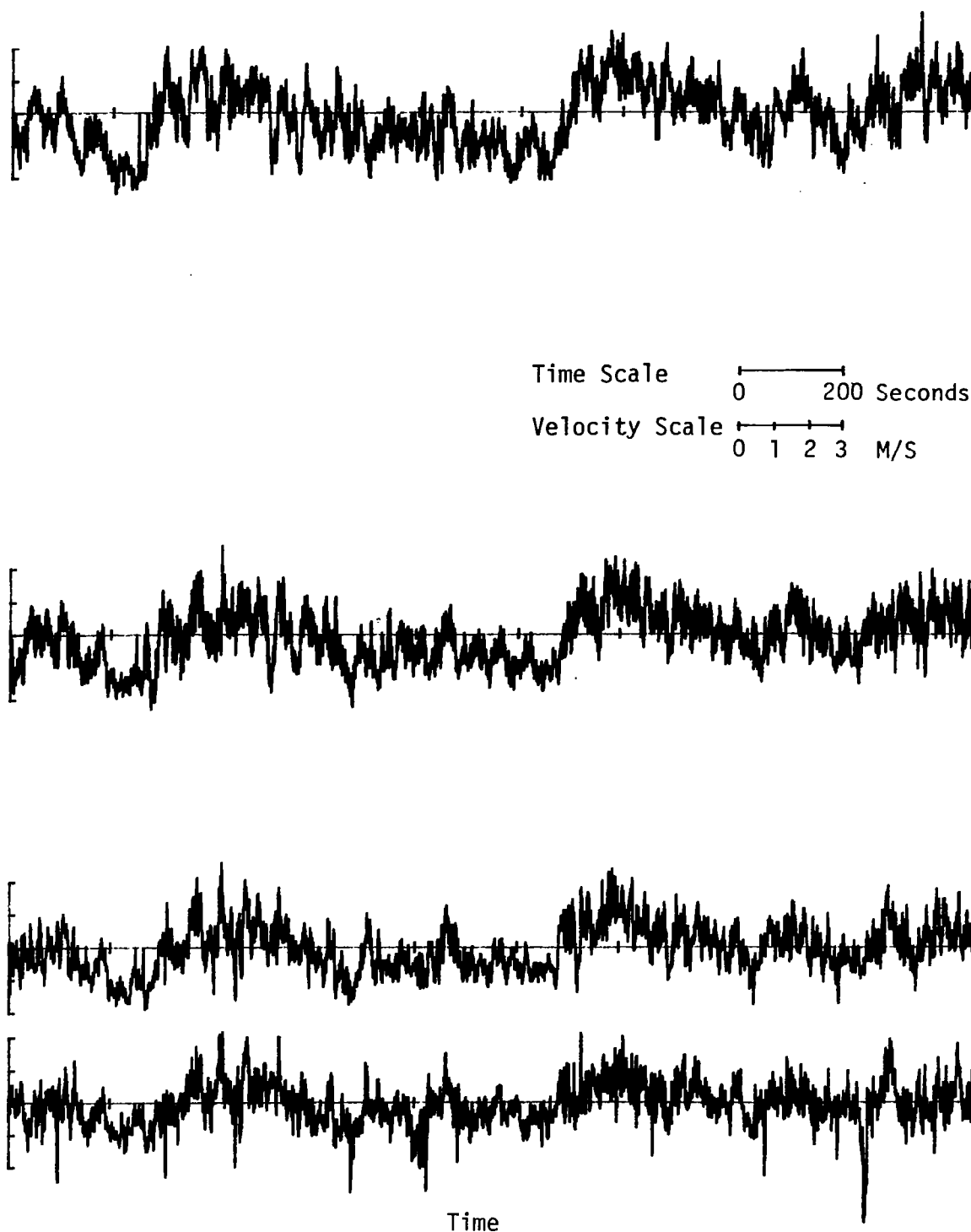
Figure B.29.   Time history of turbulent fluctuations.   (Run #8624, T2, Component 1).

205

Time Scale

0   200 Seconds

Velocity Scale
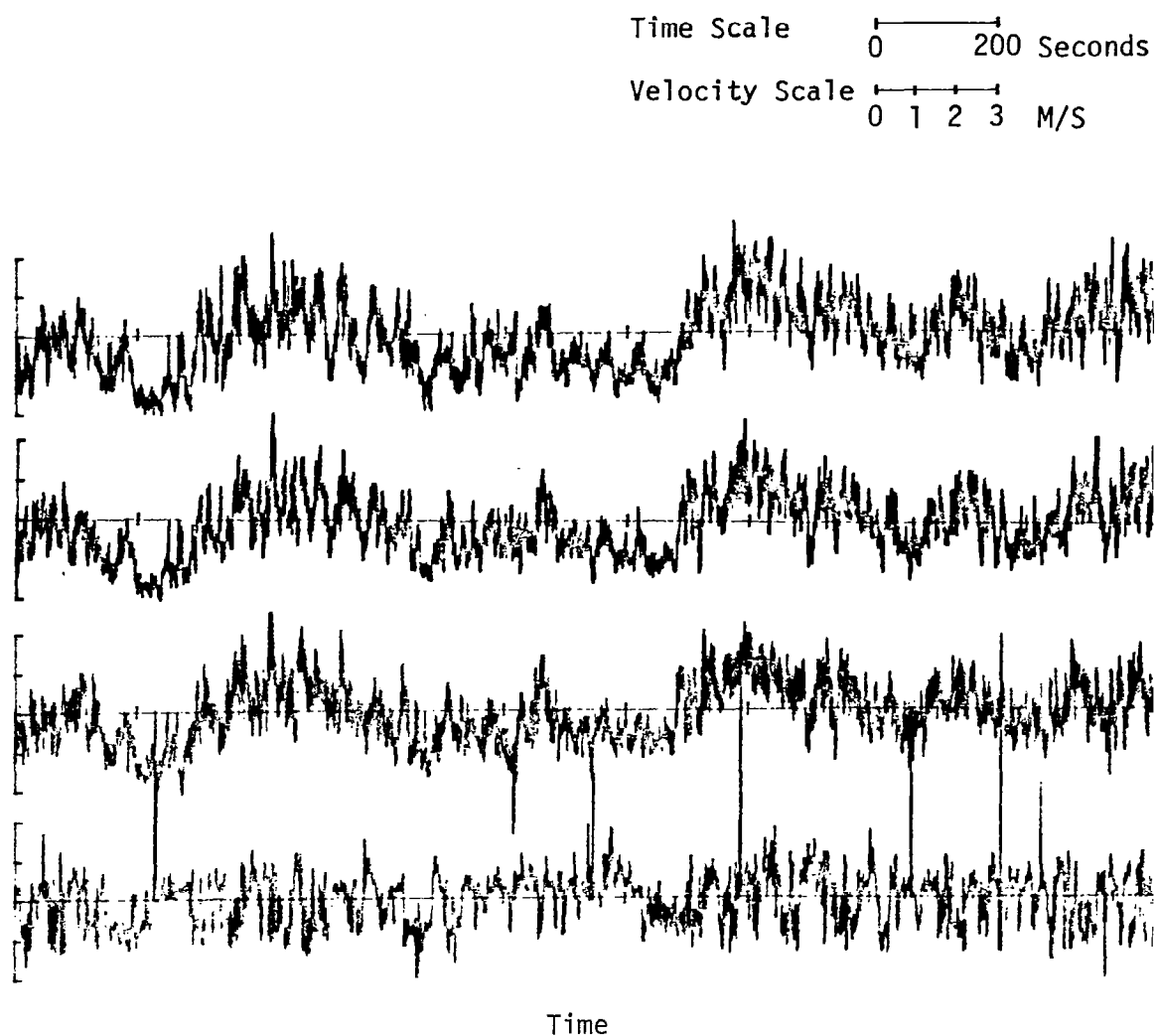
0 1 2 3   M/S

Time

Figure B.30.   Time history of turbulent fluctuations.   (Run #8624, T3, Component 1).

206
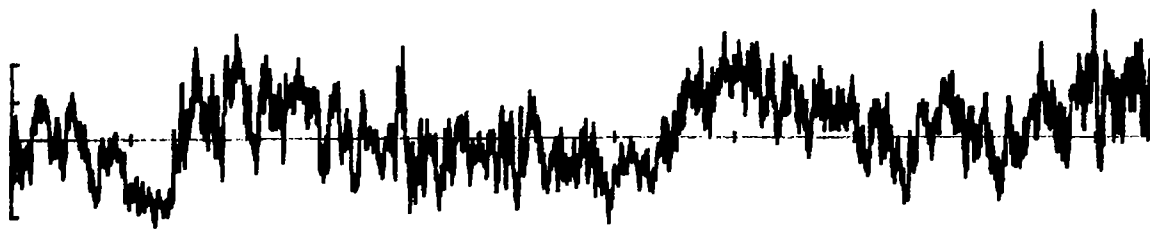
Time Scale   0   200 Seconds

Velocity Scale   0 1 2 3   M/S
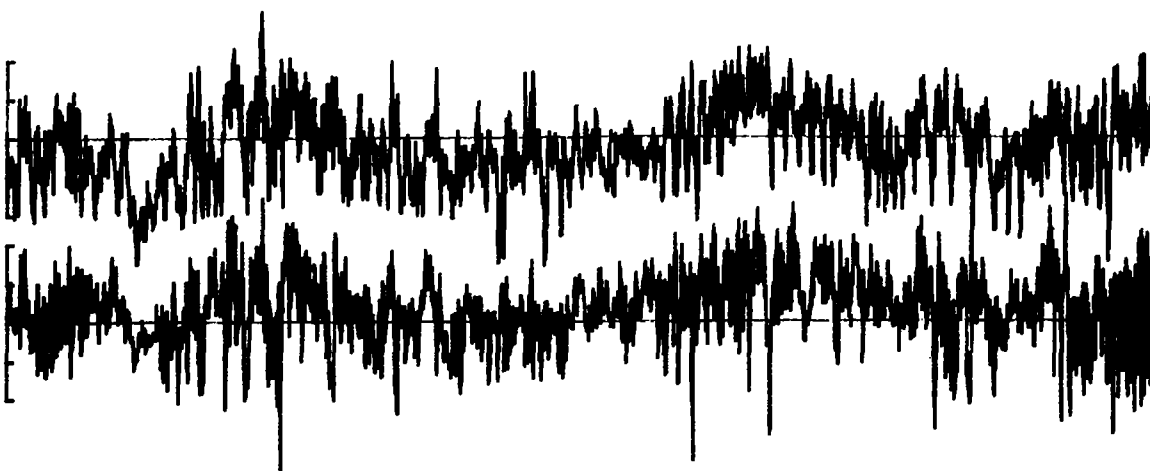
Time

Figure B.31.   Time history of turbulent fluctuations.   (Run #8624, T4, Component 1).

Time Scale | 0 ────── 200 Seconds
Velocity Scale | 0 1 2 3 M/S
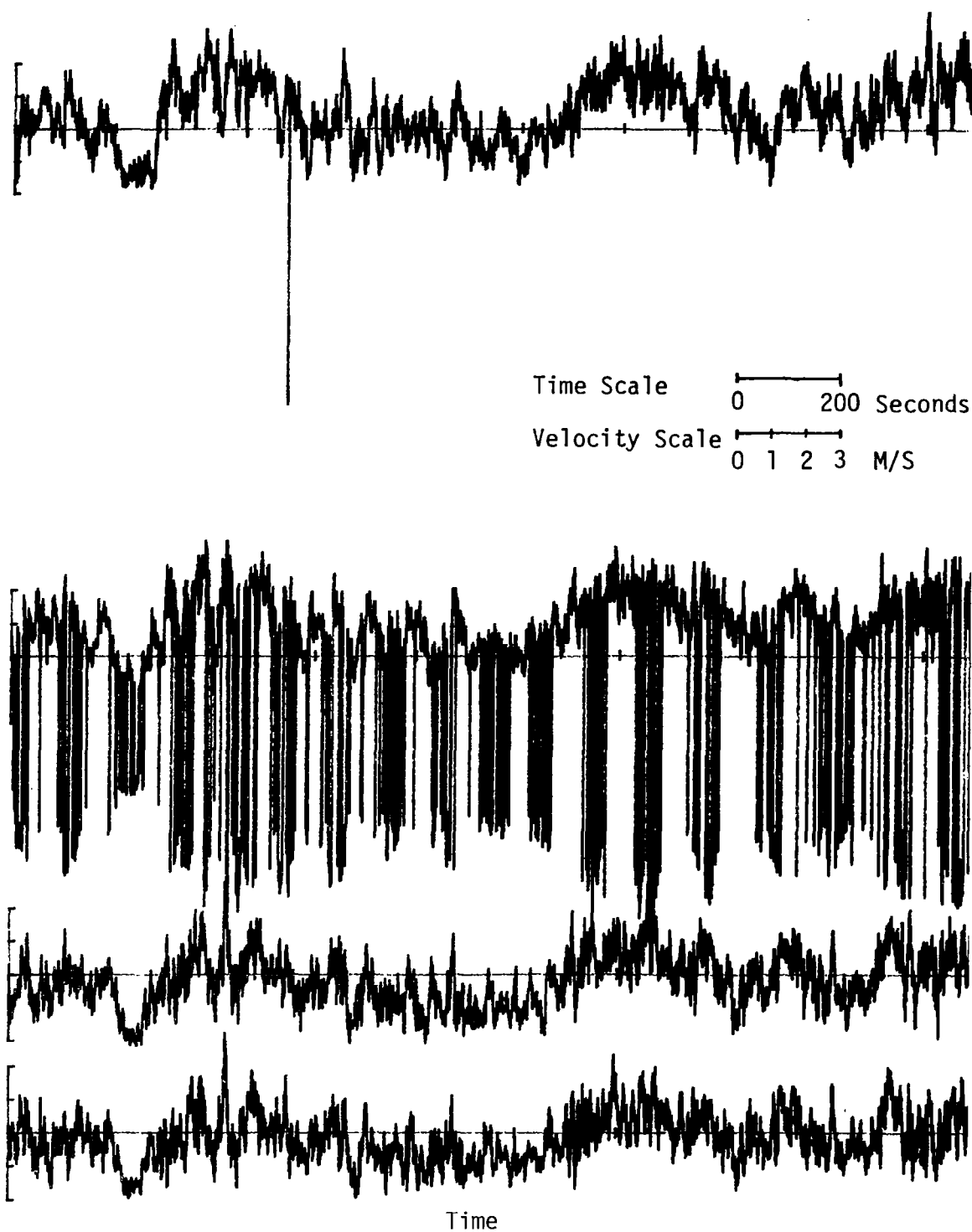
Time

Figure B.32. Time history of turbulent fluctuations. (Run #8624, T5, Component 1).

Time Scale

0   200 Seconds

Velocity Scale

0 1 2 3 M/S
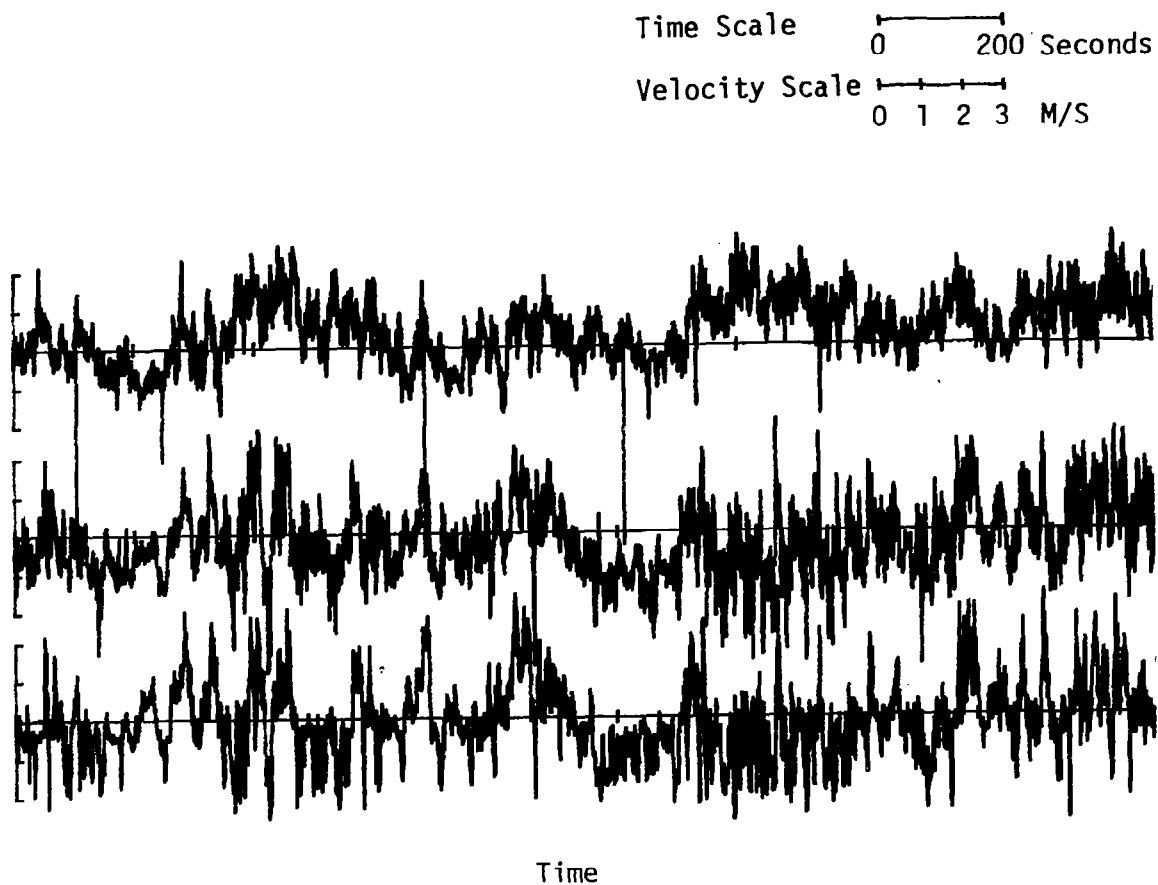
Time

Figure B.33.   Time history of turbulent fluctuations.   (Run #8624, S1, Component 1).

Time Scale

0   200 Seconds

Velocity Scale

0 1 2 3 M/S
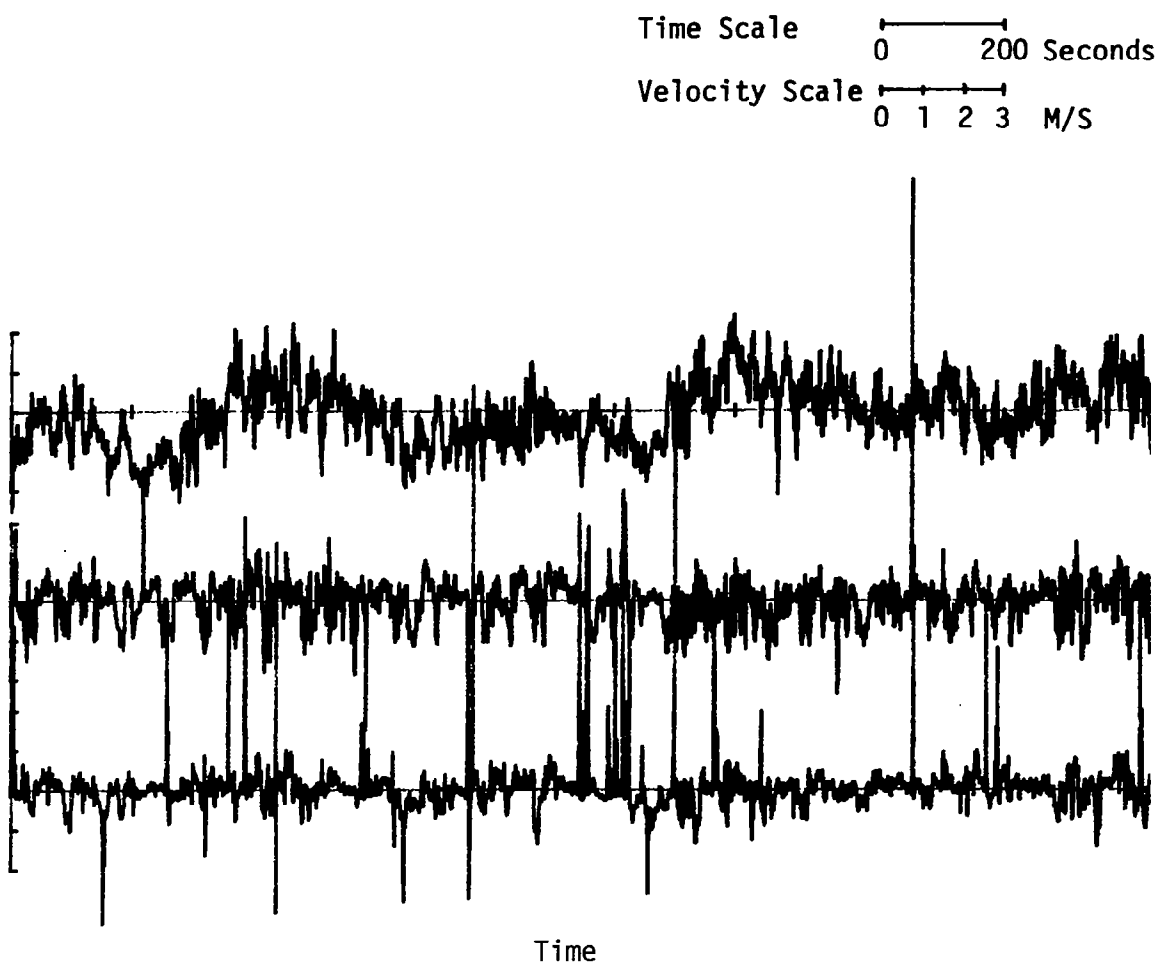
Time

Figure B.34. Time history of turbulent fluctuations. (Run #8624, S2, Component 1).

Time Scale 0   200 Seconds

Velocity Scale 0 1 2 3 M/S
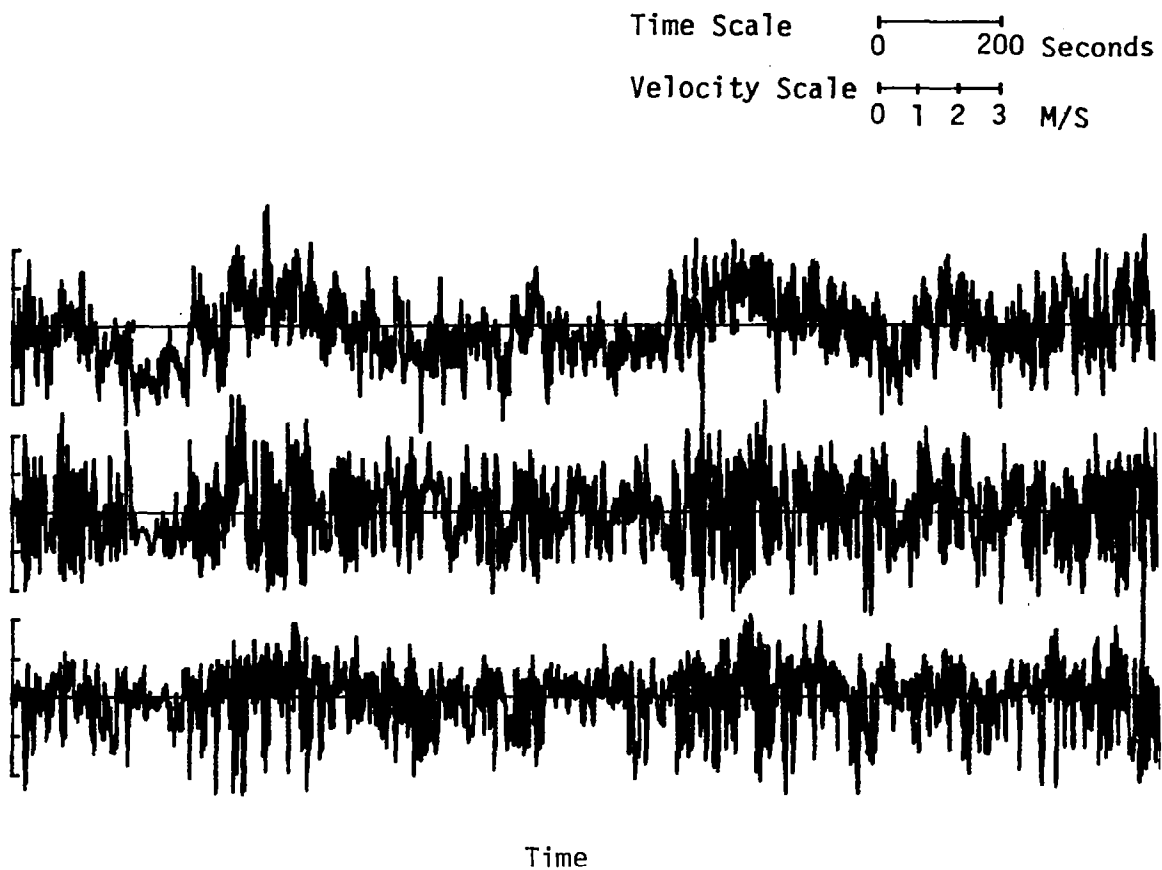
Time

Figure B.35. Time history of turbulent fluctuations. (Run #8624, S3, Component 1).

Time Scale

0   200 Seconds

Velocity Scale
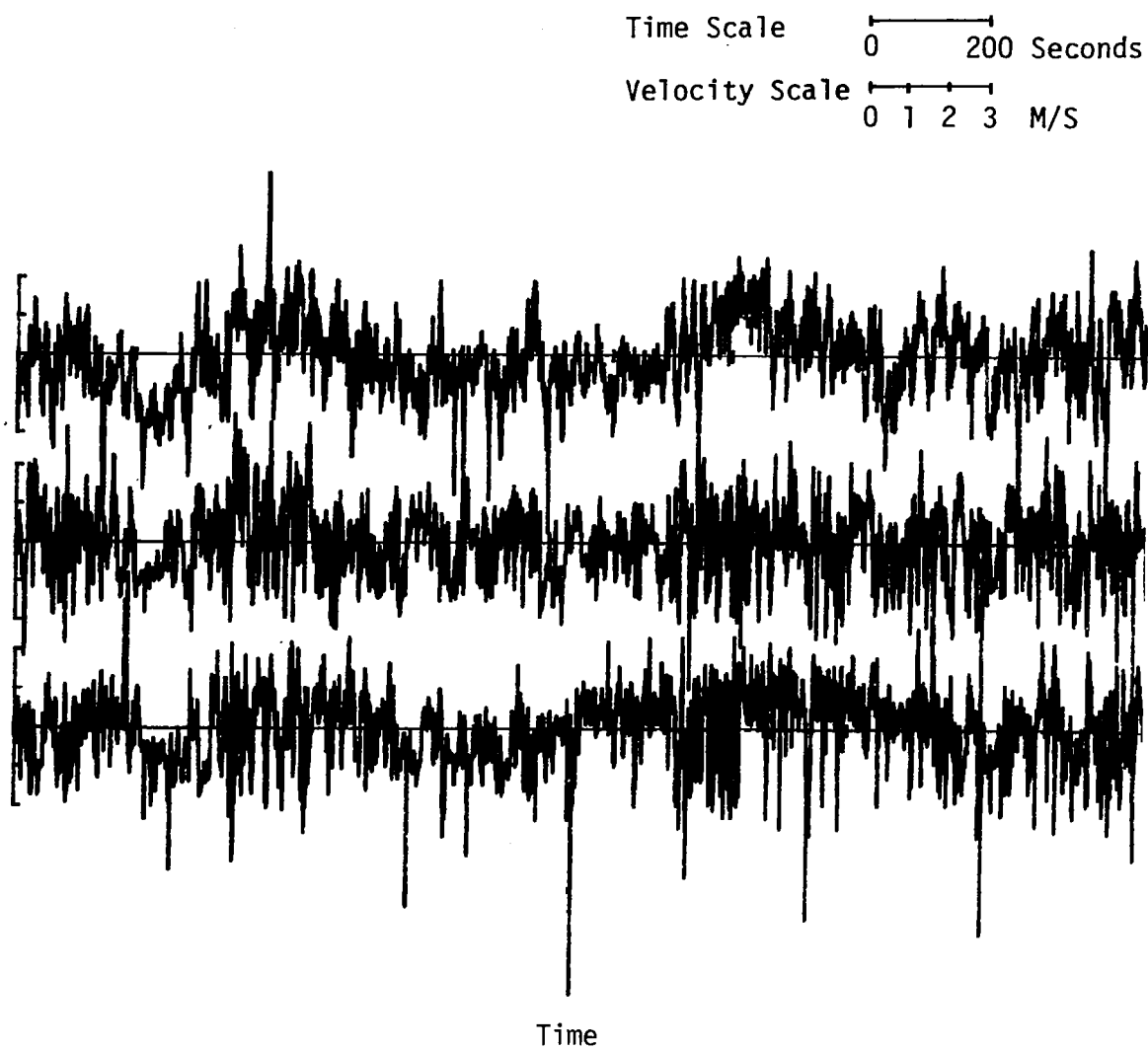
0 1 2 3 M/S

Time

Figure B.36.   Time history of turbulent fluctuations. (Run #8624, S4, Component 1).

Time Scale ⊢━━━━┥
0   200 Seconds

Velocity Scale ⊢┼┼┤
0 1 2 3 M/S
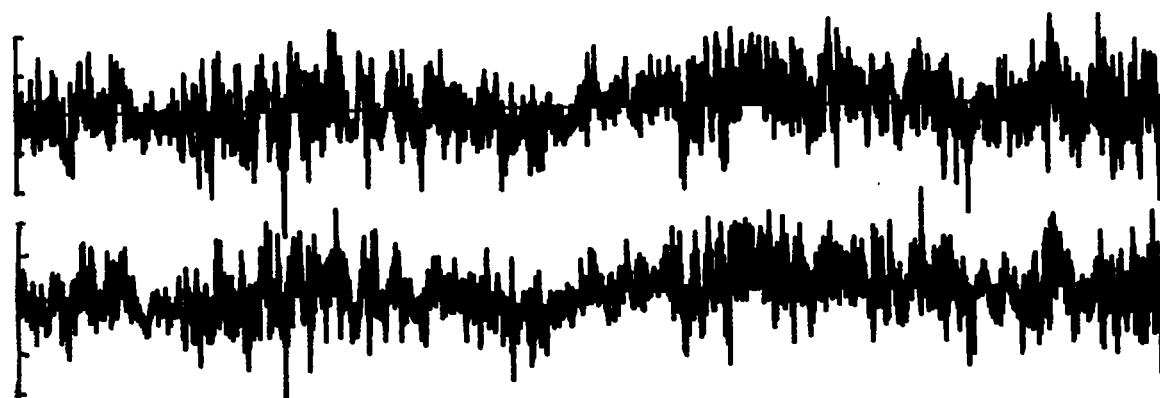
Time

Figure B.37.   Time history of turbulent fluctuations.   (Run #8624, T1, Component 2).

Time Scale ├──────────┤
0   200 Seconds
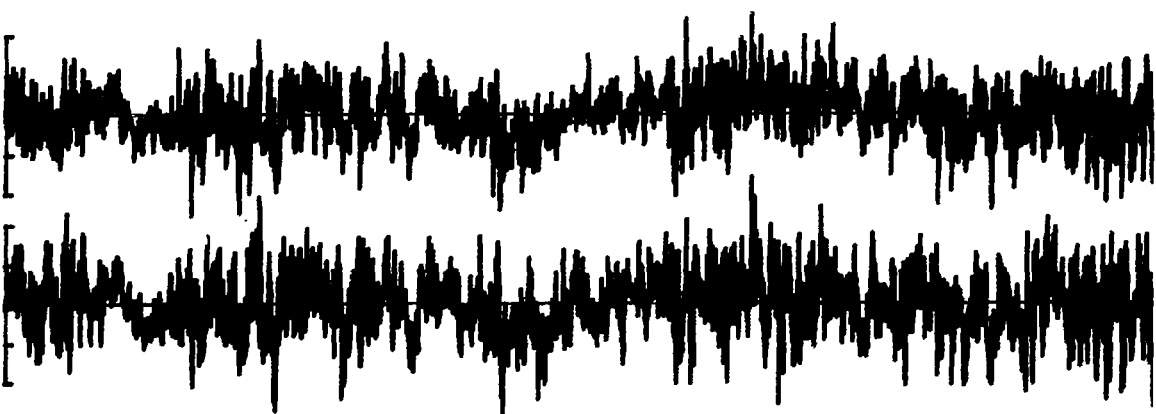
Velocity Scale ├──┼──┼──┤
0 1 2 3 M/S

Figure B.38. Time history of turbulent fluctuations. (Run #8624, T2, Component 2).

214

Time Scale

0 200 Seconds

Velocity Scale
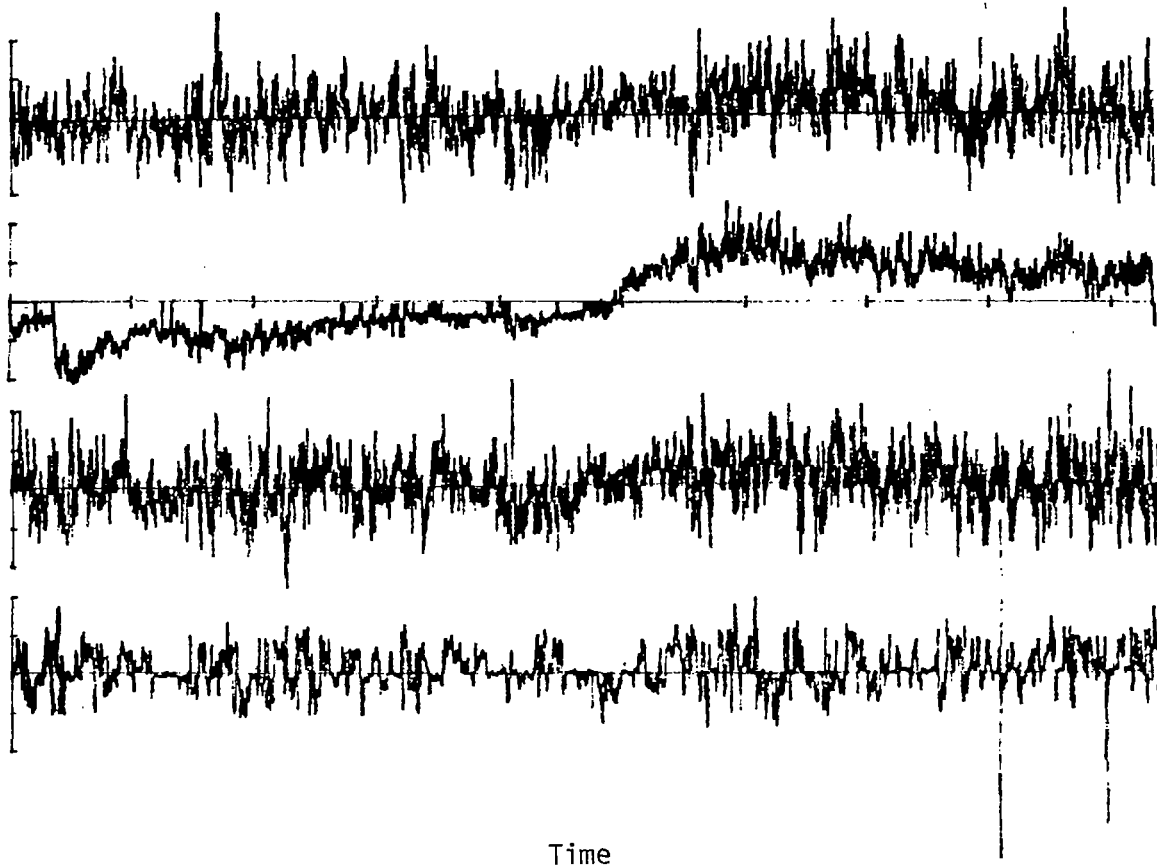
0 1 2 3 M/S

Time

Figure B.39. Time history of turbulent fluctuations. (Run #8624, T3,
Component 2).

215

Time Scale ⊢————⊣
0   200 Seconds

Velocity Scale ⊢—+—+—⊣
0 1 2 3 M/S
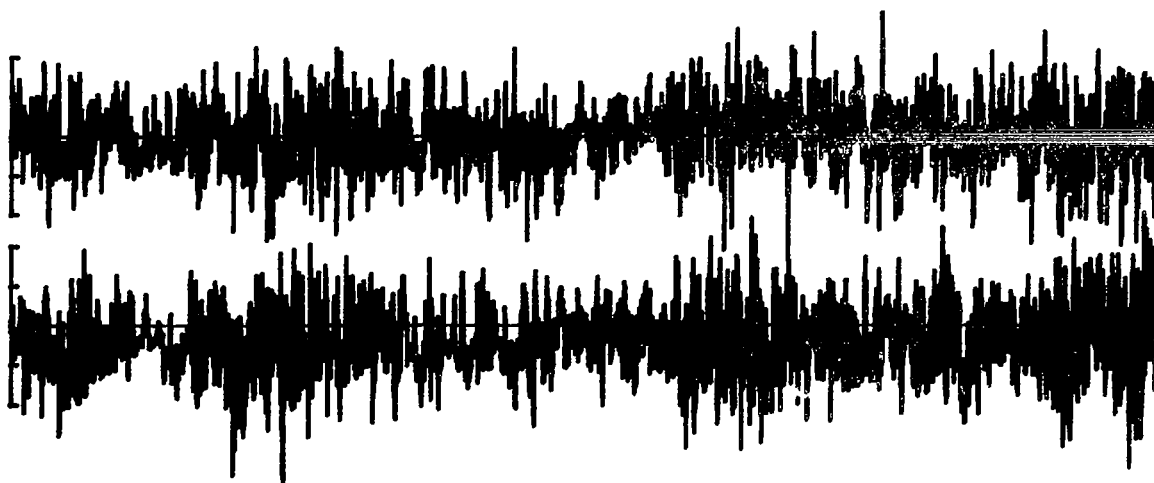
Time

Figure B.40. Time history of turbulent fluctuations. (Run #8624, T4, Component 2).

216

Time Scale $\vdash\!\!-\!\!-\!\!-\!\!-\!\!\dashv$
0   200 Seconds

Velocity Scale $\vdash\!\!-\!\!+\!\!-\!\!+\!\!\dashv$
0 1 2 3 M/S
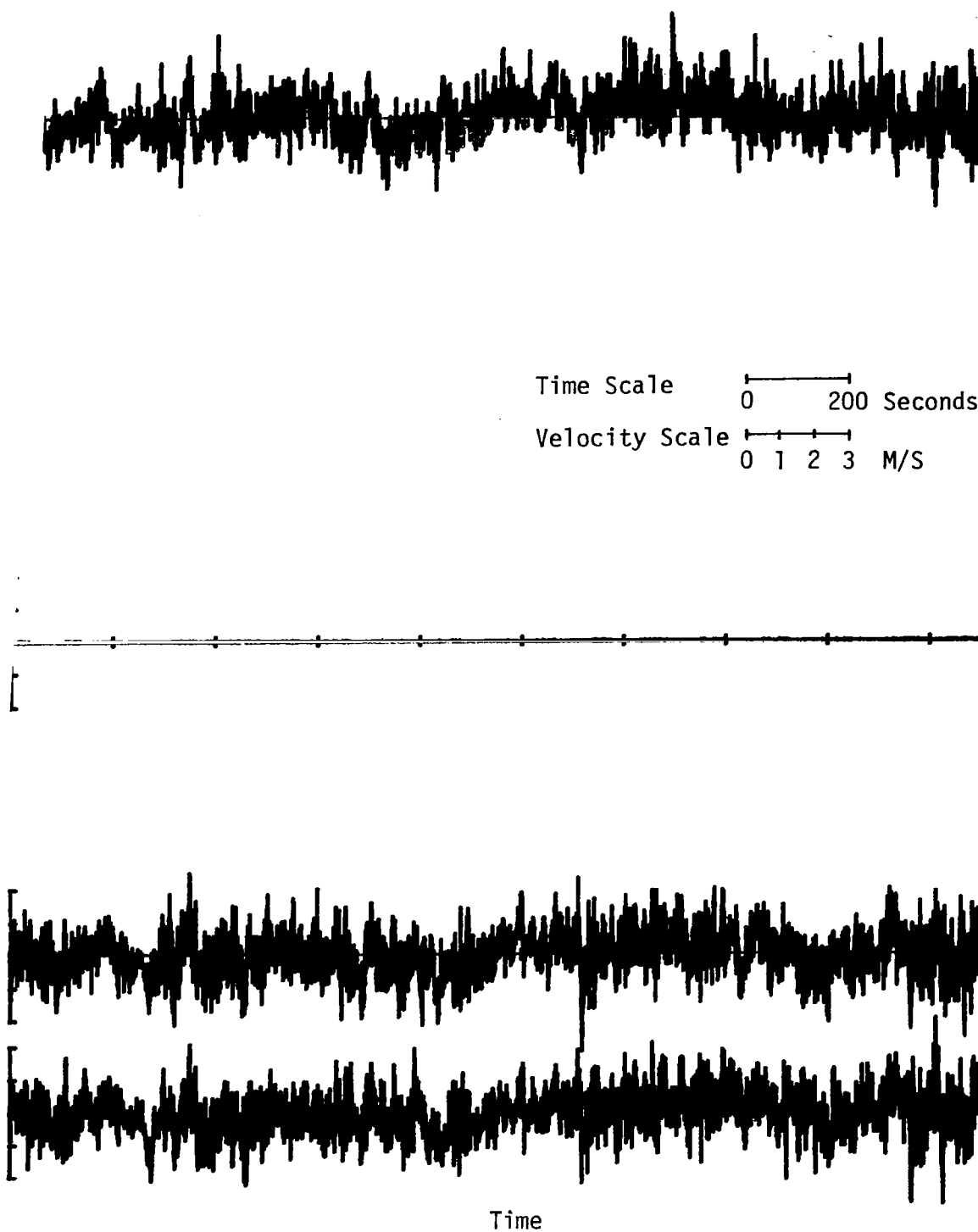
Time

Figure B.41.   Time history of turbulent fluctuations.   (Run #8624, T5, Component 2).

Time Scale

0   200 Seconds

Velocity Scale

0 1 2 3 M/S
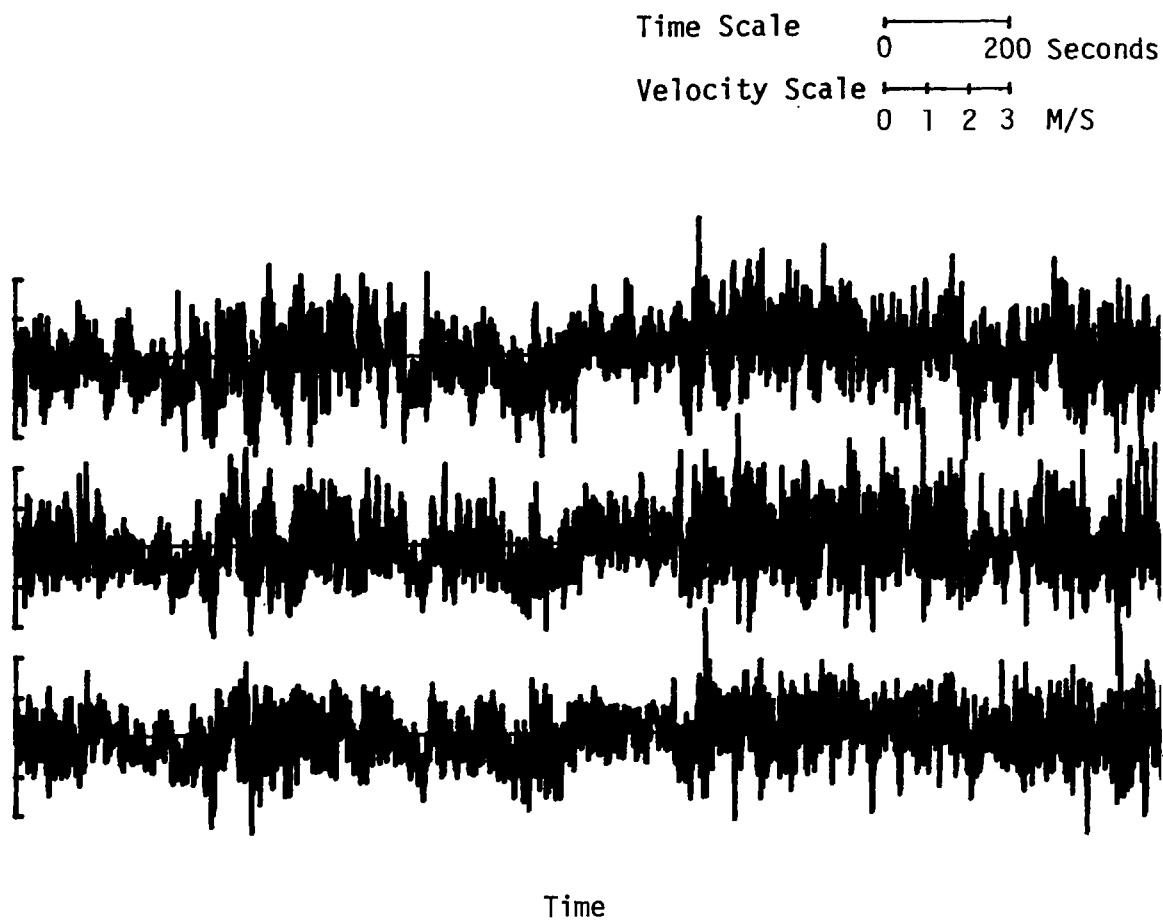
Time

Figure B.42.   Time history of turbulent fluctuations.   (Run #8624, S1, Component 2).

Time Scale ⊢——————⊣
            0   200 Seconds

Velocity Scale ⊢—+—+—⊣
                0 1 2 3 M/S
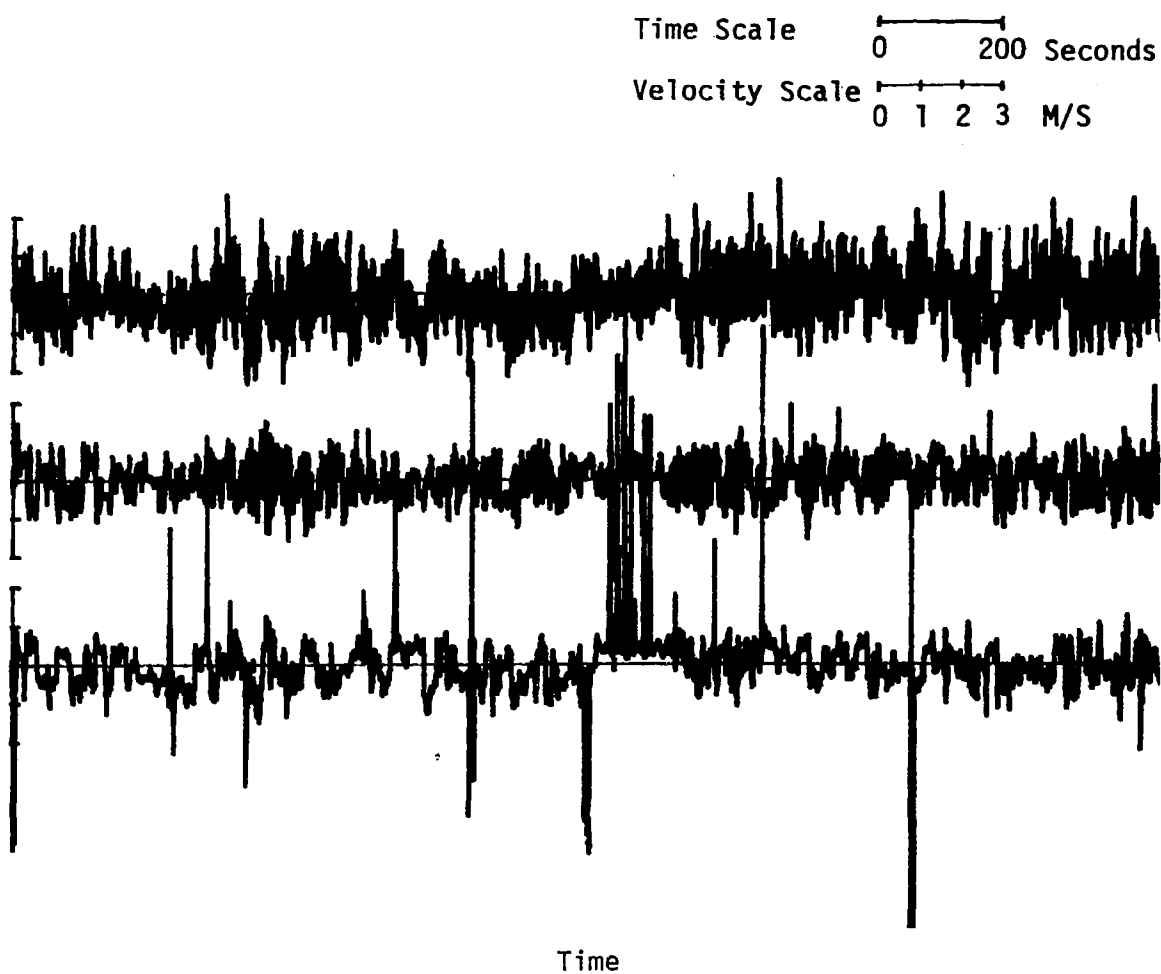
Time

Figure B.43.   Time history of turbulent fluctuations. (Run #8624, S2, Component 2).

Time Scale

0   200 Seconds

Velocity Scale
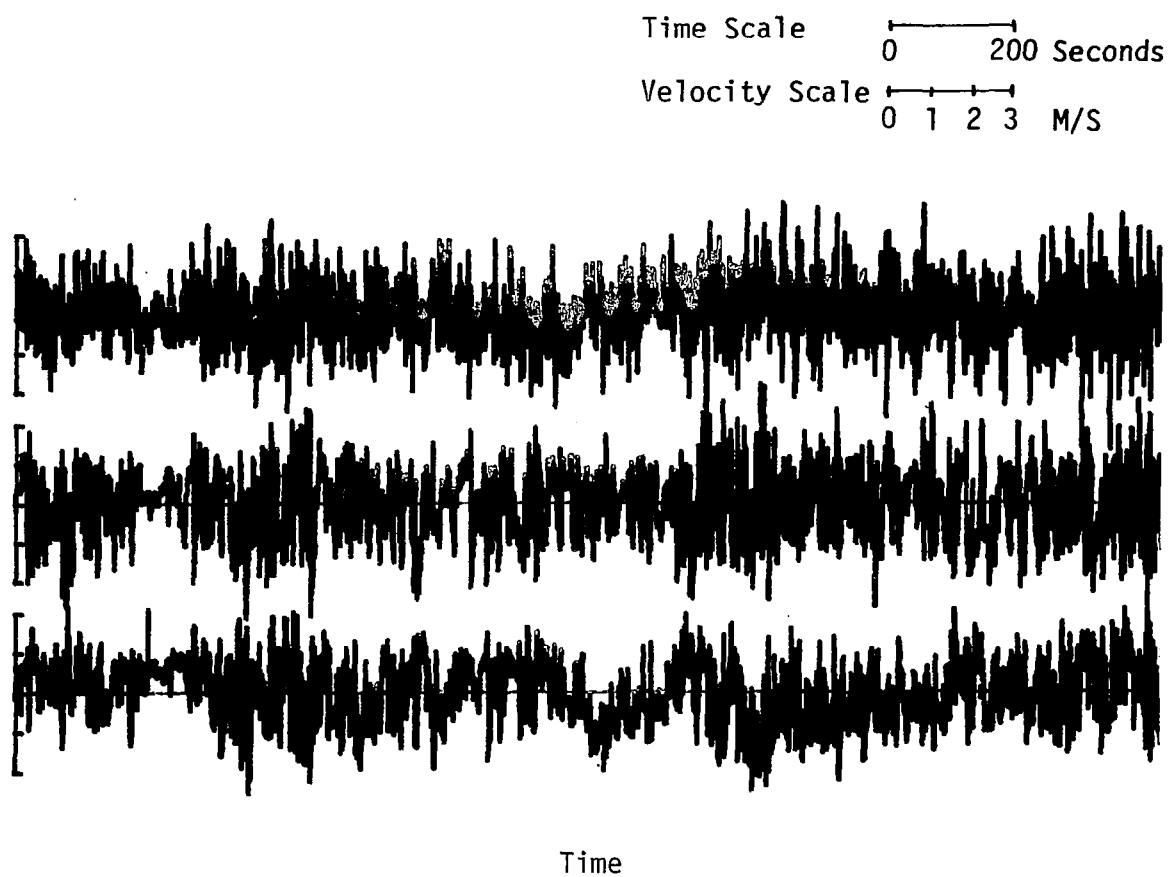
0 1 2 3   M/S

Time

Figure B.44.   Time history of turbulent fluctuations.   (Run #8624, S3, Component 2).

Time Scale ├────────┤
           0   200 Seconds

Velocity Scale ├──┼──┼──┤
               0 1 2 3 M/S
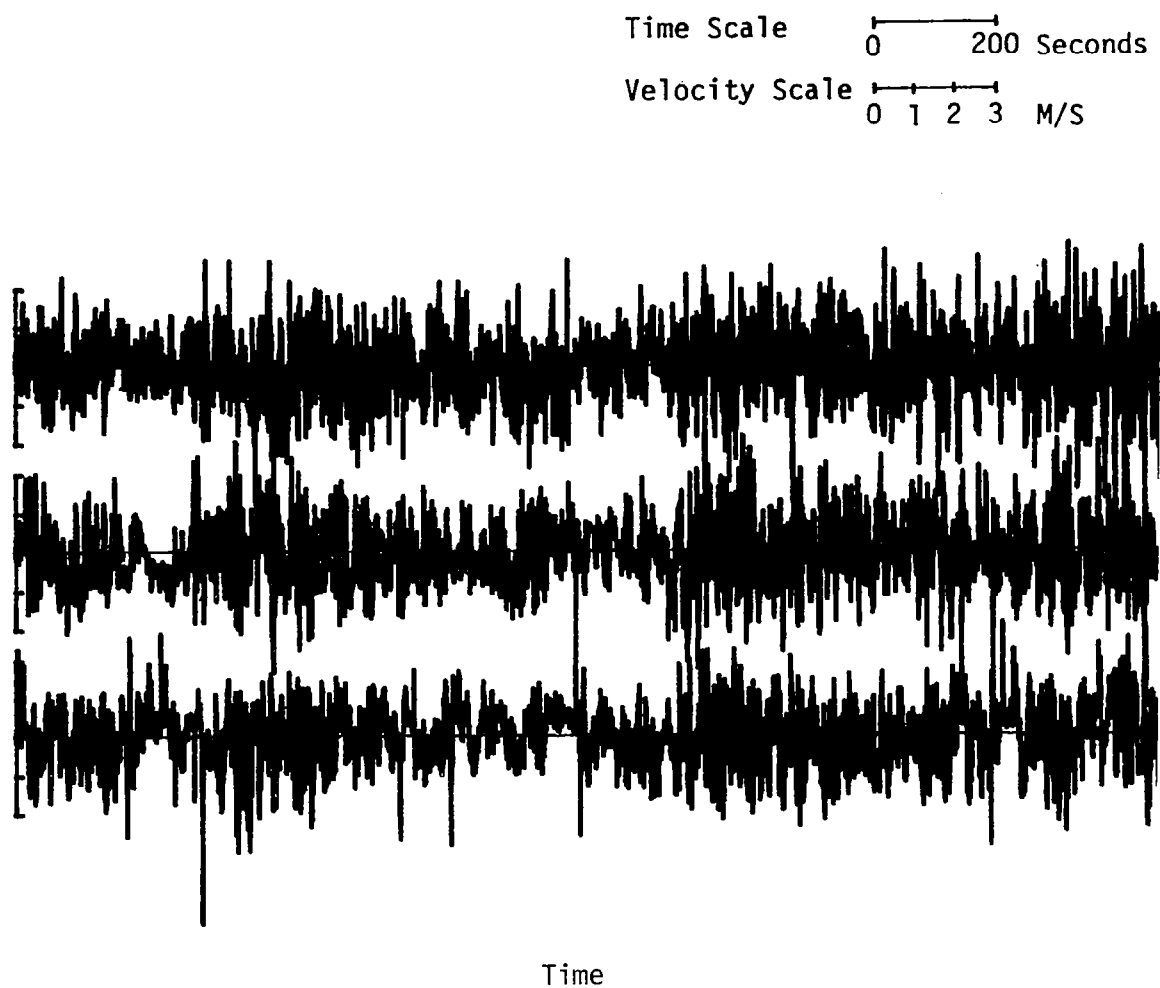
Time

Figure B.45. Time history of turbulent fluctuations. (Run #8624, S4, Component 2).

221

Time Scale ⊢————————⊣
0   200 Seconds

Velocity Scale ⊢—⊢—⊢—⊣
0 1 2 3 M/S
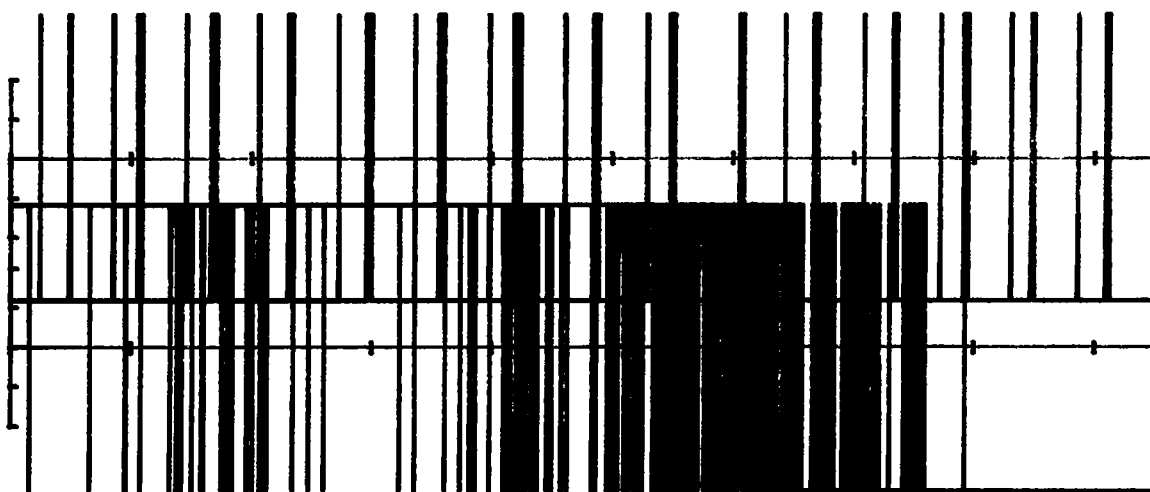
Time

Figure B.46.   Time history of turbulent fluctuations.   (Run #8624, T1, Component 3).

Time Scale 0 ——— 200 Seconds

Velocity Scale 0 1 2 3 M/S

Time

Figure B.47. Time history of turbulent fluctuations. (Run #8624, T2, Component 3).
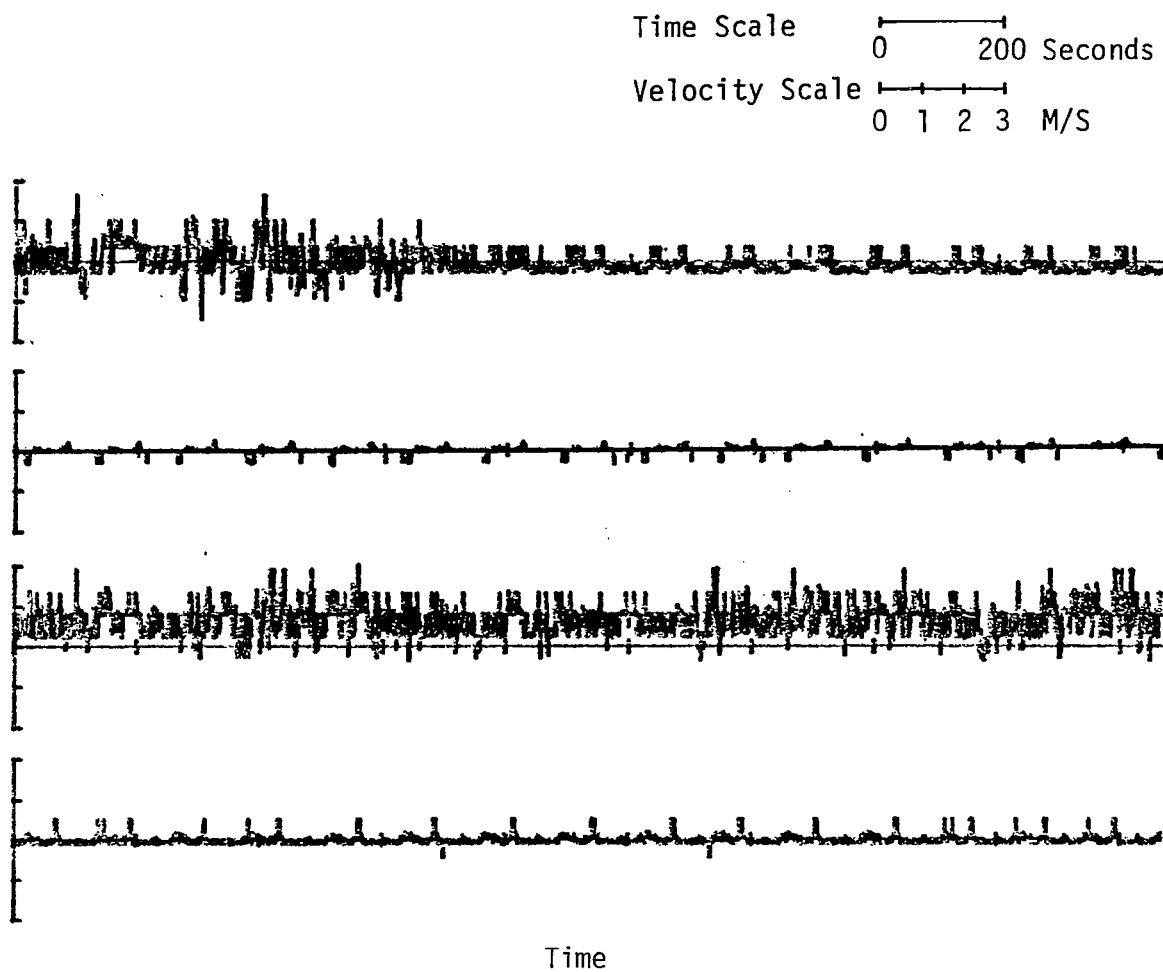
Figure B.48. Time history of turbulent fluctuations. (Run #8624, T3, Component 3).

Time Scale   ├───────┤
          0   200 Seconds

Velocity Scale ├──┬──┬──┤
              0 1 2 3   M/S

Time

Figure B.49.   Time history of turbulent fluctuations.   (Run #8624, T4, Component 3).

Time Scale ├──────────┤
0   200 Seconds

Velocity Scale ├──┬──┬──┤
0 1 2 3 M/S
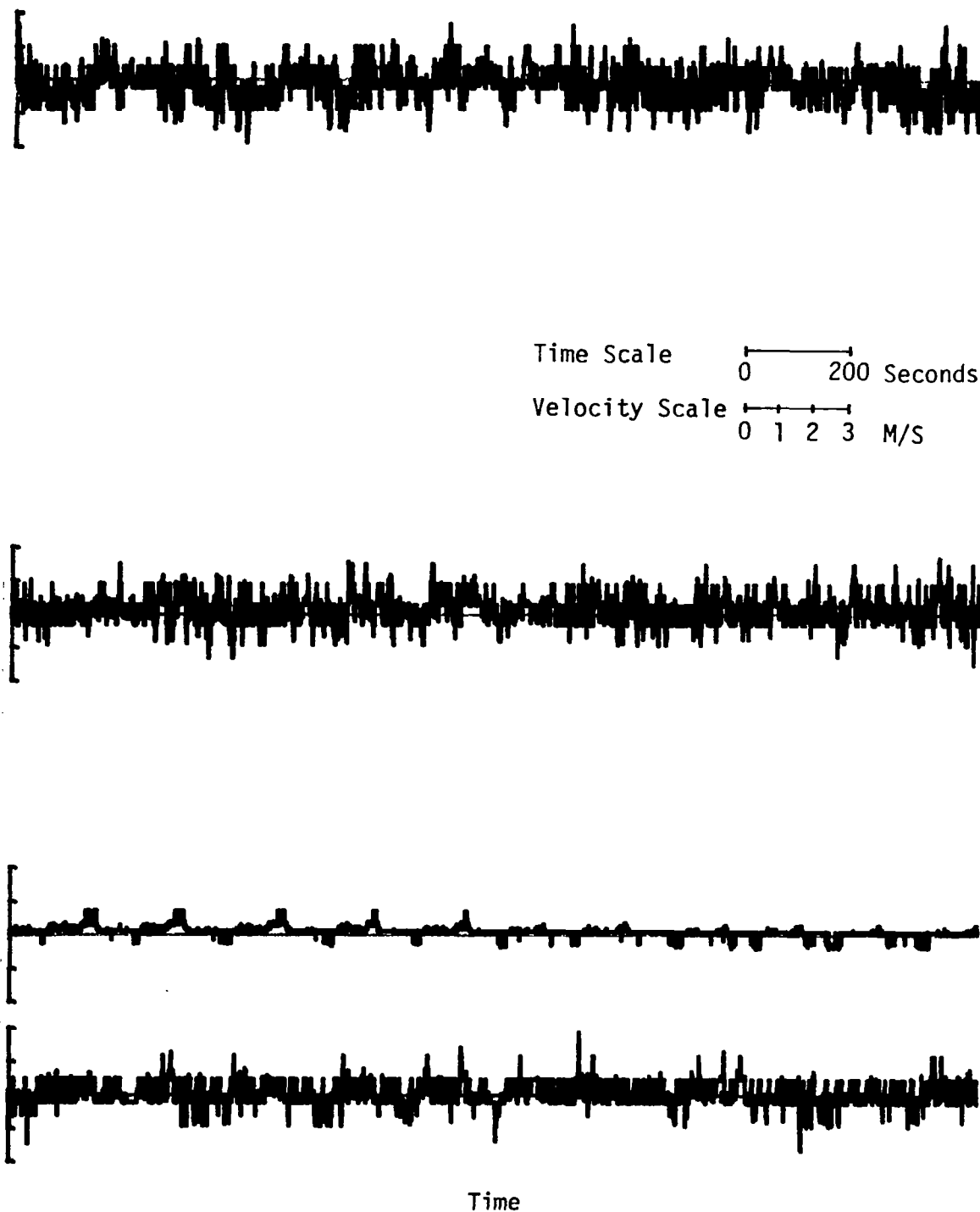
Time

Figure B.50. Time history of turbulent fluctuations. (Run #8624, T5, Component 3).
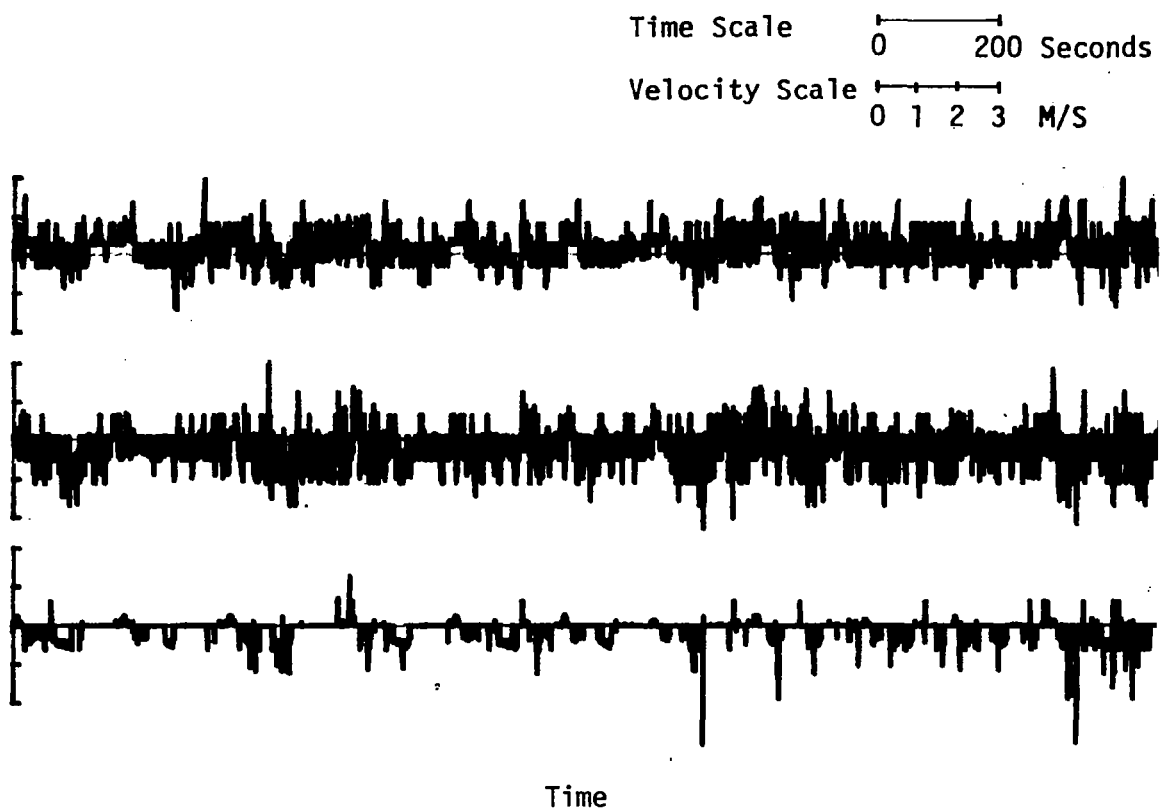
Figure B.51. Time history of turbulent fluctuations. (Run #8624, S1, Component 3).
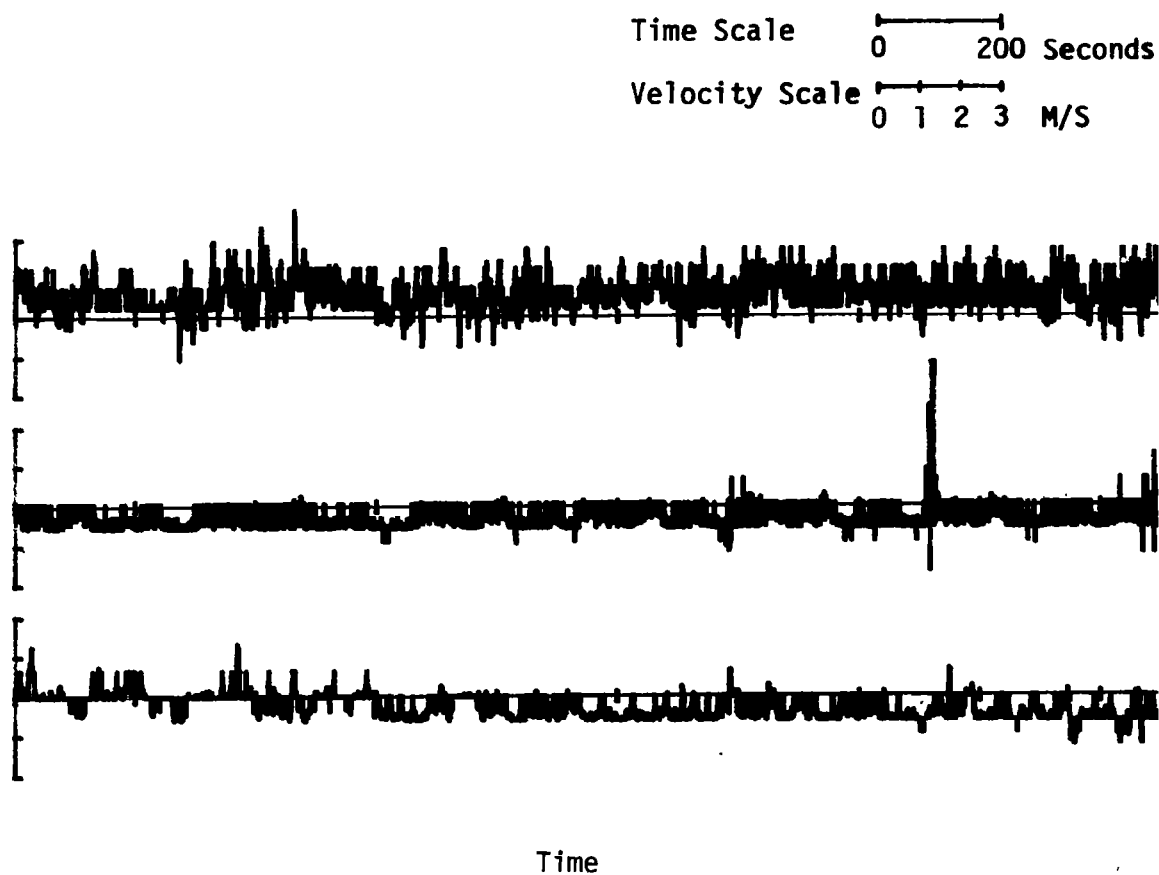
Figure B.52.   Time history of turbulent fluctuations. (Run #8624, S2,
Component 3).

Time Scale ⊢━━━━━┥
0   200 Seconds

Velocity Scale ⊢━┿━┿━┥
0 1 2 3 M/S
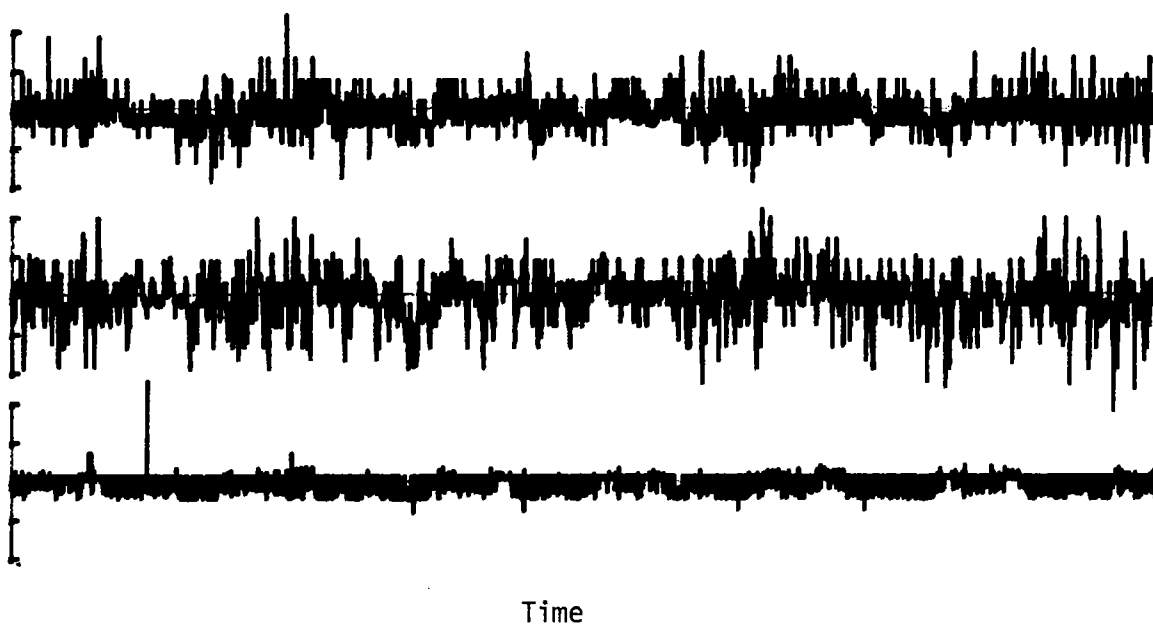
Time

Figure B.53.   Time history of turbulent fluctuations. (Run #8624, S3, Component 3).

Time Scale   0   200 Seconds

Velocity Scale   0 1 2 3   M/S
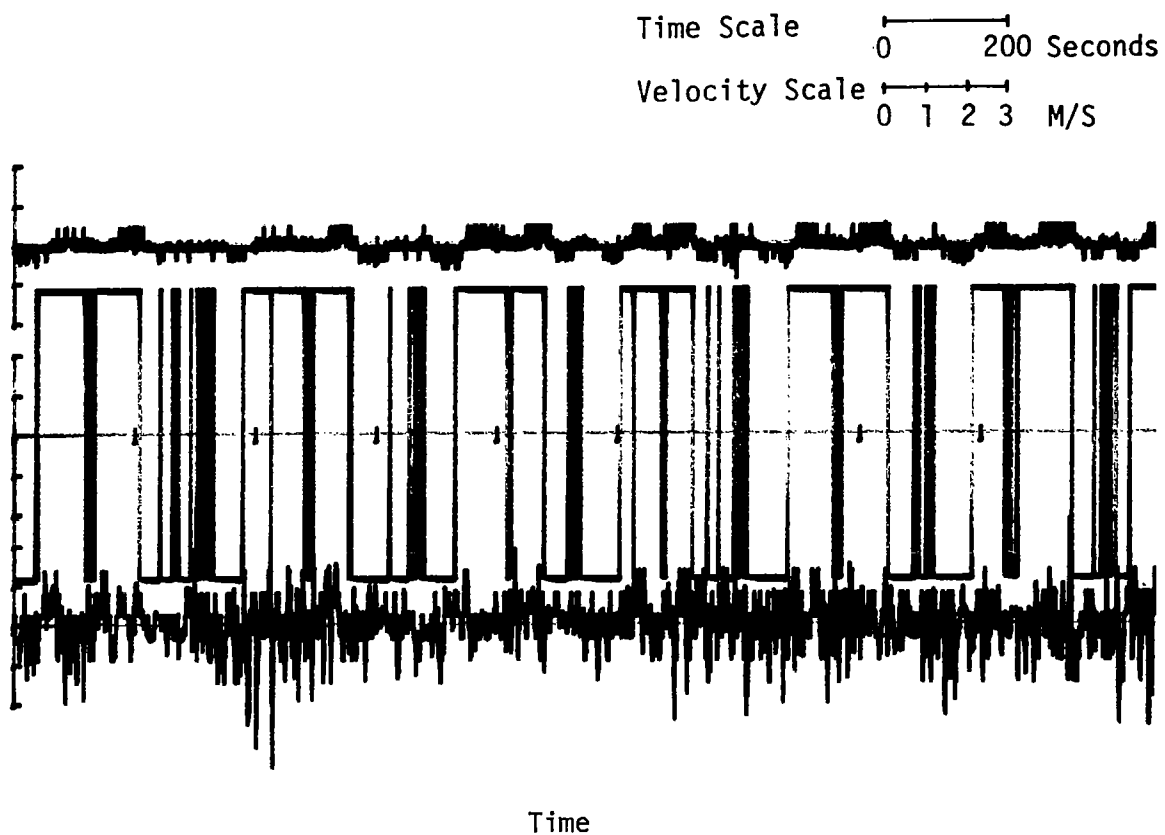
Time

Figure B.54.   Time history of turbulent fluctuations.   (Run #8624, S4, Component 3).

230

APPENDIX C

PROBABILITY DENSITY FUNCTIONS FOR THE LONGITUDINAL, LATERAL, AND VERTICAL VELOCITY COMPONENTS

The probability density functions for the longitudinal, lateral, and vertical velocity components are given in this appendix. The results are compared with the theoretical Gaussian distribution curve represented by the solid line on the figures. The data for the vertical velocities, in most cases, have very anomalous behavior. The reason for this is not clear.

Inspection of the time histories suggests that the propeller-type anemometers have a lag time when reversing direction. This effect is also apparent in the correlation functions shown in Appendix E. In the single-point spectra shown in Chapter VII and the two-point spectra shown in Chapter VIII, this effect is believed to be present as a spike in the data at $fz/\overline{W} \simeq 0.024$. This suggests a harmonic signal is present in the data with roughly a time period of 3 minutes. In future work, the possibility of filtering this effect will be studied.
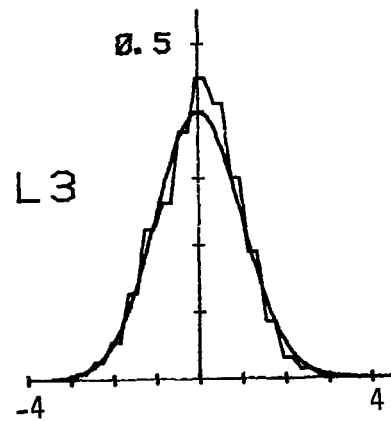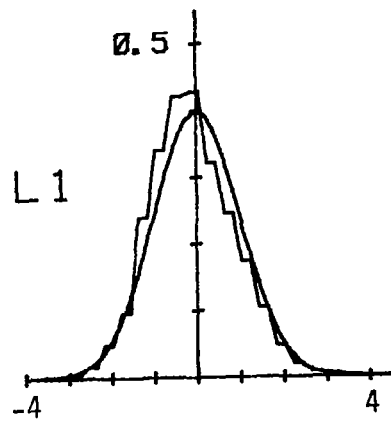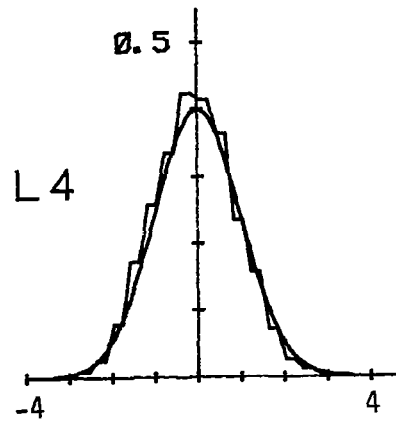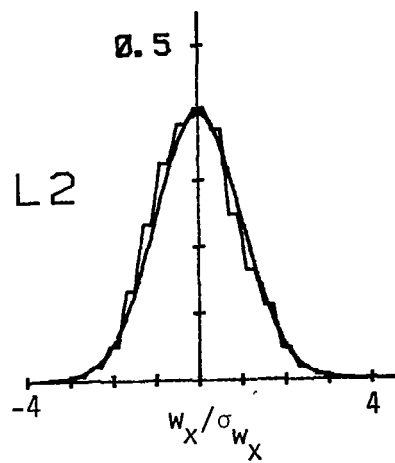
Figure C.1. Probability density function for longitudinal velocity
component normalized with σ_{w_x} (Run #8623, Tl, Component 1).
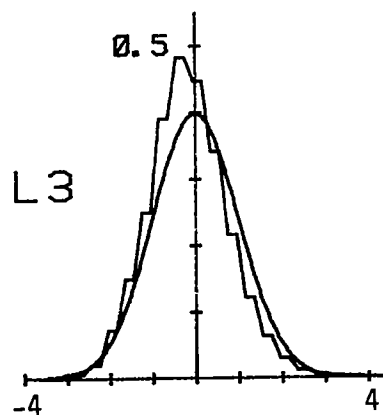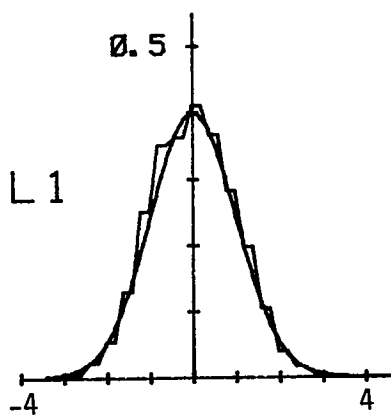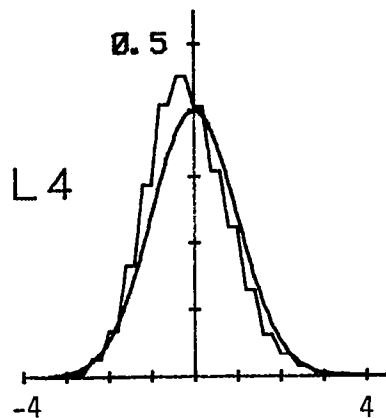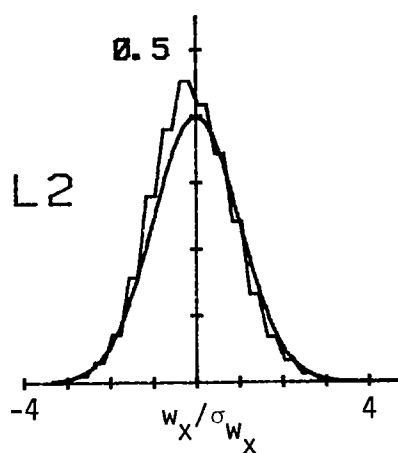
Figure C.2. Probability density function for longitudinal velocity component normalized with σ_{w_x} (Run #8623, T2, Component 1).
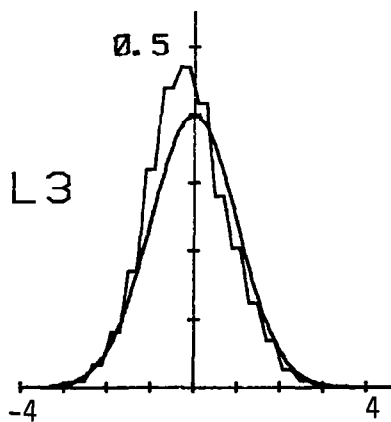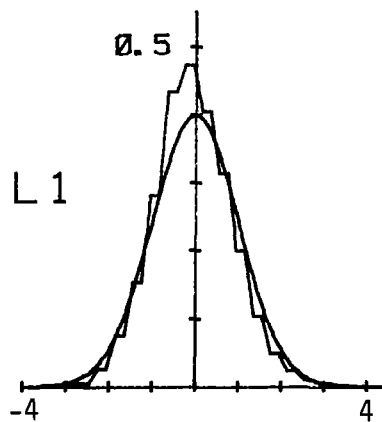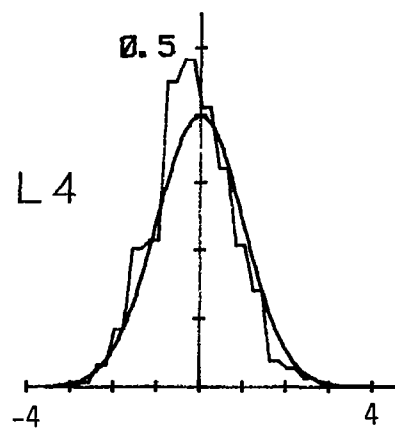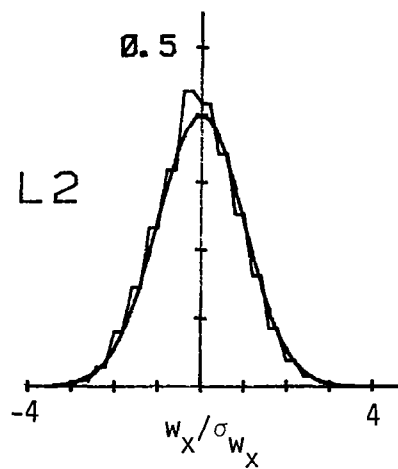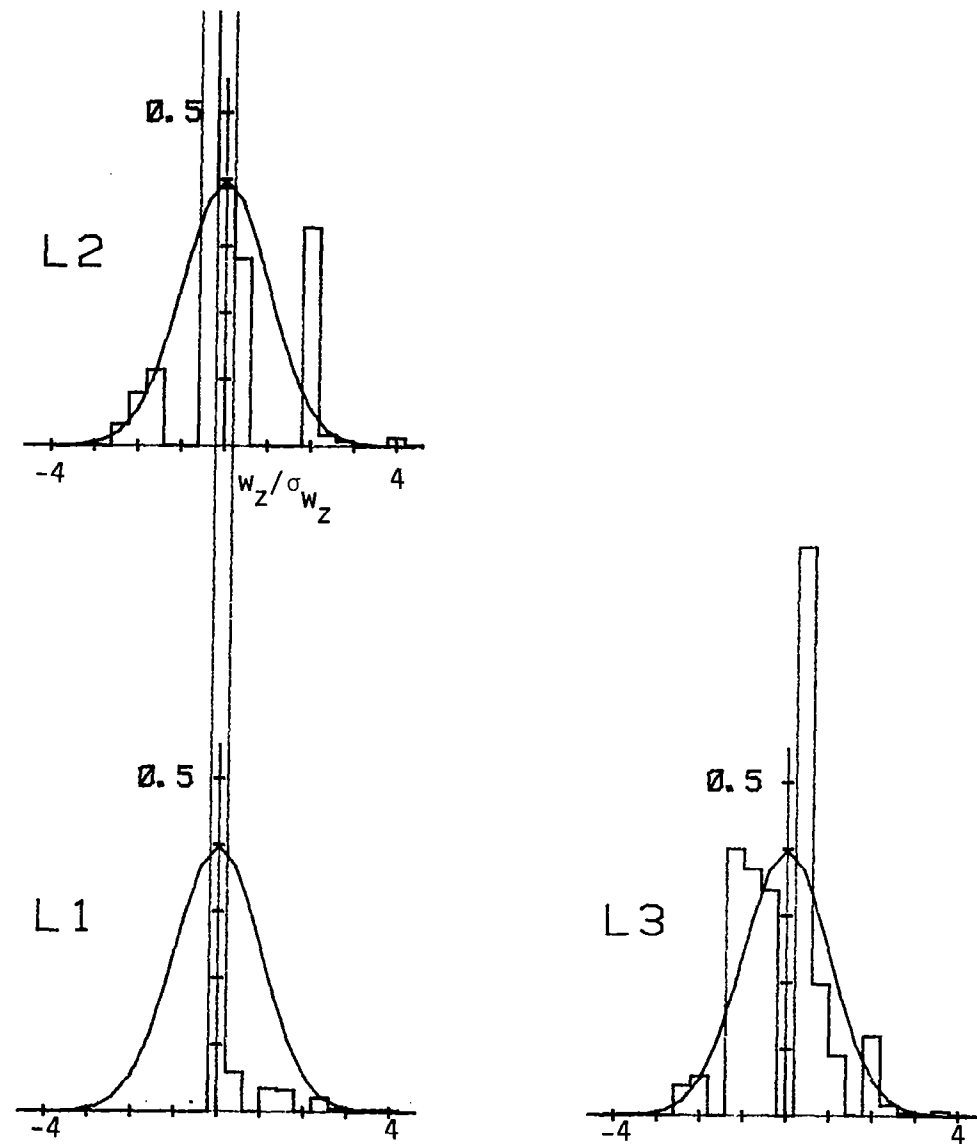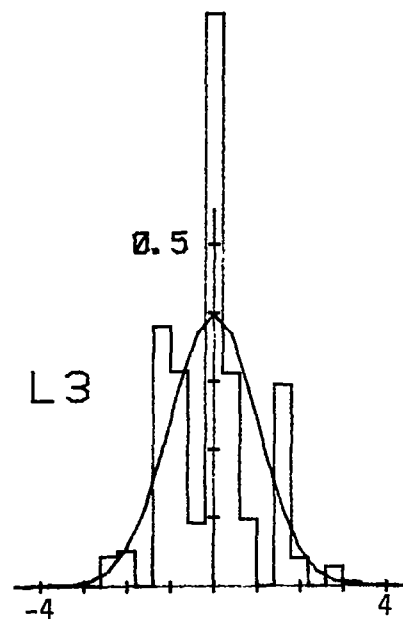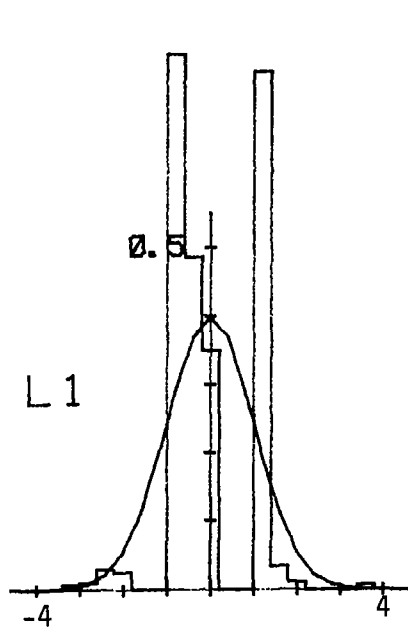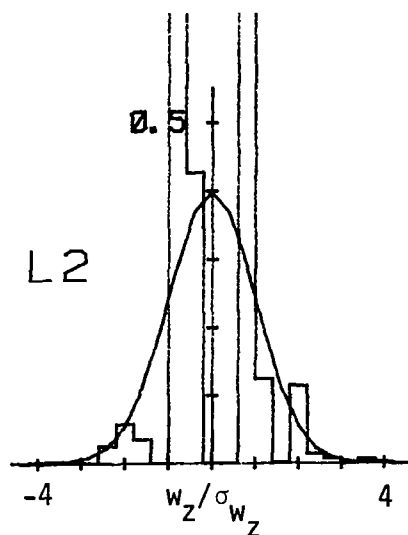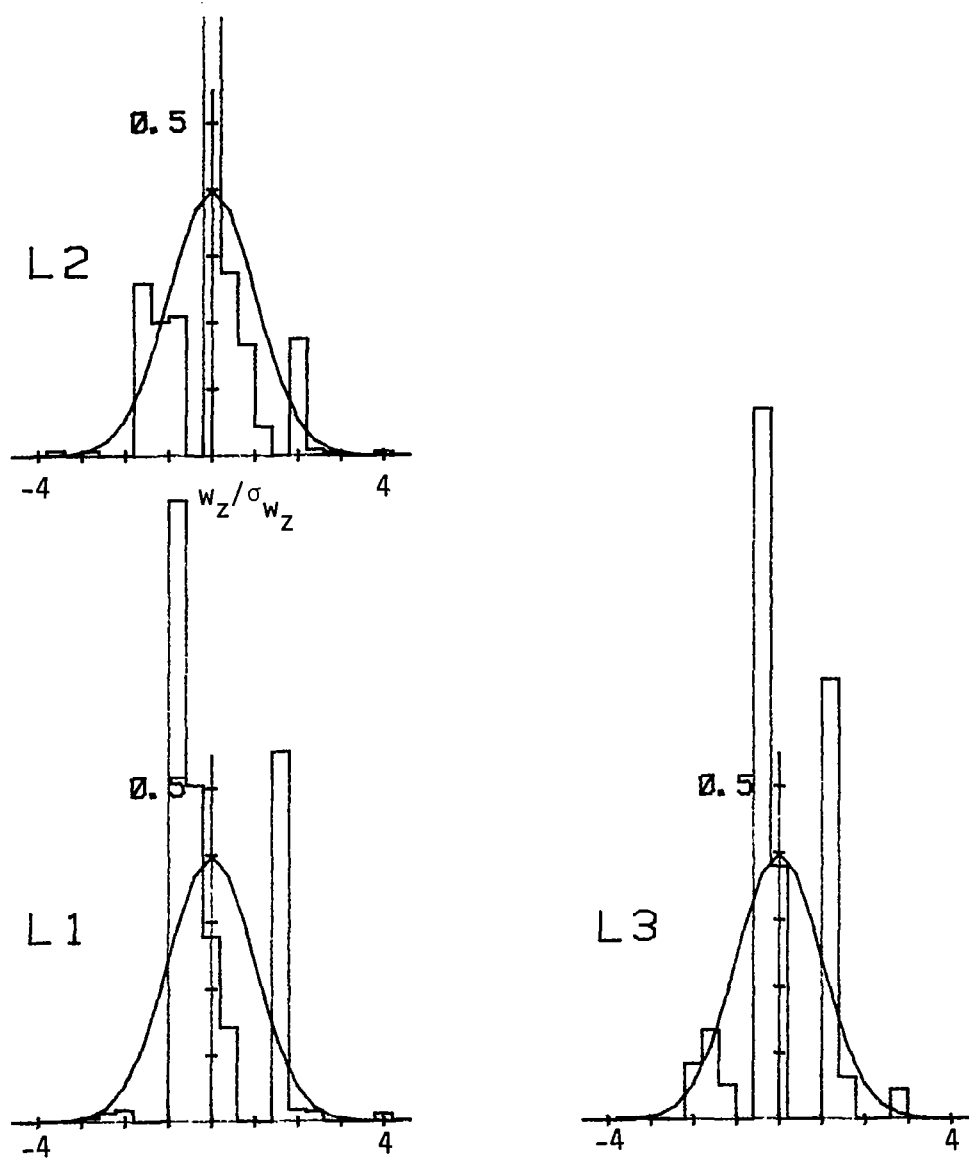
Figure C.3. Probability density function for longitudinal velocity
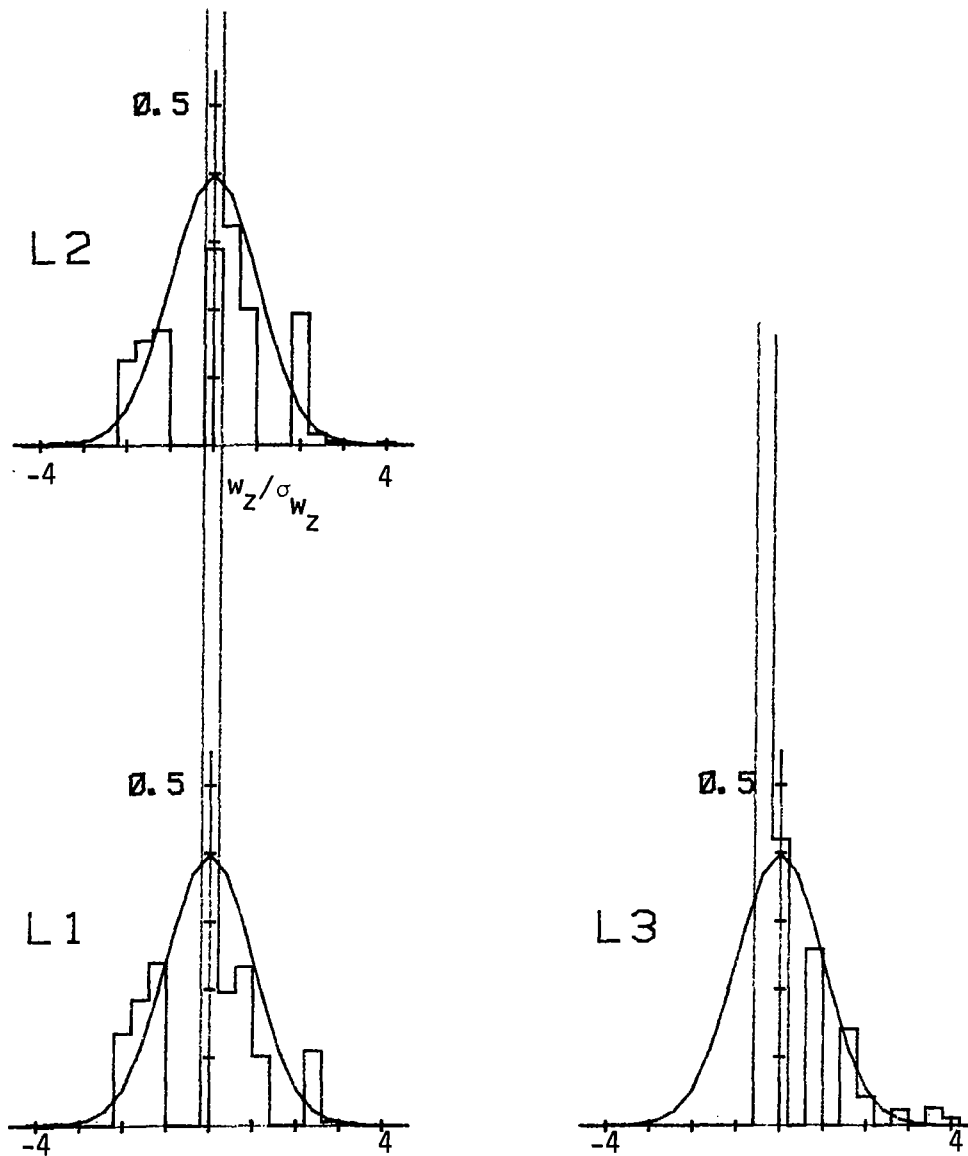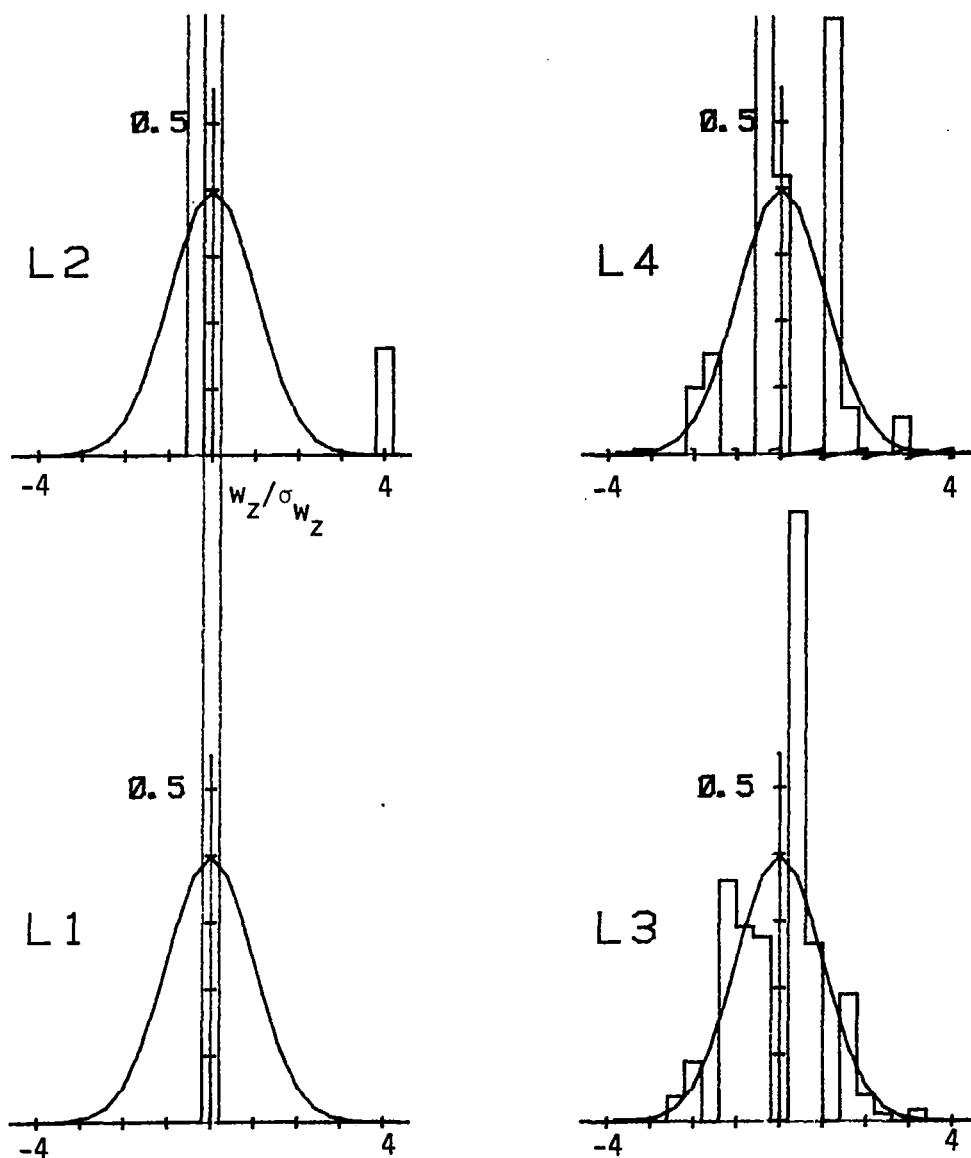component normalized with σ_{w_x} (Run #8623, T3, Component 1).
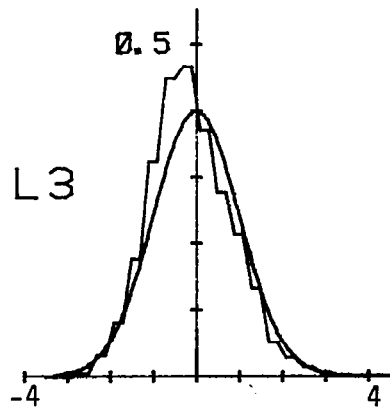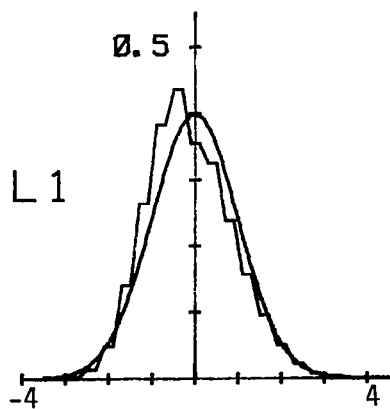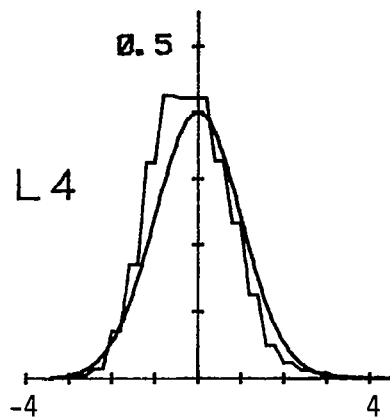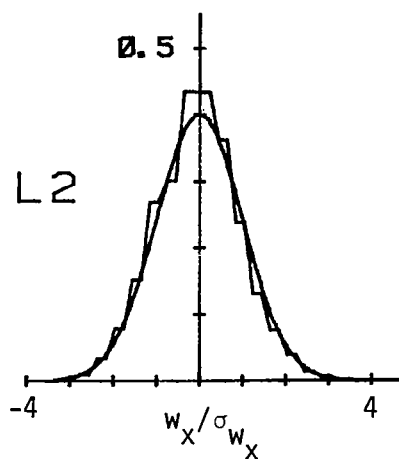
Figure C.4. Probability density function for longitudinal velocity
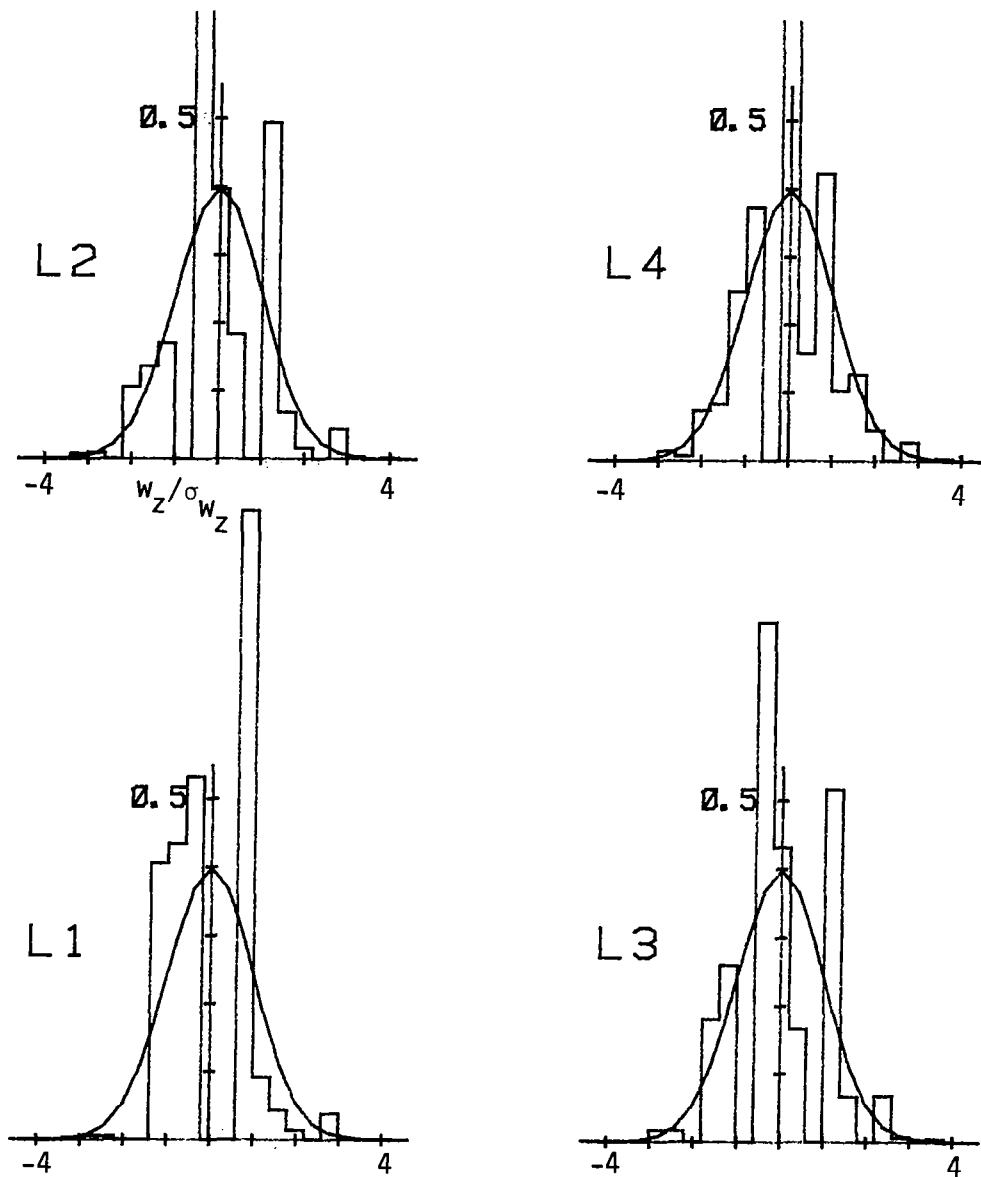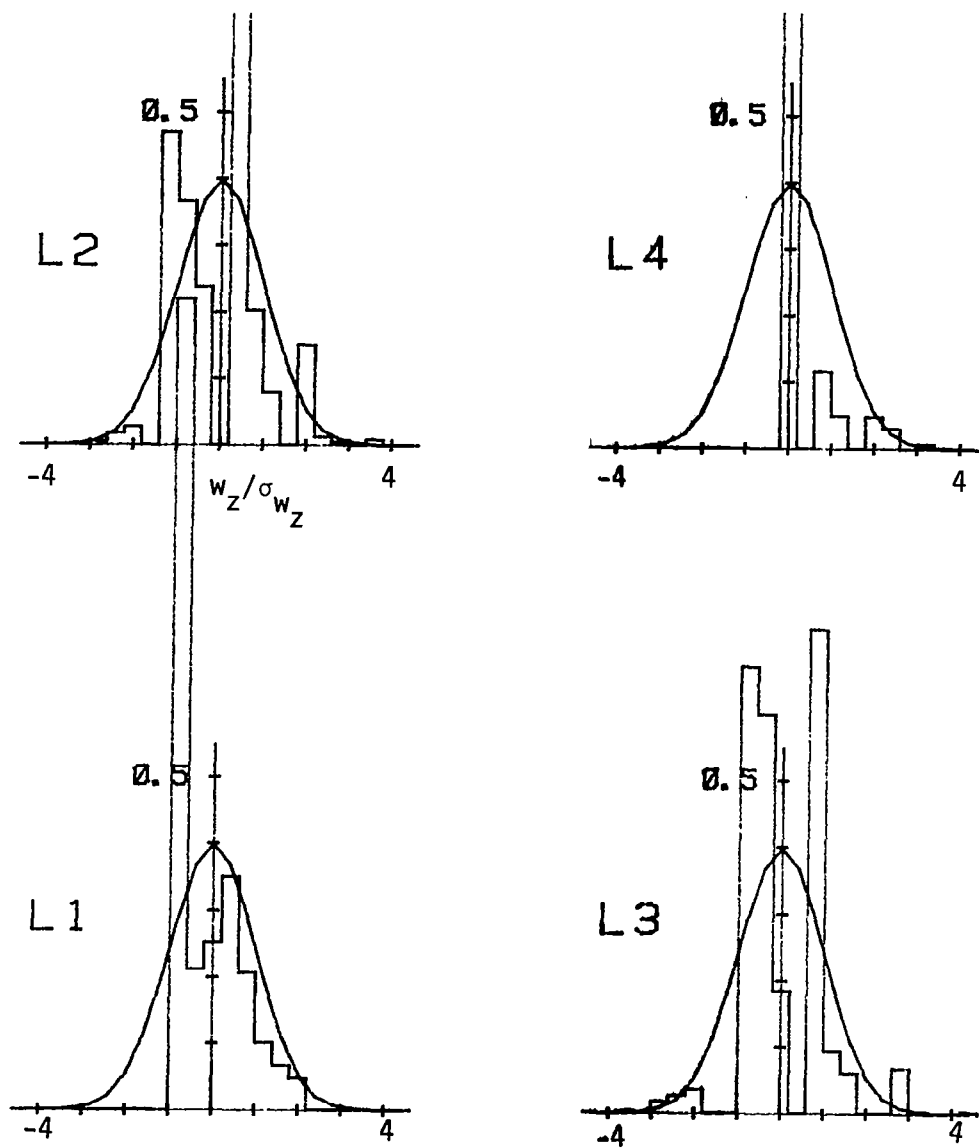component normalized with σ_{w_x} (Run #8623, T4, Component 1).
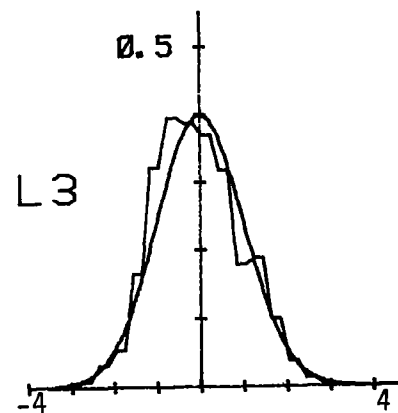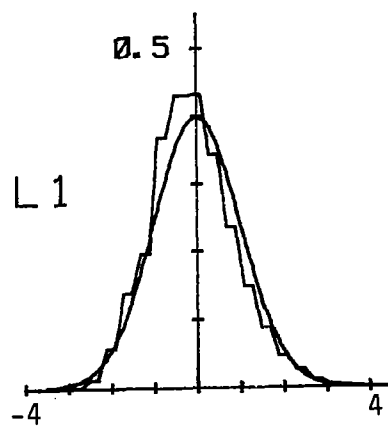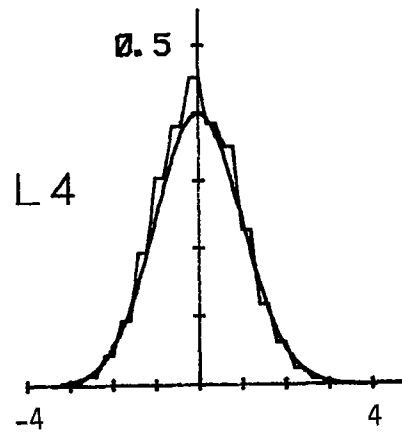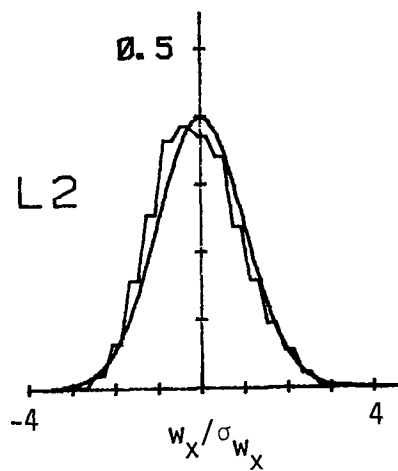
Figure C.5. Probability density function for longitudinal velocity component normalized with σ_{w_x} (Run #8623, T5, Component 1).

236
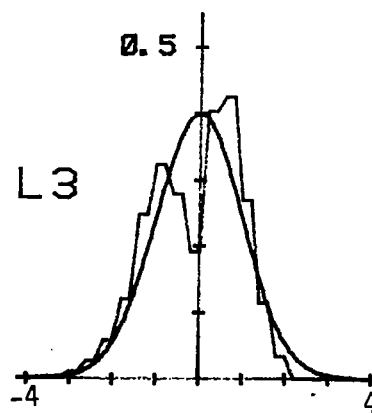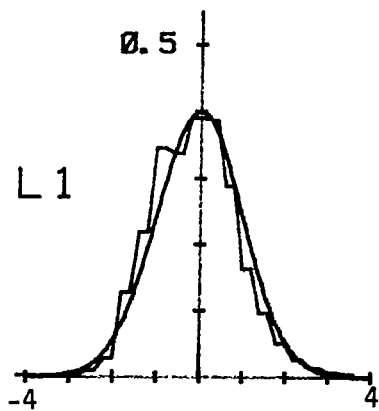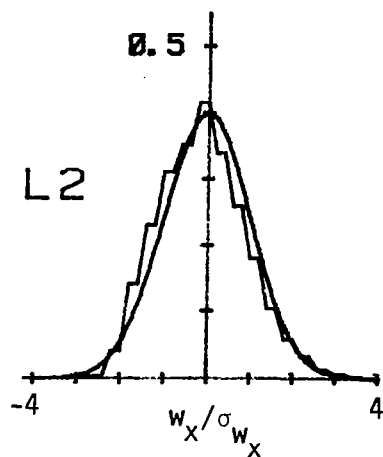
Figure C.6. Probability density function for longitudinal velocity
component normalized with σ_{w_x} (Run #8623, S1, Component 1).
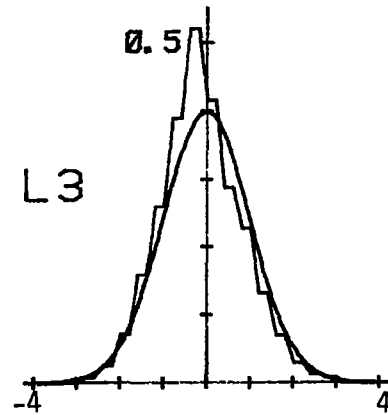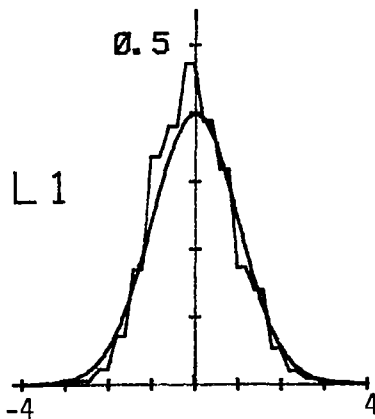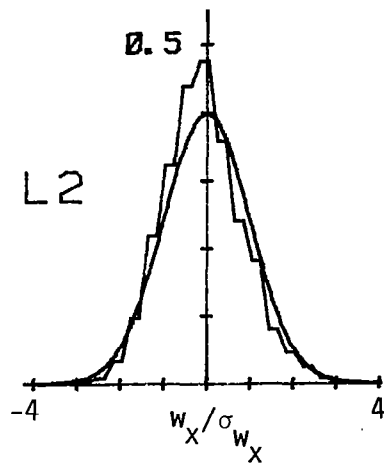
Figure C.7. Probability density function for longitudinal velocity component normalized with σ_{w_x} (Run #8623, S2, Component 1).
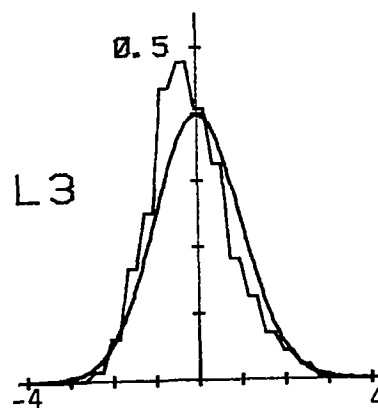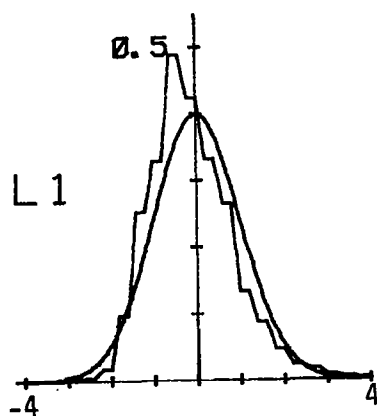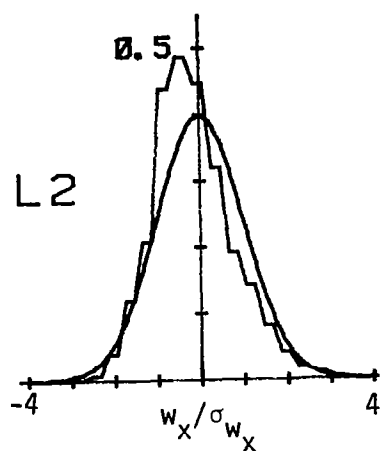
Figure C.8. Probability density function for longitudinal velocity component normalized with σ_{w_x} (Run #8623, S3, Component 1).
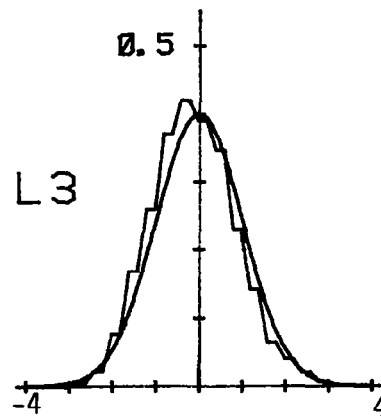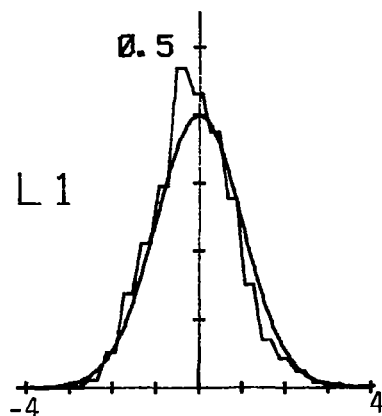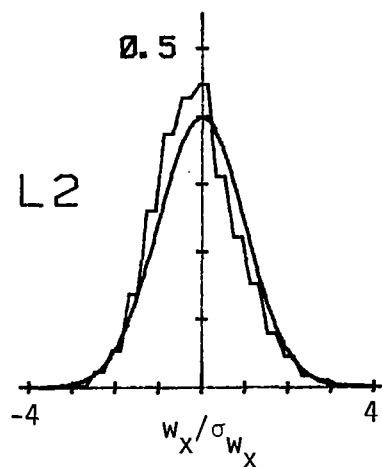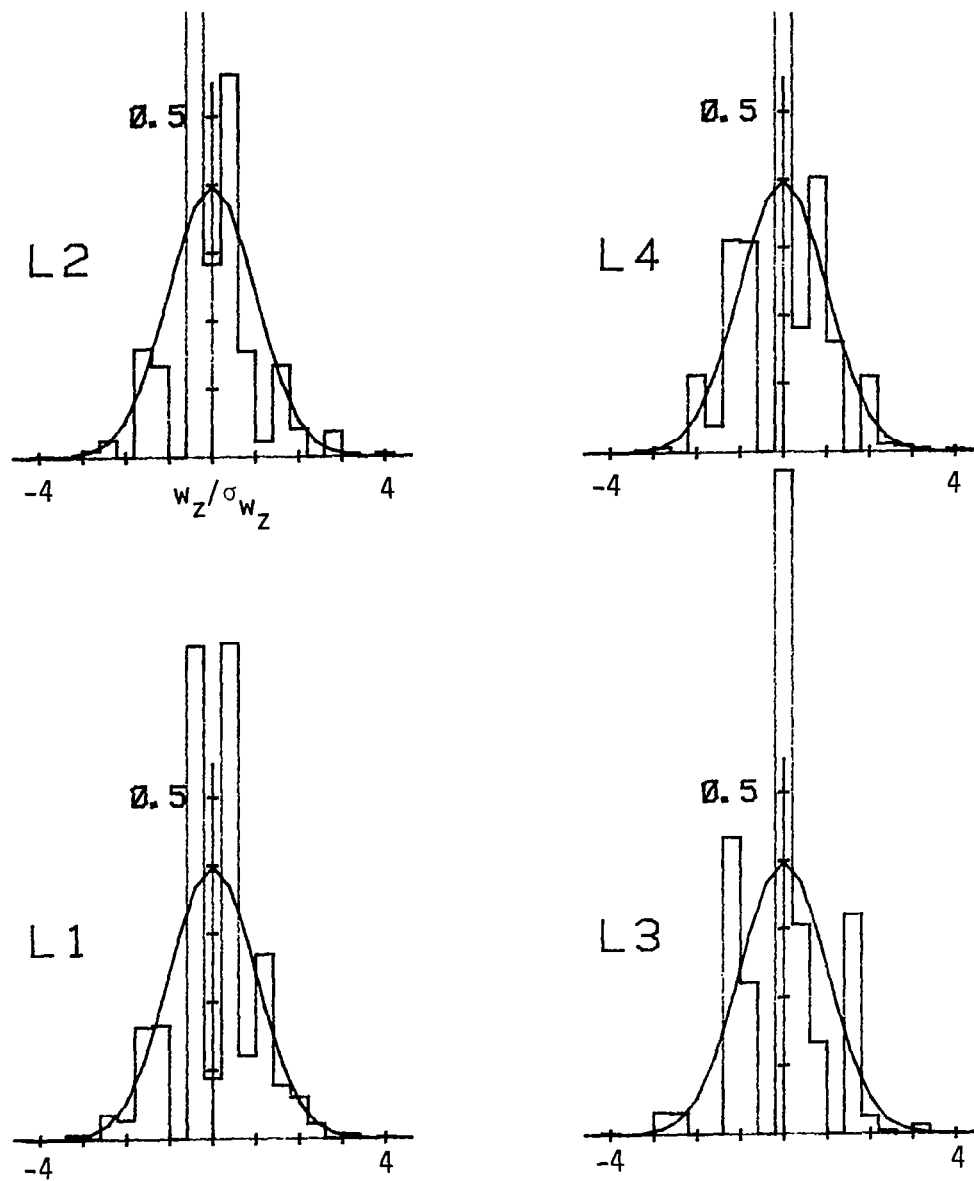
Figure C.9. Probability density function for longitudinal velocity component normalized with σ_{w_X} (Run #8623, S4, Component 1).
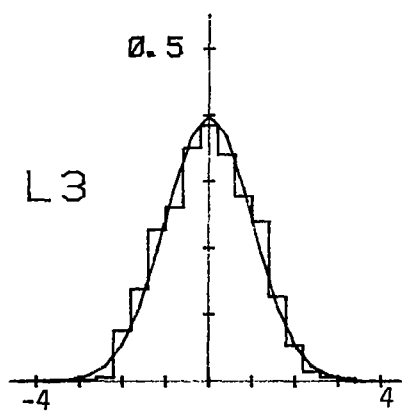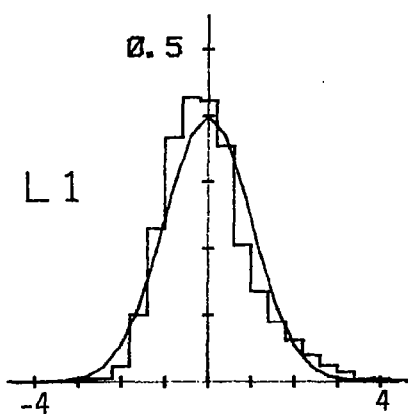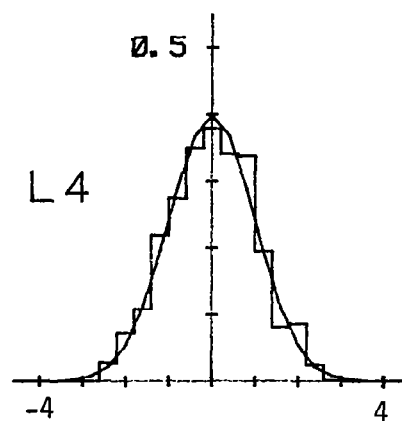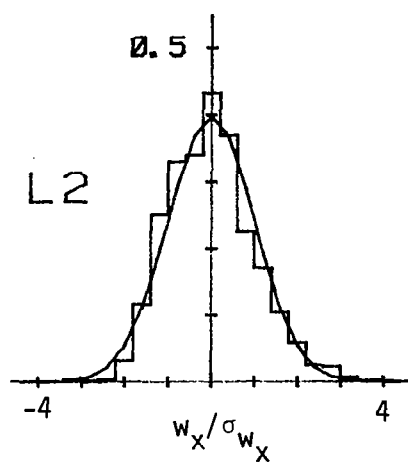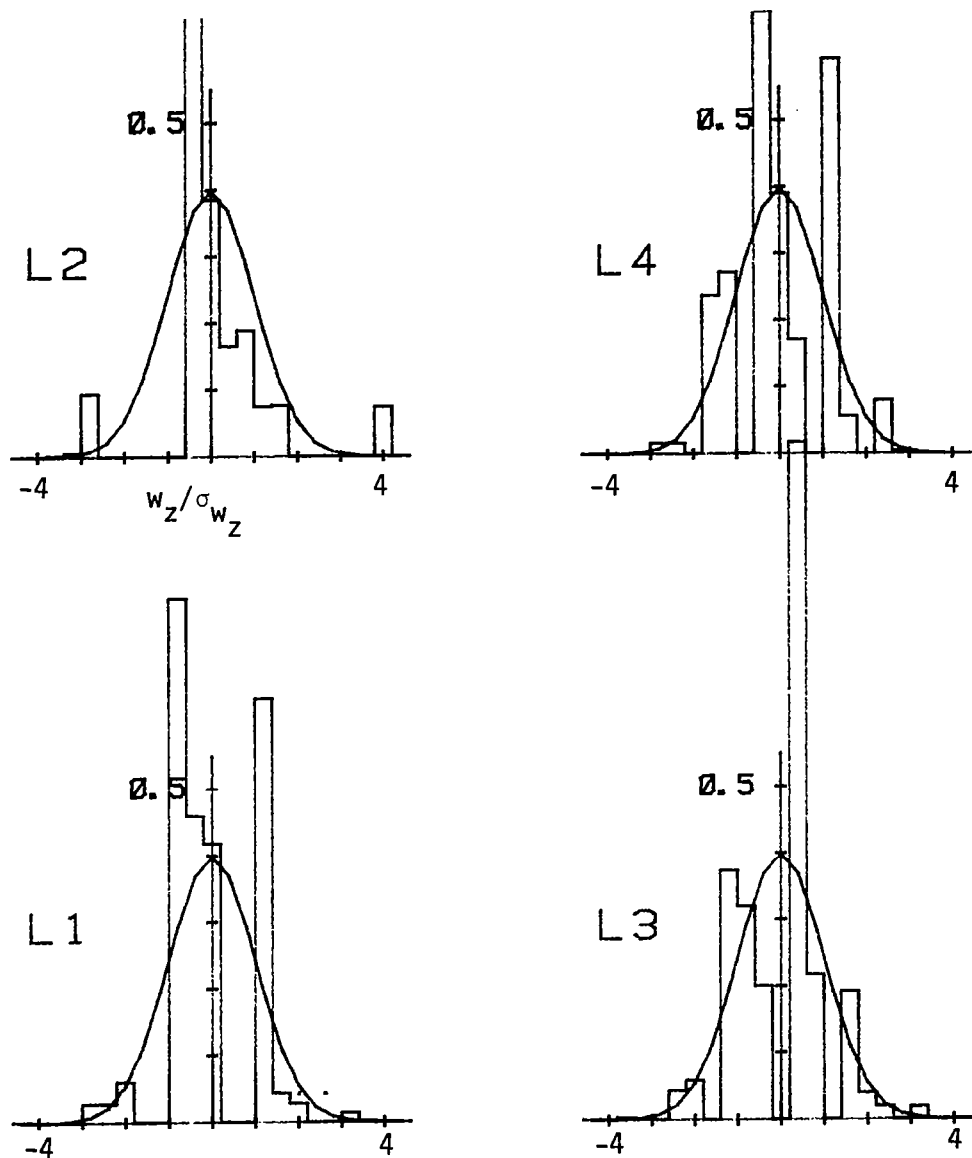
Figure C.10. Probability density function for longitudinal velocity
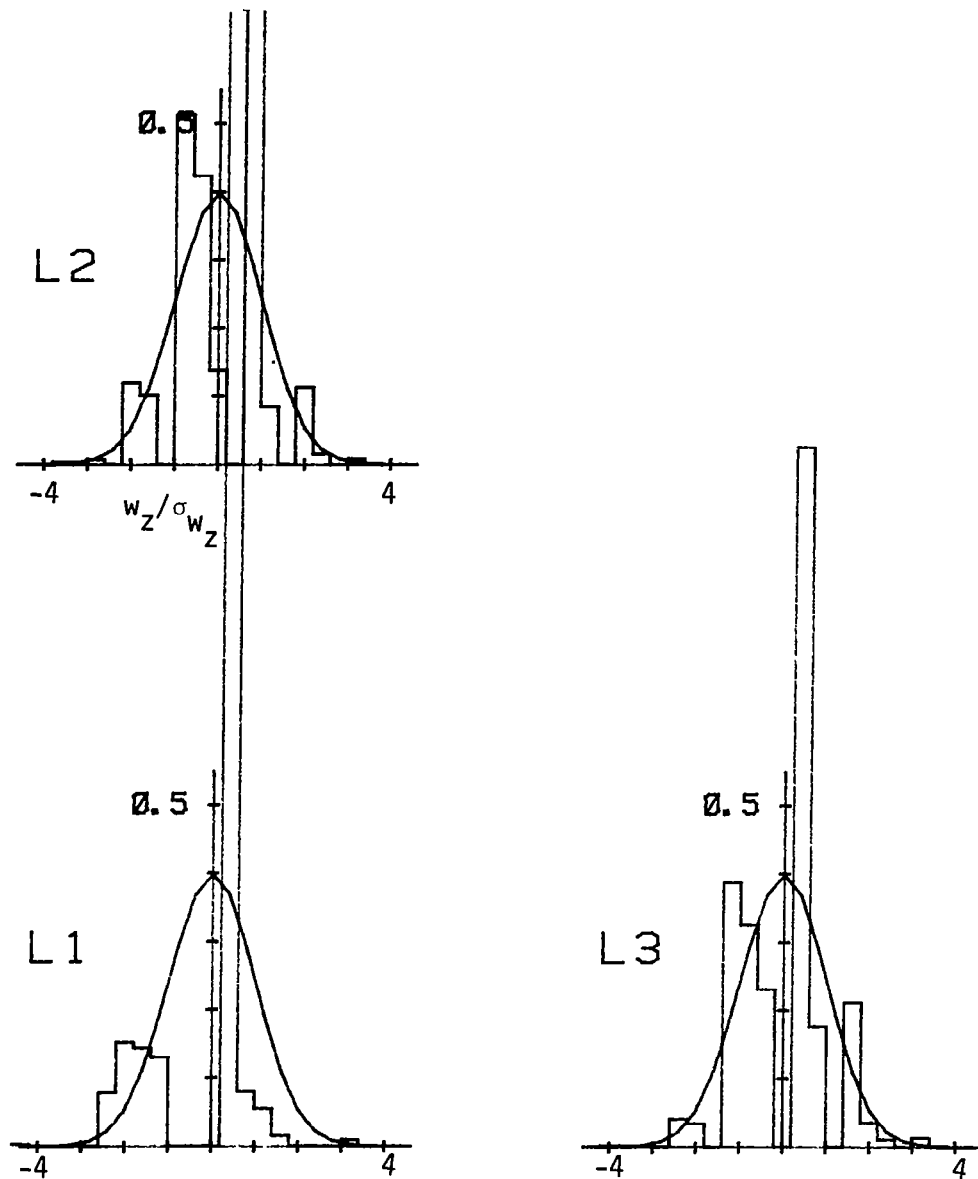component normalized with σ_{w_x} (Run #8624, Tl, Component 1).
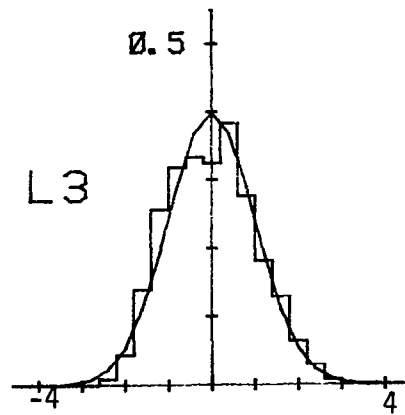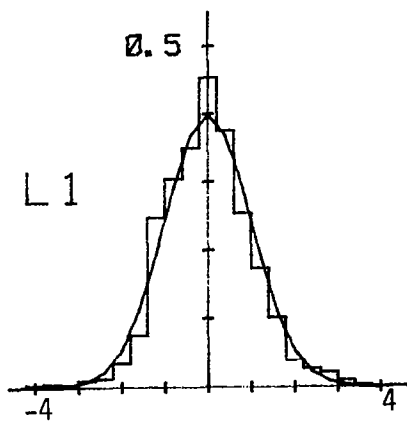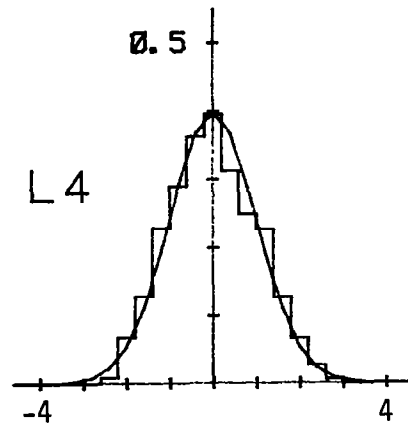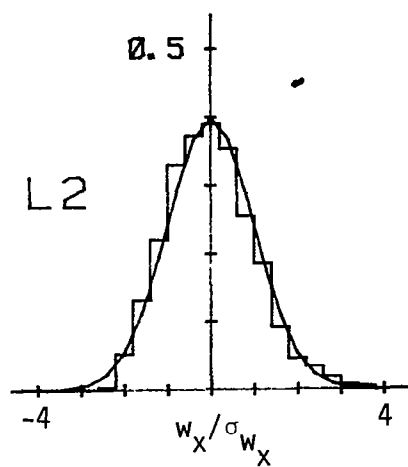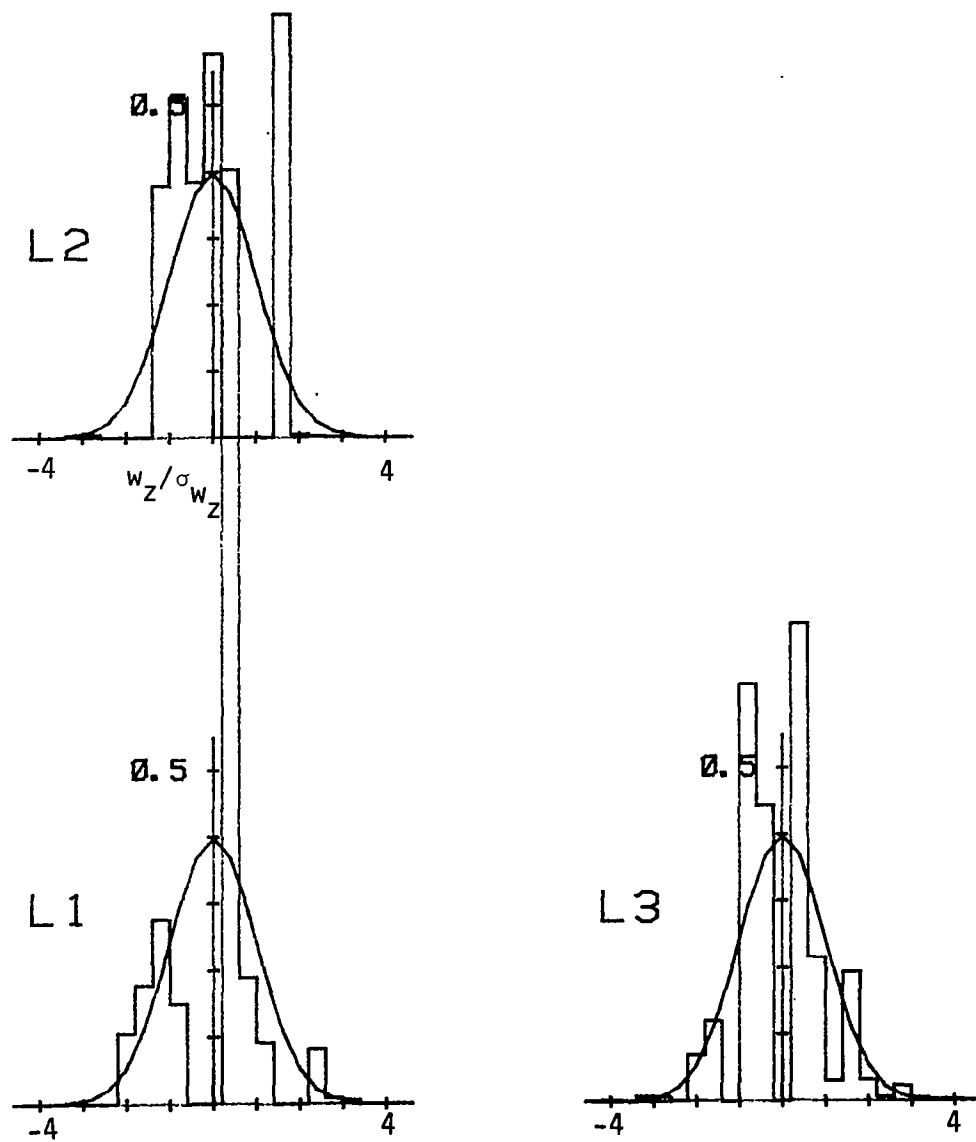
Figure C.11. Probability density function for longitudinal velocity
component normalized with σ_{w_x} (Run #8624, T2, Component 1).
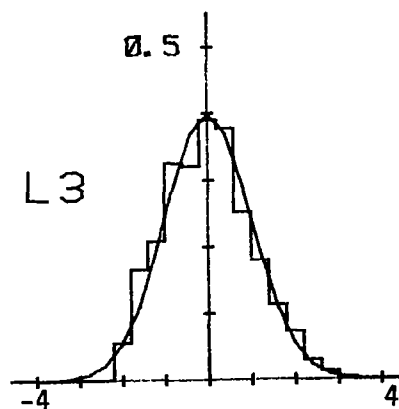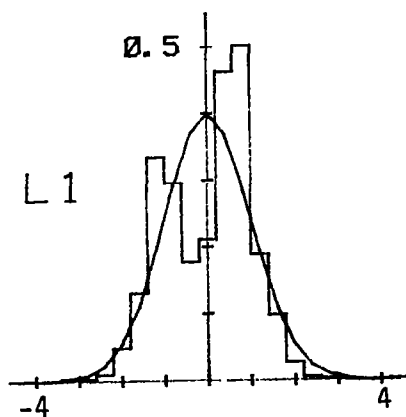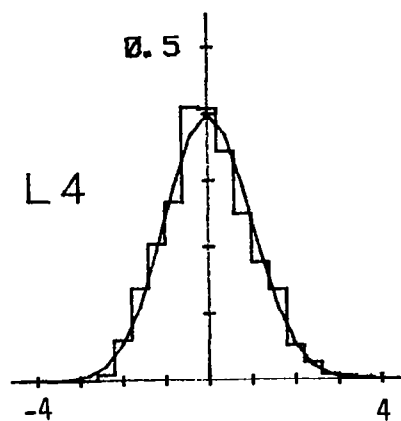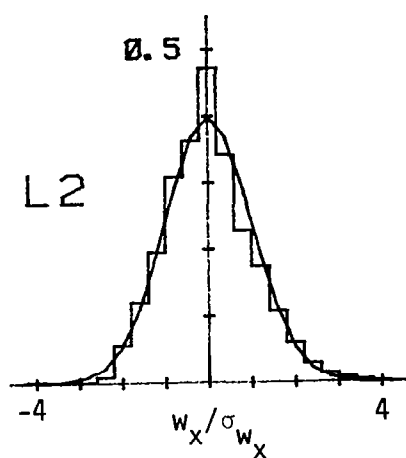
Figure C.12. Probability density function for longitudinal velocity component normalized with σ_{w_x} (Run #8624, T3, Component 1).
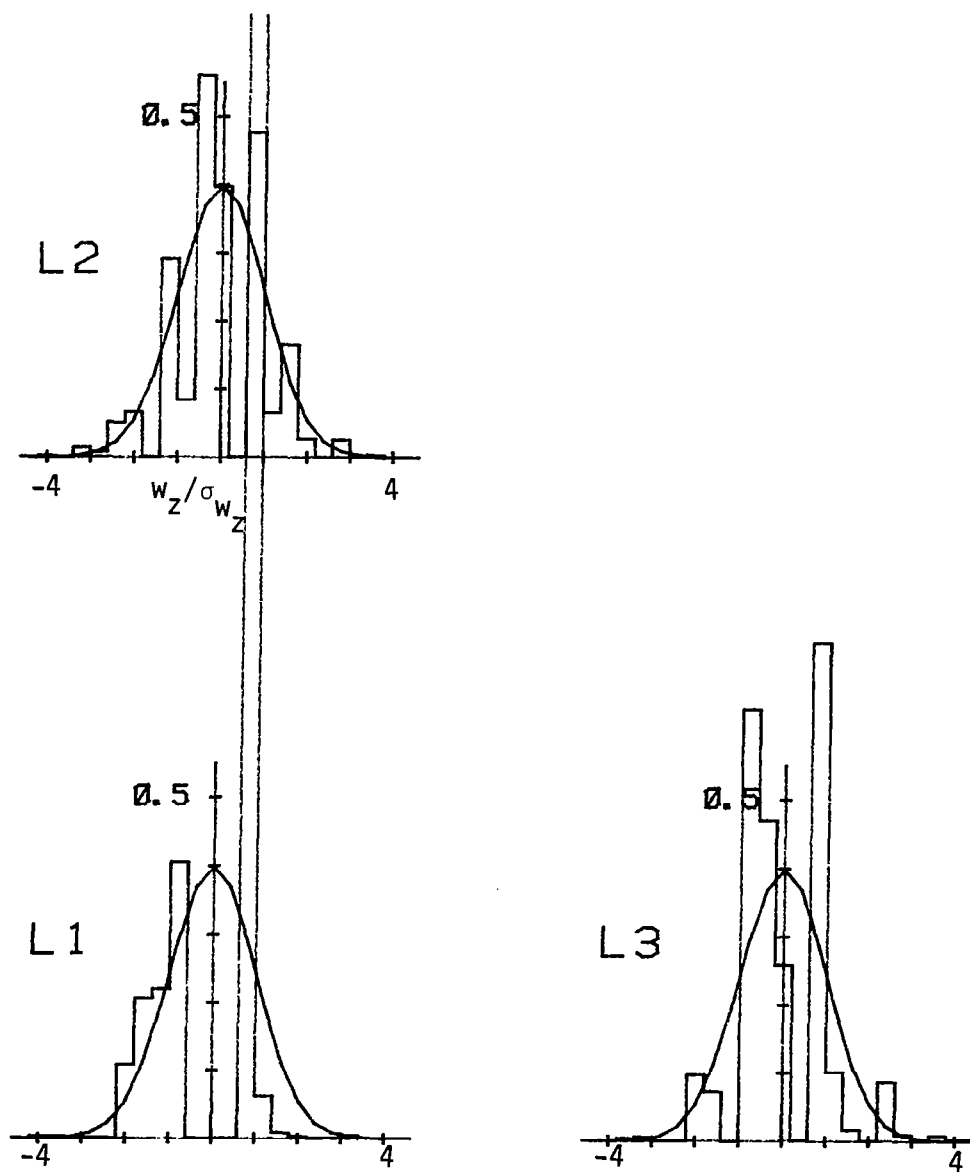
243
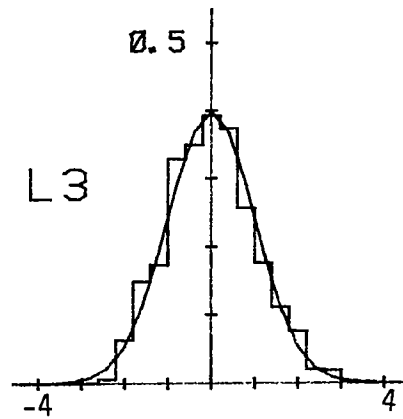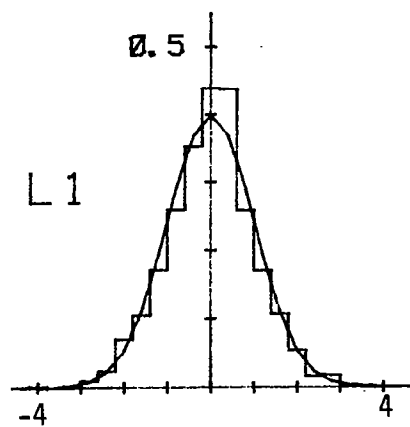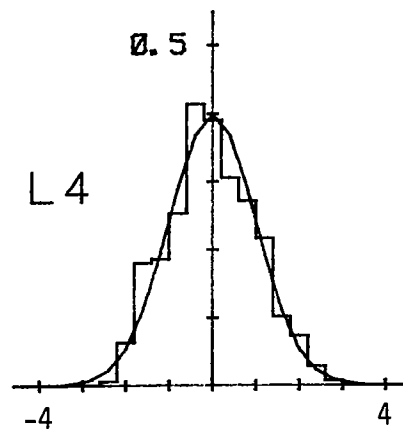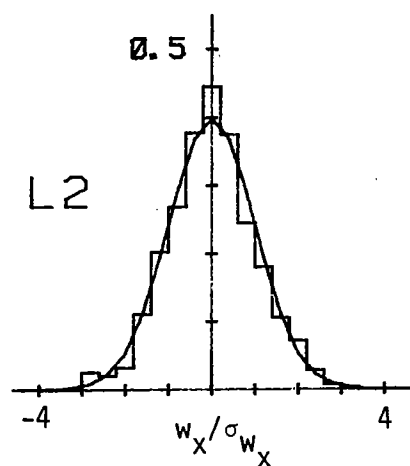
Figure C.13. Probability density function for longitudinal velocity component normalized with σ_{w_x} (Run #8624, T4, Component 1).
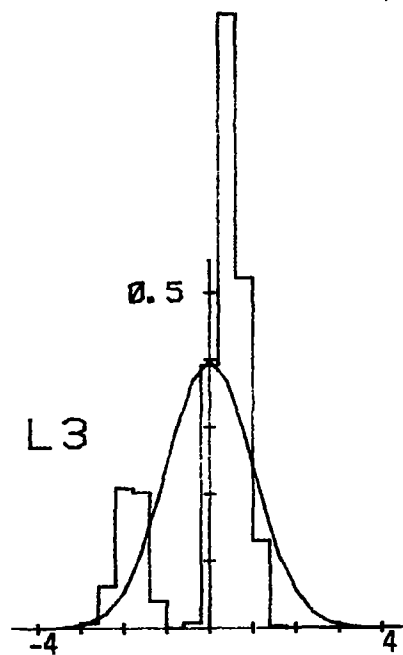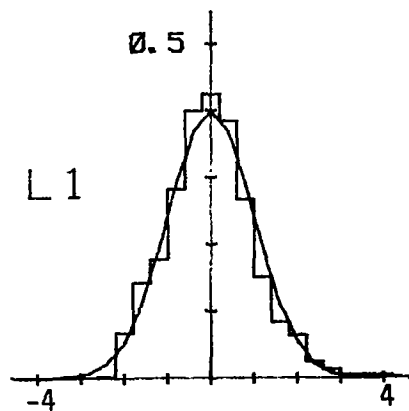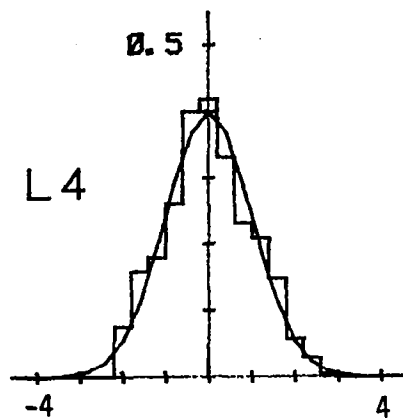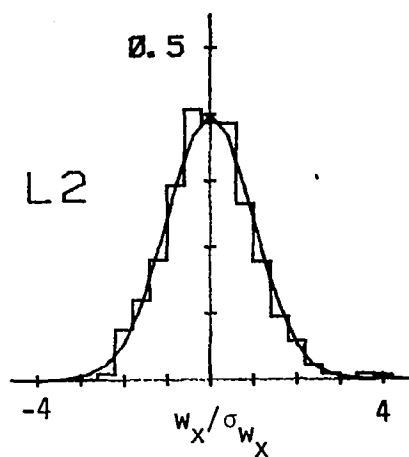
Figure C.14. Probability density function for longitudinal velocity component normalized with σ_{w_x} (Run #8624, T5, Component 1).
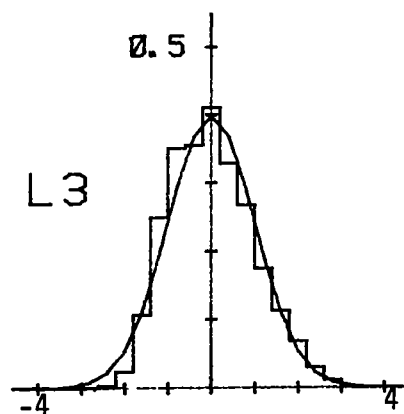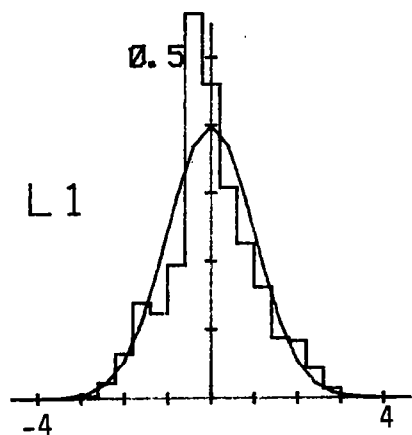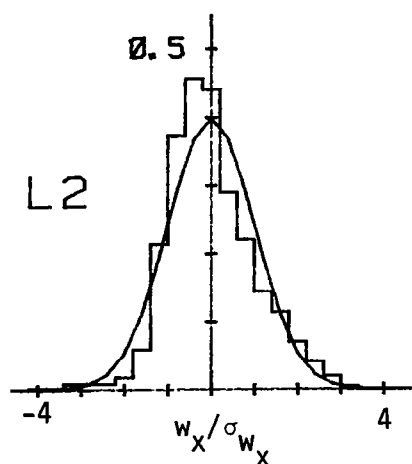
Figure C.15. Probability density function for longitudinal velocity
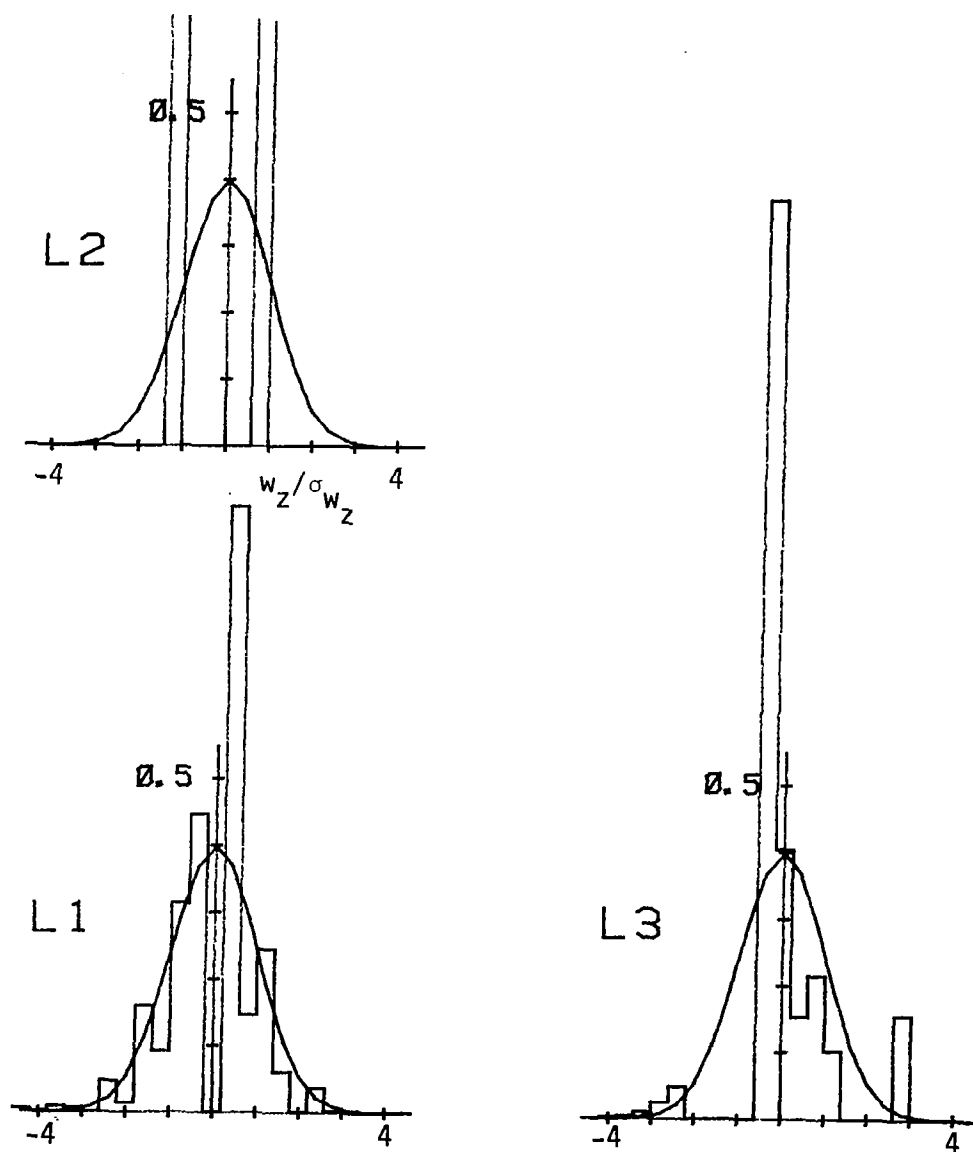component normalized with σ_{w_x} (Run #8624, S1, Component 1).
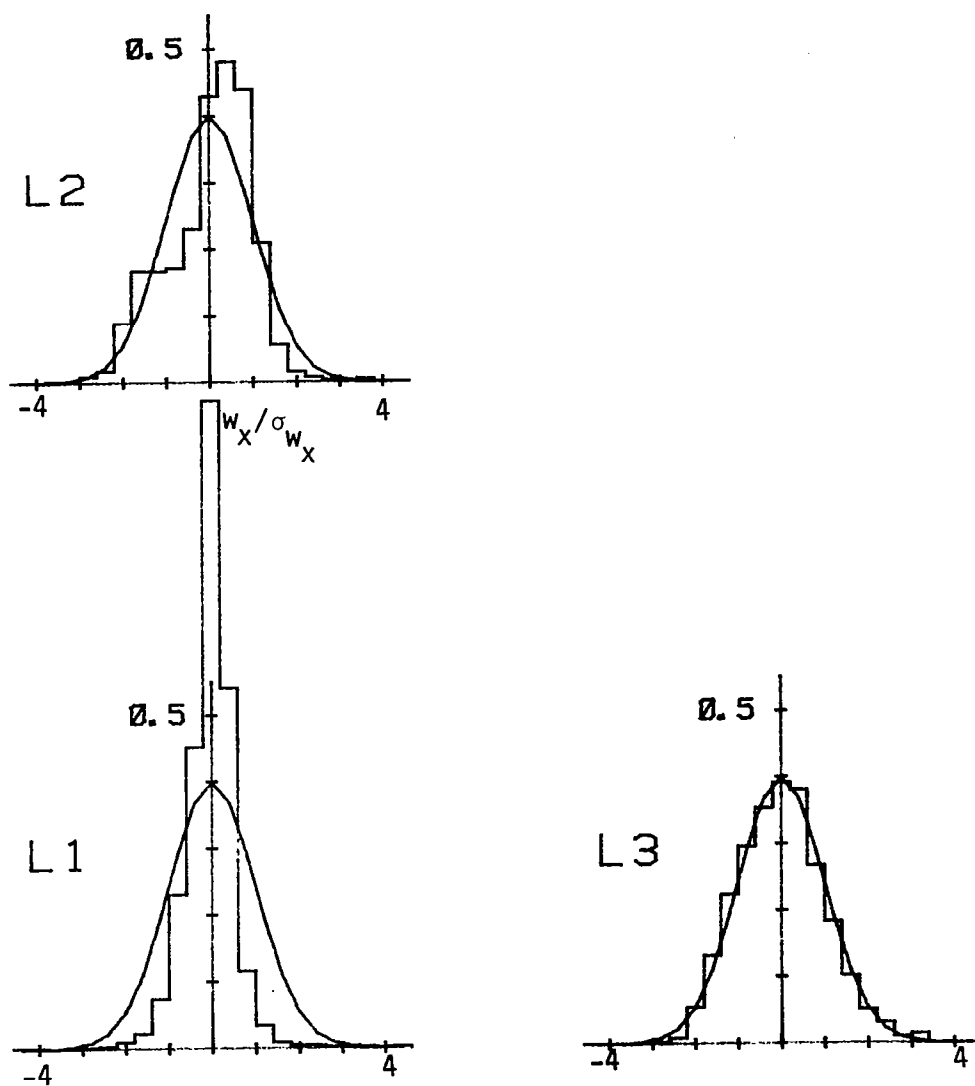
Figure C.16. Probability density function for longitudinal velocity
component normalized with σ_{w_x} (Run #8624, S2, Component 1).
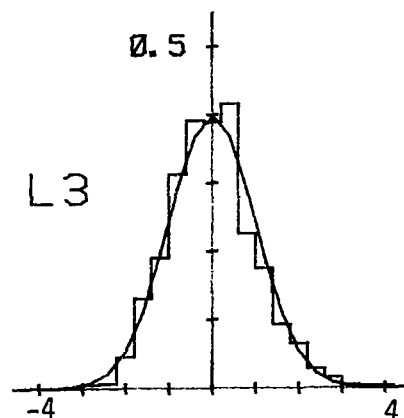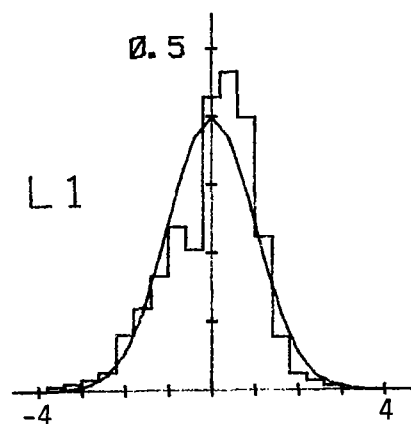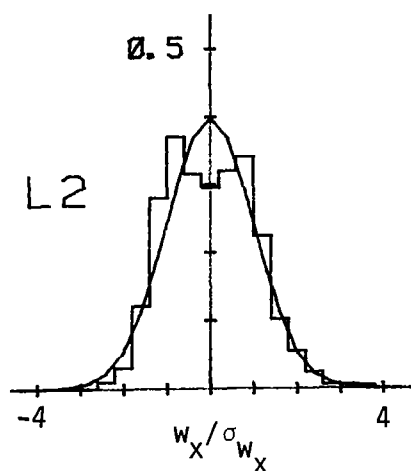
Figure C.17. Probability density function for longitudinal velocity component normalized with σ_{w_x} (Run #8624, S3, Component 1).
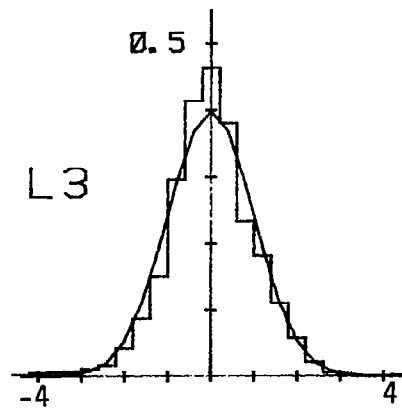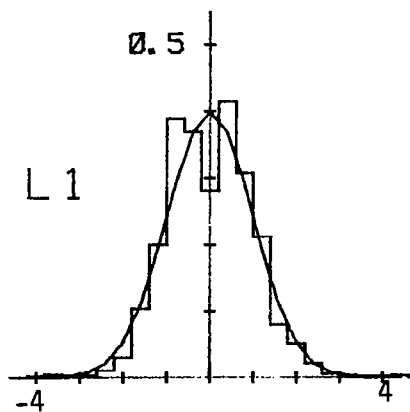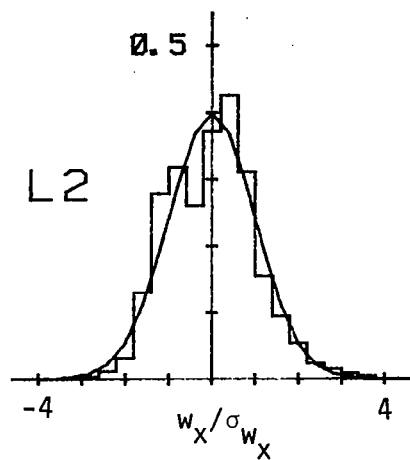
Figure C.18.   Probability density function for longitudinal velocity component normalized with σ_{w_x} (Run #8624, S4, Component 1).
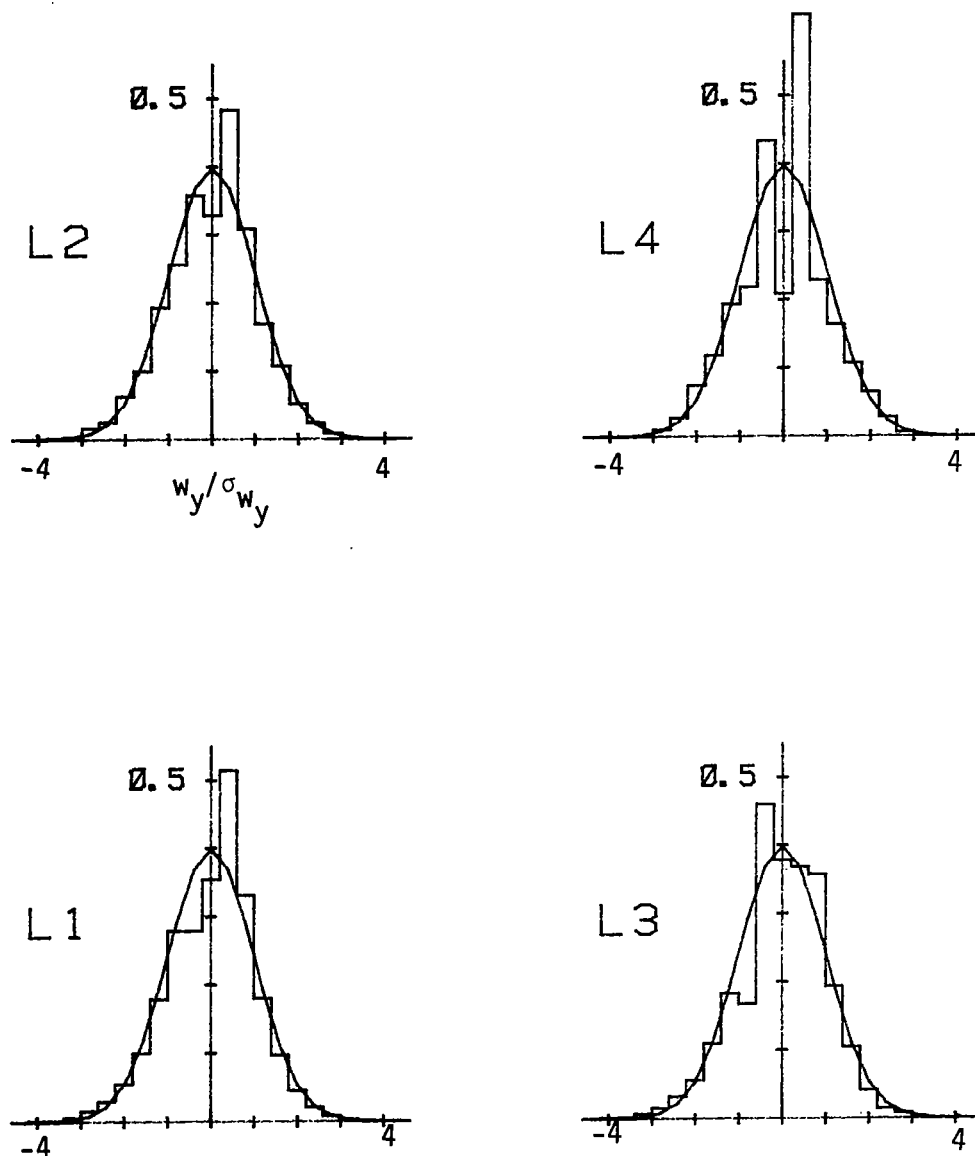
Figure C.19. Probability density function for lateral velocity
component normalized with σ_{w_y} (Run #8623, T1, Component 2).
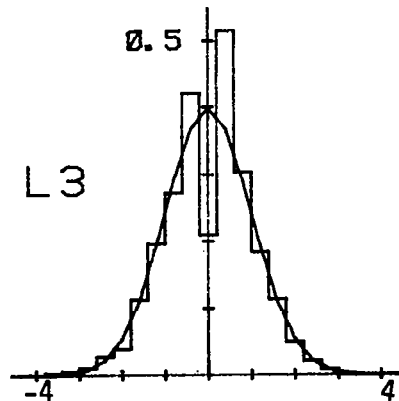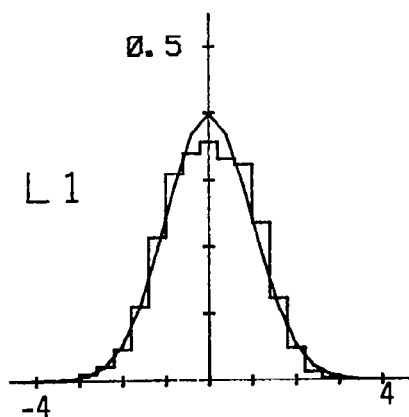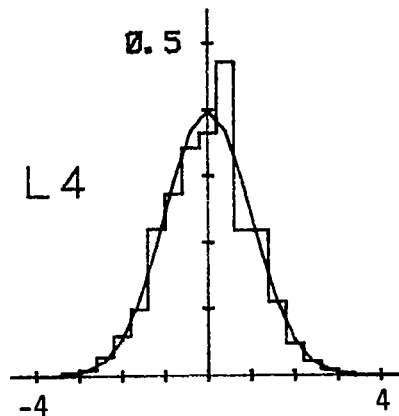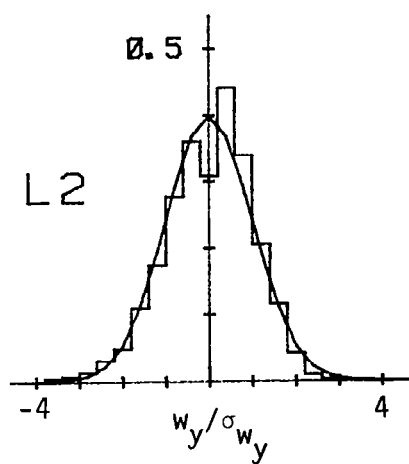
Figure C.20. Probability density function for lateral velocity
component normalized with σ_{w_y} (Run #8623, T2, Component 2).
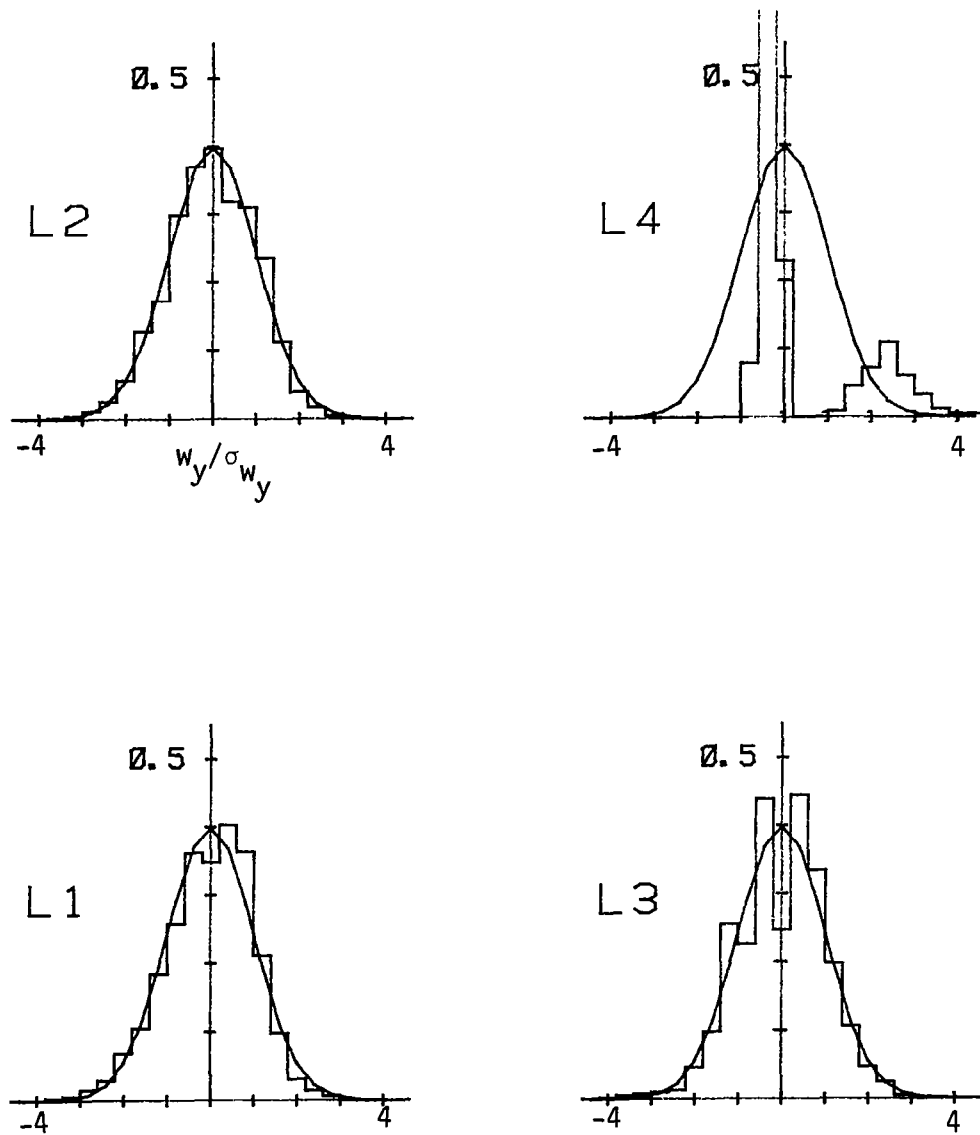
Figure C.21. Probability density function for lateral velocity component normalized with σ_{w_y} (Run #8623, T3, Component 2).

252
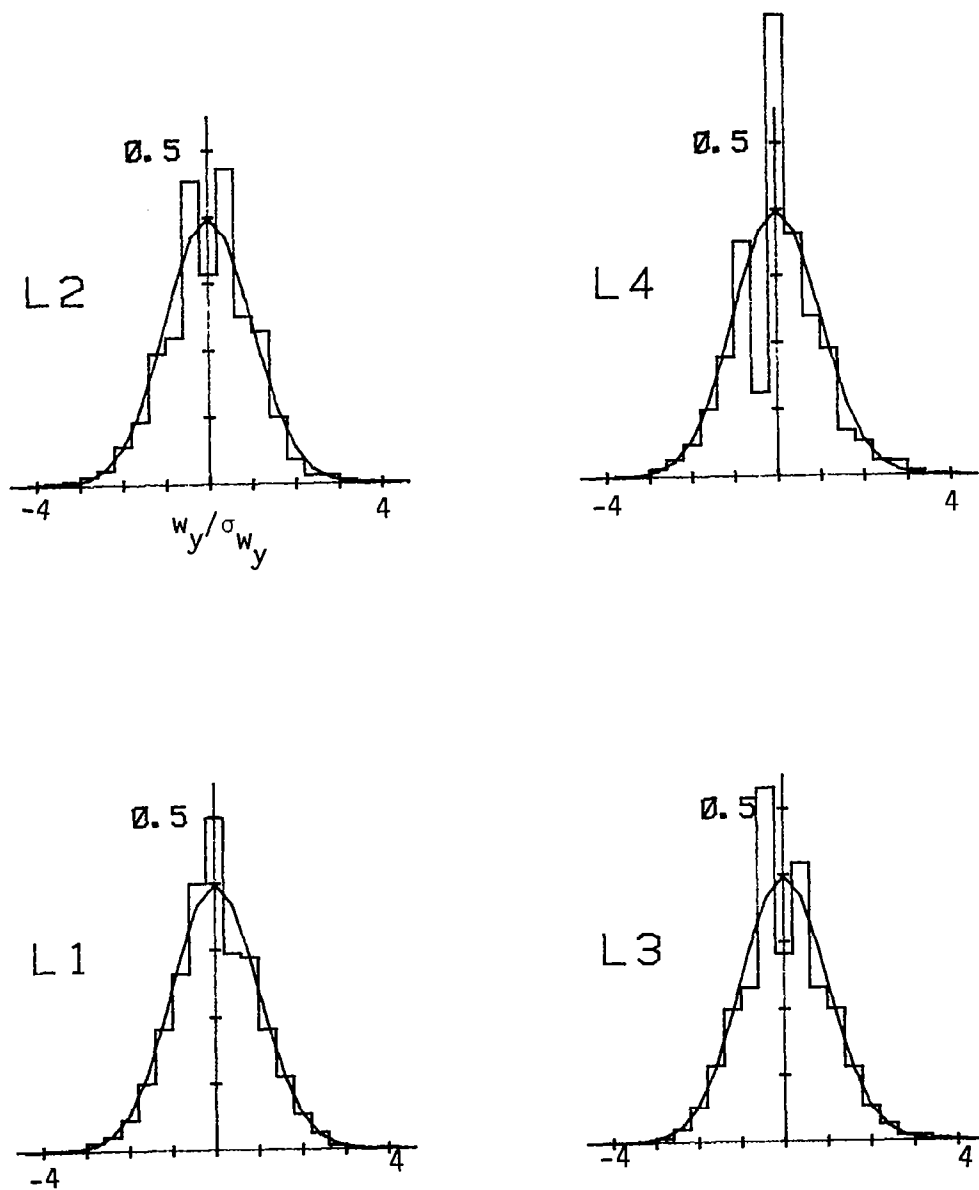
Figure C.22. Probability density function for lateral velocity component normalized with σ_{w_y} (Run #8623, T4, Component 2).
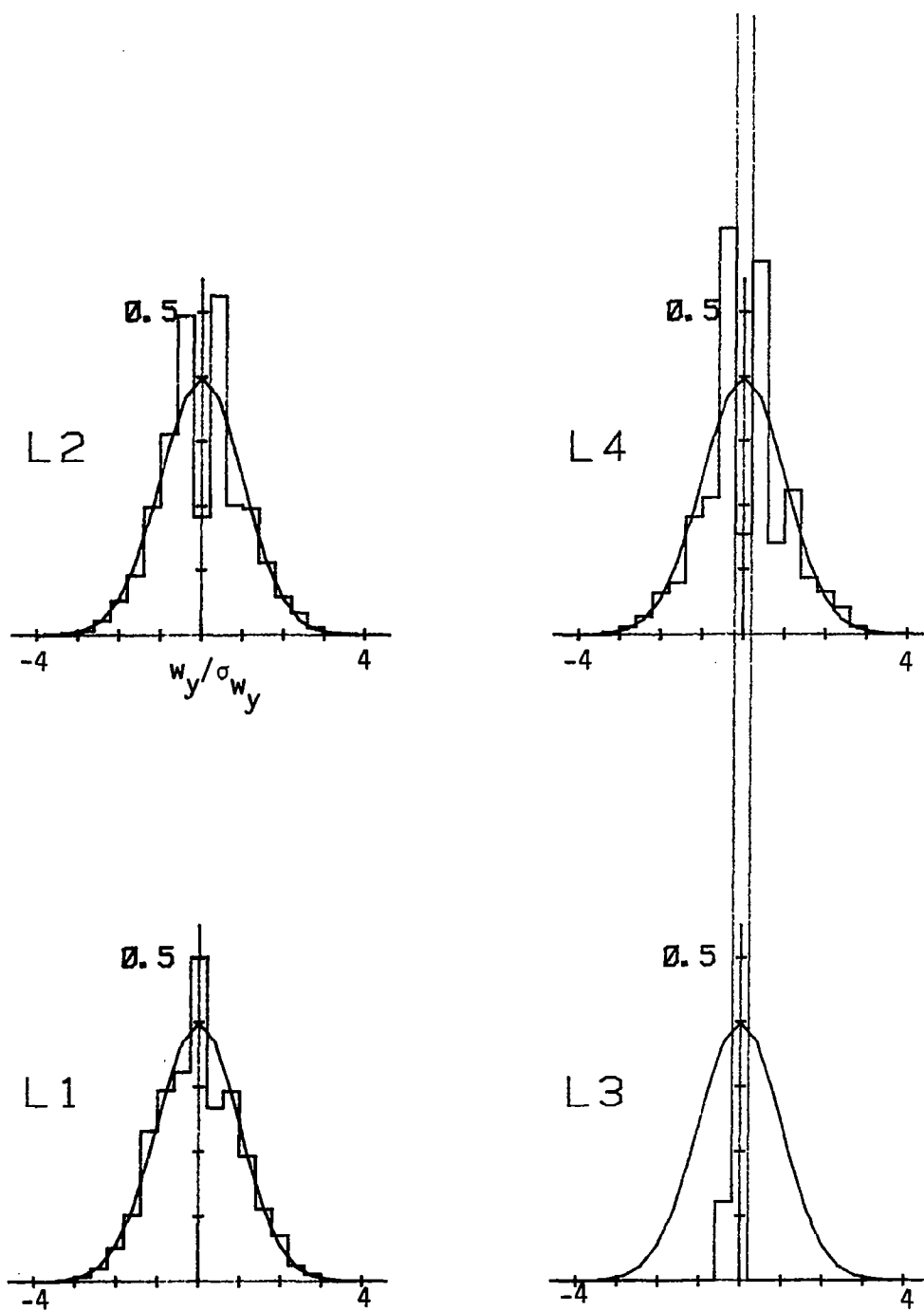
Figure C.23.   Probability density function for lateral velocity
            component normalized with σ_{w_y} (Run #8623, T5, Component 2).
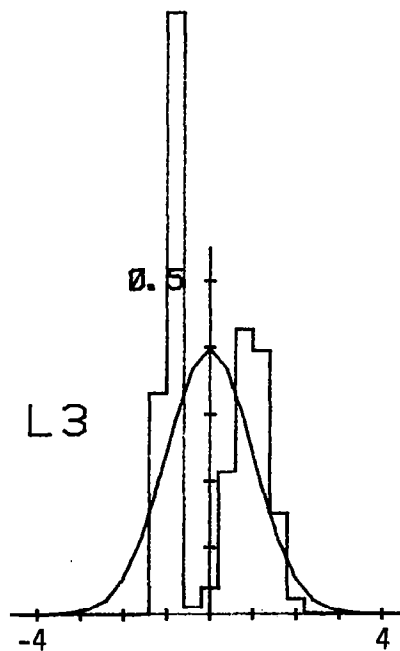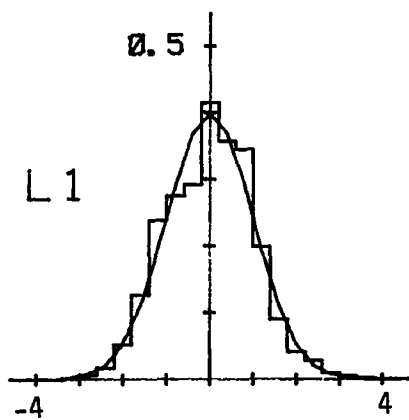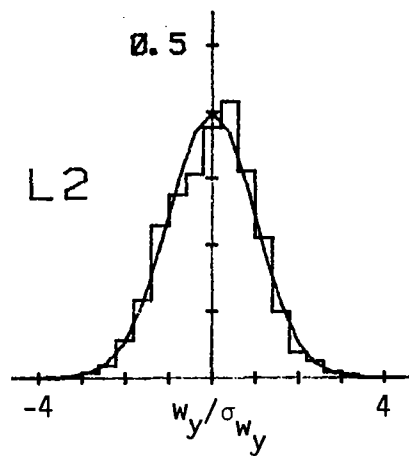
Figure C.24. Probability density function for lateral velocity
component normalized with σ_{w_y} (Run #8623, S1, Component 2).
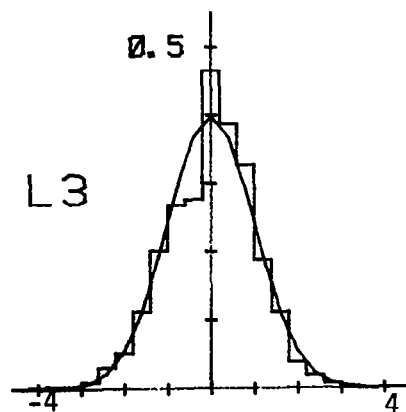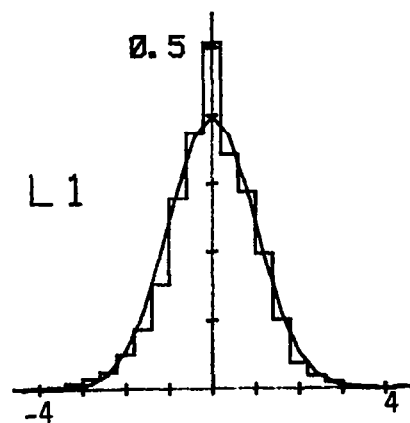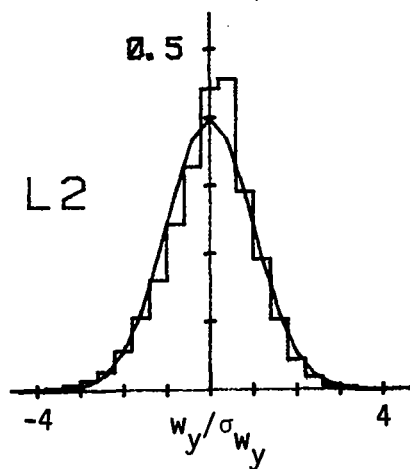
Figure C.25. Probability density function for lateral velocity component normalized with σ_{w_y} (Run #8623, S2, Component 2).
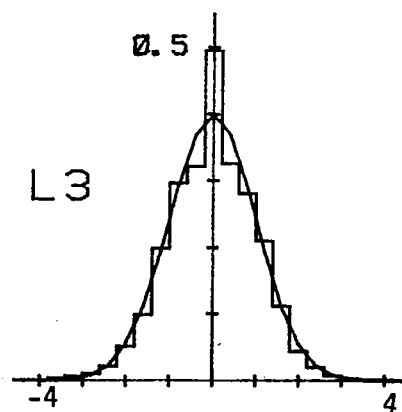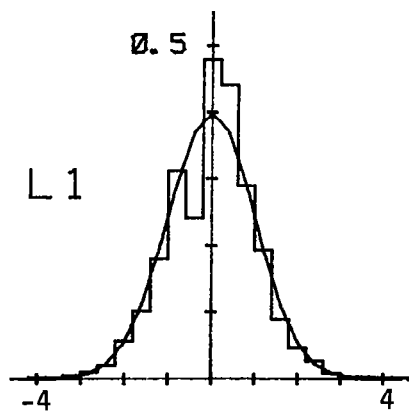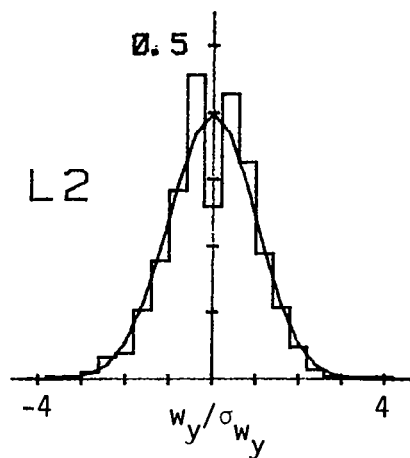
Figure C.26. Probability density function for lateral velocity component normalized with σ_{w_y} (Run #8623, S3, Component 2).
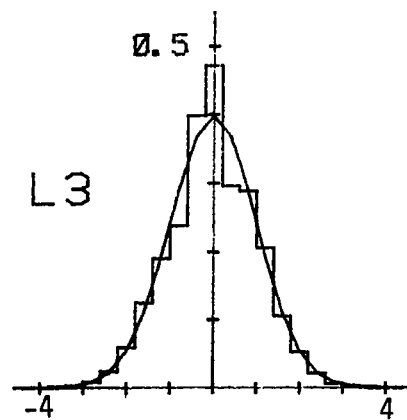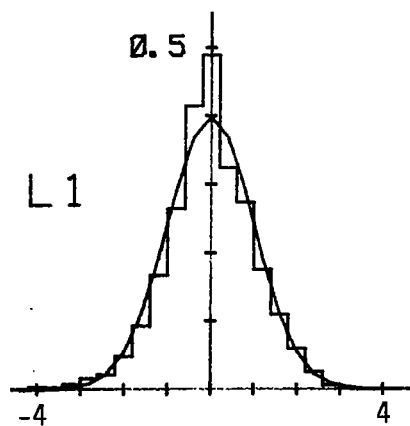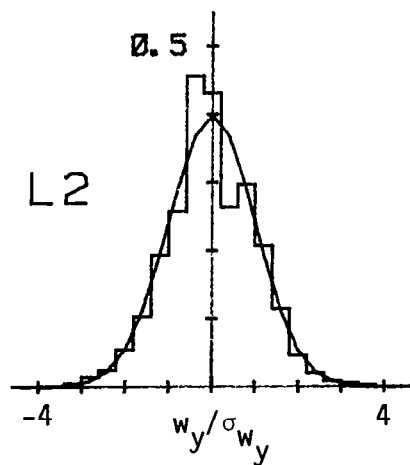
Figure C.27. Probability density function for lateral velocity
component normalized with σ_{w_y} (Run #8623, S4, Component 2).
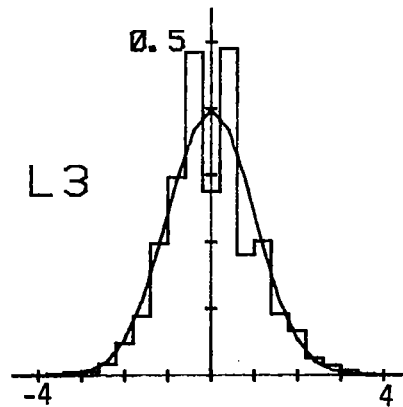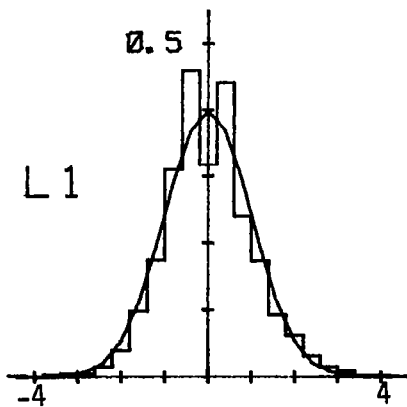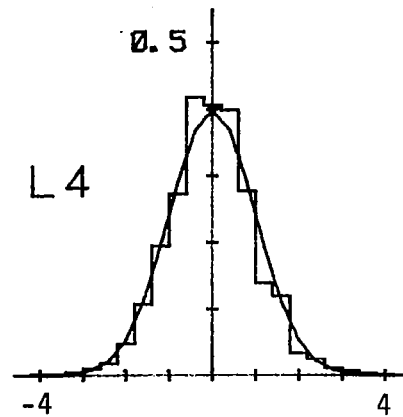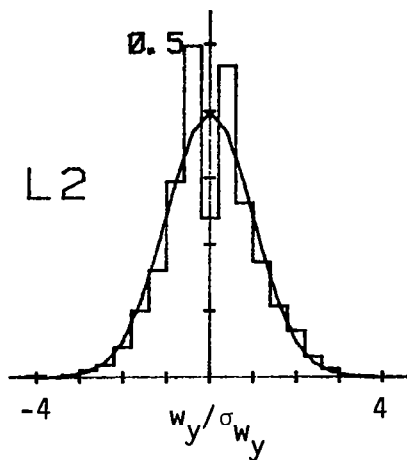
Figure C.28. Probability density function for lateral velocity component normalized with σ_{w_y} (Run #8624, T1, Component 2).
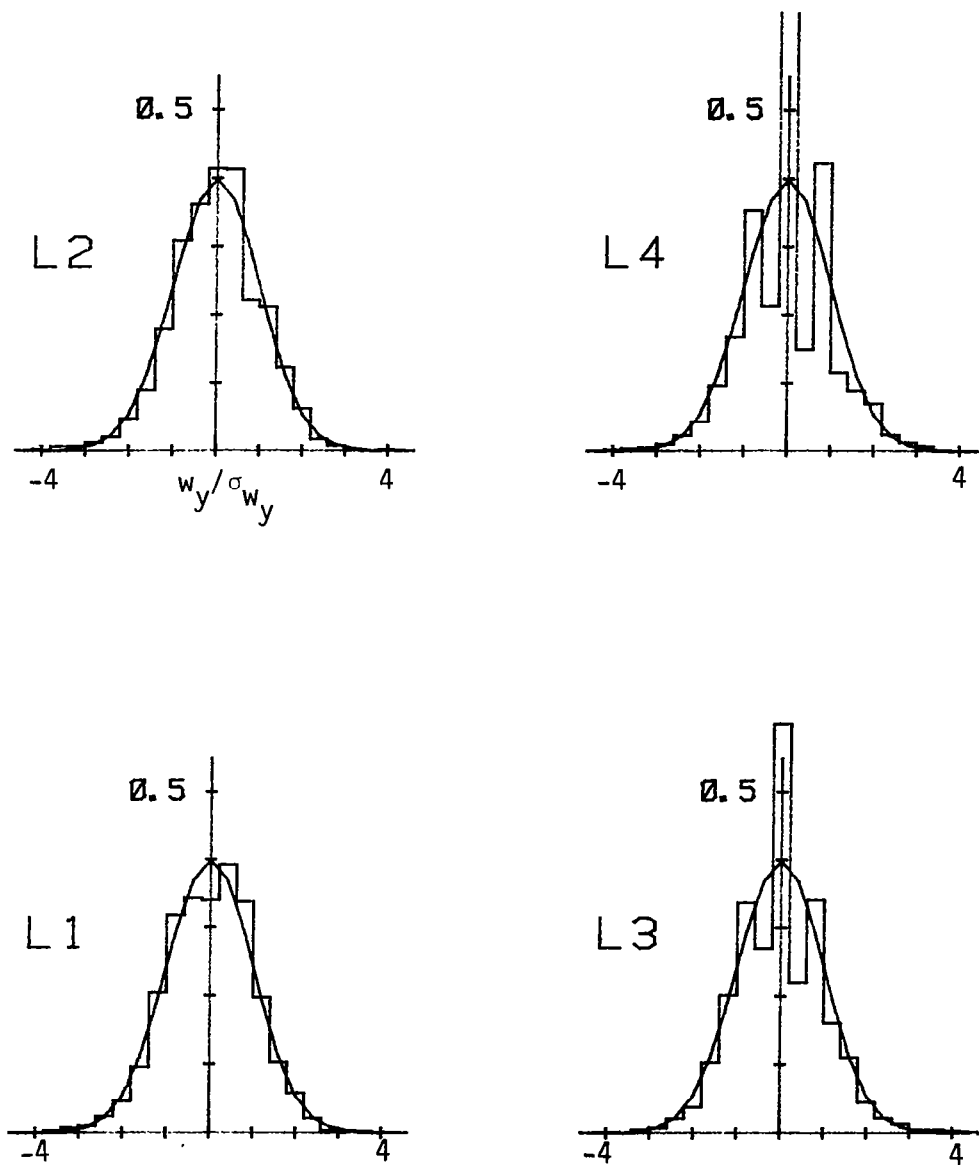
Figure C.29. Probability density function for lateral velocity component normalized with σ_{w_y} (Run #8624, T2, Component 2).
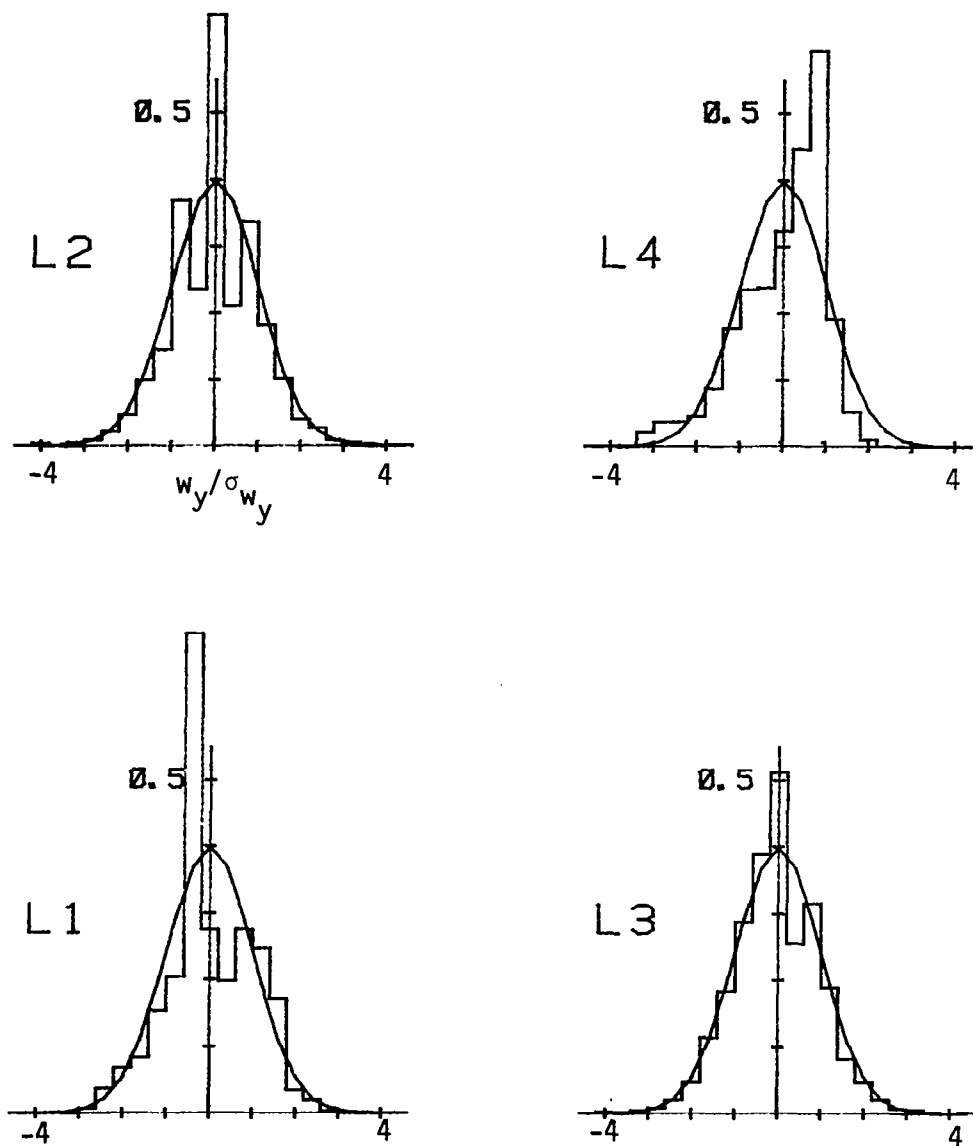
Figure C.30. Probability density function for lateral velocity
component normalized with σ_{w_y} (Run #8624, T3, Component 2).
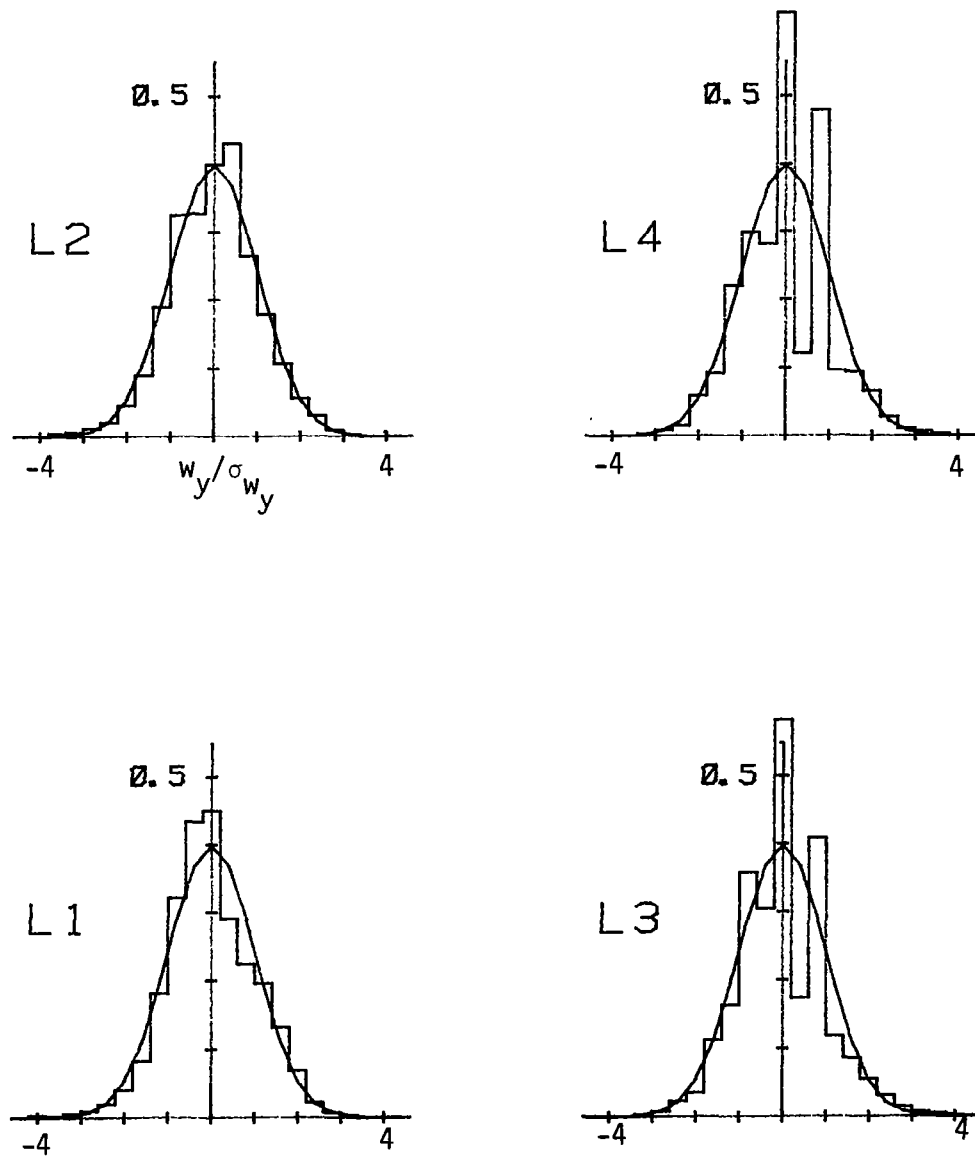
Figure C.31. Probability density function for lateral velocity
component normalized with σ_{w_y} (Run #8624, T4, Component 2).
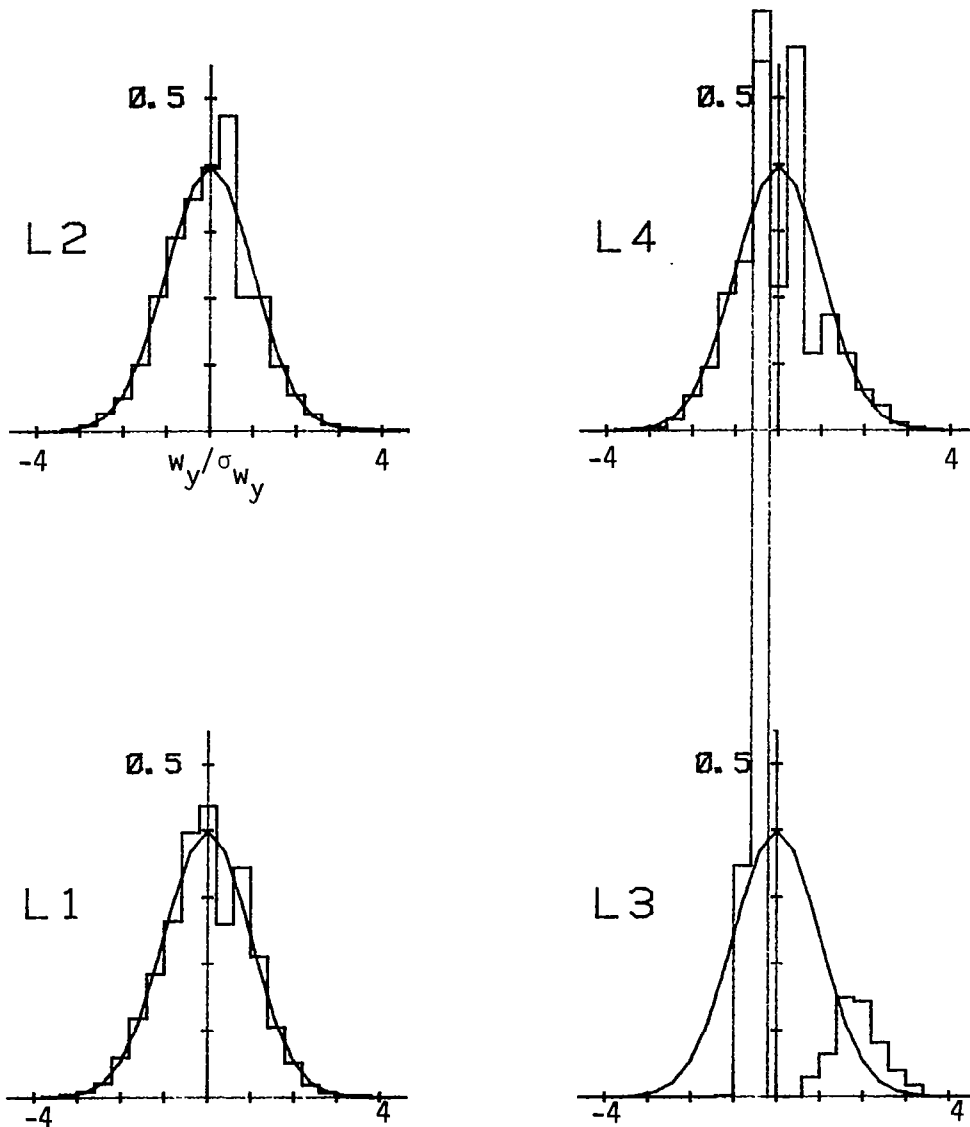
Figure C.32. Probability density function for lateral velocity component normalized with σ_{w_y} (Run #8624, T5, Component 2).
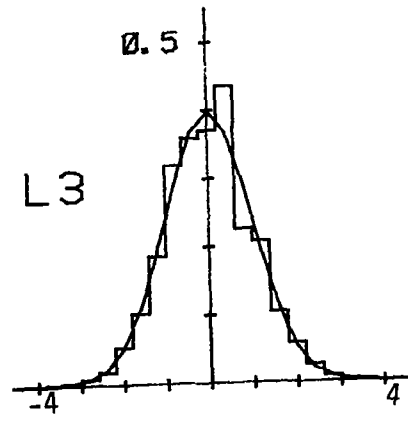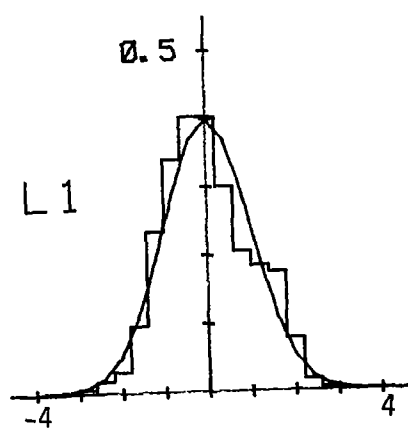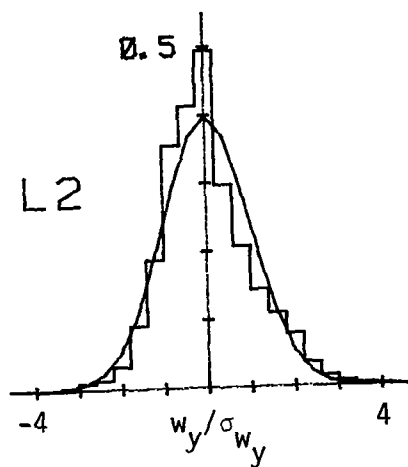
Figure C.33. Probability density function for lateral velocity
component normalized with σ_{w_y} (Run #8624, S1, Component 2).
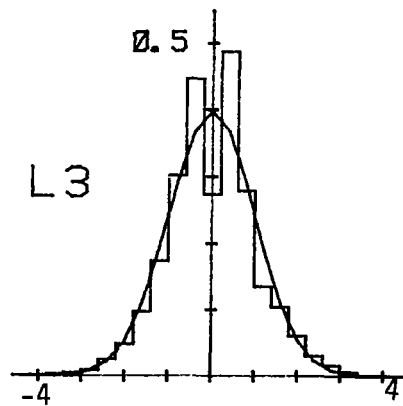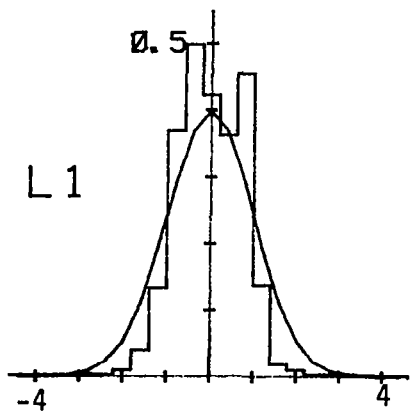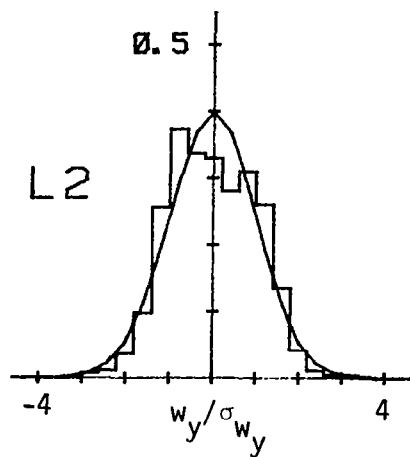
Figure C.34. Probability density function for lateral velocity component normalized with σ_{w_y} (Run #8624, S2, Component 2).
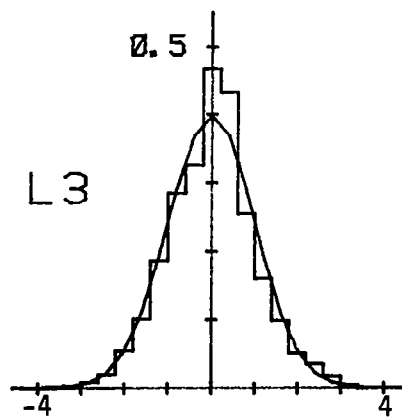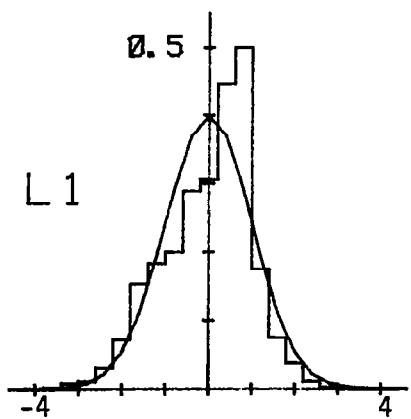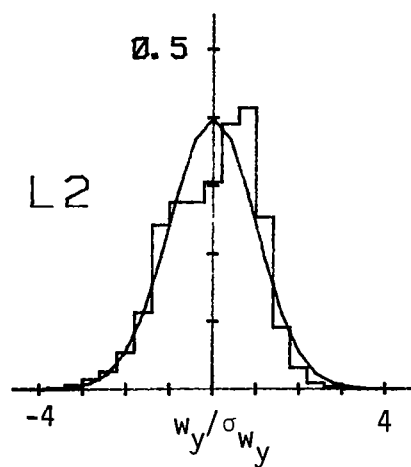
Figure C.35. Probability density function for lateral velocity component normalized with σ_{w_y} (Run #8624, S3, Component 2).
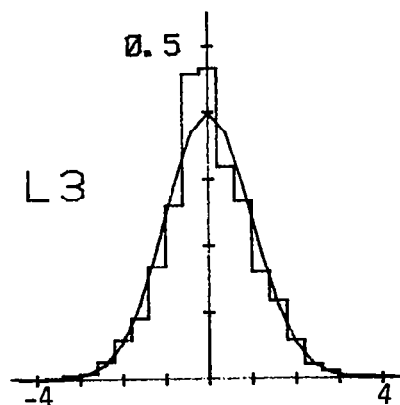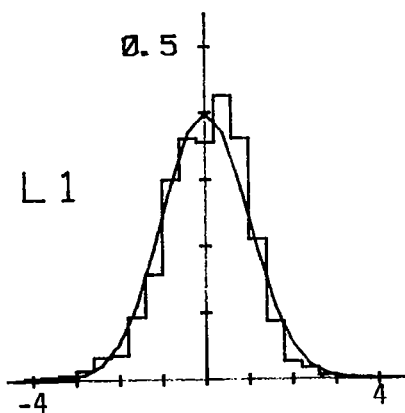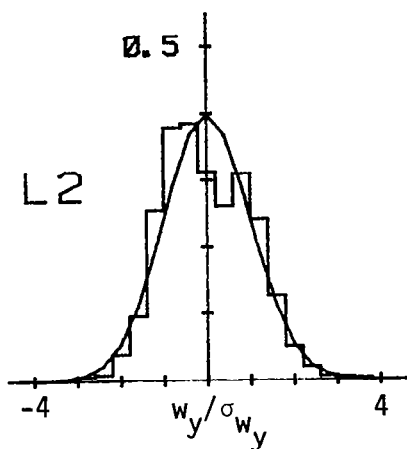
Figure C.36.   Probability density function for lateral velocity
                component normalized with σ_{w_y} (Run #8624, S4, Component 2).
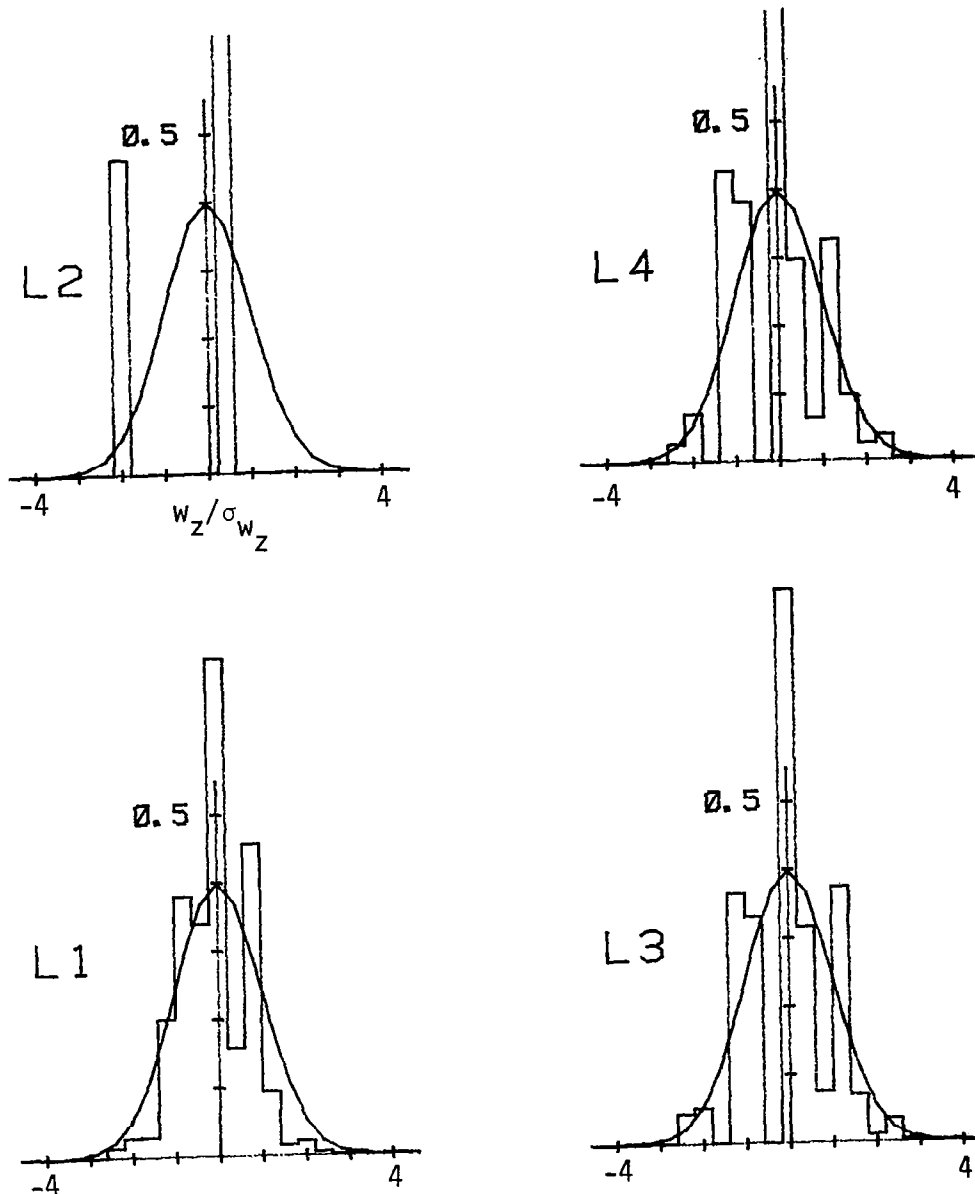
Figure C.37.   Probability density function for vertical velocity
component normalized with σ_{w_z} (Run #8623, T1, Component 3).
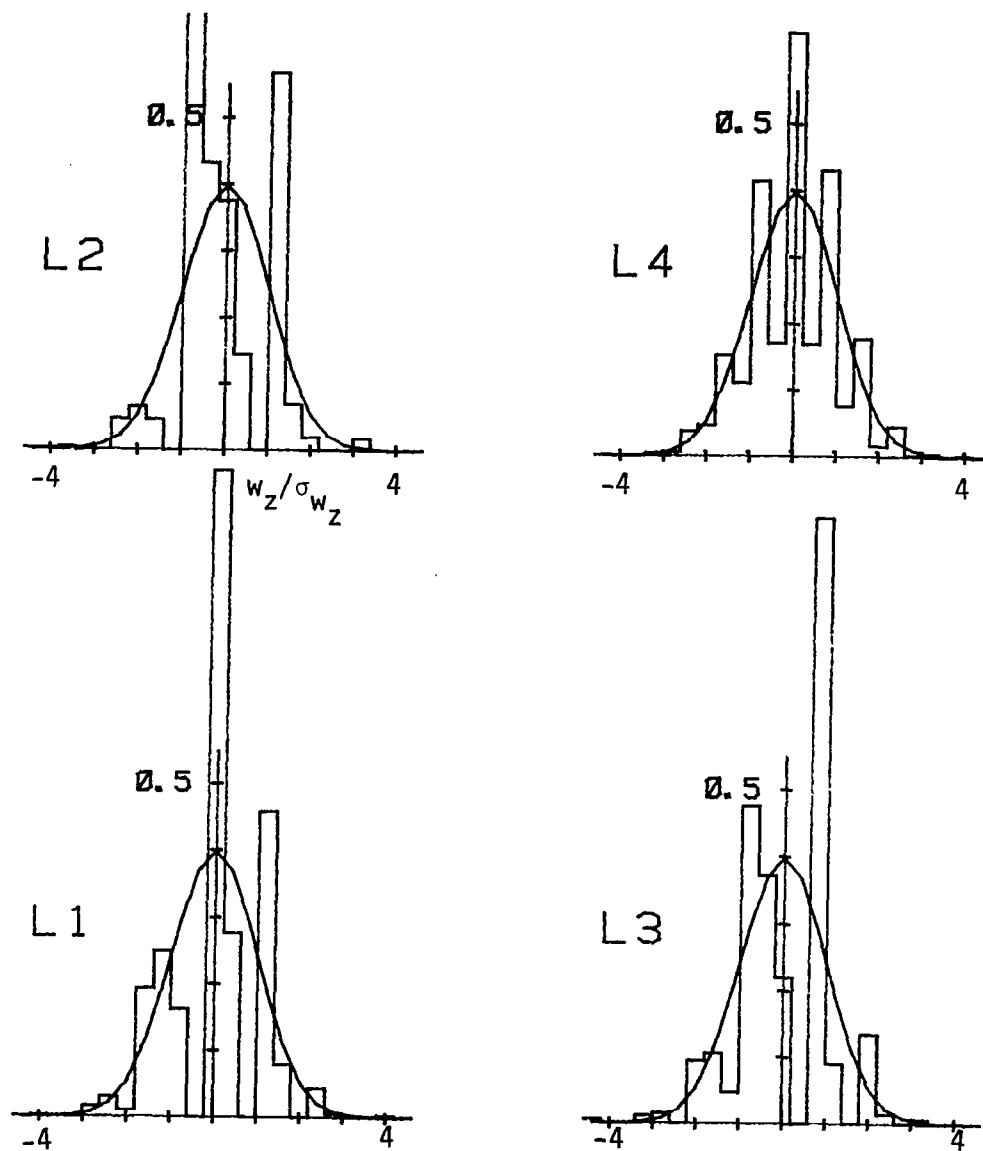
Figure C.38. Probability density function for vertical velocity component normalized with σ_{w_z} (Run #8623, T2, Component 3).
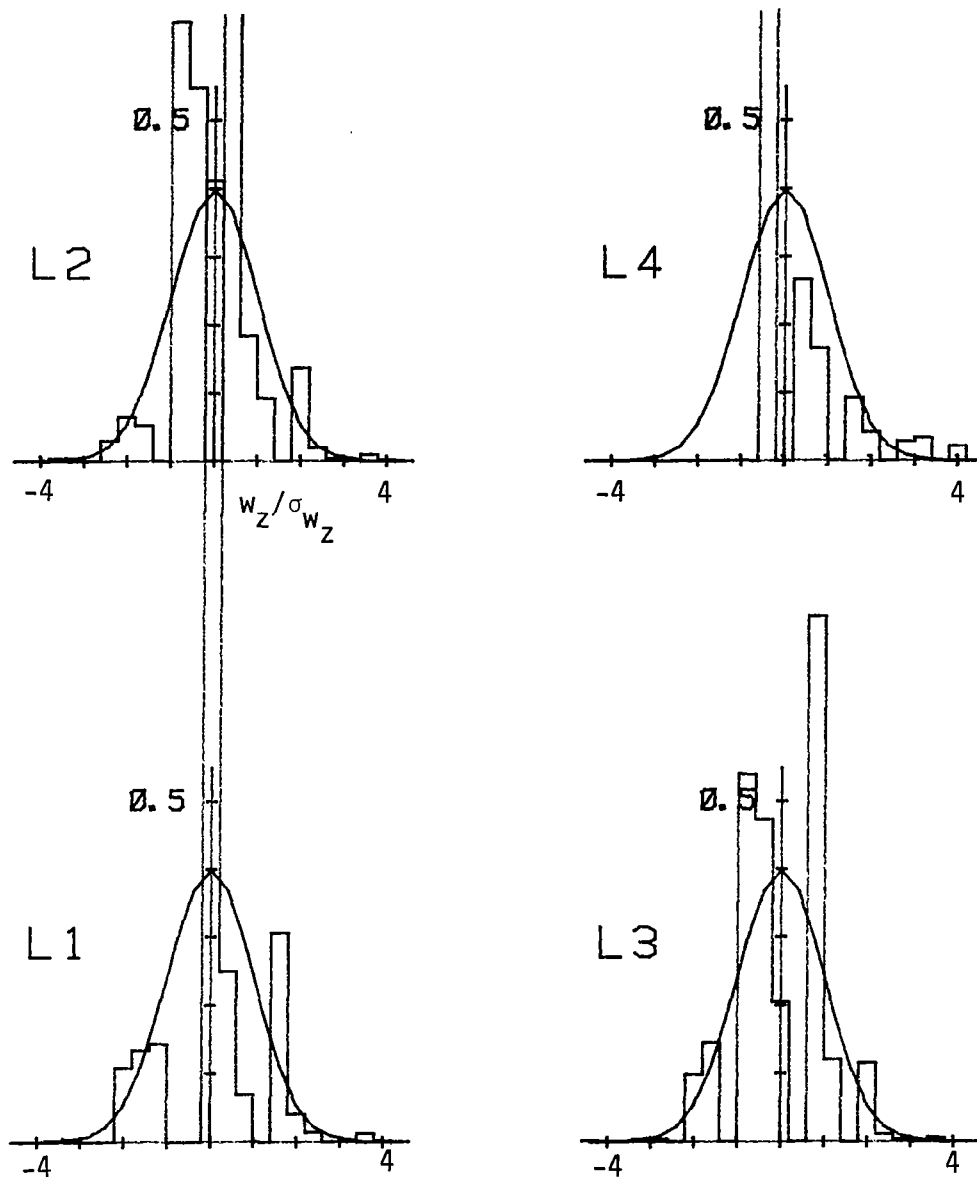
Figure C.39. Probability density function for vertical velocity component normalized with σ_{w_z} (Run #8623, T3, Component 3).
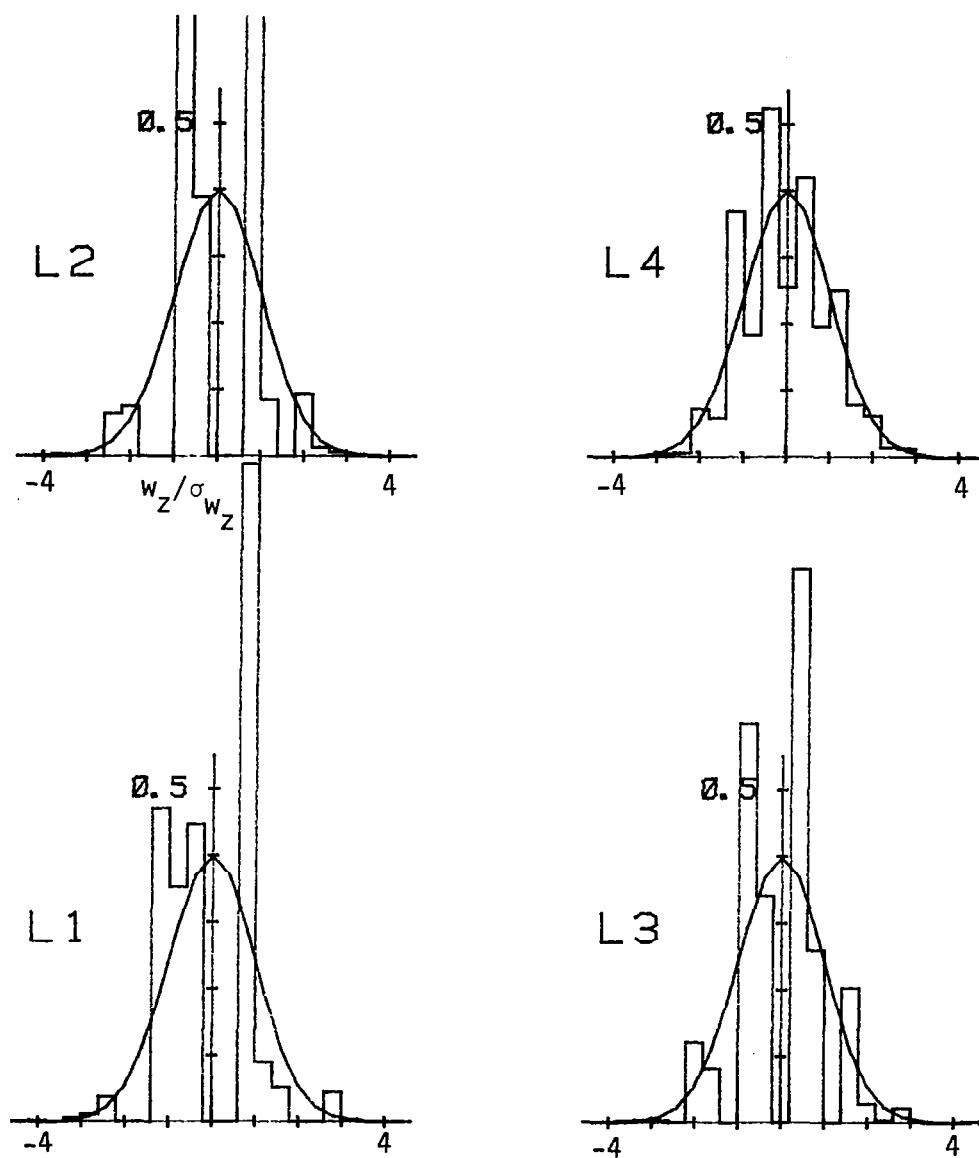
Figure C.40. Probability density function for vertical velocity
component normalized with σ_{w_z} (Run #8623, T4, Component 3).

271
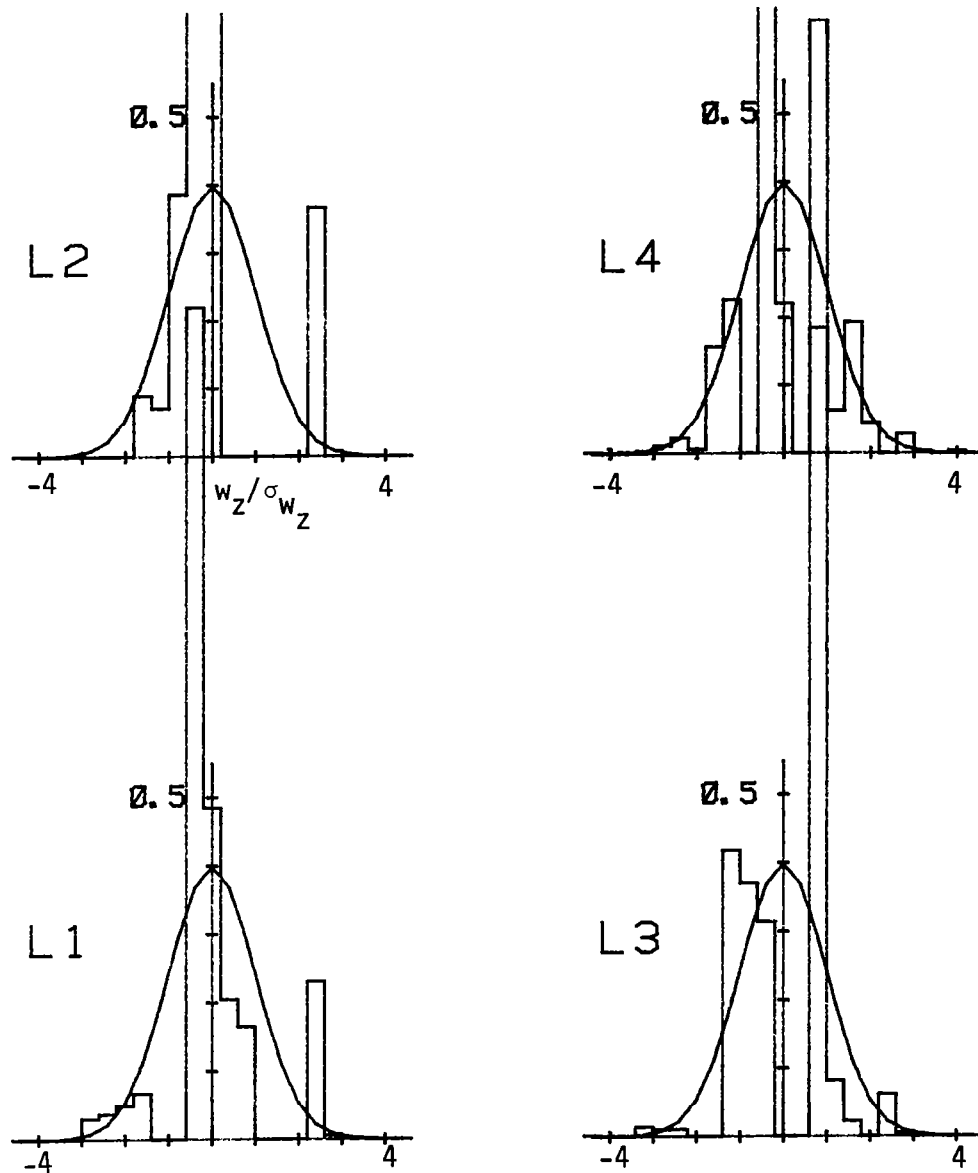
Figure C.41. Probability density function for vertical velocity
component normalized with σ_{w_z} (Run #8623, T5, Component 3).

Figure C.42. Probability density function for vertical velocity component normalized with σ_{w_z} (Run #8623, S1, Component 3).

Figure C.43.   Probability density function for vertical velocity
component normalized with σ_{w_z} (Run #8623, S2, Component 3).

Figure C.44. Probability density function for vertical velocity
component normalized with σ_{w_z} (Run #8623, S3, Component 3).

Figure C.45. Probability density function for vertical velocity component normalized with σ_{w_z} (Run #8623, S4, Component 3).

Figure C.46. Probability density function for vertical velocity
component normalized with σ_{w_z} (Run #8624, T1, Component 3).

277

Figure C.47. Probability density function for vertical velocity component normalized with σ_{w_z} (Run #8624, T2, Component 3).

Figure C.48. Probability density function for vertical velocity
component normalized with σ_{w_z} (Run #8624, T3, Component 3).

279

Figure C.49.   Probability density function for vertical velocity
component normalized with σ_{w_z} (Run #8624, T4, Component 3).

Figure C.50.   Probability density function for vertical velocity
component normalized with σ_{w_z} (Run #8624, T5, Component 3).

Figure C.51. Probability density function for vertical velocity
component normalized with σ_{w_z} (Run #8624, S1, Component 3).

Figure C.52. Probability density function for vertical velocity component normalized with σ_{w_z} (Run #8624, S2, Component 3).

Figure C.53. Probability density function for vertical velocity
component normalized with σ_{w_z} (Run #8624, S3, Component 3).

Figure C.54. Probability density function for vertical velocity component normalized with σ_{w_z} (Run #8624, S4, Component 3).

APPENDIX D

LONGITUDINAL SPECTRA

Spectral data for the longitudinal velocity component at all measuring stations for Runs #8623 and #8624 are given in this appendix. The results are plotted in dimensional form, i.e., $\phi(f)$ versus f.
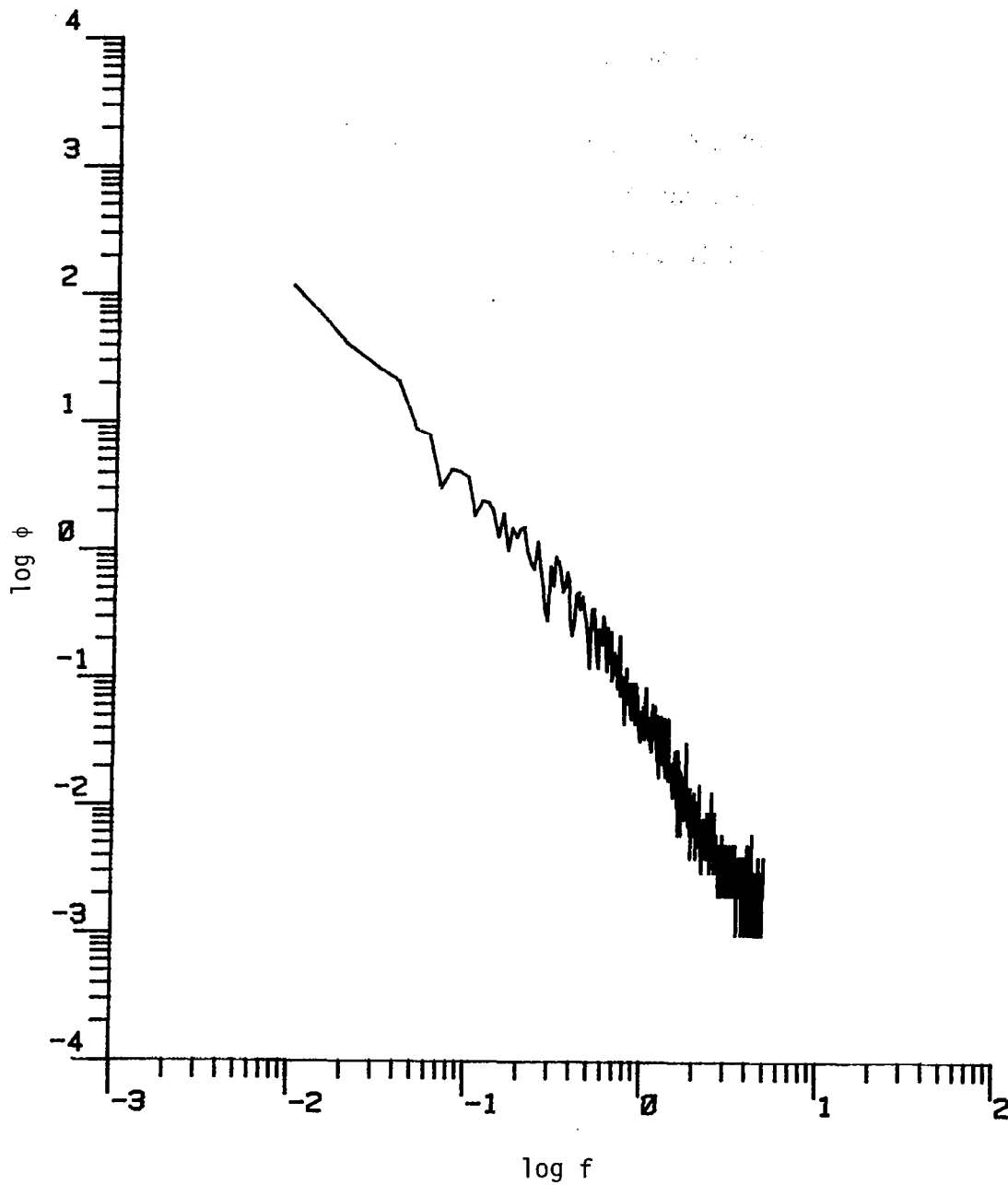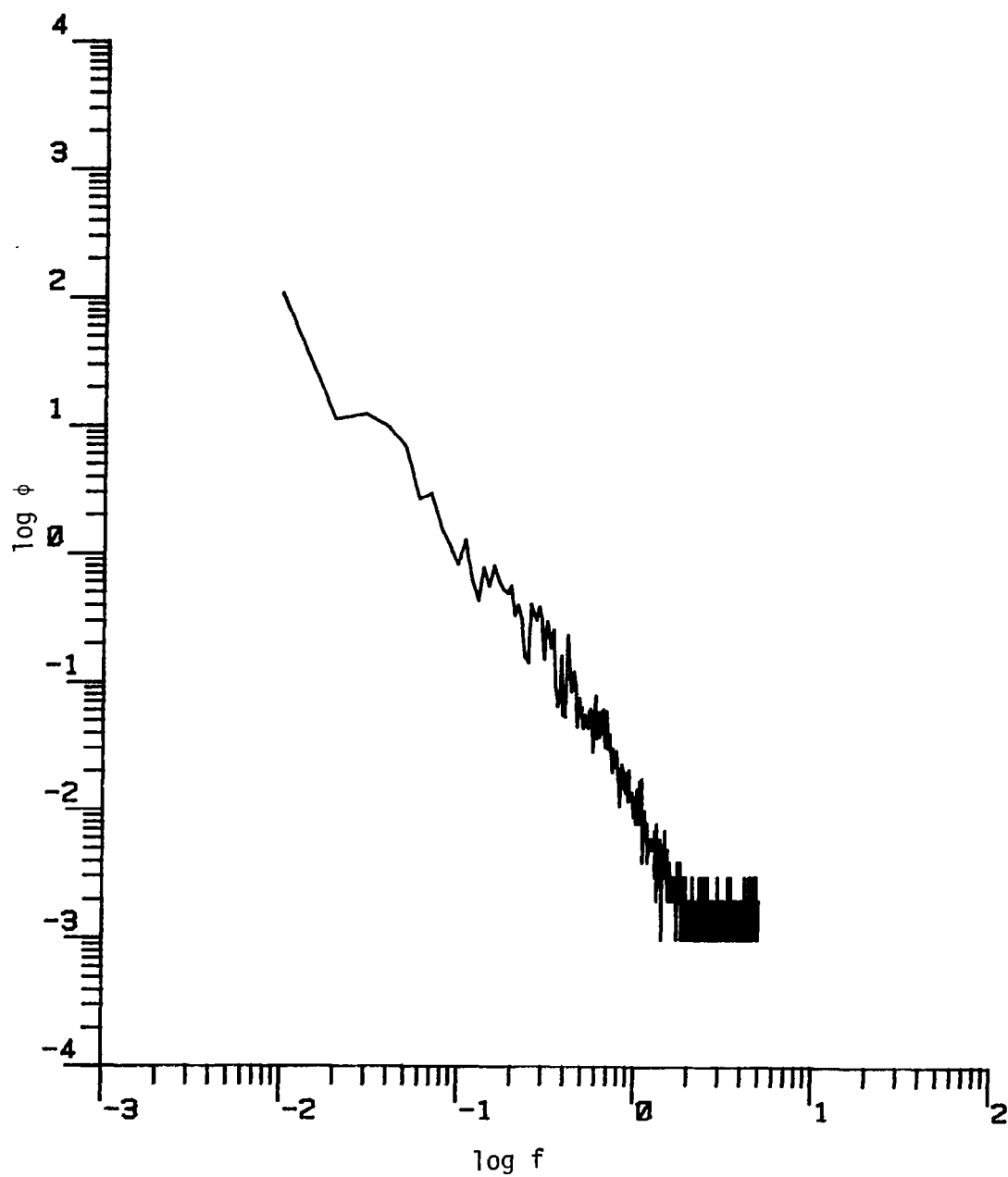
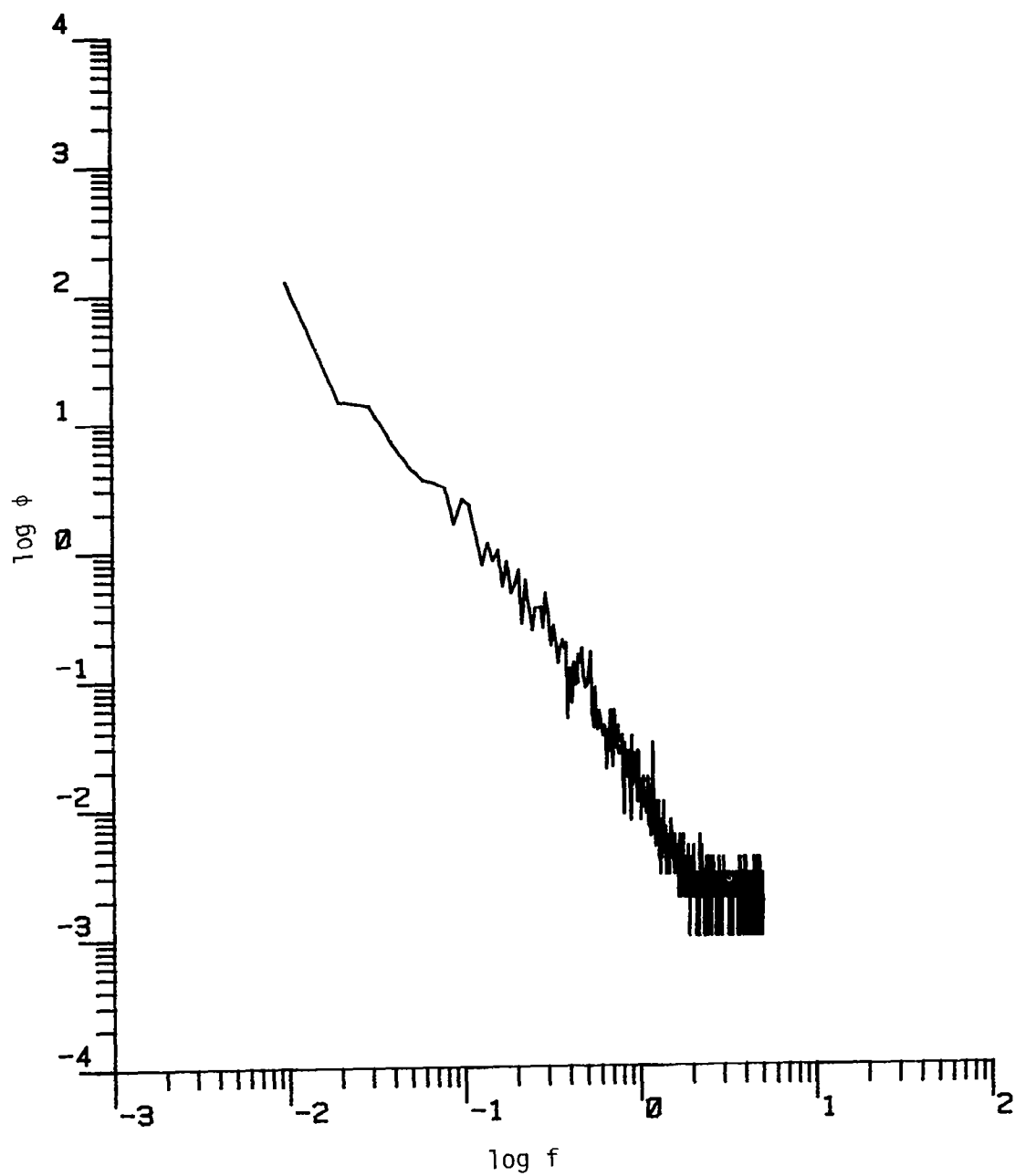Figure D.1.   The longitudinal power spectrum (Run #8623, T1L1, Component 1).

287
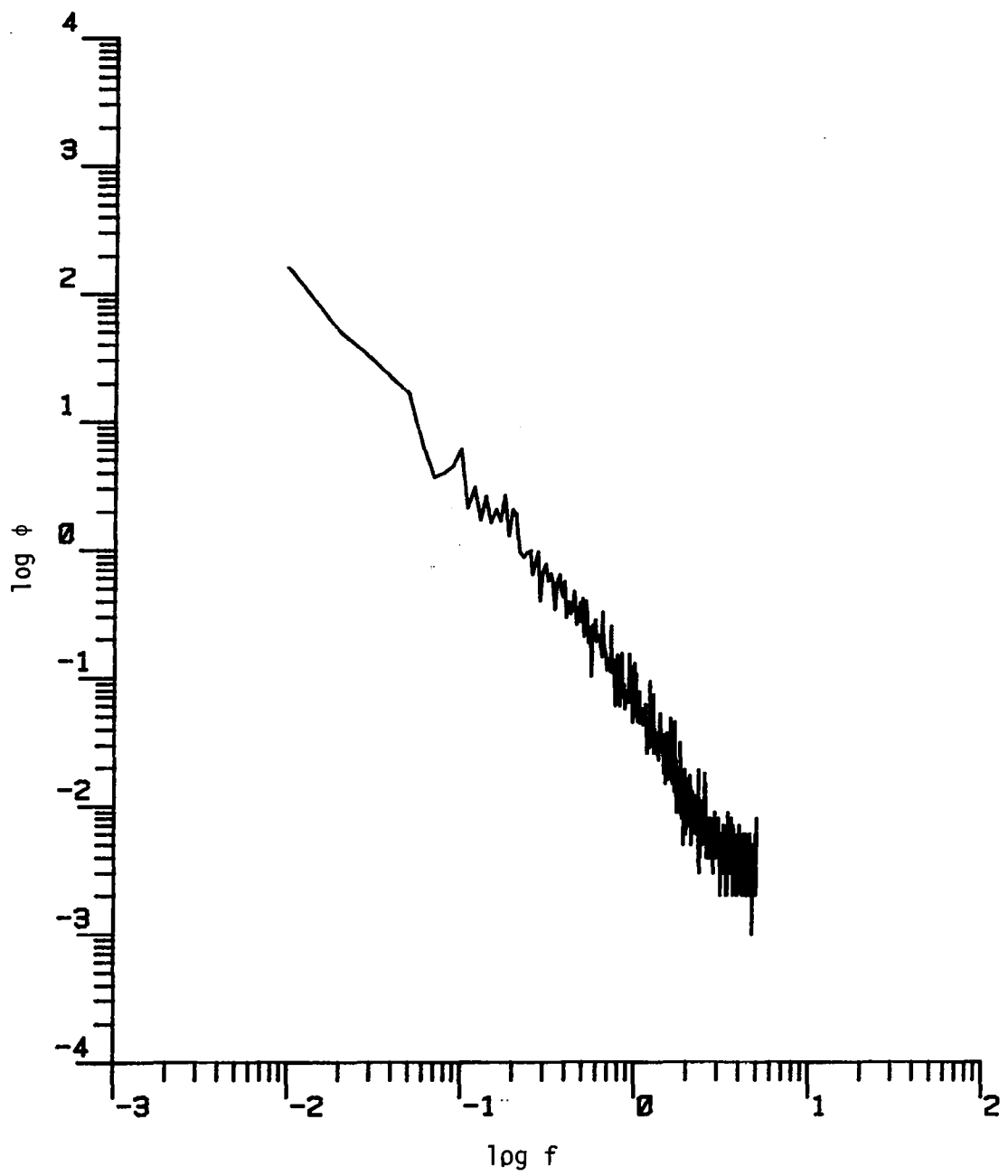
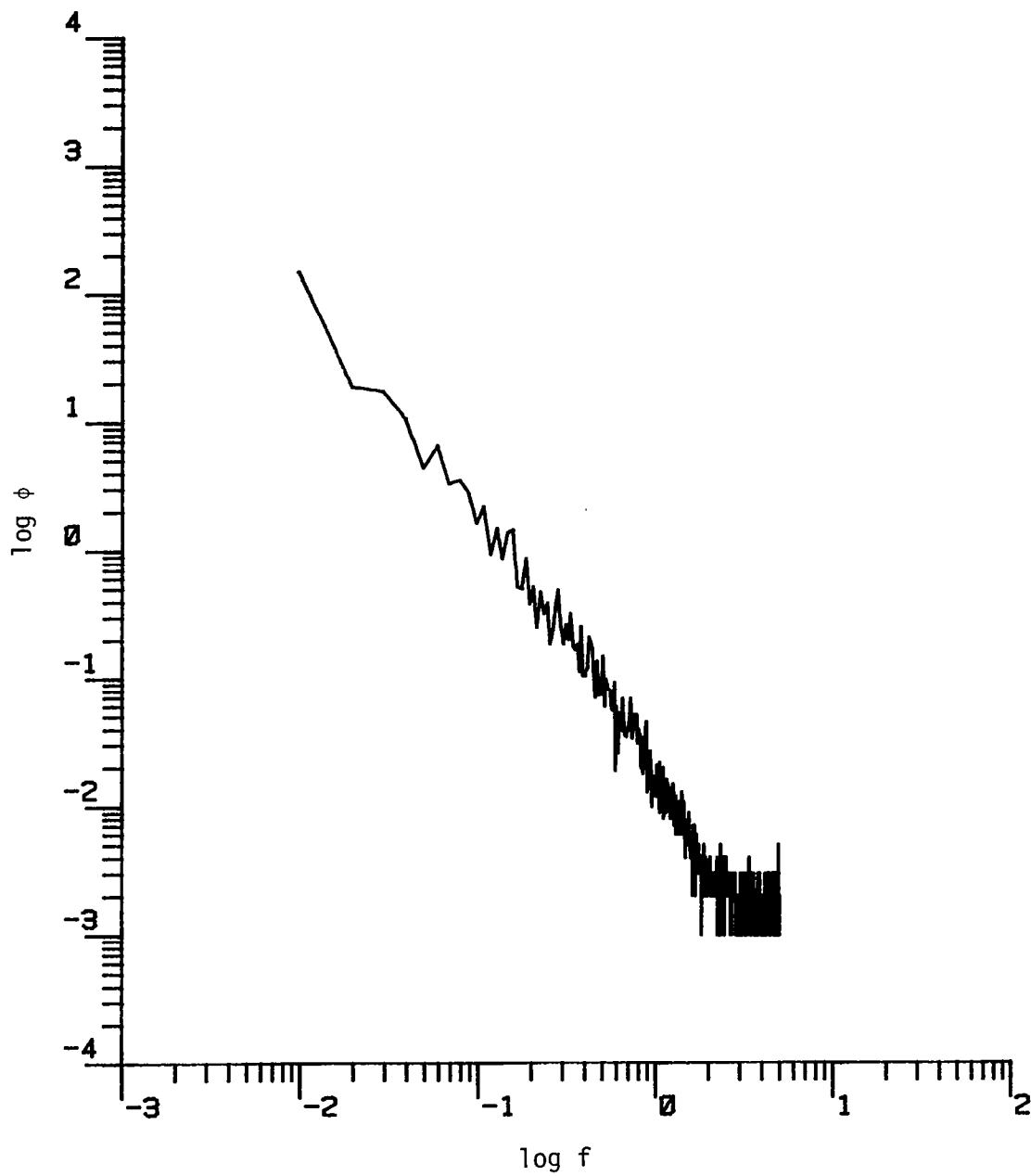Figure D.2.   The longitudinal power spectrum (Run #8623, T1L2, Component 1).
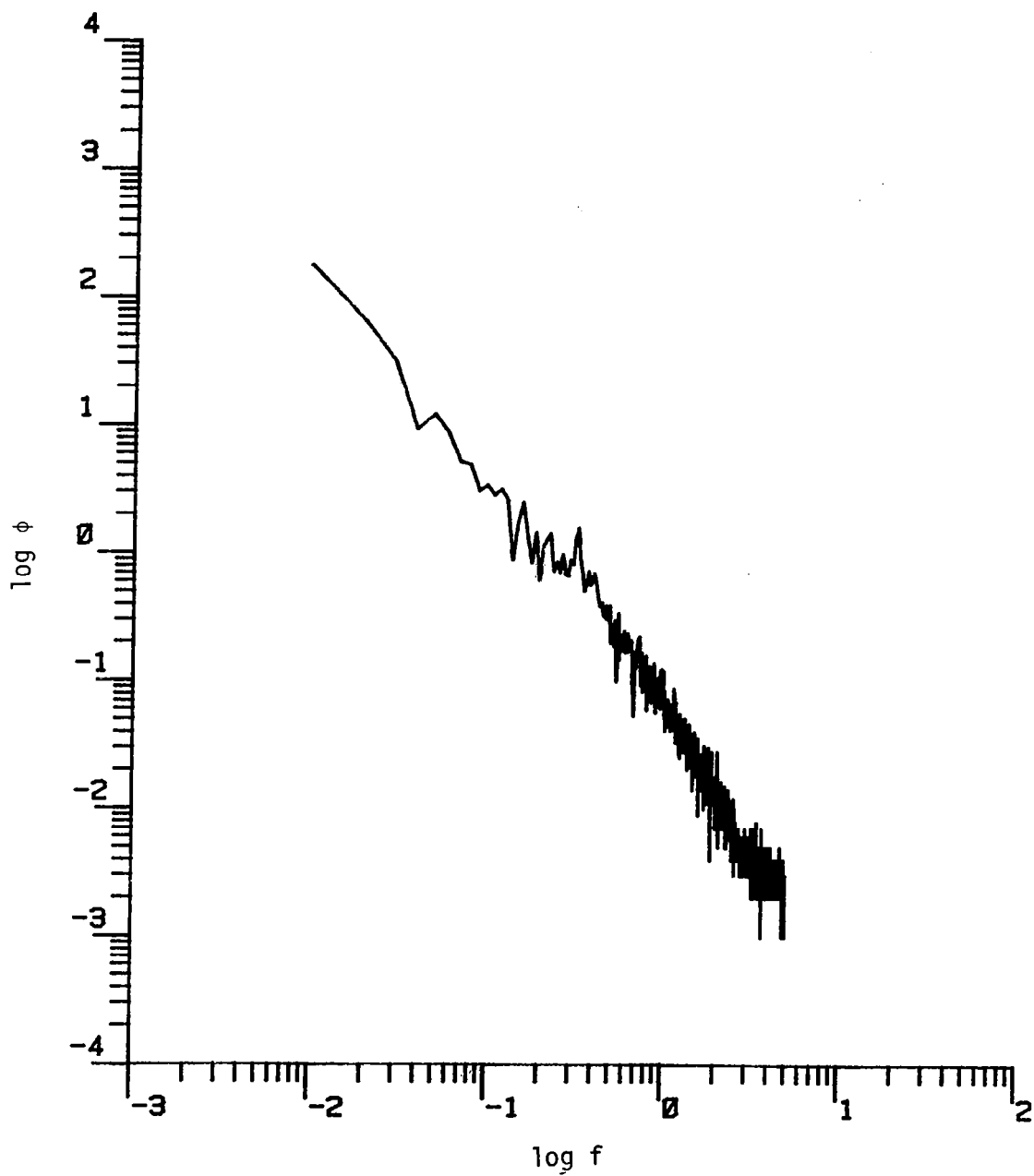
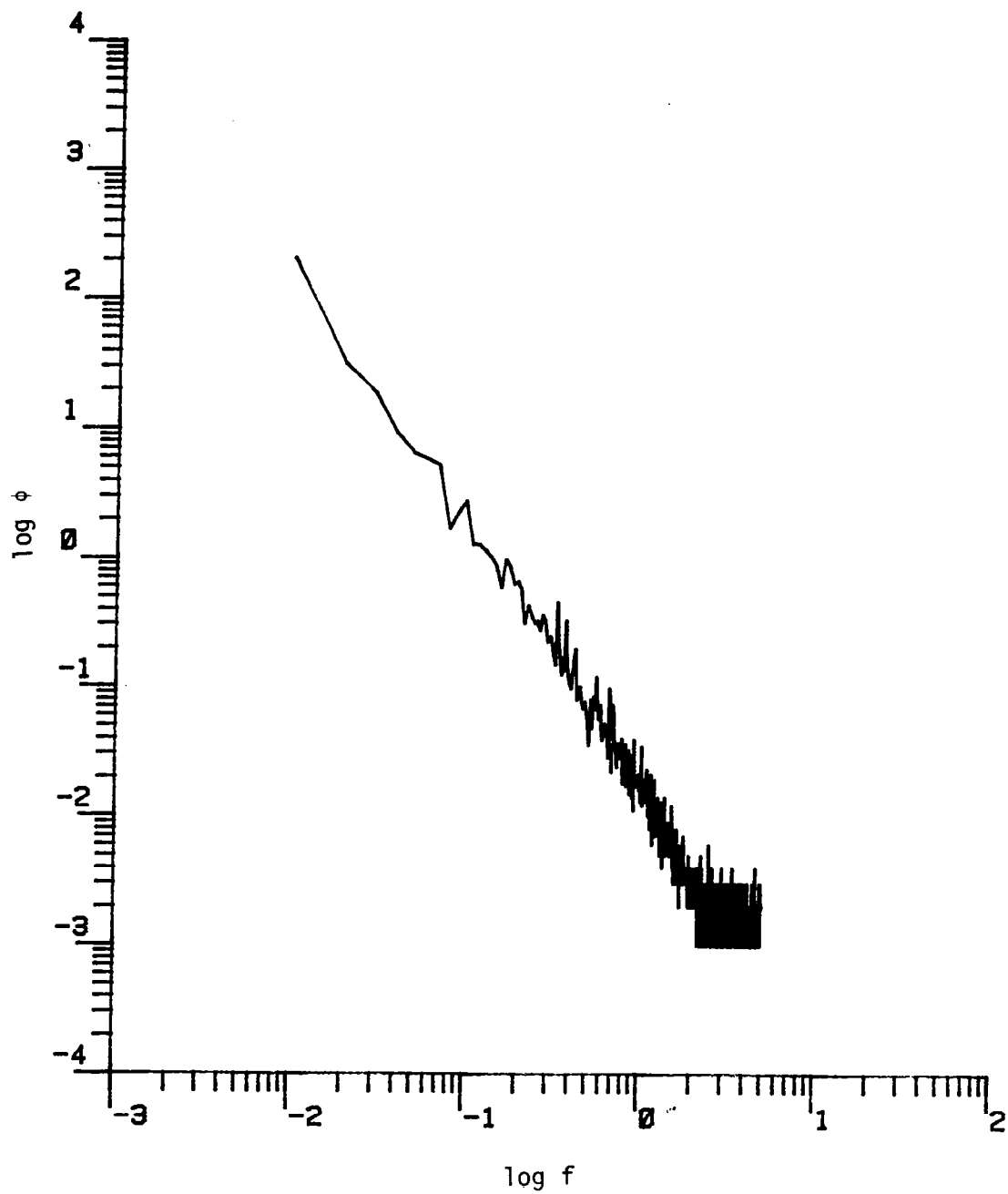Figure D.3. The longitudinal power spectrum (Run #8623, T1L3, Component 1).
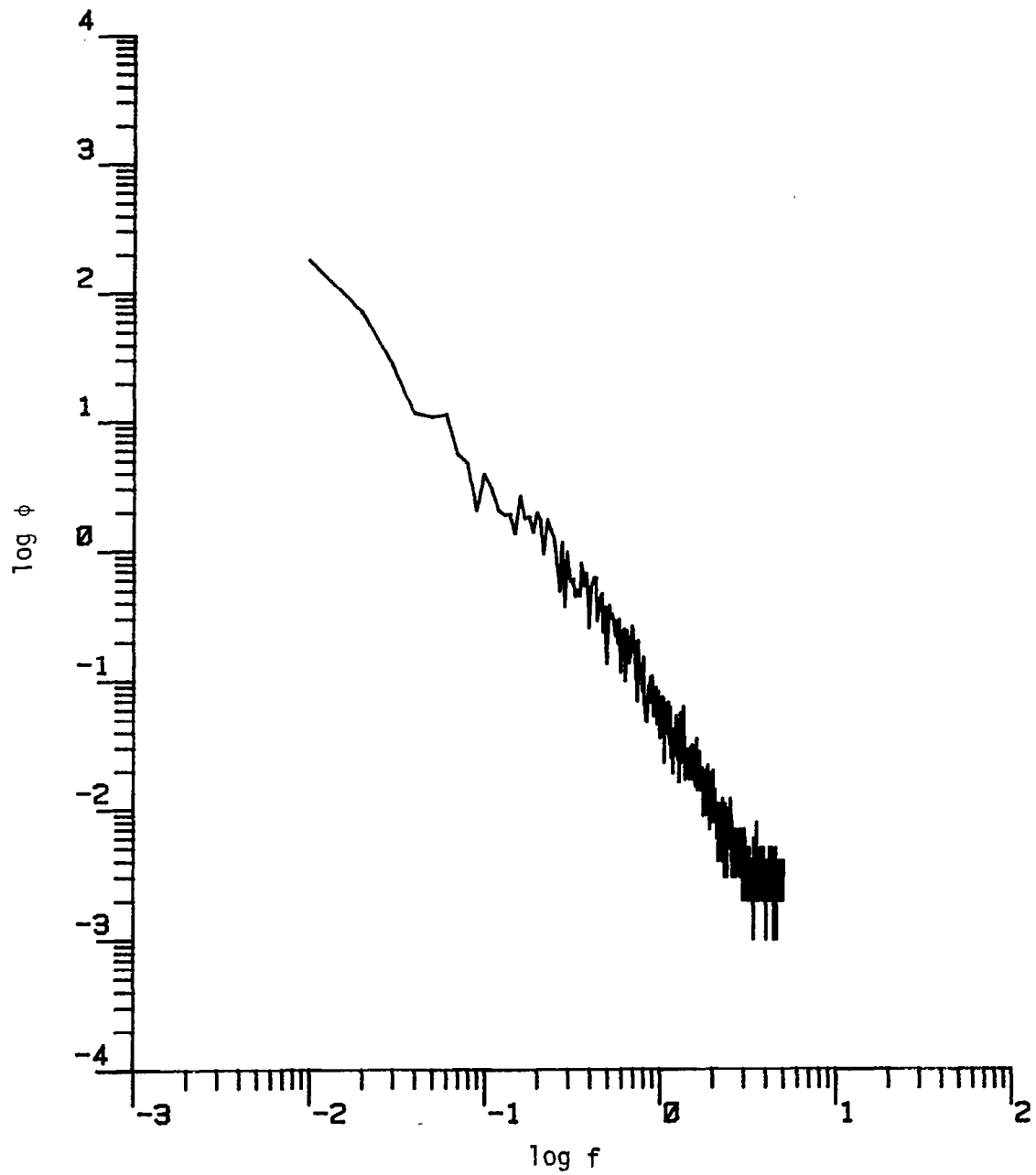
Figure D.4. The longitudinal power spectrum (Run #8623, T1L4, Component 1).
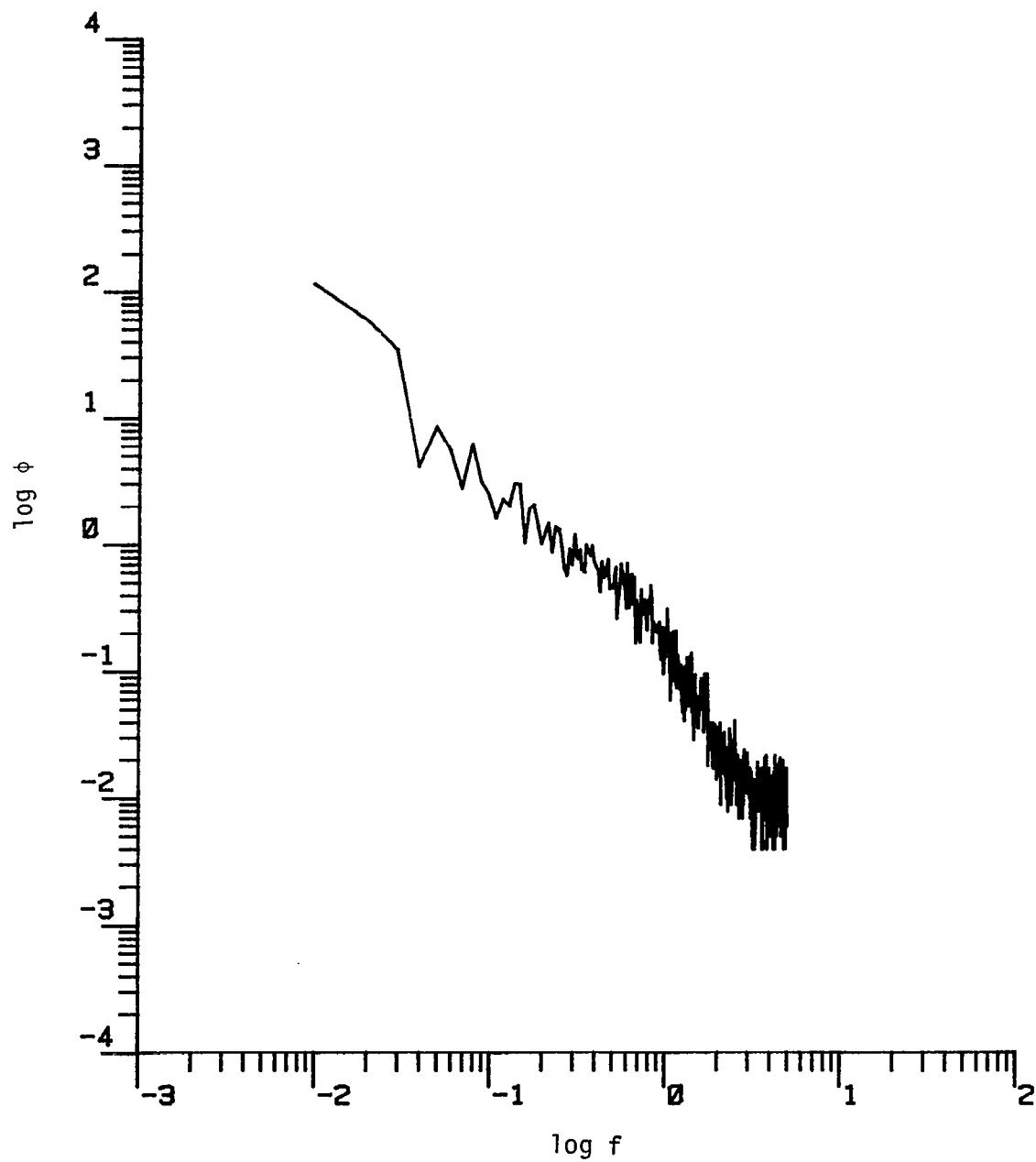
Figure D.5. The longitudinal power spectrum (Run #8623, T2L1, Component 1).

291
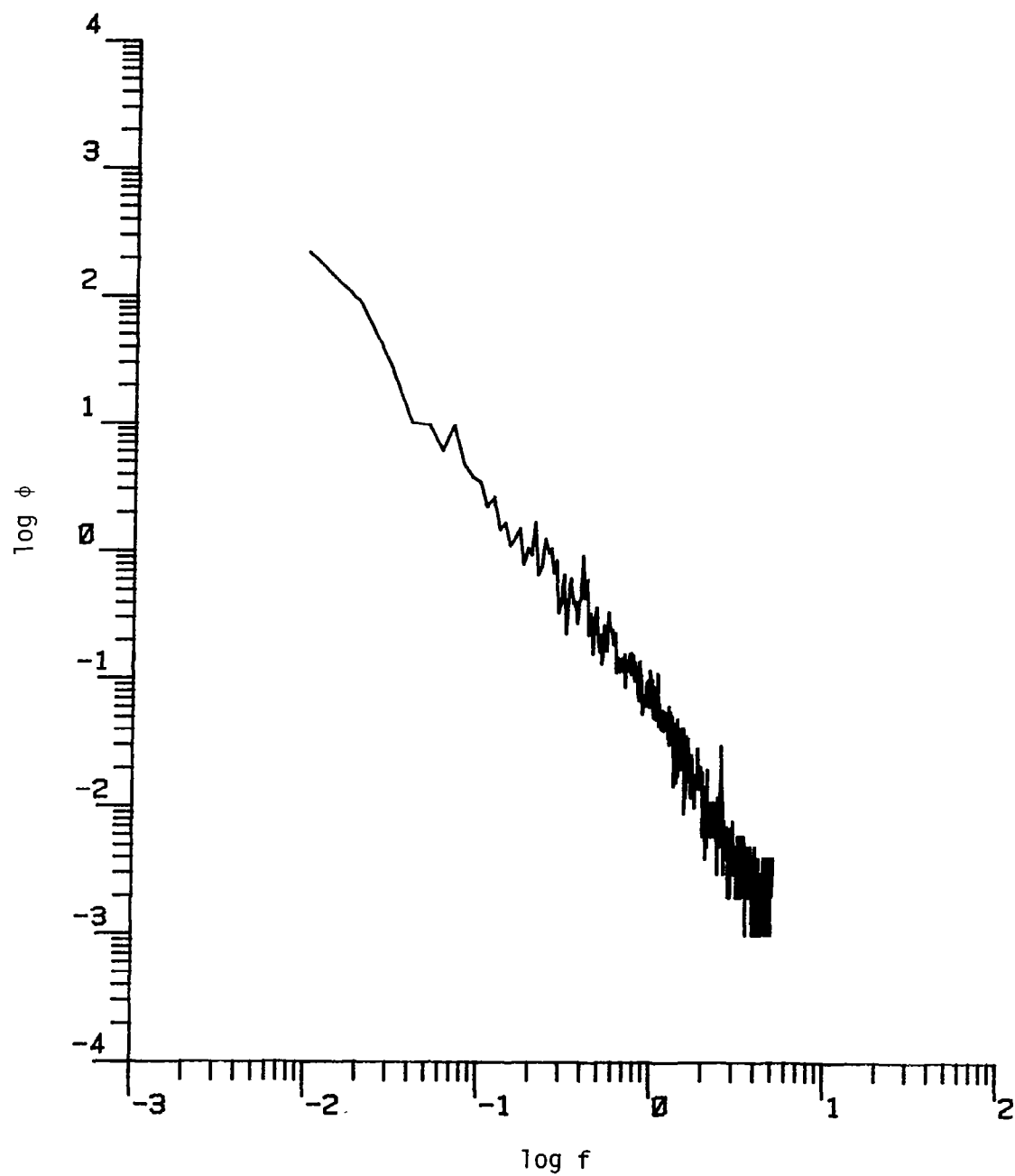
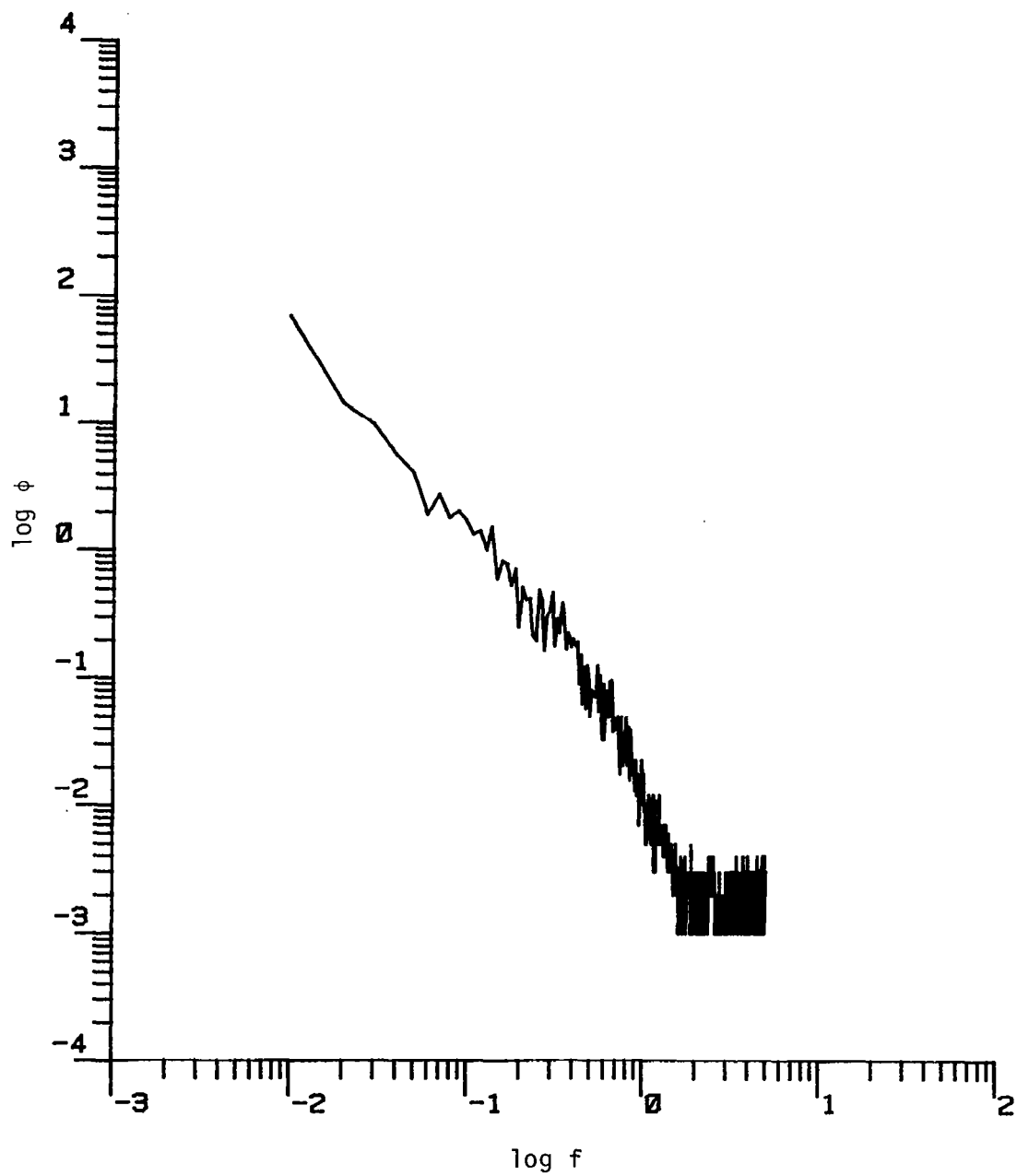Figure D.6.   The longitudinal power spectrum (Run #8623, T2L2,
Component 1).
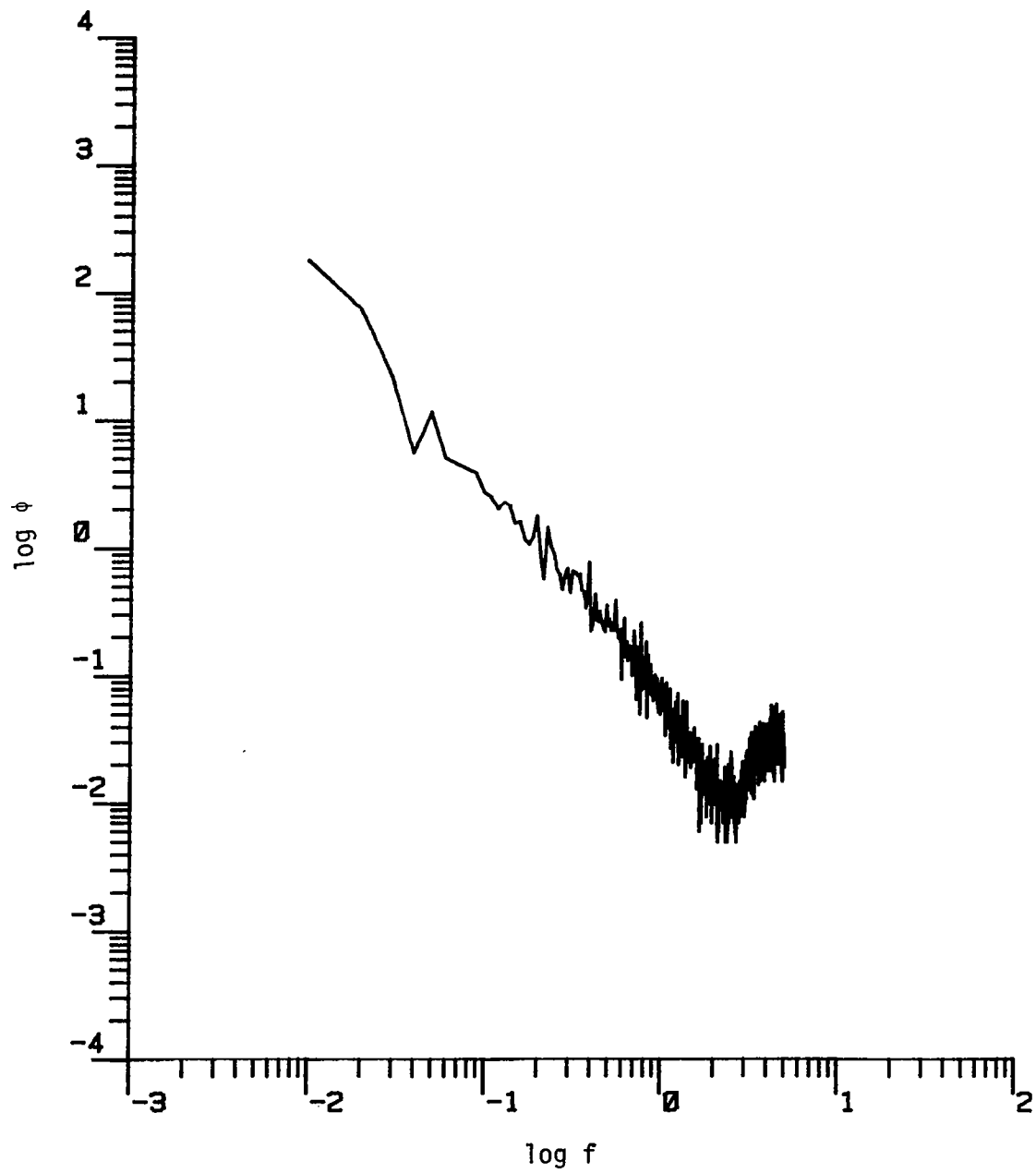
Figure D.7. The longitudinal power spectrum (Run #8623, T2L3, Component 1).
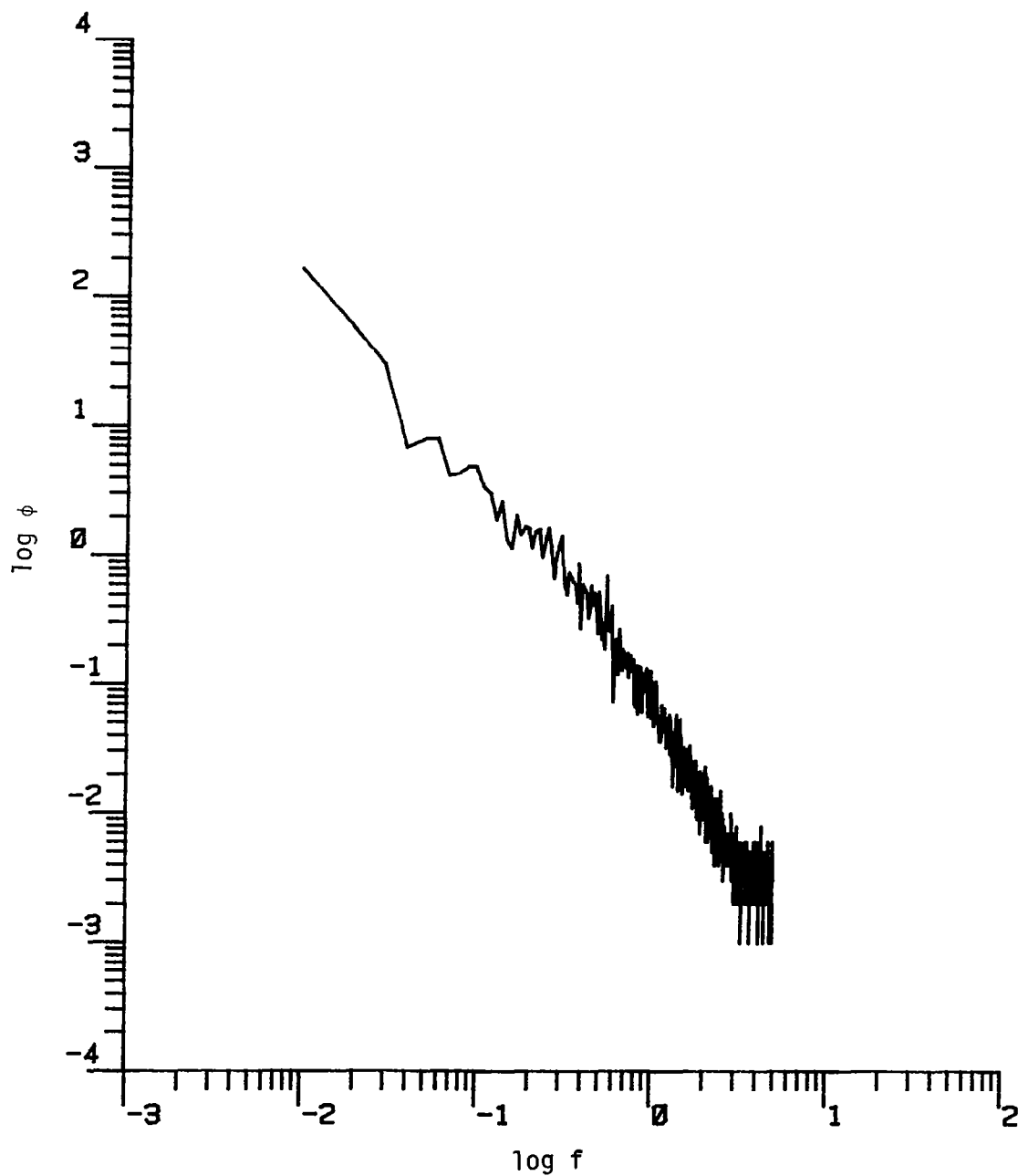
Figure D.8.   The longitudinal power spectrum (Run #8623, T2L4, Component 1).
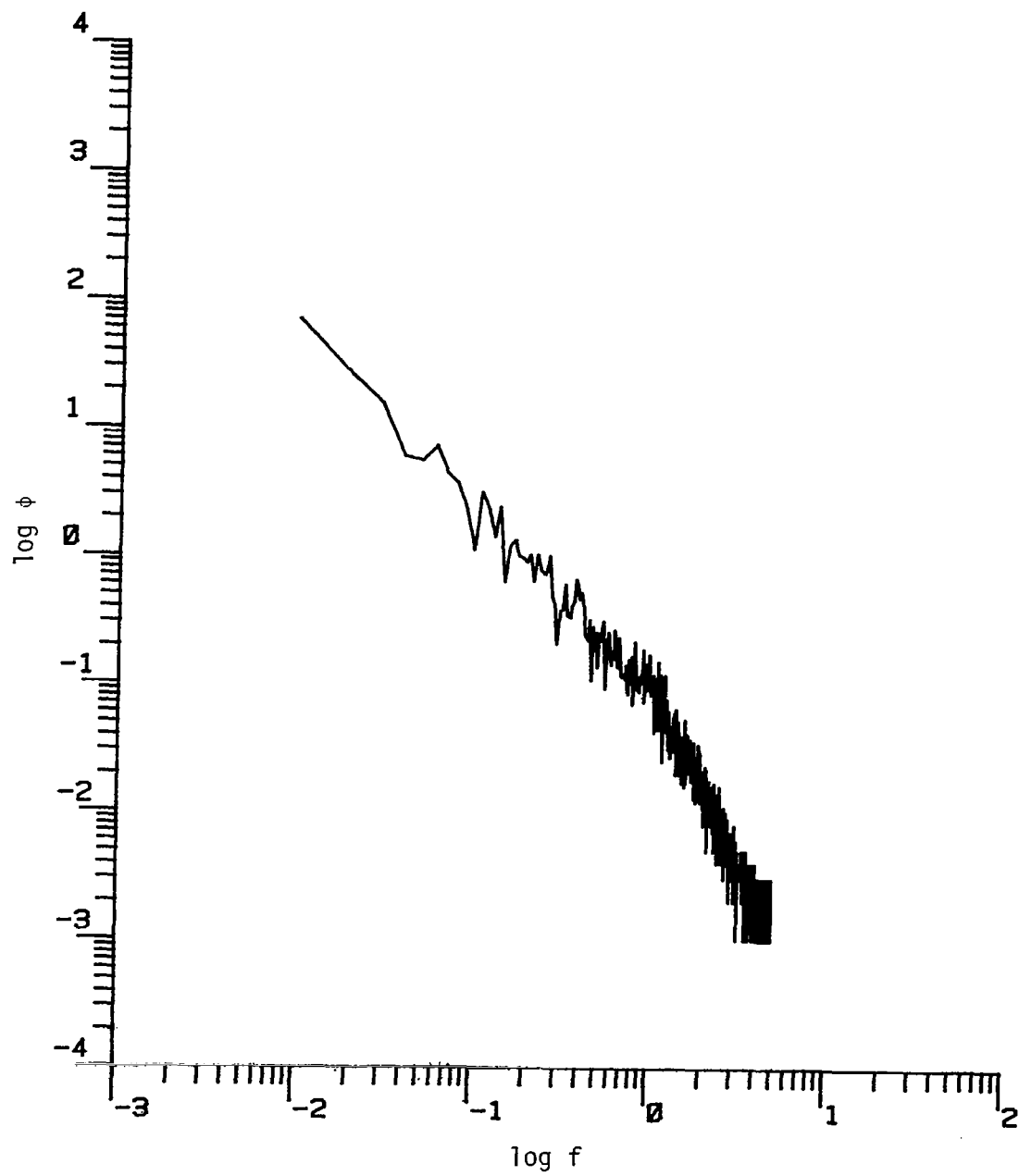
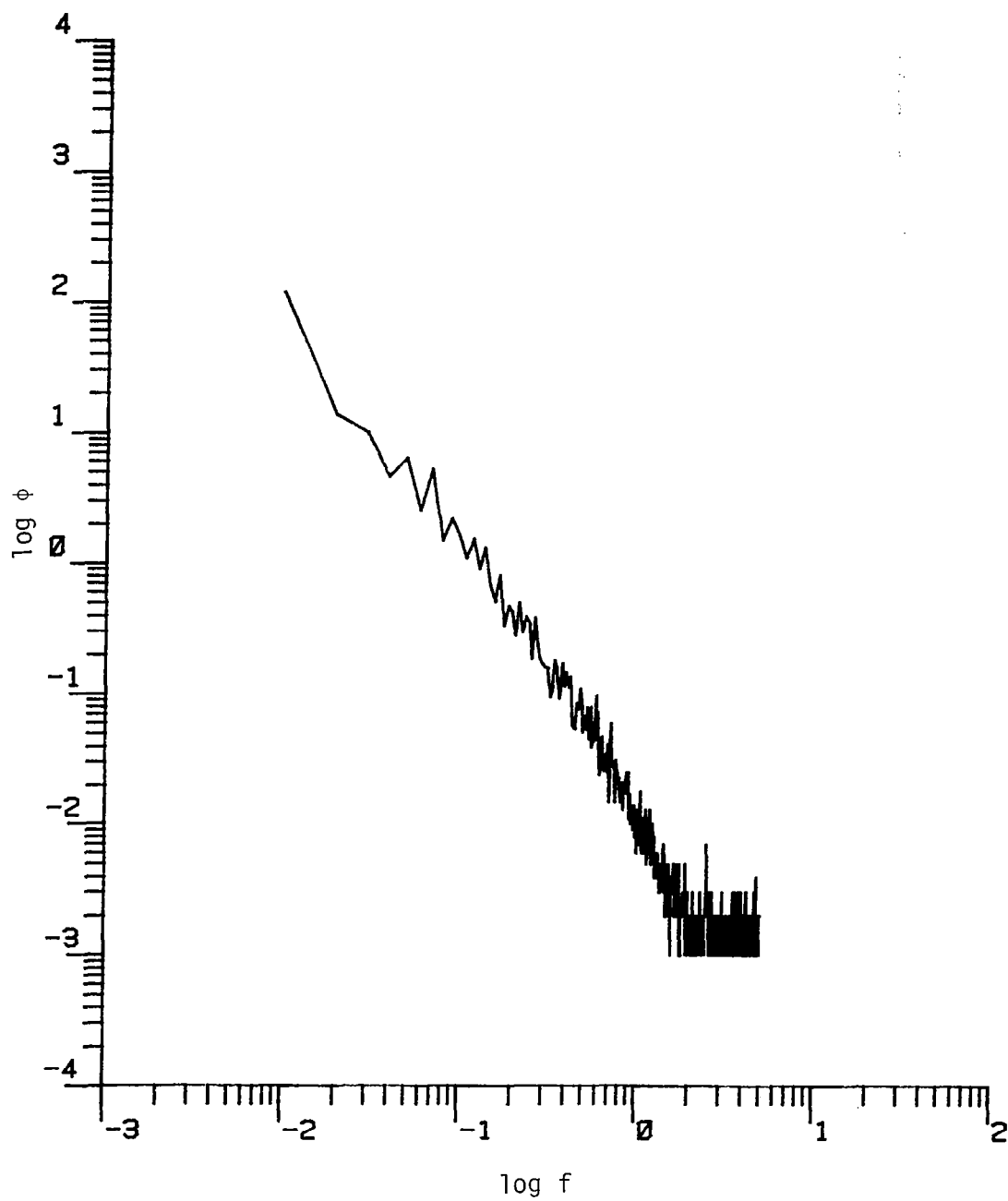Figure D.9.   The longitudinal power spectrum (Run #8623, T3L1, Component 1).
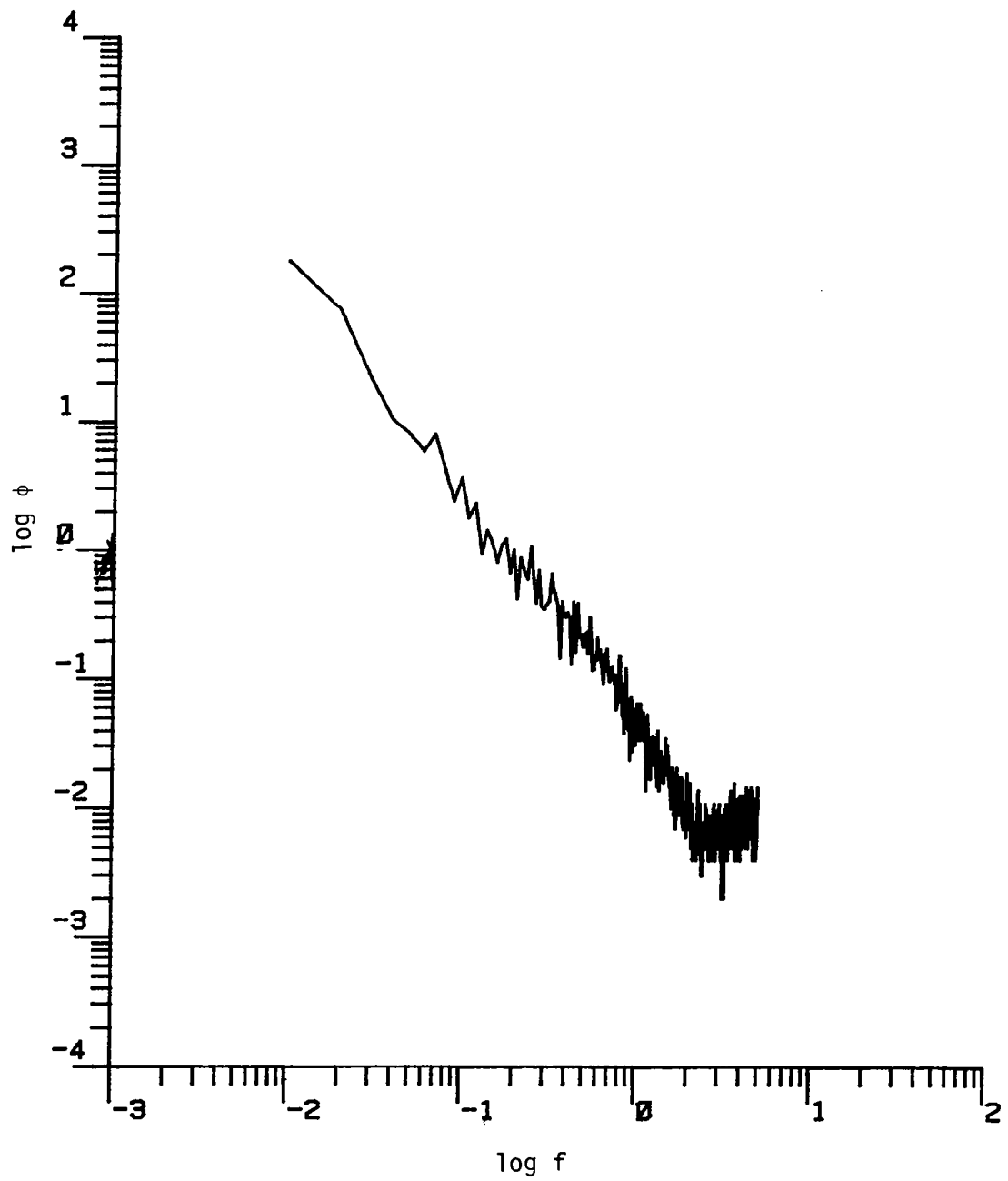
Figure D.10.   The longitudinal power spectrum (Run #8623, T3L2, Component 1).
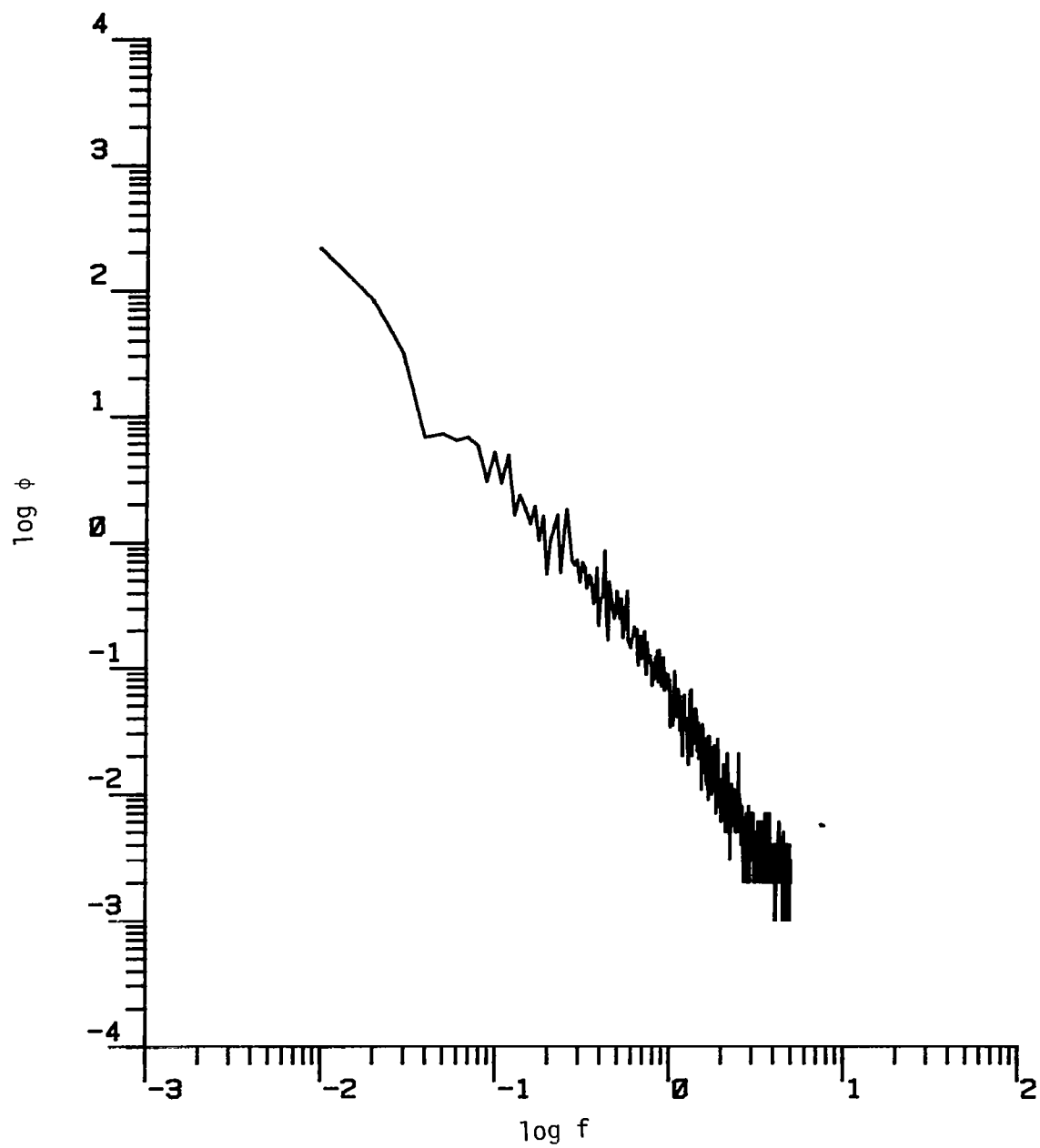
Figure D.11. The longitudinal power spectrum (Run #8623, T3L3, Component 1).
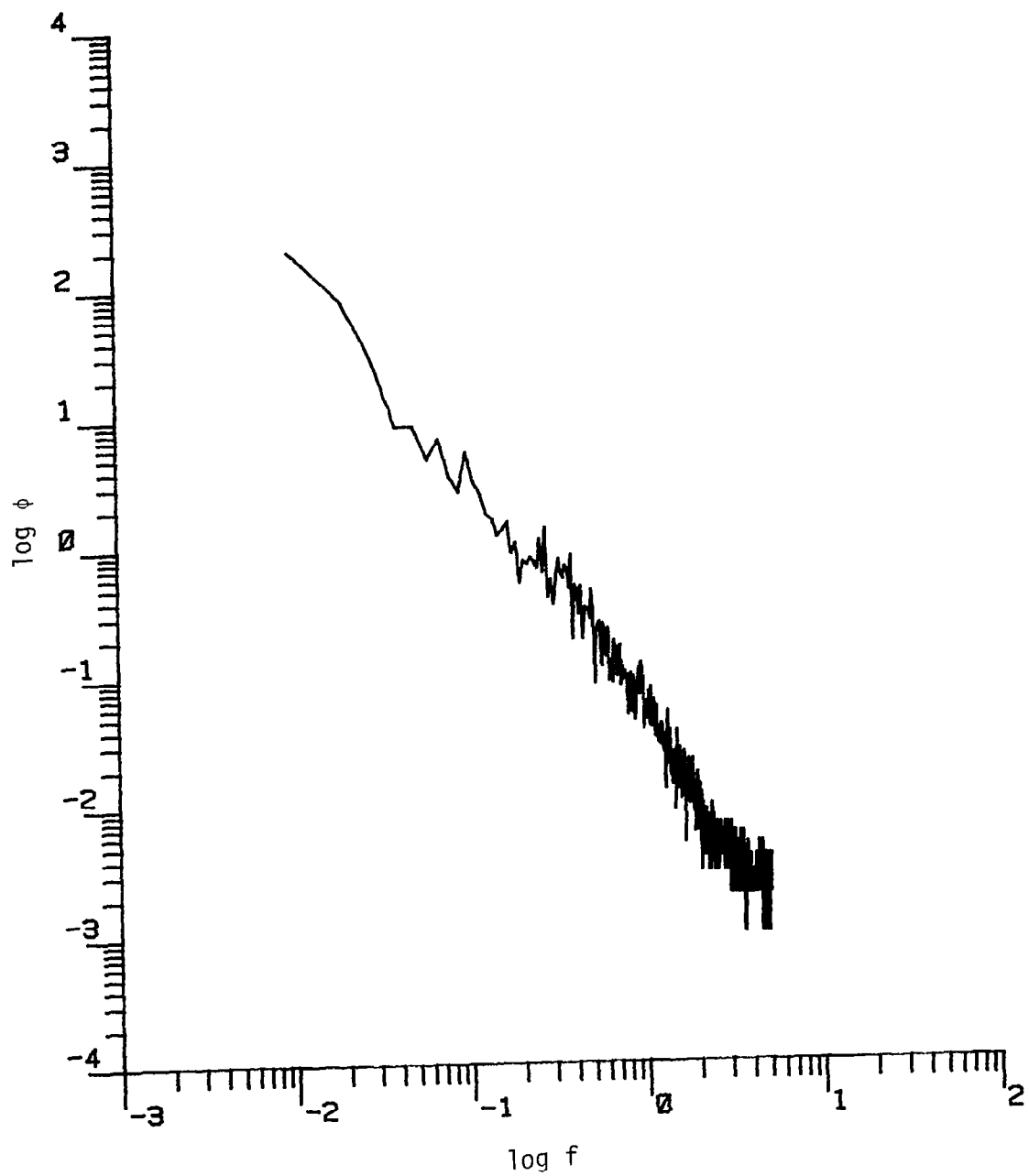
Figure D.12.   The longitudinal power spectrum (Run #8623, T3L4, Component 1).
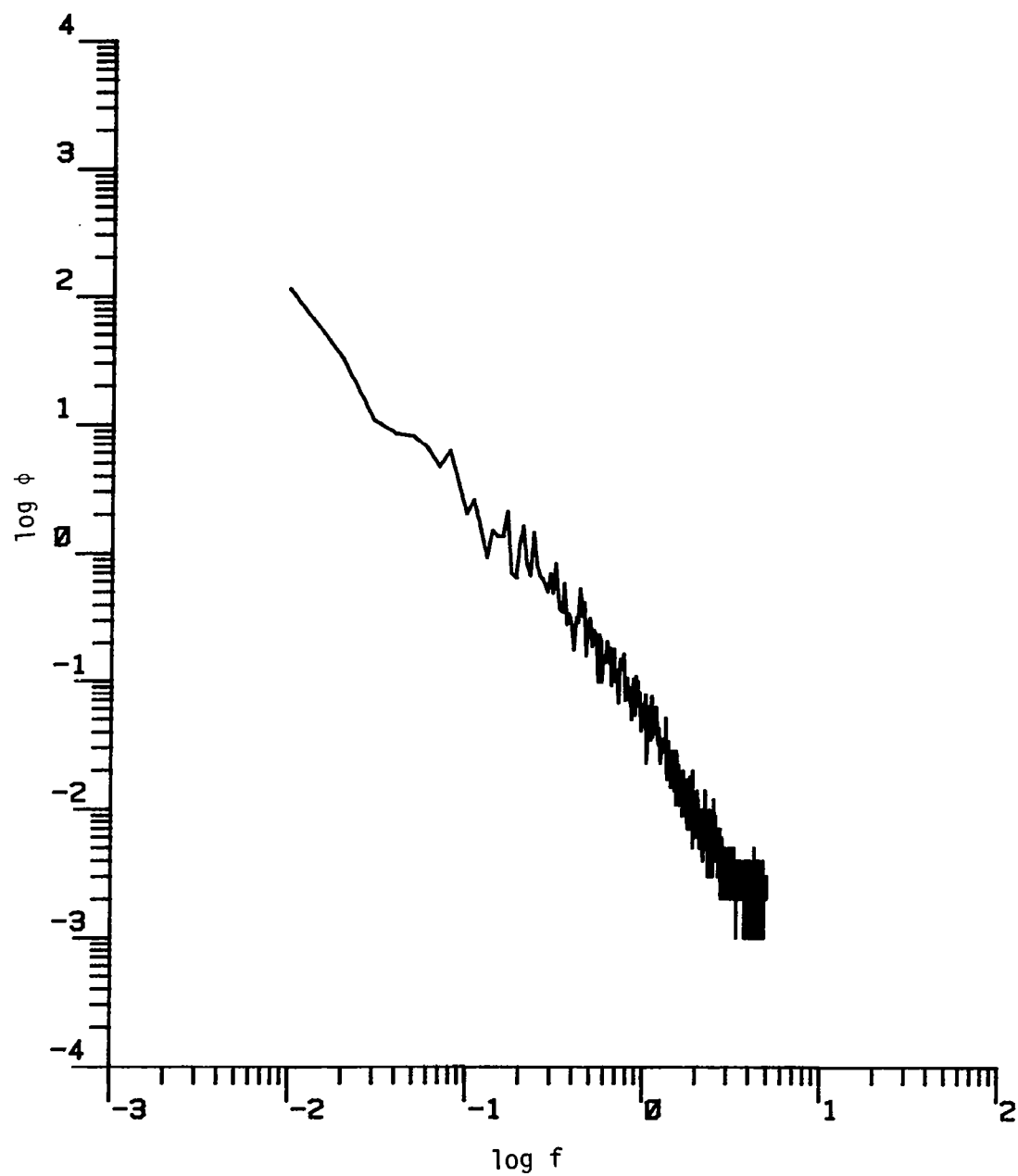
Figure D.13.   The longitudinal power spectrum (Run #8623, T4L1, Component 1).
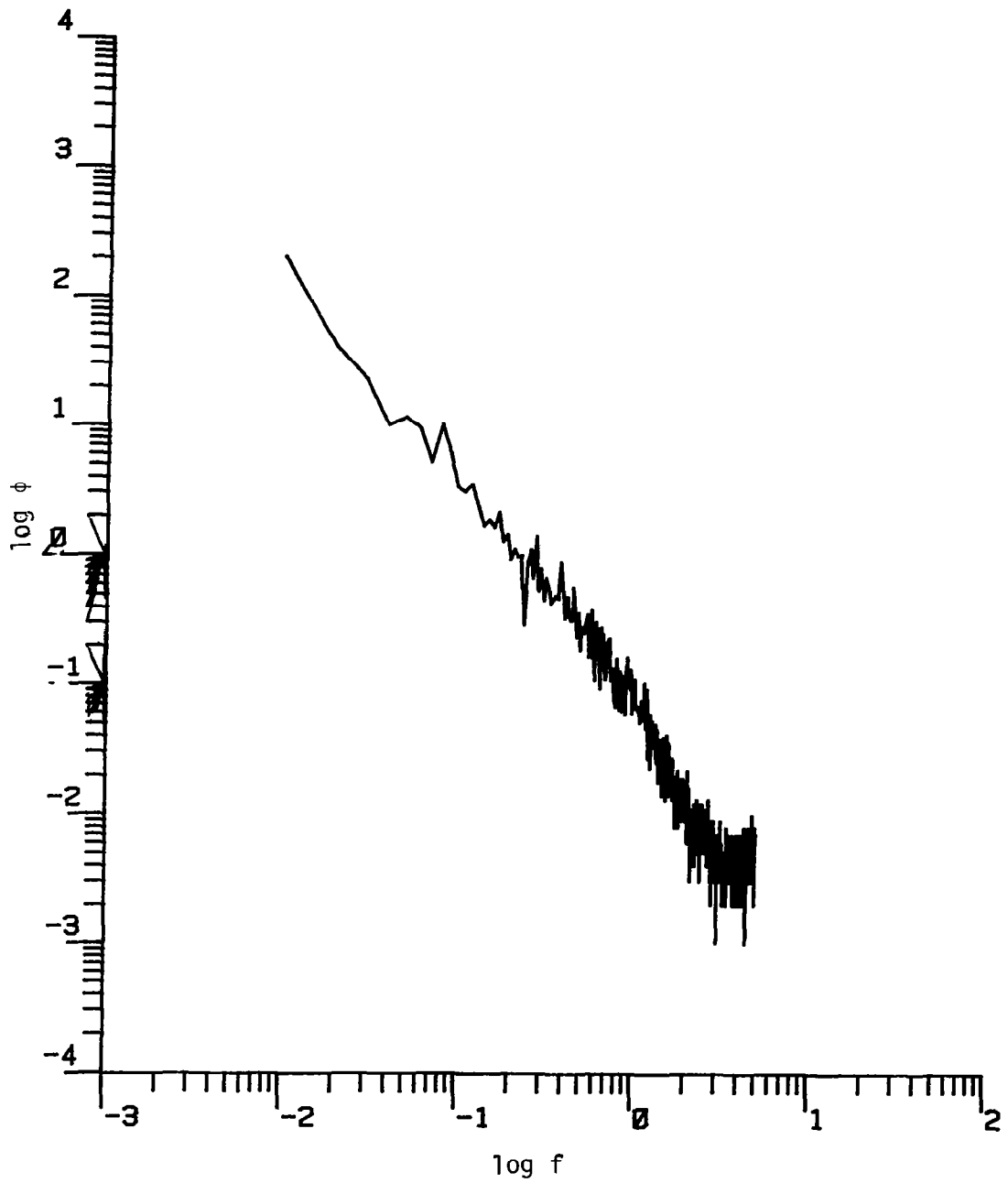
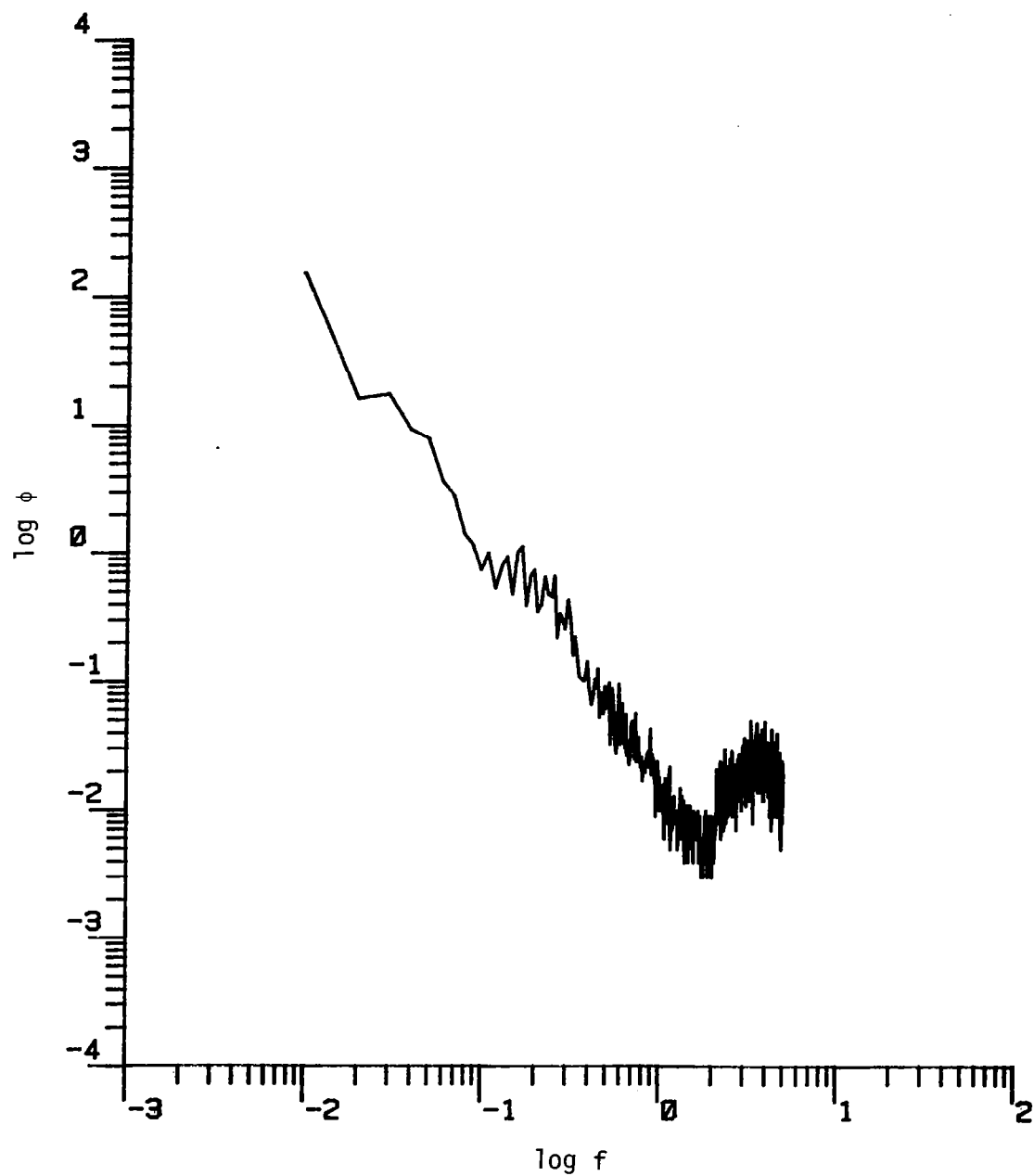Figure D.14. The longitudinal power spectrum (Run #8623, T4L2, Component 1).
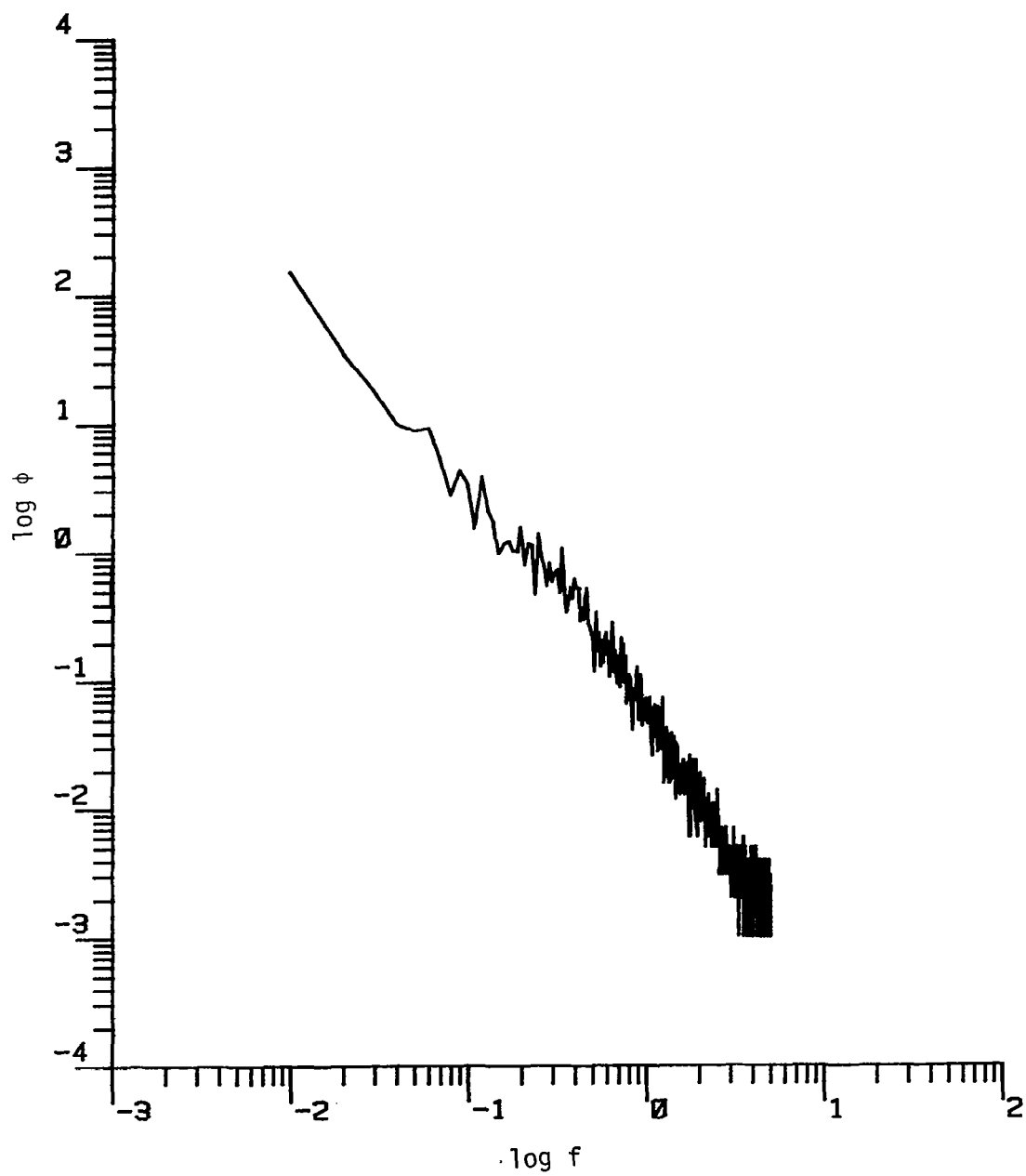
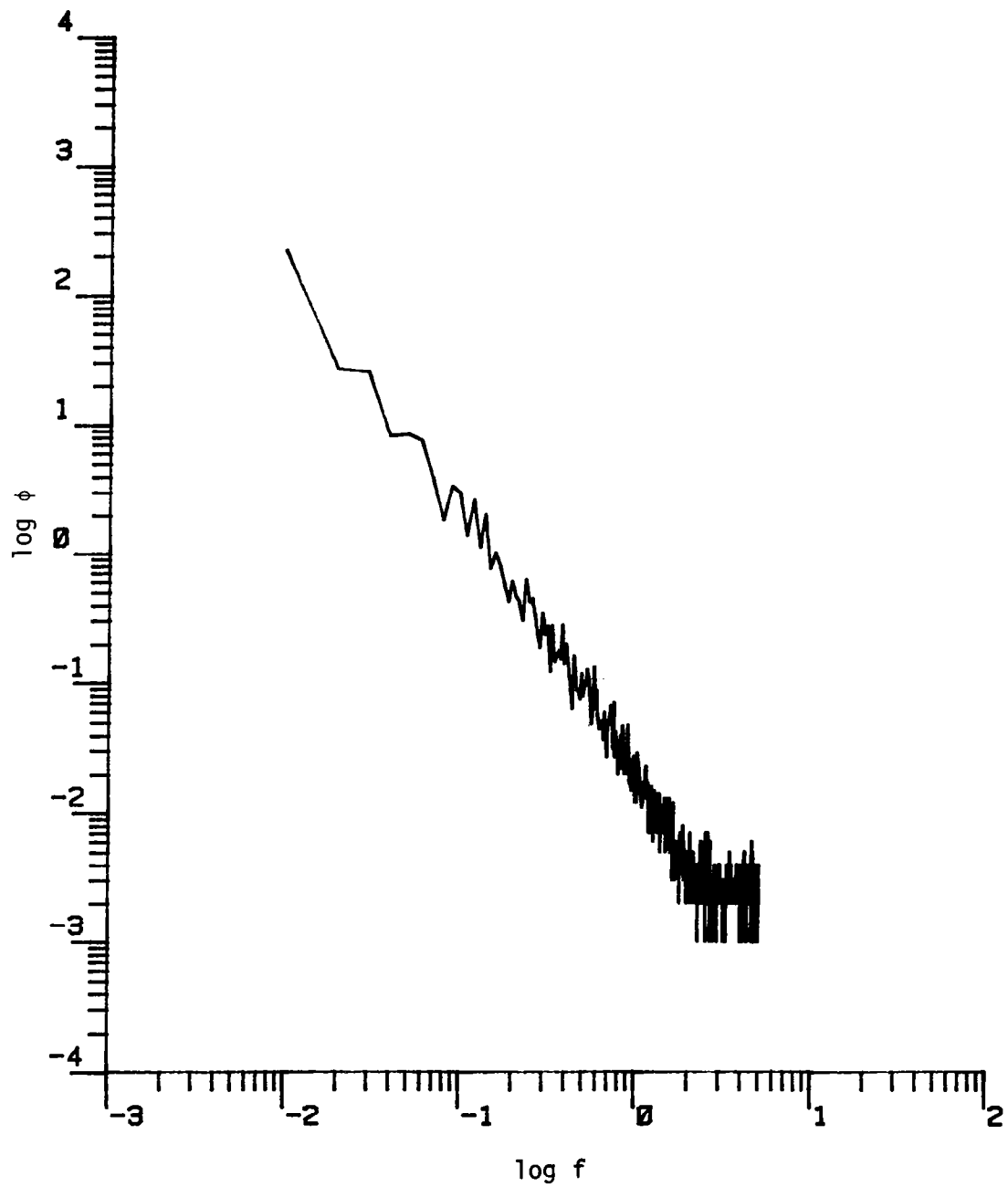Figure D.15.   The longitudinal power spectrum (Run #8623, T4L3,
Component 1).
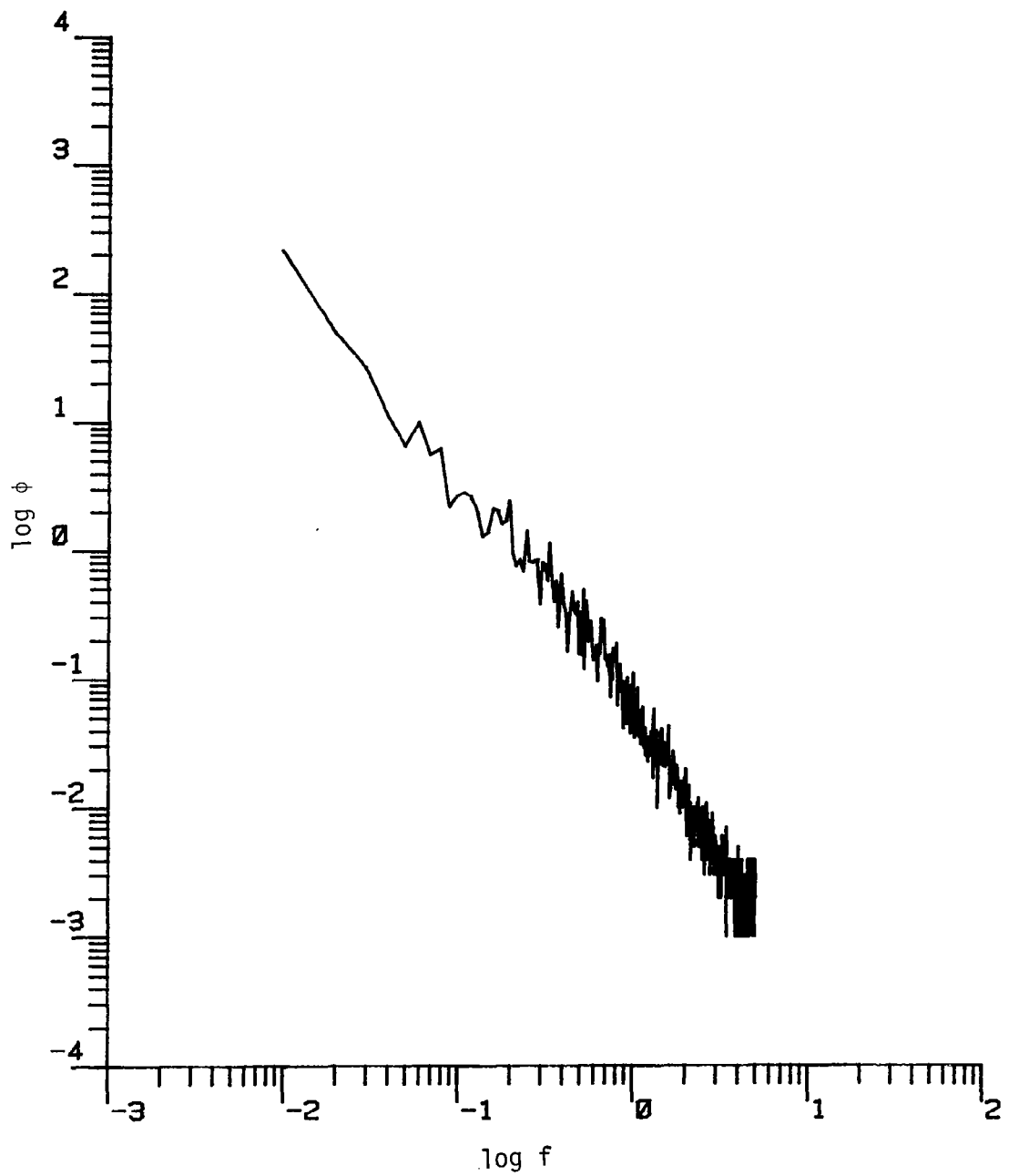
Figure D.16. The longitudinal power spectrum (Run #8623, T4L4, Component 1).
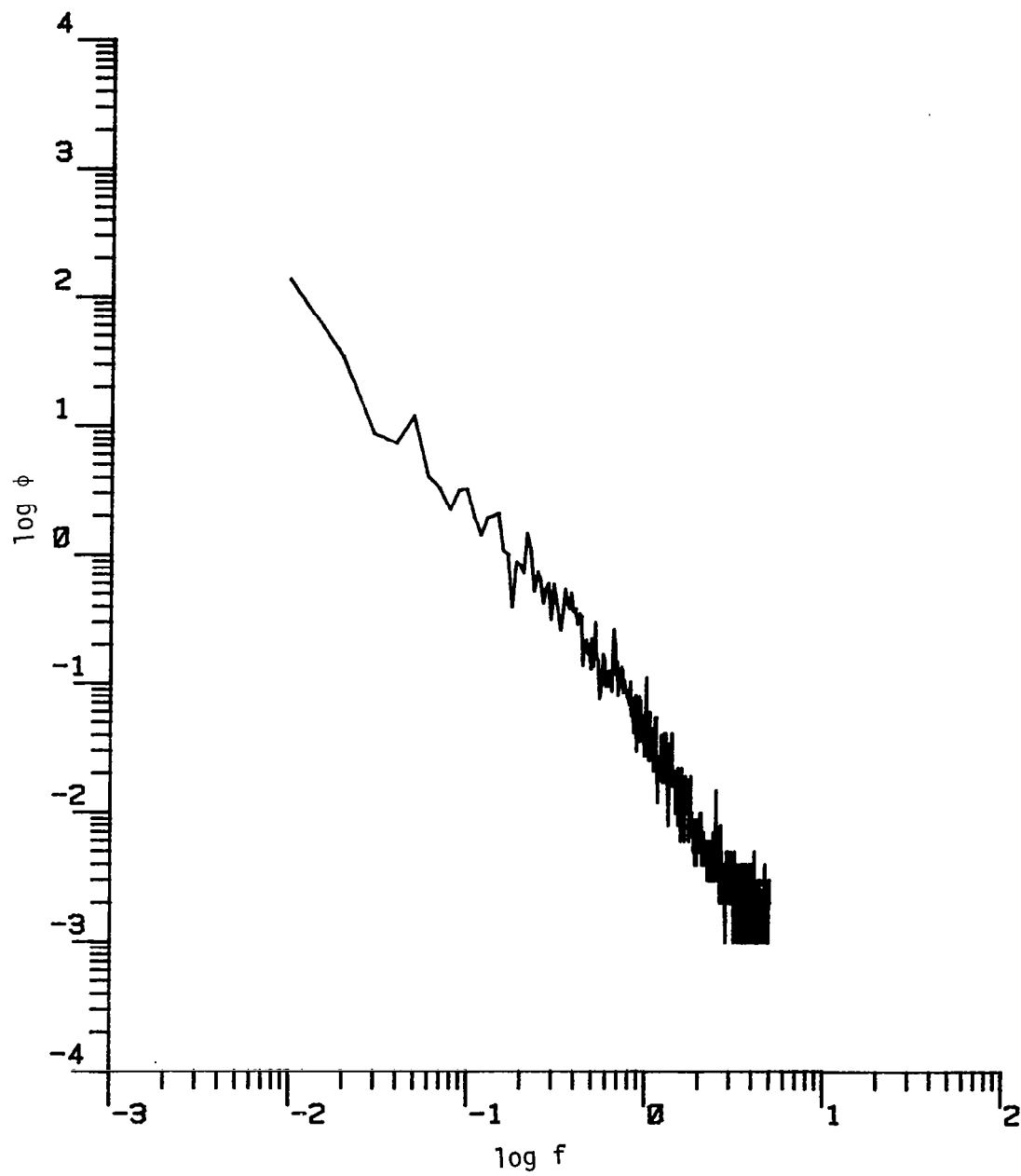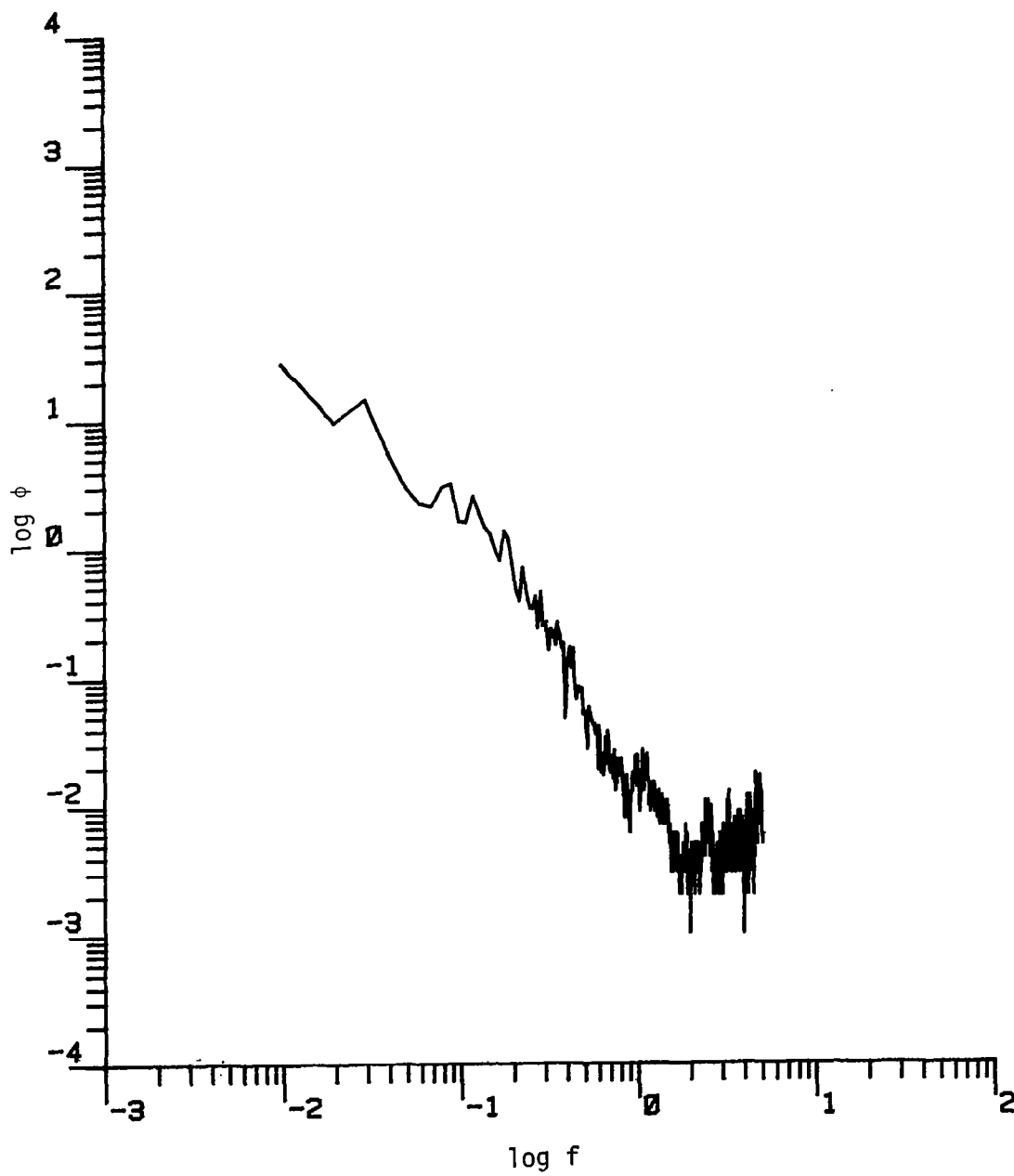
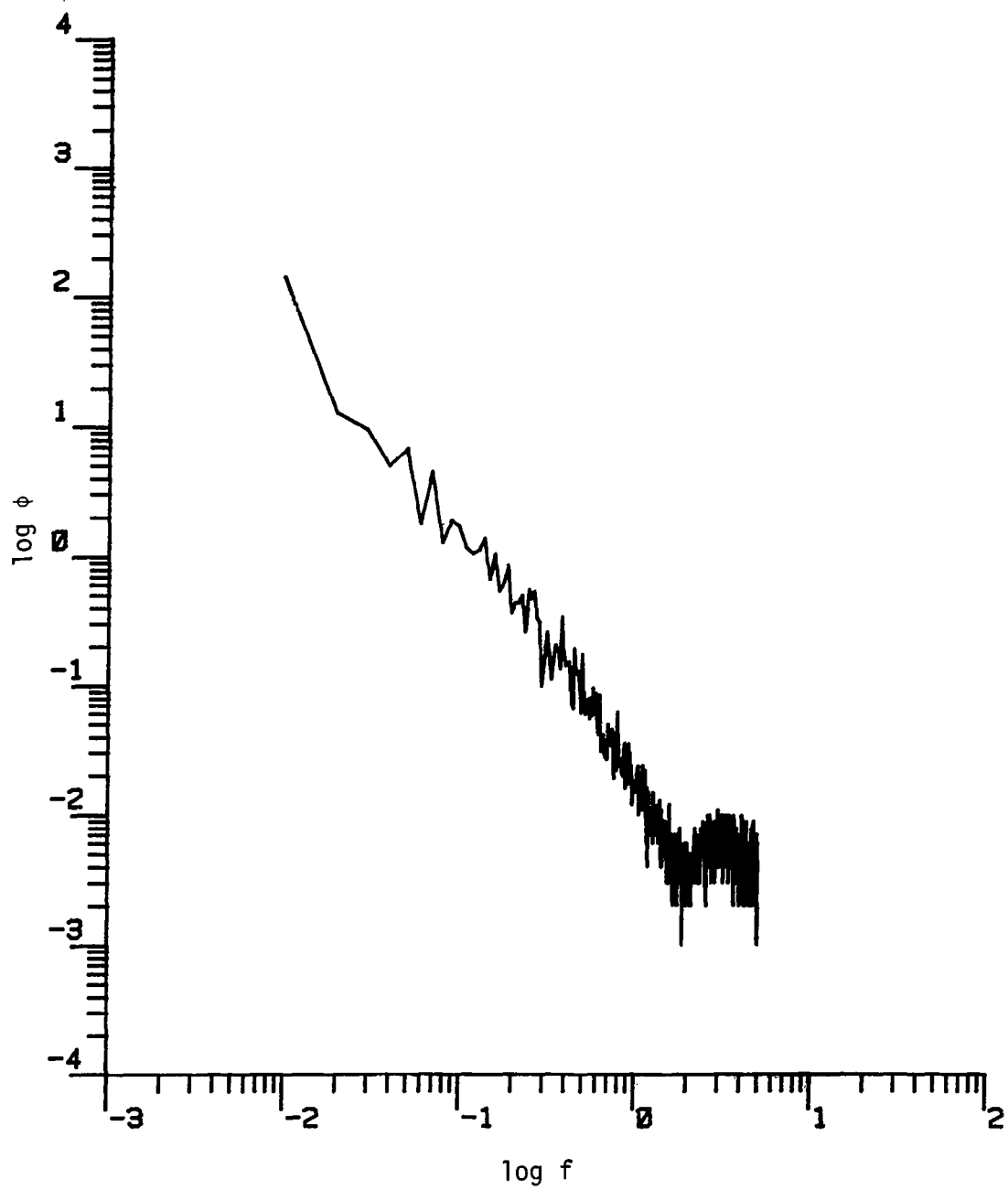Figure D.17. The longitudinal power spectrum (Run #8623, T5L1, Component 1).
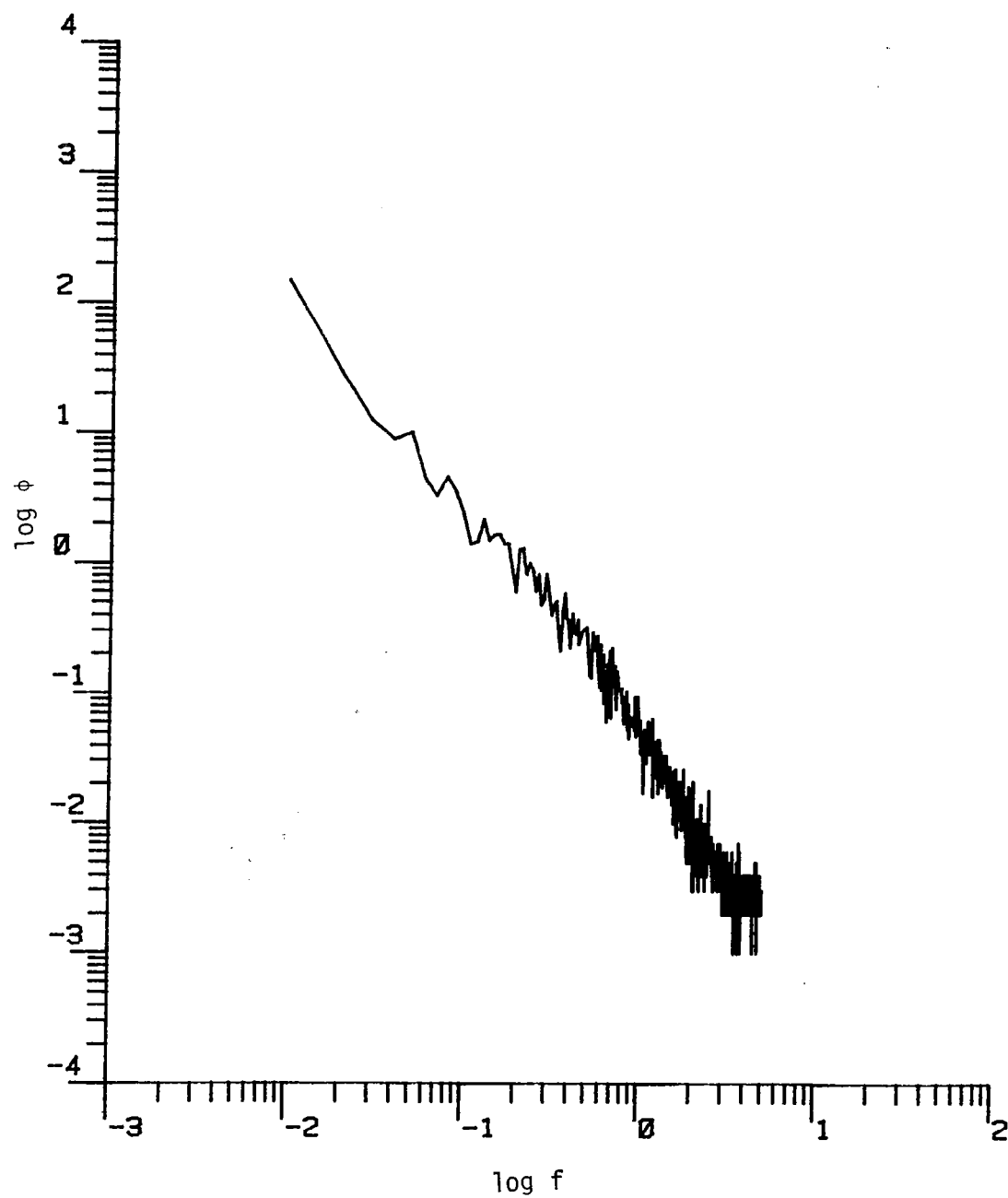
Figure D.18.   The longitudinal power spectrum (Run #8623, T5L2, Component 1).
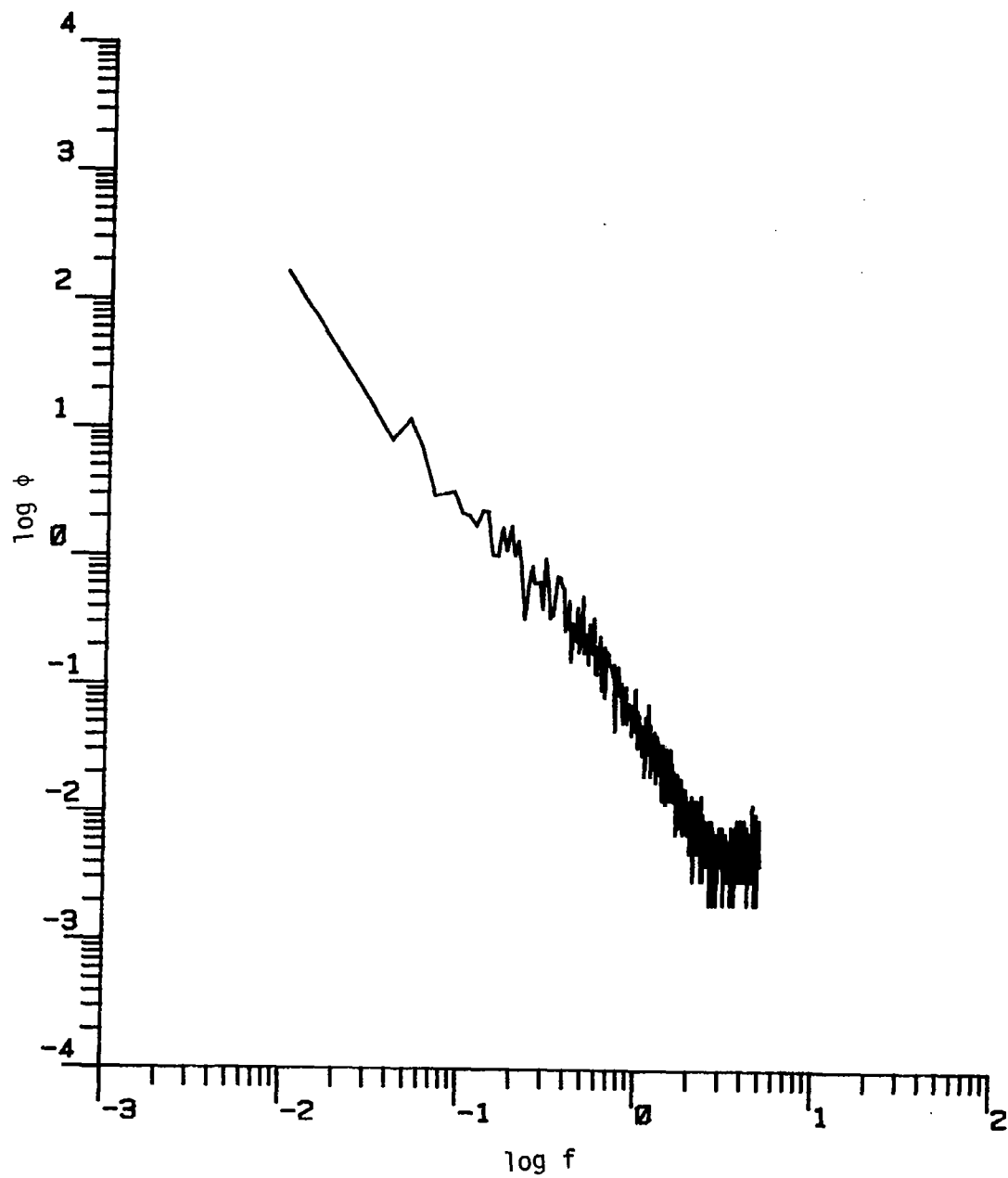
Figure D.19. The longitudinal power spectrum (Run #8623, T5L3, Component 1).

305
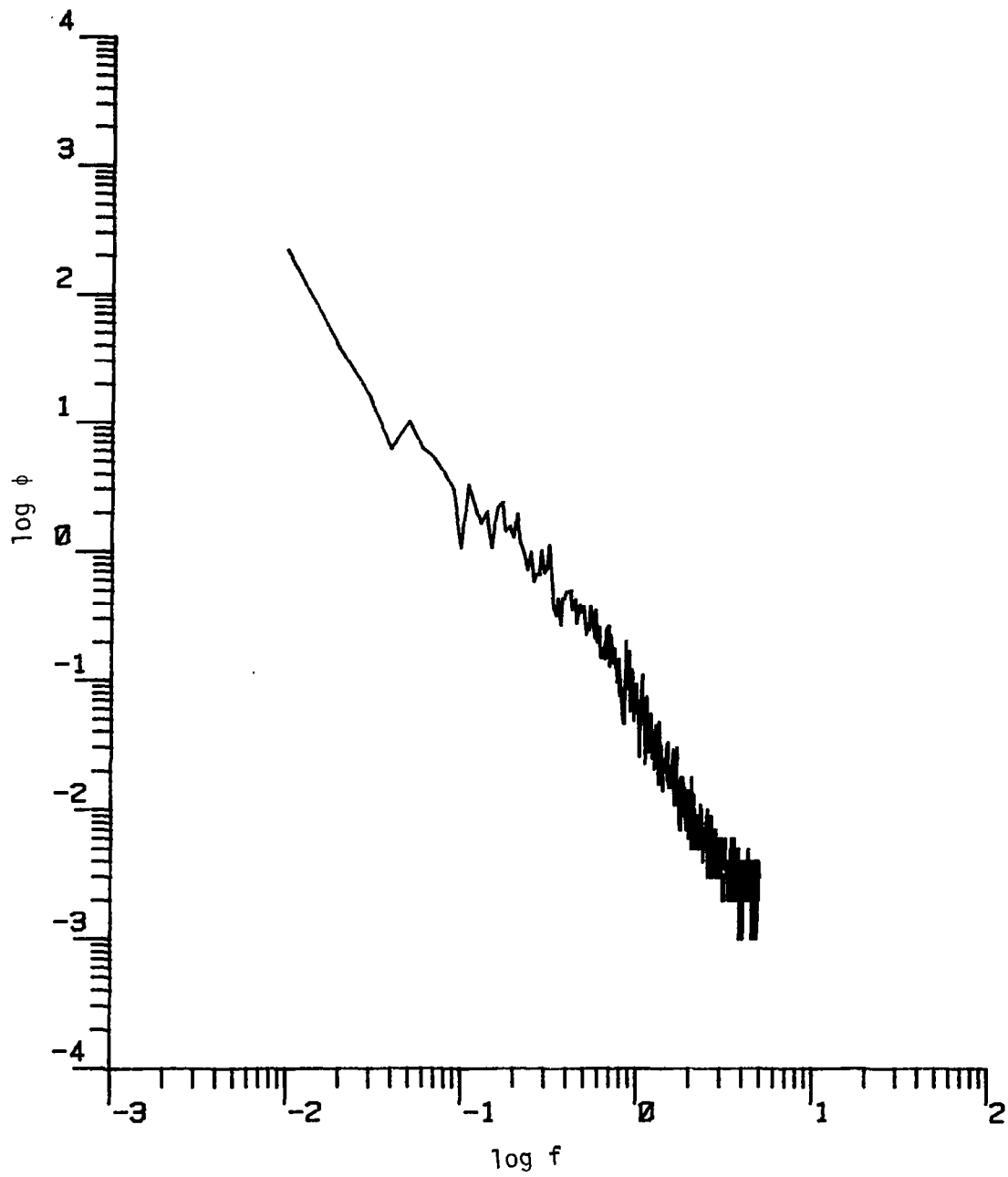
Figure D.20. The longitudinal power spectrum (Run #8623, T5L4, Component 1).

306
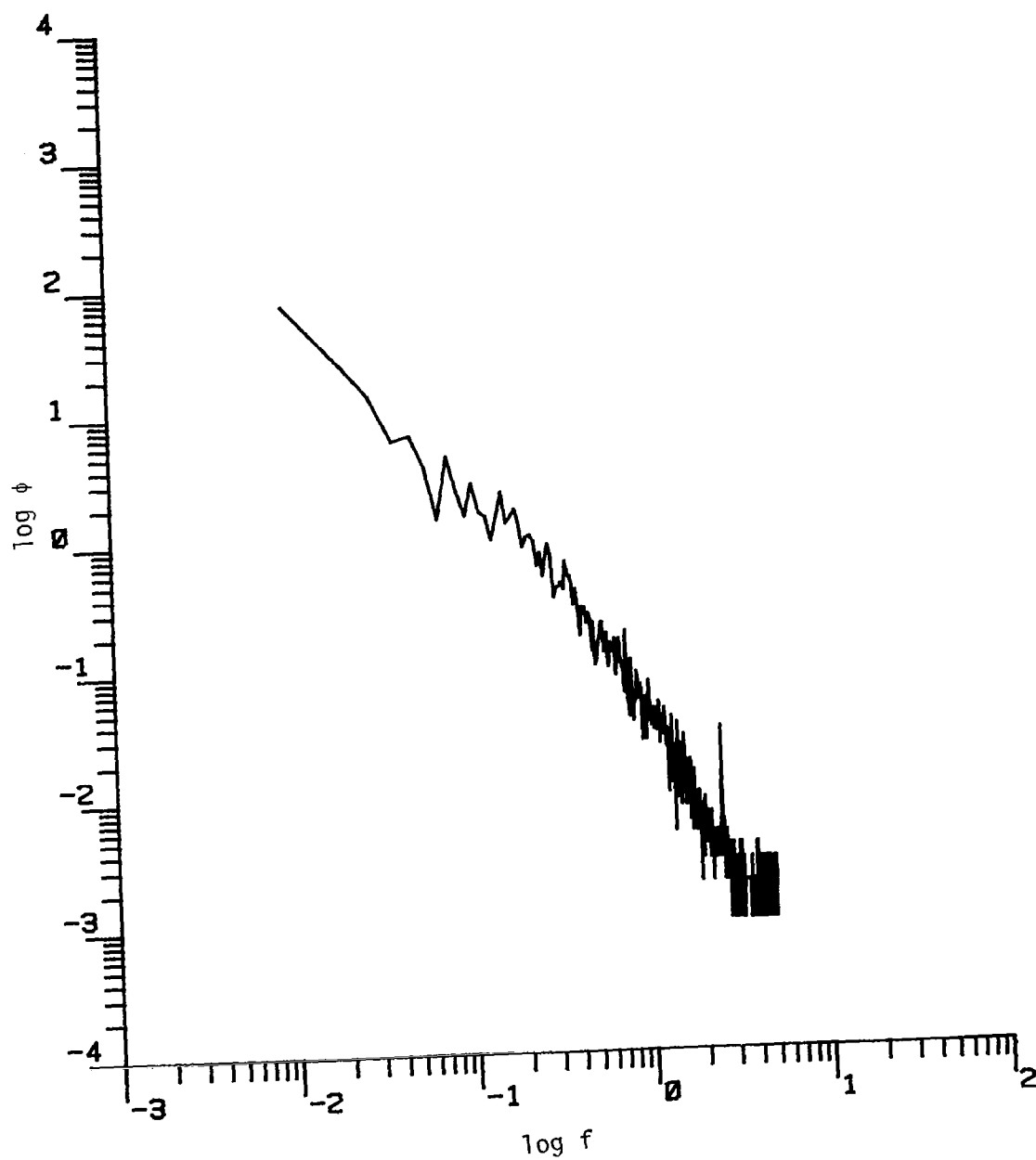
Figure D.21.   The longitudinal power spectrum (Run #8623, S1L1, Component 1).
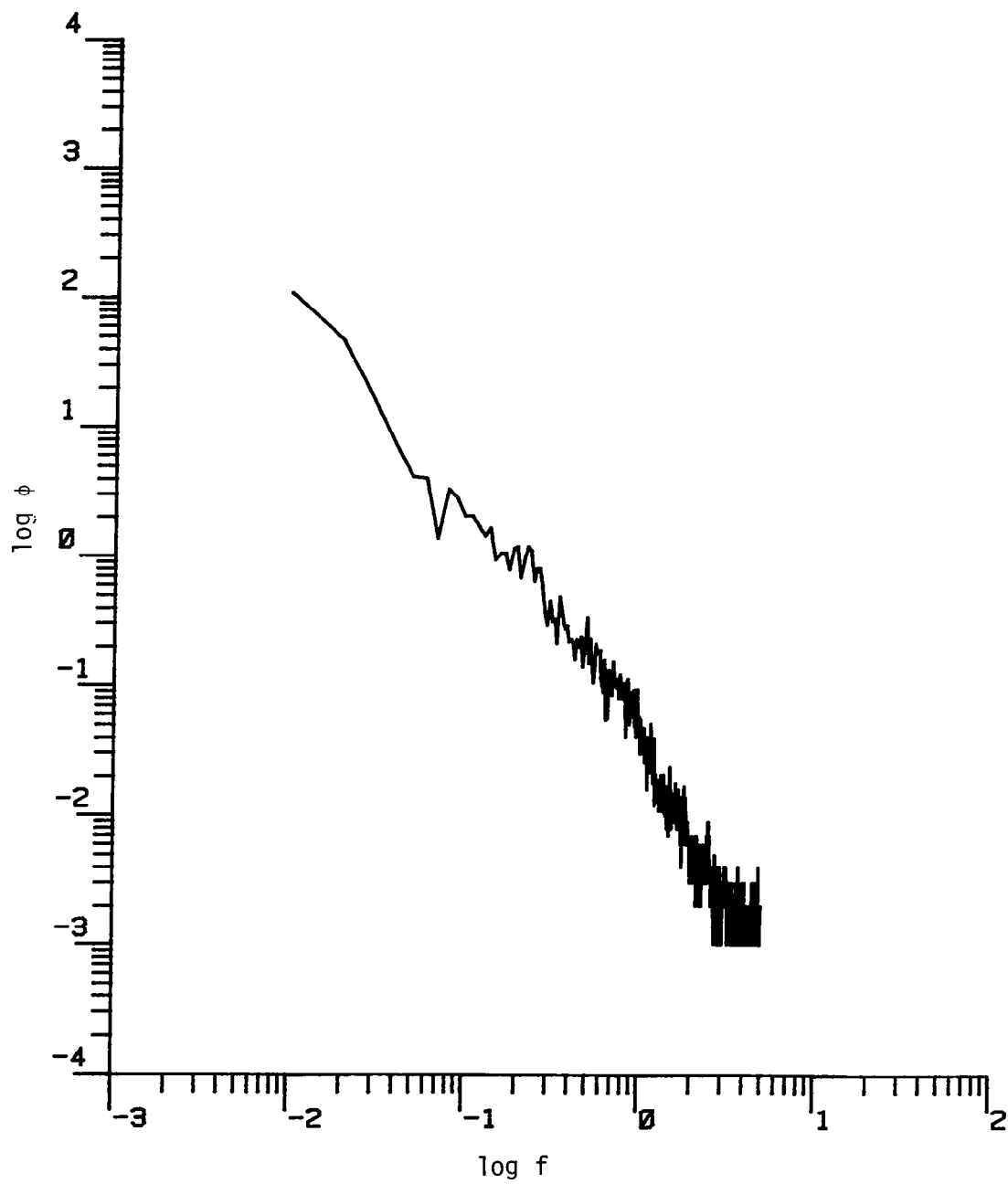
Figure D.22. The longitudinal power spectrum (Run #8623, S1L2, Component 1).
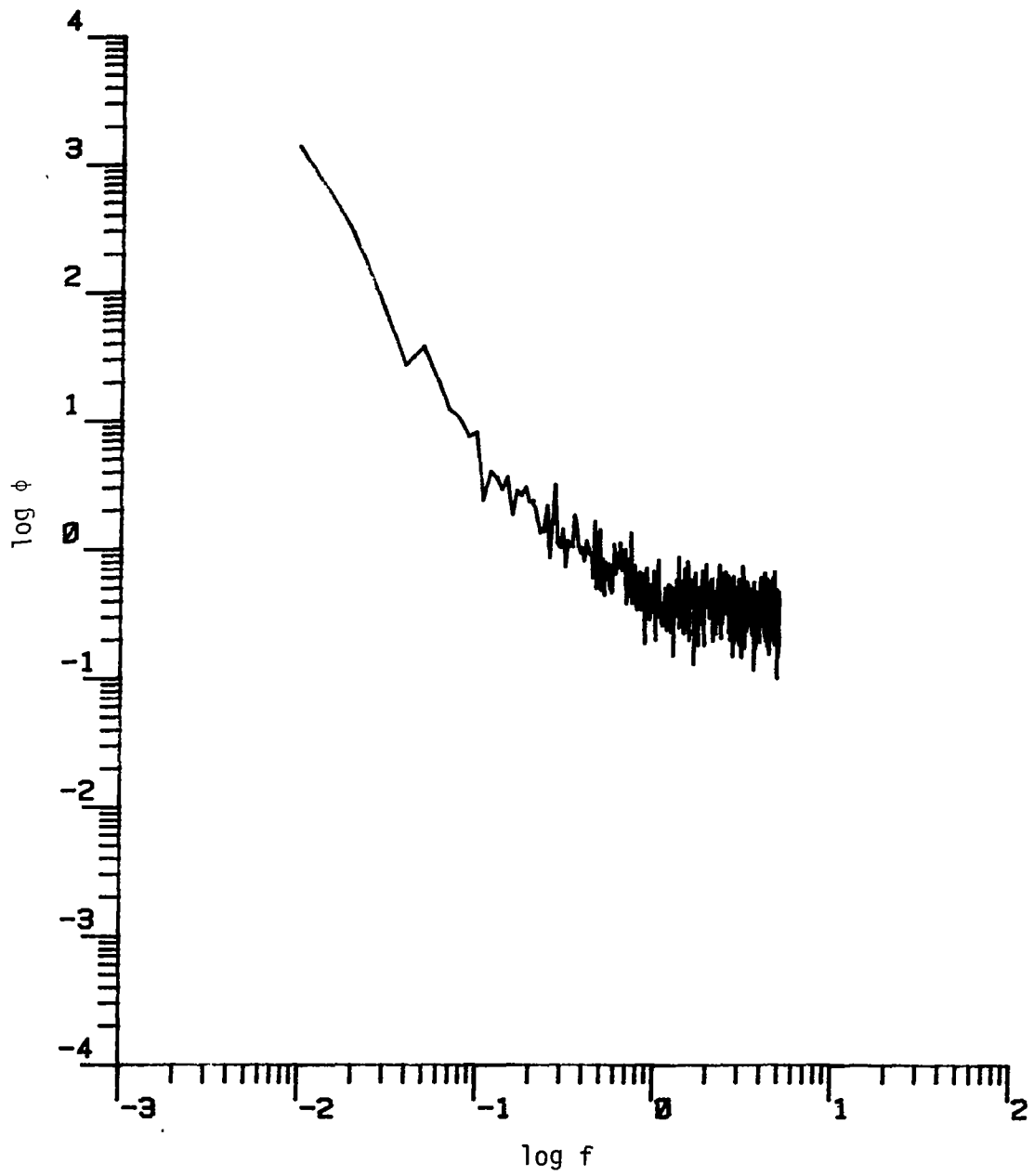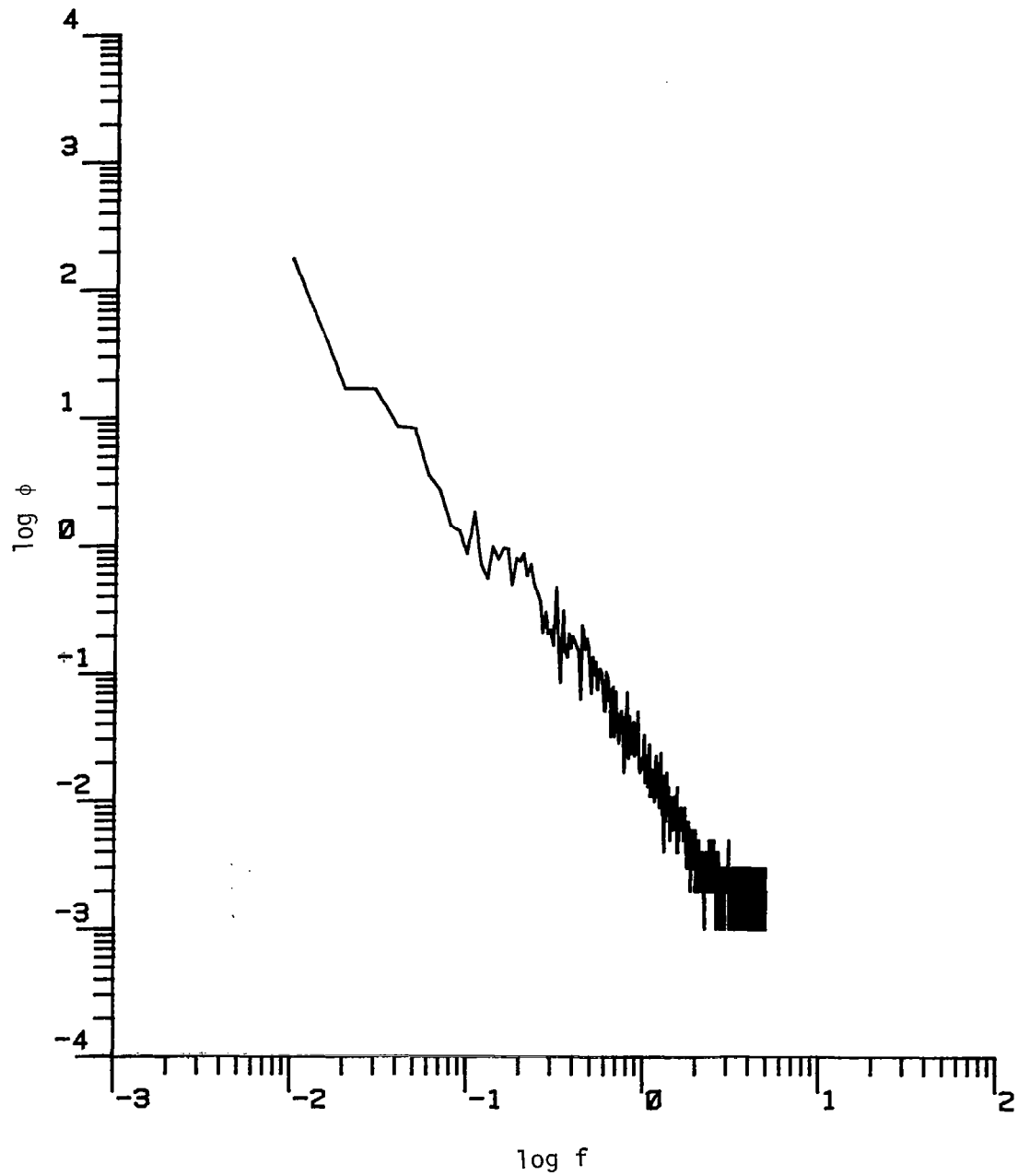
Figure D.23. The longitudinal power spectrum (Run #8623, S1L3, Component 1).
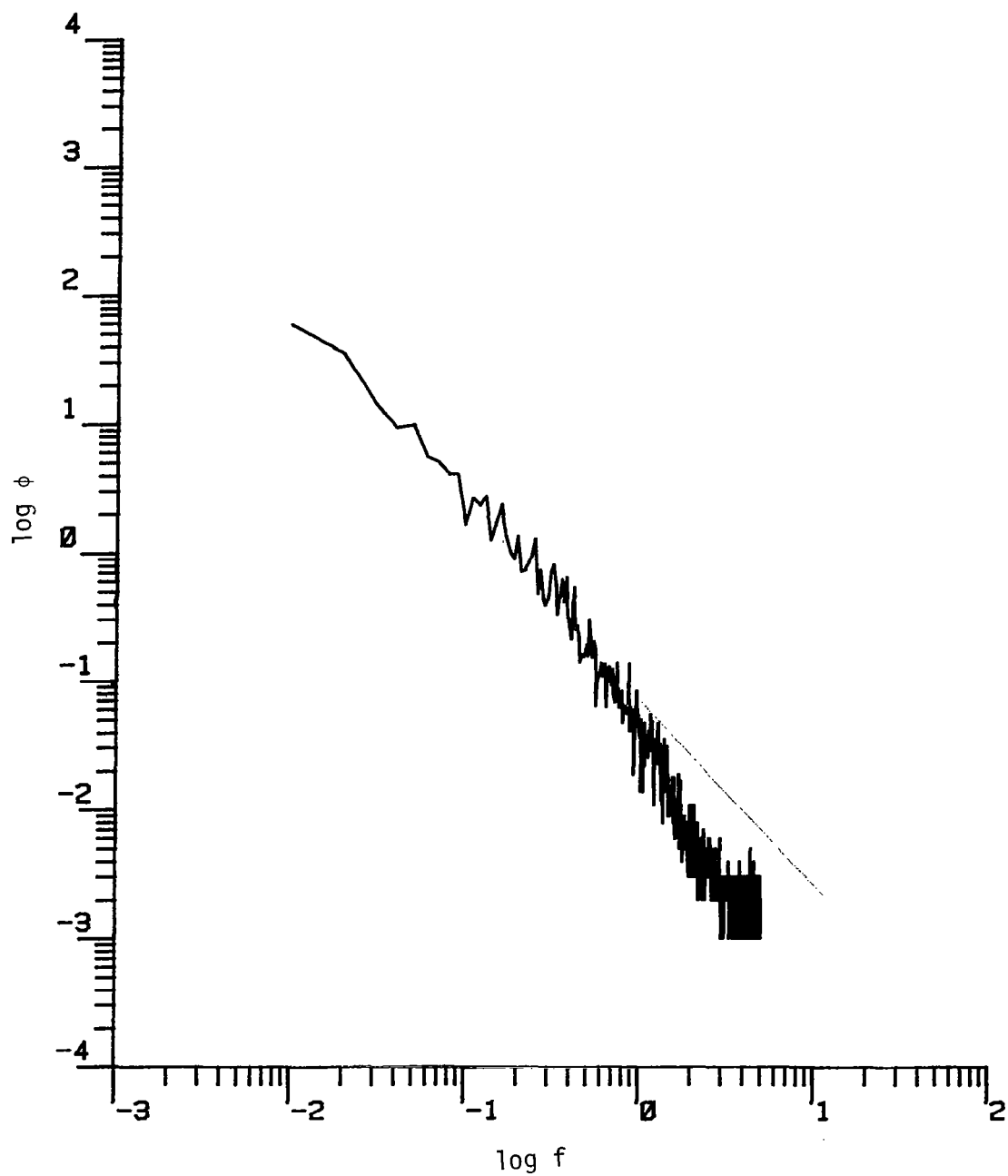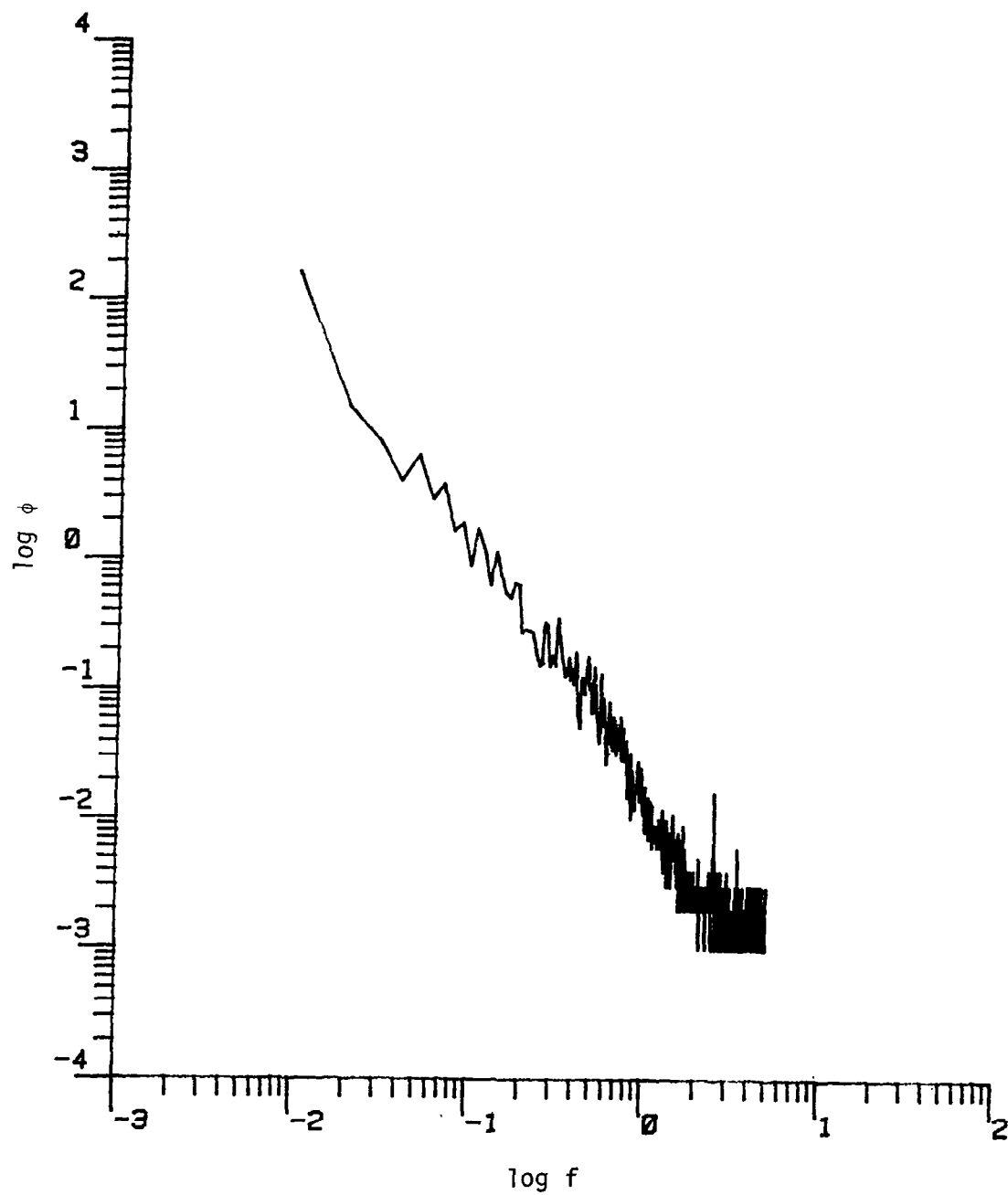
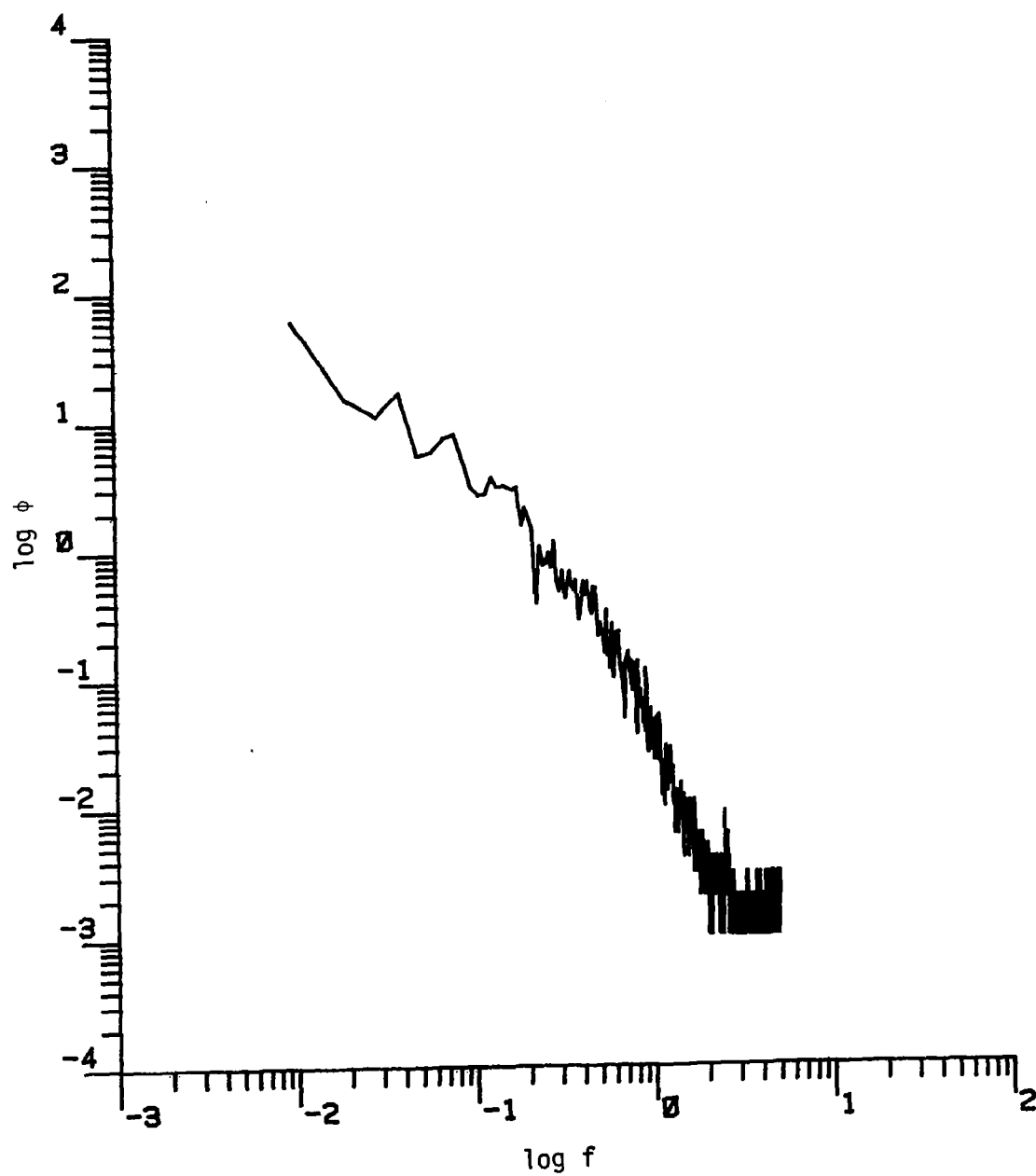Figure D.24. The longitudinal power spectrum (Run #8623, S2L1, Component 1).
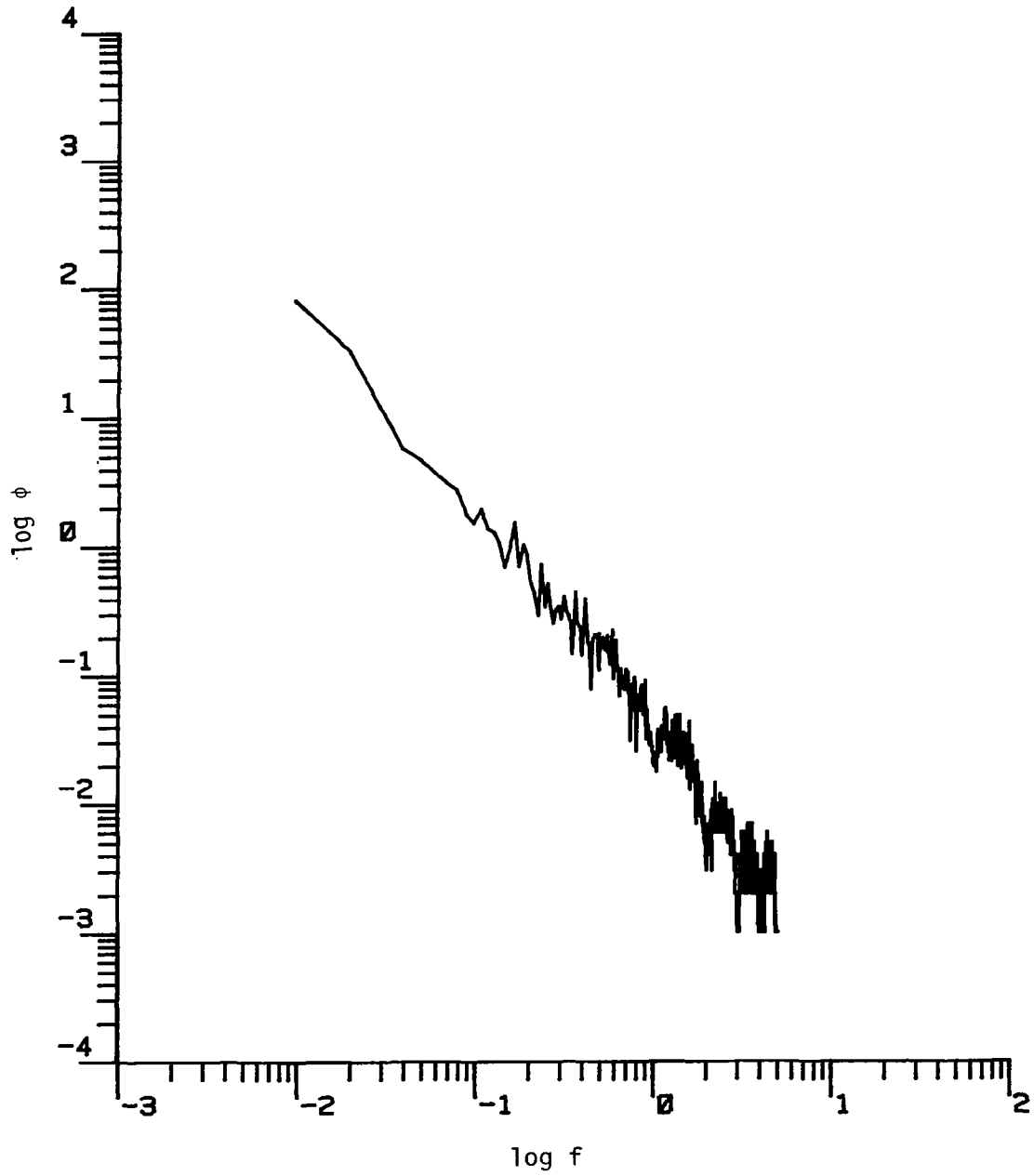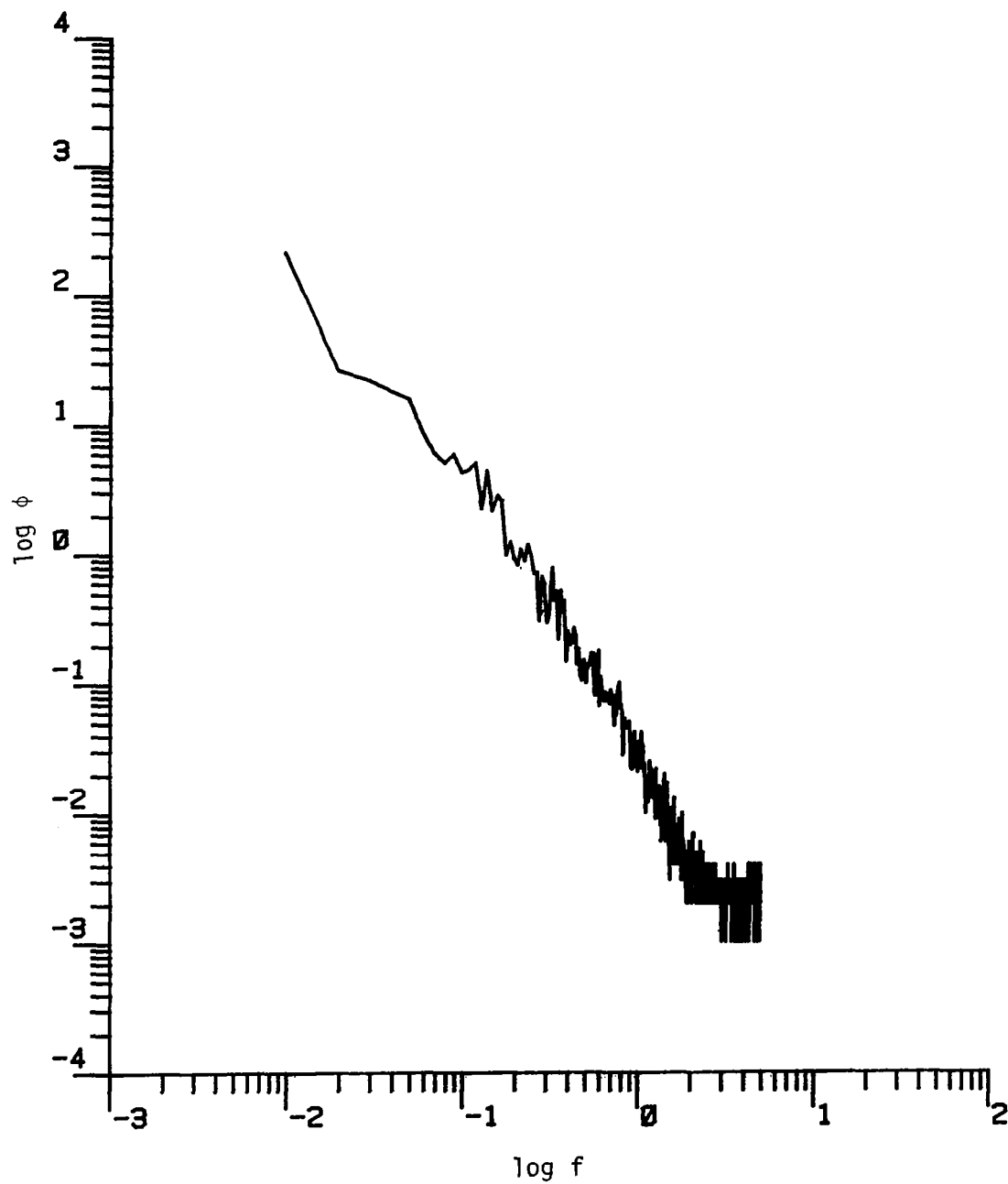
Figure D.25.   The longitudinal power spectrum (Run #8623, S2L2, Component 1).
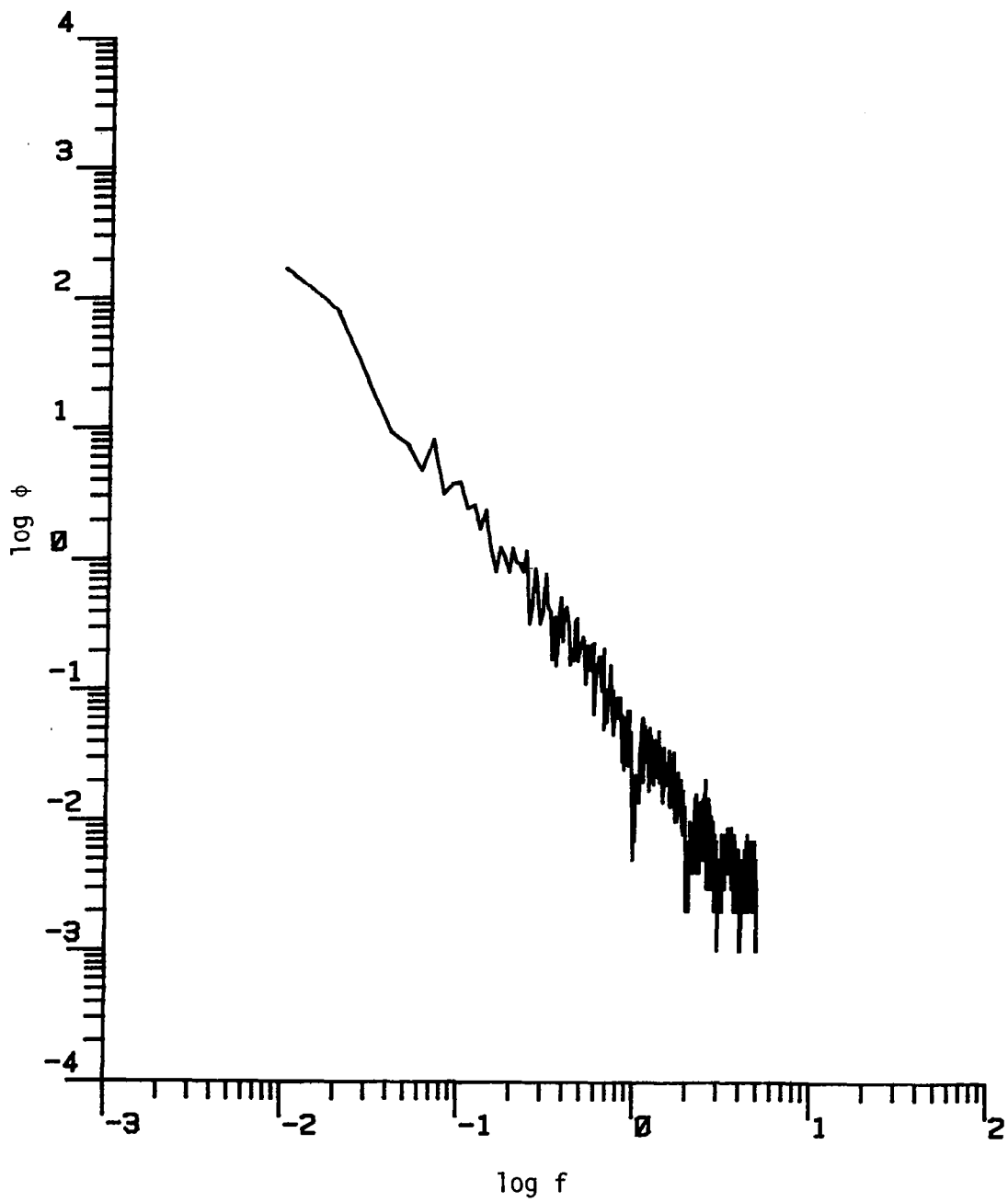
Figure D.26. The longitudinal power spectrum (Run #8623, S2L3, Component 1).
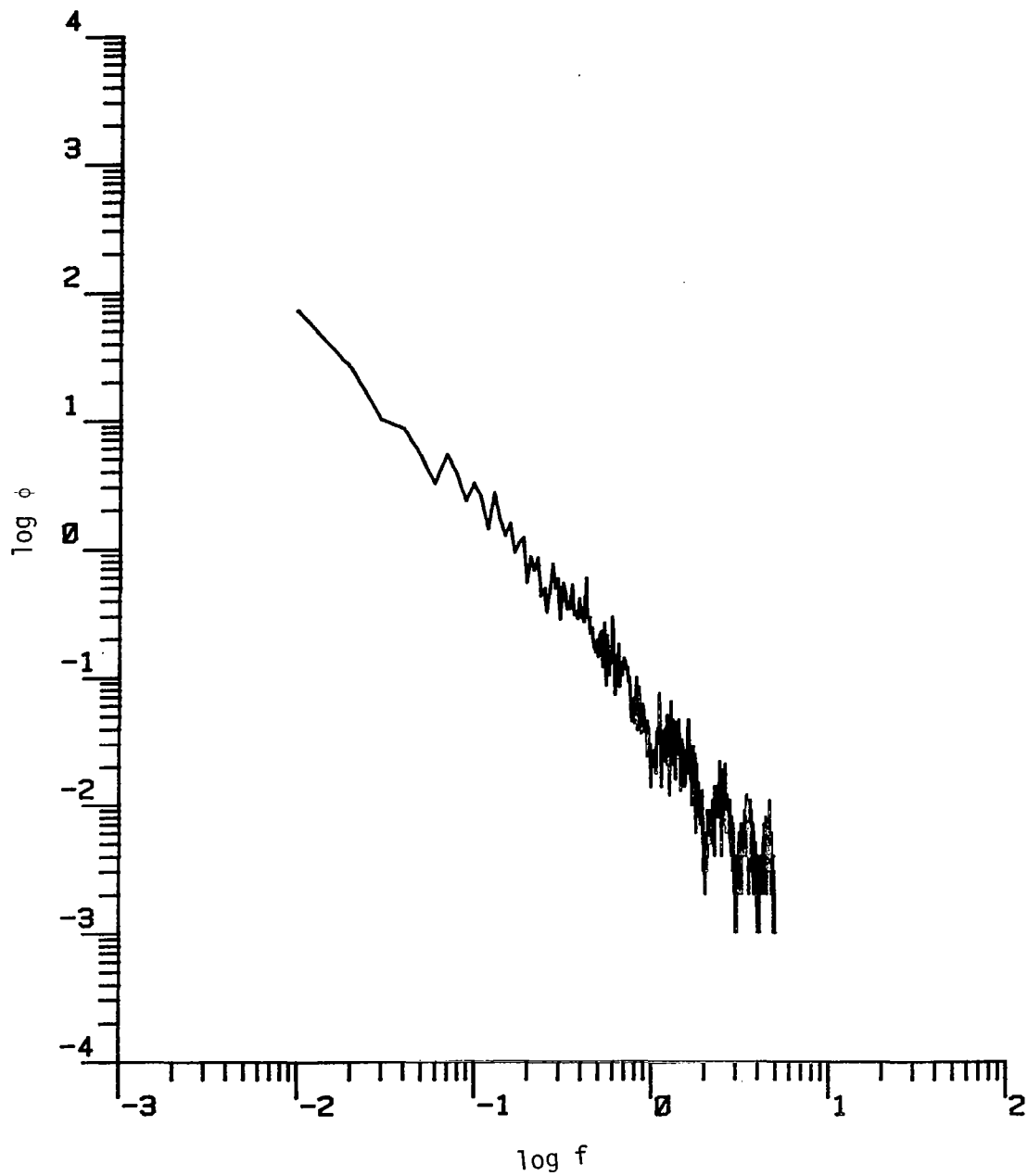
Figure D.27. The longitudinal power spectrum (Run #8623, S3L1, Component 1).
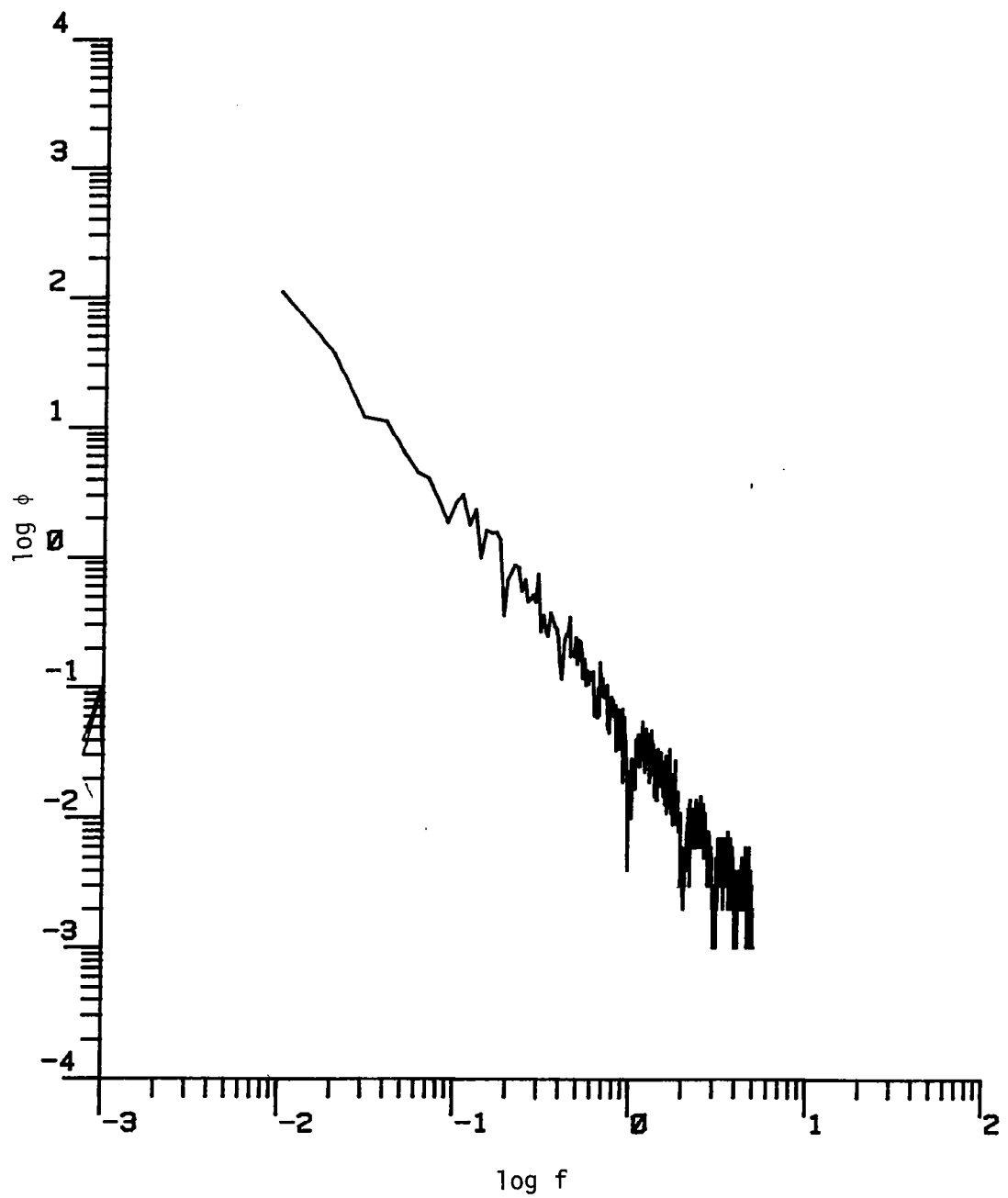
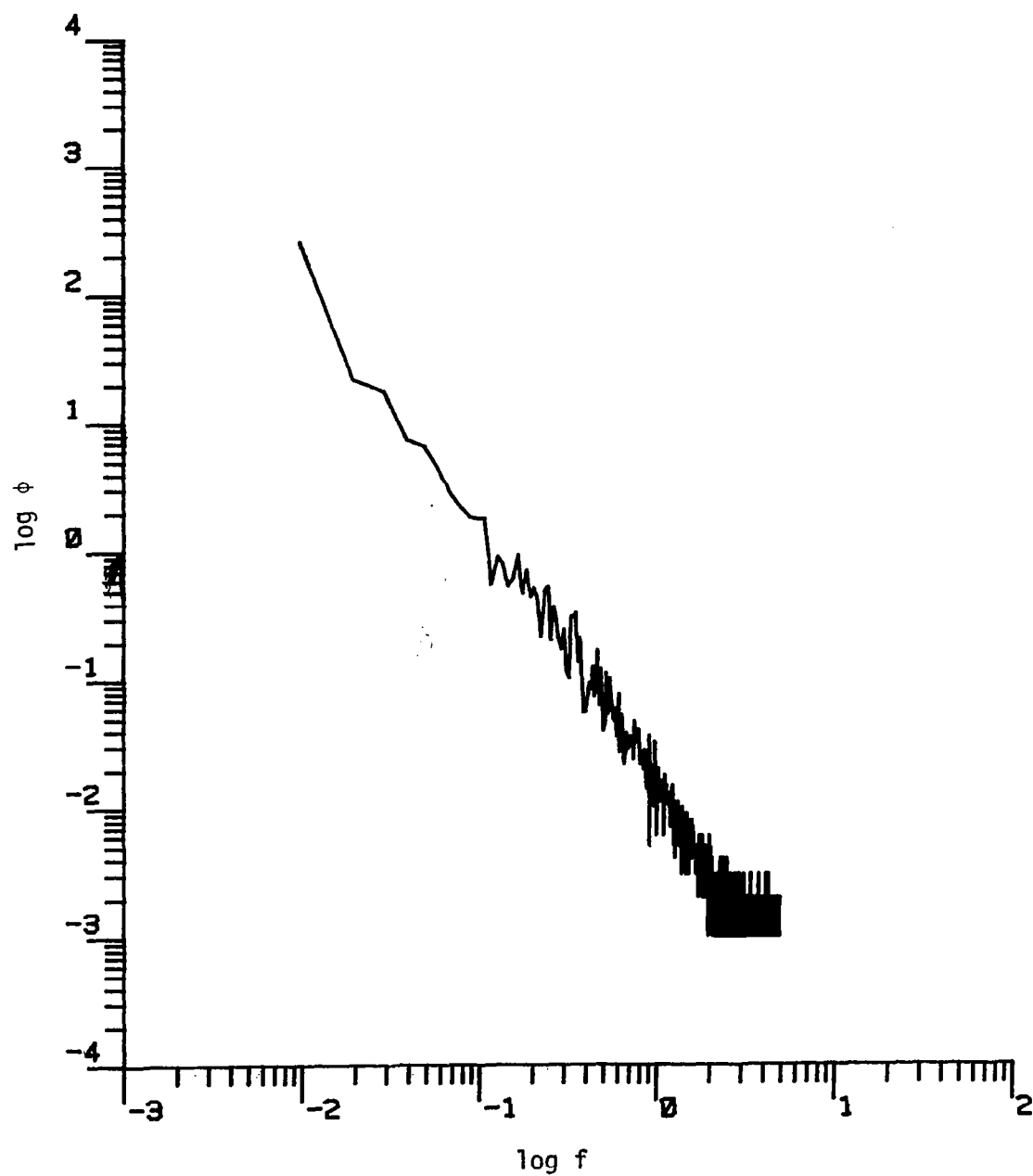Figure D.28. The longitudinal power spectrum (Run #8623, S3L2, Component 1).
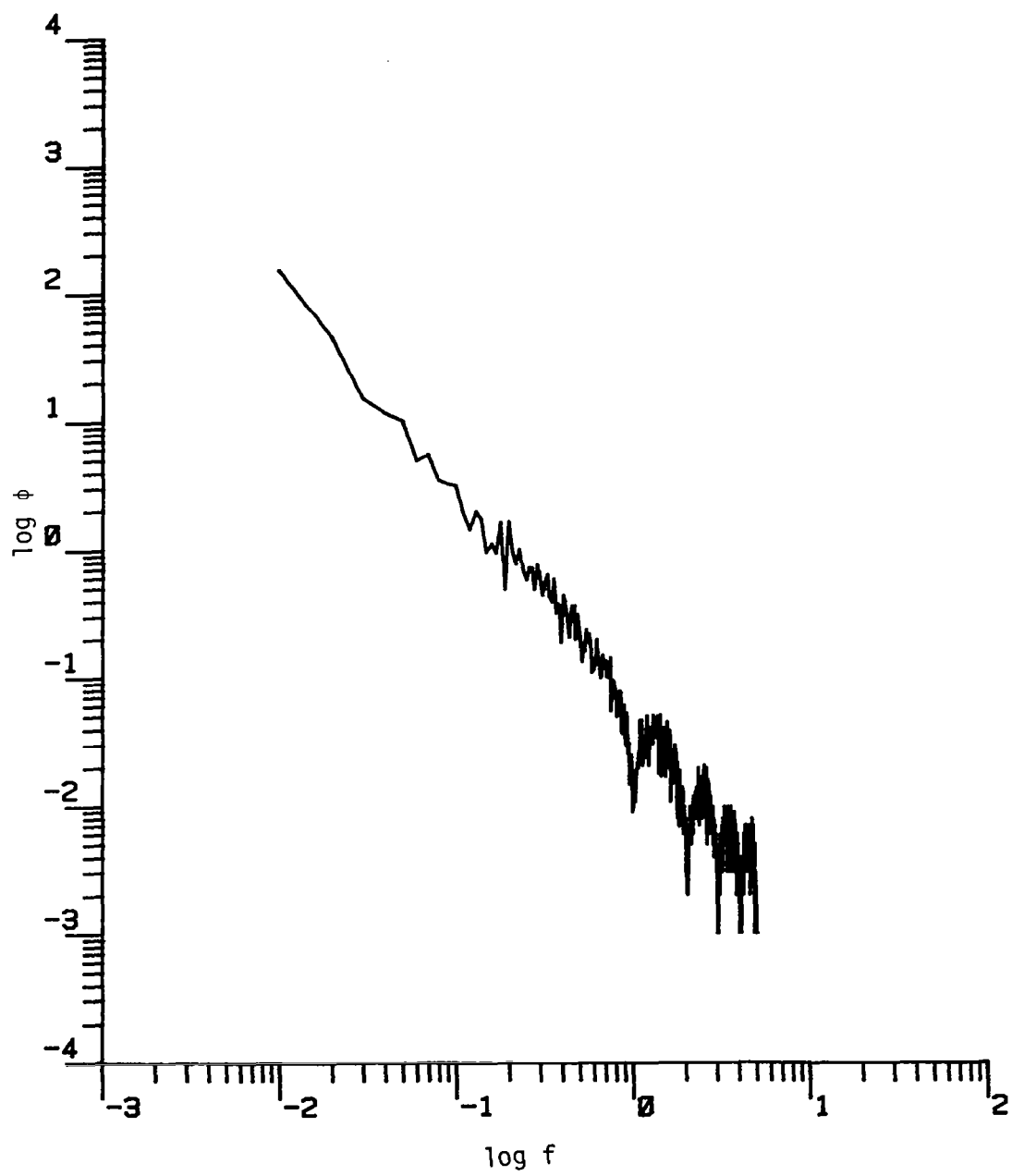
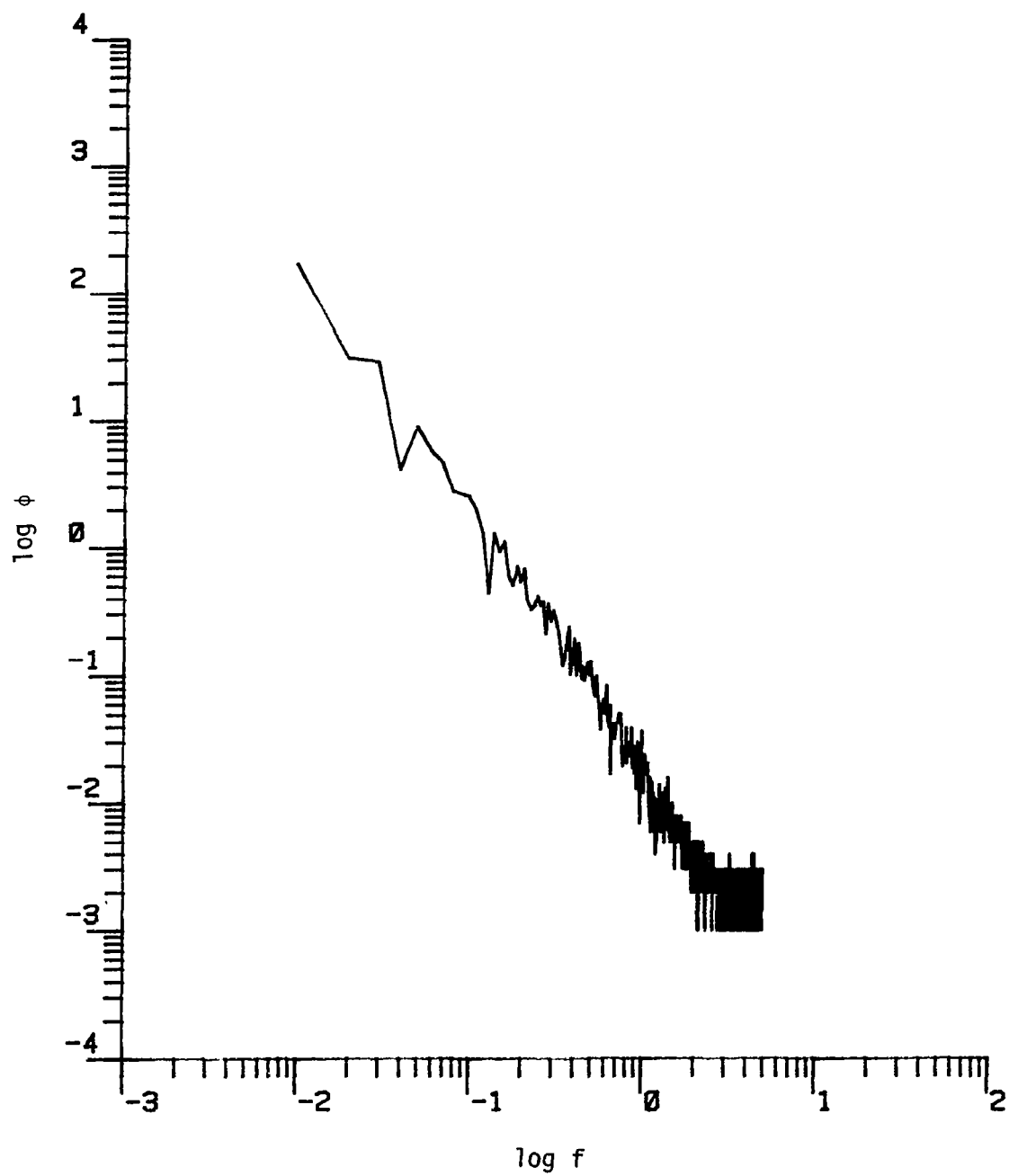Figure D.29. The longitudinal power spectrum (Run #8623, S3L3, Component 1).
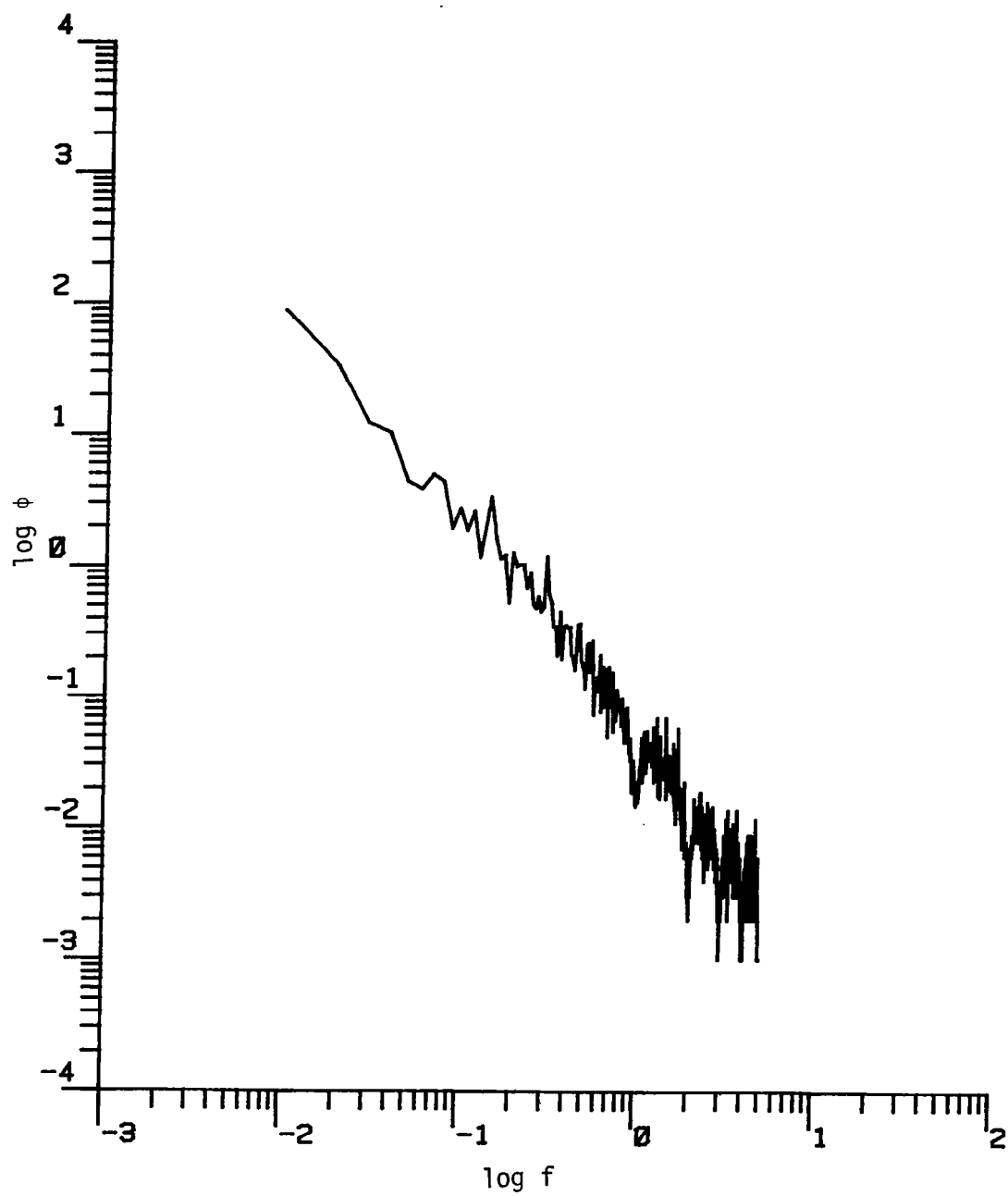
Figure D.30. The longitudinal power spectrum (Run #8623, S4L1, Component 1).
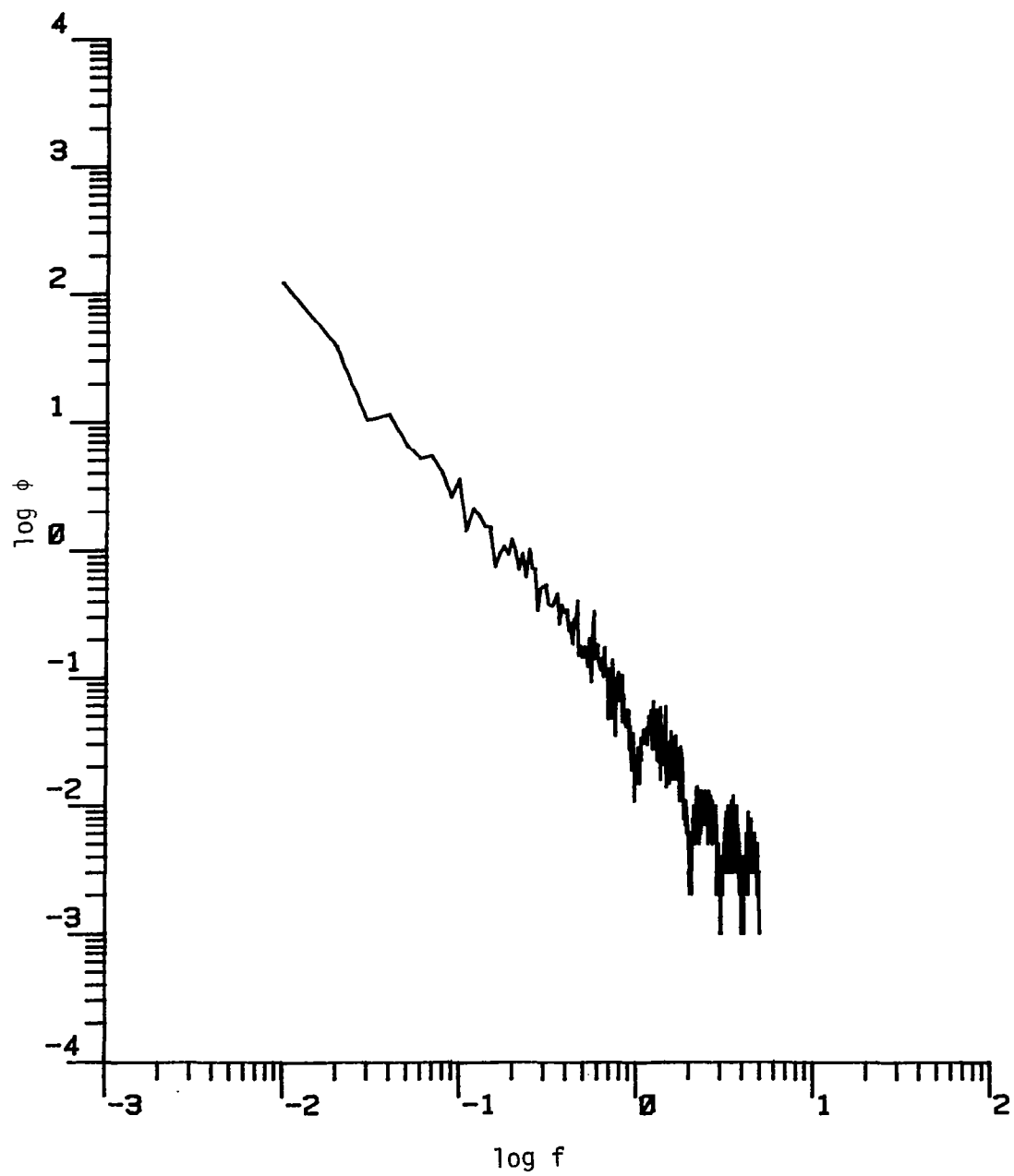
Figure D.31. The longitudinal power spectrum (Run #8623, S4L2, Component 1).
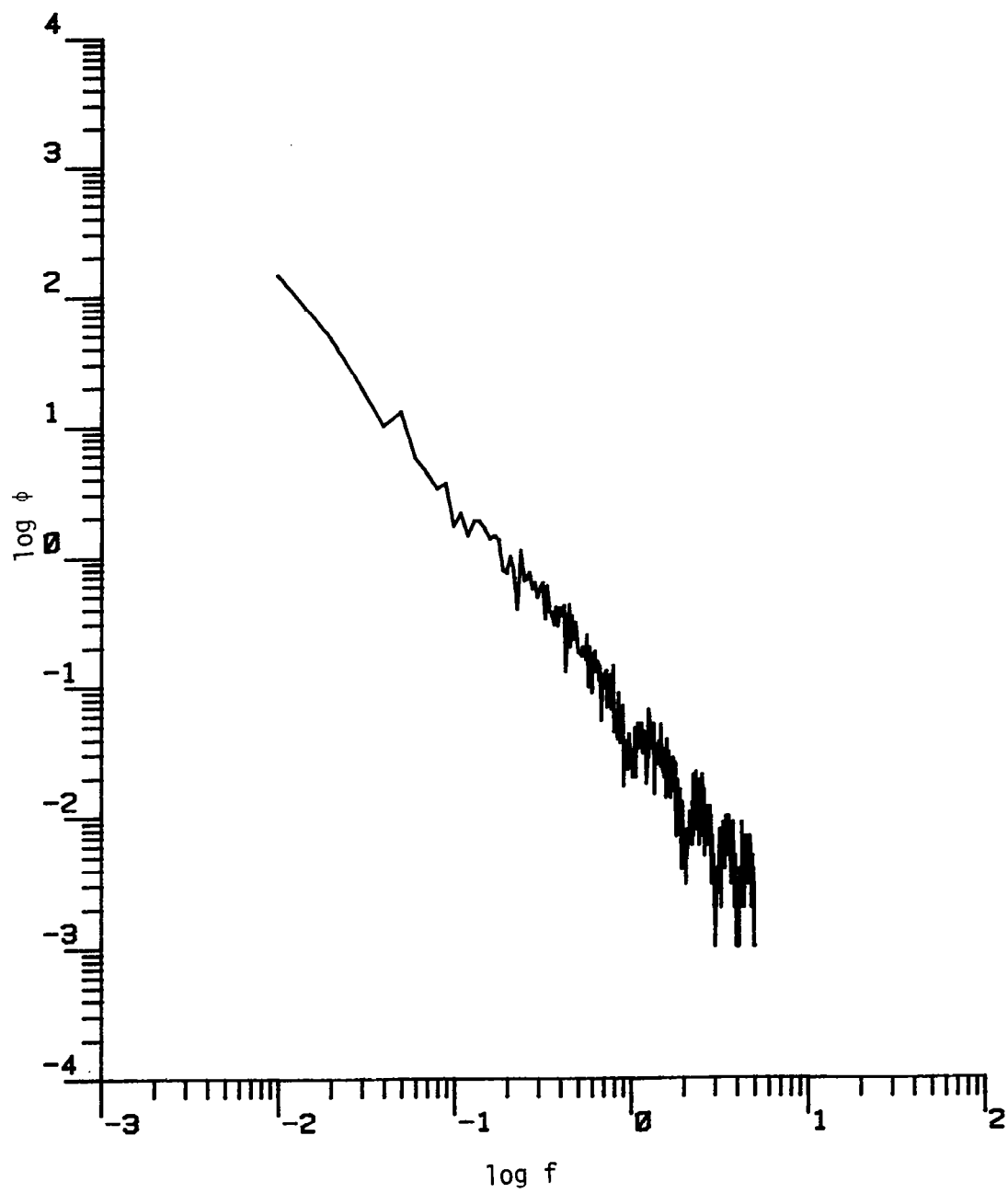
Figure D.32.   The longitudinal power spectrum (Run #8623, S4L3, Component 1).

Figure D.33.   The longitudinal power spectrum (Run #8624, T1L1, Component 1).

Figure D.34.   The longitudinal power spectrum (Run #8624, T1L2, Component 1).

Figure D.35.   The longitudinal power spectrum (Run #8624, T1L3, Component 1).

Figure D.36. The longitudinal power spectrum (Run #8624, T1L4, Component 1).
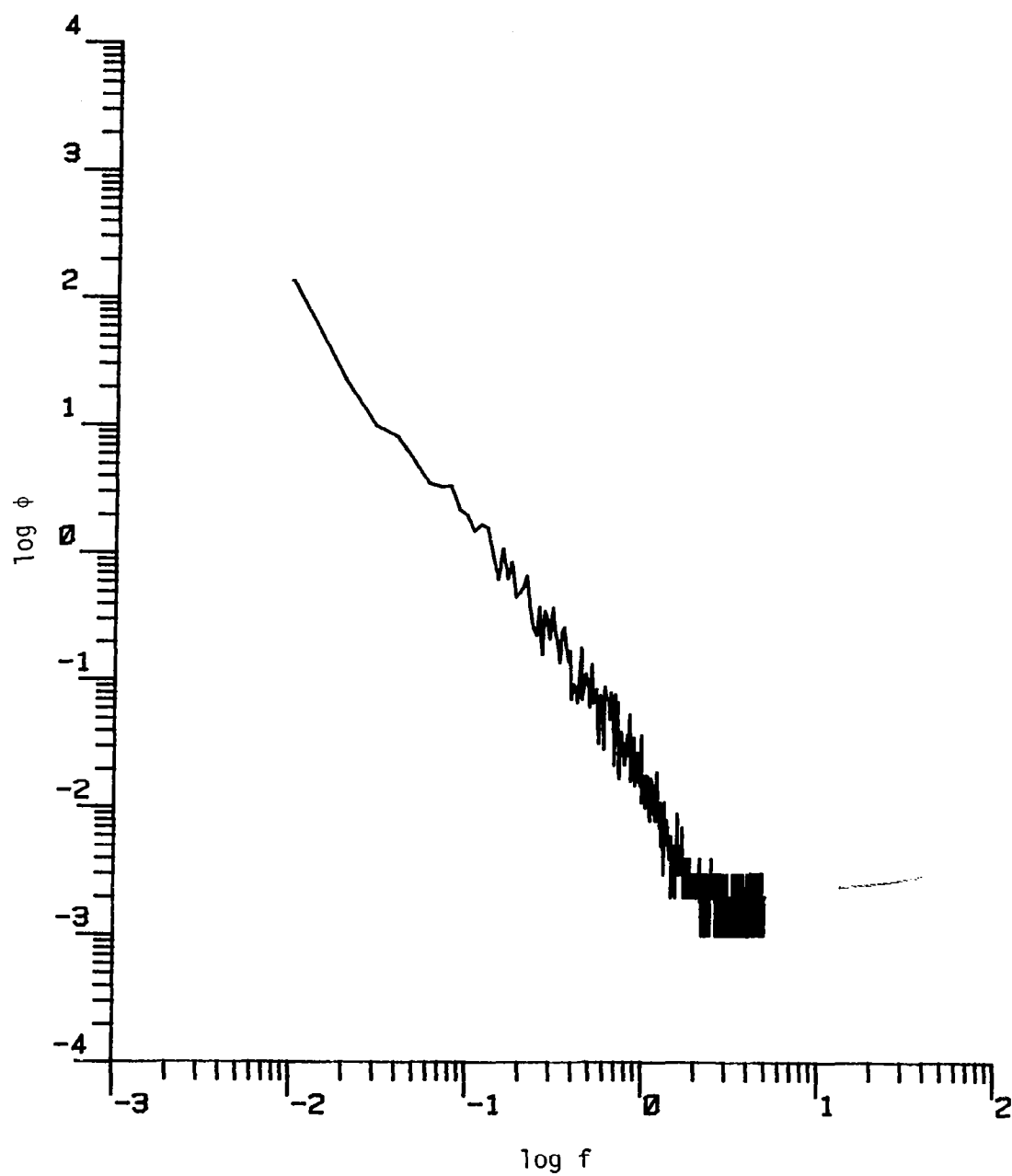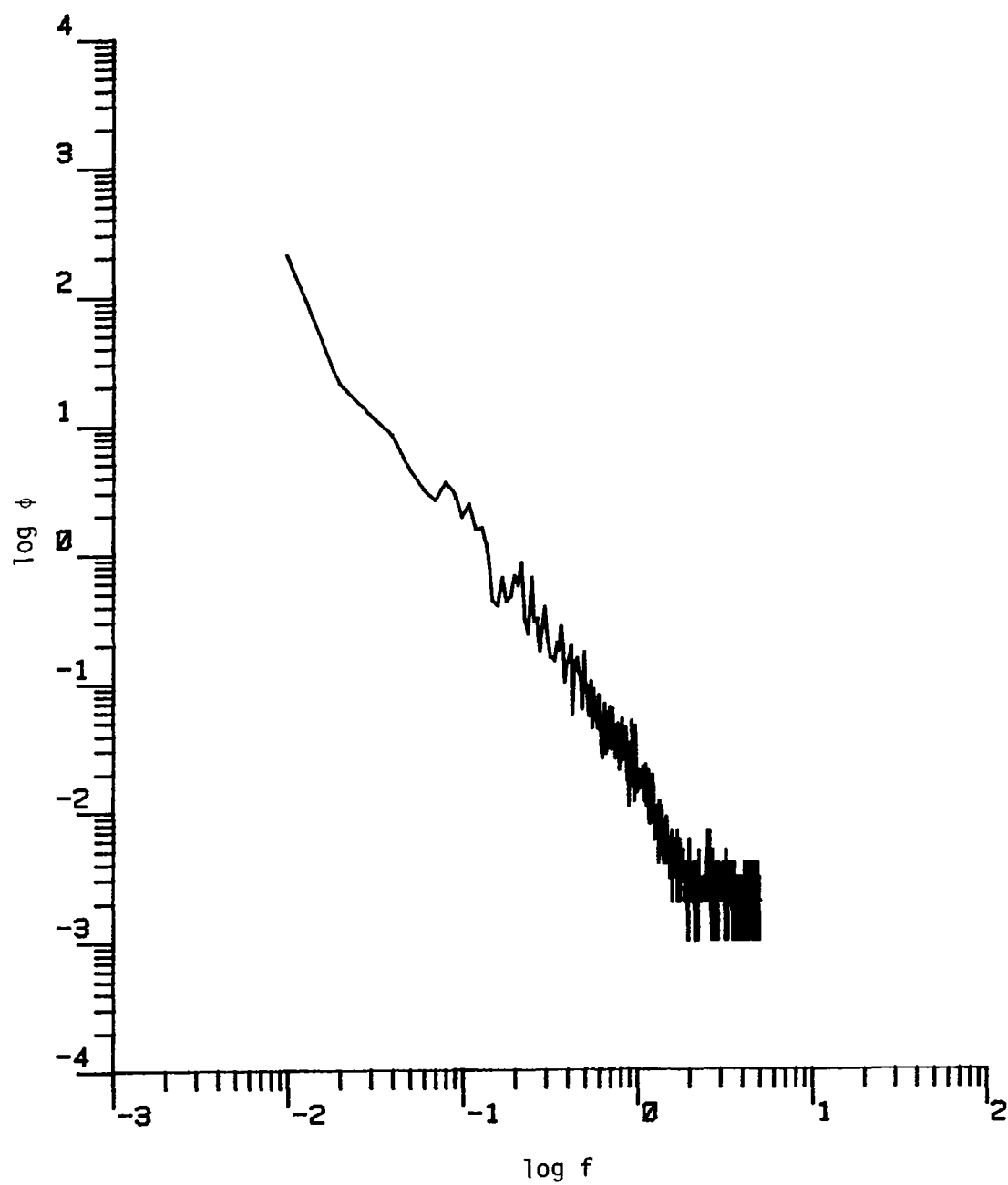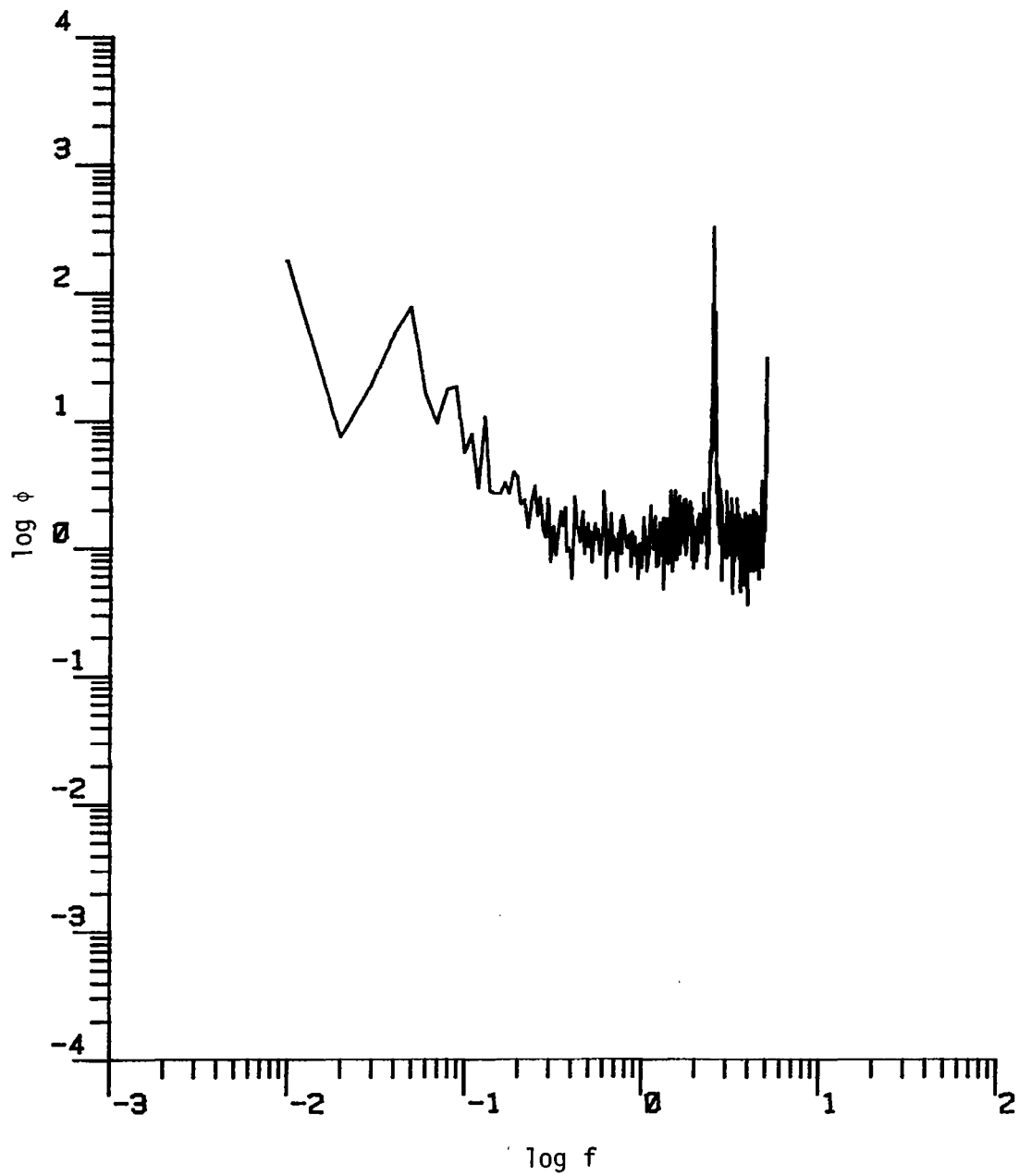
322

Figure D.37.   The longitudinal power spectrum (Run #8624, T2L1, Component 1).

Figure D.38. The longitudinal power spectrum (Run #8624, T2L2, Component 1).

324

Figure D.39. The longitudinal power spectrum (Run #8624, T2L3, Component 1).

Figure D.40.   The longitudinal power spectrum (Run #8624, T2L4, Component 1).

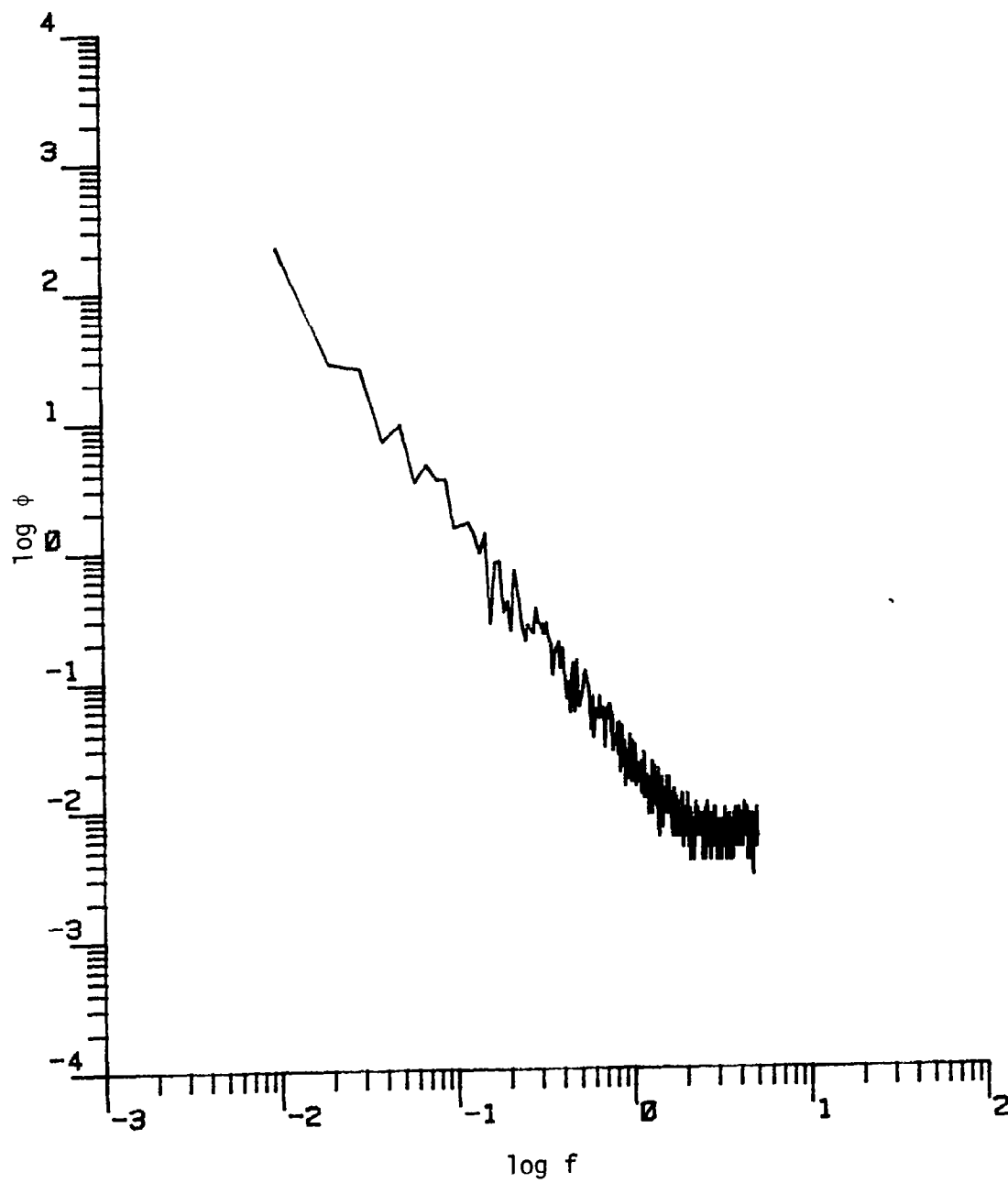Figure D.41.   The longitudinal power spectrum (Run #8624, T3L1, Component 1).

Figure D.42. The longitudinal power spectrum (Run #8624, T3L2, Component 1).
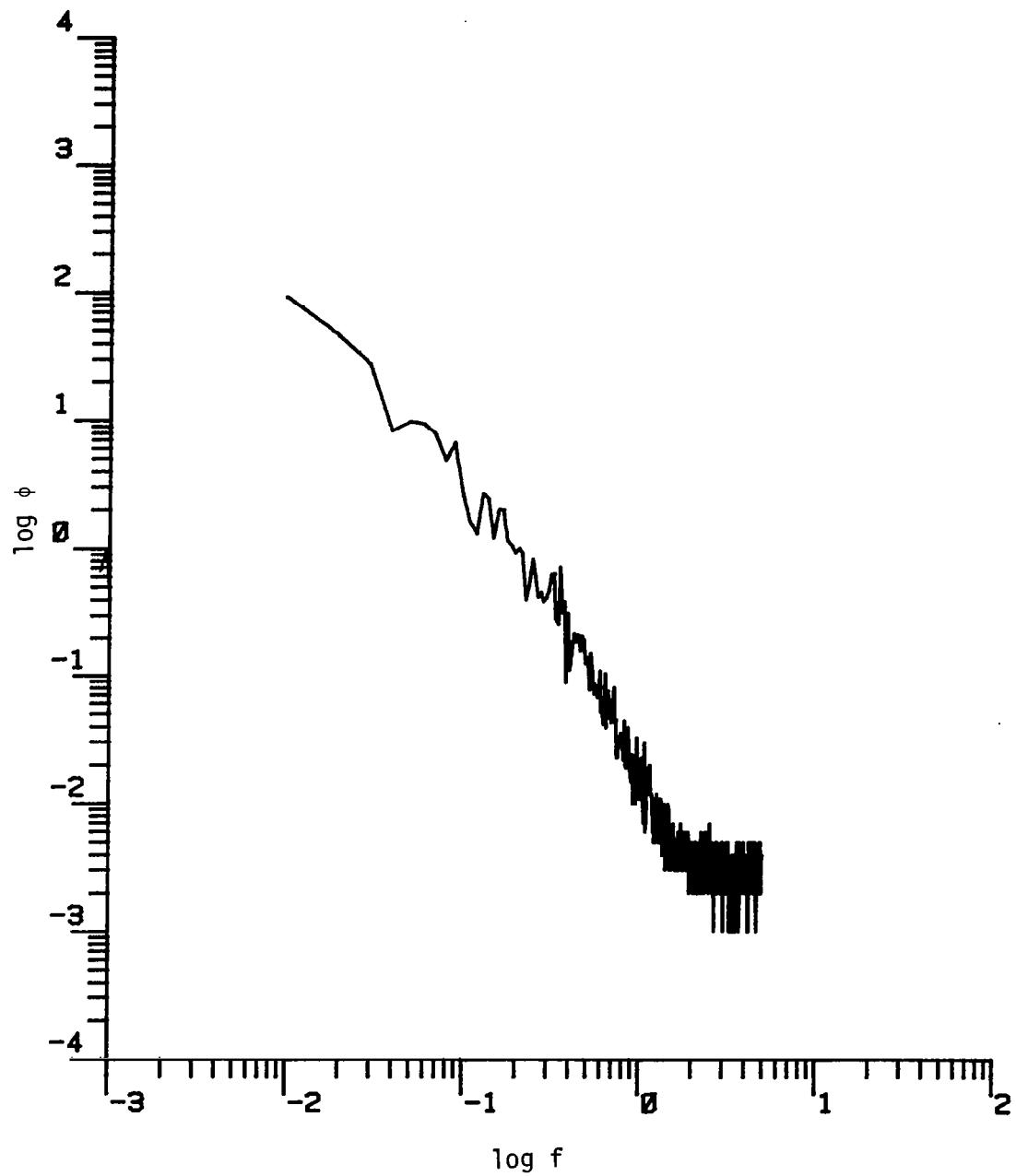
Figure D.43. The longitudinal power spectrum (Run #8624, T3L3,
Component 1).

329

Figure D.44. The longitudinal power spectrum (Run #8624, T3L4, Component 1).

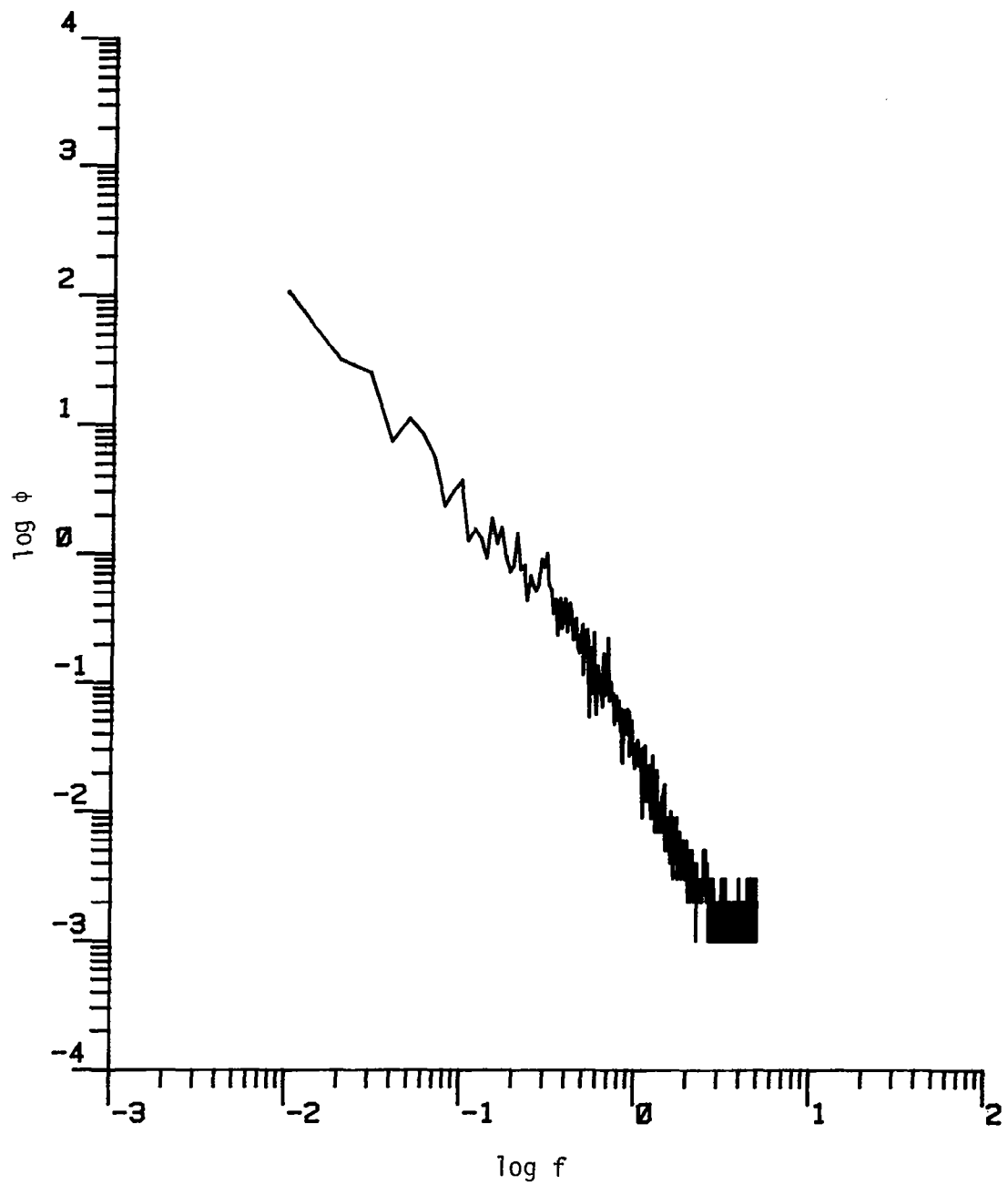Figure D.45. The longitudinal power spectrum (Run #8624, T4L1, Component 1).

Figure D.46. The longitudinal power spectrum (Run #8624, T4L2, Component 1).
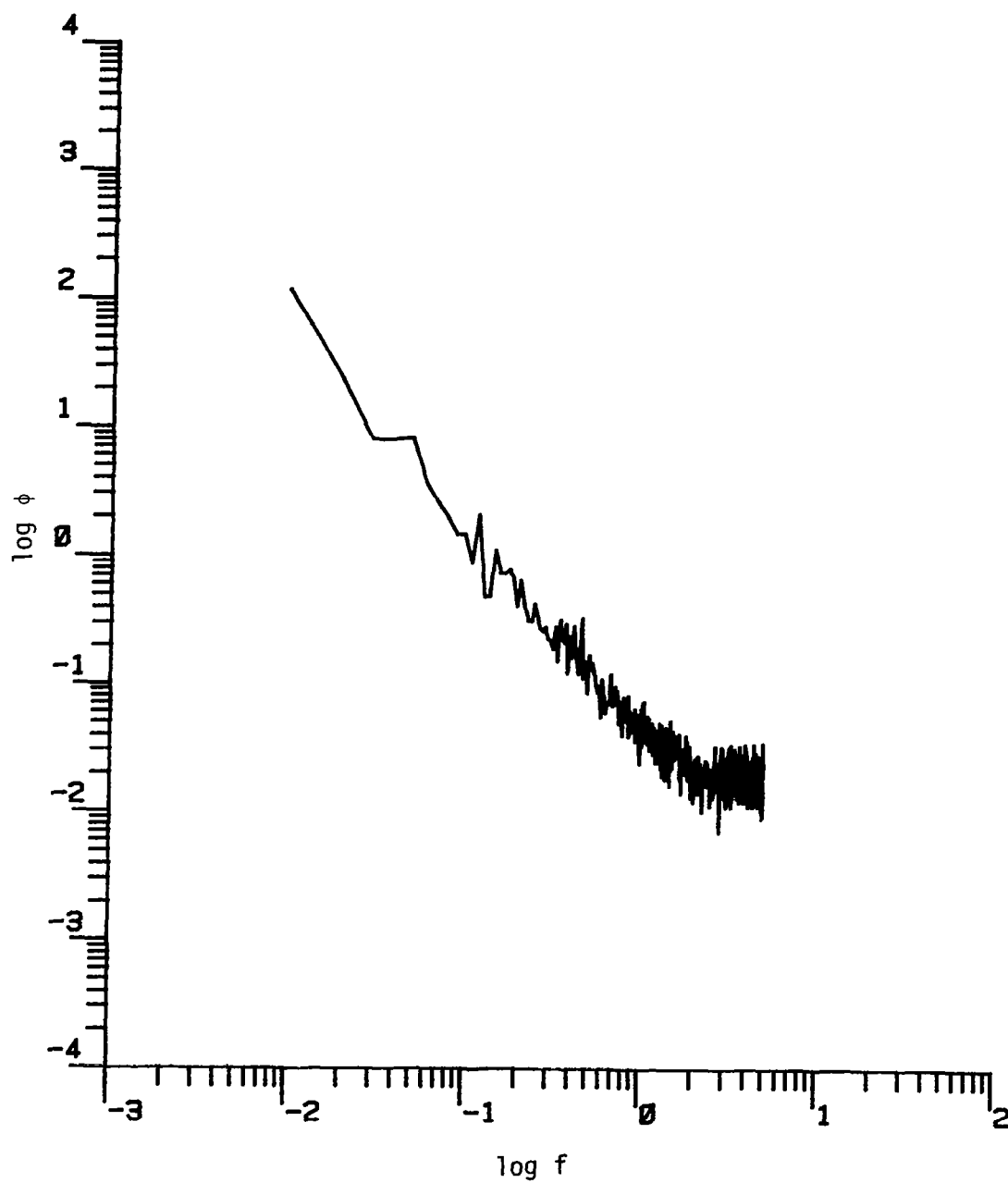
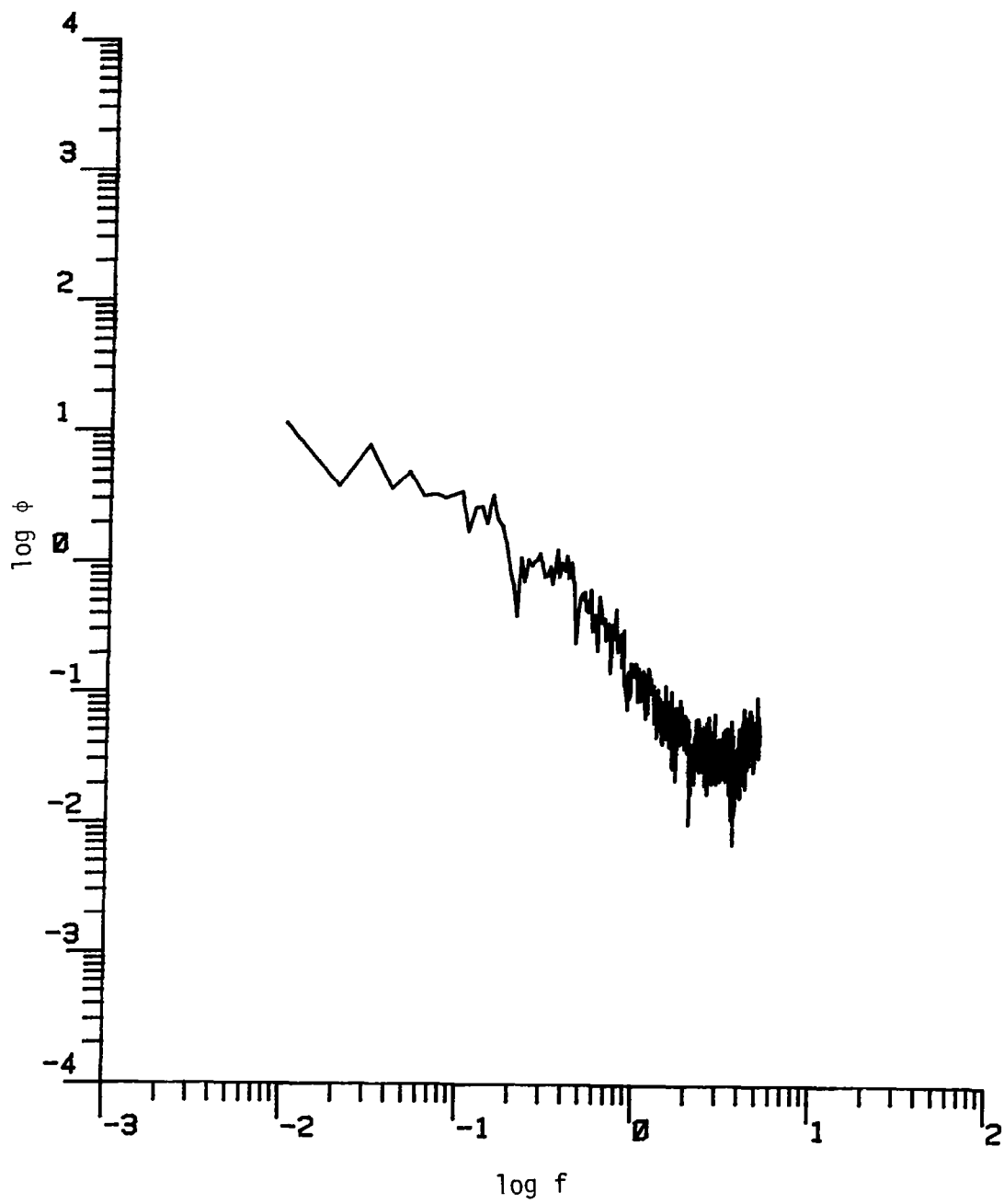Figure D.47. The longitudinal power spectrum (Run #8624, T4L3, Component 1).

Figure D.48. The longitudinal power spectrum (Run #8624, T4L4, Component 1).

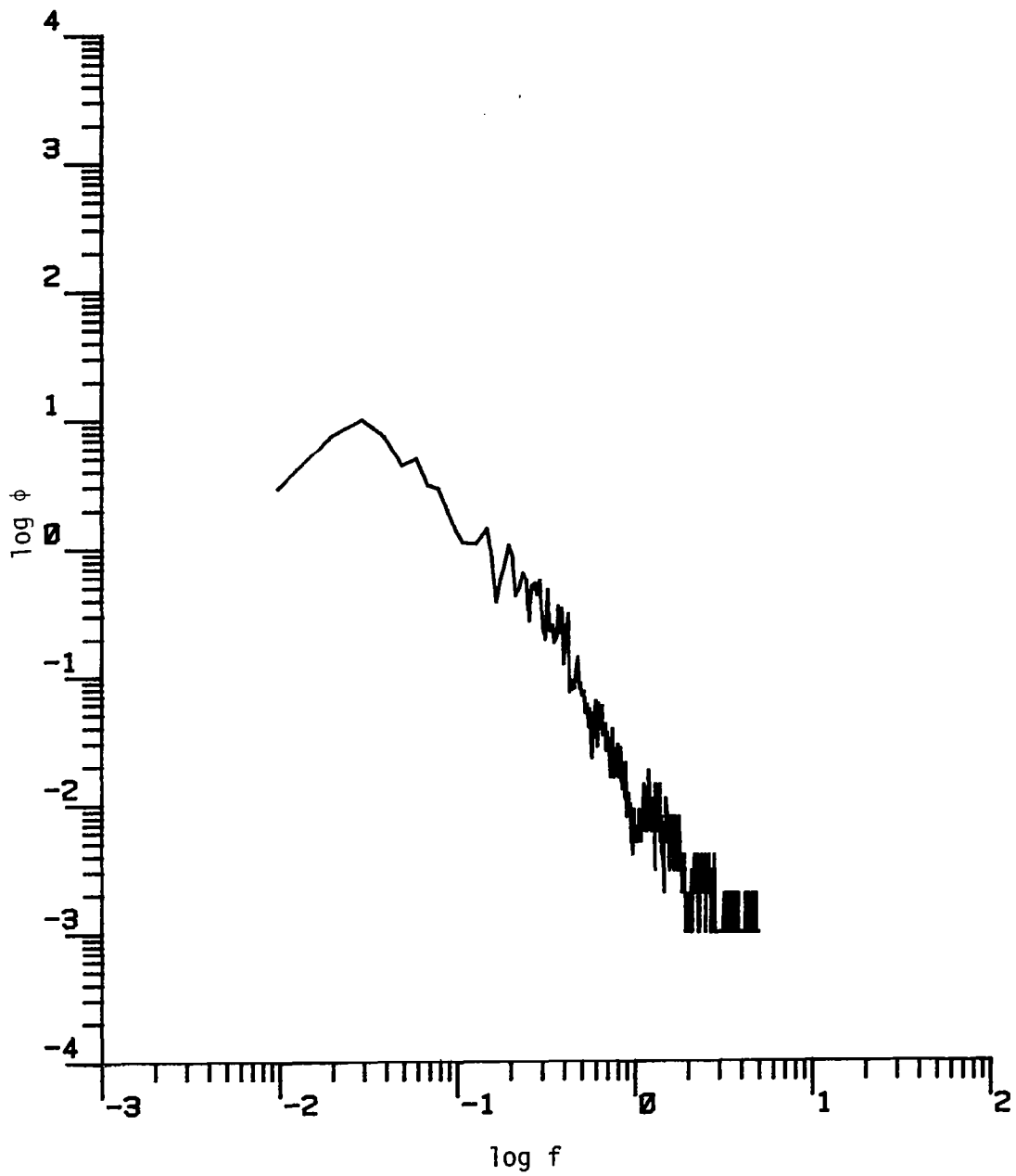Figure D.49.   The longitudinal power spectrum (Run #8624, T5L1, Component 1).

Figure D.50. The longitudinal power spectrum (Run #8624, T5L2, Component 1).

Figure D.51. The longitudinal power spectrum (Run #8624, T5L3, Component 1).

Figure D.52. The longitudinal power spectrum (Run #8624, T5L4, Component 1).

Figure D.53. The longitudinal power spectrum (Run #8624, S1L1, Component 1).

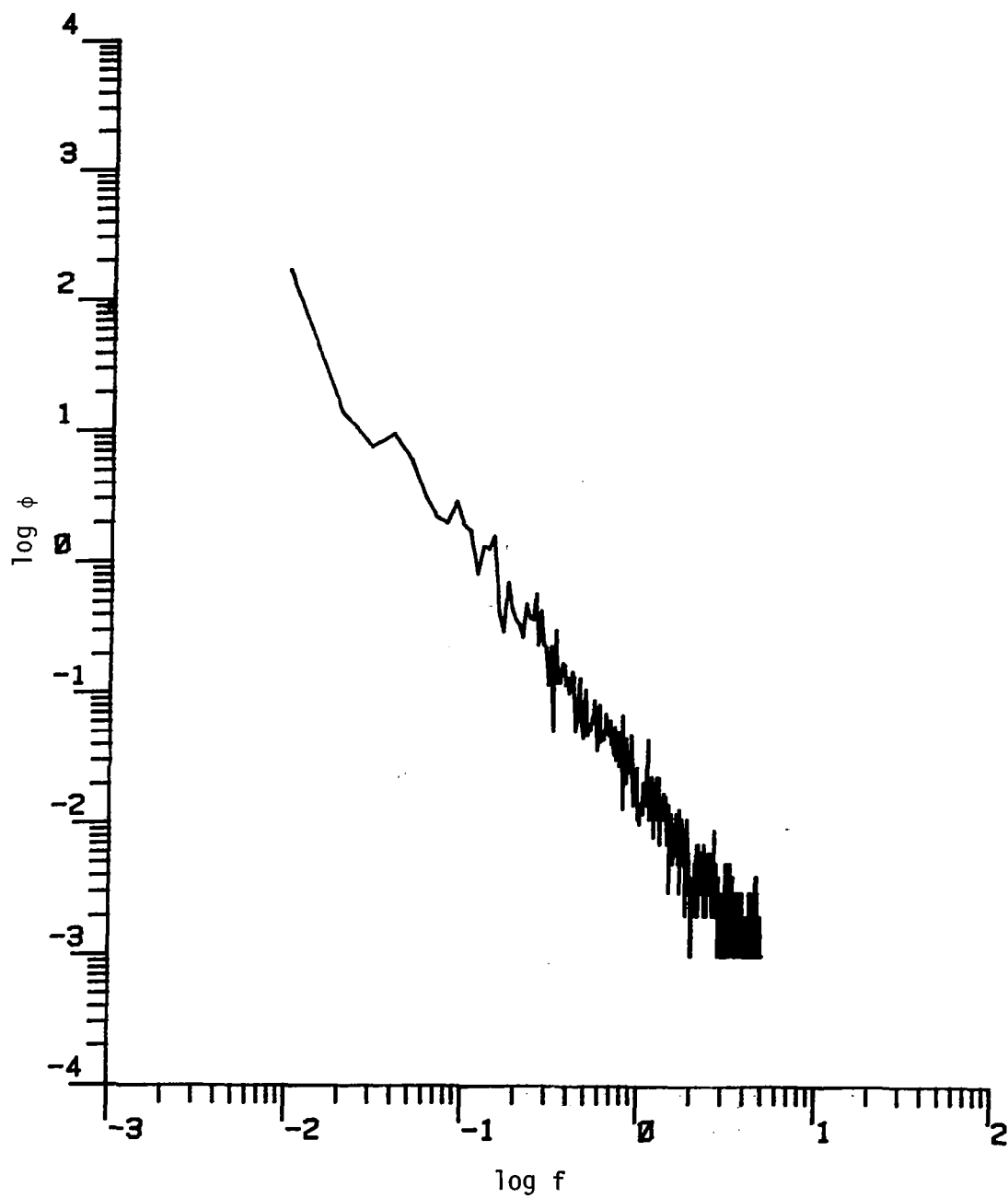Figure D.54. The longitudinal power spectrum (Run #8624, S1L2, Component 1).

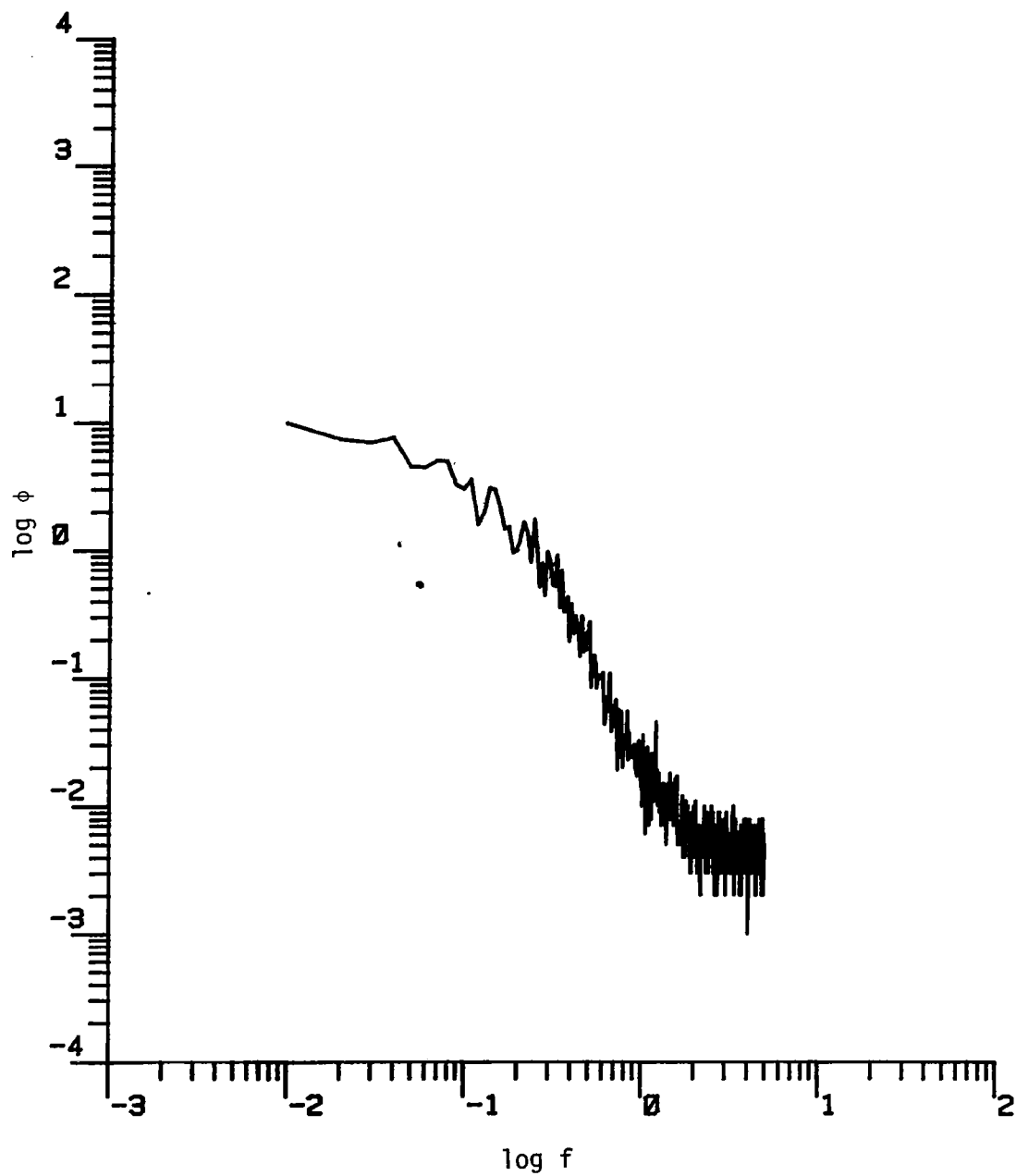Figure D.55. The longitudinal power spectrum (Run #8624, S1L3, Component 1).

Figure D.56.   The longitudinal power spectrum (Run #8624, S2L1, Component 1).
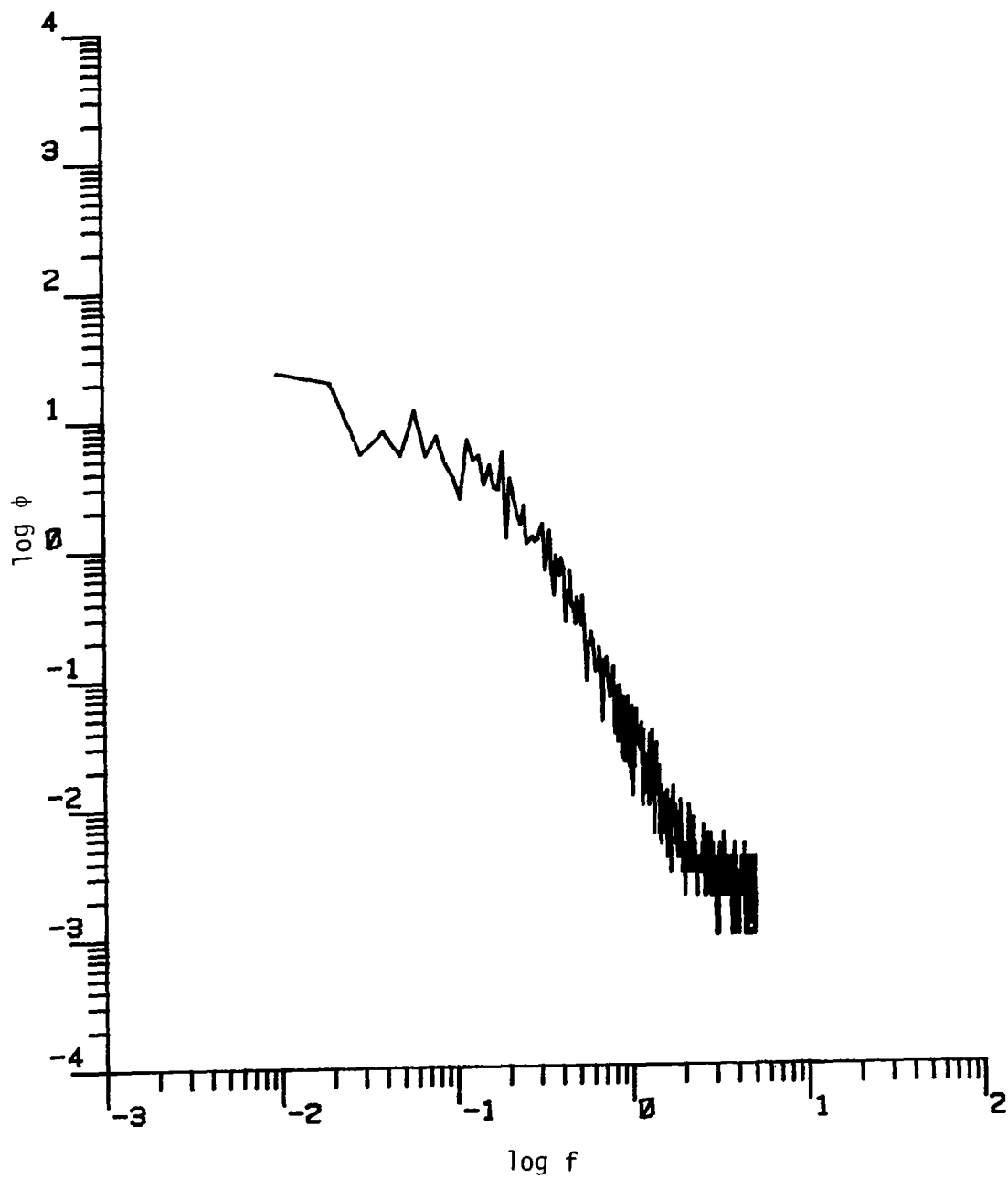
Figure D.57. The longitudinal power spectrum (Run #8624, S2L2, Component 1).

Figure D.58. The longitudinal power spectrum (Run #8624, S2L3,
Component 1).

Figure D.59. The longitudinal power spectrum (Run #8624, S3L1, Component 1).

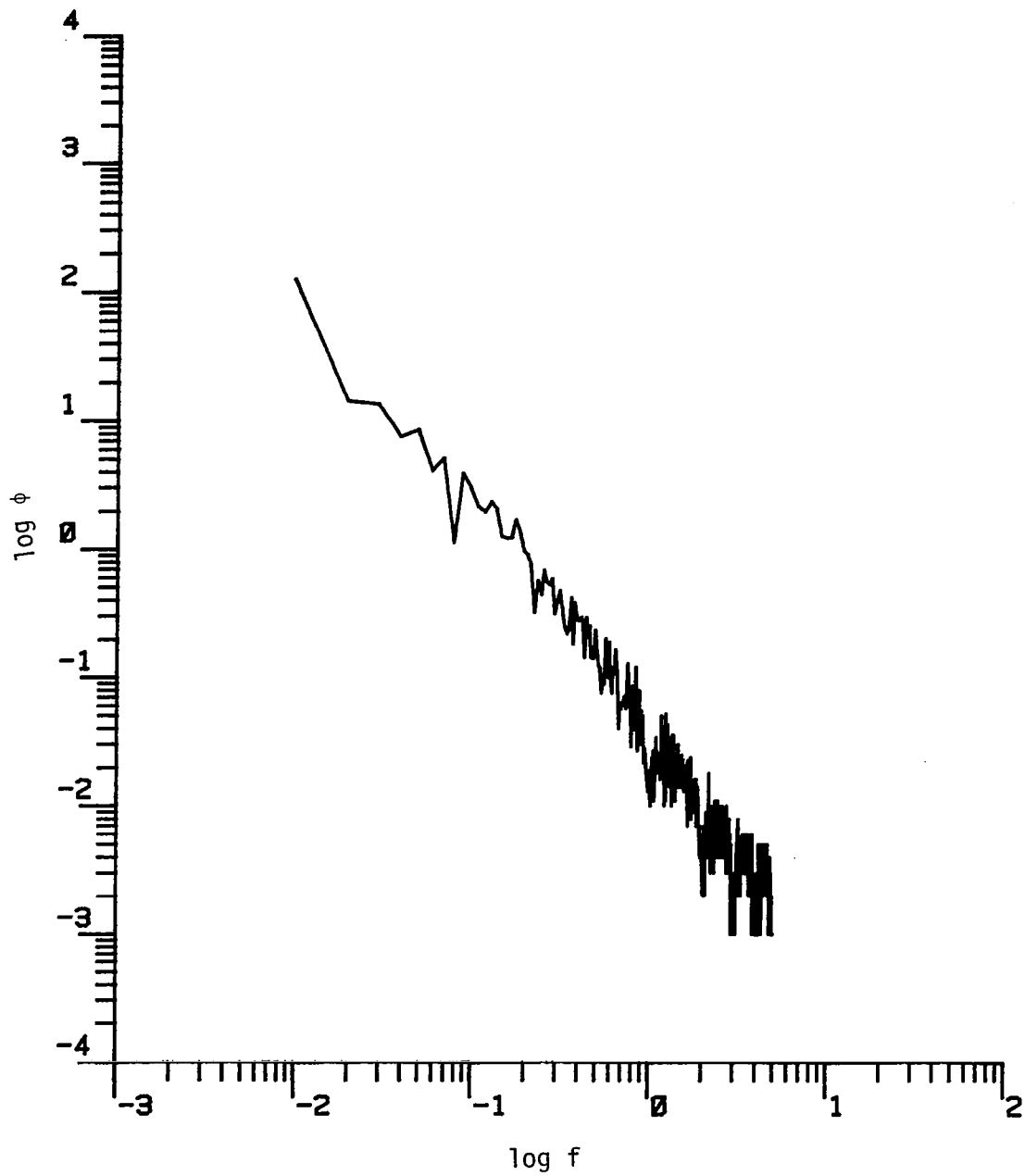Figure D.60. The longitudinal power spectrum (Run #8624, S3L2, Component 1).

Figure D.61.   The longitudinal power spectrum (Run #8624, S3L3, Component 1).
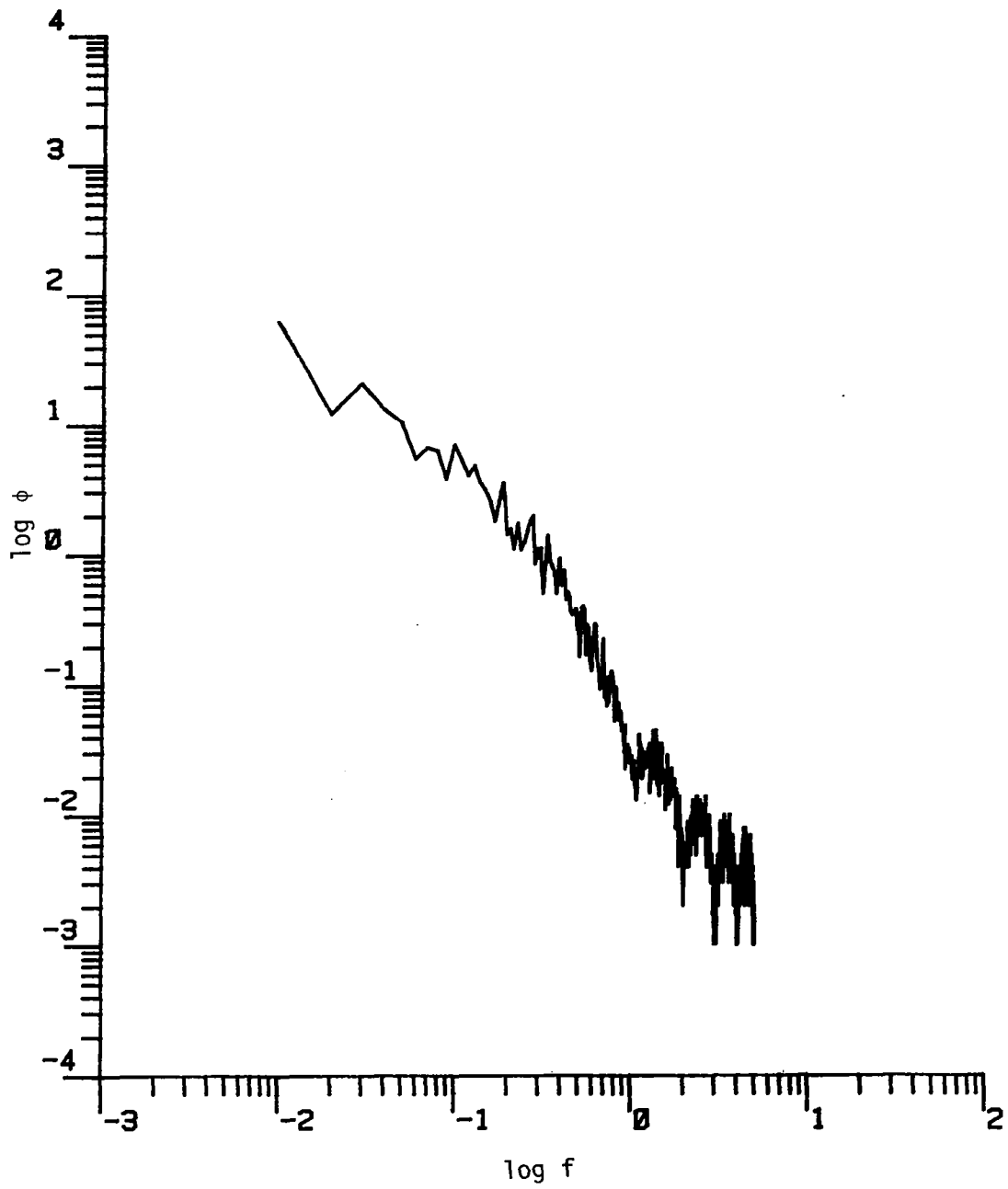
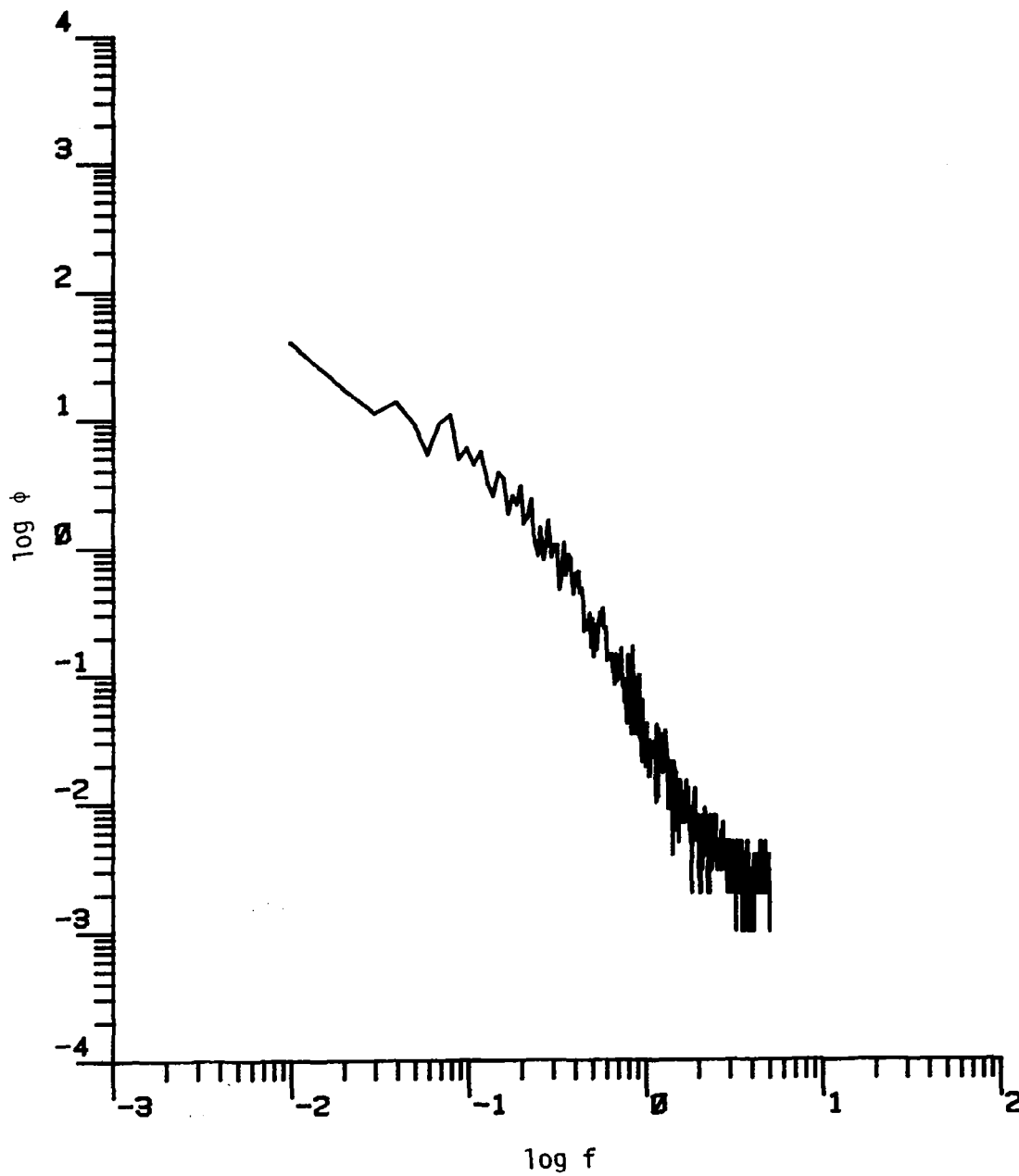Figure D.62.   The longitudinal power spectrum (Run #8624, S4L1, Component 1).

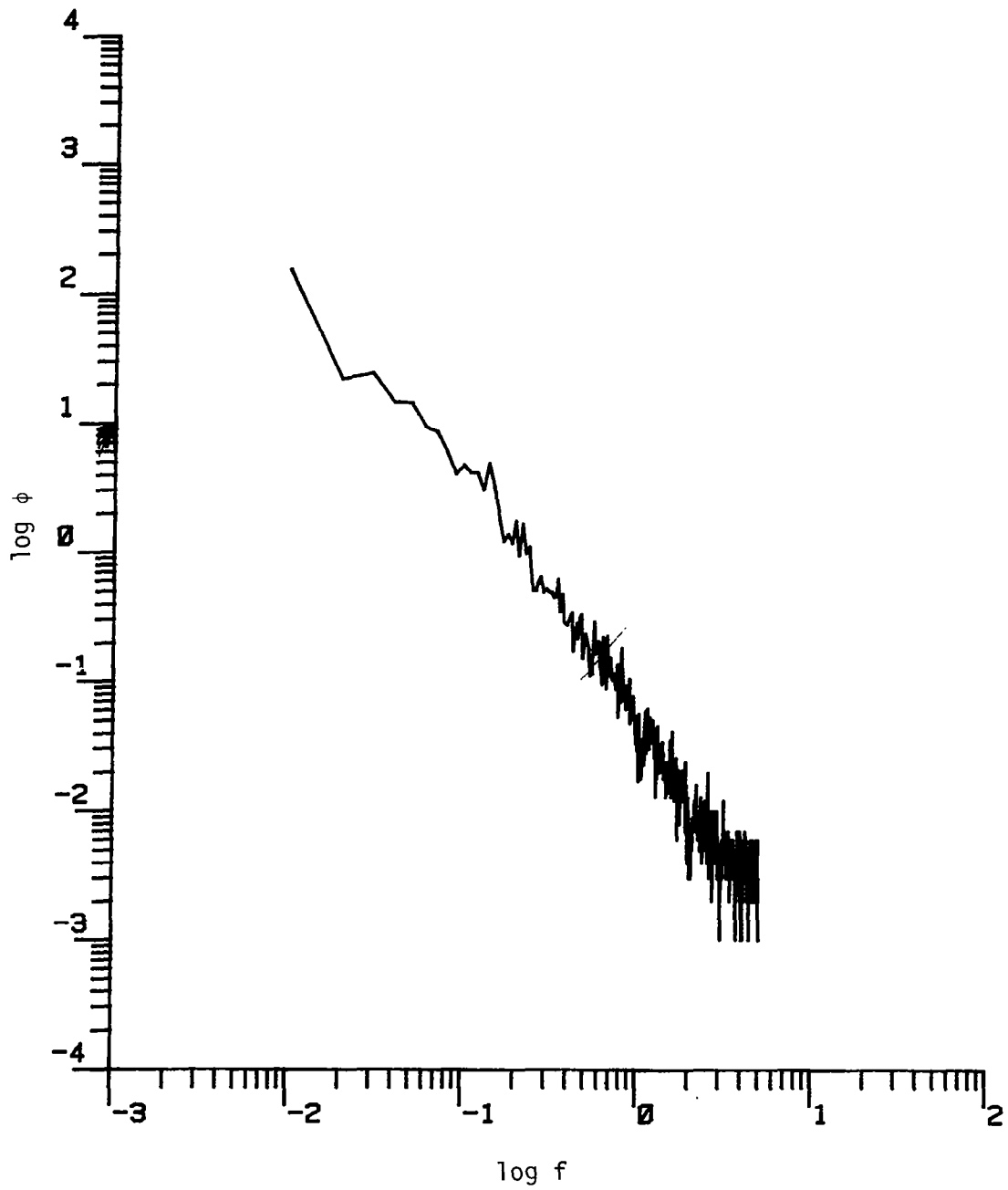Figure D.63.   The longitudinal power spectrum (Run #8624, S4L2, Component 1).

Figure D.64.   The longitudinal power spectrum (Run #8624, S4L3, Component 1).

APPENDIX E

VERTICAL VELOCITY CORRELATIONS

The two-point spatial correlation for the vertical component is presented in this appendix. The data represent the vertical correlation, i.e., correlation between velocities at different levels for a given tower.
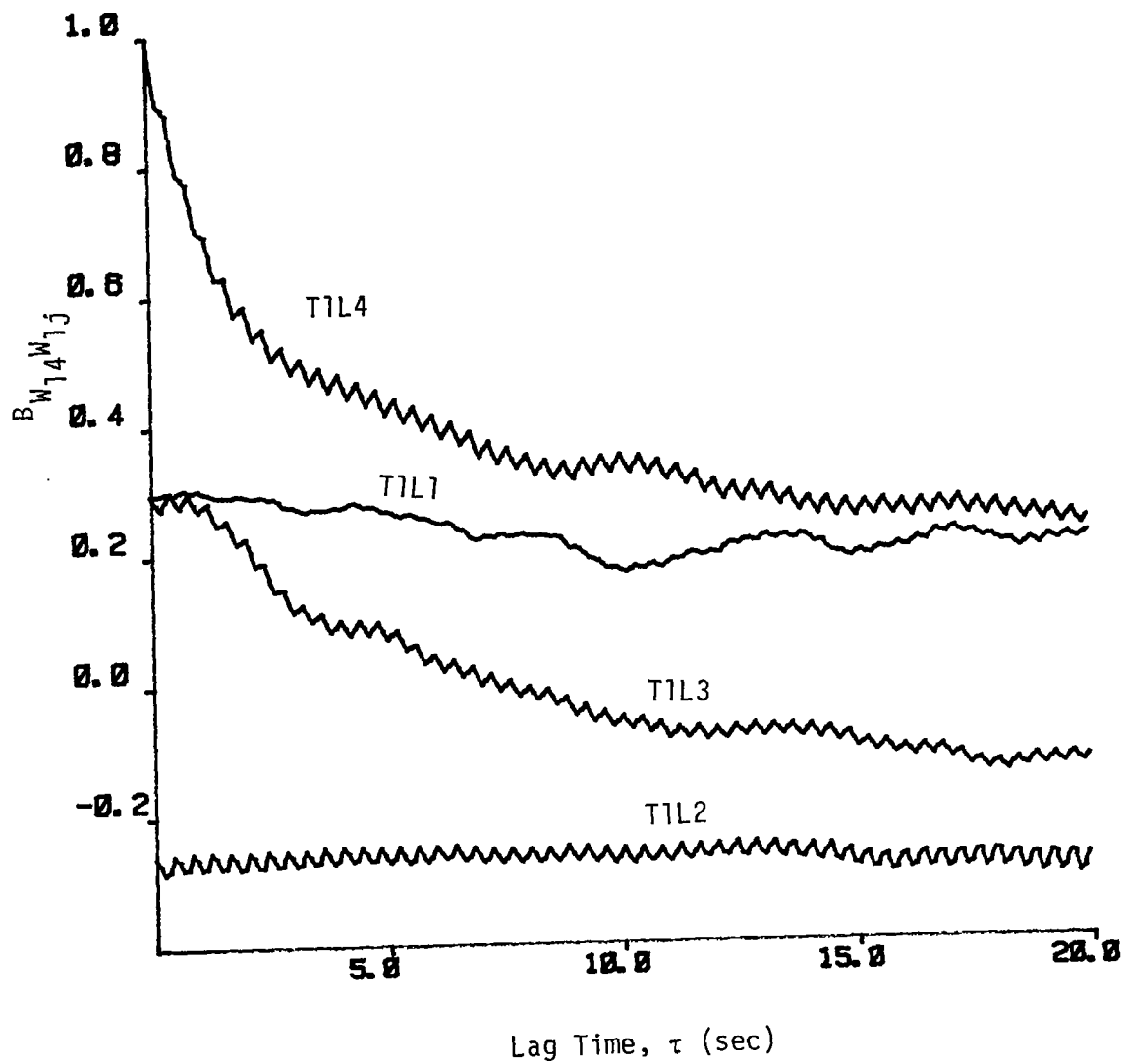
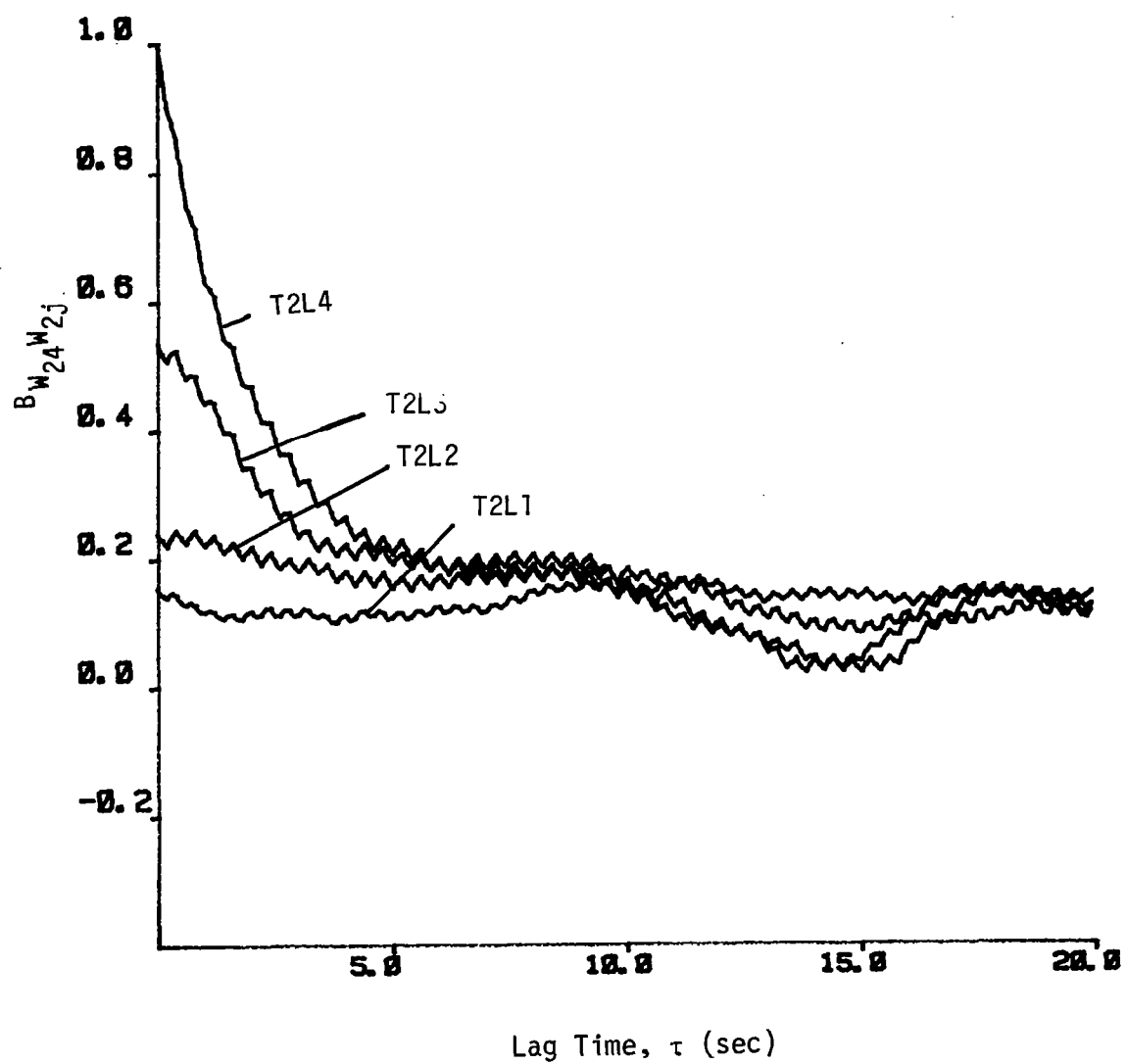Figure E.1. Two-point vertical space-time correlation relative to T1L4.

Figure E.2. Two-point vertical space-time correlation relative to
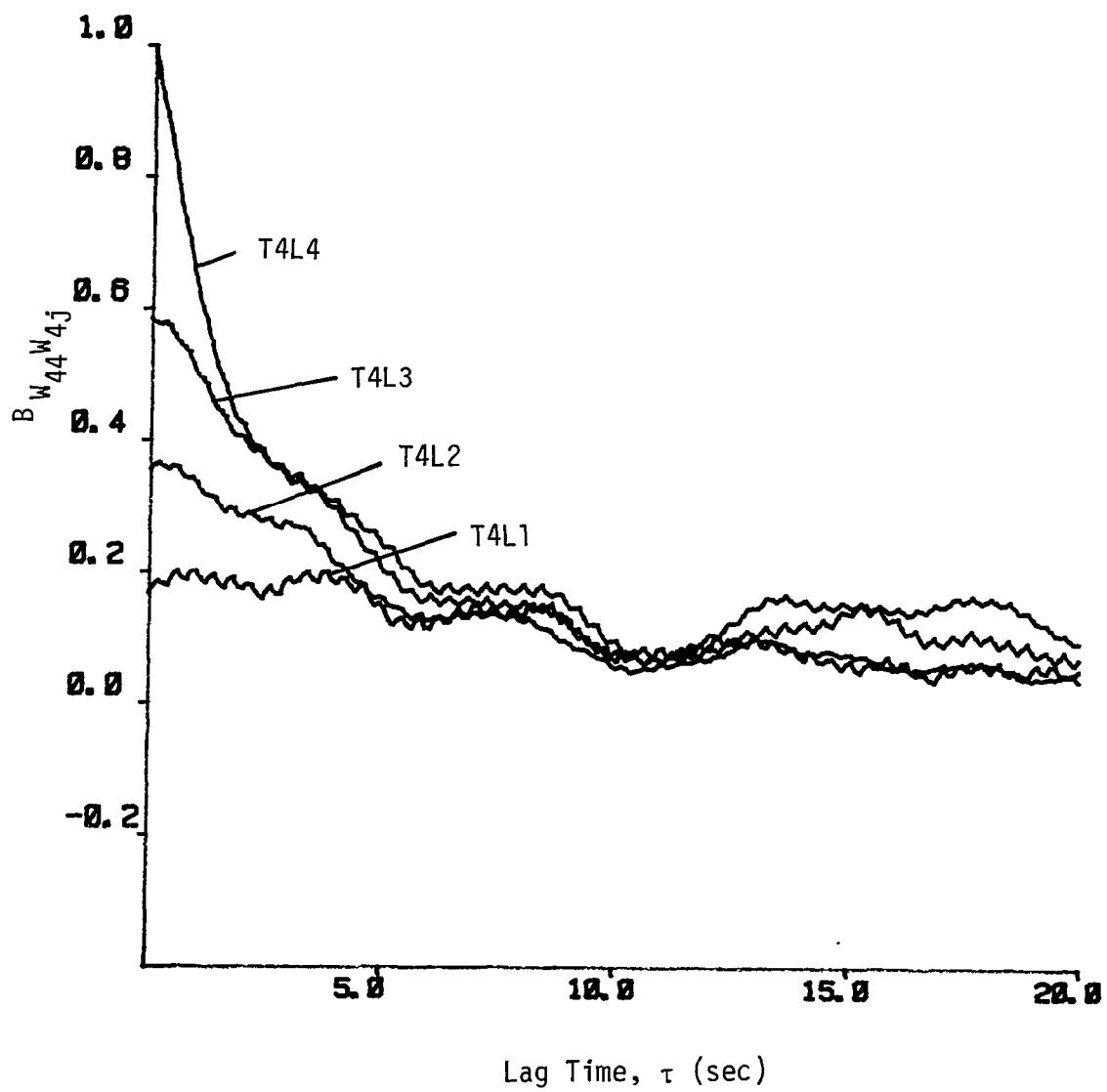   T2L4.

353

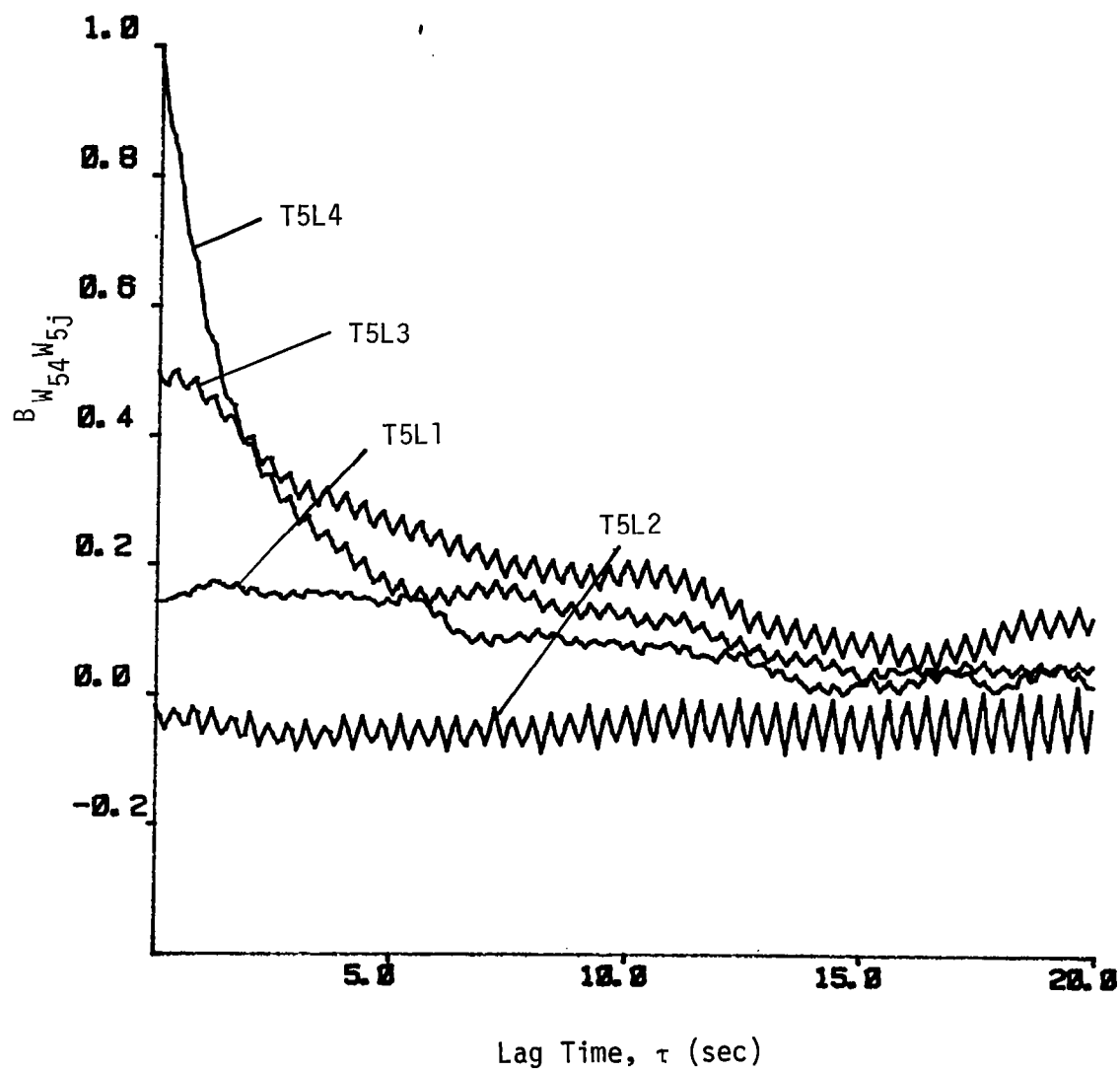Figure E.3. Two-point vertical space-time correlation relative to T4L4.

Figure E.4. Two-point vertical space-time correlation relative to T5L4.

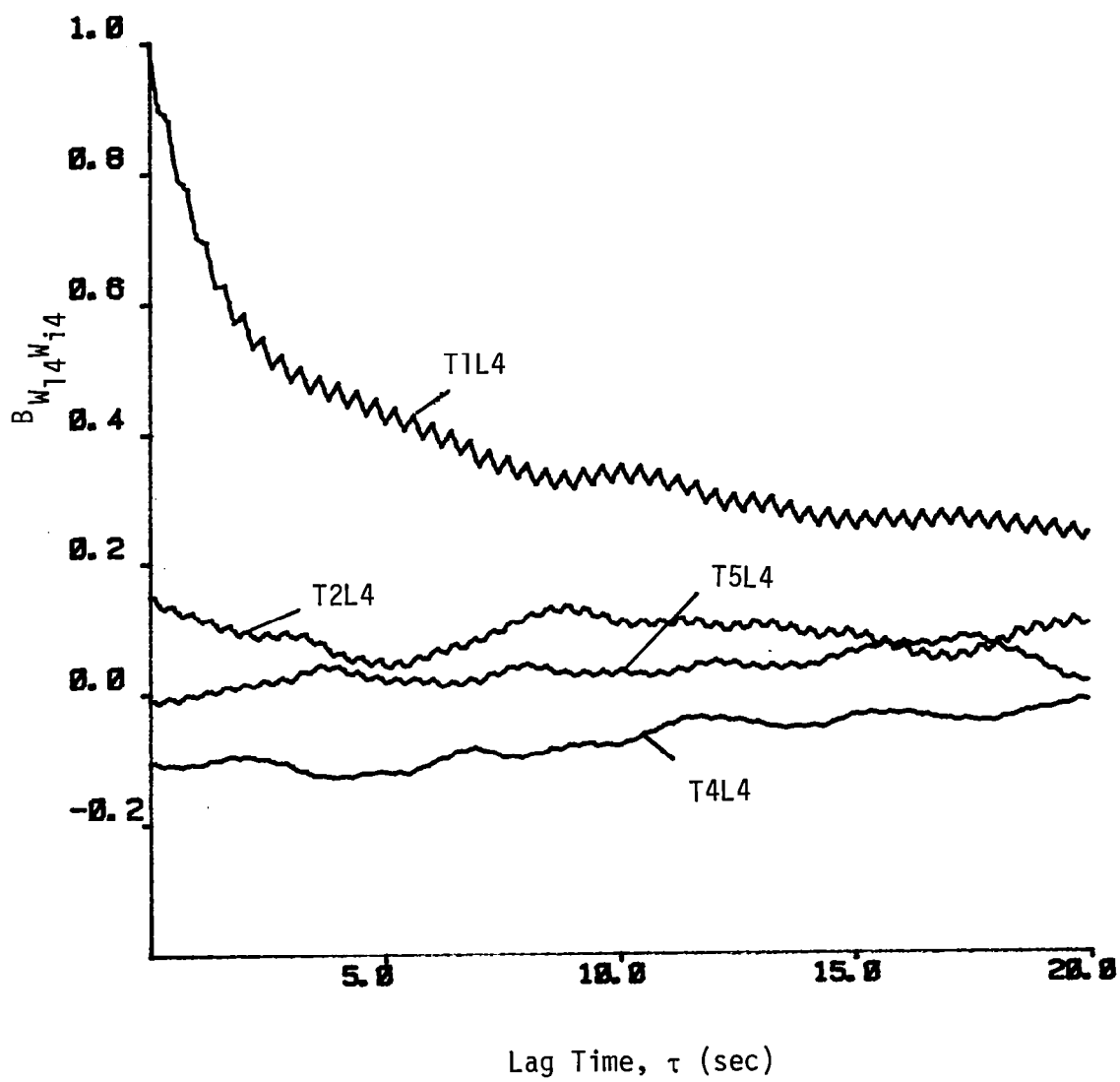Figure E.5. Two-point horizontal space-time correlation relative to T1L4.
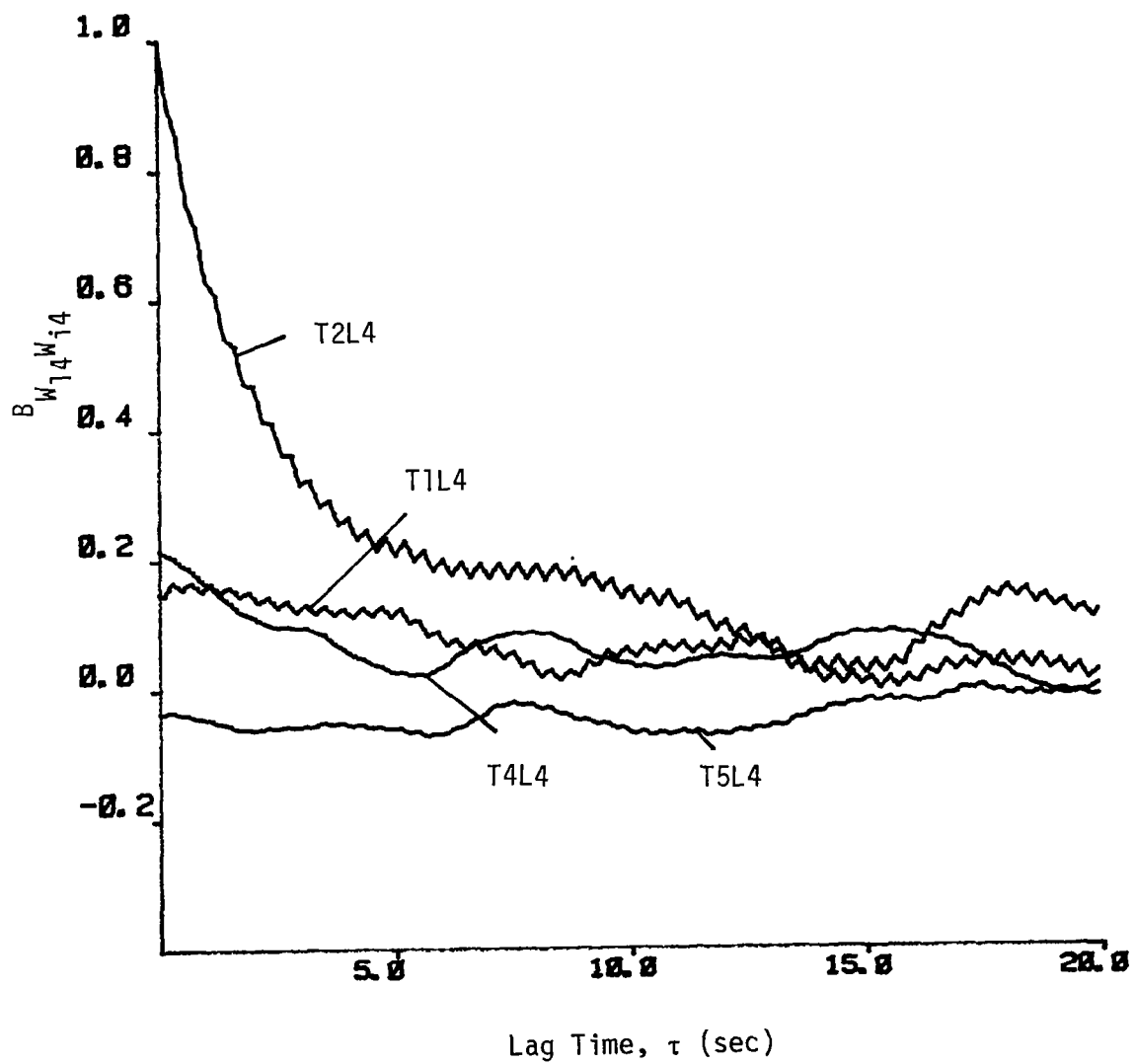
Figure E.6. Two-point horizontal space-time correlation relative to T2L4.
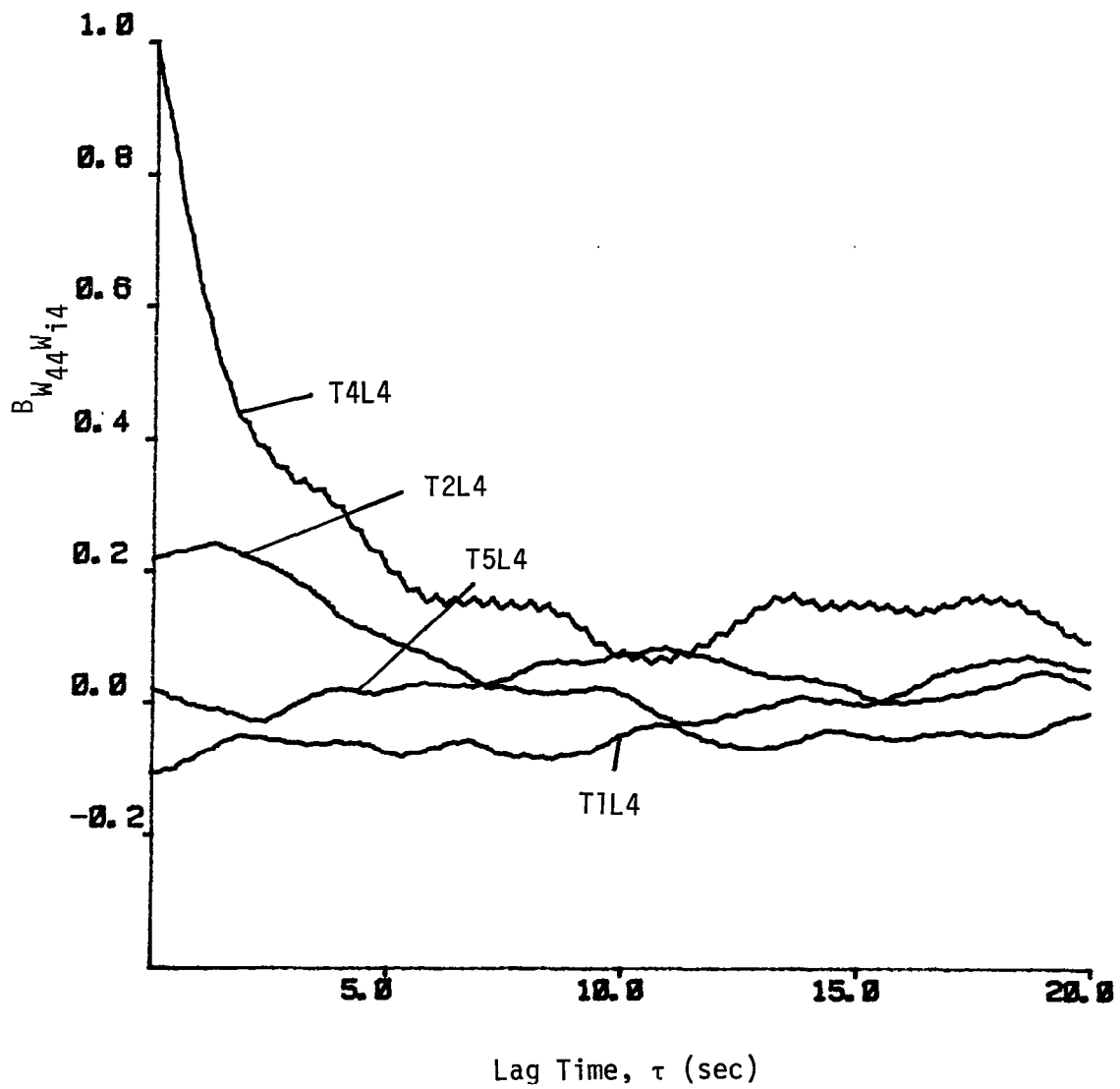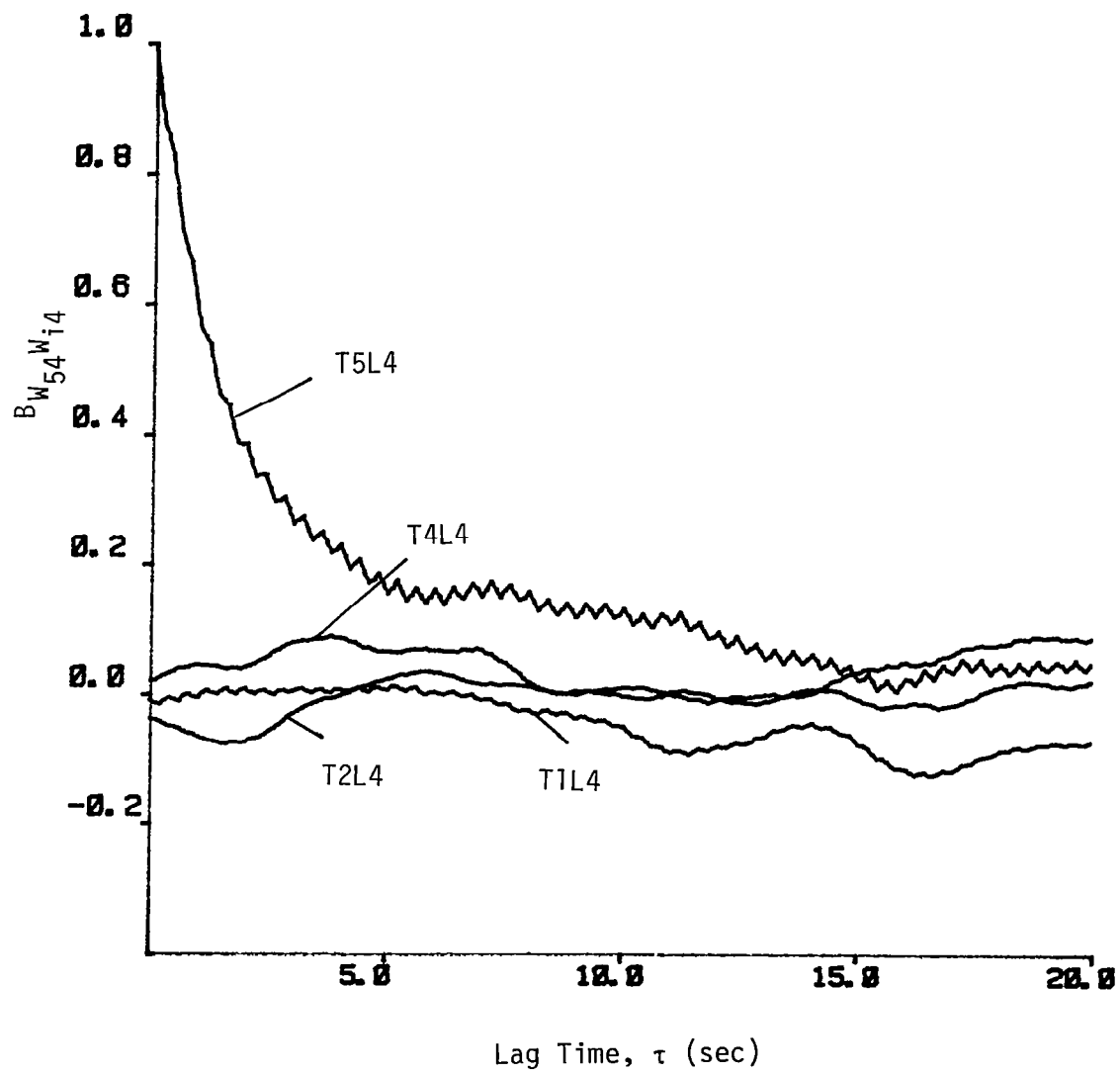
357

Figure E.7. Two-point horizontal space-time correlation relative to T4L4.

Figure E.8.   Two-point horizontal space-time correlation relative to T5L4.

1. REPORT NO. NASA CR-3737	2. GOVERNMENT ACCESSION NO.	3. RECIPIENT'S CATALOG NO.
4. TITLE AND SUBTITLE Statistical Analysis of Turbulence Data From the NASA Marshall Space Flight Center Atmospheric Boundary Layer Tower Array Facility		5. REPORT DATE November 1983
		6. PERFORMING ORGANIZATION CODE
7. AUTHOR(S) Walter Frost and Ming-Chang Lin		8. PERFORMING ORGANIZATION REPORT #
9. PERFORMING ORGANIZATION NAME AND ADDRESS University of Tennessee Space Institute Tullahoma, Tennessee 37388		10. WORK UNIT NO. M-423
		11. CONTRACT OR GRANT NO. NAS8-34627
		13. TYPE OF REPORT & PERIOD COVERED
12. SPONSORING AGENCY NAME AND ADDRESS National Aeronautics and Space Administration Washington, DC 20546		Contractor Report
		14. SPONSORING AGENCY CODE

15. SUPPLEMENTARY NOTES

Technical Monitor: Dennis W. Camp, Atmospheric Sciences Division, Systems Dynamics Laboratory, Marshall Space Flight Center, Alabama 35812

16. ABSTRACT

Statistical properties of atmospheric turbulence near the Earth's surface are presented. Emphasis is placed on the probability density distribution, two-point spatial correlation, length scale, and two-point and single-point spectrum.

Comparison of the data with isotropic homogeneous models is made. In general, agreement with the models is poor. For the design of aircraft during operations in the lower levels associated with approach, takeoff, and terrain following, it appears necessary to improve existing models or develop new nonisotropic turbulence models.

17. KEY WORDS Low-Level Flow Turbulence Turbulence Models Aviation Safety	18. DISTRIBUTION STATEMENT Unclassified - Unlimited Subject Category 47

19. SECURITY CLASSIF. (of this report) Unclassified	20. SECURITY CLASSIF. (of this page) Unclassified	21. NO. OF PAGES 386	22. PRICE A17

MSFC - Form 3292 (May 1969)